

DISSERTATION

TOWARDS ELUCIDATING PHOTOCHEMICAL REACTION PATHWAYS IN NICKEL  
CATALYZED CROSS COUPLING AND ORGANOCATALYZED BIRCH REDUCTION

Submitted by

Max Kudisch

Department of Chemistry

In partial fulfillment of the requirements

For the Degree of Doctor of Philosophy

Colorado State University

Fort Collins, Colorado

Fall 2021

Doctoral Committee:

Advisor: Garret Miyake

Richard Finke  
Jean Chung  
Brad Reisfeld

Copyright by Max Kudisch 2021

All Rights Reserved

## ABSTRACT

### TOWARDS ELUCIDATING PHOTOCHEMICAL REACTION PATHWAYS IN NICKEL CATALYZED CROSS COUPLING AND ORGANOCATALYZED BIRCH REDUCTION

Carbon-nitrogen (C—N) bond forming reactions to couple aryl halides with amines are essential for the discovery and production of medicinal compounds. The state-of-the-art method uses a precious metal palladium catalyst at high temperatures which poses sustainability concerns. Recently, a method was reported in which an iridium photocatalyst (PC) works in tandem with a nickel catalyst under blue light irradiation to achieve C—N bond formation at room temperature. Herein, it was discovered that the iridium PC could be omitted if 365 nm light is used, constituting a precious metal-free approach. This discovery suggests that a nickel-centered excited state can mediate C—N bond formation, raising the possibility of an energy transfer type pathway in dual catalytic systems. The nickel complexes formed were identified for the first time and mechanistic evidence was found that is consistent with energy transfer with both  $[\text{Ru}(\text{bpy})_3]^{2+}$  (bpy = 2,2'-bipyridine) and a phenoxazine PC. A series of  $[\text{NiBr}_2(\text{amine})_n]$  complexes were isolated, characterized, and detected in C—N coupling reaction mixtures. A theoretical framework for predicting energy transfer rate constant ratios based on Förster theory and UV-visible spectroscopy was developed. The phenoxazine PC was both predicted and found to exhibit faster energy transfer and enhanced reaction performance when compared with  $[\text{Ru}(\text{bpy})_3]^{2+}$ . In addition, a light-driven, organocatalyzed system for Birch reduction was developed. Historically, Birch reduction to reduce an arene to a 1,4-cyclohexadiene has been limited by the required use of alkali metals which are pyrophoric and can be explosive. Under violet light, a benzo[ghi]perylene imide PC was found to

reduce challenging arenes such as benzene, constituting the first visible light driven approach capable of this reactivity. Mechanistic studies were performed that are consistent with a catalytic cycle involving addition of  $\text{OH}^-$  to the PC to form an adduct,  $[\text{PC}-\text{OH}]^-$ . Photolysis of the adduct forms  $\text{OH}\cdot$  and the PC radical anion which subsequently undergoes photoionization, ejecting a solvated electron that reduces the substrate.

## ACKNOWLEDGEMENTS

### **General Acknowledgements**

I would like to thank my thesis committee – Prof. Garret Miyake, Prof. Richard Finke, Prof. Jean Chung, and Prof. Brad Reisfeld, for their support throughout my graduate studies. I would like to offer Garret my deepest thanks for mentoring me throughout my graduate journey, from the time I spent working in the group prior to graduate school to my final months wrapping up my research projects. Throughout these years of my life, Garret has helped me develop the skills needed to be a successful scientist. His input has been pivotal in terms of accomplishing my research goals as well as shaping my career trajectory as a chemist. I can't thank him enough for his support throughout this critical time in my life. Further, I would like to thank Prof. Finke for his advice and thoughtful discussions regarding my mechanistic work, especially early on in my graduate career. The joint group meetings between the Finke and Miyake groups were immensely helpful in preparing for my candidacy exams.

I would also like to thank all the graduate students and postdoctoral researchers who were or are currently part of the Miyake group as they have provided countless hours of useful discussion and advice related to my research and life in general. Overall, these talented chemists and my collaborators have made my graduate studies both enjoyable and successful. I would especially like to thank those who have mentored me in various capacities. Firstly, I would not have gotten where I am today without the insightful guidance of Dr. Chern-Hooi Lim. Thank you Chern for teaching me the skills needed to gain independence in my research through learning to ask the right questions. In addition, thank you for teaching me about quantum chemistry – learning to do computational investigations has changed the way I think about chemistry.

I would also like to thank my colleagues I have collaborated with in my graduate research: Prof. Niels Damrauer, Yisrael Lattke, Nicholas Pompetti, Dr. Dmitry Zubarev, Dr. Justin Cole, Dr. Dianfeng Chen, Dr. Bin Liu, Dr. Ryan Pearson, Alex Green, Simone Bernsten, Cameron Chrisman, Prof. Pall Thordarson, Dr. Jeffrey Johannes, and Dr. Randolph Escobar. Your dedication, knowledge, and expertise have made work possible that is far beyond what I could have achieved on my own.

In addition, I would like to thank the staff of the CSU Materials and Molecular Analysis center for their help in instrument trainings. In particular, I would like to thank Dr. Brian Newell for teaching me the challenging technique of single crystal x-ray diffraction well enough that I have become mostly self-sufficient.

Finally, I would like to thank my family: Marc, Pearl, Steph, and my partner, Ariel – my success in graduate school would not have been possible without your love and support.

### **Acknowledgements of Co-author Contributions and Funding Agencies**

**Chapter 2:** This dissertation chapter includes a published article: Lim, C.-H.; Kudisch, M.; Liu, B.; Miyake, G. M., C–N Cross-Coupling via Photoexcitation of Nickel–Amine Complexes. *Journal of the American Chemical Society* 2018, 140 (24), 7667-7673. M. K. and C.-H. L. conceived of the project. M. K. performed the initial experiment in which the method was discovered, followed by initial reaction optimization and photoreactor development. Using the new photoreactor, C.-H. L. performed experiments to optimize the reaction, explore the substrate scope, and measure the kinetic isotope effect. C.-H. L. performed density functional theory calculations and wrote the manuscript. B. L. performed experiments to synthesize flibanserin and derivatives. M.K. performed UV-visible and emission spectroscopic experiments and wrote the relevant sections of the SI. Research reported in this chapter was supported by Colorado State

University and by the National Institute of General Medical Sciences (Award Number R35GM119702) of the National Institutes of Health. C.-H. L. was supported by an NIH F32 Postdoctoral Fellowship (F32GM122392). We acknowledge the use of computational resources provided by the XSEDE - Comet supercomputer (NSF ACI-1053575).

**Chapter 3:** This dissertation chapter includes a published article: Kudisch, M.; Lim, C.-H.; Thordarson, P.; Miyake, G. M., Energy Transfer to Ni-Amine Complexes in Dual Catalytic, Light-Driven C–N Cross-Coupling Reactions. *Journal of the American Chemical Society* 2019, 141 (49), 19479-19486. M. K. performed all experiments and wrote the manuscript. P. T. analyzed the titration data, performed the global fitting and statistical analysis, and aided in writing the discussion of that data. C.-H. L. contributed intellectually through mentorship of M. K. This work was supported by Colorado State University, the NIH (R35GM119702), and the Alfred P. Sloan Foundation. P.T. would like to thank the ARC for support (CE140100036 and DP190101892).

**Chapter 5:** This dissertation chapter includes a published article: Cole, J. P.; Chen, D.-F.; Kudisch, M.; Pearson, R. M.; Lim, C.-H.; Miyake, G. M., Organocatalyzed Birch Reduction Driven by Visible Light. *Journal of the American Chemical Society* 2020, 142 (31), 13573-13581. R. M. P. discovered and synthesized the first benzo[ghi]perylene imides. J. P. C. and D.-F. C. performed optimization and substrate scope experiments. M. K. performed mechanistic experiments and wrote the mechanistic discussion in the manuscript. J. P. C., D.-F. C., and G. M. M. wrote the other sections of the manuscript. C.-H. L. performed the density functional theory calculations and modeling of EPR data. This work was supported by Colorado State University and the National Institutes of Health under Award Number R35GM119702. The content is solely the responsibility of the authors and does not necessarily represent the official views of the

National Institutes of Health. This work used the Extreme Science and Engineering Discovery Environment (XSEDE), which is supported by National Science Foundation Grant ACI-1548562.



## DEDICATION

This dissertation is dedicated to my family and colleagues.

## TABLE OF CONTENTS

ABSTRACT.....	ii
ACKNOWLEDGEMENTS.....	iv
DEDICATION.....	viii
PART 1 – LIGHT-DRIVEN, NICKEL-CATALYZED CROSS COUPLING REACTIONS.....	xi
CHAPTER 1   INTRODUCTION TO PART 1.....	1
THESIS STRUCTURE.....	1
MOTIVATIONS.....	2
REFERENCES.....	11
CHAPTER 2   C–N CROSS COUPLING VIA PHOTOEXCITATION OF NICKEL–AMINE COMPLEXES.....	13
OVERVIEW.....	13
INTRODUCTION.....	13
RESULTS AND DISCUSSION.....	16
CONCLUSION.....	27
EXPERIMENTAL 1: SUPPLEMENTARY INFORMATION FOR CHAPTER 2.....	29
REFERENCES.....	136
CHAPTER 3   ENERGY TRANSFER TO NI-AMINE COMPLEXES IN DUAL CATALYTIC, LIGHT-DRIVEN C–N CROSS COUPLING REACTIONS.....	140
OVERVIEW.....	140
INTRODUCTION.....	140
RESULTS AND DISCUSSION.....	143
CONCLUSION.....	157
EXPERIMENTAL 2: SUPPLEMENTARY INFORMATION FOR CHAPTER 3.....	159
REFERENCES.....	257
PART 2: ORGANOCATALYZED BIRCH REDUCTION DRIVEN BY VISIBLE LIGHT.....	260
CHAPTER 4   INTRODUCTION TO PART 2.....	261
REFERENCES.....	266
CHAPTER 5   ORGANOCATALYZED BIRCH REDUCTION DRIVEN BY VISIBLE LIGHT.....	268
OVERVIEW.....	268
INTRODUCTION.....	268
RESULTS AND DISCUSSION.....	271
CONCLUSION.....	282

EXPERIMENTAL 3 — SUPPLEMENTARY INFORMATION FOR CHAPTER 5.....	284
REFERENCES .....	435
CHAPTER 6   SUMMARY AND CONCLUSIONS .....	438
REFERENCES .....	442

## PART 1 – LIGHT-DRIVEN, NICKEL-CATALYZED CROSS COUPLING REACTIONS

## CHAPTER 1 | INTRODUCTION TO PART 1

### THESIS STRUCTURE

This thesis consists of 2 main parts, beginning with Part 1 which focuses on the development and mechanistic studies of light-driven, nickel-catalyzed cross coupling reactions. A general introduction to the field of research will be followed by Chapters 2 and 3 which are modeled off of published research articles. Additional work is also ongoing in this area involving a collaborative mechanistic study with researchers at AstraZeneca which will be published in due course upon its completion. Part 2 introduces light-driven, organocatalyzed Birch reductions as a new class of multi-photon excitation reactions. Chapter 4 introduces the field and motivations underpinning this work. Chapter 5 is modelled off of a published research article on the development and initial mechanistic study of the light-driven Birch reduction reaction. A more in-depth and collaborative mechanistic study of this system is currently ongoing, involving a 5-part team that includes the Damrauer Group (CU Boulder) and industrial collaborators New Iridium, IBM, and Merck; the findings from this work will be reported in due course. I have also done other work during my graduate career that will not be discussed in this thesis – some of these projects will be taken over by younger graduate students and will be reported in future publications. Briefly, one such project involves synthesis and polymerization of a new class of cyclic polysiloxanes. The other major project involves the development of multi-photon absorption reactions involving phenoxazine catalysts.

The topics covered in this thesis are presented in five chapters with the following titles:

1. INTRODUCTION TO PART 1
2. C–N CROSS-COUPLING VIA PHOTOEXCITATION OF NI-AMINE COMPLEXES

3. ENERGY TRANSFER TO NI-AMINE COMPLEXES IN DUAL CATALYTIC, LIGHT-DRIVEN C–N CROSS-COUPLING REACTIONS
4. INTRODUCTION TO PART 2
5. ORGANOCATALYZED BIRCH REDUCTION DRIVEN BY VISIBLE LIGHT

## MOTIVATIONS

In the last decade, the use of photochemistry in organic synthesis to discover and enable new reaction methodologies has skyrocketed. The use of light to provide driving force in a chemical reaction has distinct advantages over heat-driven methods in terms of selectivity in the activation of specific catalysts or reagents (i.e., those capable of absorbing the wavelengths of light applied) and the propensity of photoexcited states of molecules to engage in radical chemistry. Mechanistic reaction pathways involving radicals can in many cases lead to novel reactivity that could not be achieved with heat under the same conditions, and there are now multiple examples where this advantage has been explicitly shown.<sup>1-2</sup> Furthermore, light represents a clean and renewable primary source of energy, whereas traditional heat-driven methods require a heat source that may not be renewable and necessarily involves efficiency losses due to transduction of energy to produce the heat. Overall, the chemical industry consumes ~10% of the global final energy which is obtained primarily from fossil fuels – 42% of which is utilized to drive chemical processes.<sup>3</sup> This reliance on fossil fuels as the energy source to provide heating in large scale industrial reactions is unsustainable, motivating the development of more environmentally friendly reaction methods.

Ultimately, large scale solar chemical synthesis would both solve this problem and avoid transduction losses, although the intermittency of solar irradiation presents a significant engineering challenge and limitation.<sup>4</sup> On a smaller scale the issue of intermittency can be

circumvented through the use of electrically-powered light sources such as light emitting diodes (LEDs), incandescent bulbs, compressed gas arc lamps, or lasers that can provide constant and precisely controlled irradiation. However, the use of electronic lighting involves two energy conversion steps, first from the primary energy source to generate electricity (e.g., wind, solar, etc.) and second from the conversion of electricity to light (i.e. electroluminescent device efficiency).

For academic scale research into novel photoreactions, electronic lighting is primarily used due to the simplicity of experimentation, although sometimes direct solar photochemistry is also done as a proof-of-concept (e.g., in light-driven, organocatalyzed atom transfer radical polymerization).<sup>5</sup> Recent improvements in LED technology have led to the rise of LEDs as the preferred light source for organic photochemistry largely due to their narrow emission spectra, efficiency, and availability over a wide range of output wavelengths spanning the ultraviolet to near infrared electromagnetic spectral regions. The narrow emission of LEDs enables selective excitation of single photocatalyst (PC) species in a mixture of light absorbing compounds, whereas the use of wavelength selective filters would be required with an incandescent bulb or arc lamp that produces a broad emission output.<sup>4</sup> This selectivity is often desirable as the excitation of substrates can lead to side reactivity, limiting the utility of the reaction being developed.

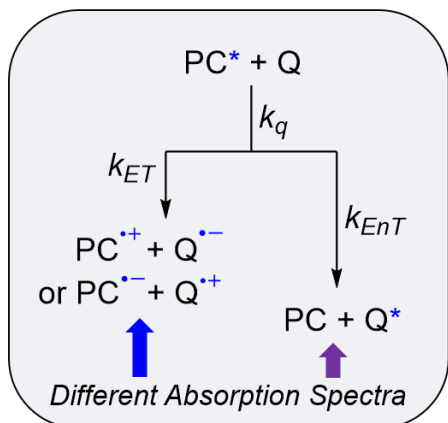
Early work in the field – often termed photoredox catalysis – largely utilized PCs based on the precious metals ruthenium and iridium to mediate a wide range of organic reactions which have been reviewed comprehensively.<sup>6-9</sup> However, the term “photoredox catalysis” contains within it an inherent mechanistic claim. Specifically, the term refers to catalysis involving photoinduced electron transfer (PET) as part of the catalytic cycle. However, many works which are commonly considered part of the field of photoredox catalysis have not been studied in

sufficient mechanistic detail to determine whether they do or do not, in fact, involve a PET step. For that reason, the term “photocatalysis” which is mechanistically neutral will be used throughout this work, and its use is encouraged for systems that have not obtained positive evidence for PET. Indeed, a wide range of reactions involving energy transfer in catalysis have been discovered, reported, and reviewed;<sup>10</sup> as such, energy transfer should be considered as a possible mechanistic step when designing or engaging in a mechanistic study of a photoreaction.

In practice, differentiating between energy transfer and electron transfer can be quite difficult experimentally, and one method of doing so that is used in later chapters will be described. For a more detailed discussion, see the review article by McCusker.<sup>11</sup> A PC molecule will be used as an example here, although an excited state of some other reagent would be equally applicable. An excited state PC in fluid solution at room temperature that reacts bimolecularly with another molecule, termed a quencher, will typically react through one of these two pathways to generate distinct products (Fig. 1.1). Quenching through PET forms a biradical ion pair, while energy transfer (EnT) forms the ground state PC and excited state of the quencher. These products are chemically distinct and, in most cases, will have distinct absorption spectra that can serve as an experimental handle for differentiating between these pathways. In this work, a time resolved absorption spectrometer with nanosecond resolution will be used frequently to measure the absorption of these reactive intermediates (Fig. 1.1). Briefly, these measurements consist of two steps – in the first, a UV-vis spectrum of the sample is measured. In the second step, a fast laser pulse excites the sample, followed by a UV-vis measurement timed to start immediately after the end of the laser pulse. This step measures the absorption of both excited state and ground state species. As such, the first step is subtracted from the second to obtain a difference spectrum which “isolates” the absorption of excited state species.



## Electron vs. Energy Transfer



## Pump-Probe Spectroscopy

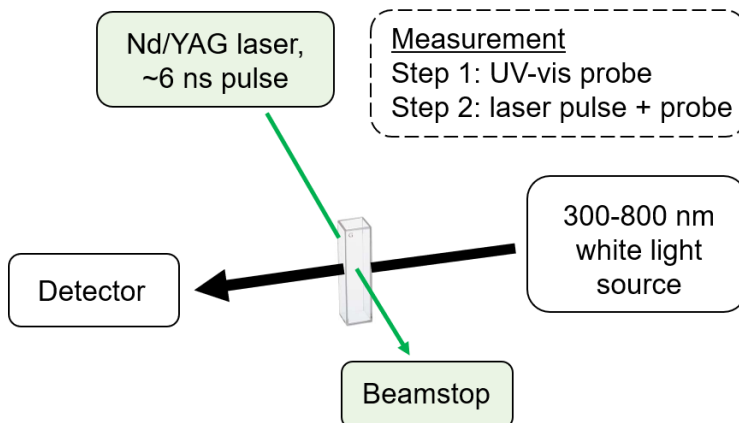


Figure 1.1. (left) Scheme defining electron vs. energy transfer mechanistic steps. Blue asterisk indicates excited state species.  $k_q$  = rate constant for quenching;  $k_{ET}$  = rate constant for electron transfer;  $k_{EnT}$  = rate constant for energy transfer. (right) Simplified schematic of pump-probe spectroscopy, specifically detailing the key components of a time-resolved absorption setup.

The difference spectrum therefore contains positive signals which reflect excited state absorptions (ESA, the absorption of an excited state to a higher lying excited state), as well as negative signals which may represent a ground state bleach (GSB, a spectral region where the ground state species absorb more than excited state species) or stimulated emission (Fig. 1.2). One can also obtain a difference spectrum at varying time delays after the laser pulse to observe the evolution of signals to follow a photoreaction. Similarly, one can monitor any of these signals at a single wavelength as a function of time to obtain a kinetic trace (Fig. 1.2) which will typically exhibit first order kinetics due to excited state relaxation processes (i.e. internal conversion, vibrational relaxation, nonradiative decay, intersystem crossing, and fluorescence/phosphorescence). A kinetic trace of a sample without a quencher can be fit with a single exponential function (the need for use of multiple exponentials would suggest a more complicated reaction than the decay of an excited state to the ground state) for which the excited

state lifetime,  $\tau_{\text{obs}}$ , which is the inverse of the observed excited state decay rate constant,  $k_{\text{obs}}$ , can be defined (For a derivation, see work by McCusker):<sup>11</sup>

$$[\text{PC}^*] = [\text{PC}^*]_0 e^{-k_{\text{obs}} t} = [\text{PC}^*]_0 e^{\frac{-t}{\tau_{\text{obs}}}} \quad (\text{Eq. 1.1})$$

In the presence of a quencher molecule that reacts with the excited state being followed, pseudo-first-order kinetics will be observed as long as the quencher is in sufficient excess to the excited state (typically at least 10-fold excess over the starting PC concentration is used).

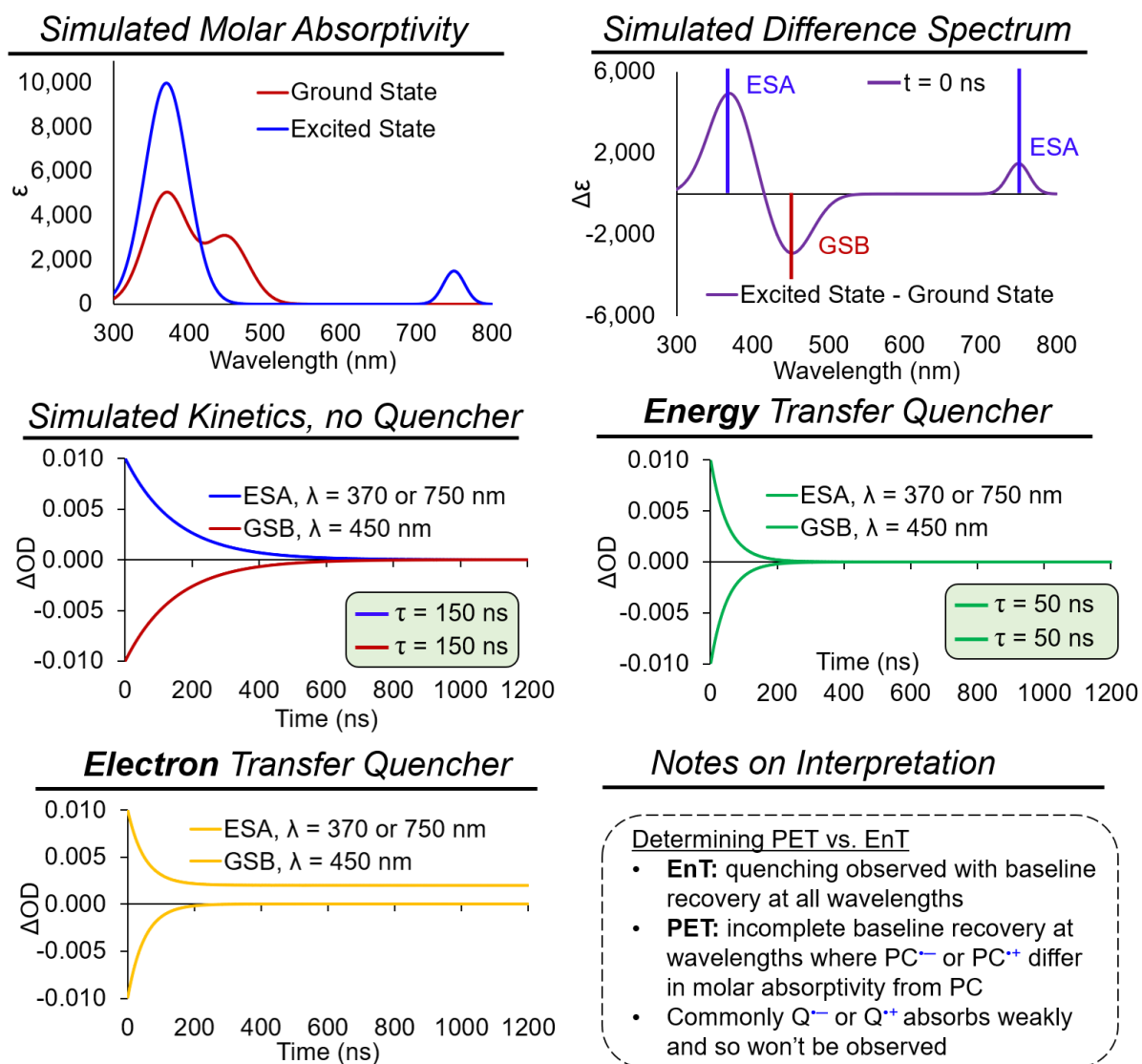


Figure 1.2. (top left) Simulated molar absorptivity spectrum for a hypothetical PC comparing the ground state and excited state absorptions. (top right) Difference spectrum subtracting the ground state absorptivity from excited state absorptivity with wavelengths of interest marked with colored bars. ESA = excited state absorption. GSB = ground state bleach. (middle left) Simulated kinetic

*trace following either ESA or GSB signal over time. (middle right) Effect on the observed kinetics of hypothetical PC reacting with a quencher via energy transfer. (bottom left) Effect on the observed kinetics of hypothetical PC reacting with a quencher via electron transfer. In this example, the electron transfer product absorbs at 370 nm and 750 nm and has the same absorption as the PC at 450 nm. (bottom right) Notes on interpreting these types of data.*

Incomplete recovery of the baseline in kinetic data indicates incomplete recovery of the starting ground state species, a scenario which implies the formation of new species. This situation will manifest as a shelf which persists beyond the time range of the experiment (unless the new species formed is comparably short-lived, in which case its decay may be able to be fit with a second exponential function). If the absorption of reactive intermediates (e.g., radical ions) is known, these signals which persist can be explicitly assigned.

Importantly, obtaining these types of data it becomes possible to distinguish between quenching by energy transfer or electron transfer. In the case of energy transfer, the products are the ground state PC and excited state quencher. Since the excited state quencher typically has weak absorption compared to the PC, the kinetics will in most cases reflect complete recovery of the PC at all wavelengths of measurement. This recovery will occur more rapidly in the presence of the quencher and can be quantified through measuring a shortened  $\tau_{\text{obs}}$ . In the case of PET, a similar shortening of  $\tau_{\text{obs}}$  occurs along with wavelength dependent kinetics. Specifically, the baseline will not be fully recovered at wavelengths where the molar absorptivity of the PC and PET products differ. It is worth noting that incomplete baseline recovery typically will appear as a shelf that persists beyond the experimental timescale since radical ions commonly survive several orders of magnitude longer than excited states. Since the lifetime of the radical ion depends on the particular species in question, this generalization is not always valid and the presence of biexponential kinetic data should be interpreted with care. **Note:** the reader ought to remain skeptical of assignment of such signals without comparison to known spectra, a mistake which is occasionally seen in

published work that can lead to a false assignment (e.g., confusion of a degradation product with a radical ion). Many more detailed discussions of pump-probe spectroscopy or time-resolved emission spectroscopy exist in the literature and the reader is referred to these works for further inquiry.<sup>11-14</sup>

In the following chapters, nanosecond time-resolved absorption spectroscopy will be used in mechanistic studies of nickel-catalyzed C—N bond forming reactions. These reactions are among the most used in medicinal chemistry and are vital for the discovery and production of medicinal compounds and chemical products. The state-of-the-art method for forming these bonds relies on a palladium catalyst which is unsustainable for long term use on an industrial scale due to the scarcity, increasing demand, and low recycling statistics of palladium.<sup>15</sup> Nickel, in contrast, is one of the most abundant elements and can catalyze many of the same types of reactions as palladium. However, the chemistry of Ni in catalysis is fundamentally different from Pd in its proclivity towards taking on odd oxidation states (i.e. Ni(I) and Ni(III)) and engaging in radical chemistry.<sup>16</sup>

As such, it is not surprising that photochemistry would pair well with nickel catalysis. An entire sub-field of photocatalysis known as dual nickel catalysis has emerged based on this pairing where a PC is used cooperatively with a nickel catalyst. In most examples, the PC is proposed to engage in PET with either the Ni catalyst, a substrate, or a sacrificial reagent, although a few examples of EnT have also been reported – rather than include them here, these reactions will be discussed in detail in Chapters 2 and 3. A wide range of reactions of this type have now been developed, and this topic has been reviewed in the literature.<sup>6, 17-18</sup>

Mechanistically, a wide range of catalytic cycles have been reported, usually involving multiple oxidation states of the Ni catalyst (e.g., Ni(I)/Ni(II)/Ni(III) or Ni(0)/Ni(I)/Ni(II)).

Typically, the precatalyst employed in these reactions is either a Ni(0) source (e.g., Ni(cod)<sub>2</sub> where cod = cyclooctadiene) or a Ni(II) source (e.g., NiX<sub>2</sub>•glyme) that is typically a Ni halide salt. Since Ni(0) precatalysts were studied first historically, the proposed mechanisms from those early works have been often extended to newer methods utilizing Ni(II) precatalysts, sometimes without sufficient evidence for the formation of Ni(0) from Ni(II). In the two cases, the most important difference is that oxidative addition of an aryl halide will occur spontaneously with a Ni(0) source as shown in 1979 in seminal work by Kochi<sup>19</sup> or with a Ni(I) source (*vide infra*) but not with a Ni(II) source.

Rather, a lower oxidation state of Ni(I) or Ni(0) must be formed to enable oxidative addition. Therefore, an initiation event is required to form Ni(I) either directly via PET or indirectly through EnT with a following electron transfer event. At this point, a second reduction event would be required to form Ni(0); while such a reaction has been observed to contribute to catalyst death via off-cycle formation of Ni nanoparticles,<sup>20</sup> direct evidence of Ni(0) complexes being formed as transient intermediates involved in productive catalysis when Ni(II) precatalysts are used has not been reported. Further, electrochemical reduction of [Ni(II)(Mebpy)<sub>3</sub>]<sup>2+</sup>, where Mebpy = 4,4'-dimethyl-2,2'-bipyridine, to form Ni(0) at the electrode results in fast comproportionation with Ni(II) in bulk solution to form two Ni(I) complexes,<sup>21</sup> a reaction that would compete with useful catalysis involving Ni(0). In contrast, multiple examples of detection of Ni(I) intermediates have been reported,<sup>22-24</sup> and the rate of oxidative addition at Ni(I) has been observed directly with aryl iodides.<sup>23</sup> As such, the reader is urged to be wary of reports that claim the involvement of Ni(0) in the catalytic cycle when a Ni(II) source is used in the reaction.

In most reported dual catalytic Ni/PC reaction systems, a ruthenium or iridium PC is used to engage in a photoreaction with the Ni complex or a reagent, motivating the development of

more sustainable Ni-catalyzed methods that do not require a precious metal PC. More specifically, while multiple examples have now been reported which solve this problem in C—N bond forming reactions to couple aryl halides with amines either through the use of an organic PC<sup>20, 25-26</sup> or through omitting the PC,<sup>2</sup> two of these systems were developed in the work described herein. First, it was discovered that a Ni-amine complex can function as a PC if ultraviolet light is used, avoiding the need for an added precious metal PC. This reaction is the subject of Chapter 2. Next, it was found that certain PCs (i.e. [Ru(bpy)<sub>3</sub>]<sup>2+</sup>) and a phenoxazine PC) can engage in energy transfer to produce a Ni-centered excited state similar to that formed when a Ni catalyst is directly irradiated. This reaction is the subject of Chapter 3. The types of Ni-amine complexes that form in these reaction mixtures either with or without an added PC were identified and characterized for the first time. A theoretical framework was developed for predicting energy transfer rate constants and the phenoxazine PC was both predicted and found experimentally to exhibit a higher rate constant as compared to [Ru(bpy)<sub>3</sub>]<sup>2+</sup>. Use of the phenoxazine led to improved performance in the reaction, achieving a broader substrate scope and higher yields.

## REFERENCES

- (1) Escobar, R. A.; Johannes, J. W., *Chem. Eur. J.* 2020, *26*, 5168.
- (2) Lim, C.-H.; Kudisch, M.; Liu, B.; Miyake, G. M., *J. Am. Chem. Soc.* 2018, *140*, 7667.
- (3) Kätelhön, A.; Meys, R.; Deutz, S.; Suh, S.; Bardow, A., *Proc. Natl. Acad. Sci. U.S.A* 2019, *116*, 11187.
- (4) Oelgemöller, M., *Chem. Rev.* 2016, *116*, 9664.
- (5) Theriot, J. C.; Lim, C.-H.; Yang, H.; Ryan, M. D.; Musgrave, C. B.; Miyake, G. M., *Science* 2016, *352*, 1082.
- (6) Skubi, K. L.; Blum, T. R.; Yoon, T. P., *Chem. Rev.* 2016, *116*, 10035.
- (7) Schultz, D. M.; Yoon, T. P., *Science* 2014, *343*, 6174.
- (8) Prier, C. K.; Rankic, D. A.; MacMillan, D. W. C., *Chem. Rev.* 2013, *113*, 5322.
- (9) Romero, N. A.; Nicewicz, D. A., *Chem. Rev.* 2016, *116*, 10075.
- (10) Strieth-Kalthoff, F.; James, M. J.; Teders, M.; Pitzer, L.; Glorius, F., *Chem. Soc. Rev.* 2018, *47*, 7190.
- (11) Arias-Rotondo, D. M.; McCusker, J. K., *Chem. Soc. Rev.* 2016, *45*, 5803.
- (12) Buzzetti, L.; Crisenza, G. E. M.; Melchiorre, P., *Angew. Chem. Int. Ed.* 2019, *58*, 3730.
- (13) Berera, R.; van Grondelle, R.; Kennis, J. T. M., *Photosynth. Res.* 2009, *101*, 105.
- (14) Quenching of Fluorescence. In *Principles of Fluorescence Spectroscopy*, Lakowicz, J. R., Ed. Springer US: Boston, MA, 2006; pp 277-330.
- (15) Nahra, F.; Cazin, C. S. J., *Chem. Soc. Rev.* 2021, *50*, 3094.
- (16) Tasker, S. Z.; Standley, E. A.; Jamison, T. F., *Nature* 2014, *509*, 299.
- (17) Zhu, C.; Yue, H.; Chu, L.; Rueping, M., *Chem. Sci.* 2020, *11*, 4051.
- (18) Zhu, C.; Yue, H.; Jia, J.; Rueping, M., *Angew. Chem. Int. Ed.* 2020, Early View.

- (19) Tsou, T. T.; Kochi, J. K., *J. Am. Chem. Soc.* 1979, *101*, 6319.
- (20) Gisbertz, S.; Reischauer, S.; Pieber, B., *Nat. Catal.* 2020, *3*, 611.
- (21) Barman, K.; Edwards, M. A.; Hickey, D. P.; Sandford, C.; Qiu, Y.; Gao, R.; Minteer, S. D.; White, H. S., *ChemElectroChem* 2020, *7*, 1473.
- (22) Sun, R.; Qin, Y.; Ruccolo, S.; Schnedermann, C.; Costentin, C.; Daniel, G. N., *J. Am. Chem. Soc.* 2018, *141*, 89.
- (23) Qin, Y.; Sun, R.; Gianoulis, N. P.; Nocera, D. G., *J. Am. Chem. Soc.* 2021, *143*, 2005.
- (24) Yang, L.; Lu, H.-H.; Lai, C.-H.; Li, G.; Zhang, W.; Cao, R.; Liu, F.; Wang, C.; Xiao, J.; Xue, D., *Angew. Chem. Int. Ed.* 2020, *59*, 12714.
- (25) Kudisch, M.; Lim, C.-H.; Thordarson, P.; Miyake, G. M., *J. Am. Chem. Soc.* 2019, *141*, 19479.
- (26) Du, Y.; Pearson, R. M.; Lim, C.-H.; Sartor, S. M.; Ryan, M. D.; Yang, H.; Damrauer, N. H.; Miyake, G. M., *Chem. Eur. J.* 2017, *23*, 10962.



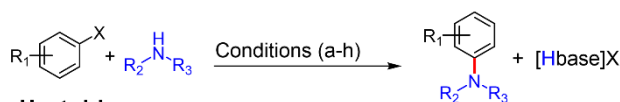
## CHAPTER 2 | C–N CROSS COUPLING VIA PHOTOEXCITATION OF NICKEL–AMINE COMPLEXES

### OVERVIEW

C–N cross-coupling is an important class of reactions with far-reaching impacts across chemistry, materials science, biology, and medicine. Transition metal complexes can elegantly orchestrate diverse aminations but typically require demanding reaction conditions, precious metal catalysts, or oxygen-sensitive procedures. Here, we introduce a mild nickel-catalyzed C–N cross-coupling methodology that operates at room temperature using an inexpensive nickel source ( $\text{NiBr}_2 \cdot 3\text{H}_2\text{O}$ ), is oxygen tolerant, and proceeds through direct irradiation of the nickel–amine complex. This operationally robust process was employed for the synthesis of diverse C–N-coupled products (40 examples) by irradiating a solution containing an amine, an aryl halide, and a catalytic amount of  $\text{NiBr}_2 \cdot 3\text{H}_2\text{O}$  with a commercially available 365 nm LED at room temperature without added photoredox catalyst and the amine substrate serving additional roles as the ligands and base. Density functional theory calculations and kinetic isotope effect experiments were performed to elucidate the observed C–N cross-coupling reactivity.

### INTRODUCTION

Aryl carbon–nitrogen (C–N) bonds are ubiquitous across a wide range of natural products and medicinally relevant compounds,<sup>1,2</sup> making aminations one of the most important and frequently used reactions in medicinal chemistry.<sup>3</sup> Copper catalyzed Ullmann condensations constitute one of the oldest methods to construct an aryl C–N bond but commonly require elevated temperatures (e.g., 200 °C) that can limit reaction scope (Figure 2.1).<sup>4,5</sup> In the past two decades, however, there has been renewed interest in Ullmann-type cross-coupling reactions, largely due to



**Heat-driven**

- a) Cu, ligand, high temp., mild base
- b) Pd, ligand, high temp., strong base
- c) Ni(0), ligand, high temp., strong base

**Light or electricity-driven**

- d) Cu(I), room temp., UV light (i.e. 254 nm), strong base
- e) Ni(II), Ir PC, room temp., blue LED, mild base
- f) Ni(II), organic PC, room temp., white LED, mild base
- g) Ni(II), ligand, room temp., electrolysis, no added base

**This work**

- h) NiBr<sub>2</sub>·3H<sub>2</sub>O, room temp., 365 nm LED
  - no added photocatalyst
  - no added ligand or base
  - cost-effective and abundant Ni source
  - tolerant to O<sub>2</sub> and H<sub>2</sub>O
  - broad scope (40 examples)

*Figure 2.1. Scheme describing historical development of the C–N Cross Coupling Reaction.*

the significant advances in new Cu/ligand systems that have drastically lowered reaction temperatures (e.g., 100 °C) and have employed catalytic, rather than stoichiometric, amounts of Cu species.<sup>6,7</sup>

Since the development of Ullmann-type coupling, the field of transition-metal-catalyzed C–N bond formation has evolved to provide a plethora of approaches for efficient aminations. Notably, palladium-catalyzed C–N cross-coupling has become the predominant method for constructing aryl C–N bonds.<sup>2,8,9</sup> As such, the potential to use abundant nickel catalysts<sup>10</sup> has received significant interest.<sup>11–13</sup> The widespread use of Ni is, however, hampered by the required use of high temperatures, strong alkoxide bases, and air-sensitive Ni(0) compounds.<sup>14</sup> Although methods that implement air-stable Ni(II) complexes have been developed,<sup>15,16</sup> excess reductants or strong bases are required to generate the Ni(0) in situ, which can severely limit functional group tolerance.

In recent years a new paradigm has arisen in aryl C–N bond formation as methods have emerged that are driven by light or electricity.<sup>17</sup> For example, photoinduced Ullmann C–N crosscoupling proceeds through light irradiation of the Cu–amine complex and an aryl halide,

which participate in a single electron transfer event to facilitate aryl C–N bond formation at room temperature.<sup>18,19</sup> Although a significant advance, the reaction typically requires a strong alkoxide base and high-energy UV irradiation (e.g., 254 nm), and has a limited reaction scope.

More recently, dual photoredox systems driven by light through a union of photoredox catalysts (PCs) and Ni catalysis for C–N cross-couplings have been reported.<sup>20,21</sup> The use of precious-metal-based PCs (e.g., Ir) in these systems, however, raises sustainability and cost concerns for the proliferation of such technology. As such, we have focused on developing strongly reducing organic PCs and have demonstrated dihydrophenazine<sup>22</sup> and phenoxazine<sup>23</sup> organic PCs as sustainable replacements for the precious metal PCs, achieving dual Ni/photoredox catalysis for aryl C–N bond formation under similar mild reaction conditions.<sup>24</sup> These organic PCs were also shown to be effective in replacing Ir PCs in applications such as lightdriven atom transfer radical polymerization, trifluoromethylation, and C–S cross-coupling.<sup>24–26</sup>

Herein, we describe a light-driven and Ni-catalyzed C–N cross-coupling methodology that does not use an added PC. The amine substrate further serves as the ligand in Ni complexes, significantly blue-shifting the UV–vis spectrum, and acts as the base to neutralize the acid byproduct. The exclusion of the added PC is enabled through direct photoexcitation of the nickel–amine complex (*vide infra*). This work establishes that the catalytically active Ni state for C–N cross-coupling can be efficiently accessed through electronic excitation of a nickel–amine complex without the aid of a supplementary PC to effect electron or energy transfer.<sup>27,28</sup> By eliminating the need for a PC, this work is expected to further contribute to the mechanistic understanding of Ni-catalyzed cross-coupling chemistry<sup>29–33</sup> in addition to improving the potential and sustainability of this technology. Comparable success was achieved with Ni-catalyzed C–C

and C–O bond formation;<sup>34,35</sup> however, the mechanistic steps involved in these coupling reactions are expected to be distinct from the aryl C–N bond formation described here.

## RESULTS AND DISCUSSION

We hypothesized that such a C–N coupling reaction could utilize air-stable Ni(II) salts for a photoinduced electron transfer reaction between an electron-rich amine and the electron-poor Ni(II) to generate an amino radical<sup>36,37</sup> and Ni(I),<sup>38</sup> the proposed active species for C–N cross-coupling. During reaction development, we determined that C–N cross-coupling between 4-bromobenzotrifluoride and morpholine was efficient under irradiation with a 365 nm ultraviolet LED in a DMAc solution containing 5 mol% NiBr<sub>2</sub>·3H<sub>2</sub>O and 1.5 equiv of quinuclidine under a nitrogen atmosphere at room temperature. Active fan cooling of the LED maintained the reaction temperature <30 °C (see EXPERIMENTAL 1, Figure S2.11). After 3 h of irradiation, C–N-coupled product 1 was obtained in 95% yield (determined from <sup>19</sup>F NMR, see EXPERIMENTAL 1, Figure S2.1) and was isolated at 91% yield (Figure 2.2).

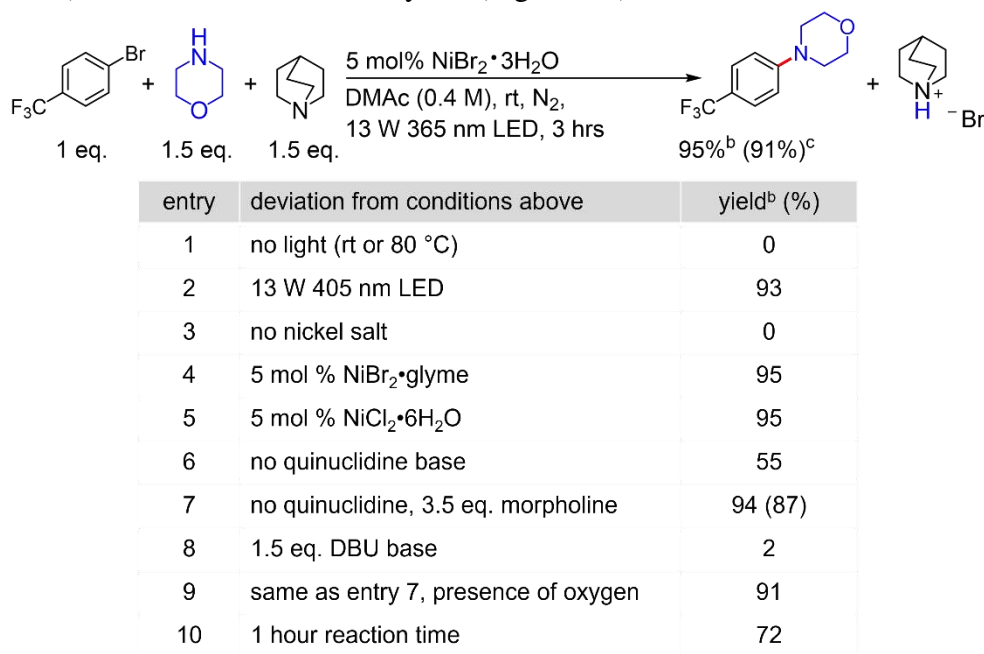


Figure 2.2. Reaction Development and Control Experiments. Reactions conducted at 0.4 mmol scale. Abbreviations: DMAc, *N,N*-dimethylacetamide; rt, room temperature; LED, light-emitting

*diode; DBU, 1,8-diazabicyclo-[5.4.0]undec-7-ene.* <sup>b</sup>Yield determined by <sup>19</sup>F NMR. <sup>c</sup>Isolated yield. <sup>d</sup>Deoxygenated reaction mixture sparged with air for 2 min prior to light irradiation.

Control experiments revealed that no reaction occurred in the absence of light at either room temperature or 80 °C (Table 1, entry 1). Irradiation using a visible light 405 nm LED was similarly effective at promoting aryl C–N bond formation (93%, entry 2) but proceeded at a slower rate (see EXPERIMENTAL 1, Figure S2.2). The nickel salt is crucial for amination as no reaction was observed when it was omitted (entry 3). At 95% yield, both hydrated nickel salts NiBr<sub>2</sub>·3H<sub>2</sub>O and NiCl<sub>2</sub>·6H<sub>2</sub>O (entry 5) gave identical yield to NiBr<sub>2</sub>·glyme (entry 4), which was used in previous light-driven or electrochemically driven C–N cross-coupling reactions (Scheme 1e–g).<sup>17,20,21,24</sup> Markedly, hydrated nickel salts are at least 2 orders of magnitude cheaper than NiBr<sub>2</sub>·glyme, thus rendering this aryl C–N cross-coupling methodology economically attractive.

The choice of base significantly impacts the success of the reaction. Quinuclidine outperformed other organic bases (Figure S5) such as triethylamine, N,N-diisopropylethylamine, and DABCO (1,4-diazabicyclo[2.2.2]octane), while the stronger base DBU (1,8-diazabicyclo[5.4.0]undec-7-ene) almost completely halted the reaction (2% yield, entry 8). Unexpectedly, 55% yield was obtained in the absence of quinuclidine base (entry 6), where excess morpholine presumably acted to neutralize the HBr byproduct. As such, using a larger excess of morpholine (3.5 equiv, entry 7), the yield improved to 94% (87% isolated). In addition to water tolerance (through use of NiBr<sub>2</sub>·3H<sub>2</sub>O), the presence of oxygen also did not appreciably affect the yield (91%, entry 9). Notably, oxygen tolerance was similarly observed in previously reported light- or electricity-driven C–N cross-coupling systems catalyzed by Ni salts.<sup>17,20</sup> Kinetically, this C–N cross-coupling reaction is reasonably fast, reaching 72% after 1 h of irradiation (entry 10).

With the optimized conditions at hand, we sought to investigate the amine and aryl halide scope (Figure 2.3). Secondary (Figure 2.3, species 1–9), primary alkyl (10–13), and primary (hetero)aryl

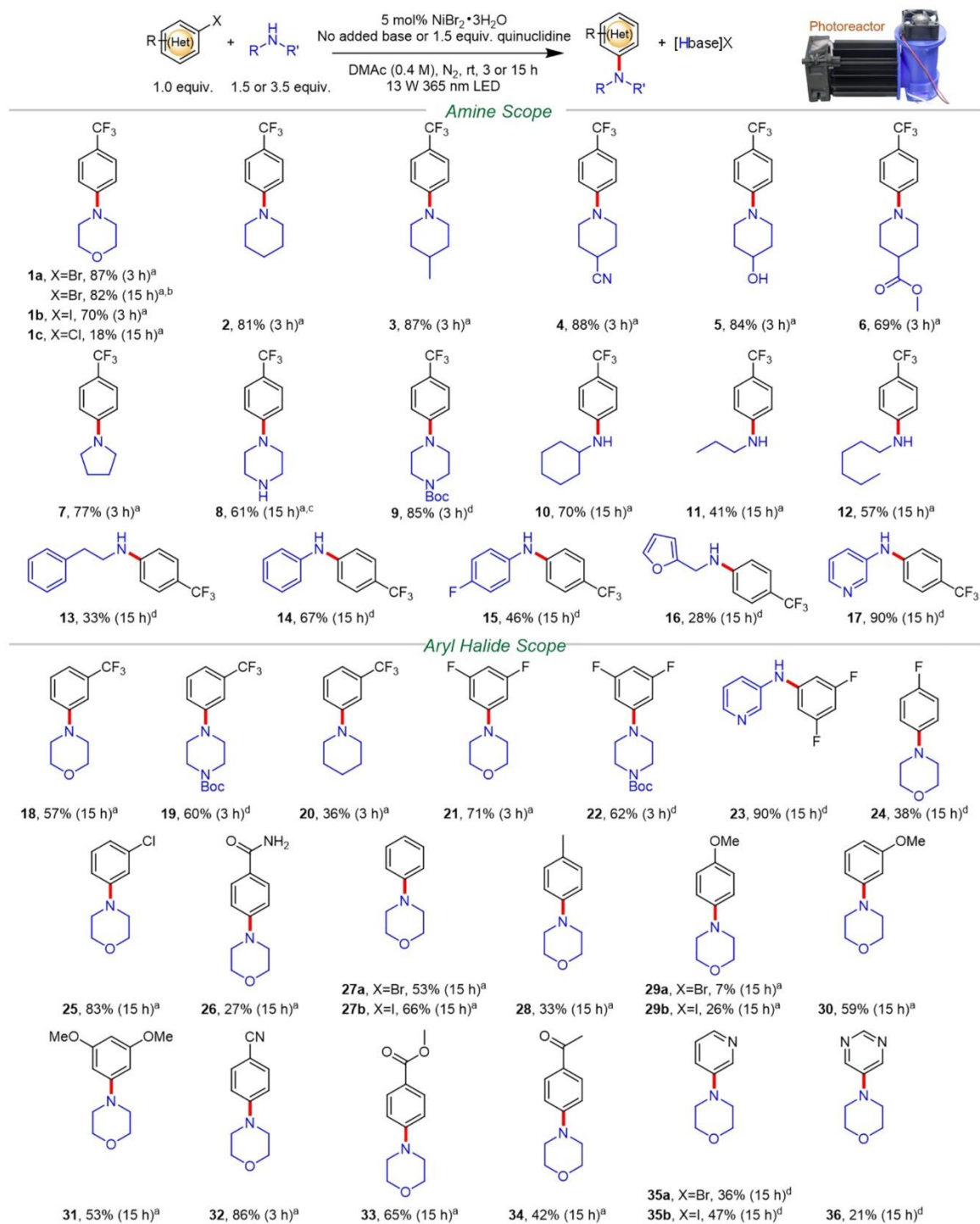


*Figure 2.3. C–N Cross-Coupling via Photoexcitation of Nickel–Amine Complexes: Amine and Aryl Halide Scope. Unless otherwise specified the reaction was conducted at 0.4 mmol scale and aryl bromide was used as the coupling partner. Percent isolated yield is reported next to the product's boldface number. A photograph depicts the 3D-printed photoreactor equipped with the 365 nm LED used in this study (See EXPERIMENTAL 1, Figures S2.8 and S2.9). The LED consumes 13 W with 3.3 W radiant flux at 700 mA and 15.5 V (top right). Abbreviations: DMAc, N,N-dimethylacetamide; rt, room temperature; LED, light-emitting diode; Boc, tert-butyloxycarbonyl. <sup>a</sup>3.5 equiv amine used with no added base. <sup>b</sup>6.4 mmol scale reaction. <sup>c</sup>Dimethyl sulfoxide (DMSO) used as solvent. <sup>d</sup>1.5 equiv amine used with 1.5 equiv quinuclidine base. See EXPERIMENTAL 1 for further details.*

amines (14–17) were all successfully coupled with 4-bromobenzotrifluoride to yield the corresponding C–N products. For morpholine, in addition to aryl bromide (1a, 87%), 4-iodobenzotrifluoride (1b) was also effectively coupled in 70% isolated yield in 3 h. 4-chlorobenzotrifluoride (1c), in contrast, was proven to be a challenging substrate and only gave 18% yield after 15 h of irradiation. C–N cross-coupling between morpholine and 4-bromobenzotrifluoride was further scaled to 6.4 mmol and isolated in 82% yield (1.21 g) after 15 h of irradiation using the same photoreactor setup.

Piperidine (2, 81%) and pyrrolidine (7, 77%) were both coupled in high yield without added base. A variety of functional groups were tolerated under these reaction conditions. For example, piperidine derivatives containing methyl (3, 87%), cyano (4, 88%), hydroxyl (5, 84%), and ester (6, 69%) functional groups were efficiently coupled. Highlighting the tolerance to oxygen, 3 was isolated in 86% yield when the solvent and reagents were used as received, without degassing. Significantly, hydroxyl groups are tolerated by this C–N coupling condition as a strong base (e.g., alkoxide) is not employed. The efficacious coupling of unprotected piperazine (8, 61%), not demonstrated in previous photochemical or electrochemical approaches,<sup>17,20,21</sup> is particularly important<sup>39</sup> as the aryl C–N-coupled piperazine moiety is prevalent among therapeutic compounds<sup>40</sup> such as aripiprazole and flibanserin. The Boc-protected piperazine (9) was shown to be more reactive, yielding the C–N product in 85%.

Primary alkyl amines were typically less reactive than secondary amines, generally resulting in lower yield while requiring longer irradiation times (e.g., 15 h). Nonetheless, cyclohexylamine (10, 70%), propylamine (11, 41%), hexylamine (12, 57%), and phenethylamine (13, 33%) were successfully coupled to 4-bromobenzotrifluoride in moderate to good yield. It is noteworthy that phenethylamine and its analogues are naturally occurring alkaloids that are commonly found in psychoactive drugs.<sup>41</sup> Furfuryl amine (16, 28%) and aromatic amines such as aniline (14, 67%), 4-fluoroaniline (15, 46%) and 3-aminopyridine (17, 90%) were also effectively coupled. Since aromatic amines are less basic than primary or secondary alkyl amines, 1.5 equiv of quinuclidine as the base was required to obtain appreciable yields.

In a previous photochemical system employing Ni and Ir PC, the addition of 10 mol% of pyrrolidine was required to effect the coupling of aniline and therefore resulted in a mixture of two C–N-coupled products derived from both pyrrolidine and aniline.<sup>21</sup> On the contrary, our approach does not require the addition of a secondary amine or elevated temperature (e.g., 55 °C) to promote coupling of aniline, thus avoiding undesirable product mixtures. For example, coupling under our approach proceeds effectively at room temperature for 9, 10, and 14 where 55 °C was required previously.<sup>21</sup> For 3-aminopyridine, few examples have been reported using Ni to catalyze C–N cross-coupling. A light-driven Ni/Ir PC system was employed for the cross coupling of 3-aminopyridine and 4-iodotoluene with 33% yield,<sup>20</sup> which is increased to 90% yield in our approach using 4-bromobenzotrifluoride (17) as the coupling partner. Furthermore, Pd catalysis has not been implemented for the synthesis of compound 17 using 3-aminopyridine. Cu was previously used to catalyze formation of 17;<sup>42</sup> however, an aryl boronic acid was used as the coupling partner instead of an aryl bromide as demonstrated here.



Regarding the scope of aryl halides, this C–N cross-coupling method is compatible with aryl halides containing trifluoromethyl (Figure 2.3, species 1–20), fluoro (21–24), chloro (25), amide (26), methyl (28), methoxy (29–31), cyano (32), ester (33), and carbonyl (34) functional groups. In addition, heteroaryl halides containing pyridine (35) and pyrimidine (36) were also successfully coupled. Generally, aryl halides containing electron-withdrawing groups are more reactive than their electron-neutral or electron-donating counterparts. For example, when comparing substituents in the para position of an aryl bromide under similar reaction conditions, the yield of cyano (32, 86%) > hydrogen (27a, 53%) > methoxy (29a, 7%). The use of aryl iodides such as iodobenzene (27b, 66%), 4-iodoanisole (29b, 26%), and 3-iodopyridine (35b, 47%) resulted in increased yields relative to using aryl bromides.

To further establish its utility, this C–N cross-coupling method was employed in multistep syntheses (Figure 2.4A,B). Recently, we reported a visible light-driven aryl C–S cross coupling methodology that proceeds under mild conditions to synthesize a wide range of diaryl thioether products through white LED irradiation of a solution containing (hetero)aryl thiol, (hetero)aryl halide and Cs<sub>2</sub>CO<sub>3</sub> in DMSO at room temperature in the absence of catalysts.<sup>43</sup> Using this method, we synthesized aryl thioether 37 at 56% yield and subsequently subjected it to the C–N cross-coupling conditions developed here, coupling it with 3-aminopyridine to yield novel compound 38 in 88% yield (Figure 2.4A). This example highlights two industrially important processes, namely aryl C–S and C–N cross-couplings, that can be driven by light irradiation under mild conditions to achieve molecular complexity.

The piperazine functionality is abundant across pharmaceutical products (*vide supra*).<sup>40</sup> Using established methods,<sup>44</sup> in four synthetic steps we converted aryl-coupled piperazine

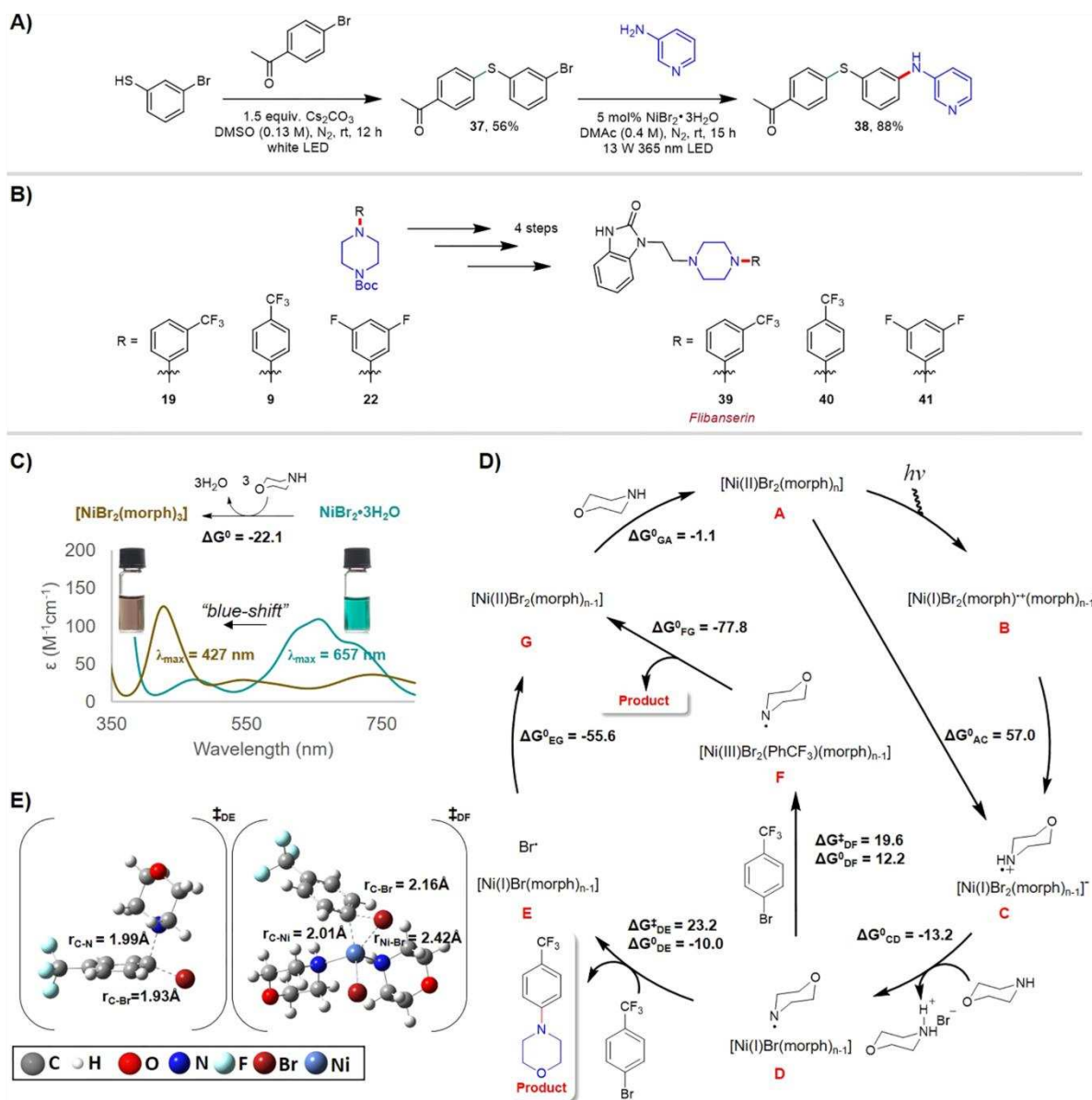


**Figure 2.4. Synthetic applications and mechanistic studies.** (A) Light-driven sequential C–S and C–N cross-couplings to construct molecular complexity. For the synthesis of 37, 1.0 equiv of 4'-bromoacetophenone and 1.5 equiv of 3-bromothiophenol were used; for the synthesis of 38, 1.5 equiv of 3-aminopyridine and 1.5 equiv of quinuclidine base were used. DMSO = dimethyl sulfoxide. (B) Synthesis of flibanserin and two structurally related derivatives; the yields of 19, 9, and 22 are shown in Figure 2.3. Using 19, 9, and 22 as the reagents, 39, 40, and 41 were obtained in the yields of 50%, 40%, and 70%, respectively. (C) UV–vis spectra of  $\text{NiBr}_2 \cdot 3\text{H}_2\text{O}$  and  $\text{NiBr}_2 \cdot 3\text{H}_2\text{O} + \text{morpholine}$  in DMAc; 70 equiv of morpholine was added with respect to  $\text{NiBr}_2 \cdot 3\text{H}_2\text{O}$  in accordance to our standard reaction conditions. Photographs showing the teal color of  $\text{NiBr}_2 \cdot 3\text{H}_2\text{O}$  solution in DMAc transformed to brownish yellow upon morpholine addition. (D) Proposed C–N cross-coupling mechanism derived from density functional theory (DFT) calculations for  $n = 3$ . Reported free energies (in kcal/mol at 298 K and 1 M in solution)

were computed at  $uM06/6-311+G(d,p)//uM06/6-31+G(d,p)$  level of theory with CPCM-described solvation in DMAc solvent. (E) Computed transition state structures for steps DE and DF (for  $n = 3$ ). *morph* = morpholine, *PhCF<sub>3</sub>Br* = 4-bromobenzotrifluoride, CPCM = conductor-like polarizable continuum model;  $\lambda_{max}$  is the maximum absorption wavelength and  $\epsilon$  the molar absorptivity.

derivatives 19, 9, and 22 to flibanserin (39) and two flibanserin derivatives (40 and 41, Figure 2.4B). We note that 40 can also be accessed from 8, therefore eliminating both Boc protection and deprotection steps. These examples illuminate the prospect of efficient and sustainable access to medicinally relevant precursors using this C–N coupling procedure for the development and manufacturing of pharmaceutical products.

To gain insight into this mechanism, density functional theory (DFT) calculations were performed to compute the energetics of intermediates involved in the proposed lowest energy potential energy surface (Figure 2.4C–E).<sup>26,45</sup> Specifically, to construct possible mechanistic pathways the mechanism to produce 1a was investigated.

A hypothesized mechanism commences with formation of nickel–amine complexes  $[\text{NiBr}_2(\text{morph})_n]$ , where  $n = 2$  or  $3$  and *morph* = morpholine (Figure 1C,D). The  $\lambda_{max}$  of a  $\text{NiBr}_2 \cdot 3\text{H}_2\text{O}$  solution in DMAc blue-shifted from 657 nm to  $\sim 550$  nm as 1–4 equiv of morpholine (relative to Ni) was sequentially added (See EXPERIMENTAL 1, Figure S2.18). We assign the species absorbing at  $\sim 550$  nm as  $\text{NiBr}_2(\text{morph})_2$ . Further, as 8–70 equiv. of morpholine was successively added to the Ni solution, the  $\sim 550$  nm peak gradually decreased while the peak at  $\sim 430$  nm increased. We assign the absorption peak at  $\sim 430$  nm to  $[\text{NiBr}_2(\text{morph})_3]$ . These assignments are based on previous reported  $[\text{NiBr}_2(\text{morph})_2]$  and  $[\text{NiBr}_2(\text{morph})_3]$  complexes, which displayed  $\lambda_{max} = 580$  and 454 nm, respectively.<sup>46</sup> Notably, these  $\lambda_{max}$  values, which were recorded as Nujol mulls, are systematically offset from our values in a DMAc solution by  $\sim 30$  nm.

Under these reaction conditions, containing 70 equiv. of morpholine relative to Ni, we

suggest that  $[\text{NiBr}_2(\text{morph})_3]$  exists as the predominant species in equilibrium with  $[\text{NiBr}_2(\text{morph})_2]$ ; this is supported by the relatively strong peak absorbance at 427 nm and weak absorbance at 543 nm (Figure 2.4C). In addition,  $[\text{NiBr}_2(\text{morph})_3]$  is a brownish yellow solid that is very distinct from the deep blue color of  $[\text{NiBr}_2(\text{morph})_2]$ .<sup>46</sup> Thus, the observed color change from the teal  $\text{NiBr}_2 \cdot 3\text{H}_2\text{O}$  solution in DMAc ( $\lambda_{\text{max}} = 657$  nm) to brownish yellow ( $\lambda_{\text{max}} = 427$  nm) upon addition of 70 equiv. of morpholine further supports the presence of  $[\text{NiBr}_2(\text{morph})_3]$  as the predominant nickel–amine complex (Figure 2.4C). Importantly, the blue-shifting of the UV–vis spectrum upon amine addition was similarly observed for basic alkyl amines such as pyrrolidine, piperidine, and cyclohexyl amine (See EXPERIMENTAL 1, Figure S2.19). Here, we further note that the UV–vis spectrum in the region from 350–800 nm remained identical upon addition of 4-bromobenzotrifluoride to a solution containing  $\text{NiBr}_2 \cdot 3\text{H}_2\text{O}$  and morpholine, demonstrating that only the nickel–amine complexes are responsible for photon absorption in the region of 350–800 nm to effect C–N cross-coupling (See EXPERIMENTAL 1, Figures S2.12–S2.17).

Computationally, the displacement of three water molecules by three morpholine molecules to generate  $[\text{NiBr}_2(\text{morph})_3]$  was determined to be exergonic by 22.1 kcal/mol (Figure 2.4C). In addition, the ground state of  $[\text{NiBr}_2(\text{morph})_3]$  was computationally determined to be a triplet that is 14.0 kcal/mol more stable than the corresponding singlet (See EXPERIMENTAL 1, Figure S2.25). Corroborating DFT predictions,  $[\text{NiBr}_2(\text{morph})_3]$  was reported to exhibit a magnetic moment of 2.95  $\mu\text{B}$ , reaffirming the triplet ground state.<sup>46</sup> We propose that catalytic activity for aryl C–N bond formation begins with photon absorption by  $[\text{NiBr}_2(\text{morph})_n]$  (A), where  $n = 2$  or 3 (Figure 2.4D); for  $n = 3$ ,  $\lambda_{\text{max}} = 427$  nm and  $\epsilon_{\text{max}} = 126\text{M}^{-1} \text{cm}^{-1}$ . Using 365 nm as the excitation wavelength, we were able to measure the emission spectrum of a DMAc solution containing predominantly the proposed  $[\text{NiBr}_2(\text{morph})_3]$  species (See EXPERIMENTAL 1, Figure S2.20),

which features sharp and broad emission peaks at 386 and 484 nm, respectively. Interestingly, measuring the emission intensity (at  $\lambda = 484$  nm) as a function of excitation wavelength revealed that the maximum emission intensity at this wavelength occurs with excitation at 359 nm (See EXPERIMENTAL 1, Figure S2.21). Thus, despite the low molar absorptivity at 365 nm (Figure 2.4C), excitation is efficient using this irradiation wavelength. Under 365 nm LED irradiation, we propose that photoinduced electron transfer from electron-rich morpholine to the electron-poor Ni(II) metal center results in the reduced Ni(I) and oxidized morpholine radical cation (B), which can subsequently dissociate into the corresponding ion pairs (C). Thermodynamically, the free energy cost to produce C from A ( $\Delta G^0_{AC}$ ) is endergonic by 57.0 kcal/mol (for  $n = 3$ ), which is energetically supplied by photon absorption (365 nm or 78.3 kcal/mol). The proton of the morpholine radical cation is relatively acidic and the bromide anion of Ni(I) complex C is also comparatively labile such that excess morpholine in solution can act as a base to neutralize the HBr to form D ( $\Delta G^0_{CD} = -13.2$  kcal/mol,  $n = 3$ ).

The Ni(I) species and morpholine radical in D are both reactive intermediates that can react with 4-bromobenzotrifluoride through either step DE or DF. In step DE, the morpholine radical adds to 4-bromobenzotrifluoride to form the desired product 1a through bromine atom displacement (E). The DFT-predicted free energy of activation ( $\Delta G^{\ddagger}_{DE}$ ) for this step is 23.3 kcal/mol, while the free energy of reaction is thermodynamically favored by 10.0 kcal/mol. The Ni(I) species and the bromine atom in E can then quench ( $\Delta G^0_{EG} = -55.6$  kcal/mol,  $n = 3$ ) to form the closed-shell  $[\text{NiBr}_2(\text{morph})_{n-1}]$  complex (G). Subsequently, G can associate with morpholine in solution ( $\Delta G^0_{GA} = -1.1$  kcal/mol,  $n = 3$ ) to re-enter the catalytic cycle as A.

Alternatively, 4-bromobenzotrifluoride can oxidatively add to Ni(I) species in D to form a Ni(III) intermediate (F) ( $\Delta G^{\ddagger}_{DF} = 19.6$  kcal/mol and  $\Delta G^0_{DF} = 12.2$  kcal/mol,  $n = 3$ ). This Ni(III)

and the morpholine radical can then react energetically ( $\Delta G_{\text{FG}}^0 = -77.8$  kcal/mol,  $n = 3$ ) to eliminate the C–N product 1a while forming the aforementioned G. The DFT-predicted transition state structures for steps DE and DF are shown in Figure 2.4E. We note that the commonly employed entropy evaluations within the rigid rotor, harmonic oscillator, and ideal gas approximations normally overestimate the entropic cost ( $>5$  kcal/mol) for reactions occurring in solution phase<sup>45,47,48</sup> such that the predicted  $\Delta G_{\text{DE}}^{\ddagger}$  and  $\Delta G_{\text{DF}}^{\ddagger}$  values are likely overestimated.

Investigating the reaction in the presence of 0.2 equiv. of 2,2,6,6-tetramethyl-1-piperidinyloxy (TEMPO), the production of 1a was significantly decreased such that only 59% conversion was observed after 15 h of irradiation. Addition of 0.5 equiv. of TEMPO or more completely halted the C–N coupling reaction. These observations suggest that radical intermediates are involved in the mechanism of this transformation.

Next, we compared the rate of C–N product formation between piperidine and piperidine-*d*11 using 4-bromobenzotrifluoride as the coupling partner (Figure 2.5) in order to determine the  $k_{\text{H}}/k_{\text{D}}$  ratio to investigate the presence of a kinetic isotope effect (KIE).<sup>49–51</sup> In monitoring the

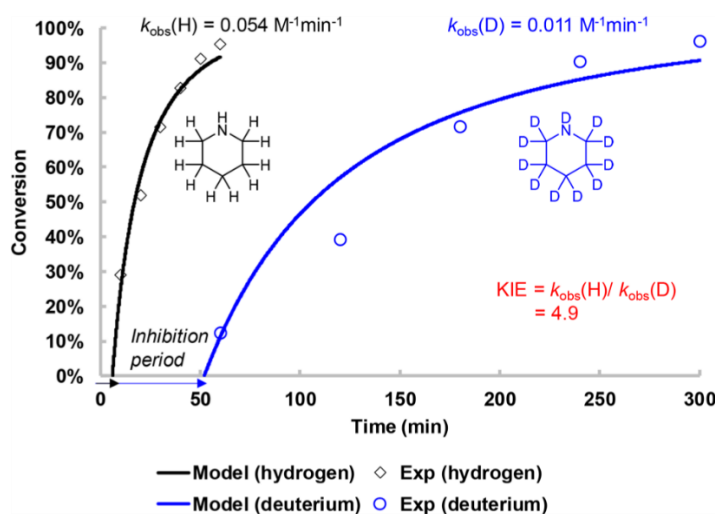


Figure 2.5. Kinetic Isotope Effect (KIE) Experiment. The rate of C–N cross-coupling was compared between piperidine and piperidine-*d*11 using 4-bromobenzotrifluoride as the coupling partner. Reaction conditions: 1.0 equiv. of 4-bromobenzotrifluoride (0.4 mmol), 3.5 equiv. of

*piperidine (H or D), 5 mol% NiBr<sub>2</sub>·3H<sub>2</sub>O, and irradiation at 365 nm. The observed rate constant ( $k_{obs}$ ) was determined by solving a second order rate equation model via numerical integration (RK4 method, see EXPERIMENTAL 1, Figures S2.23 and S2.24); inhibition periods of 6 and 52 min were included in the model fitting of piperidine and piperidine-*d*11, respectively.*

reactions, we observed an inhibition period of 6 min for piperidine and much longer 52 min for piperidine-*d*11. The involvement of O<sub>2</sub> in this inhibition was ruled out because the solutions were carefully deoxygenated, and the cause of this inhibition period is currently unknown. With incorporation of the inhibition period values, we numerically solved the second-order rate equation to obtain  $k_{obs(H)} = 0.054 \text{ M}^{-1} \text{ min}^{-1}$  and  $k_{obs(D)} = 0.011 \text{ M}^{-1} \text{ min}^{-1}$  for piperidine and piperidine-*d*11, respectively. As a result, the KIE value was determined to be 4.9. The large KIE = 4.9 value is consistent with a primary KIE for dissociating a N–H(D) bond in the rate-determining step prior to forming a C–N bond.

## CONCLUSION

We have developed a light-driven and nickel-catalyzed C–N cross-coupling methodology that proceeds via direct photoexcitation of nickel–amine complexes. This work reveals that catalytically active nickel states can be efficiently accessed without requiring energy or electron transfer mechanisms from a supplemental photoredox catalyst. By irradiating a solution containing an amine, an aryl halide, and a catalytic amount of NiBr<sub>2</sub>·3H<sub>2</sub>O with a commercially available 365 nm LED at room temperature, this operationally simple process was applied for the coupling of secondary, primary alkyl, or primary (hetero)aryl amines and aryl halides with diverse electronics (40 examples) without added photoredox catalyst or ligand and, in most cases, without added base. The effectiveness of this method was highlighted by the successive use of light-driven C–S/C–N cross-couplings to synthesize complex structures as well as *en route* to the synthesis of flibanserin and structurally related derivatives. DFT calculations suggest the production of an amino radical

through irradiation of the nickel–amine complex. Concomitantly, the large H/D kinetic isotope effect value of 4.9 (for piperidine) suggests the dissociation of a N–H(D) bond as the rate-determining step to generate the amino radical for the observed C–N cross-coupling reactivity.



## EXPERIMENTAL 1: SUPPLEMENTARY INFORMATION FOR CHAPTER 2

### 1. General Information

Anhydrous DMAc solvent, aryl halides and amines were purchased from Sigma-Aldrich, TCI or Alfa Aesar. 2,2,6,6-tetramethyl-1-piperidinyloxy (TEMPO) and piperidine-*d*11 were purchased from Sigma-Aldrich. All commercially available solvents and reagents were degassed and used without further purifications. The photoreactor was custom designed and built (see section below). Organic solutions were concentrated under reduced pressure on a Büchi rotary evaporator using a water bath. Flash column chromatography was performed using the CombiFlash® Rf+ Lumen instrument. Reactions were analyzed by TLC using TLC silica gel F254 250 µm pre-coated-plates from Merck. Developed chromatogram was visualized using a UV lamp and permanganate stain was used for UV-inactive compounds.

The  $^1\text{H}$ ,  $^{13}\text{C}$ ,  $^{19}\text{F}$  NMR spectra were recorded on a Bruker Avance Neo (400, 101, and 376 MHz, respectively) instrument. Deuterated solvents were purchased from Cambridge Isotope Laboratories (Andover, MA) and used as received. All  $^1\text{H}$  NMR experiments are reported in  $\delta$  units, parts per million (ppm), and were measured relative to the signals for residual chloroform (7.26 ppm) or dimethylsulfoxide (2.50 ppm) in the deuterated solvents. Data for  $^1\text{H}$  NMR are reported as follows: chemical shift ( $\delta$  ppm), multiplicity (s = singlet, d = doublet, t = triplet, q = quartet, p = quintet, m = multiplet, dd = doublet of doublets, dt = doublet of triplets...etc, br = broad), coupling constant (Hz) and integration. All  $^{13}\text{C}$  NMR spectra are reported in ppm relative to  $\text{CDCl}_3$  (77.16 ppm) or  $\text{DMSO-}d_6$  (39.52 ppm). Mass spectrometry analysis was performed using an Agilent 6220 TOF LC/MS (“OTOF”) interfaced to an Agilent 1200 HPLC with electrospray (ESI), multi-mode (combined ESI and APCI), atmospheric pressure photoionization (APPI), and Direct Analysis in Real Time (DART) sources at Colorado State University.

## 2. Reaction Development and Optimization

### General Procedure A:

Under nitrogen atmosphere in a glovebox, a stir bar, an aryl halide (0.40 mmol, 1.0 equiv.) and 1 mL of DMAc solution containing dissolved  $\text{NiBr}_2 \cdot 3\text{H}_2\text{O}$  (0.02 mmol, 0.05 equiv., 5.5 mg) was added to a 0.5 dram glass vial. The glass vial was then capped using a screw cap equipped with a PTFE/silicone septum and sealed with a strip of Parafilm®. The capped vial was then brought out of the glovebox and liquid amine (degassed, 1.40 mmol, 3.5 equiv.) was added via a Hamilton® syringe. Solid amines were weighed and added inside the glovebox. The capped glass vial containing the reaction mixture was then placed in a 3D-printed vial holder and subjected to 365 nm LED irradiation with fan cooling to maintain the vial at room temperature. After the time specified in the reaction schemes, the reaction mixture was washed with water, extracted with EtOAc or DCM and concentrated under vacuum. Purification of the crude product by flash chromatography on silica gel using the indicated solvent system afforded the desired product.

### General Procedure B:

Under nitrogen atmosphere in a glovebox, a stir bar, an aryl halide (0.40 mmol, 1.0 equiv.), quinuclidine (0.60 mmol, 1.5 equiv., 66.7 mg) and 1 mL of DMAc solution containing dissolved  $\text{NiBr}_2 \cdot 3\text{H}_2\text{O}$  (0.02 mmol, 0.05 equiv., 5.5 mg) was added to a 0.5 dram glass vial. The glass vial was then capped using a screw cap equipped with a PTFE/silicone septum and sealed with a strip of Parafilm®. The capped vial was then brought out of the glovebox and liquid amine (degassed, 0.60 mmol, 1.5 equiv.) was added via a Hamilton® syringe. Solid amines were weighed and added inside the glovebox. The capped glass vial containing the reaction mixture was then placed in a 3D-printed vial holder and subjected to 365 nm LED irradiation with fan cooling to maintain the

vial at room temperature. After the time specified in the reaction schemes, the reaction mixture was washed with water, extracted with EtOAc or DCM and concentrated under vacuum. Purification of the crude product by flash chromatography on silica gel using the indicated solvent system afforded the desired product.

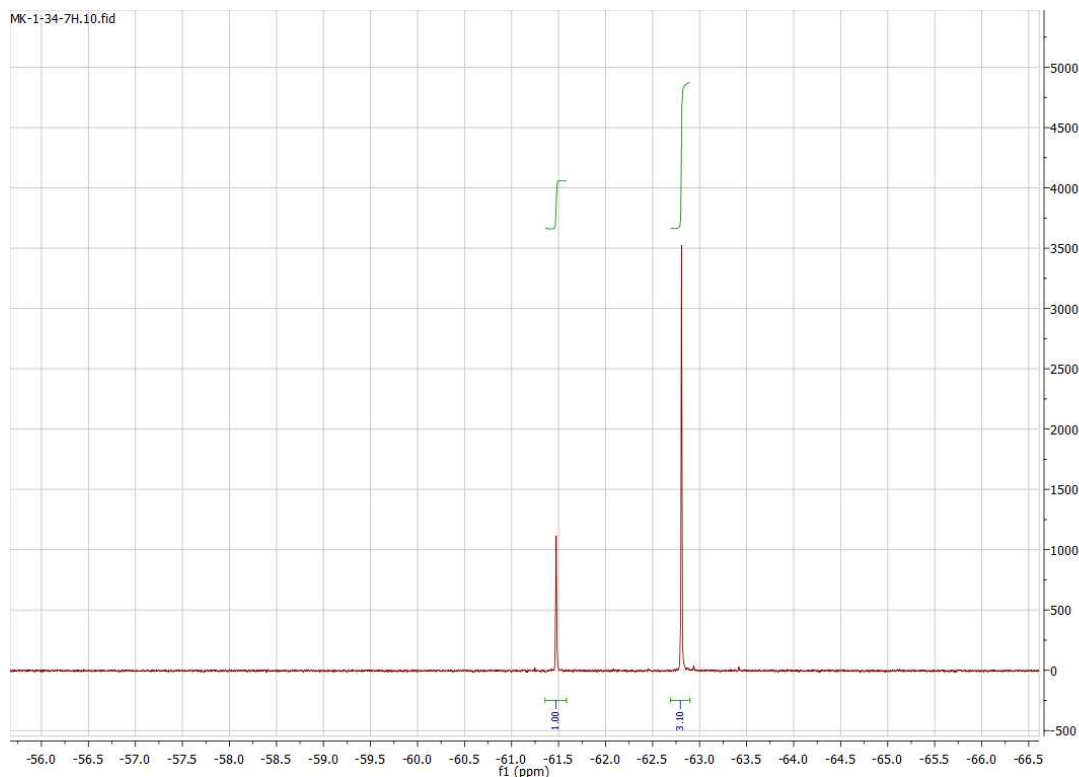
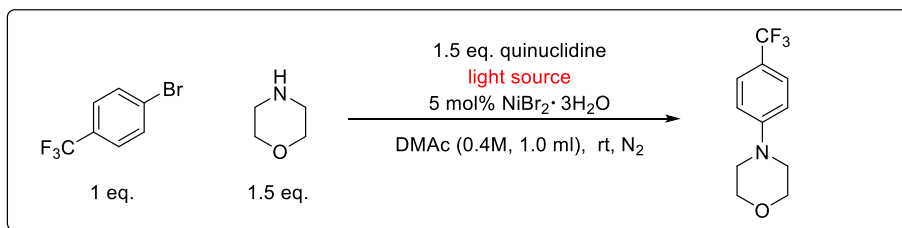


Figure S2.1. Conversion of the C-N coupled product determined from  $^{19}\text{F}$  NMR.

We used 4-bromobenzotrifluoride and morpholine as our model substrates and employed general procedure B to perform control experiments and reaction optimizations detailed below (Fig. S2.2-S2.7). We monitored the conversion of the C-N coupled product (4-(4-(trifluoromethyl)phenyl)morpholine) as a function of time (e.g., 1 h, 2 h, and 3 h) using  $^{19}\text{F}$  NMR (Fig. S2.1). We assumed that during the course of the reaction, the number of  $\text{CF}_3$  groups in the reaction mixture is conserved, allowing the conversion of the C-N coupled product to be calculated (see Fig. S2.1). This method is sufficiently accurate that  $^{19}\text{F}$  NMR conversion closely matches isolated yield. For example, C-N coupled product was isolated at 91% yield with  $^{19}\text{F}$  NMR

conversion of 95%. To obtain  $^{19}\text{F}$  NMR conversion as a function of time, we withdrew a  $\sim 10\ \mu\text{L}$  aliquot from the reaction mixture under oxygen-free conditions and diluted the sample with  $\sim 600\ \mu\text{L}$  of deuterated chloroform before subjecting the sample to  $^{19}\text{F}$  NMR spectroscopy.

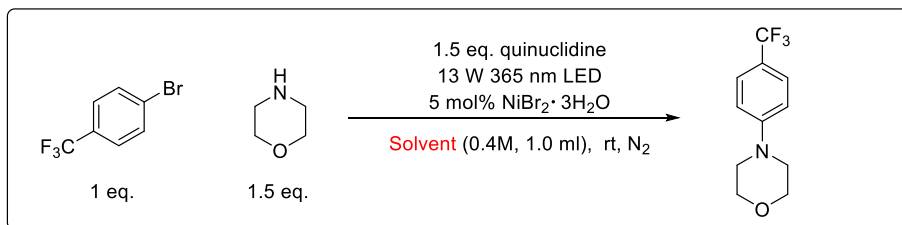
During reaction optimization, we determined that no reaction occurred in the absence of nickel salts or without irradiation at either room temperature or  $80\ ^\circ\text{C}$  (Fig. S2.2). 405 nm light gave slower conversion than 365 nm light (52% vs. 72% at 1 hour) but achieved similar conversion at 3 hours. With no added quinuclidine, 55% conversion was obtained. DMF and DMSO gave similarly high conversion ( $>90\%$ ) to DMAc while MeOH and MeCN gave considerably lower conversion (Fig. S2.3). Various nickel salts at different loadings have similar performance (Fig. S2.4). The effect of types of added organic bases were also investigated (Fig. S2.5 and S2.6). Quinuclidine gave the best performance while bases such as DMAP, DBU and PMDETA almost completely shut off reactivity. Fig. S2.7 shows that excess morpholine substrate can also function as a base. For example, when morpholine substrate was introduced at 3.5 eq., 94% of conversion was obtained with no added base.



hv	$^{19}\text{F}$ -NMR Conversion		
	1 hr	2 hr	3 hr
no light	-----	-----	0%
no light ( $80^\circ\text{C}$ )	-----	-----	0%
405 nm	52%	81%	93%
365 nm	72%	94%	95% (91%)*
365 nm (no nickel)	-----	-----	0%
365 nm (no base)	-----	-----	55%

\*Isolated yield

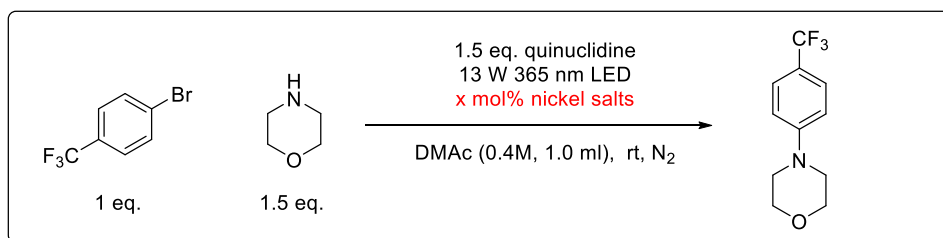
Figure S2.2. Control experiment and effect of light source.



Solvent	<sup>19</sup> F-NMR Conversion		
	1 hr	2 hr	3 hr
DMAc (365 nm)	72%	94%	95% (91%)*
DMSO (365 nm)	-----	-----	93%
MeOH (365 nm)	-----	-----	60%
DMF (365 nm)	-----	-----	93%
MeCN (365 nm)	-----	-----	46%

\*Isolated yield

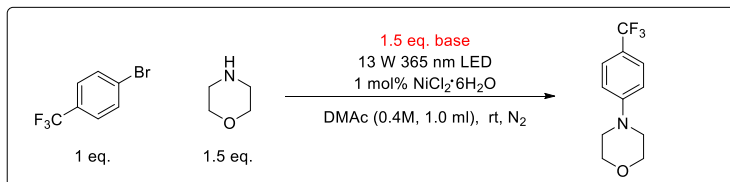
Figure S2.3. Effect of solvent.



Nickel salts	<sup>19</sup> F-NMR Conversion		
	1 hr	2 hr	3 hr
NiBr <sub>2</sub> •glyme 5%	81%	96%	95%
NiCl <sub>2</sub> •6H <sub>2</sub> O 5%	76%	96%	95%
NiCl <sub>2</sub> •glyme 5%	68%	95%	95%
NiBr <sub>2</sub> •3H <sub>2</sub> O 5%	72%	94%	95% (91%)*
NiBr <sub>2</sub> •3H <sub>2</sub> O 1%	82%	95%	95%
NiBr <sub>2</sub> •3H <sub>2</sub> O 2%	85%	96%	95%
NiBr <sub>2</sub> •3H <sub>2</sub> O 8%	74%	95%	95%
NiBr <sub>2</sub> •3H <sub>2</sub> O 10%	74%	95%	95%

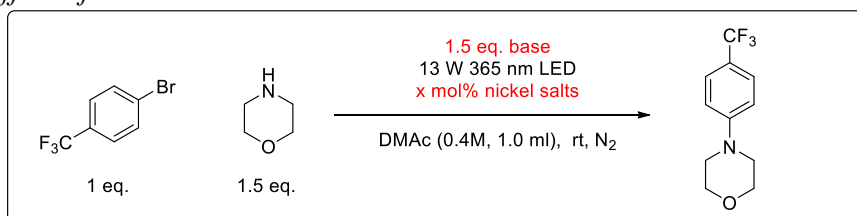
\*Isolated yield

Figure S2.4. Effect of types and loadings of nickel salts. The lower light penetration into the  $\text{NiBr}_2 \cdot 3\text{H}_2\text{O}$  5%, 8% and 10% solutions could explain their lower conversions compared to  $\text{NiBr}_2 \cdot 3\text{H}_2\text{O}$  1% in the 1st hour.



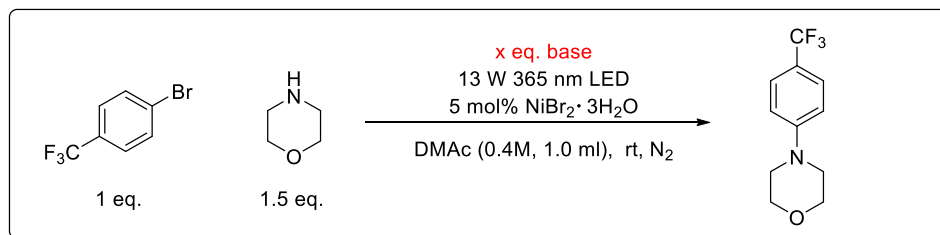
Base	<sup>19</sup> F-NMR Conversion		
	1 hr	2 hr	3 hr
quinuclidine 1.5eq	79%	94%	94%
DABCO 1.5eq	14%	26%	35%
DIPEA 1.5eq	21%	48%	68%
morpholine 1.5eq	20%	47%	64%
N-Me morpholine 1.5eq	31%	46%	52%
DMAP 1.5eq	0%	1%	2%
TEA 1.5eq	43%	70%	78%
DBU 1.5eq	0%	0%	2%
PMDETA 1.5eq	0%	0%	0%
proton sponge 1.5eq	2%	4%	7%

Figure S2.5. Effect of added base.



Base	Nickel	<sup>19</sup> F-NMR Conversion		
		1 hr	2 hr	3 hr
morpholine 1.5eq	$\text{NiBr}_2 \cdot 3\text{H}_2\text{O}$ 5%	65%	85%	93%
morpholine 1.5eq	$\text{NiBr}_2 \cdot 3\text{H}_2\text{O}$ 2%	57%	80%	88%
morpholine 1.5eq	$\text{NiBr}_2 \cdot 3\text{H}_2\text{O}$ 1%	34%	63%	74%
morpholine 1.5eq	$\text{NiCl}_2 \cdot 6\text{H}_2\text{O}$ 5%	34%	65%	79%
morpholine 1.5eq	$\text{NiCl}_2 \cdot 6\text{H}_2\text{O}$ 2%	27%	58%	75%
morpholine 1.5eq	$\text{NiCl}_2 \cdot 6\text{H}_2\text{O}$ 1%	20%	47%	64%
DIPEA 1.5eq	$\text{NiBr}_2 \cdot 3\text{H}_2\text{O}$ 5%	45%	79%	85%
DIPEA 1.5eq	$\text{NiBr}_2 \cdot 3\text{H}_2\text{O}$ 2%	44%	76%	81%
DIPEA 1.5eq	$\text{NiBr}_2 \cdot 3\text{H}_2\text{O}$ 1%	23%	50%	68%
DIPEA 1.5eq	$\text{NiCl}_2 \cdot 6\text{H}_2\text{O}$ 5%	29%	69%	84%
DIPEA 1.5eq	$\text{NiCl}_2 \cdot 6\text{H}_2\text{O}$ 2%	28%	65%	79%
DIPEA 1.5eq	$\text{NiCl}_2 \cdot 6\text{H}_2\text{O}$ 1%	21%	48%	68%
TEA 1.5eq	$\text{NiBr}_2 \cdot 3\text{H}_2\text{O}$ 5%	51%	77%	86%
TEA 1.5eq	$\text{NiBr}_2 \cdot 3\text{H}_2\text{O}$ 2%	50%	78%	86%
TEA 1.5eq	$\text{NiBr}_2 \cdot 3\text{H}_2\text{O}$ 1%	36%	65%	77%
TEA 1.5eq	$\text{NiCl}_2 \cdot 6\text{H}_2\text{O}$ 5%	36%	68%	82%
TEA 1.5eq	$\text{NiCl}_2 \cdot 6\text{H}_2\text{O}$ 2%	31%	64%	81%
TEA 1.5eq	$\text{NiCl}_2 \cdot 6\text{H}_2\text{O}$ 1%	43%	70%	78%

Figure S2.6. Effect of nickel salts and added base.



Base	<sup>19</sup> F-NMR Conversion		
	1 hr	2 hr	3 hr
morpholine 0.0eq	-----	-----	55%
morpholine 1.0eq	52%	75%	84%
morpholine 1.5eq	65%	85%	93%
morpholine 1.8eq	63%	86%	94%
morpholine 2.0eq	66%	90%	94%
DIPEA 1.5eq	45%	79%	85%
DIPEA 1.8eq	27%	66%	83%
DIPEA 2.0eq	23%	60%	81%
TEA 1.5eq	51%	77%	86%
TEA 1.8eq	50%	78%	87%

Figure S2.7. Effect of base loading.

### 3. Photoreactor Development

This C-N coupling reaction utilizes a high radiant flux setup to achieve reduced reaction times. To this end, a photoreactor was developed (Fig. S2.8) that makes use of industrial strength light-emitting diodes (LEDs) which provide high radiant flux at 365 nm or 405 nm. Such powerful LEDs produce enough heat that active cooling is needed both to protect the LED and ensure that its emission profile remains constant throughout the reaction. To facilitate this, the LEDs were mounted to a metal core printed circuit board (MCPCB) which in turn is mounted to an aluminum heatsink. The MCPCB (b) enables efficient heat transfer from the LED to the heatsink (c). This heatsink is then actively cooled by a 60mm computer fan (d). In addition, the reaction chamber is separately cooled by a 40mm computer fan (a) to allow for consistent reaction conditions. This chamber also has a reflective interior surface coating (e) consisting of aluminum tape to maximize reflection of emitted light back to the reaction vial. A removable vial holder (f) ensures consistent vial placement 5 mm from the LED and allows for irradiation of 0.5 dram, 1.5 dram, and 20 mL vials. Lastly, the LED/MCPCB mounted to the heatsink/fan assembly forms a modular block (g) which allows for facile exchange of LEDs with differing emission wavelengths. The reactor is constructed from commercially available parts (Table S2.1) with the exception of the reaction chamber and vial holder (Fig. S2.9).

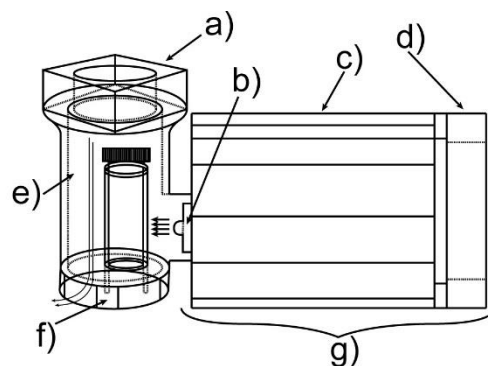


Figure S2.8. A schematic of the photoreactor.

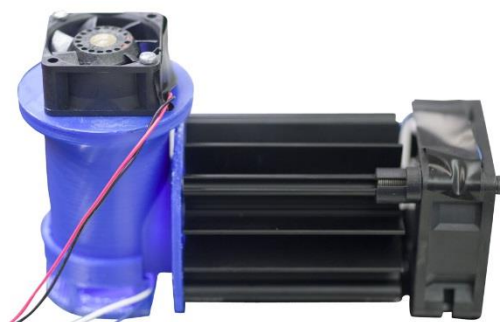


Figure S2.9. A photograph of the photoreactor with 365nm LED turned on and 0.5 dram vial holder attached.

Table S2.1. Parts needed for photoreactor construction are listed by manufacturer with specifications and part numbers.

Part	Source	Manufacturer	Specifications	Part Number
365 nm LED	commercial	LED Engin	3.3W radiant flux at 700 mA, 15.5 V	LZ4-04UV00
405 nm LED	commercial	LED Engin	4.1W radiant flux at 700 mA, 15.5 V	LZ4-00UB00
60 mm fan	commercial	Delta Electronics	51.7 cfm airflow at 750 mA, 12 V	QFR-0612DH-B
40 mm fan	commercial	Delta Electronics	20.56 cfm airflow at 430 mA, 12 V	THA0412AD
Fan power supply	commercial	Mean Well	12 V, 240 W, switching	HLG-240H-12
LED power supply	commercial	Cincon	18 V, 150 W, switching	TRH150A180
LED driver	commercial	LEDdynamics	Output: Input V – 2.5 V, 700 mA	3023-D-N-700
Heatsink	commercial	Wakefield	2.75" diameter, 3" thick aluminum	882-300AB
Reactor chamber	3D-printed	N/A	Fits 40 mm fan, 65 mm heatsink	N/A
Vial Holder	3D-printed	N/A	.5 dram, 1.5 dram, or 20mL vials	N/A

The vial holder, reactor body, and fan adapter parts were designed in-house using Autodesk Inventor software and 3D-printed using stereolithography with a Form2 printer (FormLabs) or fused filament fabrication with a Creator Pro (Flashforge). Vial position in the reaction chamber was optimized by 3D-printing vial holders with distances of 5 mm, 10 mm, and 15 mm from the



LED emitter surface to the vial. The 5 mm position yielded higher NMR conversion after 1 hour compared to other distances under standard reaction conditions on a 0.2 mmol scale (Fig. S10).

All reactions reported in the main text were performed at the 5 mm irradiation distance.

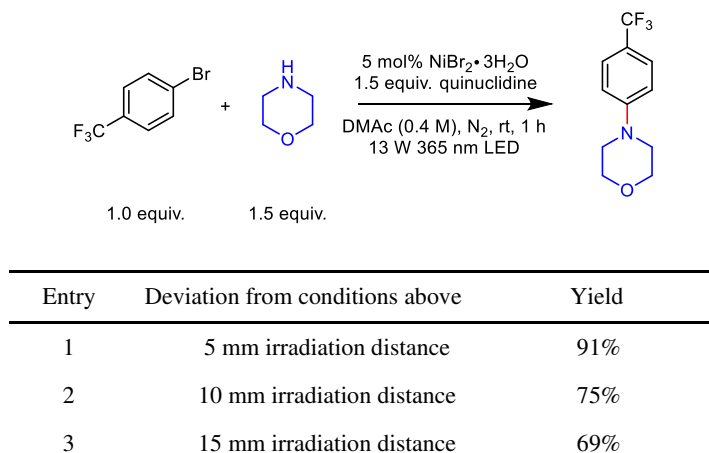


*Figure S2.10. The model reaction was performed on a 0.2 mmol scale (half scale compared to other reported reactions) with varying irradiation distances. In the main text, at 0.4 mmol scale 72% yield was achieved after 1 hour at 5mm irradiation distance. Yields were determined by <sup>19</sup>F NMR.*

Temperature monitoring of the reaction was performed by inserting a type-K thermocouple (VWR) through a septum into a 0.5 dram vial equipped with a stir bar and 1 mL DMAc to simulate reaction conditions. The temperature inside the vial was initially 23.9°C prior to irradiation. During irradiation, the temperature varied from 27.6-28.1°C over the course of 3 hours (Fig. S2.11).



*Figure S2.11. Temperature Monitoring Setup. A 0.5 dram vial equipped with a stir bar and 1 mL DMAc was monitored via a type K thermocouple inserted through the septum (left) and sealed with Parafilm. The vial was placed in the photoreactor as shown (right) and irradiated for 3 hours. The photo shown is before irradiation.*

#### **4. UV-Visible Spectroscopy**

UV-visible spectroscopy was performed for each reaction component and combination of reaction components using a Cary 5000 spectrophotometer (Agilent Technologies). Morpholine and 4-bromobenzotrifluoride (4-BrBzCF<sub>3</sub>) are both colorless liquids without significant molar absorptivity at wavelengths greater than 300 nm (Fig. S2.12) at the concentrations present in the C-N coupling reaction mixture.

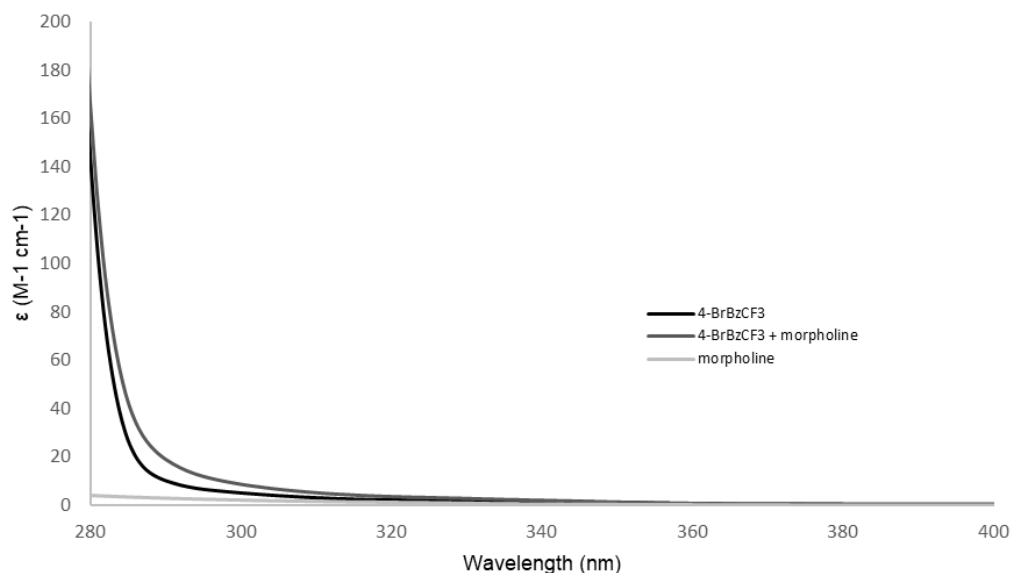


Figure S2.12. Molar absorptivity vs. wavelength for 4-bromobenzotrifluoride and morpholine individually and combined in DMAc, 0.4 M in 4-bromobenzotrifluoride and 1.4 M in morpholine.

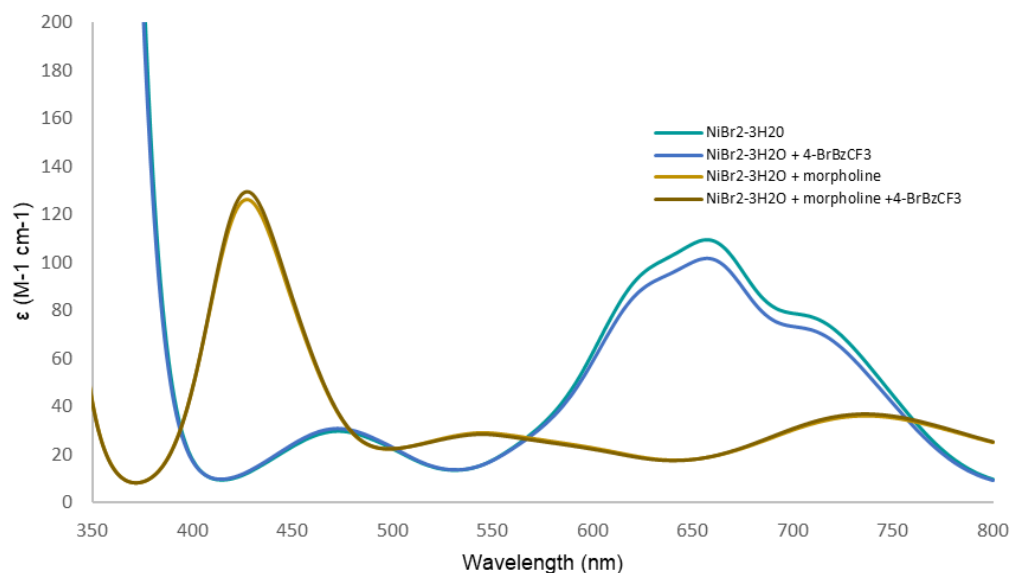


Figure S2.13. Molar absorptivity vs. wavelength for NiBr<sub>2</sub>·3H<sub>2</sub>O and its combinations with 4-bromobenzotrifluoride and morpholine in DMAc.

UV-visible spectroscopy was also performed for NiBr<sub>2</sub>·3H<sub>2</sub>O alone and in combination with 4-BrBzCF<sub>3</sub> and morpholine. NiBr<sub>2</sub>·3H<sub>2</sub>O has a distinctive absorption profile which was not altered with addition of 4-BrBzCF<sub>3</sub>. However, upon addition of morpholine, the  $\lambda_{max}$  was blue-shifted from 657 nm to 427 nm (Fig. S2.13).

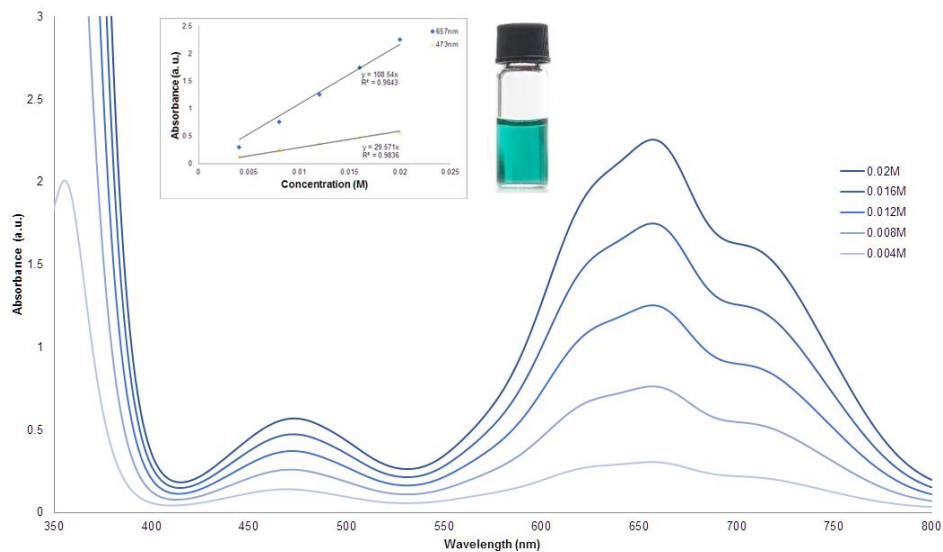


Figure S2.14. Absorption spectra of  $\text{NiBr}_2 \cdot 3\text{H}_2\text{O}$  at concentrations ranging from 0.02 – 0.004 M in DMAC. Inset: a photo of the solution and linear regressions at 657 nm and 473 nm.

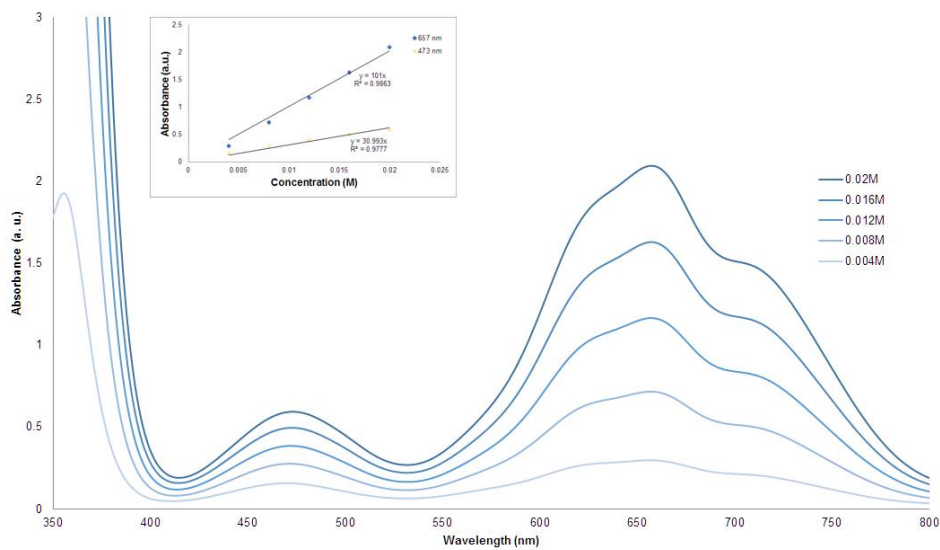


Figure S2.15. Absorption spectra of  $\text{NiBr}_2 \cdot 3\text{H}_2\text{O} + 4\text{-BrBzCF}_3$  at concentrations ranging from 0.02 – 0.004 M ( $\text{NiBr}_2 \cdot 3\text{H}_2\text{O}$ ) and 0.4 – 0.08 M ( $4\text{-BrBzCF}_3$ ) in DMAC. Inset: linear regressions at 657 nm and 473 nm.

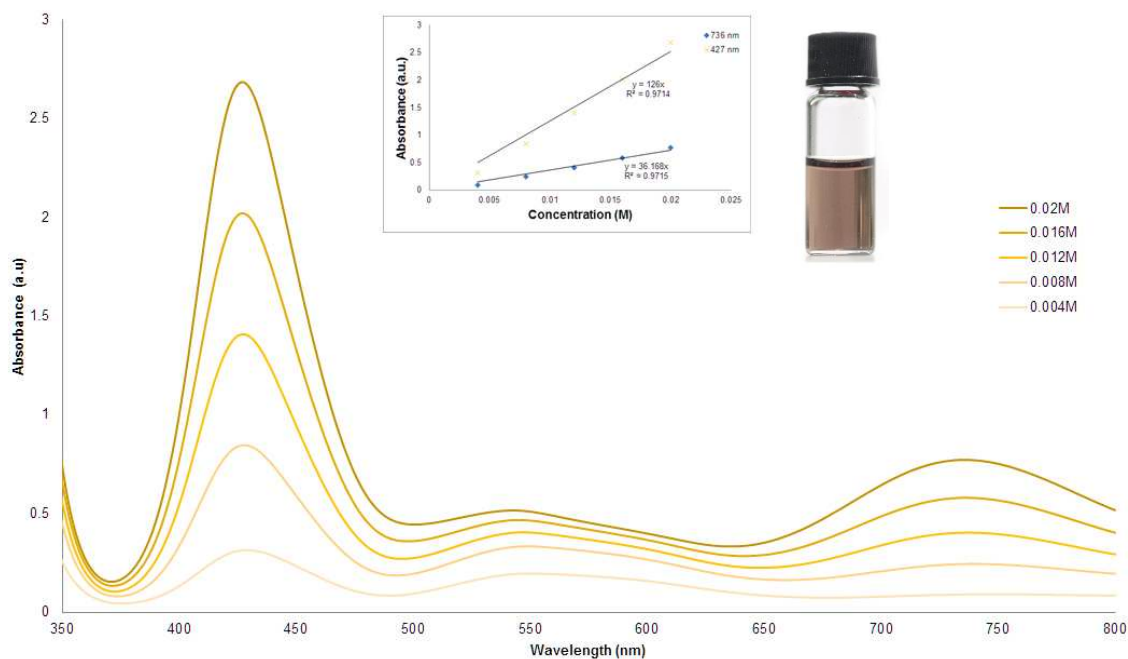


Figure S2.16. Absorption spectra of  $\text{NiBr}_2 \cdot 3\text{H}_2\text{O}$  + morpholine at concentrations ranging from 0.02 – 0.004 M ( $\text{NiBr}_2 \cdot 3\text{H}_2\text{O}$ ) and 1.4 – 0.28 M (morpholine) in DMAc. Inset: a photo of the mixture and linear regressions at 736 nm and 427 nm.

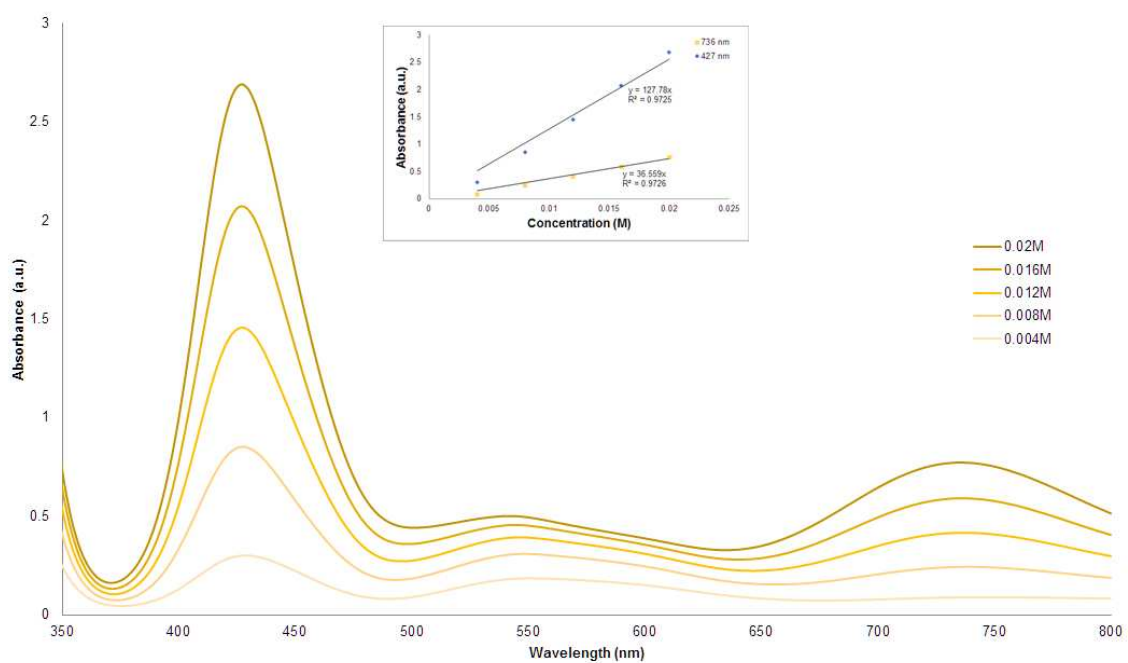
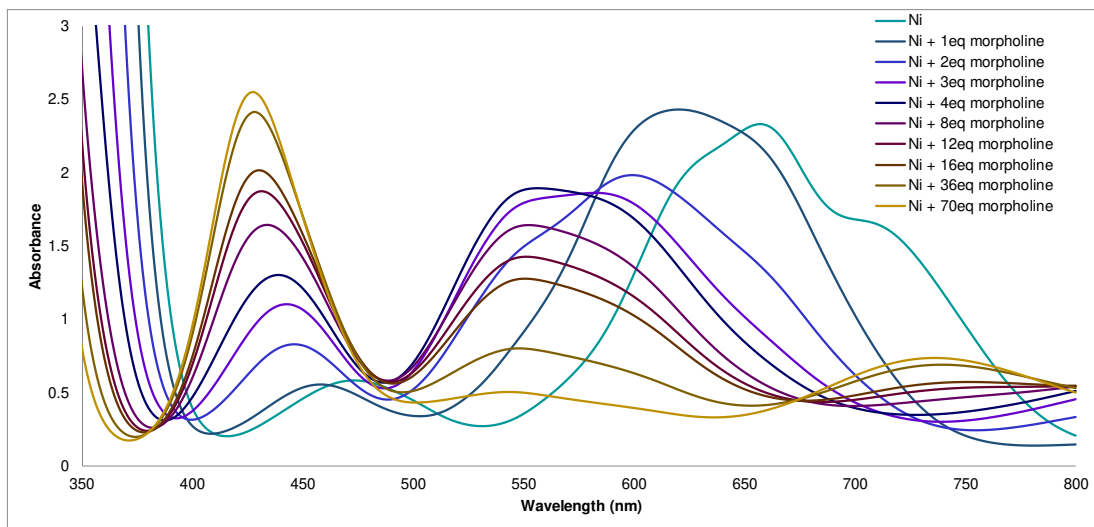


Figure S2.17. Absorption spectra of  $\text{NiBr}_2 \cdot 3\text{H}_2\text{O}$  + morpholine + 4- $\text{BrBzCF}_3$  at concentrations ranging from 0.02 – 0.004 M ( $\text{NiBr}_2 \cdot 3\text{H}_2\text{O}$ ), 1.4 – 0.28 M (morpholine), and 0.4-0.08 M (4- $\text{BrBzCF}_3$ ) in DMAc. Inset: linear regressions at 736 nm and 427 nm.

Molar absorptivity for each major peak and secondary peak of each combination were calculated according to Beer's Law (Table S2.2) with 5 data points used for each reported value (Fig. S2.13-S2.17). The  $R^2$  coefficient of determination is also reported for each peak.

*Table S2. Molar absorptivity for the most prominent peaks of each reagent combination. Data was extracted from spectra collected for 5 concentrations ranging from 0.02 - 0.008 M in  $\text{NiBr}_2 \cdot 3\text{H}_2\text{O}$ .*

Solution	$\lambda_{\text{max}}$ (nm)	$\lambda_2$ (nm)	$\epsilon_{\text{max}}$ ( $\text{s}^{-1}\text{M}^{-1}$ )	$\epsilon_2$ ( $\text{s}^{-1}\text{M}^{-1}$ )	$R^2_{\text{max}}$	$R^2_2$
$\text{NiBr}_2 \cdot 3\text{H}_2\text{O}$	657	473	109	30	.984	.984
$\text{NiBr}_2 \cdot 3\text{H}_2\text{O}$ + morpholine	427	736	126	36	.971	.971
$\text{NiBr}_2 \cdot 3\text{H}_2\text{O}$ + 4-BrBzCF <sub>3</sub>	657	473	101	31	.986	.977
$\text{NiBr}_2 \cdot 3\text{H}_2\text{O}$ + morpholine + 4-BrBzCF <sub>3</sub>	427	736	128	37	.973	.973



*Figure S2.18. Absorption spectra of  $\text{NiBr}_2 \cdot 3\text{H}_2\text{O}$  + morpholine at concentrations ranging from 0.02 M ( $\text{NiBr}_2 \cdot 3\text{H}_2\text{O}$ ), 0.02 M – 1.40 M (morpholine, 1 equiv. to 70 equiv. relative to Ni) in DMAc.*

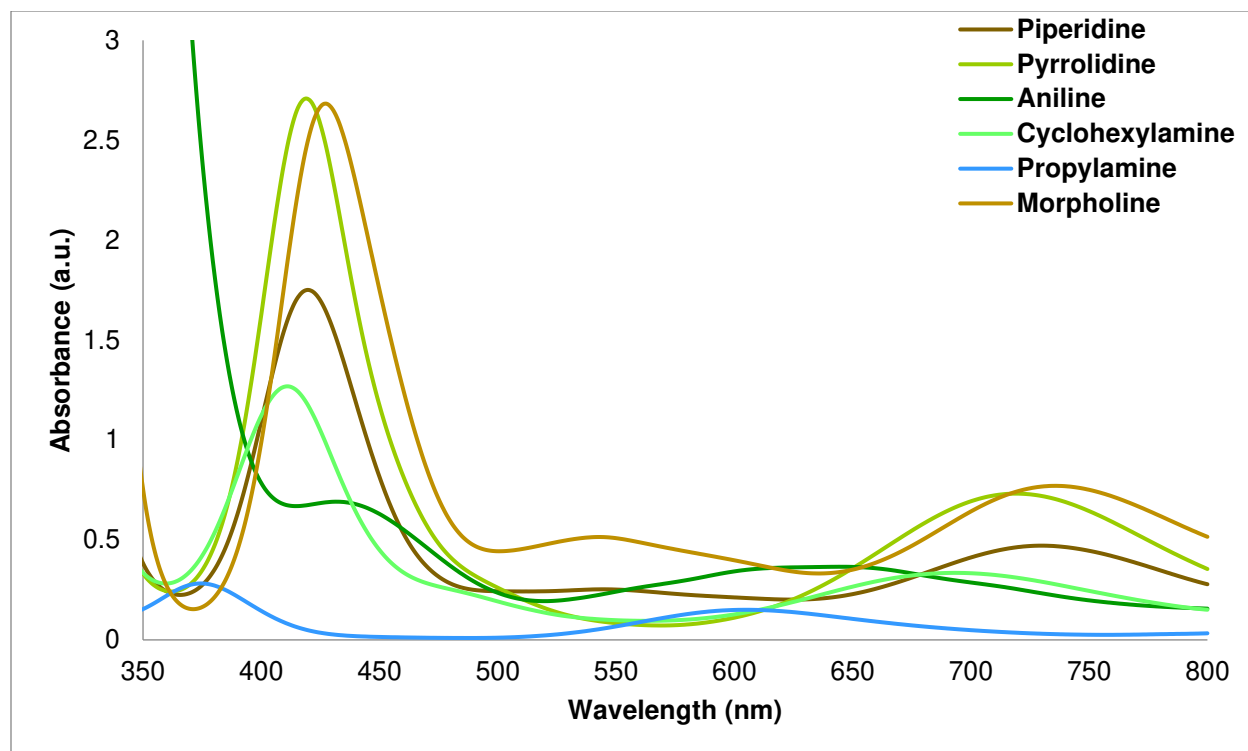


Figure S2.19. UV-visible absorption spectra of  $[\text{NiBr}_2(\text{amine})_n]$  complexes are plotted for 6 amines in DMAc. Each solution was 0.02 M in  $\text{NiBr}_2 \cdot 3\text{H}_2\text{O}$  and 1.4 M in amine.

The spectra of  $[\text{NiBr}_2(\text{morpholine})_n]$ ,  $[\text{NiBr}_2(\text{pyrrolidine})_n]$ , and  $[\text{NiBr}_2(\text{piperidine})_n]$  show similar curve shapes and  $\lambda_{\text{max}} = 427 \text{ nm}$ ,  $\lambda_{\text{max}} = 419 \text{ nm}$ , and  $\lambda_{\text{max}} = 420 \text{ nm}$ , respectively (Fig. S2.19). This appears characteristic of Ni-amine complexes with secondary amines. With primary amines, the  $\lambda_{\text{max}}$  is blue-shifted somewhat. The spectra of  $[\text{NiBr}_2(\text{cyclohexylamine})_n]$  and  $[\text{NiBr}_2(\text{propylamine})_n]$  showed  $\lambda_{\text{max}} = 411 \text{ nm}$  and  $\lambda_{\text{max}} = 375 \text{ nm}$ , respectively. The spectrum of the cyclohexylamine complex shares characteristics of both primary and secondary Ni-amine complexes in terms of how blue-shifted the  $\lambda_{\text{max}}$  is and the presence and location of secondary peaks. The  $[\text{NiBr}_2(\text{aniline})_n]$  complex shows a strikingly different absorption spectrum.

## 5. Fluorimetry

Spectrofluorometer FS5 (Edinburgh Instruments) was used to monitor the emission of the nickel-amine complex (Fig. S2.20). A solution of 0.02 M  $\text{NiBr}_2 \cdot 3\text{H}_2\text{O}$  in DMAc was prepared in a glovebox in a 1 cm quartz cuvette, capped with a septum screw cap, and the seal was reinforced

with Parafilm. Morpholine was degassed by sparging with N<sub>2</sub> for 30 minutes and added to the cuvette via syringe under N<sub>2</sub> to make a 1.4 M solution. The resulting mixture was equal in concentration to the C-N coupling reaction conditions described in this work. This mixture was excited at 365 nm with a Xenon lamp and emission was scanned from 375-800 nm. All fluorescence measurements were corrected internally with a reference detector. A sharp emission peak at 386 nm and a broad emission peak at 484 nm were observed (Fig. S2.20).

Next, excitation wavelength was varied from 240nm to 440nm, monitoring emission intensity at 484 nm ( $\lambda_{\text{max,emission}}$  determined in Fig. S2.20). Notably, the emission intensity (at 484 nm) peaks at excitation wavelength of 359 nm, which is within the range of the emission spectrum for the 365 nm LED used in C-N coupling reactions (Fig. S2.21). This suggests that 365 nm LED is an optimum light source for the C-N coupling reaction and might explain the slower reaction rate at 405 nm irradiation.

In addition, a Stern-Volmer quenching study was attempted by introducing 4-bromobenzotrifluoride, degassed by sparging with N<sub>2</sub>, in increments of 0.01 eq (Fig. S2.22). While quenching was not observed, the shoulder of the  $\lambda_{\text{max}} = 484$  nm emission peak grew in height and a new side peak appeared at  $\lambda = 524$  nm. Thus, addition of aryl halide altered the emission of the Ni-amine complex. Work is underway to determine the structural change that underlies the formation of this new emission peak.



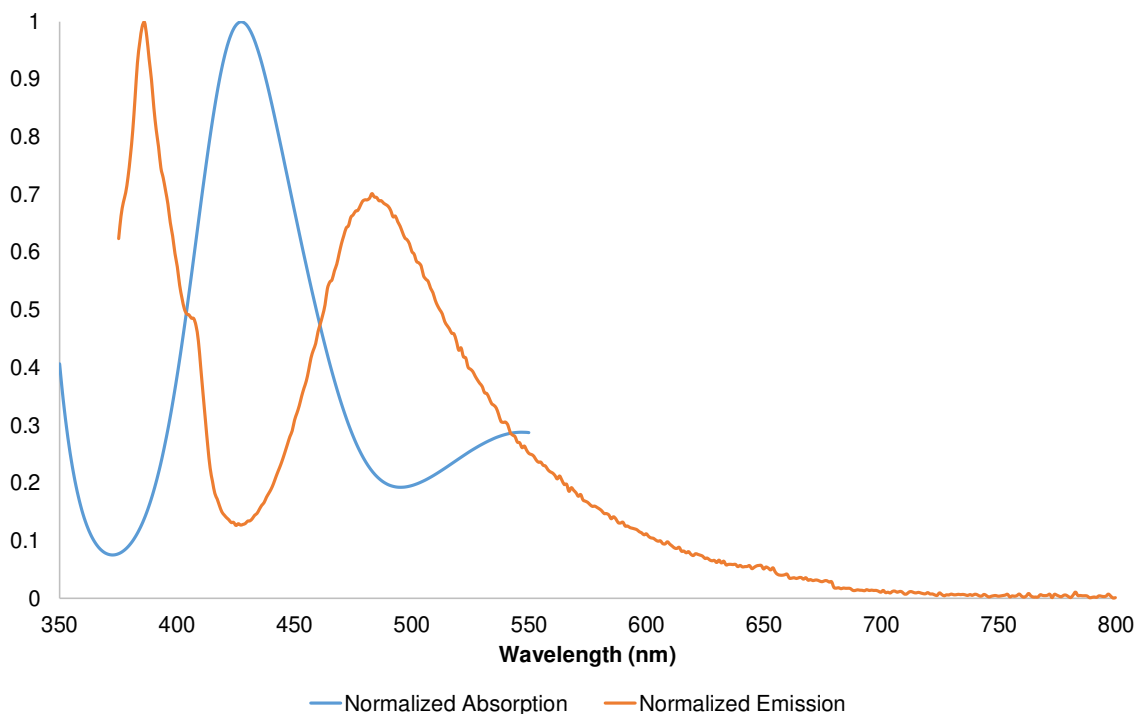


Figure S2.20. Normalized UV-vis absorption and emission spectrums of nickel-morpholine complex. 0.02 M of  $\text{NiBr}_2 \cdot 3\text{H}_2\text{O}$  and 1.4 M of morpholine were dissolved in DMAc. For the emission spectrum, the complex was excited at 365 nm and emission was monitored from 375-800 nm (orange trace).

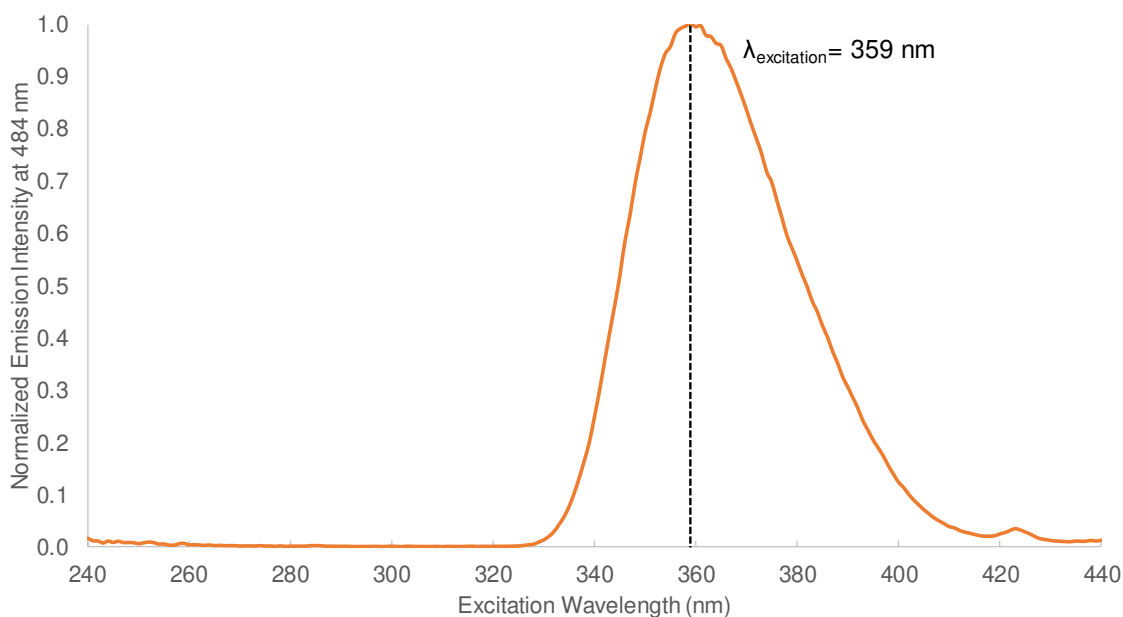


Figure S2.21. Normalized emission intensity (at  $\lambda = 484$  nm) as a function of excitation wavelength. 0.02 M of  $\text{NiBr}_2 \cdot 3\text{H}_2\text{O}$  and 1.4 M of morpholine were dissolved in DMAc. The emission intensity at  $\lambda = 484$  nm is maximum when excitation source at 359 nm is used.

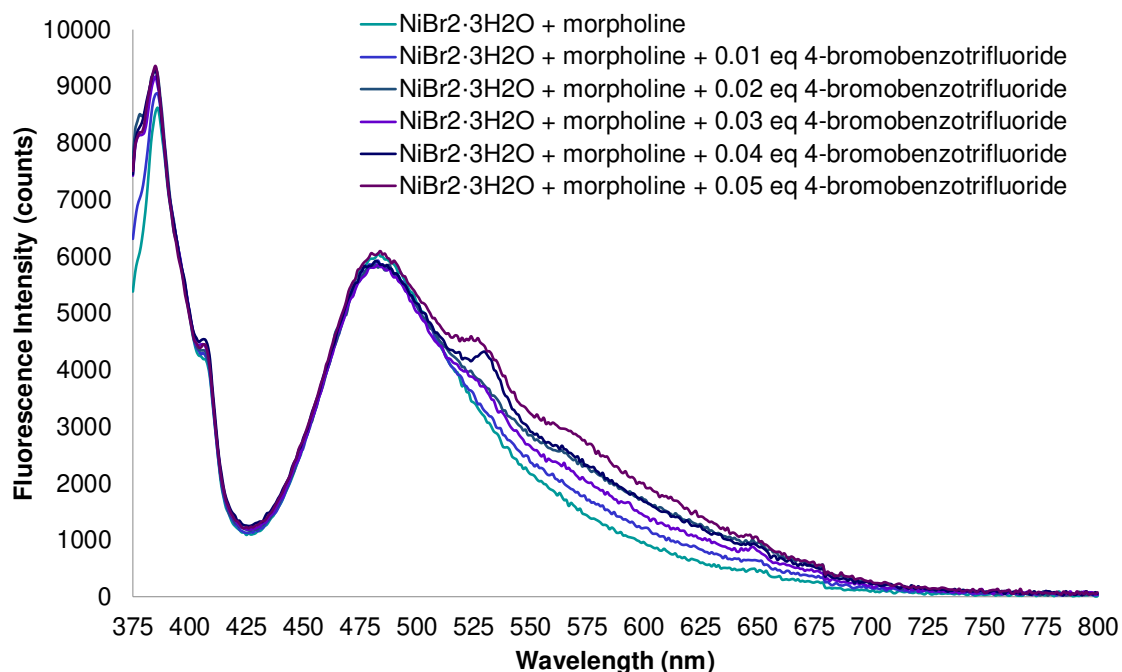


Figure S2.22. Emission spectrum as a function of increasing 4-bromobenzotrifluoride concentration. 0.02 M of  $\text{NiBr}_2 \cdot 3\text{H}_2\text{O}$  and 1.4 M of morpholine were dissolved in DMAc. 4-bromobenzotrifluoride was increasingly added from 0.004M (0.01 eq) to 0.020M (0.05 eq).

## 6. Kinetic Isotope Effect

The following second order rate expression was solved numerically by the Runge–Kutta RK4 method to obtain the observed second order rate constant  $k_{\text{obs}}$  (Fig. S23 and S24).

A = amine; B = aryl halide; C = C-N coupled product.

$$\frac{d[A]}{dt} = -2k_{\text{obs}}[A][B], [A]_0 = 1.4M$$

The factor of 2 here accounts for the consumption of the amine as both the substrate and base to neutralize the produced acid.

$$\frac{d[B]}{dt} = -k_{obs}[A][B], [B]_0 = 0.4M$$

$$\frac{d[C]}{dt} = k_{obs}[A][B], [C]_0 = 0.0M$$

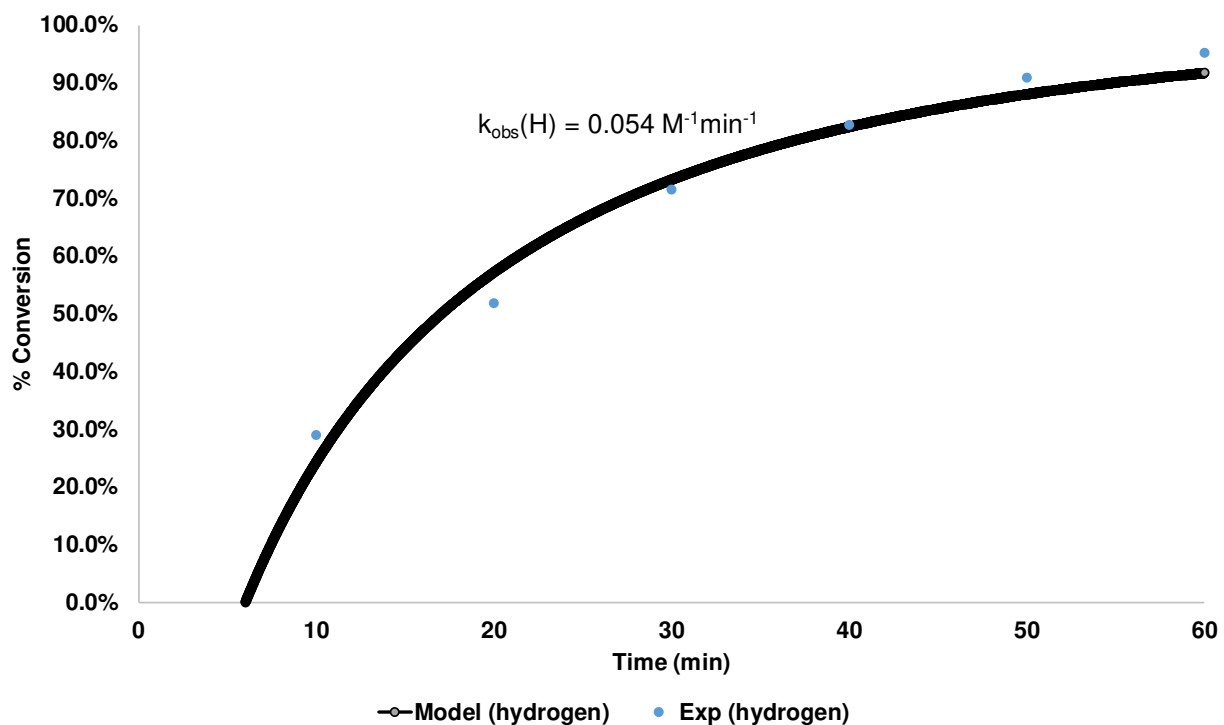


Figure S2.23. Reactions conditions: 1.0 equiv. of 4-bromobenzotrifluoride (0.4 mmol), 3.5 equiv. of piperidine (H), 5 mol% NiBr<sub>2</sub>•3H<sub>2</sub>O and irradiation at 365 nm. The observed rate constant ( $k_{obs}$ ) was determined by solving the second order rate equation model via numerical integration (RK4 method, time step = 0.01 min). An inhibition period of 6 min was included in the model fitting. The determined rate constant value is  $k_{obs}(H) = 0.054 M^{-1}min^{-1}$ .

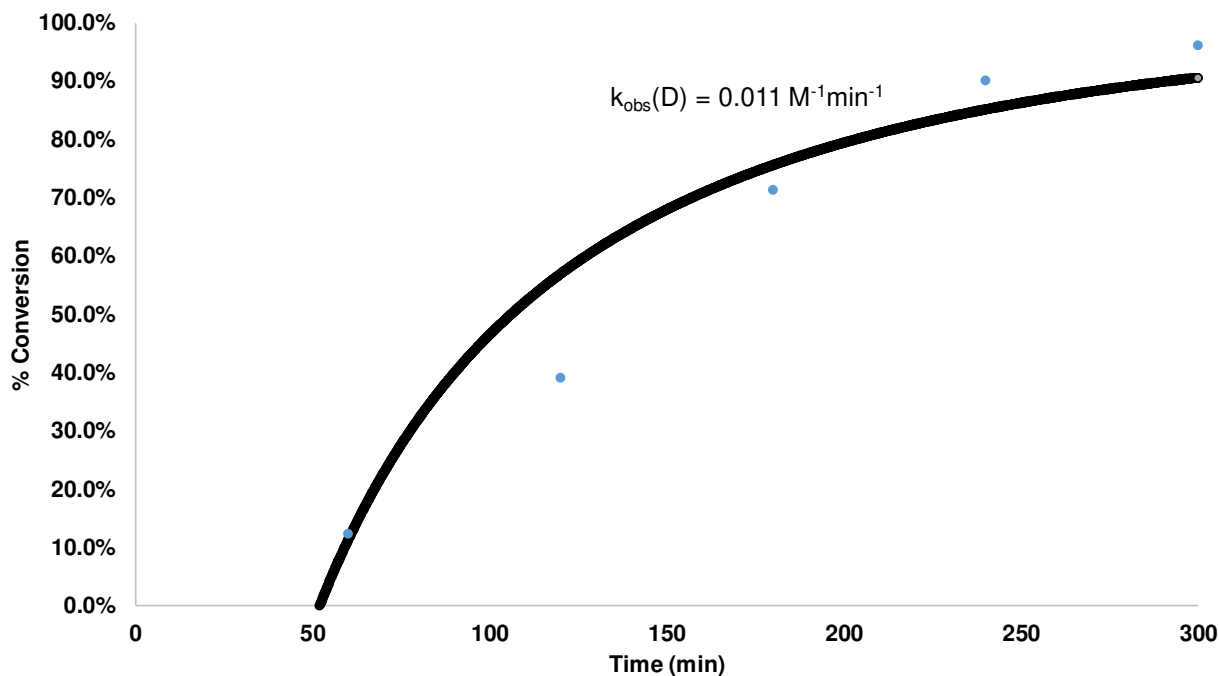


Figure S2.24. Reactions conditions: 1.0 equiv. of 4-bromobenzotrifluoride (0.4 mmol), 3.5 equiv. of piperidine (D), 5 mol%  $\text{NiBr}_2 \cdot 3\text{H}_2\text{O}$  and irradiation at 365 nm. The observed rate constant ( $k_{\text{obs}}$ ) was determined by solving the second order rate equation model via numerical integration (RK4 method, time step = 0.1 min). An inhibition period of 52 min was included in the model fitting. The determined rate constant value is  $k_{\text{obs}}(\text{D}) = 0.011 \text{ M}^{-1}\text{min}^{-1}$ .

## 7. Computational Details

All calculations were performed using computational chemistry software package Gaussian 09 ver. D01. We acknowledge the use of computational resources provided by the XSEDE - Comet supercomputer (grant number CHE 160041).

Geometries of all molecular structures were optimized at the uM06/6-31+G(d,p)/CPCM-DMAc level of theory followed by frequency calculations to obtain zero point energy (ZPE) corrections, thermal corrections, and entropic TS terms using ideal gas approximations. The obtained Gibbs free energy,  $G^{0*}(298\text{K}, 1\text{atm})$ , by default has a standard reference state of 298.15K and 1 atm. However, a standard reference state of 298.15K and 1 mole/liter [ $G^0(298\text{K}, 1\text{M})$ ] is

more relevant to our examined systems as the C-N cross-coupling reactions are carried out in the liquid phase in DMAc.

To obtain the Gibbs free energy with relevant standard state reference,  $G^0(298\text{K}, 1\text{M}) = G^{0*}(298\text{K}, 1\text{atm}) + RT \ln(0.08206T)$ , where  $R$  is the gas constant and  $T$  is the temperature.  $\Delta G^0(298\text{K}, 1\text{M}) = \Delta G^{0*}(298\text{K}, 1\text{atm})$  when there is no mole change from the reactant to the product. However, for every net mole change  $\Delta G^0(298\text{K}, 1\text{M}) = \Delta G^{0*}(298\text{K}, 1\text{atm}) - 1.89$  kcal/mol.

At the converged geometries, single point calculations at uM06/6-311+G(d,p)/CPCM-DMAc were performed; the various corrections and entropic TS terms from uM06/6-31+G(d,p) calculations were then applied to the energy obtained with uM06/6-311+G(d,p).

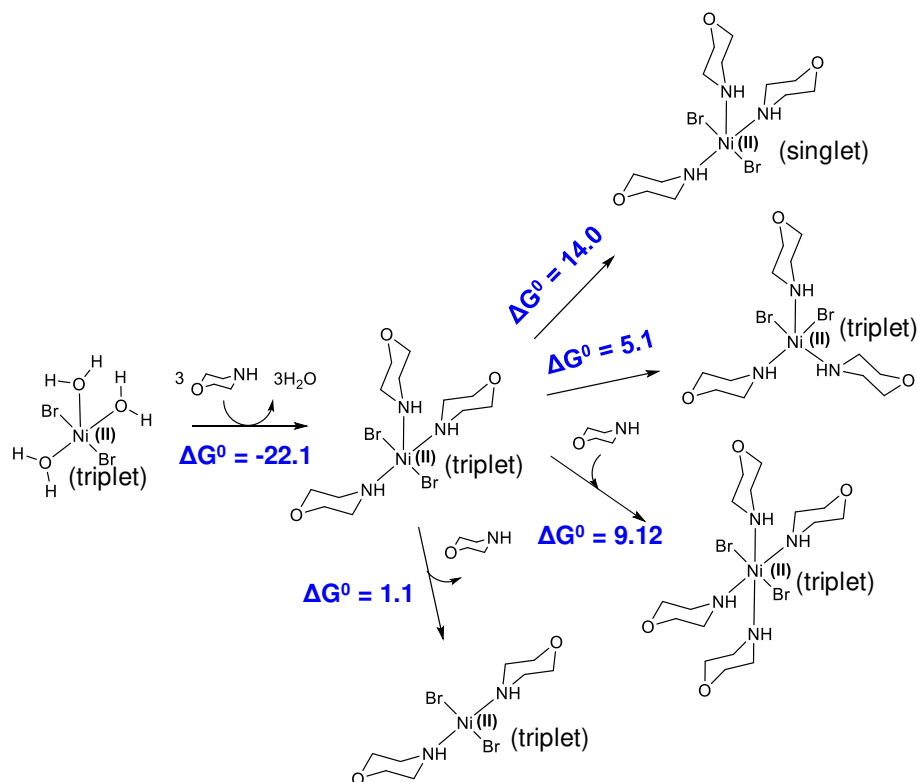
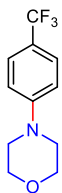


Figure S2.25. Stability of various nickel-amine complexes; unit in kcal/mol.

## 8. Characterizations



### 4-(4-(trifluoromethyl)phenyl)morpholine (1a)

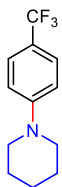
General procedure A was followed using 4-bromobenzotrifluoride as the aryl halide, and morpholine as the amine. The reaction was run at room temperature for 3 hours. Purification was done by flash chromatography on silica gel, eluting with a gradient of 0-15% EtOAc/hexanes to give the product as a white solid (80.2 mg, 87%). NMR data matched previously reported spectra.<sup>1-2</sup>

<sup>1</sup>H NMR (400 MHz, Chloroform-*d*)  $\delta$  7.50 (d,  $J$  = 8.4 Hz, 2H), 6.92 (d,  $J$  = 8.8 Hz, 2H), 3.86 (t,  $J$  = 4.8 Hz, 4H), 3.24 (t,  $J$  = 5.2 Hz, 4H).

<sup>13</sup>C NMR (101 MHz, Chloroform-*d*)  $\delta$  153.5, 126.6 (q,  $J_{C-F}$  = 3.8 Hz), 124.8 (q,  $J_{C-F}$  = 271.7 Hz), 121.1 (q,  $J_{C-F}$  = 32.9 Hz), 114.4, 66.8, 48.3.

<sup>19</sup>F NMR (376 MHz, Chloroform-*d*)  $\delta$  -61.4 (s, 3F).

HRMS (DART-TOF): calculated for C<sub>11</sub>H<sub>13</sub>F<sub>3</sub>NO ([M+H]<sup>+</sup>) 232.0944, found 232.0943.



### 1-(4-(trifluoromethyl)phenyl)piperidine (2)

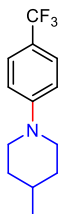
General procedure A was followed using 4-bromobenzotrifluoride as the aryl halide, and piperidine as the amine. The reaction was run at room temperature for 3 hours. Purification was done by flash chromatography on silica gel, eluting with a gradient of 0-15% EtOAc/hexanes to give the product as a pale yellow oil (74.5 mg, 81%). NMR data matched previously reported spectra.<sup>3</sup>

<sup>1</sup>H NMR (400 MHz, Chloroform-*d*)  $\delta$  7.46 (d,  $J$  = 8.7 Hz, 2H), 6.92 (d,  $J$  = 8.7 Hz, 2H), 3.27 (t,  $J$  = 5.2 Hz, 4H), 1.77 – 1.58 (m, 6H).

<sup>13</sup>C NMR (101 MHz, Chloroform-*d*)  $\delta$  154.0, 126.5 (q,  $J_{C-F}$  = 3.7 Hz), 124.9 (q,  $J_{C-F}$  = 271.6 Hz), 119.7 (q,  $J_{C-F}$  = 32.7 Hz), 114.7, 49.4, 25.6, 24.4.

<sup>19</sup>F NMR (376 MHz, Chloroform-*d*)  $\delta$  -61.2 (s, 3F).

HRMS (DART-TOF): calculated for C<sub>12</sub>H<sub>15</sub>F<sub>3</sub>N ([M+H]<sup>+</sup>) 231.1151, found 230.1162.



### 4-methyl-1-(4-(trifluoromethyl)phenyl)piperidine (3)

General procedure A was followed using 4-bromobenzotrifluoride as the aryl halide, and 4-methylpiperidine as the amine. The reaction was run at room temperature for 3 hours. Purification was done by flash

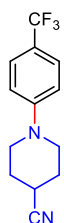
chromatography on silica gel, eluting with a gradient of 0-15% EtOAc/hexanes to give the product as a white solid (84.4 mg, 87%).

$^1\text{H}$  NMR (400 MHz, Chloroform-*d*)  $\delta$  7.46 (d,  $J$  = 8.4 Hz, 2H), 6.92 (d,  $J$  = 8.6 Hz, 2H), 3.83 – 3.72 (m, 2H), 2.80 (td,  $J$  = 12.5, 2.7 Hz, 2H), 1.80 – 1.69 (m, 2H), 1.67 – 1.49 (m, 1H), 1.39 – 1.23 (m, 2H), 0.99 (d,  $J$  = 6.5 Hz, 3H).

$^{13}\text{C}$  NMR (101 MHz, Chloroform-*d*)  $\delta$  153.7, 126.5 (q,  $J_{\text{C-F}}$  = 3.7 Hz), 125.0 (q,  $J_{\text{C-F}}$  = 271.4 Hz), 119.6 (q,  $J_{\text{C-F}}$  = 32.7 Hz), 114.7, 48.8, 33.8, 30.9, 22.0.

$^{19}\text{F}$  NMR (376 MHz, Chloroform-*d*)  $\delta$  -61.2 (s, 3F).

HRMS (DART-TOF): calculated for  $\text{C}_{13}\text{H}_{17}\text{F}_3\text{N}$  ( $[\text{M}]$ ) 244.1308, found 244.1307.



#### 1-(4-(trifluoromethyl)phenyl)piperidine-4-carbonitrile (4)

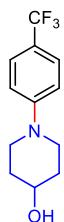
General procedure A was followed using 4-bromobenzotrifluoride as the aryl halide, and piperidine-4-carbonitrile as the amine. The reaction was run at room temperature for 3 hours. Purification was done by flash chromatography on silica gel, eluting with a gradient of 0-15% EtOAc/hexanes to give the product as a white solid (89.7 mg, 88%). NMR data matched previously reported spectra.<sup>3</sup>

$^1\text{H}$  NMR (400 MHz, Chloroform-*d*)  $\delta$  7.49 (d,  $J$  = 8.6 Hz, 2H), 6.93 (d,  $J$  = 8.5 Hz, 2H), 3.57 – 3.46 (m, 2H), 3.28 – 3.17 (m, 2H), 2.85 (tt,  $J$  = 8.0, 4.3 Hz, 1H), 2.12 – 1.91 (m, 4H).

$^{13}\text{C}$  NMR (101 MHz, Chloroform-*d*)  $\delta$  153.1, 126.6 (q,  $J_{\text{C-F}}$  = 3.7 Hz), 124.7 (q,  $J_{\text{C-F}}$  = 272.0 Hz), 121.3 (q,  $J_{\text{C-F}}$  = 33.1 Hz), 121.2, 115.4, 46.9, 28.3, 26.3.

$^{19}\text{F}$  NMR (376 MHz, Chloroform-*d*)  $\delta$  -61.5 (s, 3F).

HRMS (DART-TOF): calculated for  $\text{C}_{13}\text{H}_{14}\text{F}_3\text{N}_2$  ( $[\text{M}+\text{H}]^+$ ) 255.1104, found 255.1093.



#### 1-(4-(trifluoromethyl)phenyl)piperidin-4-ol (5)

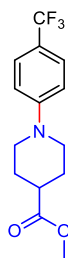
General procedure A was followed using 4-bromobenzotrifluoride as the aryl halide, and 4-hydroxypiperidine as the amine. The reaction was run at room temperature for 3 hours. Purification was done by flash chromatography on silica gel, eluting with a gradient of 0-40% EtOAc/hexanes to give the product as a white solid (82.4 mg, 84%). NMR data matched previously reported spectra.<sup>3</sup>

$^1\text{H}$  NMR (400 MHz, Chloroform-*d*)  $\delta$  7.46 (d,  $J$  = 8.7 Hz, 2H), 6.92 (d,  $J$  = 8.8 Hz, 2H), 3.89 (tt,  $J$  = 8.7, 4.0 Hz, 1H), 3.74 – 3.56 (m, 2H), 3.03 (ddd,  $J$  = 13.0, 9.7, 3.2 Hz, 2H), 2.06 – 1.92 (m, 2H), 1.79 (s, 1H), 1.74 – 1.53 (m, 2H).

$^{13}\text{C}$  NMR (101 MHz, Chloroform-*d*)  $\delta$  153.1, 126.5 (q,  $J_{\text{C-F}}$  = 3.8 Hz), 124.9 (q,  $J_{\text{C-F}}$  = 271.5 Hz), 120.1 (q,  $J_{\text{C-F}}$  = 32.7 Hz), 114.9, 67.7, 46.0, 33.8.

$^{19}\text{F}$  NMR (376 MHz, Chloroform-*d*)  $\delta$  -61.3 (s, 3F).

HRMS (DART-TOF): calculated for  $\text{C}_{12}\text{H}_{15}\text{F}_3\text{NO}$  ( $[\text{M}+\text{H}]^+$ ) 246.1100, found 246.1099.



methyl 1-(4-(trifluoromethyl)phenyl)piperidine-4-carboxylate (6)

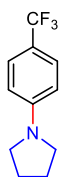
General procedure A was followed using 4-bromobenzotrifluoride as the aryl halide, and methyl 4-piperidinecarboxylate as the amine. The reaction was run at room temperature for 3 hours. Purification was done by flash chromatography on silica gel, eluting with a gradient of 0-15% EtOAc/hexanes to give the product as a white solid (78.8 mg, 69%).

$^1\text{H}$  NMR (400 MHz, Chloroform-*d*)  $\delta$  7.46 (d,  $J$  = 8.7 Hz, 2H), 6.92 (d,  $J$  = 8.6 Hz, 2H), 3.80 – 3.68 (m, 5H), 2.90 (ddd,  $J$  = 12.7, 11.3, 2.9 Hz, 2H), 2.51 (tt,  $J$  = 11.0, 4.0 Hz, 1H), 2.08 – 1.97 (m, 2H), 1.92 – 1.77 (m, 2H).

$^{13}\text{C}$  NMR (101 MHz, Chloroform-*d*)  $\delta$  175.1, 153.4, 126.5 (q,  $J_{\text{C-F}}$  = 3.8 Hz), 124.9 (q,  $J_{\text{C-F}}$  = 271.7 Hz), 120.3 (q,  $J_{\text{C-F}}$  = 32.8 Hz), 115.0, 51.9, 48.0, 40.9, 27.8.

$^{19}\text{F}$  NMR (376 MHz, Chloroform-*d*)  $\delta$  -61.3 (s, 3F).

HRMS (DART-TOF): calculated for  $\text{C}_{14}\text{H}_{17}\text{F}_3\text{NO}_2$  ( $[\text{M}+\text{H}]^+$ ) 288.1206, found 288.1210.



1-(4-(trifluoromethyl)phenyl)pyrrolidine (7)

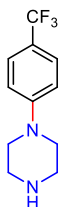
General procedure A was followed using 4-bromobenzotrifluoride as the aryl halide, and pyrrolidine as the amine. The reaction was run at room temperature for 3 hours. Purification was done by flash chromatography on silica gel, eluting with a gradient of 0-15% EtOAc/hexanes to give the product as a white solid (66.0 mg, 77%). NMR data matched previously reported spectra.<sup>1-2</sup>

$^1\text{H}$  NMR (400 MHz, Chloroform-*d*)  $\delta$  7.44 (d,  $J$  = 8.6 Hz, 2H), 6.55 (d,  $J$  = 8.6 Hz, 2H), 3.36 – 3.27 (m, 4H), 2.10 – 1.97 (m, 4H).

$^{13}\text{C}$  NMR (101 MHz, Chloroform-*d*)  $\delta$  149.9, 126.5 (q,  $J_{\text{C-F}}$  = 3.7 Hz), 125.5 (q,  $J_{\text{C-F}}$  = 270.5 Hz), 116.8 (q,  $J_{\text{C-F}}$  = 32.5 Hz), 111.0, 47.7, 25.6.

$^{19}\text{F}$  NMR (376 MHz, Chloroform-*d*)  $\delta$  -60.6 (s, 3F).

HRMS (DART-TOF): calculated for  $\text{C}_{11}\text{H}_{13}\text{F}_3\text{N}$  ( $[\text{M}+\text{H}]^+$ ) 216.0995, found 216.1001.



1-(4-(trifluoromethyl)phenyl)piperazine (8)

General procedure A was followed using 4-bromobenzotrifluoride as the aryl halide, and piperazine as the amine. DMSO was used as the solvent instead of DMAc. The reaction was run at room temperature for 15 hours. Purification was done by flash chromatography on silica gel, eluting with a gradient of 0-20%



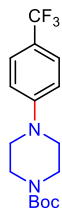
MeOH/DCM to give the product as a pale yellow solid (56.1 mg, 61%). NMR data matched previously reported spectra.<sup>4</sup>

<sup>1</sup>H NMR (400 MHz, Chloroform-*d*) δ 7.47 (d, *J* = 8.5 Hz, 2H), 6.91 (d, *J* = 8.6 Hz, 2H), 3.23 (t, *J* = 4.8 Hz, 4H), 3.02 (t, *J* = 5.0 Hz, 4H), 1.81 (s, 1H)

<sup>13</sup>C NMR (101 MHz, Chloroform-*d*) δ 153.9, 126.5 (q, *J*<sub>C-F</sub> = 3.8 Hz), 124.9 (q, *J*<sub>C-F</sub> = 271.9 Hz), 120.6 (q, *J*<sub>C-F</sub> = 32.6 Hz), 114.6, 49.2, 46.0.

<sup>19</sup>F NMR (376 MHz, Chloroform-*d*) δ -61.4 (s, 3F).

HRMS (DART-TOF): calculated for C<sub>11</sub>H<sub>14</sub>F<sub>3</sub>N<sub>2</sub> ([M+H]<sup>+</sup>) 231.1104, found 231.1101.



*tert*-butyl 4-(4-(trifluoromethyl)phenyl)piperazine-1-carboxylate (9)

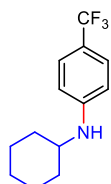
General procedure B was followed using 4-bromobenzotrifluoride as the aryl halide, and *tert*-butyl piperazine-1-carboxylate as the amine. The reaction was run at room temperature for 3 hours. Purification was done by flash chromatography on silica gel, eluting with a gradient of 0-15% EtOAc/hexanes to give the product as a white solid (112.4 mg, 85%). NMR data matched previously reported spectra.<sup>1,3</sup>

<sup>1</sup>H NMR (400 MHz, Chloroform-*d*) δ 7.49 (d, *J* = 8.0 Hz, 2H), 6.92 (d, *J* = 8.4 Hz, 2H), 3.58 (t, *J* = 4.8 Hz, 4H), 3.23 (t, *J* = 5.6 Hz, 4H), 1.49 (s, 9H).

<sup>13</sup>C NMR (101 MHz, Chloroform-*d*) δ 154.8, 153.3, 126.6 (q, *J*<sub>C-F</sub> = 3.7 Hz), 124.8 (q, *J*<sub>C-F</sub> = 271.7 Hz), 121.1 (q, *J*<sub>C-F</sub> = 32.8 Hz), 115.1, 80.2, 48.2, 28.5.

<sup>19</sup>F NMR (376 MHz, Chloroform-*d*) δ -61.4 (s, 3F).

HRMS (DART-TOF): calculated for C<sub>16</sub>H<sub>22</sub>F<sub>3</sub>N<sub>2</sub>O<sub>2</sub> ([M+H]<sup>+</sup>) 331.1628, found 331.1630.



N-cyclohexyl-4-(trifluoromethyl)aniline (10)

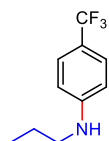
General procedure A was followed using 4-bromobenzotrifluoride as the aryl halide, and cyclohexylamine as the amine. The reaction was run at room temperature for 15 hours. Purification was done by flash chromatography on silica gel, eluting with a gradient of 0-15% EtOAc/hexanes to give the product as a pale yellow solid (68.1 mg, 70%). NMR data matched previously reported spectra.<sup>1,3</sup>

<sup>1</sup>H NMR (400 MHz, Chloroform-*d*) δ 7.38 (d, *J* = 8.5 Hz, 2H), 6.57 (d, *J* = 8.5 Hz, 2H), 3.88 (d, *J* = 7.8 Hz, 1H), 3.38 – 3.20 (m, 1H), 2.13 – 1.96 (m, 2H), 1.86 – 1.72 (m, 2H), 1.73 – 1.59 (m, 1H), 1.47 – 1.32 (m, 2H), 1.32 – 1.07 (m, 3H).

<sup>13</sup>C NMR (101 MHz, Chloroform-*d*) δ 149.9, 126.8 (q, *J*<sub>C-F</sub> = 3.8 Hz), 125.2 (q, *J*<sub>C-F</sub> = 271.1 Hz), 118.2 (q, *J*<sub>C-F</sub> = 32.7 Hz), 112.10, 51.5, 33.3, 25.9, 25.0.

<sup>19</sup>F NMR (376 MHz, Chloroform-*d*) δ -60.9 (s, 3F).

HRMS (DART-TOF): calculated for C<sub>13</sub>H<sub>17</sub>F<sub>3</sub>N ([M+H]<sup>+</sup>) 244.1308, found 244.1293.



N-propyl-4-(trifluoromethyl)aniline (11)

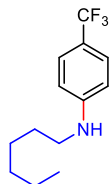
General procedure A was followed using 4-bromobenzotrifluoride as the aryl halide, and propylamine as the amine. The reaction was run at room temperature for 15 hours. Purification was done by flash chromatography on silica gel, eluting with a gradient of 0-15% EtOAc/hexanes to give the product as a pale yellow oil (33.1 mg, 41%). NMR data matched previously reported spectra.<sup>2</sup>

<sup>1</sup>H NMR (400 MHz, Chloroform-*d*)  $\delta$  7.39 (d,  $J$  = 8.4 Hz, 2H), 6.59 (d,  $J$  = 8.5 Hz, 2H), 3.97 (s, 1H), 3.11 (q,  $J$  = 5.2 Hz, 2H), 1.66 (h,  $J$  = 7.2 Hz, 2H), 1.01 (t,  $J$  = 7.4 Hz, 3H).

<sup>13</sup>C NMR (101 MHz, Chloroform-*d*)  $\delta$  151.0, 126.7 (q,  $J_{C-F}$  = 3.7 Hz), 125.2 (q,  $J_{C-F}$  = 271.2 Hz), 118.6 (q,  $J_{C-F}$  = 32.7 Hz), 111.8, 45.4, 22.75, 11.7.

<sup>19</sup>F NMR (376 MHz, Chloroform-*d*)  $\delta$  -60.9 (s, 3F).

HRMS (DART-TOF): calculated for C<sub>10</sub>H<sub>13</sub>F<sub>3</sub>N ([M+H]<sup>+</sup>) 204.0995, found 204.0989.



N-hexyl-4-(trifluoromethyl)aniline (12)

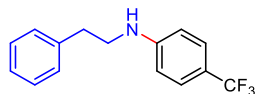
General procedure A was followed using 4-bromobenzotrifluoride as the aryl halide, and hexylamine as the amine. The reaction was run at room temperature for 15 hours. Purification was done by flash chromatography on silica gel, eluting with a gradient of 0-15% EtOAc/hexanes to give the product as a pale yellow oil (55.9 mg, 57%). NMR data matched previously reported spectra.<sup>1</sup>

<sup>1</sup>H NMR (400 MHz, Chloroform-*d*)  $\delta$  7.40 (d,  $J$  = 8.5 Hz, 2H), 6.59 (d,  $J$  = 8.5 Hz, 2H), 3.94 (s, 1H), 3.29 – 2.97 (m, 2H), 1.63 (p,  $J$  = 7.1 Hz, 2H), 1.46 – 1.28 (m, 6H), 1.00 – 0.83 (m, 3H).

<sup>13</sup>C NMR (101 MHz, Chloroform-*d*)  $\delta$  151.0, 126.7 (q,  $J_{C-F}$  = 3.9 Hz), 125.2 (q,  $J_{C-F}$  = 271.2 Hz), 118.5 (q,  $J_{C-F}$  = 32.7 Hz), 111.8, 43.7, 31.7, 29.4, 26.9, 22.8, 14.2.

<sup>19</sup>F NMR (376 MHz, Chloroform-*d*)  $\delta$  -60.9 (s, 3F).

HRMS (DART-TOF): calculated for C<sub>13</sub>H<sub>19</sub>F<sub>3</sub>N ([M+H]<sup>+</sup>) 246.1464, found 246.1462.



N-phenethyl-4-(trifluoromethyl)aniline (13)

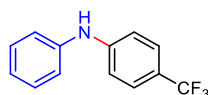
General procedure B was followed using 4-bromobenzotrifluoride as the aryl halide, and phenethylamine as the amine. The reaction was run at room temperature for 15 hours. Purification was done by flash chromatography on silica gel, eluting with a gradient of 0-15% EtOAc/hexanes to give the product as a yellow oil (34.9 mg, 33%). NMR data matched previously reported spectra.<sup>5</sup>

<sup>1</sup>H NMR (400 MHz, Chloroform-*d*)  $\delta$  7.44 (d,  $J$  = 8.5 Hz, 2H), 7.40 – 7.33 (m, 2H), 7.32 – 7.22 (m, 3H), 6.63 (d,  $J$  = 8.5 Hz, 2H), 4.04 (s, 1H), 3.47 (q,  $J$  = 6.6 Hz, 2H), 2.96 (t,  $J$  = 6.9 Hz, 2H).

<sup>13</sup>C NMR (101 MHz, Chloroform-*d*)  $\delta$  150.5, 138.9, 128.89, 128.86, 126.78 (q,  $J_{C-F}$  = 3.9 Hz), 126.77, 125.1 (q,  $J_{C-F}$  = 271.3 Hz), 119.0 (q,  $J_{C-F}$  = 32.8 Hz), 112.1, 44.6, 35.4.

<sup>19</sup>F NMR (376 MHz, Chloroform-*d*)  $\delta$  -61.0 (s, 3F)

HRMS (DART-TOF): calculated for C<sub>15</sub>H<sub>15</sub>F<sub>3</sub>N ([M+H]<sup>+</sup>) 266.1151, found 266.1154.



N-phenyl-4-(trifluoromethyl)aniline (14)

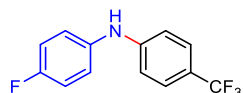
General procedure B was followed using 4-bromobenzotrifluoride as the aryl halide, and aniline as the amine. The reaction was run at room temperature for 15 hours. Purification was done by flash chromatography on silica gel, eluting with a gradient of 0-10% EtOAc/hexanes to give the product as a pale yellow solid (63.8 mg, 67%). NMR data matched previously reported spectra.<sup>1-2</sup>

<sup>1</sup>H NMR (400 MHz, Chloroform-*d*) δ 7.49 (d, *J* = 8.5 Hz, 2H), 7.36 (t, *J* = 8.4 Hz, 2H), 7.16 (d, *J* = 7.2 Hz, 2H), 7.12 – 7.02 (m, 3H), 5.91 (s, 1H).

<sup>13</sup>C NMR (101 MHz, Chloroform-*d*) δ 146.9, 141.3, 129.7, 126.8 (q, *J*<sub>C-F</sub> = 3.9 Hz), 124.8 (q, *J*<sub>C-F</sub> = 271.8 Hz), 123.1, 121.8 (q, *J*<sub>C-F</sub> = 32.8 Hz), 120.2, 115.5.

<sup>19</sup>F NMR (376 MHz, Chloroform-*d*) δ -61.4 (s, 3F).

HRMS (DART-TOF): calculated for C<sub>13</sub>H<sub>11</sub>F<sub>3</sub>N ([M+H]<sup>+</sup>) 238.0838, found 238.0826.



4-fluoro-N-(4-(trifluoromethyl)phenyl)aniline (15)

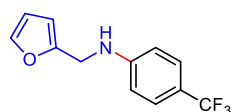
General procedure B was followed using 4-bromobenzotrifluoride as the aryl halide, and 4-Fluoroaniline as the amine. The reaction was run at room temperature for 15 hours. Purification was done by flash chromatography on silica gel, eluting with a gradient of 0-10% EtOAc/hexanes to give the product as a yellow oil (46.9 mg, 46%).

<sup>1</sup>H NMR (400 MHz, Chloroform-*d*) δ 7.46 (d, *J* = 8.5 Hz, 2H), 7.18 – 7.08 (m, 2H), 7.08 – 6.99 (m, 2H), 6.93 (d, *J* = 8.4 Hz, 2H), 5.79 (s, 1H).

<sup>13</sup>C NMR (101 MHz, Chloroform-*d*) δ 159.3 (d, *J*<sub>C-F</sub> = 243.6 Hz), 147.7, 137.1 (d, *J*<sub>C-F</sub> = 2.7 Hz), 126.9 (q, *J*<sub>C-F</sub> = 3.9 Hz), 124.8 (q, *J*<sub>C-F</sub> = 271.8 Hz), 123.2 (d, *J*<sub>C-F</sub> = 8.1 Hz), 121.5 (q, *J*<sub>C-F</sub> = 32.8 Hz), 116.4 (d, *J*<sub>C-F</sub> = 22.7 Hz), 114.7.

<sup>19</sup>F NMR (376 MHz, Chloroform-*d*) δ -61.4 (s, 3F), -119.2 (m, 1F).

HRMS (DART-TOF): calculated for C<sub>13</sub>H<sub>10</sub>F<sub>4</sub>N ([M+H]<sup>+</sup>) 256.0744, found 256.0737.



N-(furan-2-ylmethyl)-4-(trifluoromethyl)aniline (16)

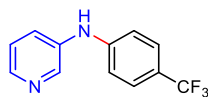
General procedure B was followed using 4-bromobenzotrifluoride as the aryl halide, and furfurylamine as the amine. The reaction was run at room temperature for 15 hours. Purification was done by flash chromatography on silica gel, eluting with a gradient of 0-20% EtOAc/hexanes to give the product as a pale yellow solid (27.3 mg, 28%). NMR data matched previously reported spectra.<sup>1-2</sup>

<sup>1</sup>H NMR (400 MHz, Chloroform-*d*) δ 7.42 (d, *J* = 8.5 Hz, 2H), 7.39 – 7.36 (m, 1H), 6.68 (d, *J* = 8.5 Hz, 2H), 6.34 (dd, *J* = 3.3, 1.9 Hz, 1H), 6.25 (d, *J* = 3.2 Hz, 1H), 4.36 (s, 3H).

<sup>13</sup>C NMR (101 MHz, Chloroform-*d*) δ 151.9, 150.1, 142.3, 126.7 (q, *J*<sub>C-F</sub> = 3.8 Hz), 125.0 (q, *J*<sub>C-F</sub> = 271.4 Hz), 119.6 (q, *J*<sub>C-F</sub> = 32.6 Hz), 112.3, 110.6, 107.5, 41.0.

<sup>19</sup>F NMR (376 MHz, Chloroform-*d*) δ -61.1 (s, 3F).

HRMS (DART-TOF): calculated for C<sub>12</sub>H<sub>11</sub>F<sub>3</sub>NO ([M+H]<sup>+</sup>) 242.0787, found 242.0776.



N-(4-(trifluoromethyl)phenyl)pyridin-3-amine (17)

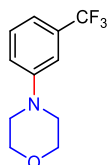
General procedure B was followed using 4-bromobenzotrifluoride as the aryl halide, and 3-aminopyridine as the amine. The reaction was run at room temperature for 15 hours. Purification was done by flash chromatography on silica gel, eluting with a gradient of 0-100% EtOAc/hexanes to give the product as a pale yellow solid (85.8 mg, 90%). NMR data matched previously reported spectra.<sup>6</sup>

<sup>1</sup>H NMR (400 MHz, DMSO-*d*<sub>6</sub>) δ 8.85 (s, 1H), 8.44 (s, 1H), 8.17 (d, *J* = 6.4, 1H), 7.64 – 7.58 (m, 1H), 7.55 (d, *J* = 8.4 Hz, 2H), 7.32 (dd, *J* = 8.3, 4.7 Hz, 1H), 7.17 (d, *J* = 8.4 Hz, 2H).

<sup>13</sup>C NMR (101 MHz, DMSO-*d*<sub>6</sub>) δ 147.2, 142.9, 141.5, 138.7, 127.1 (q, *J*<sub>C-F</sub> = 3.8 Hz), 125.5, 125.2 (q, *J*<sub>C-F</sub> = 271.8 Hz), 124.40, 119.8 (q, *J*<sub>C-F</sub> = 32.3 Hz), 115.5.

<sup>19</sup>F NMR (376 MHz, DMSO-*d*<sub>6</sub>) δ -59.7 (s, 3F).

HRMS (DART-TOF): calculated for C<sub>12</sub>H<sub>10</sub>F<sub>3</sub>N<sub>2</sub> ([M+H]<sup>+</sup>) 239.0791, found 239.0792.



4-(3-(trifluoromethyl)phenyl)morpholine (18)

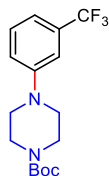
General procedure A was followed using 3-bromobenzotrifluoride as the aryl halide, and morpholine as the amine. The reaction was run at room temperature for 15 hours. Purification was done by flash chromatography on silica gel, eluting with a gradient of 0-15% EtOAc/hexanes to give the product as a pale yellow oil solid (52.7 mg, 57%). NMR data matched previously reported spectra.<sup>7</sup>

<sup>1</sup>H NMR (400 MHz, Chloroform-*d*) δ 7.42 – 7.29 (m, 1H), 7.16 – 7.08 (m, 2H), 7.08 – 7.03 (m, 1H), 3.88 (t, *J* = 4.8, 4H), 3.21 (t, *J* = 4.8, 4H).

<sup>13</sup>C NMR (101 MHz, Chloroform-*d*) δ 151.5, 131.7 (q, *J*<sub>C-F</sub> = 31.8 Hz), 129.8, 124.4 (q, *J*<sub>C-F</sub> = 273.4 Hz), 118.6, 116.4 (q, *J*<sub>C-F</sub> = 3.8 Hz), 112.0 (q, *J*<sub>C-F</sub> = 3.9 Hz), 66.9, 49.0.

<sup>19</sup>F NMR (376 MHz, Chloroform-*d*) δ -62.8 (s, 3F).

HRMS (DART-TOF): calculated for C<sub>11</sub>H<sub>13</sub>F<sub>3</sub>NO ([M+H]<sup>+</sup>) 232.0944, found 232.0934.



*tert*-butyl 4-(3-(trifluoromethyl)phenyl)piperazine-1-carboxylate (19)

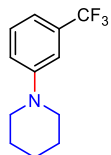
General procedure B was followed using 3-bromobenzotrifluoride as the aryl halide, and *tert*-butyl piperazine-1-carboxylate as the amine. The reaction was run at room temperature for 3 hours. Purification was done by flash chromatography on silica gel, eluting with a gradient of 0-15% EtOAc/hexanes to give the product as a pale yellow oil (79.3 mg, 60%). NMR data matched previously reported spectra.<sup>8</sup>

<sup>1</sup>H NMR (400 MHz, Chloroform-*d*) δ 7.40 – 7.31 (m, 1H), 7.13 – 7.08 (m, 2H), 7.08 – 7.02 (m, 1H), 3.60 (t, *J* = 5.2, 4H), 3.18 (t, *J* = 5.2, 4H), 1.49 (s, 9H).

<sup>13</sup>C NMR (101 MHz, Chloroform-*d*) δ 154.8, 151.5, 131.6 (q, *J*<sub>C-F</sub> = 31.8 Hz), 129.8, 124.4 (q, *J*<sub>C-F</sub> = 273.5 Hz), 119.4, 116.5 (q, *J*<sub>C-F</sub> = 3.9 Hz), 112.8 (q, *J*<sub>C-F</sub> = 3.9 Hz), 80.2, 49.0, 28.5.

<sup>19</sup>F NMR (376 MHz, Chloroform-*d*) δ -62.8 (s, 3F).

HRMS (DART-TOF): calculated for C<sub>16</sub>H<sub>22</sub>F<sub>3</sub>N<sub>2</sub>O<sub>2</sub> ([M+H]<sup>+</sup>) 331.1628, found 331.1632.



#### 1-(3-(trifluoromethyl)phenyl)piperidine (20)

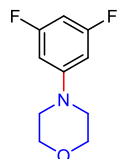
General procedure A was followed using 3-bromobenzotrifluoride as the aryl halide, and piperidine as the amine. The reaction was run at room temperature for 3 hours. Purification was done by flash chromatography on silica gel, eluting with a gradient of 0-10% EtOAc/hexanes to give the product as a pale yellow oil (33.0 mg, 36%). NMR data matched previously reported spectra.<sup>9</sup>

<sup>1</sup>H NMR (400 MHz, Chloroform-*d*) δ 7.32 (t, *J* = 8.0 Hz, 1H), 7.12 (s, 1H), 7.10 – 6.99 (m, 2H), 3.21 (t, *J* = 5.2, 4H), 1.76 – 1.67 (m, 4H), 1.66 – 1.57 (m, 2H).

<sup>13</sup>C NMR (101 MHz, Chloroform-*d*) δ 152.3, 131.4 (q, *J*<sub>C-F</sub> = 31.6 Hz), 129.5, 124.6 (q, *J*<sub>C-F</sub> = 273.5 Hz), 119.2, 115.3 (q, *J*<sub>C-F</sub> = 3.9 Hz), 112.6 (q, *J*<sub>C-F</sub> = 3.9 Hz), 50.3, 25.8, 24.3.

<sup>19</sup>F NMR (376 MHz, Chloroform-*d*) δ -62.7 (s, 3F).

HRMS (DART-TOF): calculated for C<sub>12</sub>H<sub>15</sub>F<sub>3</sub>N ([M+H]<sup>+</sup>) 230.1151, found 230.1151.



#### 4-(3,5-difluorophenyl)morpholine (21)

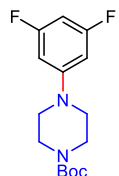
General procedure A was followed using 1-bromo-3,5-difluorobenzene as the aryl halide, and morpholine as the amine. The reaction was run at room temperature for 3 hours. Purification was done by flash chromatography on silica gel, eluting with a gradient of 0-15% EtOAc/hexanes to give the product as a white solid (56.3 mg, 71%). NMR data matched previously reported spectra.<sup>10</sup>

<sup>1</sup>H NMR (400 MHz, Chloroform-*d*) δ 6.42 – 6.23 (m, 3H), 3.83 (t, *J* = 4.8 Hz, 4H), 3.14 (t, *J* = 4.8 Hz, 4H).

<sup>13</sup>C NMR (101 MHz, Chloroform-*d*) δ 164.1 (dd, *J* = 245.4, *J* = 16.2 Hz), 153.4 (t, *J* = 12.2 Hz), 98.0 - 97.8 (m), 94.6 (t, *J* = 26.3 Hz), 66.7, 48.4.

<sup>19</sup>F NMR (376 MHz, Chloroform-*d*) δ -109.7 – -109.9 (m, 2F).

HRMS (DART-TOF): calculated for C<sub>10</sub>H<sub>12</sub>F<sub>2</sub>NO ([M+H]<sup>+</sup>) 200.0881, found 200.0874.



#### *tert*-butyl 4-(3,5-difluorophenyl)piperazine-1-carboxylate (22)

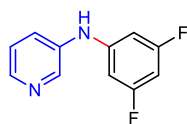
General procedure B was followed using 1-bromo-3,5-difluorobenzene as the aryl halide, and *tert*-butyl piperazine-1-carboxylate as the amine. The reaction was run at room temperature for 3 hours. Purification was done by flash chromatography on silica gel, eluting with a gradient of 0-15% EtOAc/hexanes to give the product as a white solid (73.4 mg, 62%).

$^1\text{H}$  NMR (400 MHz, Chloroform-*d*)  $\delta$  6.40 – 6.30 (m, 2H), 6.27 (tt,  $J = 8.8, 2.2$  Hz, 1H), 3.55 (t,  $J = 5.2$ , 4H), 3.14 (t,  $J = 5.2$ , 4H), 1.48 (s, 9H).

$^{13}\text{C}$  NMR (101 MHz, Chloroform-*d*)  $\delta$  164.1 (dd,  $J = 245.4, J = 15.8$  Hz), 154.7, 153.2 (t,  $J = 12.3$  Hz), 98.7 – 98.3 (m), 94.7 (t,  $J = 23.3$  Hz), 80.3, 48.3, 28.5.

$^{19}\text{F}$  NMR (376 MHz, Chloroform-*d*)  $\delta$  -109.6 – -109.8 (m, 2F).

HRMS (DART-TOF): calculated for  $\text{C}_{15}\text{H}_{21}\text{F}_2\text{N}_2\text{O}_2$  ( $[\text{M}+\text{H}]^+$ ) 299.1556, found 299.1556.



#### N-(3,5-difluorophenyl)pyridin-3-amine (23)

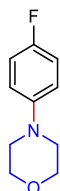
General procedure B was followed using 1-bromo-3,5-difluorobenzene as the aryl halide, and 3-aminopyridine as the amine. The reaction was run at room temperature for 15 hours. Purification was done by flash chromatography on silica gel, eluting with a gradient of 0-100% EtOAc/hexanes to give the product as a white solid (74.4 mg, 90%).

$^1\text{H}$  NMR (400 MHz, DMSO-*d*<sub>6</sub>)  $\delta$  8.81 (s, 1H), 8.39 (d,  $J = 2.7$  Hz, 1H), 8.26 – 8.07 (m, 1H), 7.68 – 7.48 (m, 1H), 7.41 – 7.21 (m, 1H), 6.83 – 6.48 (m, 3H).

$^{13}\text{C}$  NMR (101 MHz, DMSO-*d*<sub>6</sub>)  $\delta$  163.4 (dd,  $J = 243.8, J = 16.3$  Hz), 146.2 (t,  $J = 13.5$  Hz), 142.6, 141.1, 138.1, 125.1, 124.0, 98.5 – 98.0 (m), 94.5 (t,  $J = 26.7$  Hz).

$^{19}\text{F}$  NMR (376 MHz, DMSO-*d*<sub>6</sub>)  $\delta$  -109.5 (t,  $J = 9.3$  Hz, 2F).

HRMS (DART-TOF): calculated for  $\text{C}_{11}\text{H}_9\text{F}_2\text{N}_2$  ( $[\text{M}+\text{H}]^+$ ) 207.0728, found 207.0730.



#### 4-(4-fluorophenyl)morpholine (24)

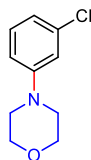
General procedure B was followed using 1-bromo-4-fluorobenzene as the aryl halide, and morpholine as the amine. The reaction was run at room temperature for 15 hours. Purification was done by flash chromatography on silica gel, eluting with a gradient of 0-15% EtOAc/hexanes to give the product as a colorless oil (27.3 mg, 38%). NMR data matched previously reported spectra.<sup>11</sup>

$^1\text{H}$  NMR (400 MHz, Chloroform-*d*)  $\delta$  7.04 – 6.92 (m, 2H), 6.92 – 6.82 (m, 2H), 3.87 (t,  $J = 4.8$  Hz, 4H), 3.09 (t,  $J = 4.8$  Hz, 4H).

$^{13}\text{C}$  NMR (101 MHz, Chloroform-*d*)  $\delta$  157.5 (d,  $J_{\text{C-F}} = 240.3$  Hz), 148.1, 117.6 (d,  $J_{\text{C-F}} = 7.8$  Hz), 115.8 (d,  $J_{\text{C-F}} = 22.2$  Hz), 67.1, 50.5.

$^{19}\text{F}$  NMR (376 MHz, Chloroform-*d*)  $\delta$  -124.2 – -124.3 (m, 1F).

HRMS (DART-TOF): calculated for  $\text{C}_{10}\text{H}_{13}\text{FNO}$  ( $[\text{M}+\text{H}]^+$ ) 182.0976, found 182.0976.



#### 4-(3-chlorophenyl)morpholine (25)

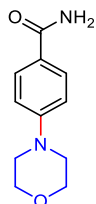
General procedure A was followed using 1-bromo-3-chlorobenzene as the aryl halide, and morpholine as the amine. The reaction was run at room temperature for 15 hours. Purification was done by flash

chromatography on silica gel, eluting with a gradient of 0-15% EtOAc/hexanes to give the product as a colorless oil (65.4 mg, 83%). NMR data matched previously reported spectra.<sup>12</sup>

<sup>1</sup>H NMR (400 MHz, Chloroform-*d*)  $\delta$  7.18 (t, *J* = 8.1 Hz, 1H), 6.89 – 6.81 (m, 2H), 6.80 – 6.74 (m, 1H), 3.85 (t, *J* = 4.8 Hz, 4H), 3.15 (t, *J* = 5.2 Hz, 4H).

<sup>13</sup>C NMR (101 MHz, Chloroform-*d*)  $\delta$  152.5, 135.2, 130.2, 119.8, 115.6, 113.7, 66.9, 49.0.

HRMS (ESI-TOF): calculated for C<sub>10</sub>H<sub>13</sub>CINO ([M+H]<sup>+</sup>) 198.0680, found 198.0691.



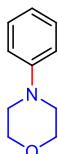
#### 4-morpholinobenzamide (26)

General procedure A was followed using 4-bromobenzamide as the aryl halide, and morpholine as the amine. The reaction was run at room temperature for 15 hours. Purification was done by flash chromatography on silica gel, eluting with a gradient of 0-10% MeOH/DCM to give the product as a white solid (22.5 mg, 27%). NMR data matched previously reported spectra.<sup>13</sup>

<sup>1</sup>H NMR (400 MHz, DMSO-*d*<sub>6</sub>)  $\delta$  7.88 – 7.64 (m, 3H), 7.09 – 6.83 (m, 3H), 3.74 (t, *J* = 4.8 Hz, 4H), 3.21 (t, *J* = 4.8 Hz, 4H).

<sup>13</sup>C NMR (101 MHz, DMSO-*d*<sub>6</sub>)  $\delta$  167.5, 152.9, 128.8, 123.9, 113.3, 65.9, 47.4.

HRMS (ESI-TOF): calculated for C<sub>11</sub>H<sub>15</sub>N<sub>2</sub>O<sub>2</sub> ([M+H]<sup>+</sup>) 207.1128, found 207.1121.



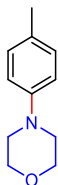
#### 4-phenylmorpholine (27)

General procedure A was followed using 4-bromobenzene as the aryl halide, and morpholine as the amine. The reaction was run at room temperature for 15 hours. Purification was done by flash chromatography on silica gel, eluting with a gradient of 0-15% EtOAc/hexanes to give the product as a white solid (34.8 mg, 53%). NMR data matched previously reported spectra.<sup>12</sup>

<sup>1</sup>H NMR (400 MHz, Chloroform-*d*)  $\delta$  7.35 – 7.26 (m, 2H), 6.99 – 6.83 (m, 3H), 3.87 (t, *J* = 4.8 Hz, 4H), 3.17 (t, *J* = 4.8 Hz, 4H).

<sup>13</sup>C NMR (101 MHz, Chloroform-*d*)  $\delta$  151.4, 129.3, 120.2, 115.8, 67.1, 49.5.

HRMS (DART-TOF): calculated for C<sub>10</sub>H<sub>14</sub>NO ([M+H]<sup>+</sup>) 164.1070, found 164.1075.



#### 4-(p-tolyl)morpholine (28)

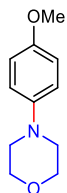
General procedure A was followed using 4-bromotoluene as the aryl halide, and morpholine as the amine. The reaction was run at room temperature for 15 hours. Purification was done by flash chromatography on

silica gel, eluting with a gradient of 0-15% EtOAc/hexanes to give the product as a white solid (23.4 mg, 33%). NMR data matched previously reported spectra.<sup>12</sup>

<sup>1</sup>H NMR (400 MHz, Chloroform-*d*) δ 7.14 – 7.05 (m, 2H), 6.88 – 6.80 (m, 2H), 3.87 (t, *J* = 4.8 Hz, 4H), 3.11 (t, *J* = 4.8 Hz, 4H), 2.28 (s, 3H).

<sup>13</sup>C NMR (101 MHz, Chloroform-*d*) δ 149.3, 129.8, 129.7, 116.2, 67.1, 50.1, 20.6.

HRMS (DART-TOF): calculated for C<sub>11</sub>H<sub>16</sub>NO ([M+H]<sup>+</sup>) 178.1226, found 178.1225.



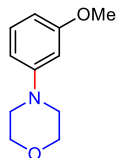
#### 4-(4-methoxyphenyl)morpholine (29)

General procedure A was followed using 4-bromoanisole as the aryl halide, and morpholine as the amine. The reaction was run at room temperature for 15 hours. Purification was done by flash chromatography on silica gel, eluting with a gradient of 0-15% EtOAc/hexanes to give the product as a white solid (5.6 mg, 7%). NMR data matched previously reported spectra.<sup>12</sup>

<sup>1</sup>H NMR (400 MHz, Chloroform-*d*) δ 6.94 – 6.81 (m, 4H), 3.86 (t, *J* = 4.4 Hz, 4H), 3.77 (s, 3H), 3.06 (t, *J* = 4.8 Hz, 4H).

<sup>13</sup>C NMR (101 MHz, Chloroform-*d*) δ 154.2, 145.8, 118.0, 114.7, 67.2, 55.7, 51.0.

HRMS (DART-TOF): calculated for C<sub>11</sub>H<sub>16</sub>NO<sub>2</sub> ([M+H]<sup>+</sup>) 194.1176, found 194.1174.



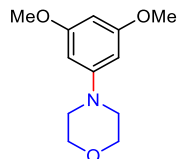
#### 4-(3-methoxyphenyl)morpholine (30)

General procedure A was followed using 3-bromoanisole as the aryl halide, and morpholine as the amine. The reaction was run at room temperature for 15 hours. Purification was done by flash chromatography on silica gel, eluting with a gradient of 0-15% EtOAc/hexanes to give the product as a colorless oil (45.8 mg, 59%). NMR data matched previously reported spectra.<sup>12</sup>

<sup>1</sup>H NMR (400 MHz, Chloroform-*d*) δ 7.24 – 7.14 (m, 1H), 6.57 – 6.50 (m, 1H), 6.48 – 6.41 (m, 2H), 3.85 (t, *J* = 4.8 Hz, 4H), 3.80 (s, 3H), 3.16 (t, *J* = 4.8 Hz, 4H).

<sup>13</sup>C NMR (101 MHz, Chloroform-*d*) δ 160.8, 152.8, 123.0, 108.6, 104.9, 102.4, 67.0, 55.3, 49.4.

HRMS (DART-TOF): calculated for C<sub>11</sub>H<sub>16</sub>NO<sub>2</sub> ([M+H]<sup>+</sup>) 194.1176, found 194.1181.



#### 4-(3,5-dimethoxyphenyl)morpholine (31)

General procedure A was followed using 1-bromo-3,5-dimethoxybenzene as the aryl halide, and morpholine as the amine. The reaction was run at room temperature for 15 hours. Purification was done by

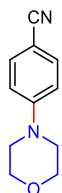


flash chromatography on silica gel, eluting with a gradient of 0-15% EtOAc/hexanes to give the product as a white solid (47.4 mg, 53%). NMR data matched previously reported spectra.<sup>14</sup>

<sup>1</sup>H NMR (400 MHz, Chloroform-*d*)  $\delta$  6.08 (d, *J* = 2.1 Hz, 2H), 6.04 (t, *J* = 2.1 Hz, 1H), 3.84 (t, *J* = 4.8 Hz, 4H), 3.78 (s, 6H), 3.14 (t, *J* = 4.8 Hz, 4H).

<sup>13</sup>C NMR (101 MHz, Chloroform-*d*)  $\delta$  161.7, 153.4, 94.9, 92.0, 67.0, 55.4, 49.5.

HRMS (DART-TOF): calculated for C<sub>12</sub>H<sub>18</sub>NO<sub>3</sub> ([M+H]<sup>+</sup>) 224.1281, found 224.1281.



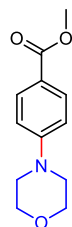
#### 4-morpholinobenzonitrile (32)

General procedure A was followed using 4-bromobenzonitrile as the aryl halide, and morpholine as the amine. The reaction was run at room temperature for 3 hours. Purification was done by flash chromatography on silica gel, eluting with a gradient of 0-30% EtOAc/hexanes to give the product as a white solid (64.5 mg, 86%). NMR data matched previously reported spectra.<sup>15</sup>

<sup>1</sup>H NMR (400 MHz, Chloroform-*d*)  $\delta$  7.54 – 7.45 (m, 2H), 6.89 – 6.81 (m, 2H), 3.83 (t, *J* = 5.2 Hz, 4H), 3.27 (t, *J* = 5.2 Hz, 4H).

<sup>13</sup>C NMR (101 MHz, Chloroform-*d*)  $\delta$  153.6, 133.6, 120.0, 114.1, 101.0, 66.5, 47.4.

HRMS (DART-TOF): calculated for C<sub>11</sub>H<sub>13</sub>N<sub>2</sub>O ([M+H]<sup>+</sup>) 189.1022, found 189.1011.



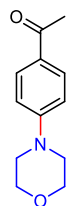
#### methyl 4-morpholinobenzoate (33)

General procedure A was followed using methyl 4-bromobenzoate as the aryl halide, and morpholine as the amine. The reaction was run at room temperature for 15 hours. Purification was done by flash chromatography on silica gel, eluting with a gradient of 0-30% EtOAc/hexanes to give the product as a white solid (57.7 mg, 65%). NMR data matched previously reported spectra.<sup>16</sup>

<sup>1</sup>H NMR (400 MHz, Chloroform-*d*)  $\delta$  7.95 – 7.91 (m, 2H), 6.89 – 6.81 (m, 2H), 3.88 – 3.80 (m, 7H), 3.27 (t, *J* = 4.8 Hz, 4H).

<sup>13</sup>C NMR (101 MHz, Chloroform-*d*)  $\delta$  167.1, 154.3, 131.3, 120.4, 113.6, 66.7, 51.8, 47.8.

HRMS (DART-TOF): calculated for C<sub>12</sub>H<sub>16</sub>NO<sub>3</sub> ([M+H]<sup>+</sup>) 222.1125, found 222.1121.



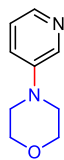
#### 1-(4-morpholinophenyl)ethan-1-one (34)

General procedure A was followed using 4'-bromoacetophenone as the aryl halide, and morpholine as the amine. The reaction was run at room temperature for 15 hours. Purification was done by flash chromatography on silica gel, eluting with a gradient of 0-30% EtOAc/hexanes to give the product as a pale yellow solid (34.4 mg, 42%). NMR data matched previously reported spectra.<sup>17</sup>

<sup>1</sup>H NMR (400 MHz, Chloroform-*d*)  $\delta$  7.88 (d,  $J$  = 8.8 Hz, 2H), 6.86 (d,  $J$  = 8.8 Hz, 2H), 3.85 (t,  $J$  = 4.8 Hz, 4H), 3.30 (t,  $J$  = 5.2 Hz, 4H), 2.52 (s, 3H).

<sup>13</sup>C NMR (101 MHz, Chloroform-*d*)  $\delta$  196.6, 154.3, 130.5, 128.3, 113.4, 66.7, 47.7, 26.3.

HRMS (DART-TOF): calculated for C<sub>12</sub>H<sub>16</sub>NO<sub>2</sub> ([M+H]<sup>+</sup>) 206.1176, found 206.1177.



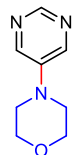
#### 4-(pyridin-3-yl)morpholine (35)

General procedure B was followed using 3-bromopyridine as the aryl halide, and morpholine as the amine. The reaction was run at room temperature for 15 hours. Purification was done by flash chromatography on silica gel, eluting with a gradient of 0-100% EtOAc/hexanes to give the product as a pale yellow oil (23.4 mg, 36%). NMR data matched previously reported spectra.<sup>12</sup>

<sup>1</sup>H NMR (400 MHz, Chloroform-*d*)  $\delta$  8.30 (s, 1H), 8.12 (t,  $J$  = 2.8 Hz, 1H), 7.18 – 7.14 (m, 2H), 3.86 (t,  $J$  = 4.8 Hz, 4H), 3.18 (t,  $J$  = 4.8 Hz, 4H).

<sup>13</sup>C NMR (101 MHz, Chloroform-*d*)  $\delta$  147.0, 141.3, 138.5, 123.6, 122.2, 66.8, 48.7.

HRMS (DART-TOF): calculated for C<sub>9</sub>H<sub>13</sub>N<sub>2</sub>O ([M+H]<sup>+</sup>) 165.1022, found 165.1018.



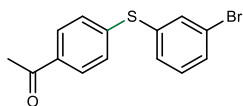
#### 4-(pyrimidin-5-yl)morpholine (36)

General procedure B was followed using 5-bromopyrimidine as the aryl halide, and morpholine as the amine. The reaction was run at room temperature for 15 hours. Purification was done by flash chromatography on silica gel, eluting with a gradient of 0-100% EtOAc/hexanes to give the product as a pale yellow oil (13.8 mg, 21%). NMR data matched previously reported spectra.<sup>18</sup>

<sup>1</sup>H NMR (400 MHz, Chloroform-*d*)  $\delta$  8.73 (s, 1H), 8.36 (s, 2H), 3.89 (t,  $J$  = 5.6 Hz, 4H), 3.23 (t,  $J$  = 4.8 Hz, 4H).

<sup>13</sup>C NMR (101 MHz, Chloroform-*d*)  $\delta$  150.3, 144.3, 143.6, 66.5, 47.6.

HRMS (DART-TOF): calculated for C<sub>8</sub>H<sub>12</sub>N<sub>3</sub>O ([M+H]<sup>+</sup>) 166.0975, found 166.0965.



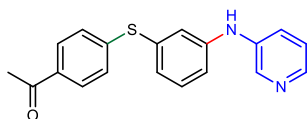
1-(4-((3-bromophenyl)thio)phenyl)ethan-1-one (37)

A 50 mL storage flask was charged with a stir bar, flame dried under vacuum and back filled with nitrogen three times. The flask was then charged with  $\text{Cs}_2\text{CO}_3$  (1.466 g, 4.5 mmol, 1.5 equiv.), 4'-bromoacetophenone (0.597 g, 3.0 mmol, 1.00 equiv.), 3-bromothiophenol (0.851 g, 4.5 mmol, 1.5 equiv.) and 23 mL DMSO. The reaction mixture was evacuated and purged with inert gas ( $\text{N}_2$ ) three times. The reaction mixture was then placed into an LED-lined beaker along with a tube for air cooling and stirred. After stirring for 12 hours, the reaction mixture was washed with water, extracted with EtOAc, and concentrated under vacuum. The product was isolated by flash chromatography (1:5 EtOAc:hexanes) as a white solid (0.516 g, 56%).

$^1\text{H}$  NMR (400 MHz, Chloroform-*d*)  $\delta$  7.89 – 7.76 (m, 2H), 7.58 (t,  $J$  = 1.8 Hz, 1H), 7.53 – 7.43 (m, 1H), 7.40 – 7.32 (m, 1H), 7.31 – 7.20 (m, 3H), 2.56 (s, 3H).

$^{13}\text{C}$  NMR (101 MHz, Chloroform-*d*)  $\delta$  197.1, 143.1, 135.4, 135.4, 135.3, 131.6, 131.5, 131.0, 129.2, 128.8, 123.4, 26.6.

HRMS (ESI-TOF): calculated for  $\text{C}_{14}\text{H}_{12}\text{BrOS}$  ( $[\text{M}+\text{H}]^+$ ) 306.9787, found 306.9813.



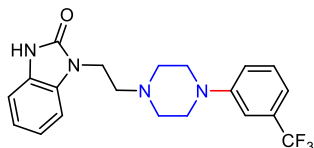
1-(4-((3-(pyridin-3-ylamino)phenyl)thio)phenyl)ethan-1-one (38)

General procedure B was followed using 1-(4-((3-bromophenyl)thio)phenyl)ethan-1-one (37) as the aryl halide, and 3-aminopyridine as the amine. The reaction was run at room temperature for 15 hours. Purification was done by flash chromatography on silica gel, eluting with a gradient of 0-80% EtOAc/hexanes to give the product as a pale yellow solid (113.4 mg, 88%).

$^1\text{H}$  NMR (400 MHz, Chloroform-*d*)  $\delta$  8.39 (d,  $J$  = 2.8 Hz, 1H), 8.20 (d,  $J$  = 4.4, 1H), 7.88 – 7.80 (m, 2H), 7.45 – 7.38 (m, 1H), 7.32 – 7.26 (m, 3H), 7.20 – 7.12 (m, 2H), 7.10 – 7.02 (m, 2H), 6.06 (s, 1H), 2.56 (s, 3H).

$^{13}\text{C}$  NMR (101 MHz, Chloroform-*d*)  $\delta$  197.3, 144.3, 143.7, 142.9, 141.0, 139.0, 134.9, 134.0, 130.7, 129.1, 128.2, 126.3, 124.5, 123.9, 121.9, 117.6, 26.6.

HRMS (ESI-TOF): calculated for  $\text{C}_{19}\text{H}_{17}\text{N}_2\text{OS}$  ( $[\text{M}+\text{H}]^+$ ) 321.1056, found 321.1063.



1-(2-(4-(3-(trifluoromethyl)phenyl)piperazin-1-yl)ethyl)-1,3-dihydro-2H-benzo[d]imidazol-2-one (39, Flibanserin)

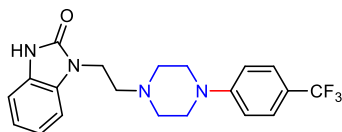
Using *tert*-butyl 4-(3-(trifluoromethyl)phenyl)piperazine-1-carboxylate (19) as the precursor, compound 39 was synthesized using previously published procedures.<sup>19</sup> NMR data matched previously reported spectra.<sup>19</sup>

$^1\text{H}$  NMR (400 MHz, Chloroform-*d*)  $\delta$  9.99 (s, 1H), 7.32 (t,  $J$  = 8.0 Hz, 1H), 7.15 – 6.97 (m, 7H), 4.07 (t,  $J$  = 6.8 Hz, 2H), 3.21 (t,  $J$  = 4.8 Hz, 4H), 2.79 (t,  $J$  = 6.9 Hz, 2H), 2.72 (t,  $J$  = 5.2 Hz, 4H).

$^{13}\text{C}$  NMR (101 MHz, Chloroform-*d*)  $\delta$  155.8, 151.5, 131.6 (q,  $J_{\text{C-F}} = 31.9$  Hz), 130.5, 129.6, 128.2, 124.5 (q,  $J_{\text{C-F}} = 273.5$  Hz), 121.7, 121.4, 118.8, 115.9 (q,  $J_{\text{C-F}} = 4.0$  Hz), 112.2 (q,  $J_{\text{C-F}} = 3.9$  Hz), 109.8, 108.1, 55.9, 53.2, 48.8, 38.7.

$^{19}\text{F}$  NMR (376 MHz, Chloroform-*d*)  $\delta$  -62.8 (s, 3F).

HRMS (ESI-TOF): calculated for  $\text{C}_{20}\text{H}_{21}\text{F}_3\text{N}_4\text{O}$  ( $[\text{M}+\text{H}]^+$ ) 391.1740, found 391.1739.



1-(2-(4-(4-(trifluoromethyl)phenyl)piperazin-1-yl)ethyl)-1,3-dihydro-2H-benzo[d]imidazol-2-one (40)

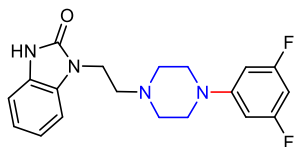
Using *tert*-butyl 4-(4-(trifluoromethyl)phenyl)piperazine-1-carboxylate (9) as the precursor, compound 40 was synthesized using previously published procedures.<sup>19</sup>

$^1\text{H}$  NMR (400 MHz, Chloroform-*d*)  $\delta$  10.02 (s, 1H), 7.45 (d,  $J = 8.7$  Hz, 2H), 7.20 – 6.99 (m, 4H), 6.87 (d,  $J = 8.6$  Hz, 2H), 4.07 (t,  $J = 6.8$  Hz, 2H), 3.24 (t,  $J = 4.8$  Hz, 4H), 2.78 (t,  $J = 6.8$  Hz, 2H), 2.71 (t,  $J = 5.6$  Hz, 4H).

$^{13}\text{C}$  NMR (101 MHz, Chloroform-*d*)  $\delta$  155.7, 153.4, 130.4, 128.0, 126.5 (q,  $J_{\text{C-F}} = 4.4$  Hz), 124.9 (q,  $J_{\text{C-F}} = 271.4$  Hz), 121.7, 121.4, 120.6 (q,  $J_{\text{C-F}} = 32.9$  Hz), 114.6, 109.7, 108.1, 55.8, 53.1, 48.1, 38.6.

$^{19}\text{F}$  NMR (376 MHz, Chloroform-*d*)  $\delta$  -61.4 (s, 3F).

HRMS (ESI-TOF): calculated for  $\text{C}_{20}\text{H}_{21}\text{F}_3\text{N}_4\text{O}$  ( $[\text{M}+\text{H}]^+$ ) 391.1740, found 391.1767.



1-(2-(4-(3,5-difluorophenyl)piperazin-1-yl)ethyl)-1,3-dihydro-2H-benzo[d]imidazol-2-one (41)

Using *tert*-butyl 4-(3,5-difluorophenyl)piperazine-1-carboxylate (22) as the precursor, compound 41 was synthesized using previously published procedures.<sup>19</sup>

$^1\text{H}$  NMR (400 MHz, Chloroform-*d*)  $\delta$  10.25 (s, 1H), 7.17 – 6.94 (m, 4H), 6.37 – 6.27 (m, 2H), 6.23 (tt,  $J = 8.9, 2.2$  Hz, 1H), 4.06 (t,  $J = 6.8$  Hz, 2H), 3.16 (t,  $J = 4.8$  Hz, 4H), 2.77 (t,  $J = 6.8$  Hz, 2H), 2.69 (t,  $J = 5.2$  Hz, 4H).

$^{13}\text{C}$  NMR (101 MHz, Chloroform-*d*)  $\delta$  164.1 (dd,  $J = 244.8, J = 16.1$  Hz), 155.9, 153.2 (t,  $J = 12.3$  Hz), 130.4, 128.2, 121.7, 121.4, 109.8, 108.0, 98.2 – 97.8 (m), 94.1 (t,  $J = 26.2$  Hz), 55.8, 53.0, 48.2, 38.7.

$^{19}\text{F}$  NMR (376 MHz, Chloroform-*d*)  $\delta$  -110.0 – -110.1 (m, 2F).

HRMS (ESI-TOF): calculated for  $\text{C}_{19}\text{H}_{21}\text{F}_2\text{N}_4\text{O}$  ( $[\text{M}+\text{H}]^+$ ) 359.1678, found 359.1690.

## 9. NMR Spectra

4-(4-(trifluoromethyl)phenyl)morpholine (1)

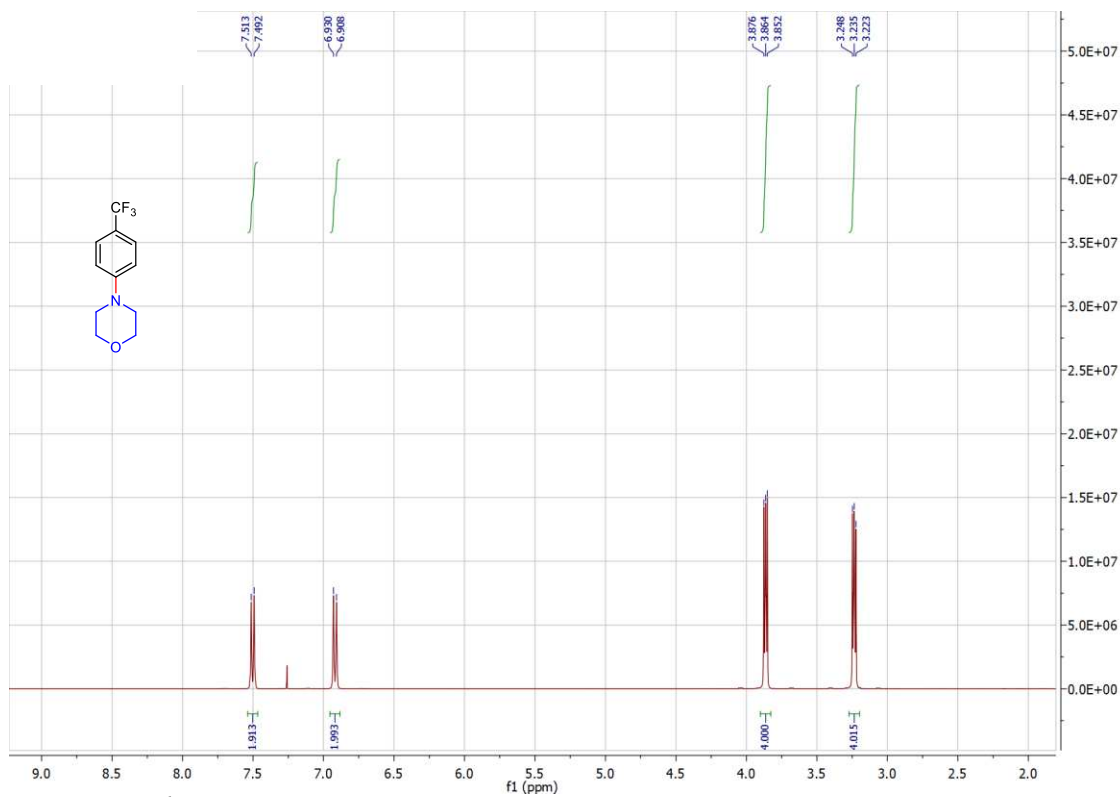


Figure S2.26.  $^1\text{H}$  NMR of 4-(4-(trifluoromethyl)phenyl)morpholine (1)

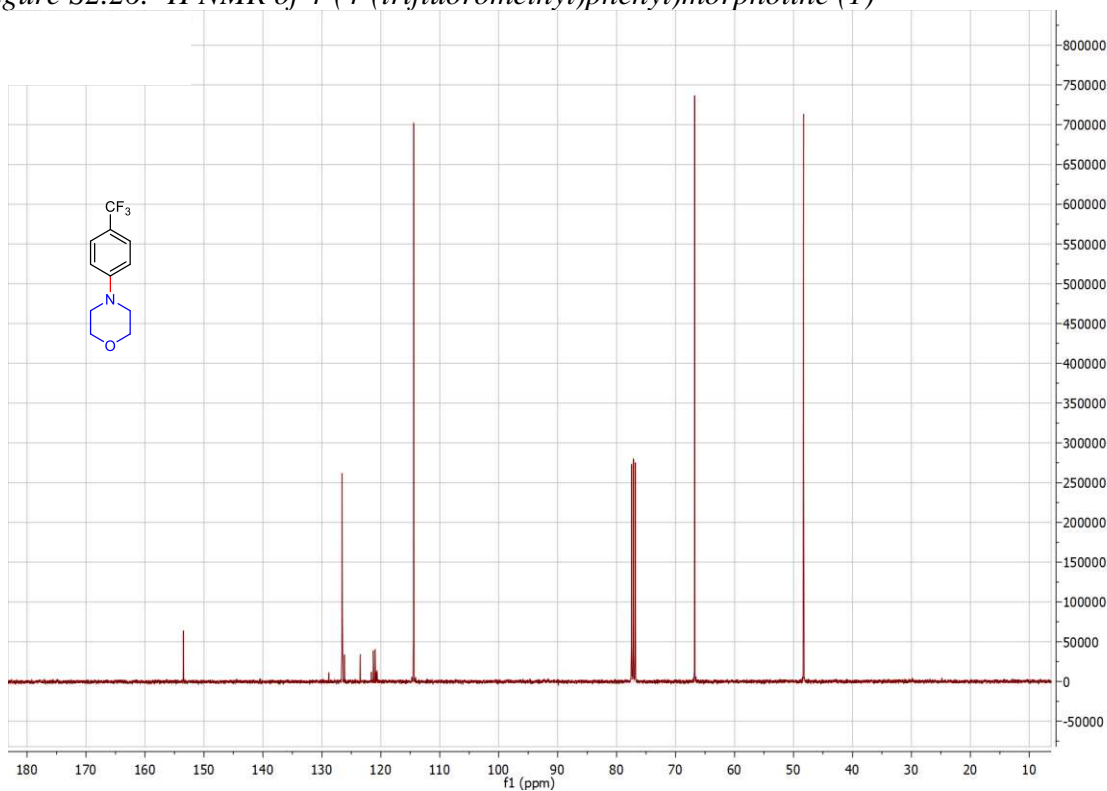


Figure S2.27.  $^{13}\text{C}$  NMR of 4-(4-(trifluoromethyl)phenyl)morpholine (1)

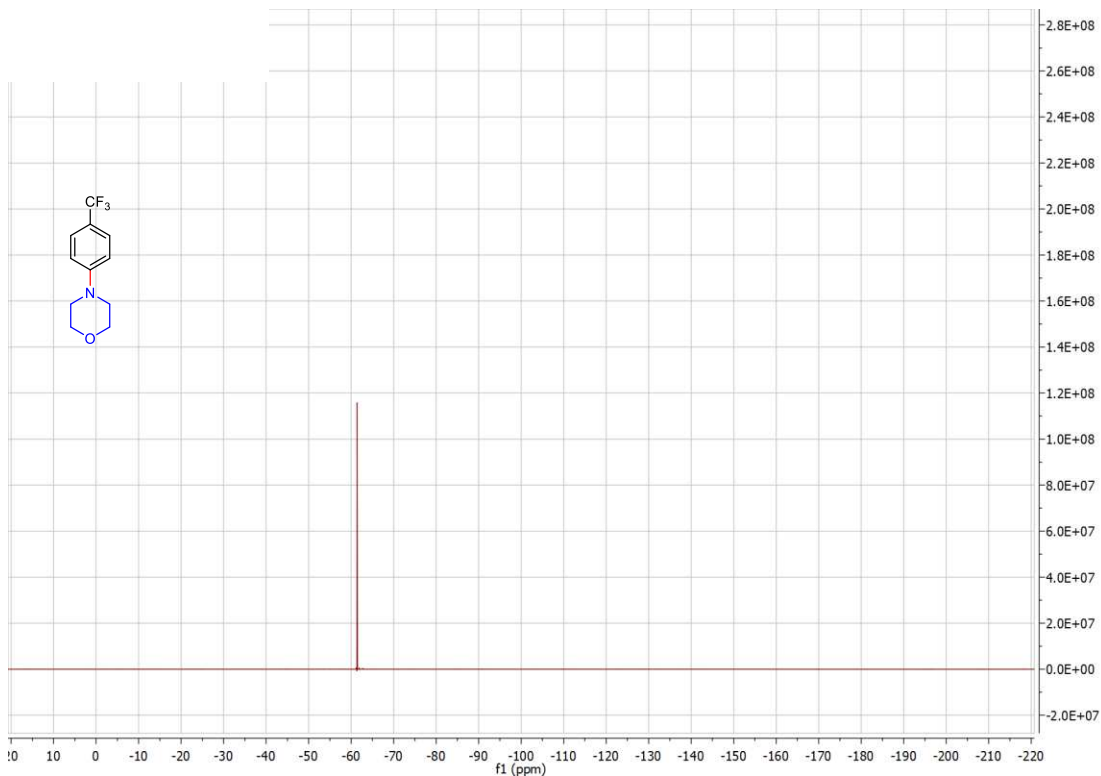


Figure S2.28.  $^{19}\text{F}$  NMR of 4-(4-(trifluoromethyl)phenyl)morpholine (1)

1-(4-(trifluoromethyl)phenyl)piperidine (2)

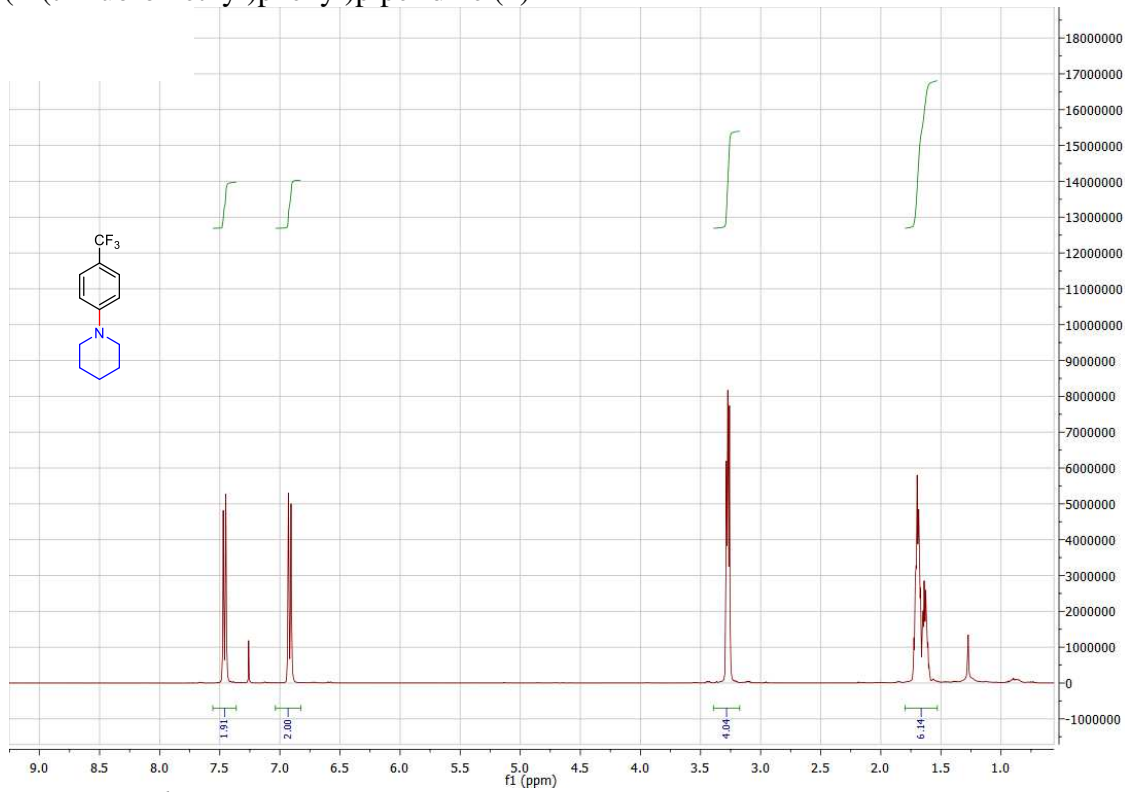


Figure S2.29.  $^1\text{H}$  NMR of 1-(4-(trifluoromethyl)phenyl)piperidine (2)

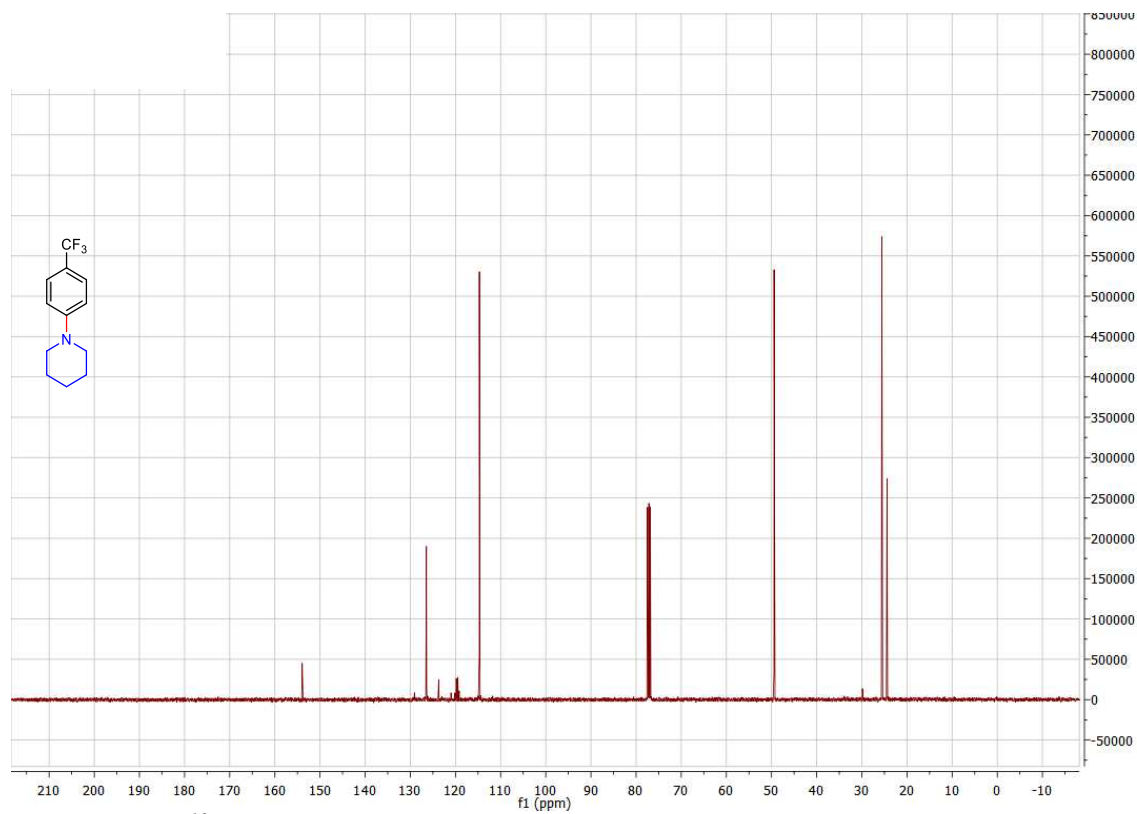


Figure S2.30.  $^{13}\text{C}$  NMR of 1-(4-(trifluoromethyl)phenyl)piperidine (2)

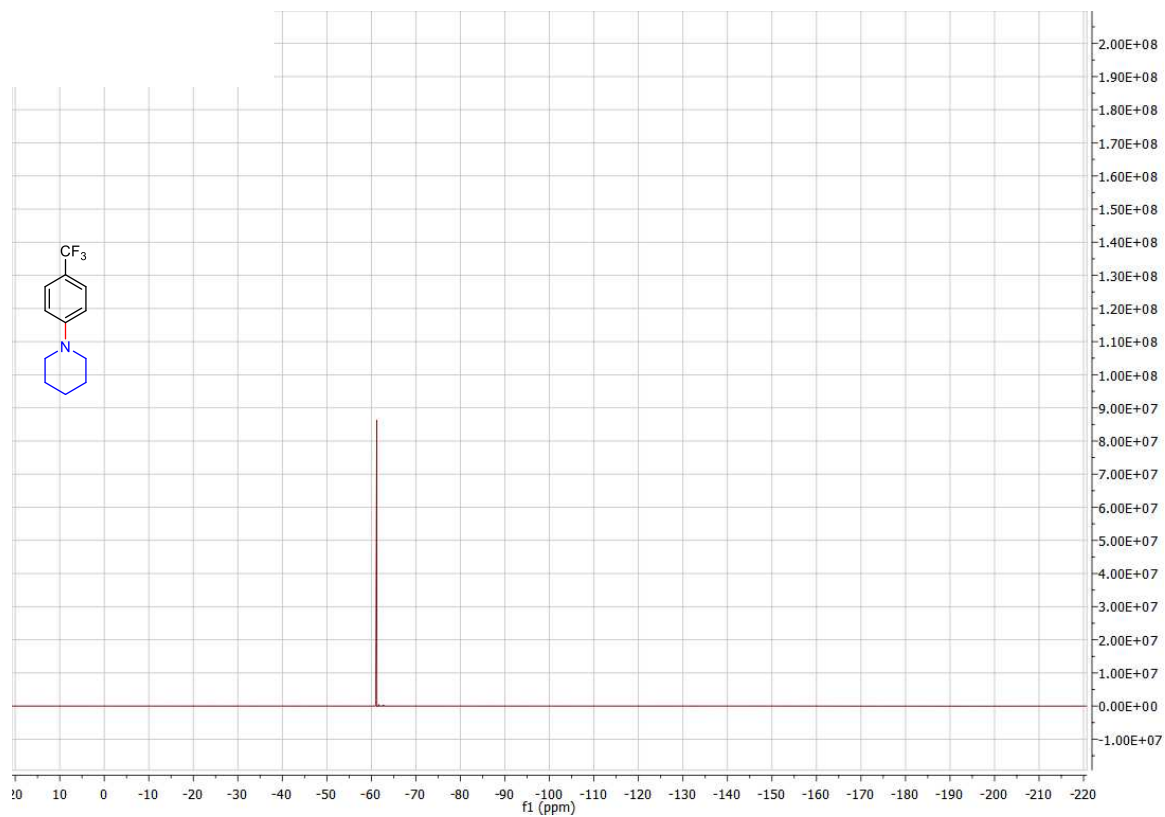


Figure S2.31.  $^{19}\text{F}$  NMR of 1-(4-(trifluoromethyl)phenyl)piperidine (2)

4-methyl-1-(4-(trifluoromethyl)phenyl)piperidine (3)

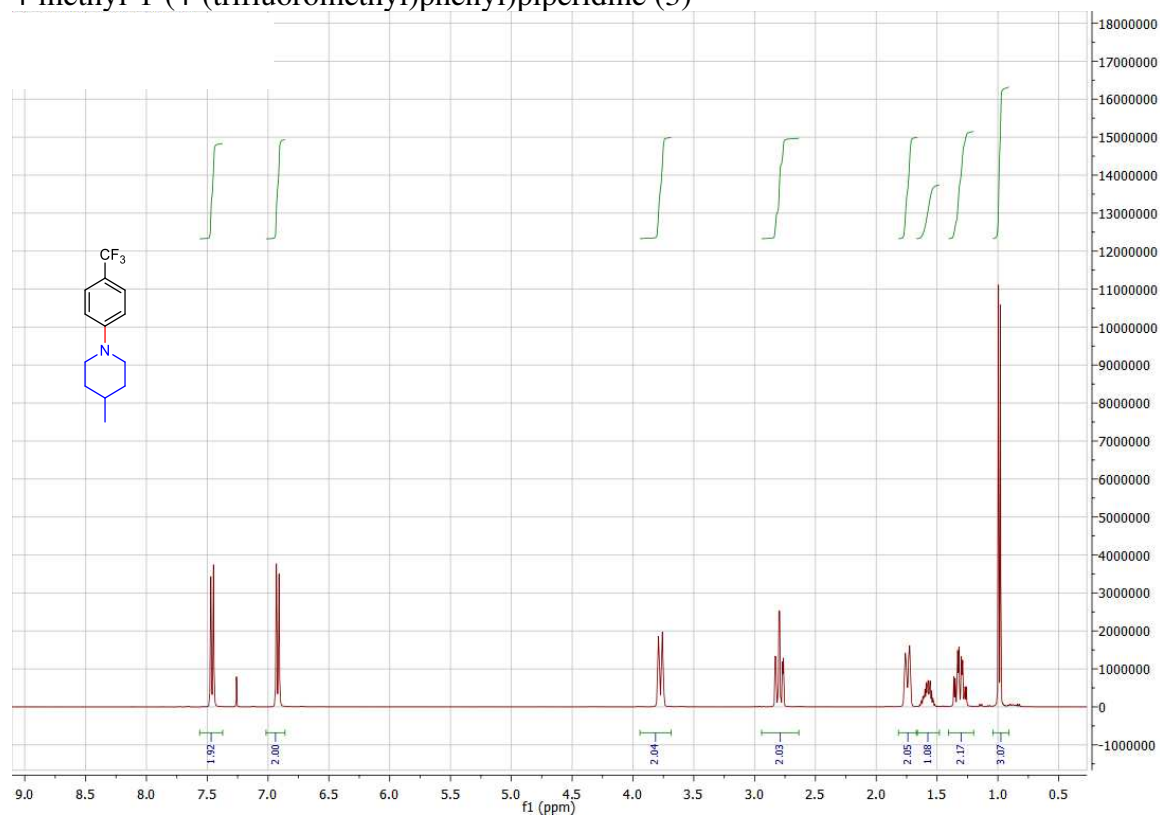


Figure S2.32. <sup>1</sup>H NMR of 4-methyl-1-(4-(trifluoromethyl)phenyl)piperidine (3)

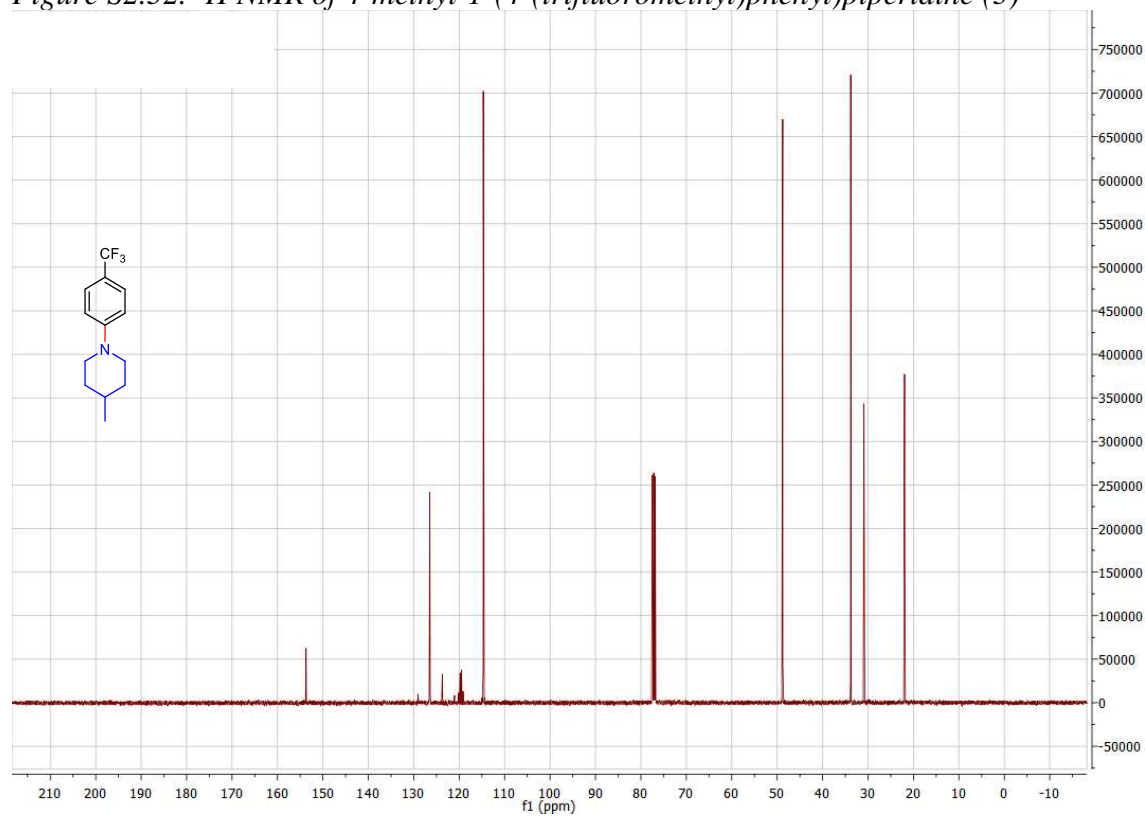




Figure S2.33.  $^{13}\text{C}$  NMR of 4-methyl-1-(4-(trifluoromethyl)phenyl)piperidine (3)

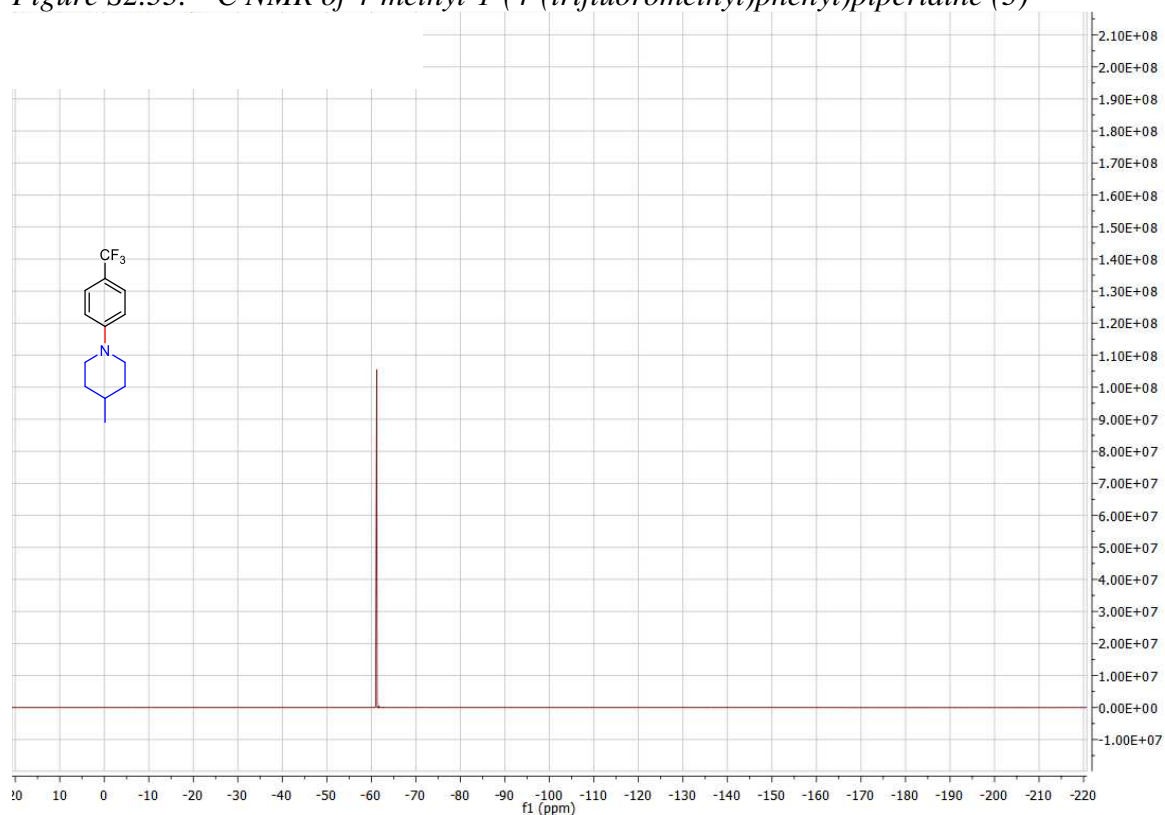


Figure S2.34.  $^{19}\text{F}$  NMR of 4-methyl-1-(4-(trifluoromethyl)phenyl)piperidine (3)

1-(4-(trifluoromethyl)phenyl)piperidine-4-carbonitrile (4)

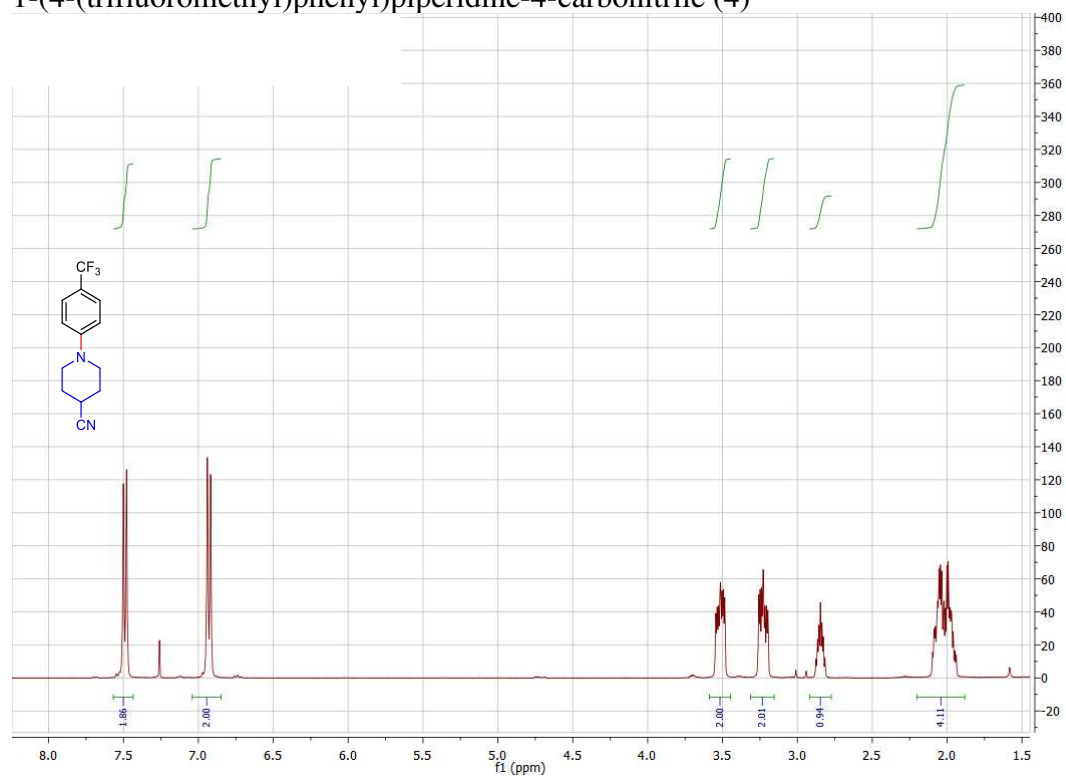


Figure S2.35.  $^1\text{H}$  NMR of 1-(4-(trifluoromethyl)phenyl)piperidine-4-carbonitrile (4)

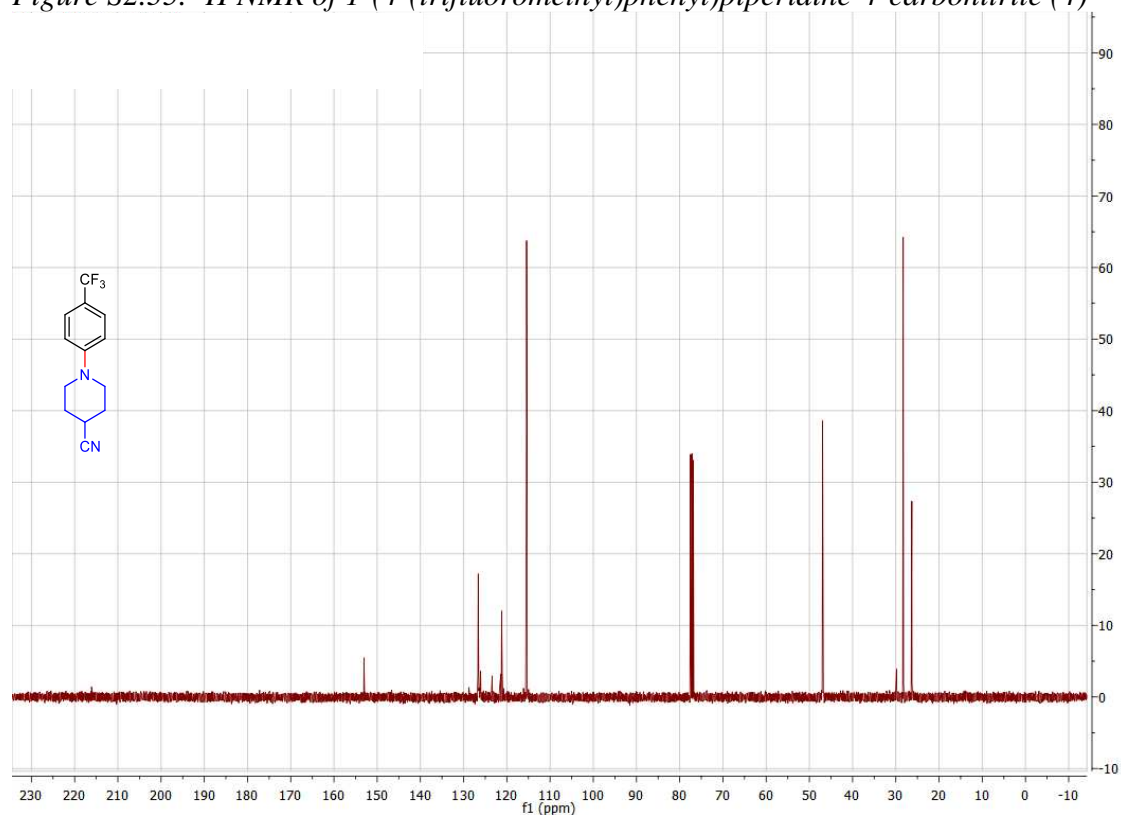


Figure S2.36.  $^{13}\text{C}$  NMR of 1-(4-(trifluoromethyl)phenyl)piperidine-4-carbonitrile (4)

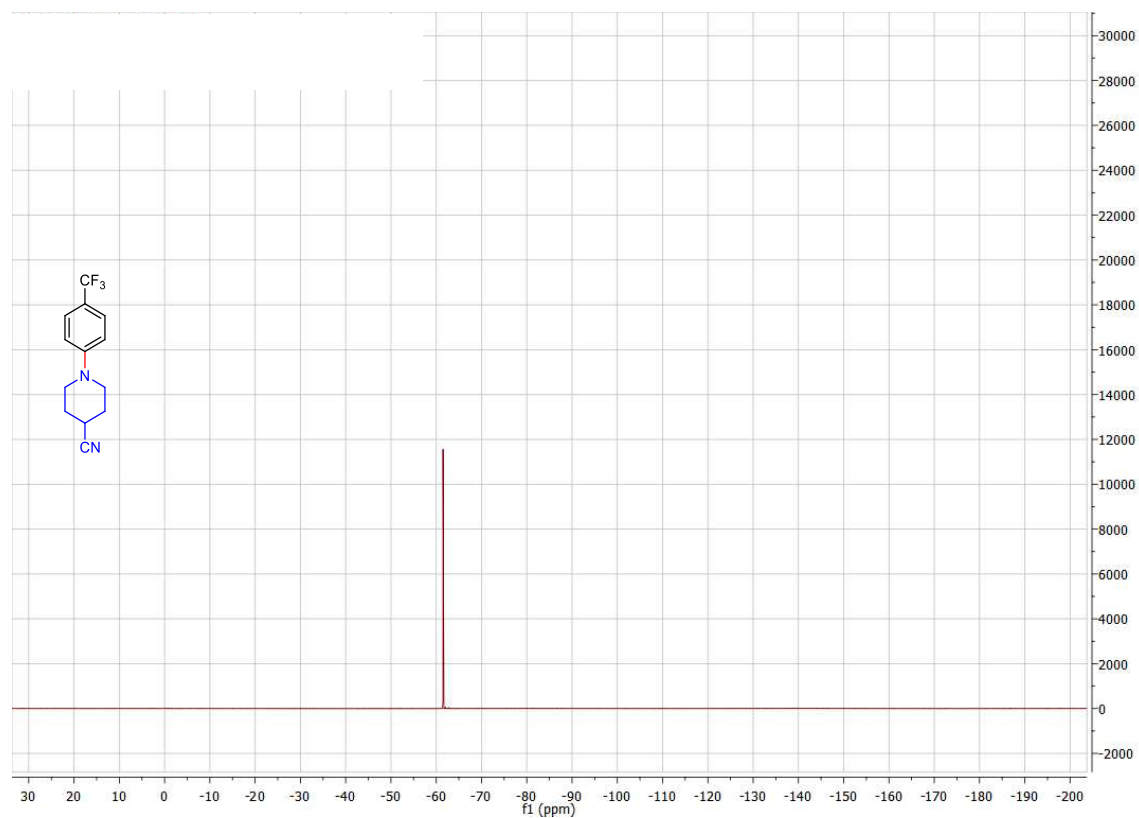


Figure S2.37.  $^{19}\text{F}$  NMR of 1-(4-(trifluoromethyl)phenyl)piperidine-4-carbonitrile (4)

1-(4-(trifluoromethyl)phenyl)piperidin-4-ol (5)

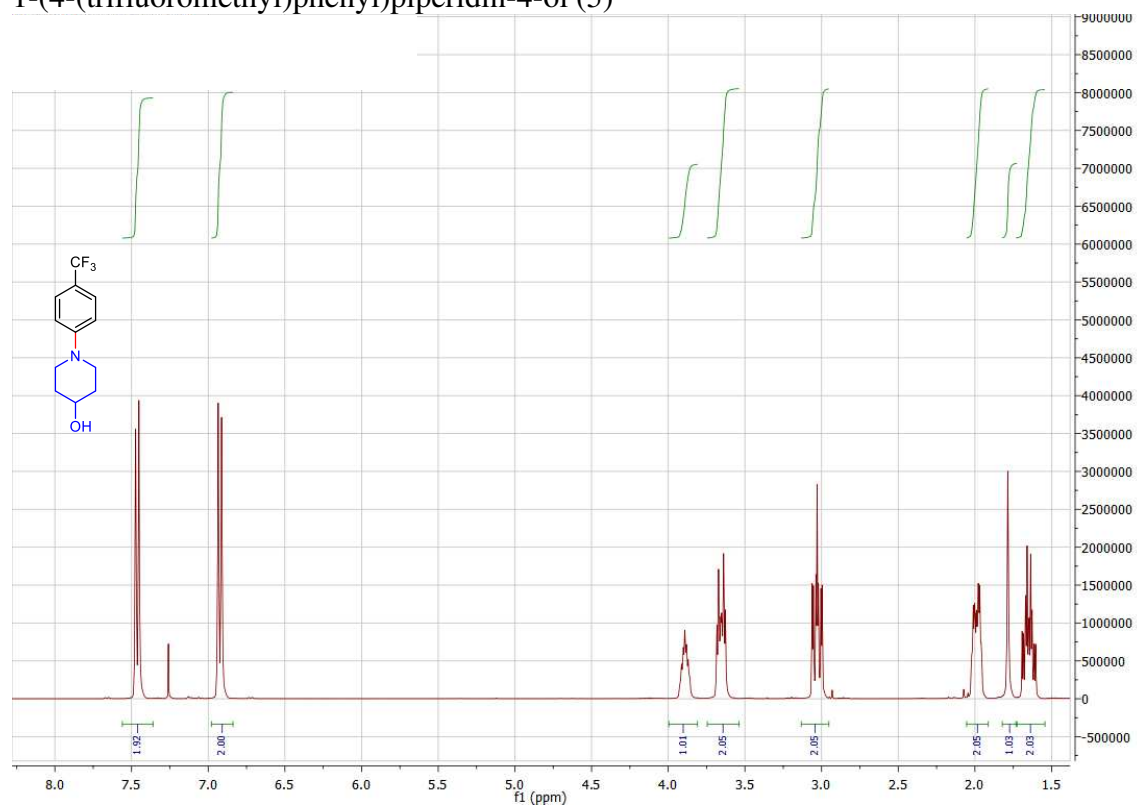


Figure S2.38.  $^1\text{H}$  NMR of 1-(4-(trifluoromethyl)phenyl)piperidin-4-ol (5)

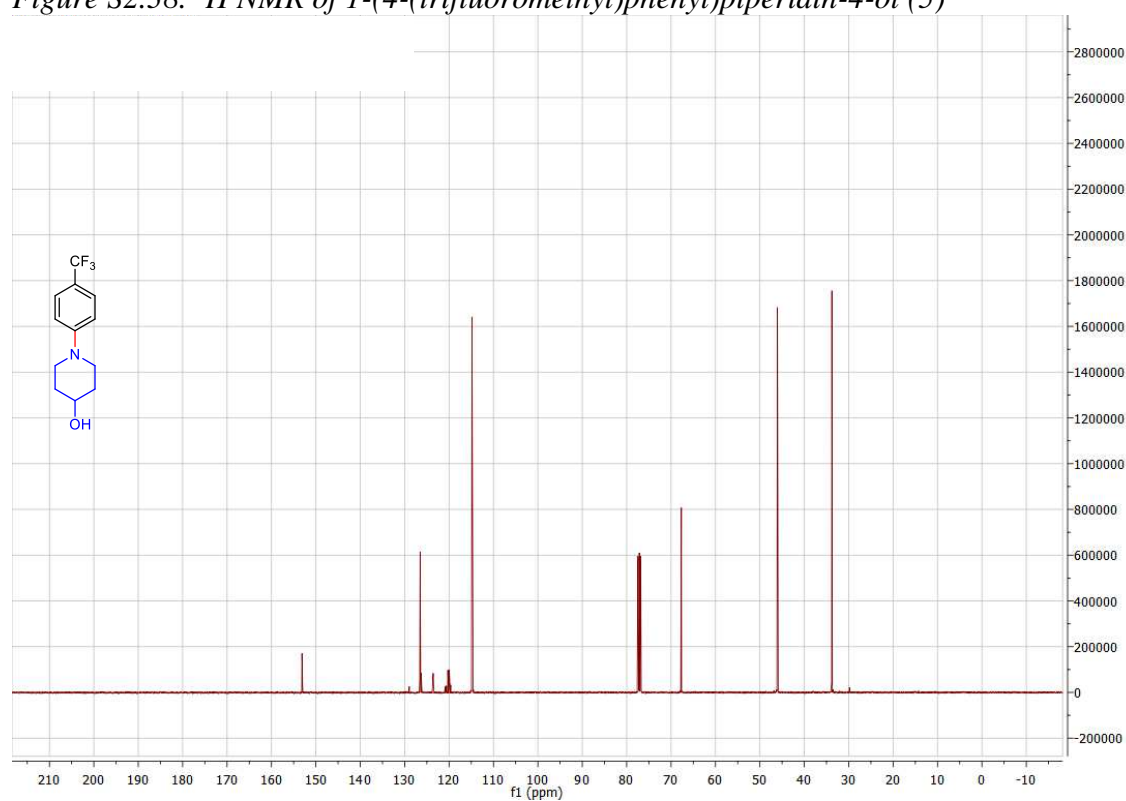


Figure S2.39.  $^{13}\text{C}$  NMR of 1-(4-(trifluoromethyl)phenyl)piperidin-4-ol (5)

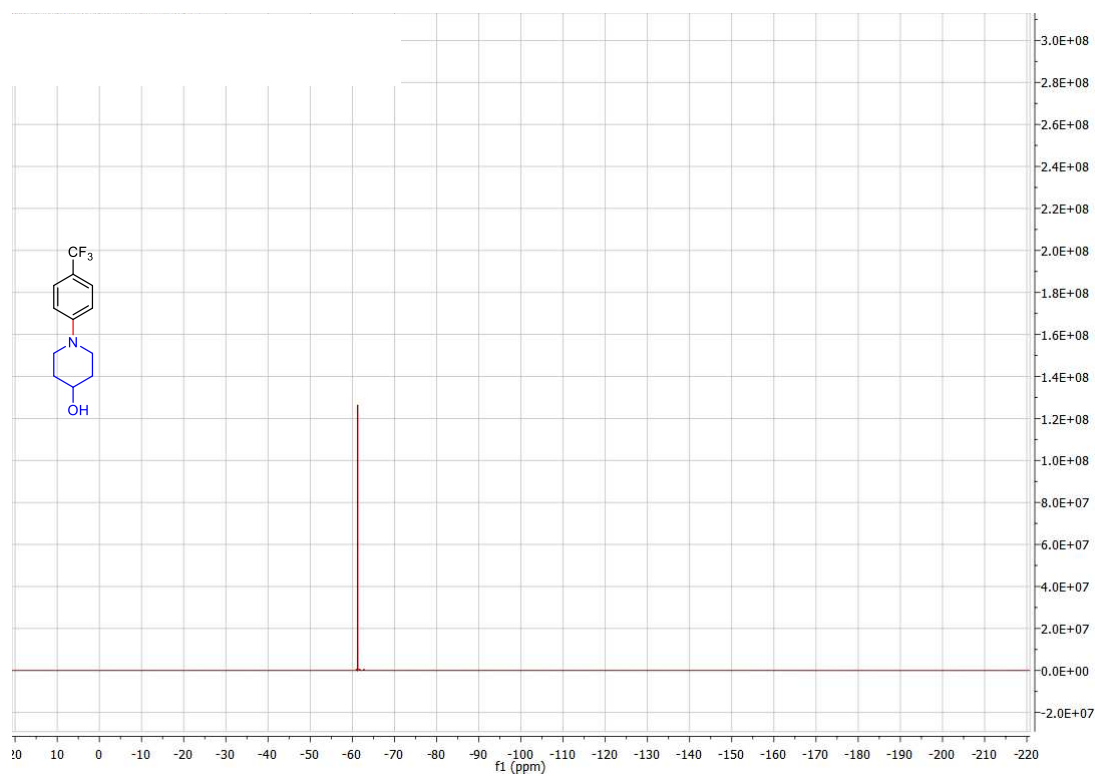


Figure S2.40.  $^{19}\text{F}$  NMR of 1-(4-(trifluoromethyl)phenyl)piperidin-4-ol (5)

methyl 1-(4-(trifluoromethyl)phenyl)piperidine-4-carboxylate (6)

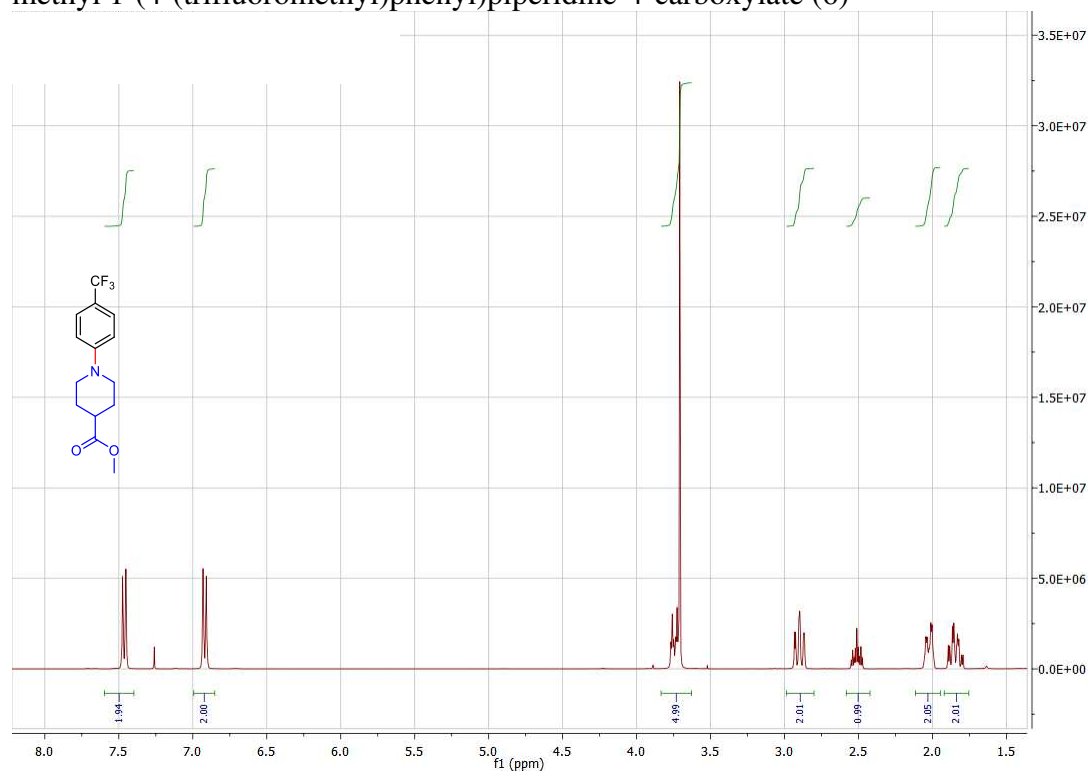


Figure S2.41.  $^1\text{H}$  NMR of methyl 1-(4-(trifluoromethyl)phenyl)piperidine-4-carboxylate (6)

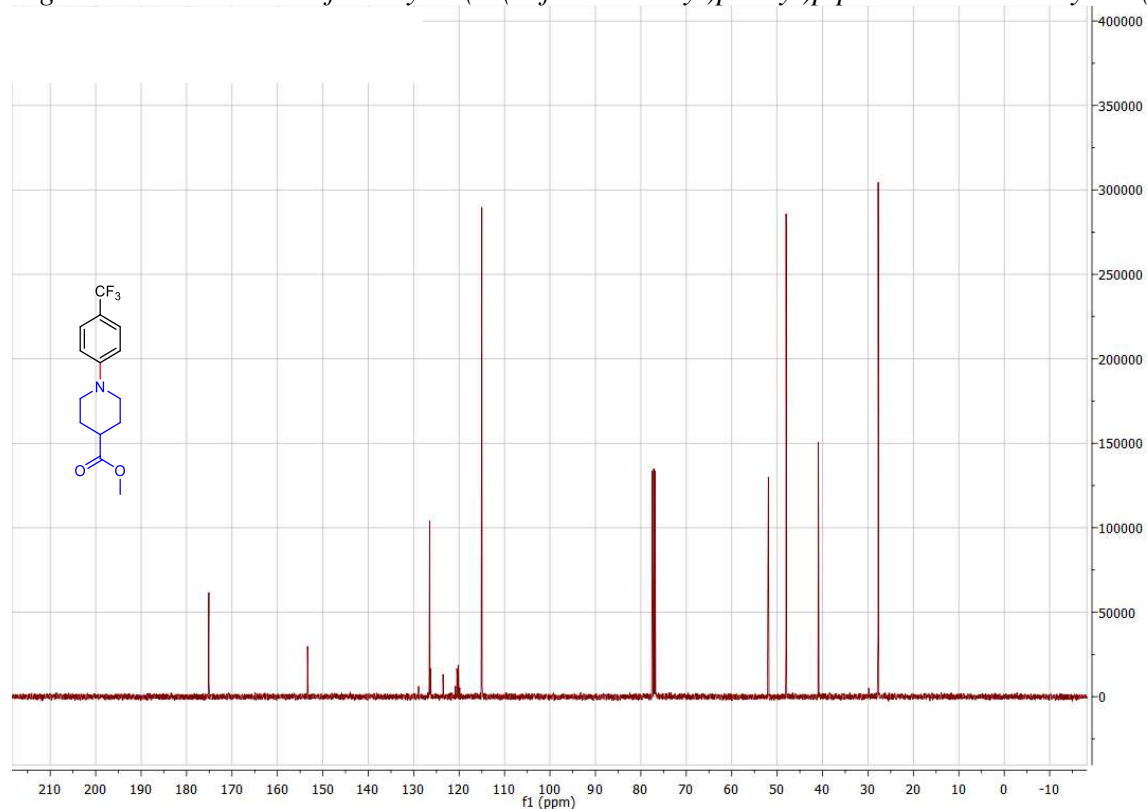


Figure S2.42.  $^{13}\text{C}$  NMR of methyl 1-(4-(trifluoromethyl)phenyl)piperidine-4-carboxylate (6)

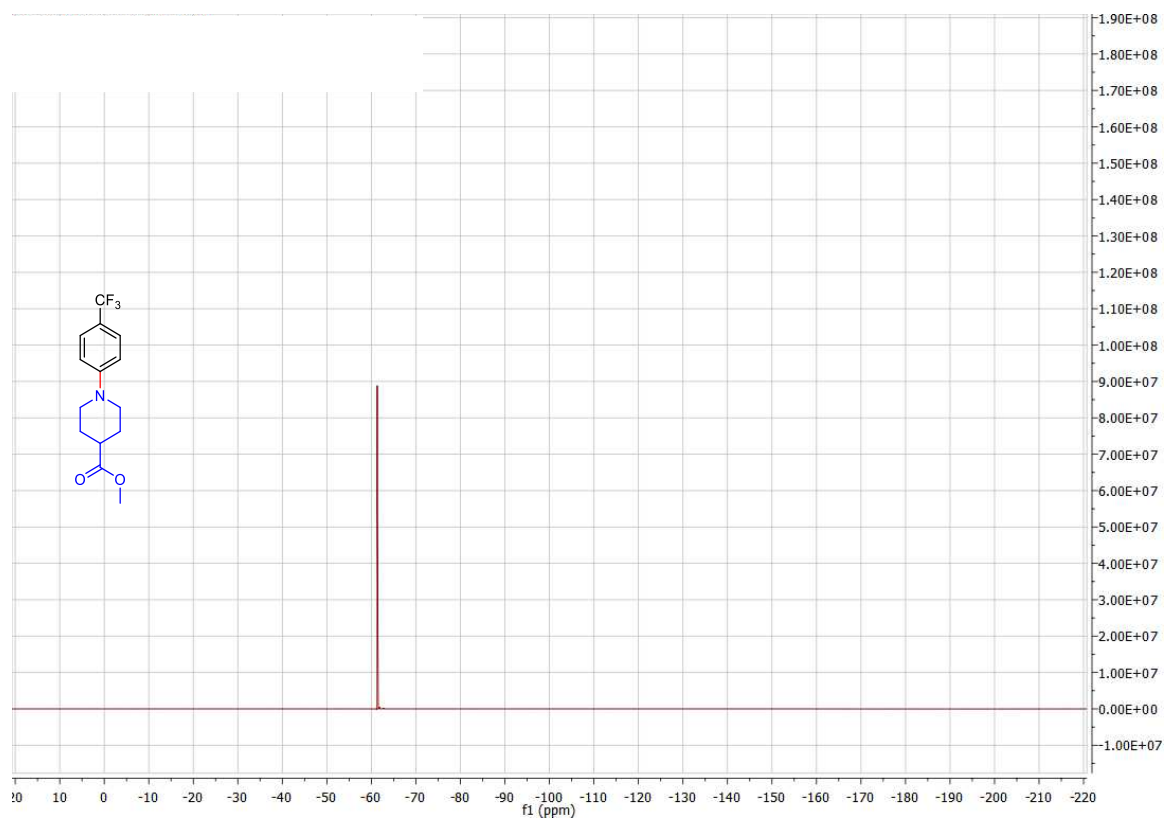


Figure S2.43.  $^{19}\text{F}$  NMR of methyl 1-(4-(trifluoromethyl)phenyl)piperidine-4-carboxylate (6)

1-(4-(trifluoromethyl)phenyl)pyrrolidine (7)

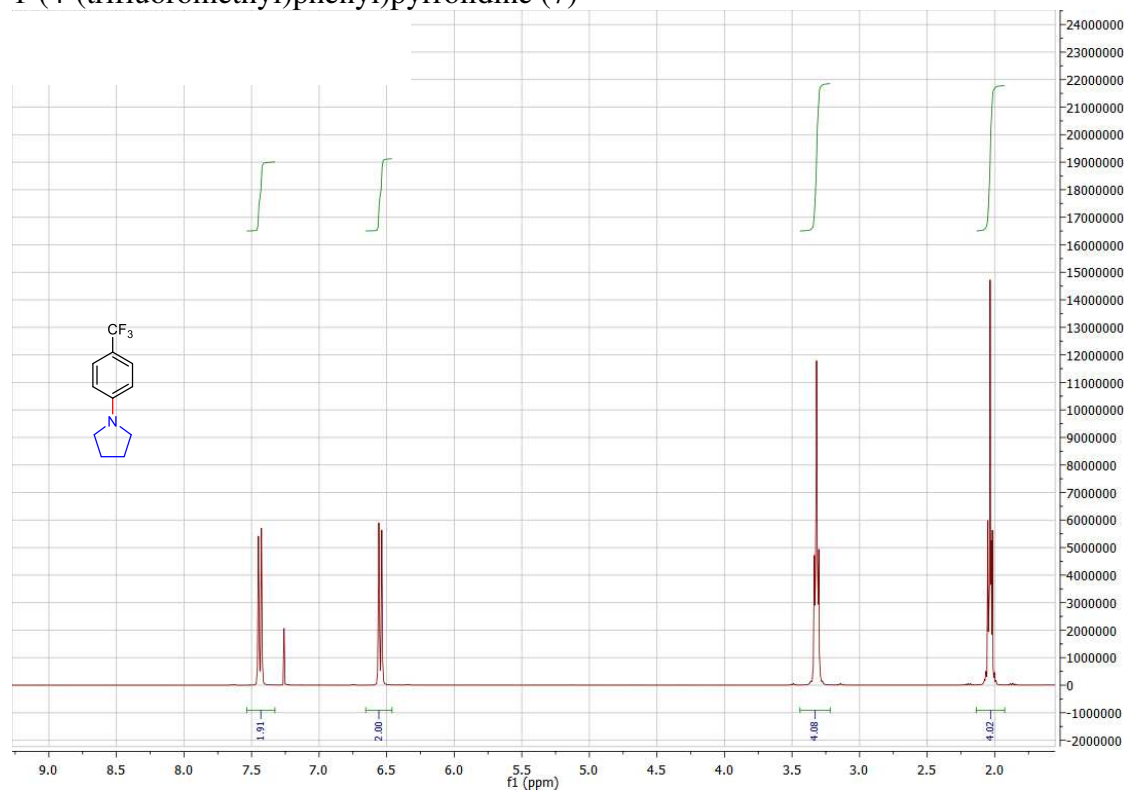


Figure S2.44.  $^1\text{H}$  NMR of 1-(4-(trifluoromethyl)phenyl)pyrrolidine (7)

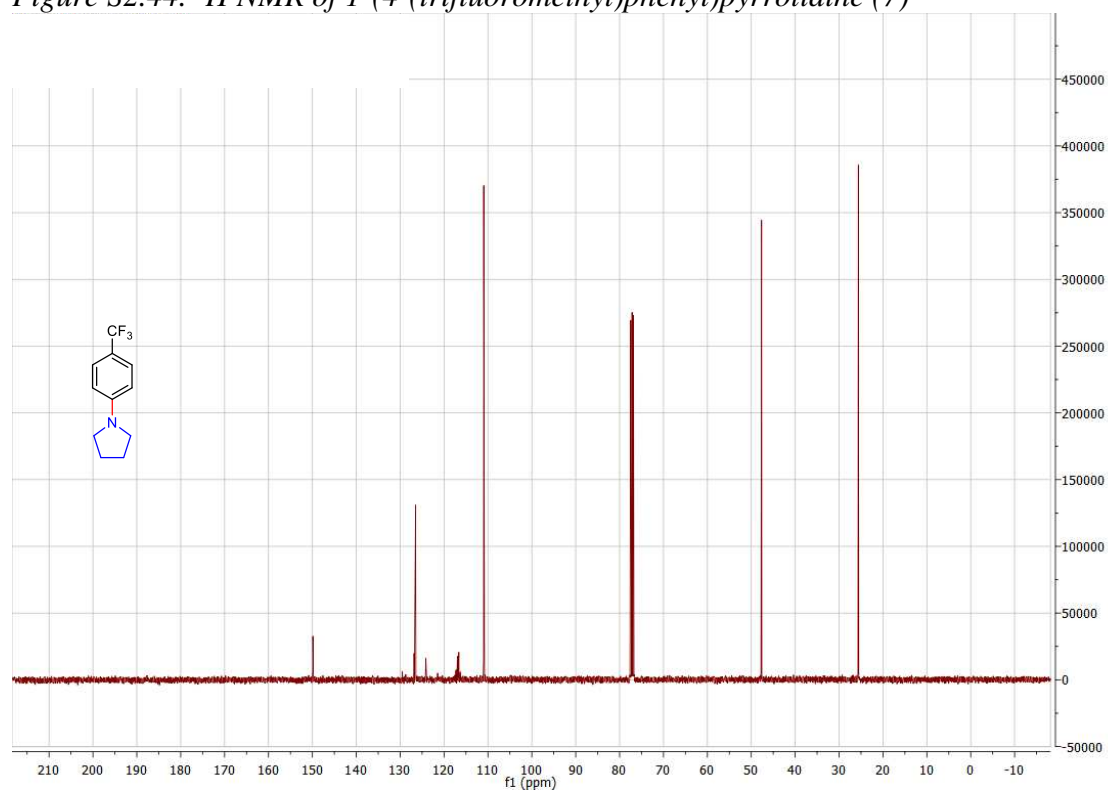


Figure S2.45.  $^{13}\text{C}$  NMR of 1-(4-(trifluoromethyl)phenyl)pyrrolidine (7)

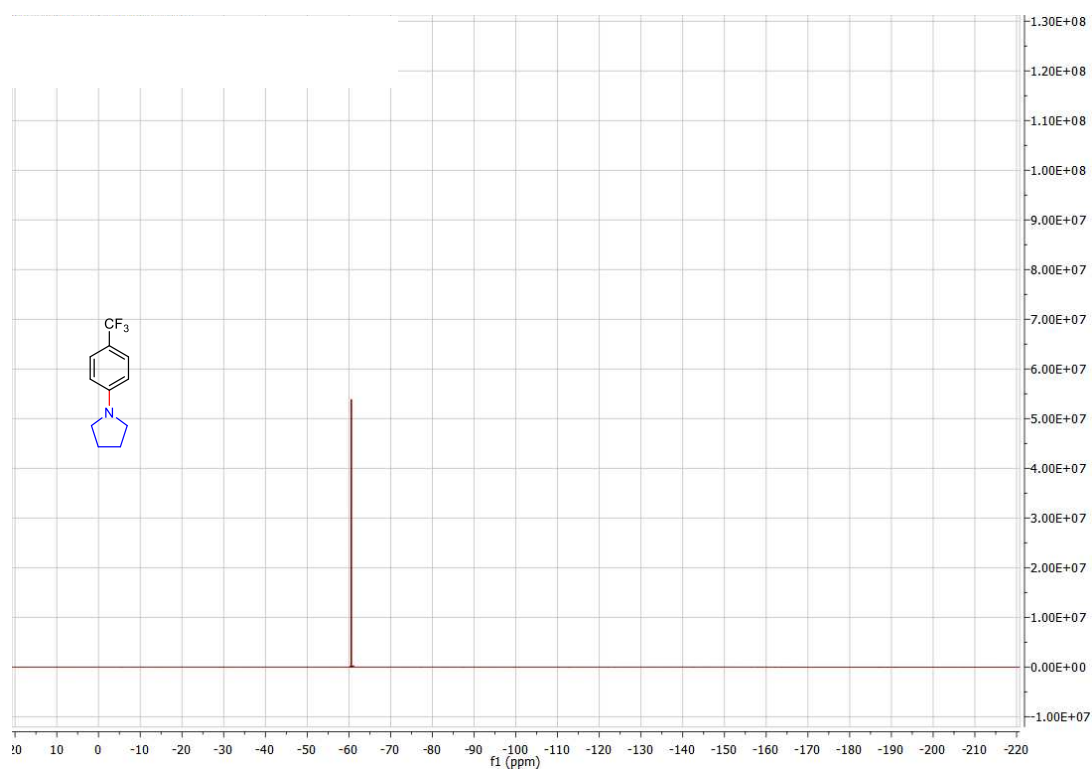


Figure S2.46.  $^{19}\text{F}$  NMR of 1-(4-(trifluoromethyl)phenyl)pyrrolidine (7)

1-(4-(trifluoromethyl)phenyl)piperazine (8)

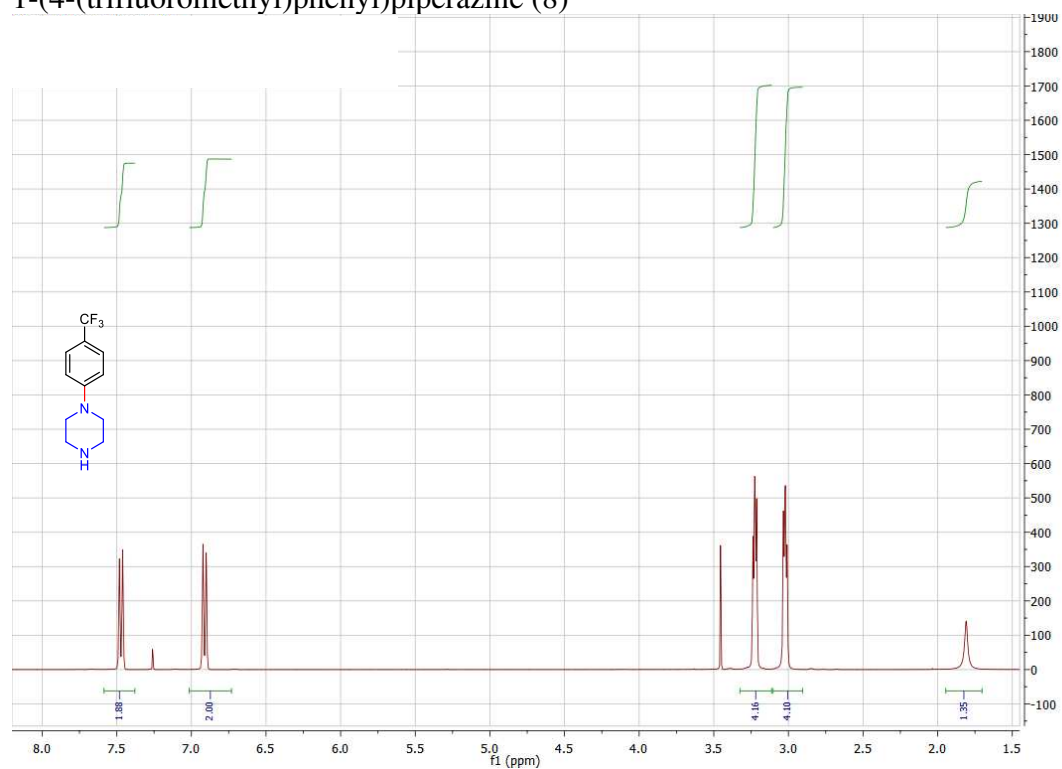


Figure S2.47.  $^1\text{H}$  NMR of 1-(4-(trifluoromethyl)phenyl)piperazine (8)

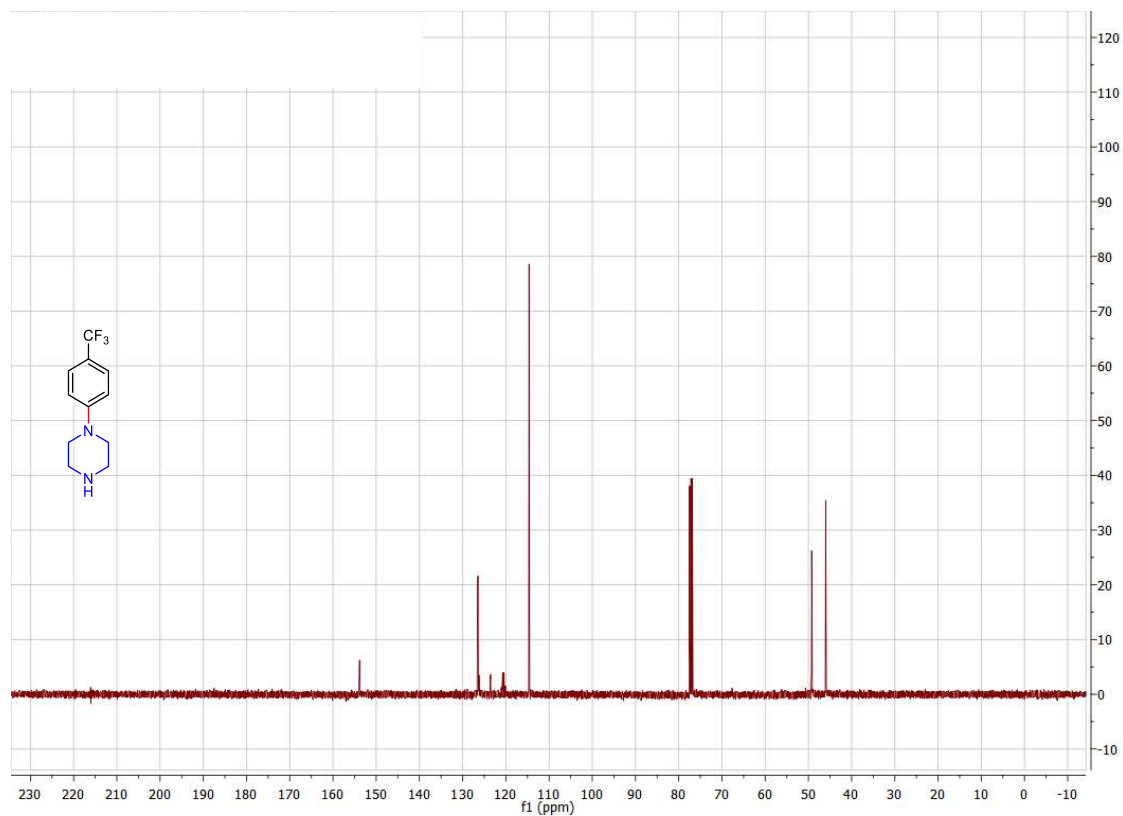


Figure S2.48.  $^{13}\text{C}$  NMR of 1-(4-(trifluoromethyl)phenyl)piperazine (8)

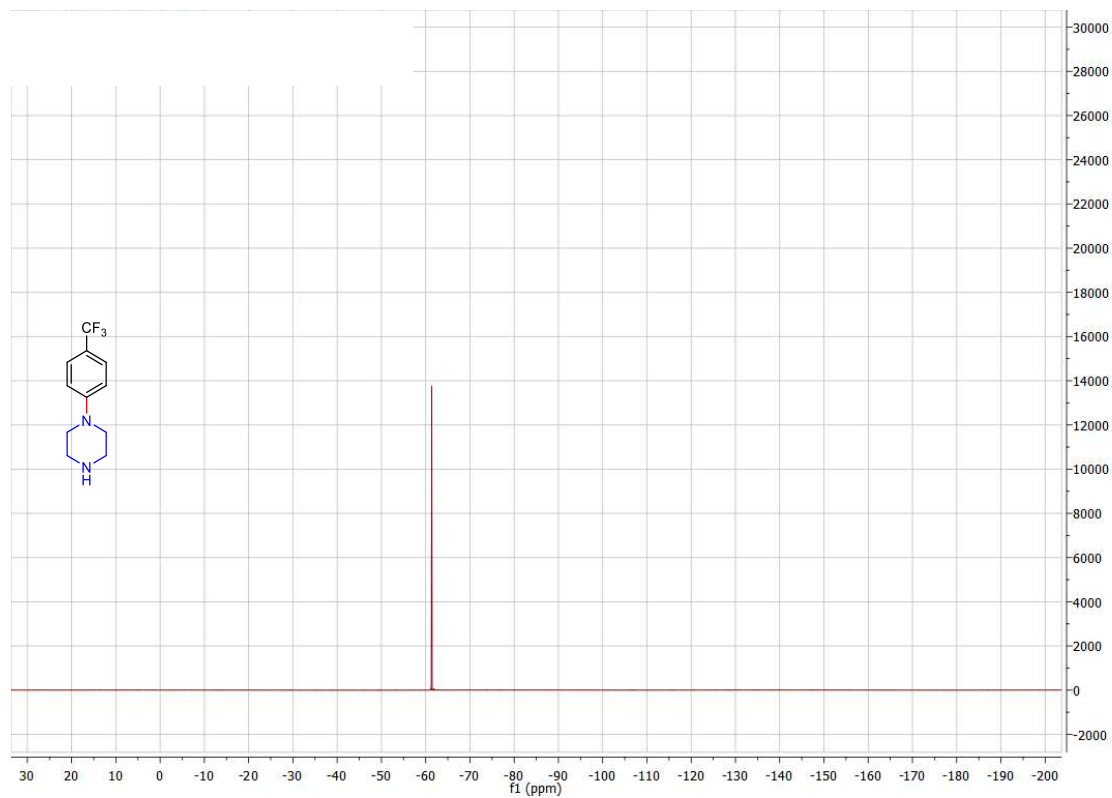


Figure S2.49.  $^{19}\text{F}$  NMR of 1-(4-(trifluoromethyl)phenyl)piperazine (8)



*tert*-butyl 4-(4-(trifluoromethyl)phenyl)piperazine-1-carboxylate (9)



Figure S2.50. <sup>1</sup>H NMR of *tert*-butyl 4-(4-(trifluoromethyl)phenyl)piperazine-1-carboxylate (9)

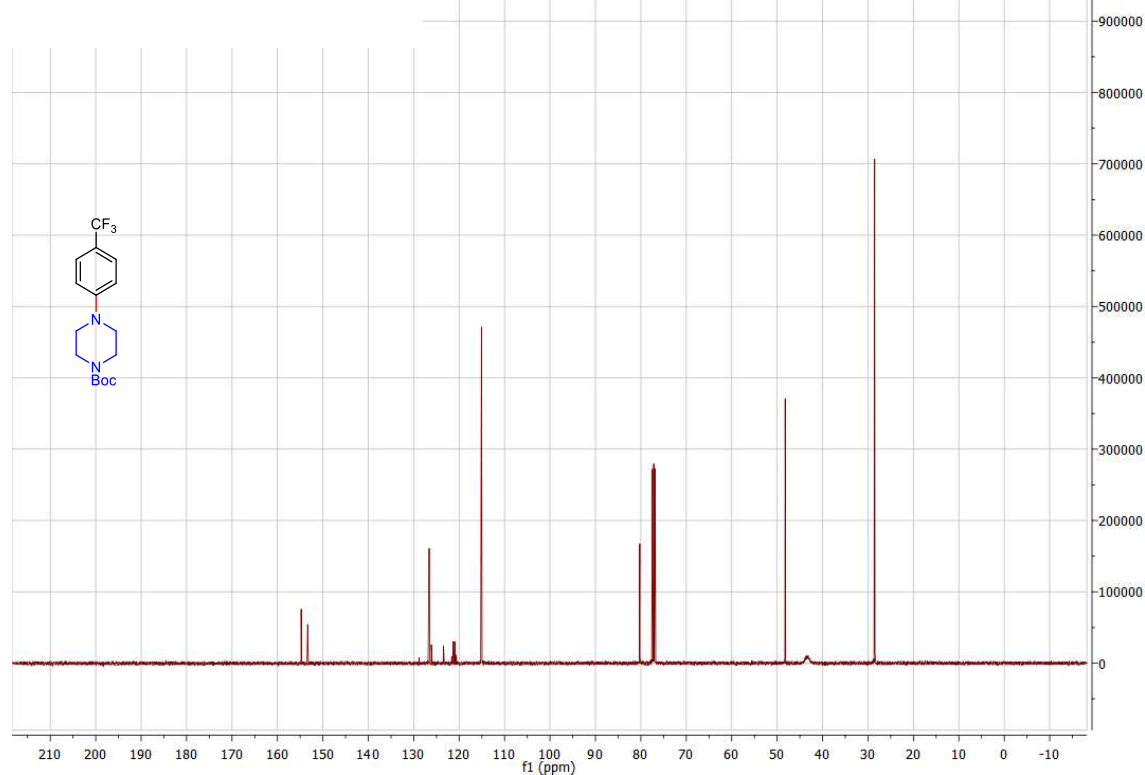


Figure S2.51. <sup>13</sup>C NMR of *tert*-butyl 4-(4-(trifluoromethyl)phenyl)piperazine-1-carboxylate (9)

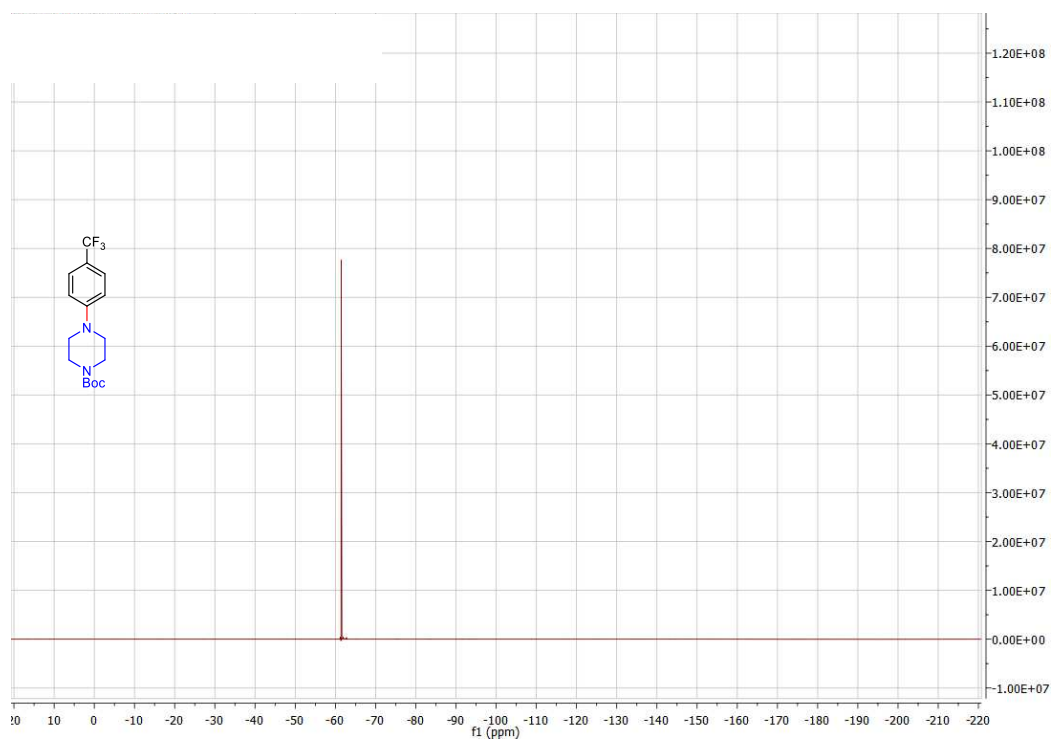


Figure S2.52.  $^{19}\text{F}$  NMR of tert-butyl 4-(4-(trifluoromethyl)phenyl)piperazine-1-carboxylate (9)

N-cyclohexyl-4-(trifluoromethyl)aniline (10)

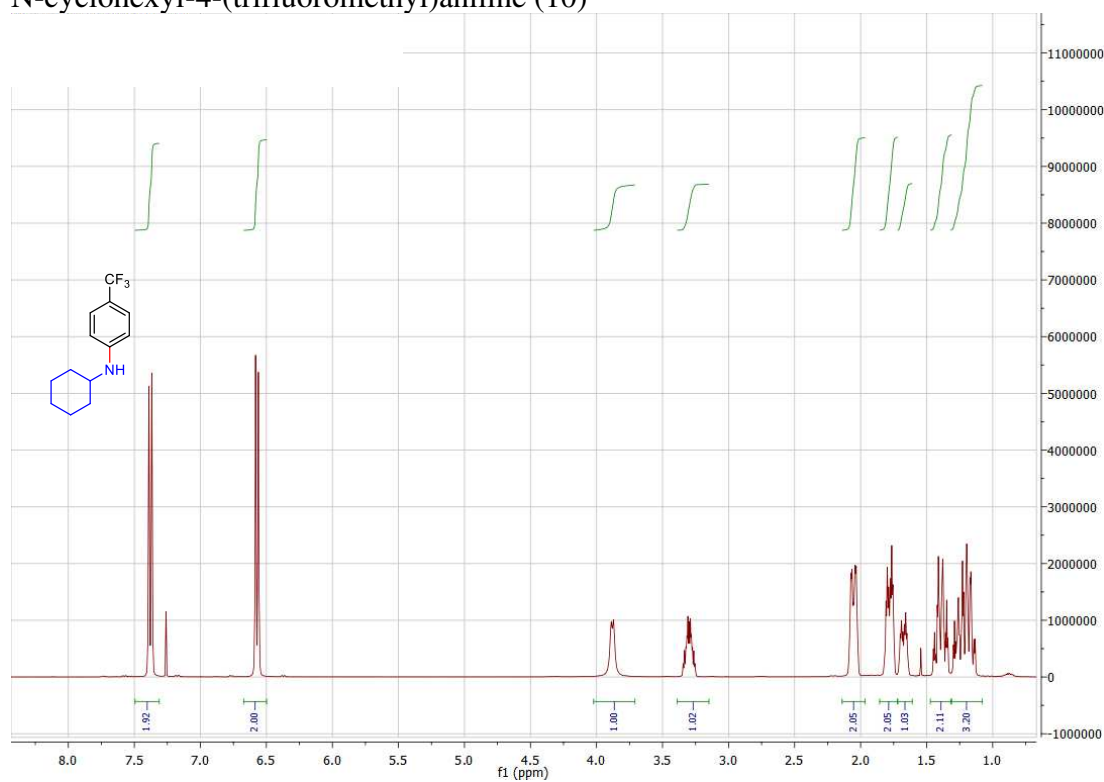


Figure S2.53.  $^1\text{H}$  NMR of N-cyclohexyl-4-(trifluoromethyl)aniline (10)

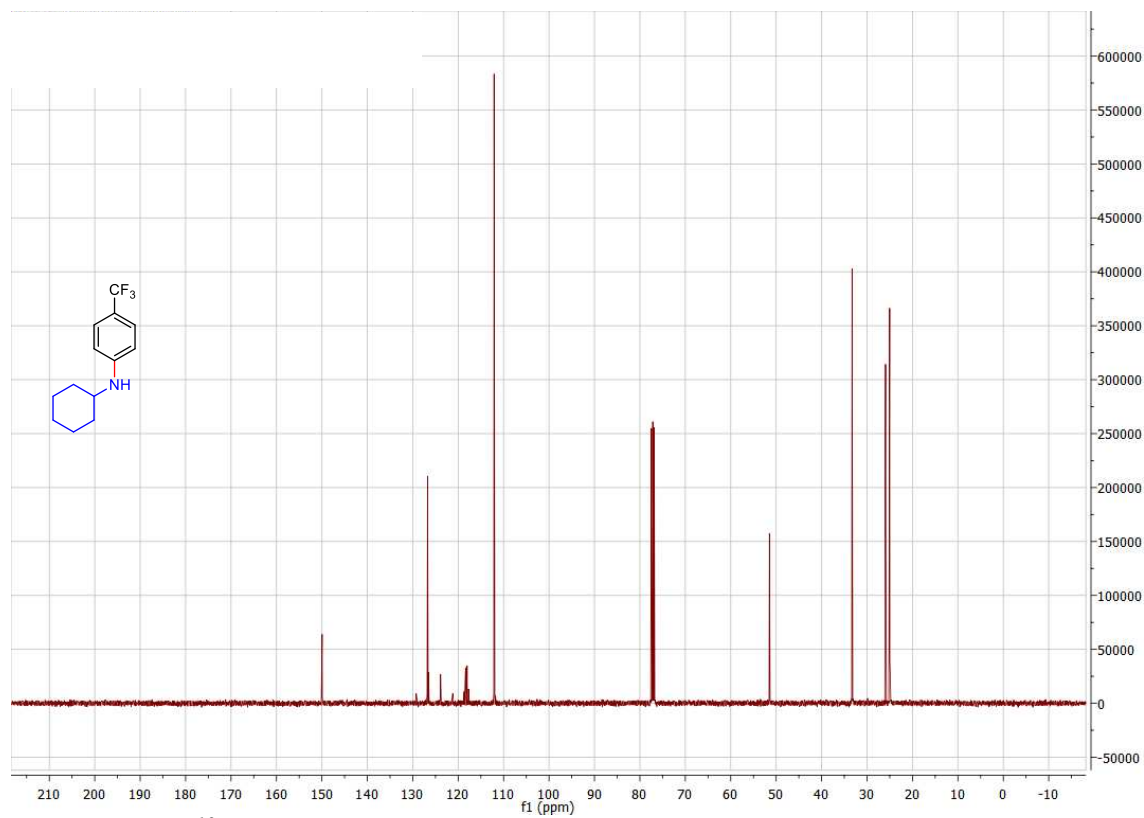


Figure S2.54.  $^{13}\text{C}$  NMR of *N*-cyclohexyl-4-(trifluoromethyl)aniline (10)

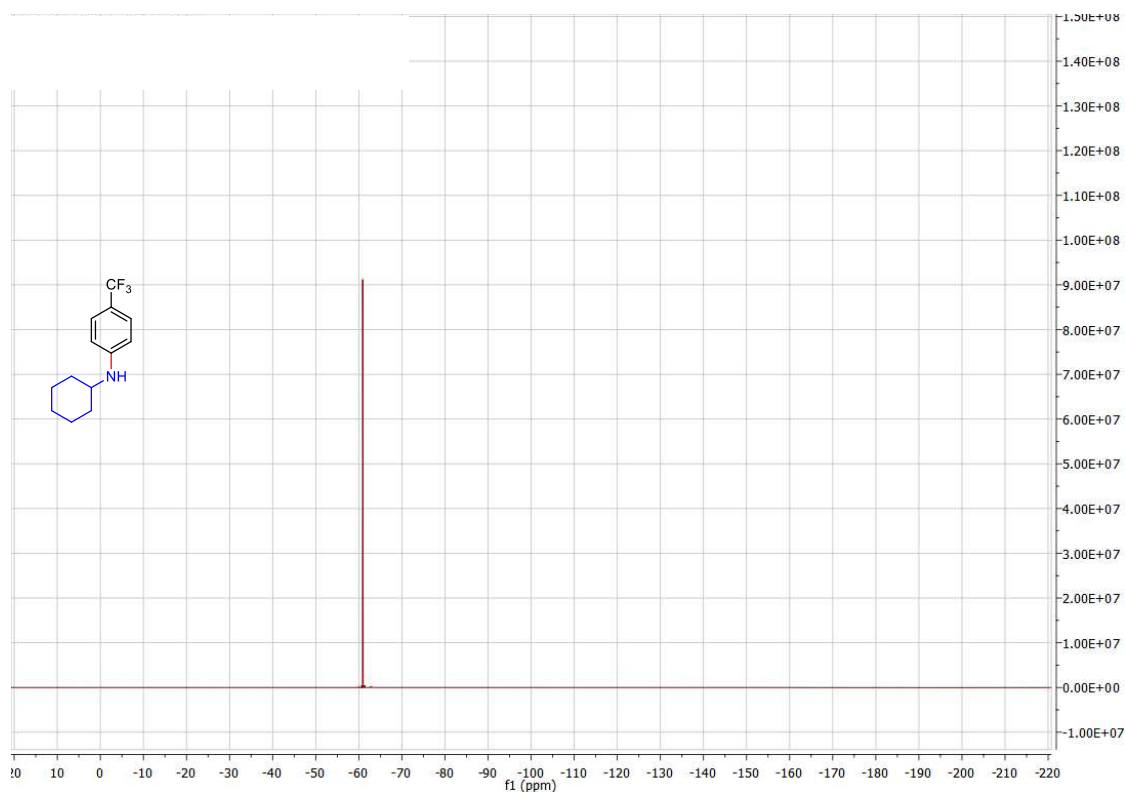


Figure S2.55.  $^{19}\text{F}$  NMR of *N*-cyclohexyl-4-(trifluoromethyl)aniline (10)

N-propyl-4-(trifluoromethyl)aniline (11)

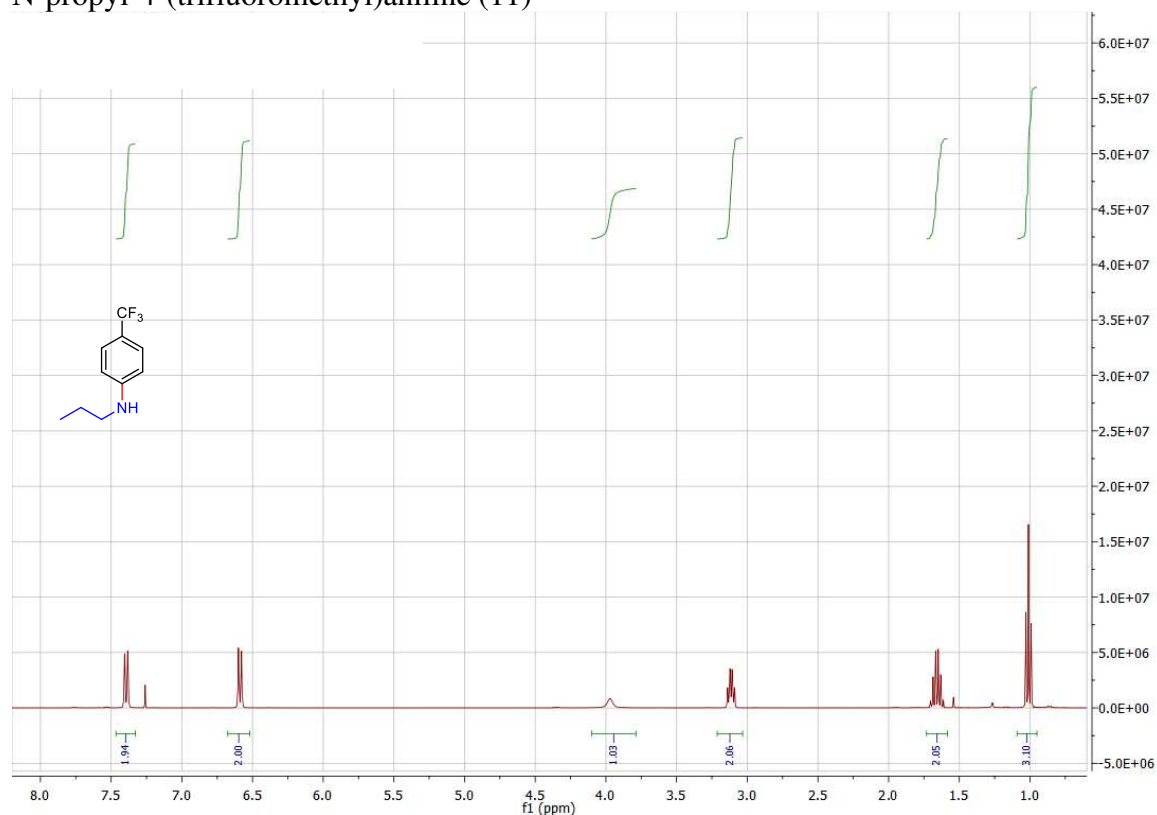


Figure S2.56.  $^1\text{H}$  NMR of N-propyl-4-(trifluoromethyl)aniline (11)

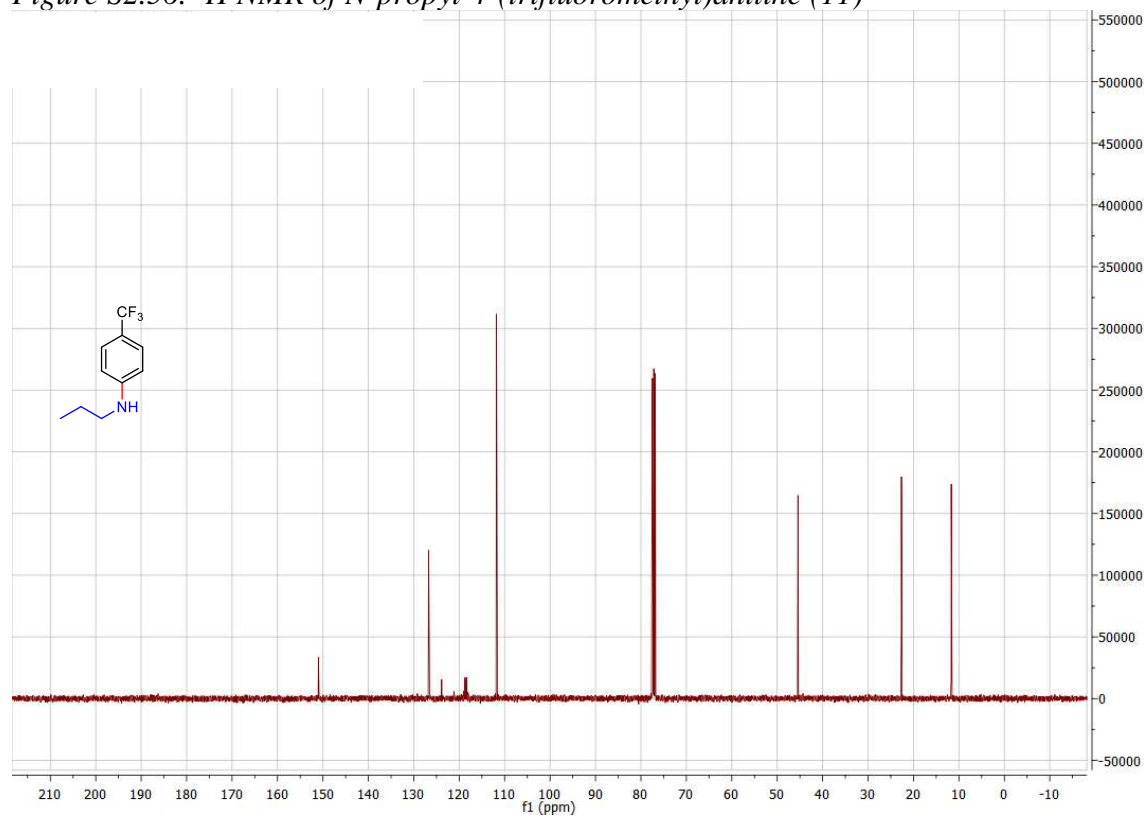
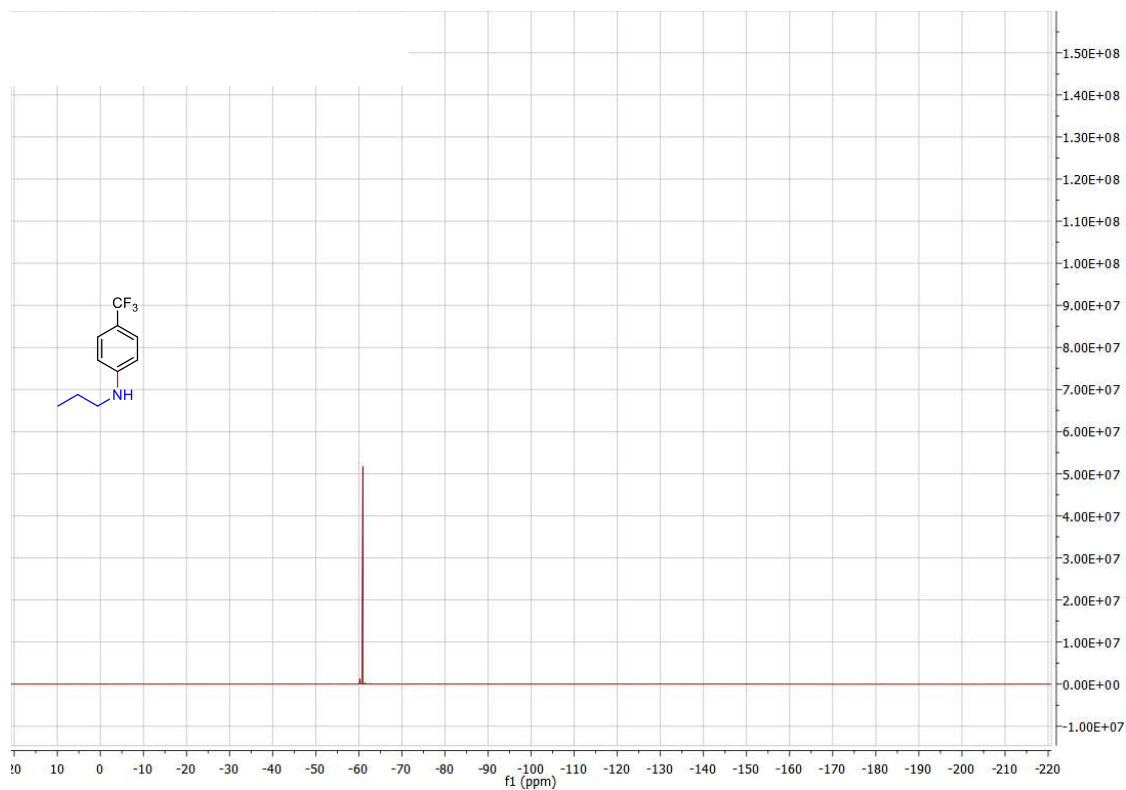
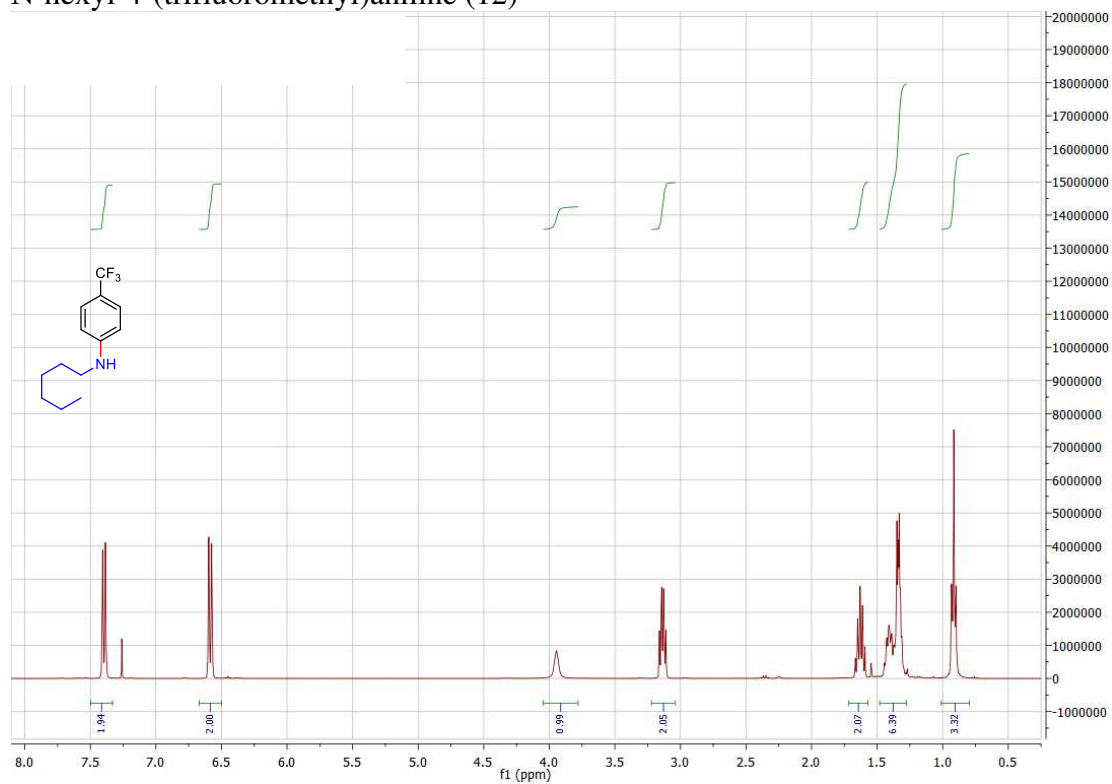


Figure S2.57.  $^{13}\text{C}$  NMR of N-propyl-4-(trifluoromethyl)aniline (11)



*N*-hexyl-4-(trifluoromethyl)aniline (12)



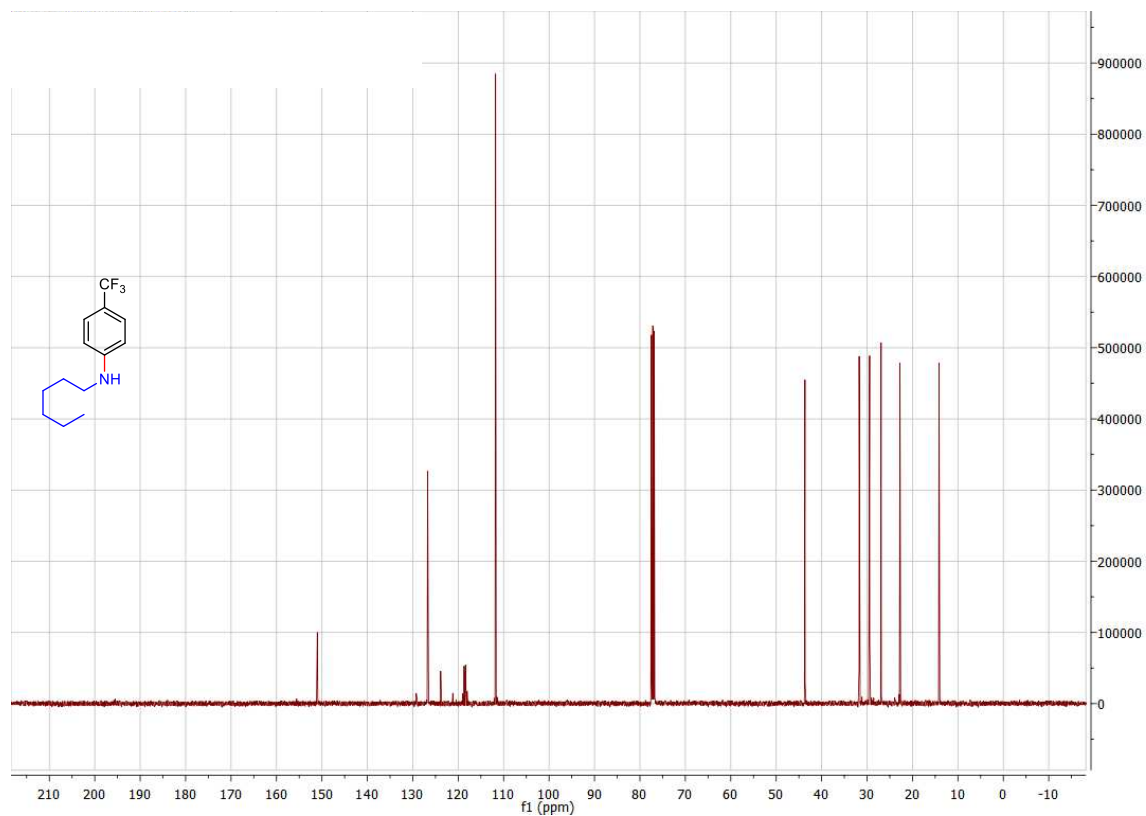


Figure S2.60.  $^{13}\text{C}$  NMR of *N*-hexyl-4-(trifluoromethyl)aniline (12)

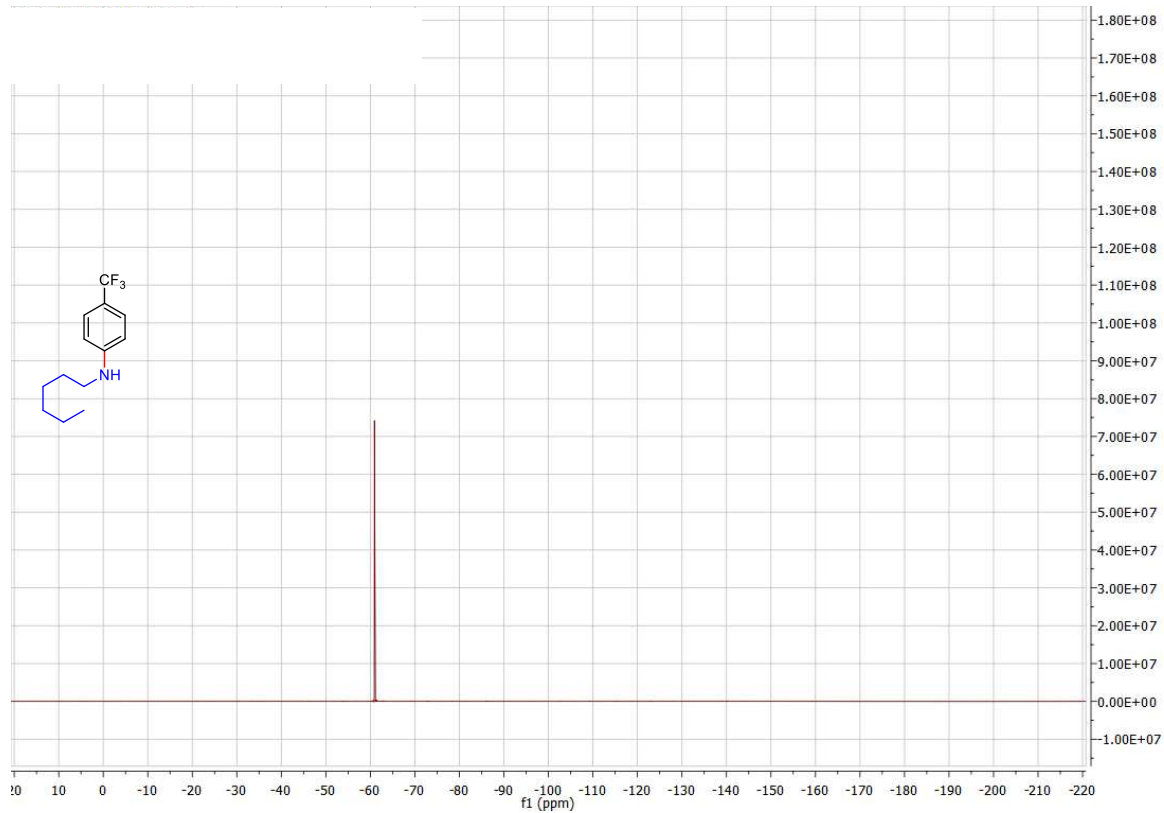


Figure S2.61.  $^{19}\text{F}$  NMR of *N*-hexyl-4-(trifluoromethyl)aniline (12)

N-phenethyl-4-(trifluoromethyl)aniline (13)

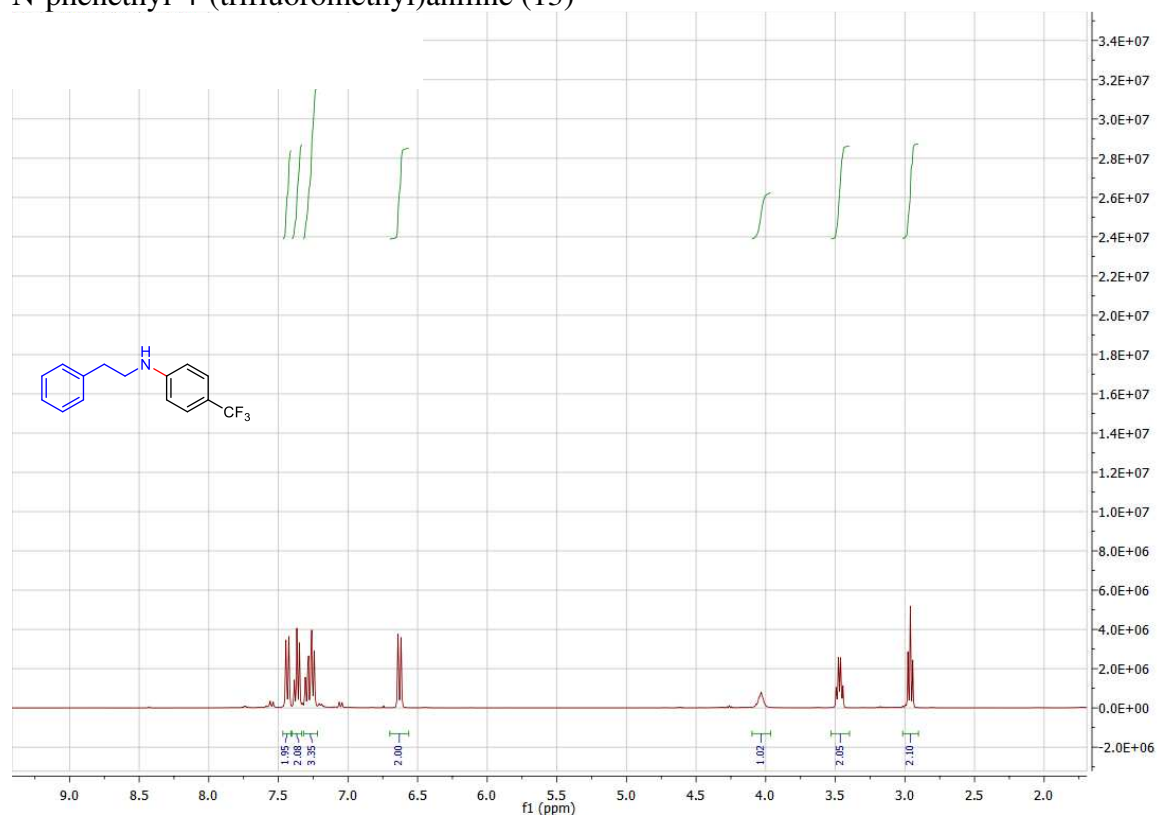


Figure S2.62. <sup>1</sup>H NMR of N-phenethyl-4-(trifluoromethyl)aniline (13)

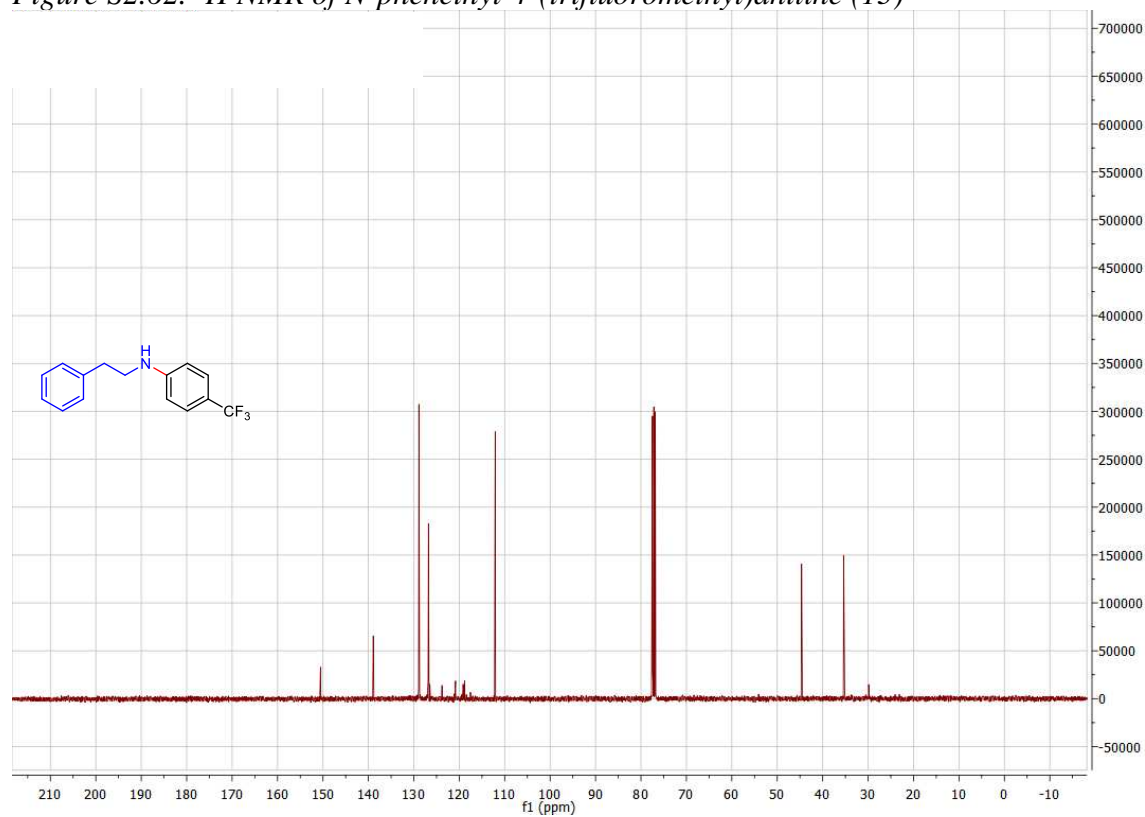


Figure S2.63. <sup>13</sup>C NMR of N-phenethyl-4-(trifluoromethyl)aniline (13)

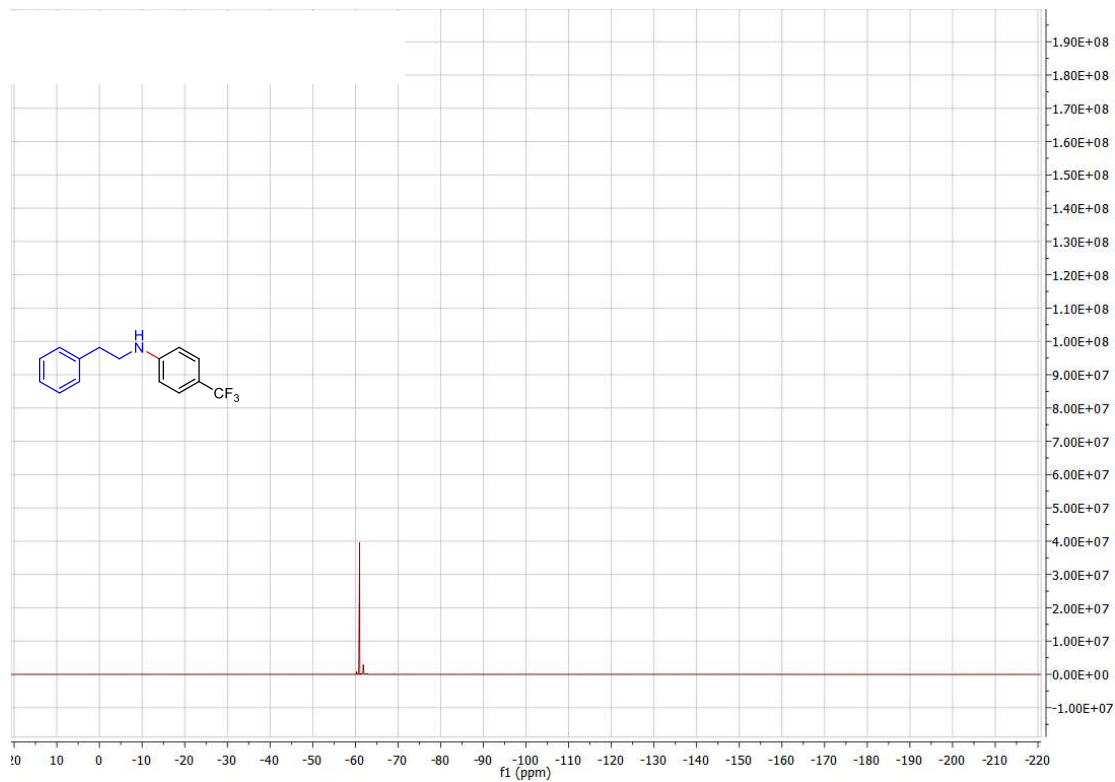


Figure S2.64.  $^{19}\text{F}$  NMR of *N*-phenethyl-4-(trifluoromethyl)aniline (13)

*N*-phenyl-4-(trifluoromethyl)aniline (14)

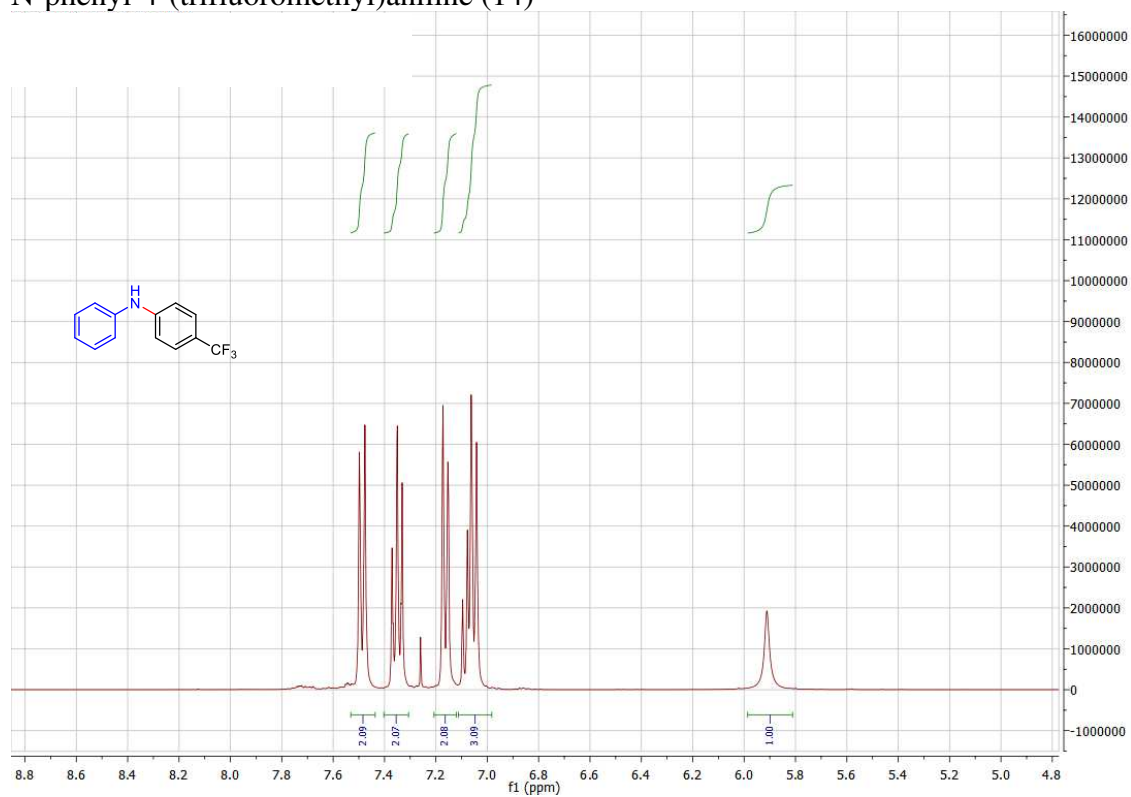


Figure S2.65.  $^1\text{H}$  NMR of *N*-phenyl-4-(trifluoromethyl)aniline (14)



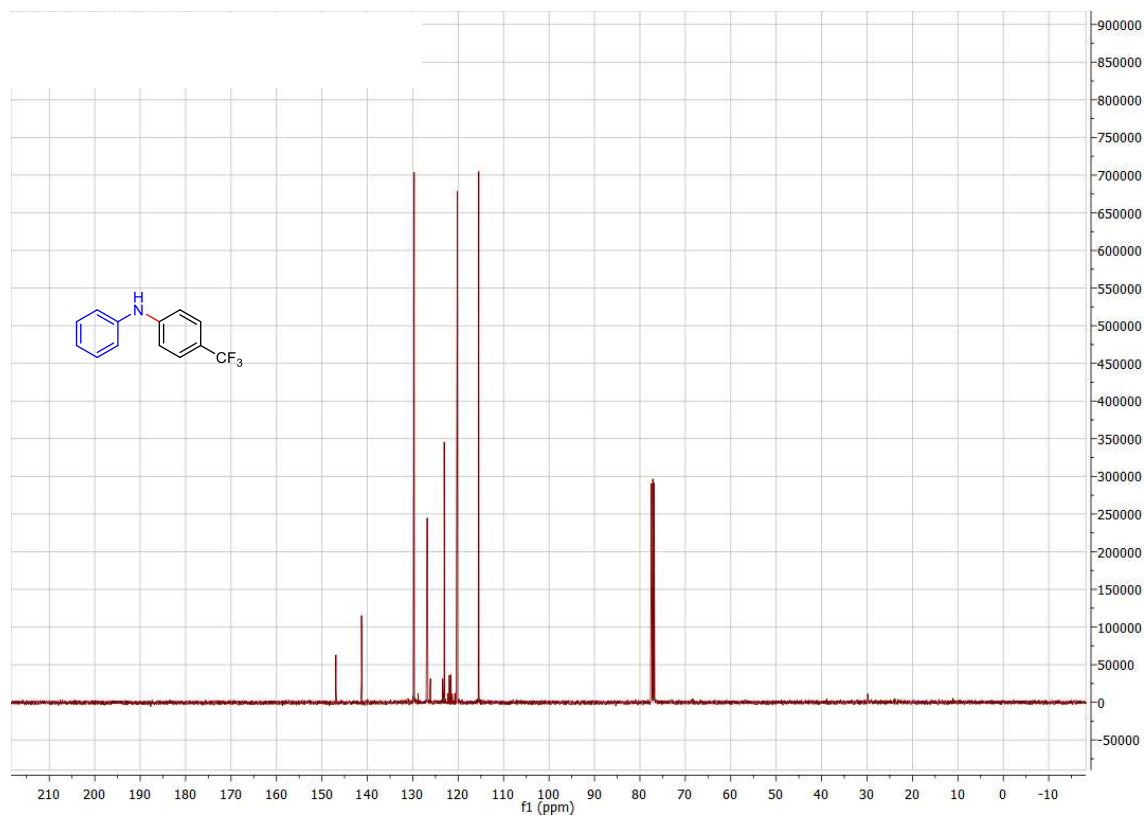


Figure S2.66.  $^{13}\text{C}$  NMR of *N*-phenyl-4-(trifluoromethyl)aniline (14)

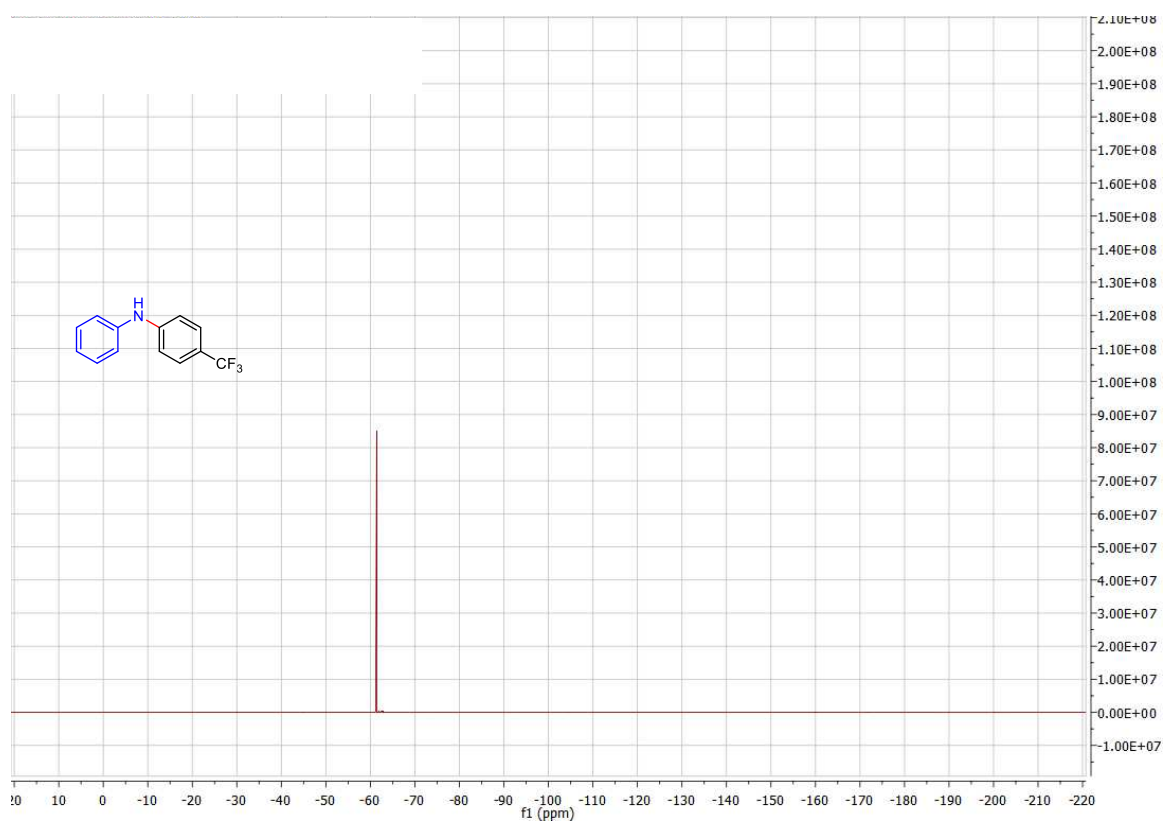


Figure S2.67.  $^{19}\text{F}$  NMR of *N*-phenyl-4-(trifluoromethyl)aniline (14)

4-fluoro-N-(4-(trifluoromethyl)phenyl)aniline (15)

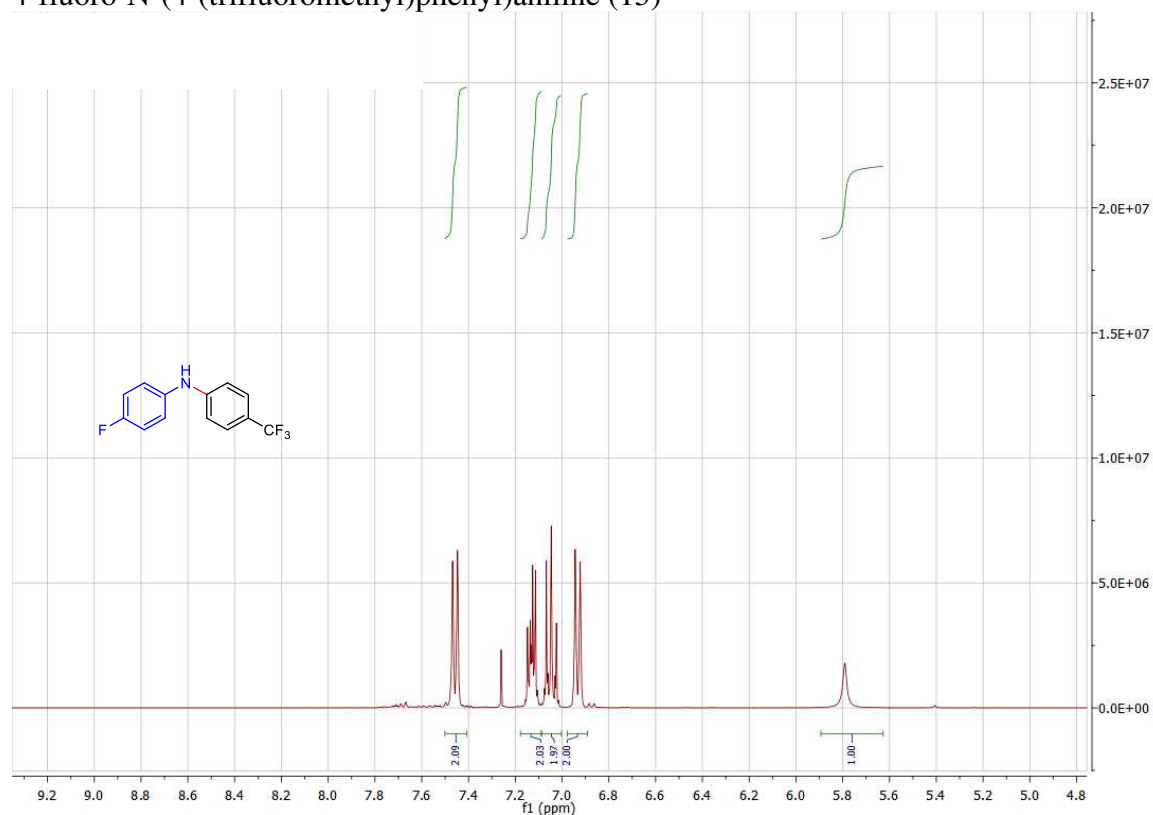


Figure S2.68. <sup>1</sup>H NMR of 4-fluoro-N-(4-(trifluoromethyl)phenyl)aniline (15)

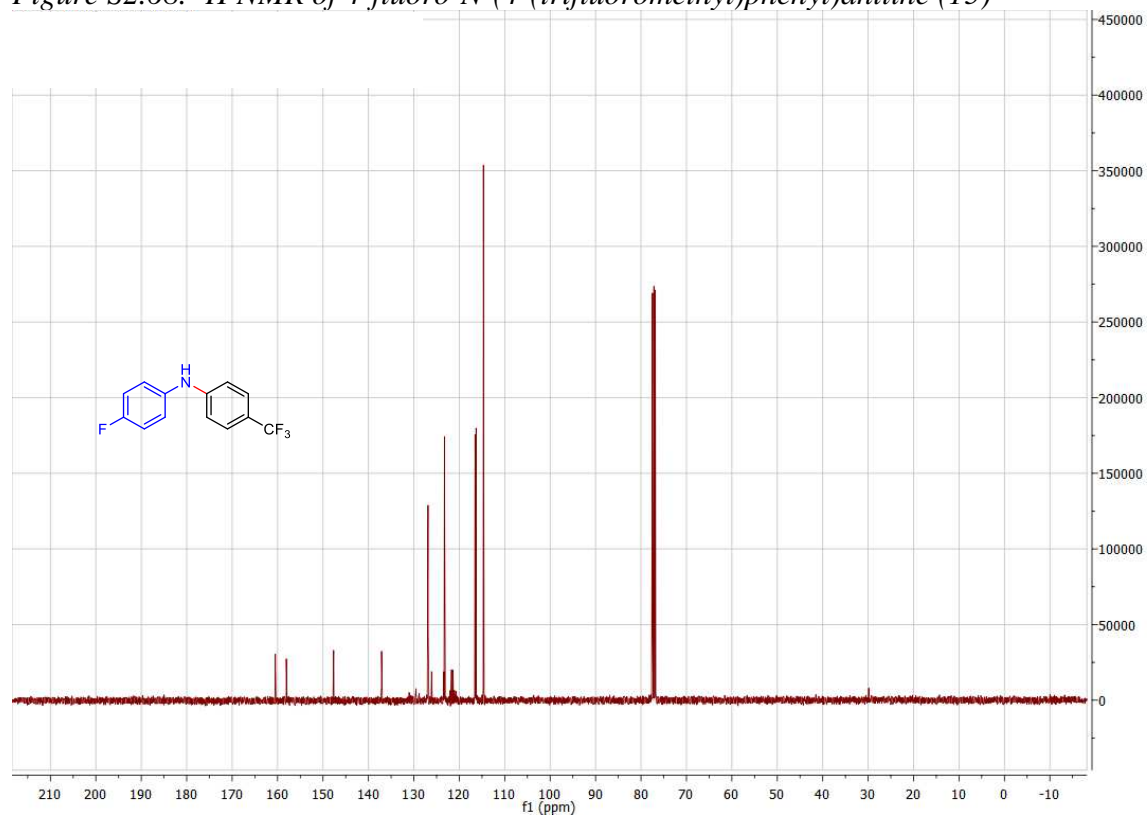


Figure S2.69. <sup>13</sup>C NMR of 4-fluoro-N-(4-(trifluoromethyl)phenyl)aniline (15)

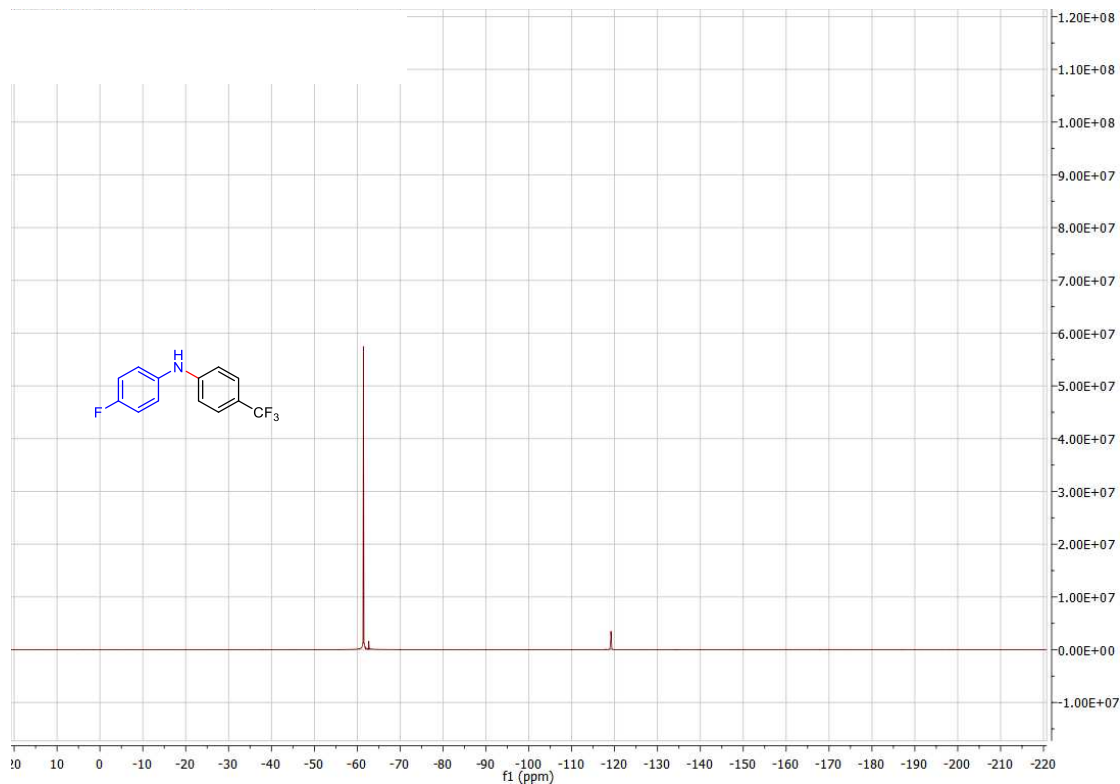


Figure S2.70.  $^{19}\text{F}$  NMR of 4-fluoro-N-(4-(trifluoromethyl)phenyl)aniline (15)

N-(furan-2-ylmethyl)-4-(trifluoromethyl)aniline (16)

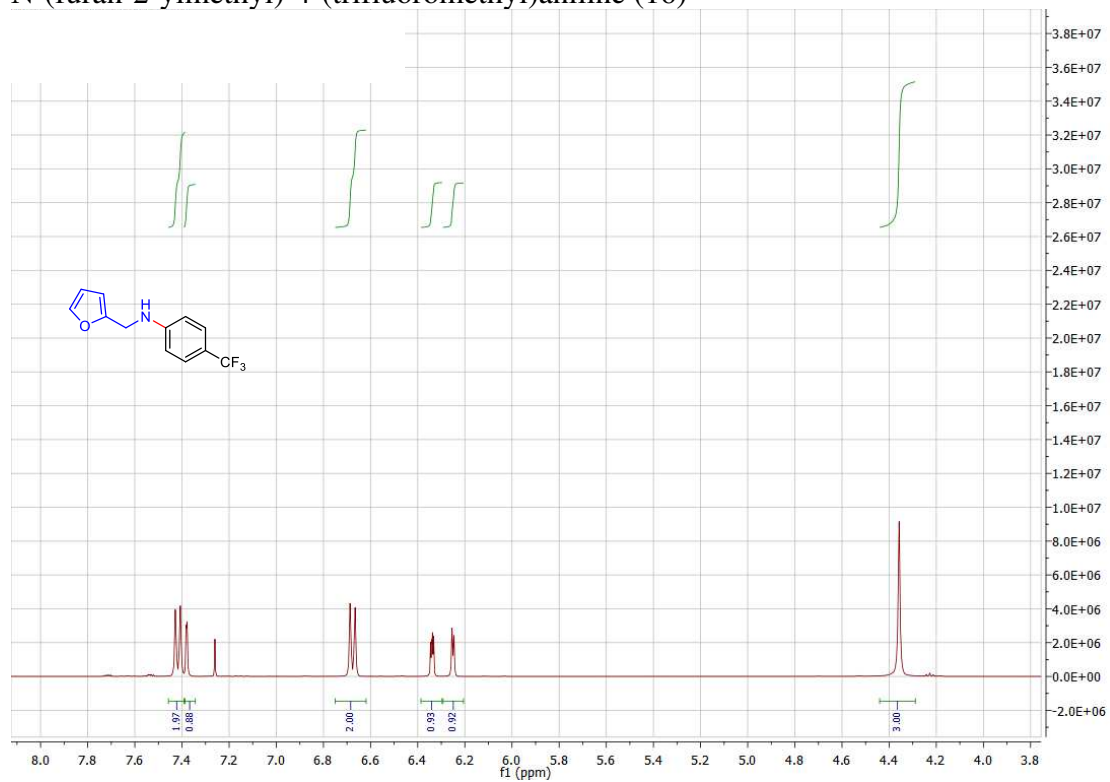


Figure S2.71.  $^1\text{H}$  NMR of N-(furan-2-ylmethyl)-4-(trifluoromethyl)aniline (16)

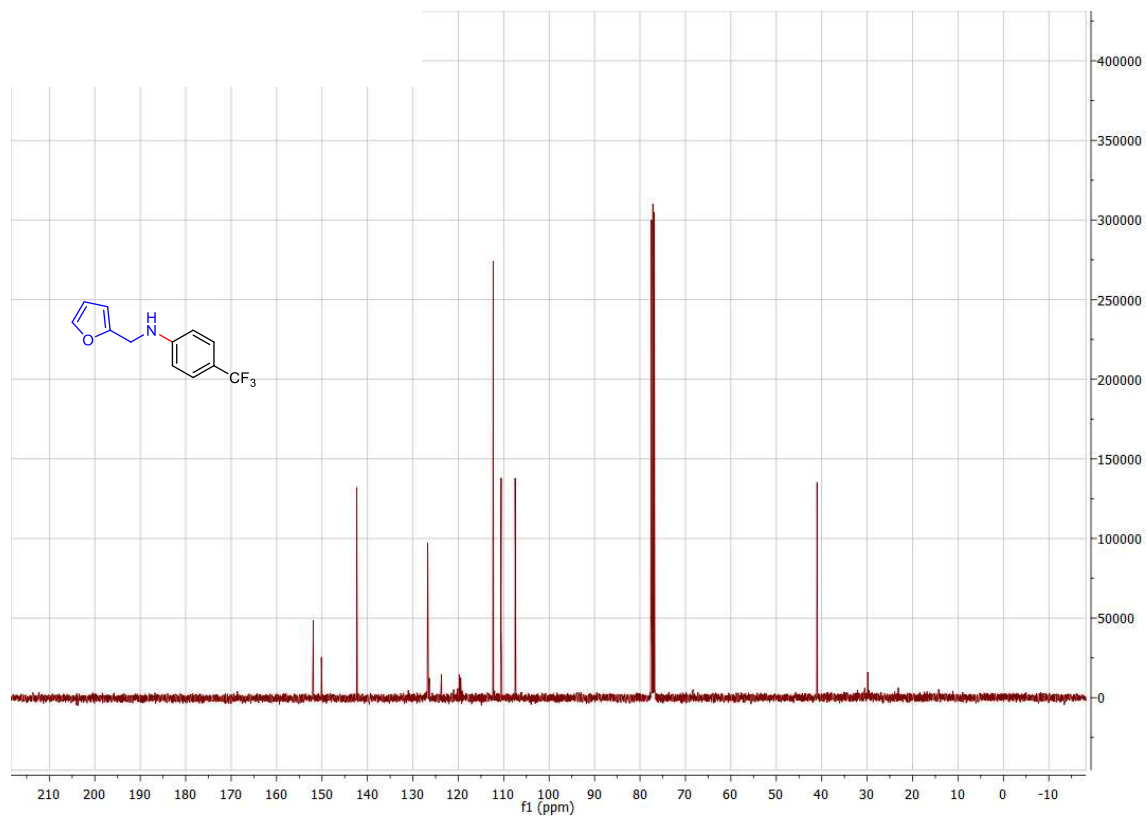


Figure S2.72.  $^{13}\text{C}$  NMR of *N*-(furan-2-ylmethyl)-4-(trifluoromethyl)aniline (16)

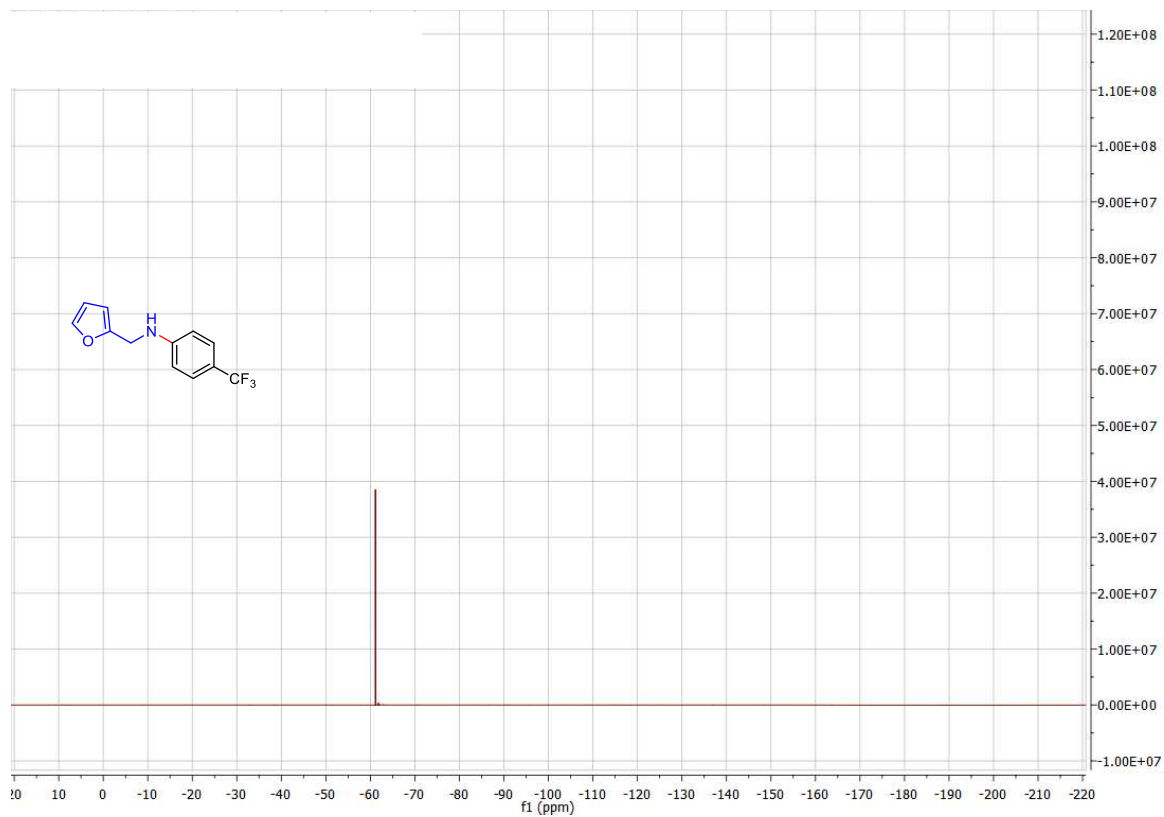


Figure S2.73.  $^{19}\text{F}$  NMR of *N*-(furan-2-ylmethyl)-4-(trifluoromethyl)aniline (16)

N-(4-(trifluoromethyl)phenyl)pyridin-3-amine (17)

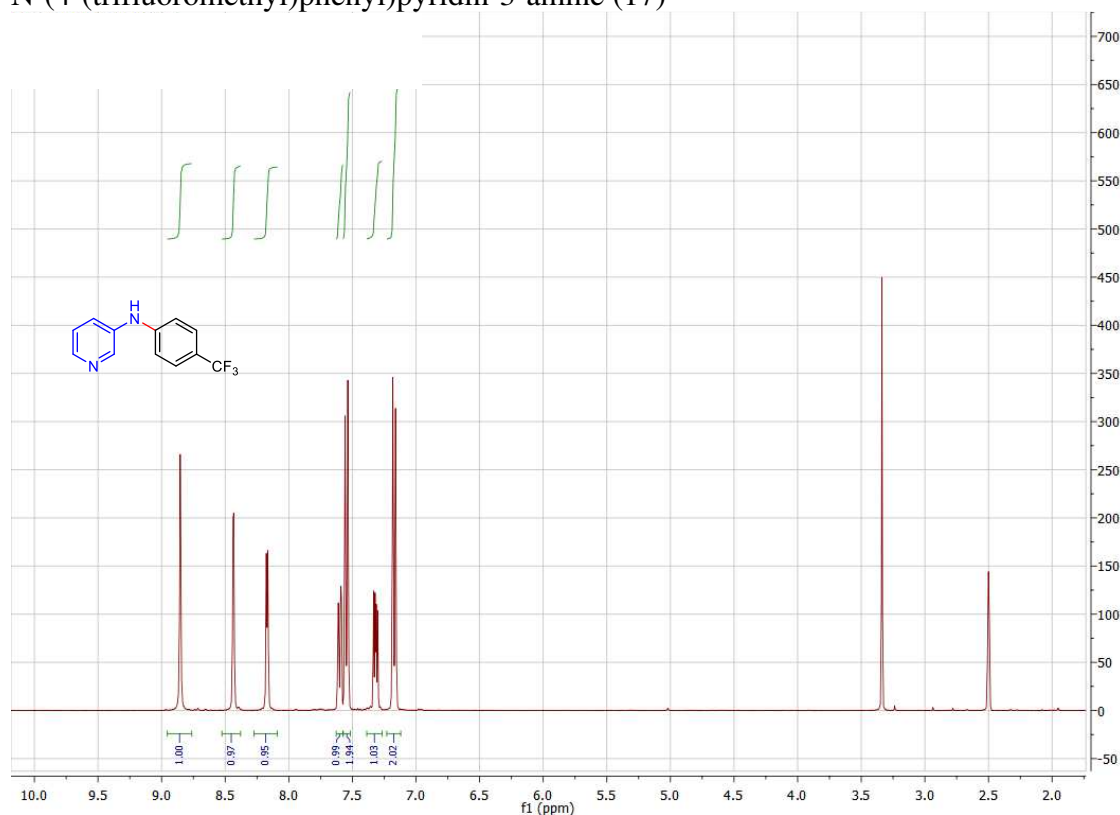


Figure S2.74.  $^1\text{H}$  NMR of N-(4-(trifluoromethyl)phenyl)pyridin-3-amine (17)

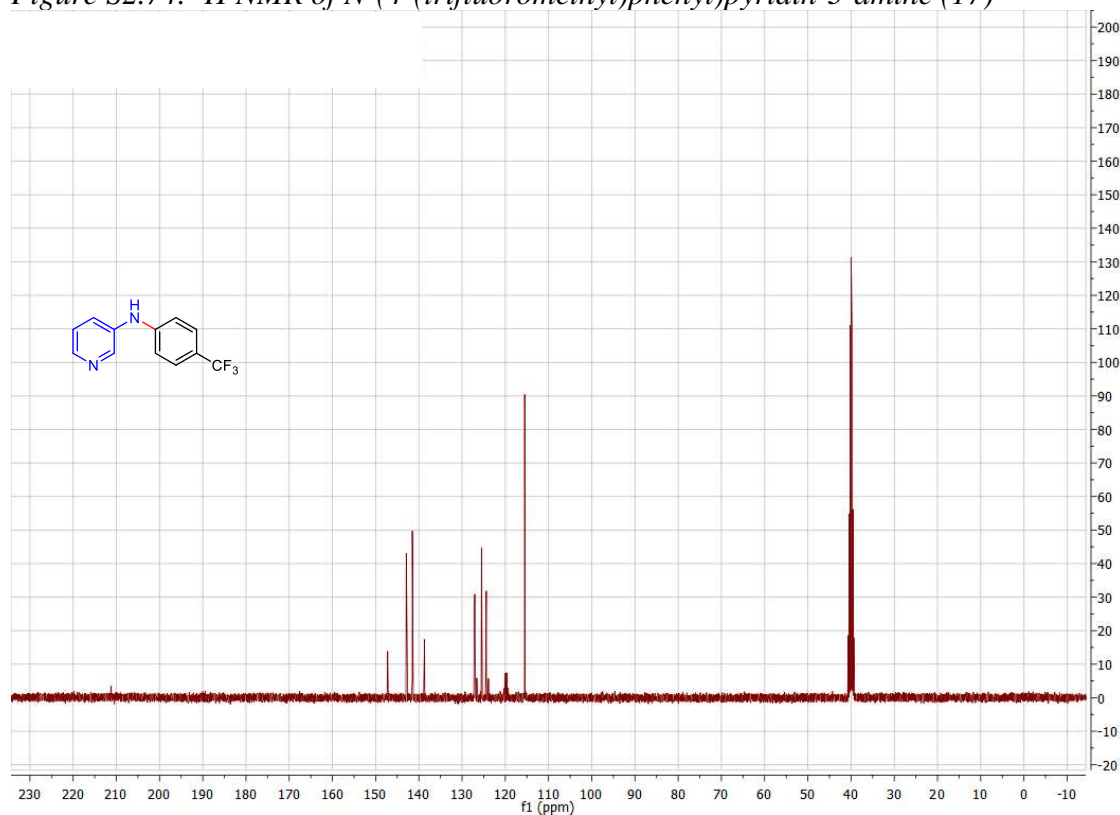


Figure S2.75.  $^{13}\text{C}$  NMR of N-(4-(trifluoromethyl)phenyl)pyridin-3-amine (17)

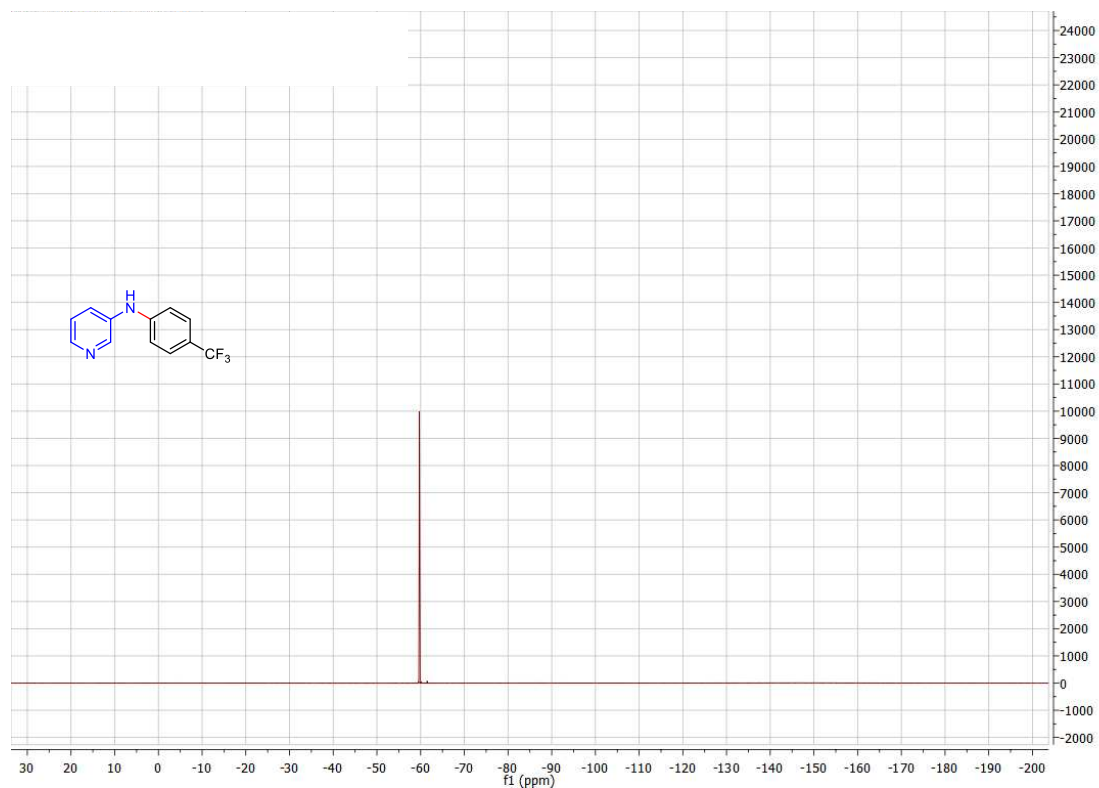


Figure S2.76.  $^{19}\text{F}$  NMR of *N*-(4-(trifluoromethyl)phenyl)pyridin-3-amine (17)

4-(3-(trifluoromethyl)phenyl)morpholine (18)

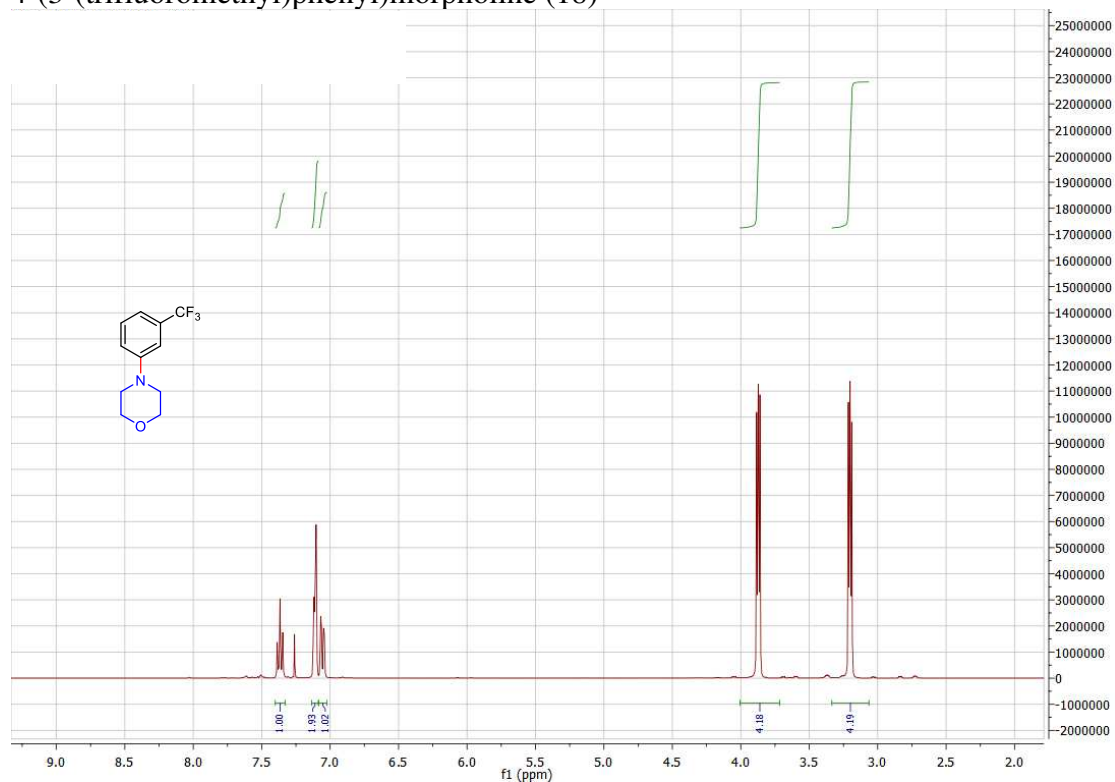


Figure S2.77.  $^1\text{H}$  NMR of 4-(3-(trifluoromethyl)phenyl)morpholine (18)

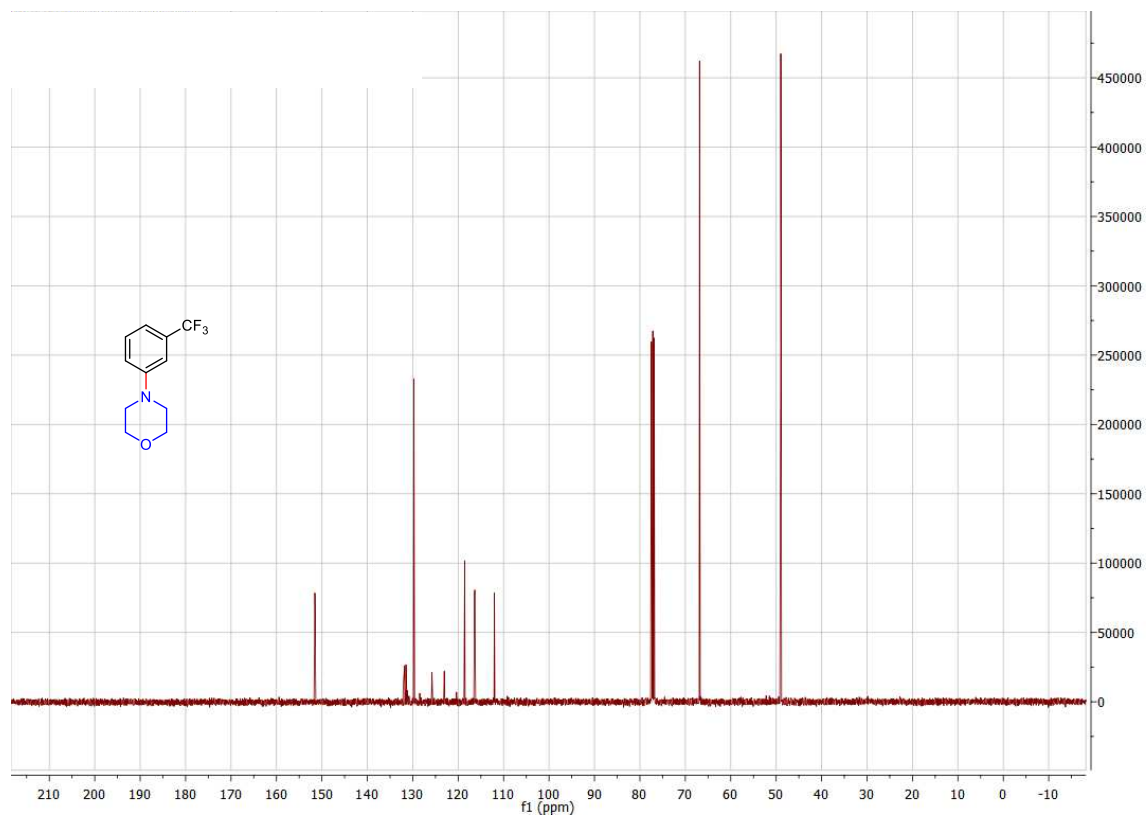


Figure S2.78.  $^{13}\text{C}$  NMR of 4-(3-(trifluoromethyl)phenyl)morpholine (18)

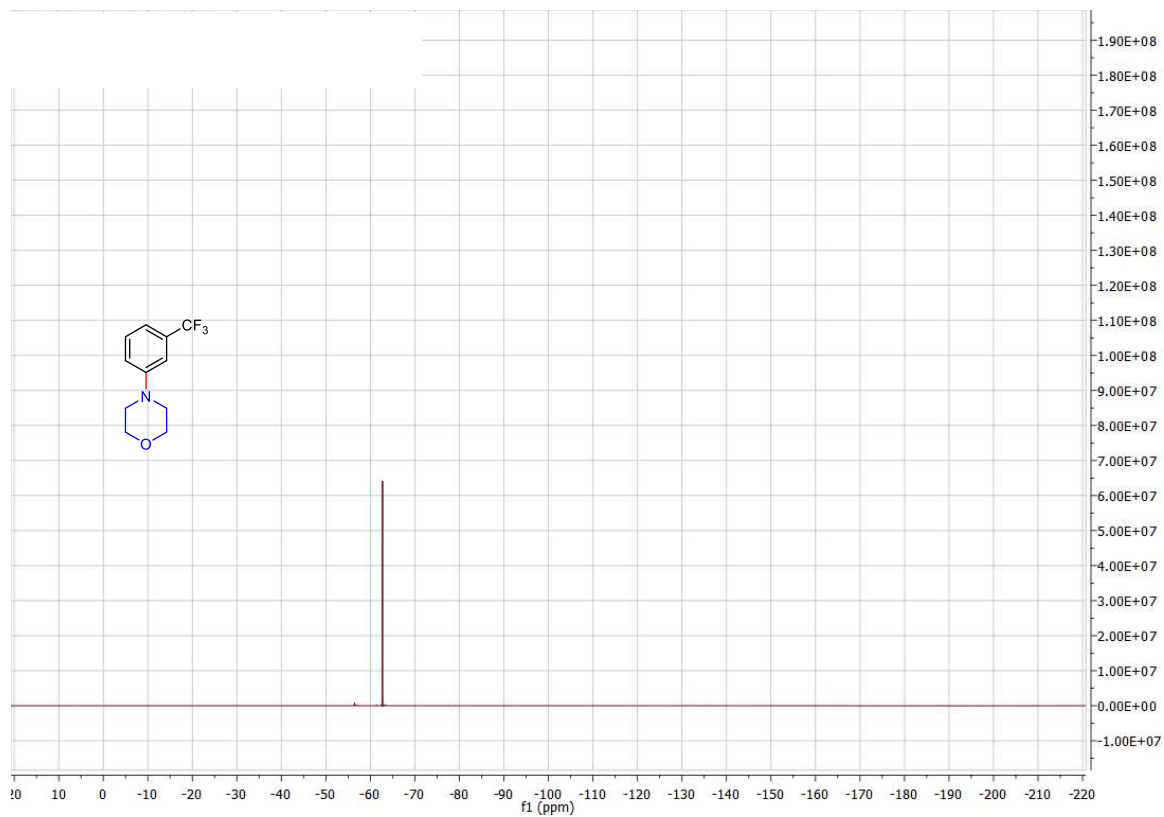


Figure S2.79.  $^{19}\text{F}$  NMR of 4-(3-(trifluoromethyl)phenyl)morpholine (18)

*tert*-butyl 4-(3-(trifluoromethyl)phenyl)piperazine-1-carboxylate (19)

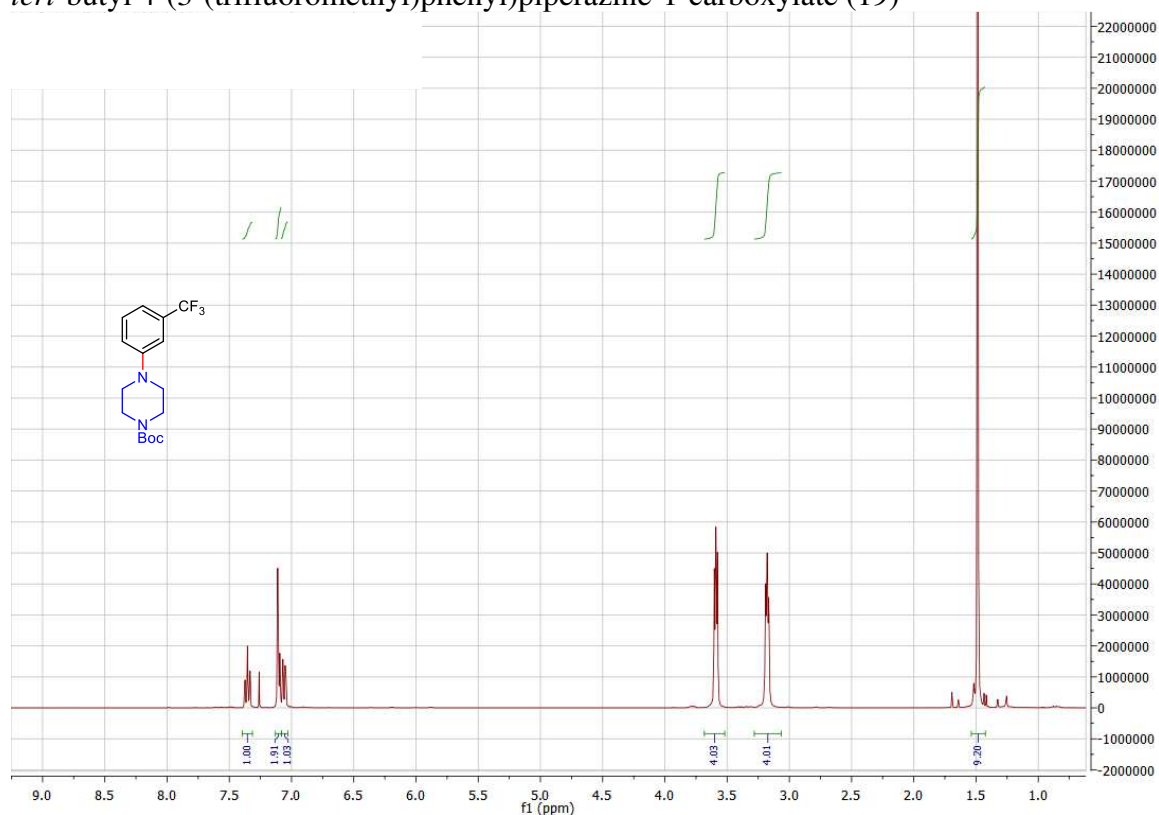


Figure S2.80.  $^1\text{H}$  NMR of *tert*-butyl 4-(3-(trifluoromethyl)phenyl)piperazine-1-carboxylate (19)

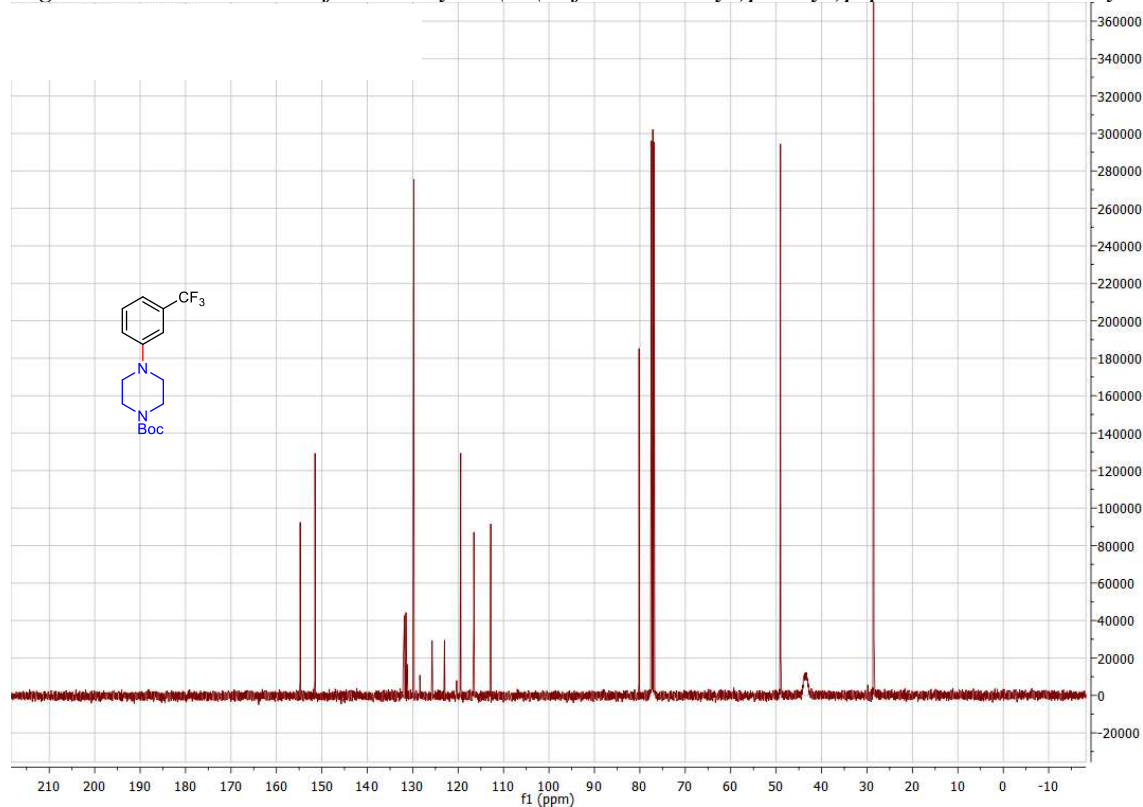


Figure S2.81.  $^{13}\text{C}$  NMR of *tert*-butyl 4-(3-(trifluoromethyl)phenyl)piperazine-1-carboxylate (19)



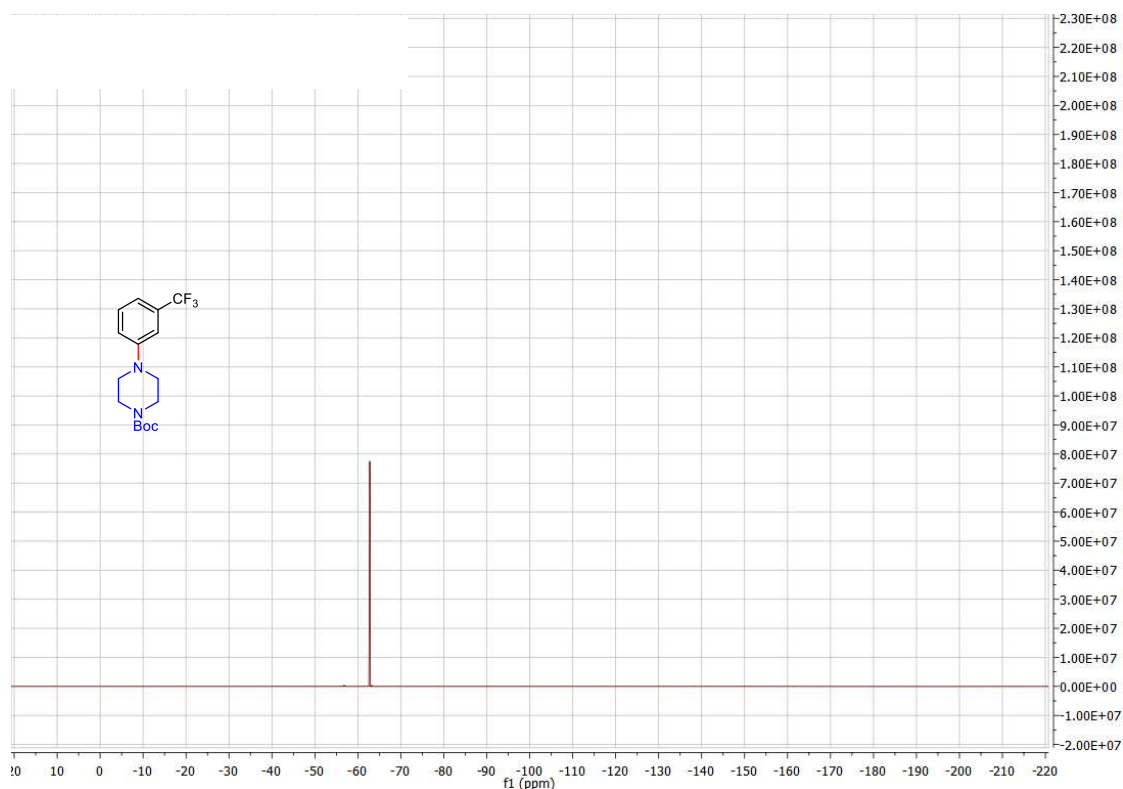


Figure S2.82.  $^{19}\text{F}$  NMR of tert-butyl 4-(3-(trifluoromethyl)phenyl)piperazine-1-carboxylate (19)

1-(3-(trifluoromethyl)phenyl)piperidine (20)

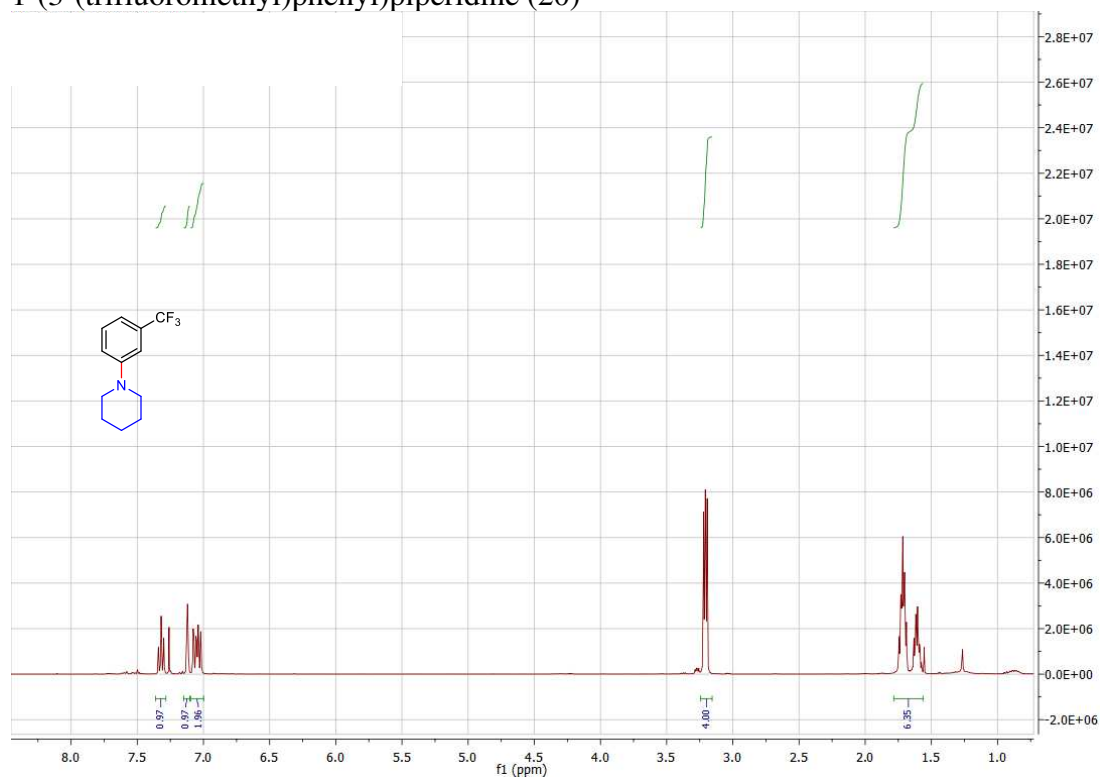


Figure S2.83.  $^1\text{H}$  NMR of 1-(3-(trifluoromethyl)phenyl)piperidine (20)

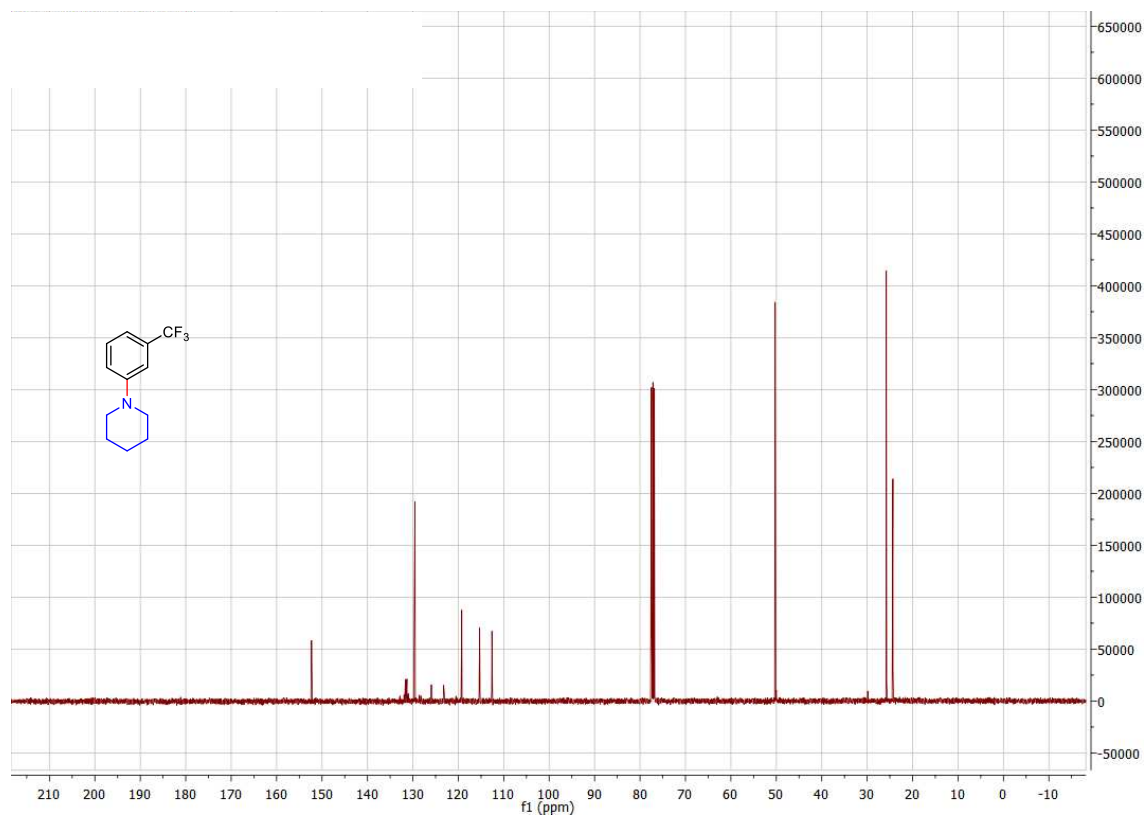


Figure S2.84.  $^{13}\text{C}$  NMR of 1-(3-(trifluoromethyl)phenyl)piperidine (20)

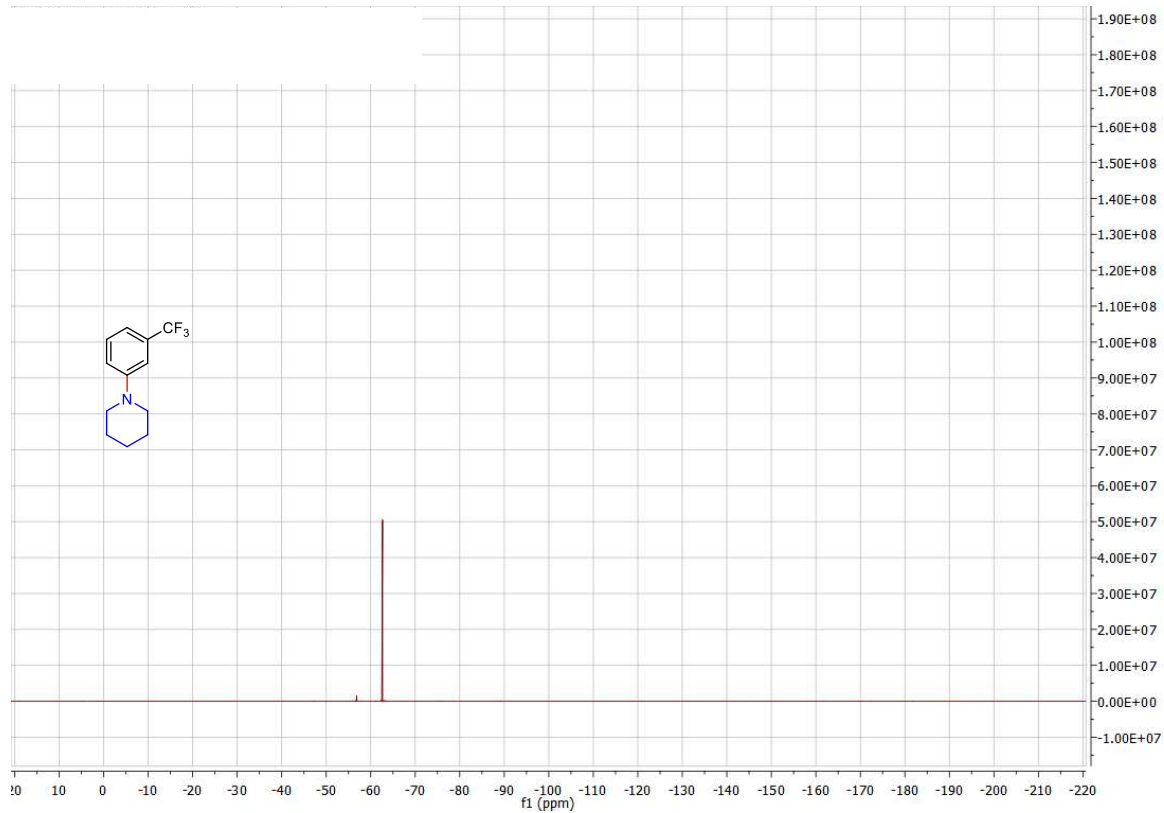
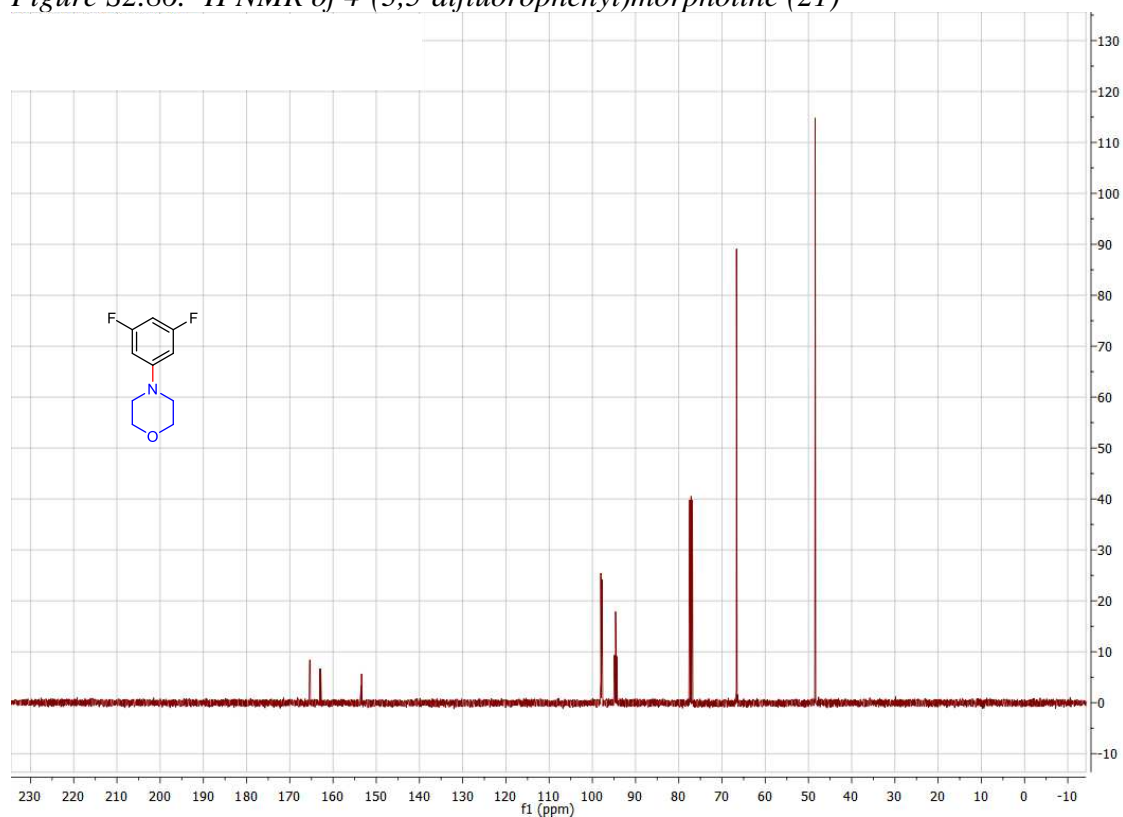
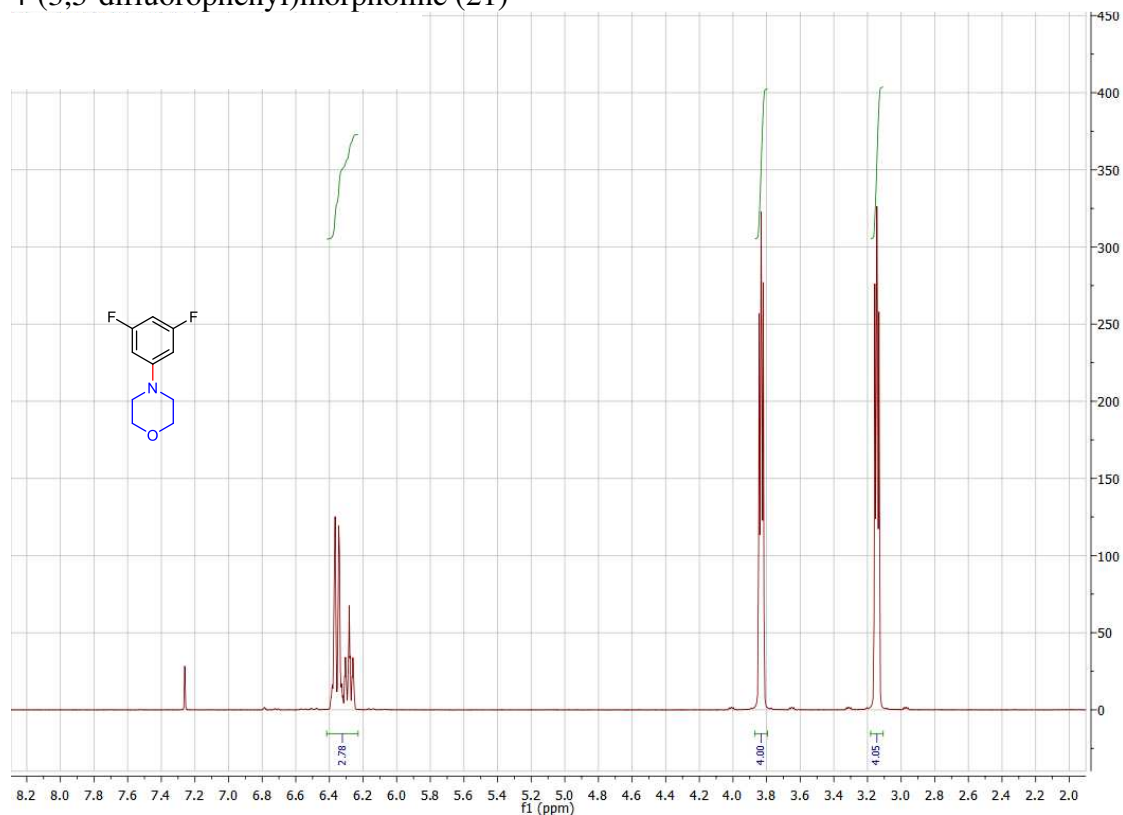
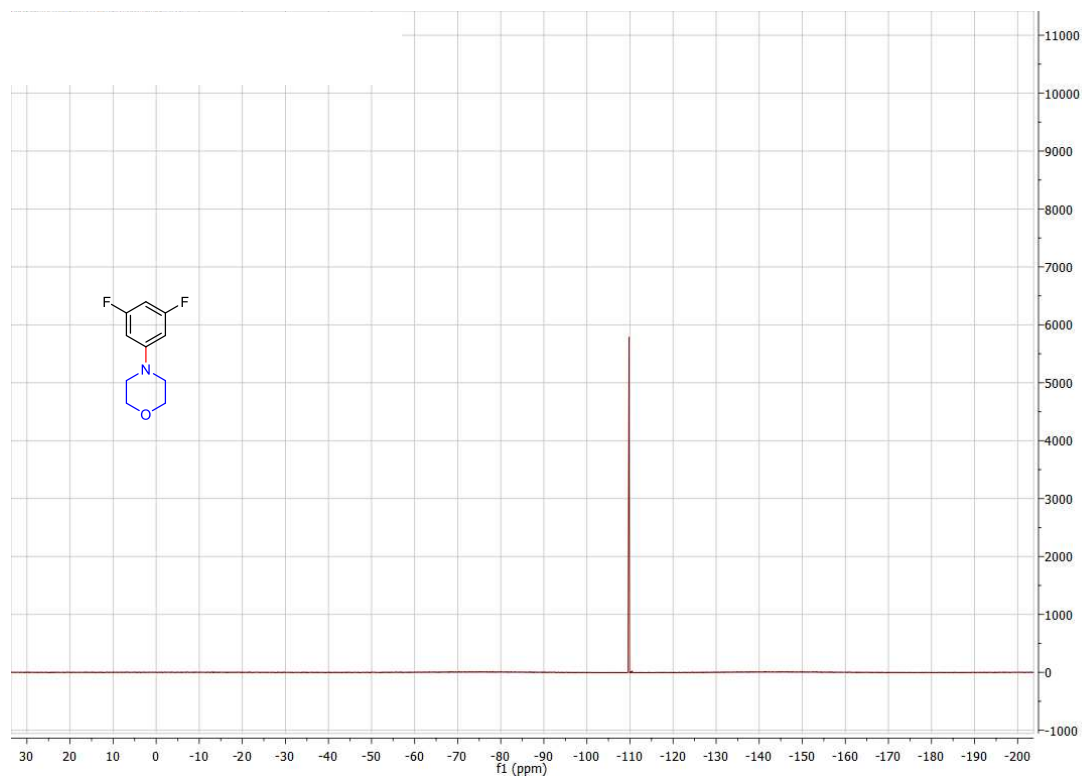


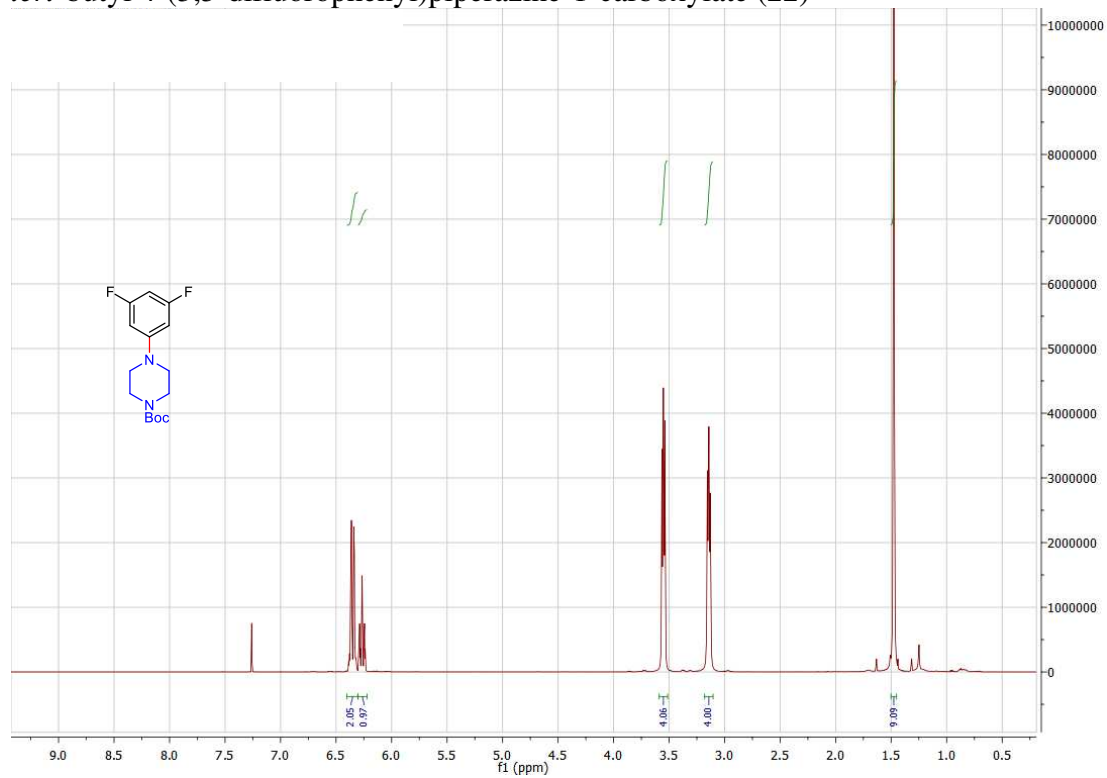
Figure S2.85.  $^{19}\text{F}$  NMR of 1-(3-(trifluoromethyl)phenyl)piperidine (20)

4-(3,5-difluorophenyl)morpholine (21)





*tert*-butyl 4-(3,5-difluorophenyl)piperazine-1-carboxylate (22)



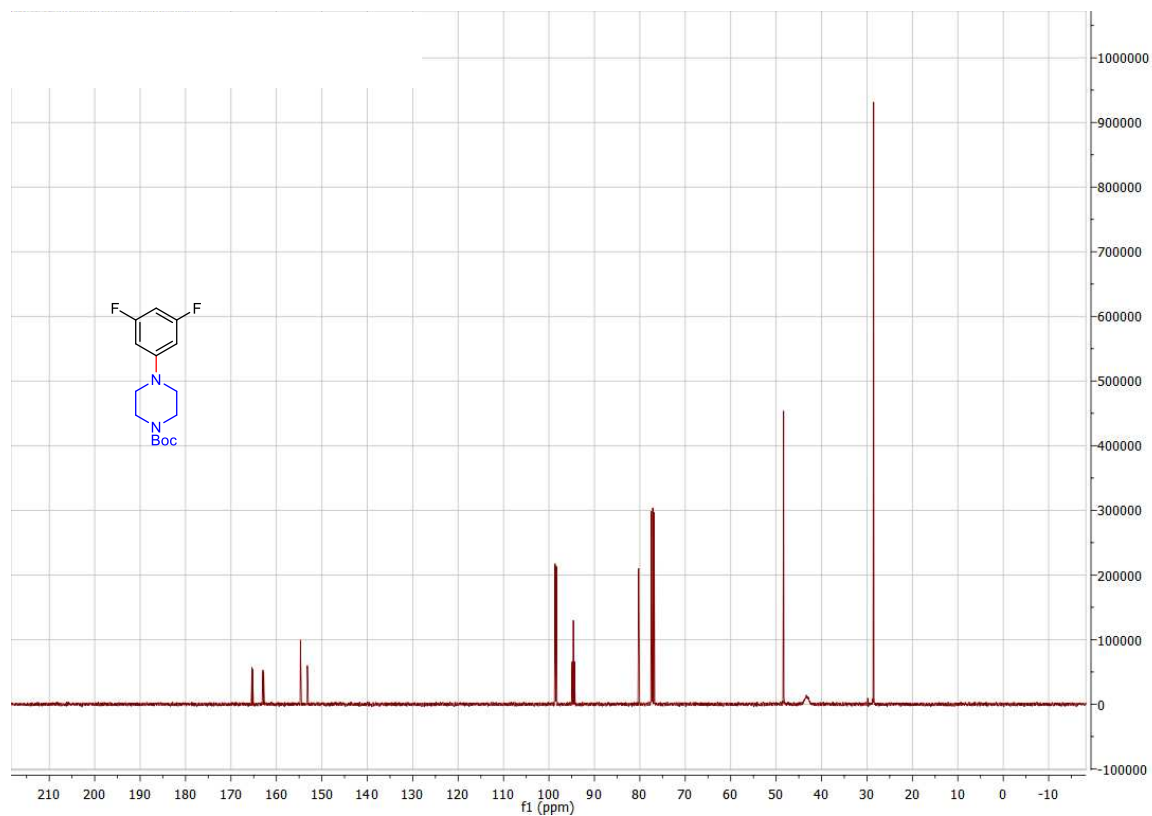


Figure S2.90.  $^{13}\text{C}$  NMR of tert-butyl 4-(3,5-difluorophenyl)piperazine-1-carboxylate (22)

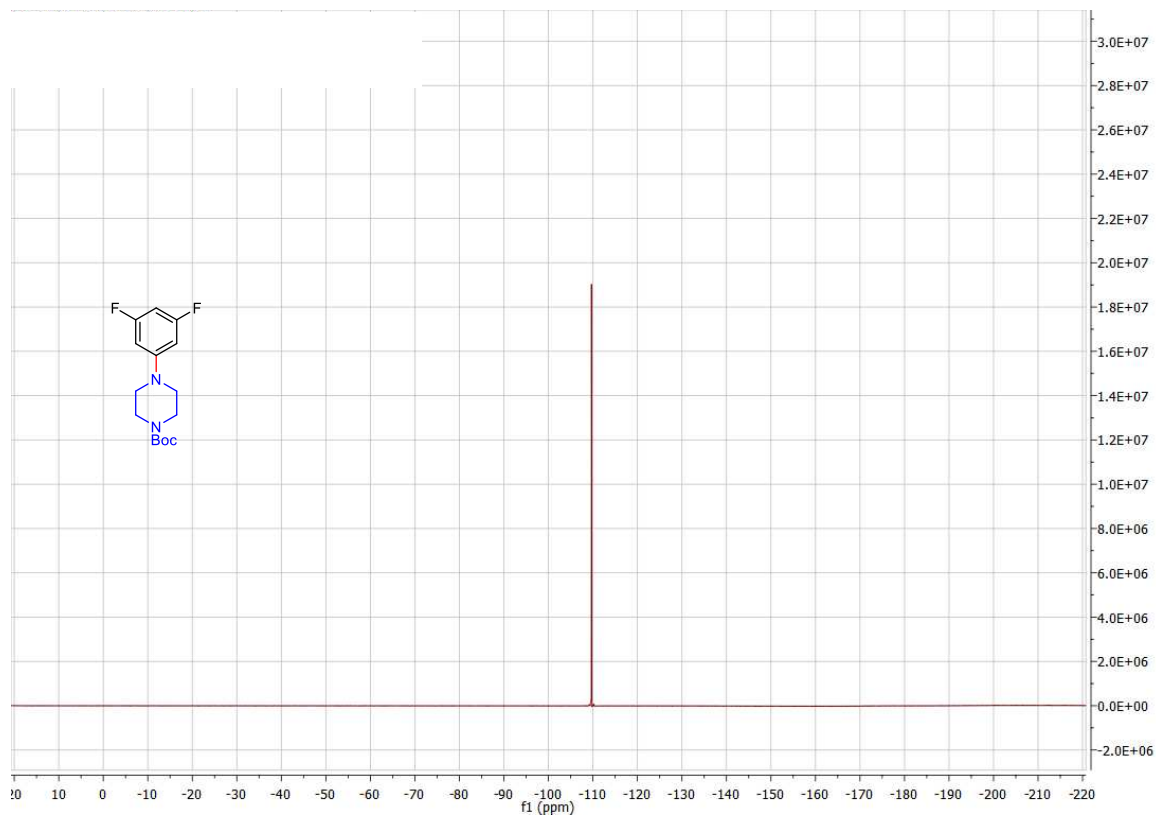


Figure S2.91.  $^{19}\text{F}$  NMR of tert-butyl 4-(3,5-difluorophenyl)piperazine-1-carboxylate (22)

N-(3,5-difluorophenyl)pyridin-3-amine (23)

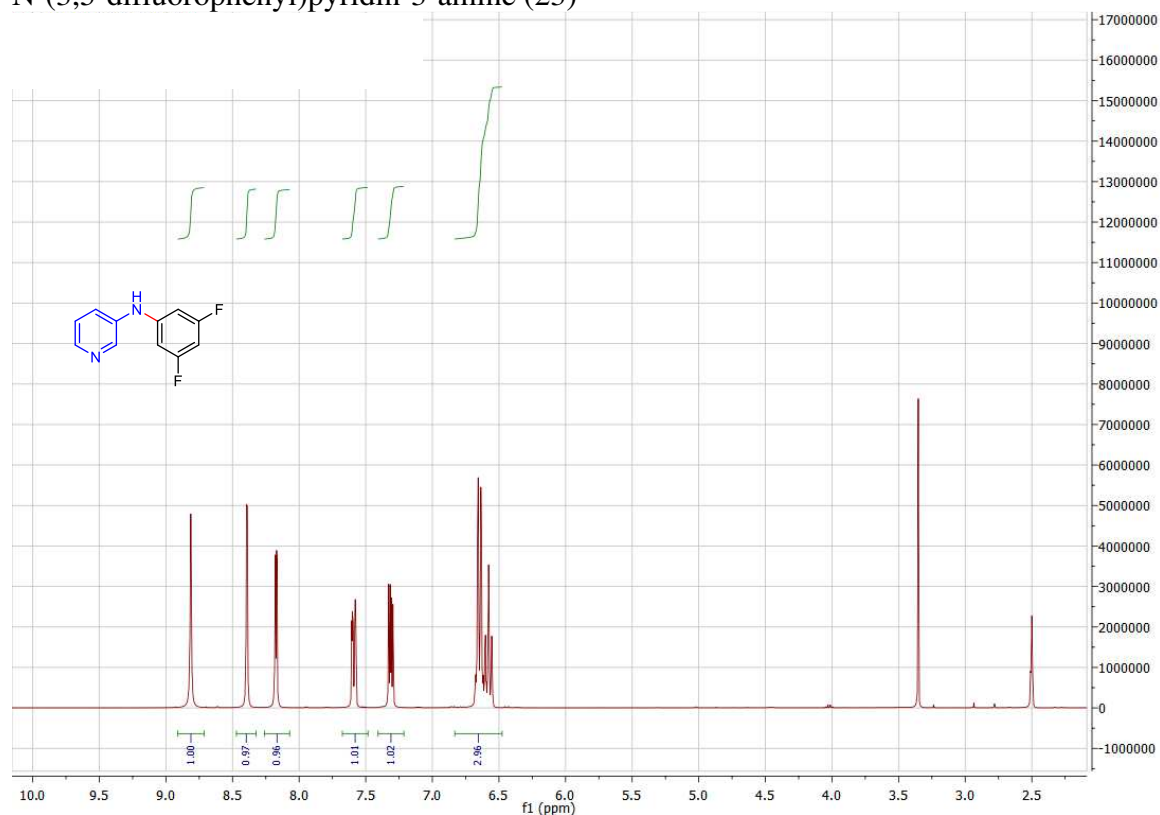


Figure S2.92.  $^1\text{H}$  NMR of N-(3,5-difluorophenyl)pyridin-3-amine (23)

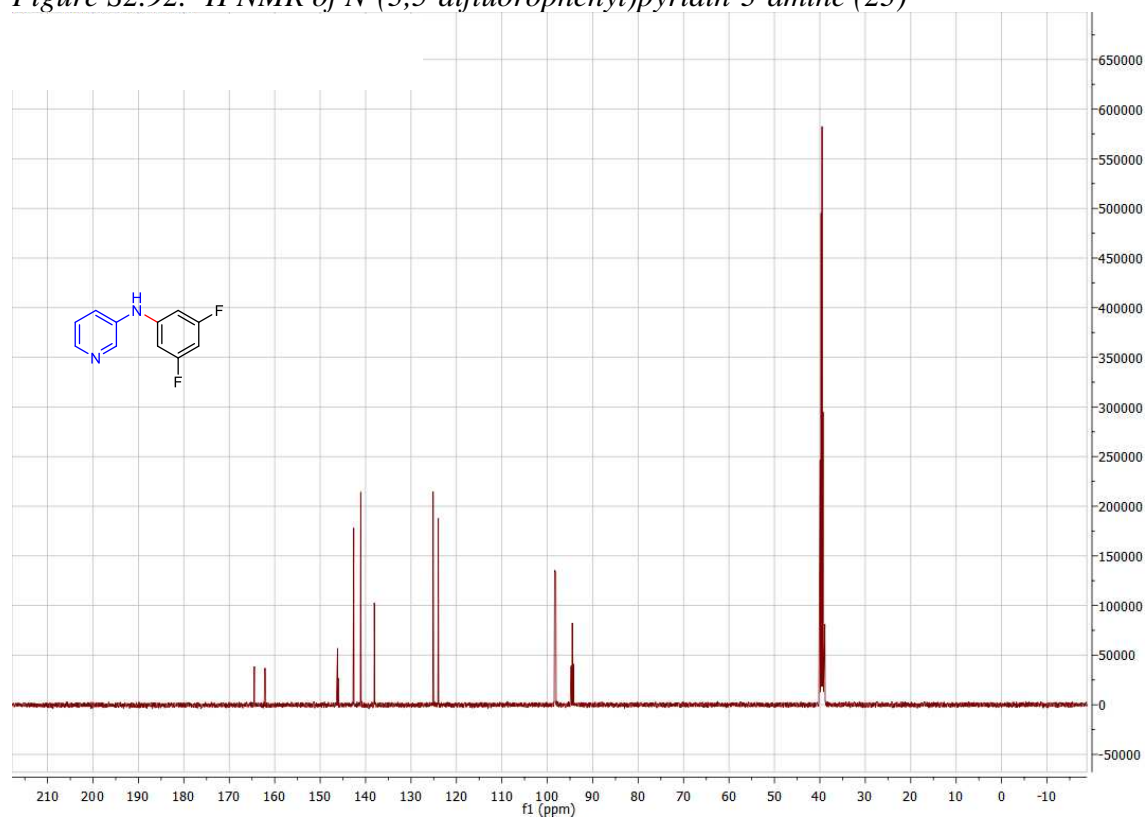
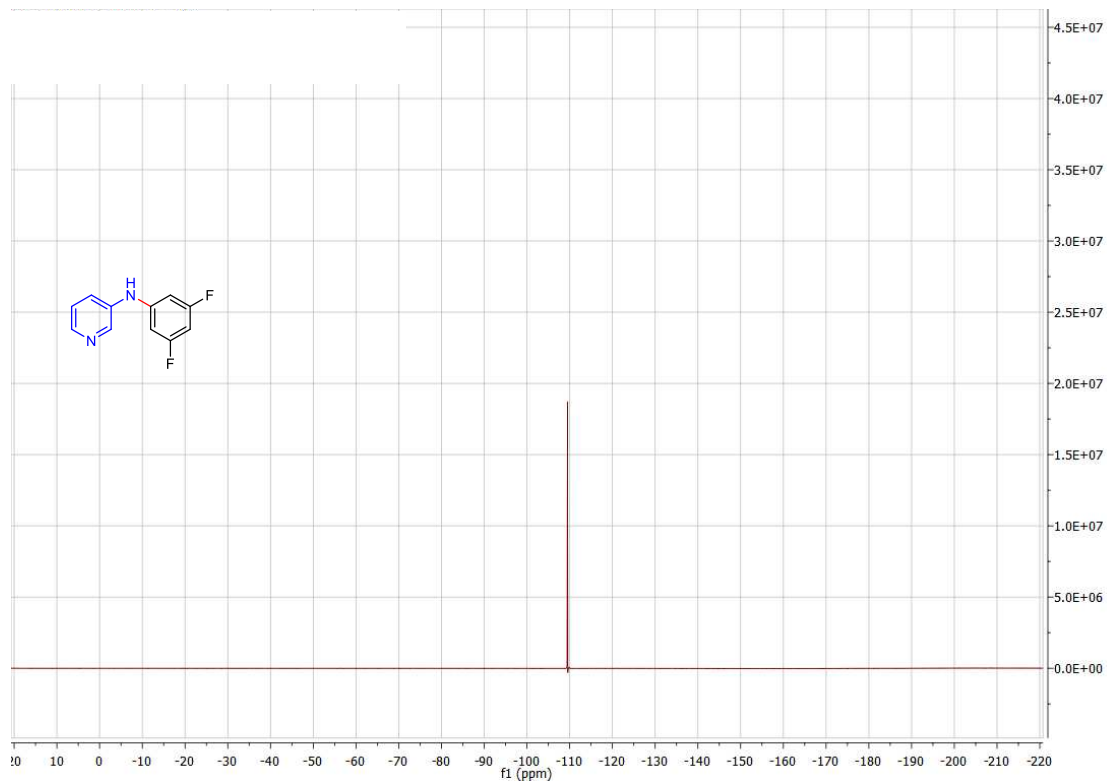
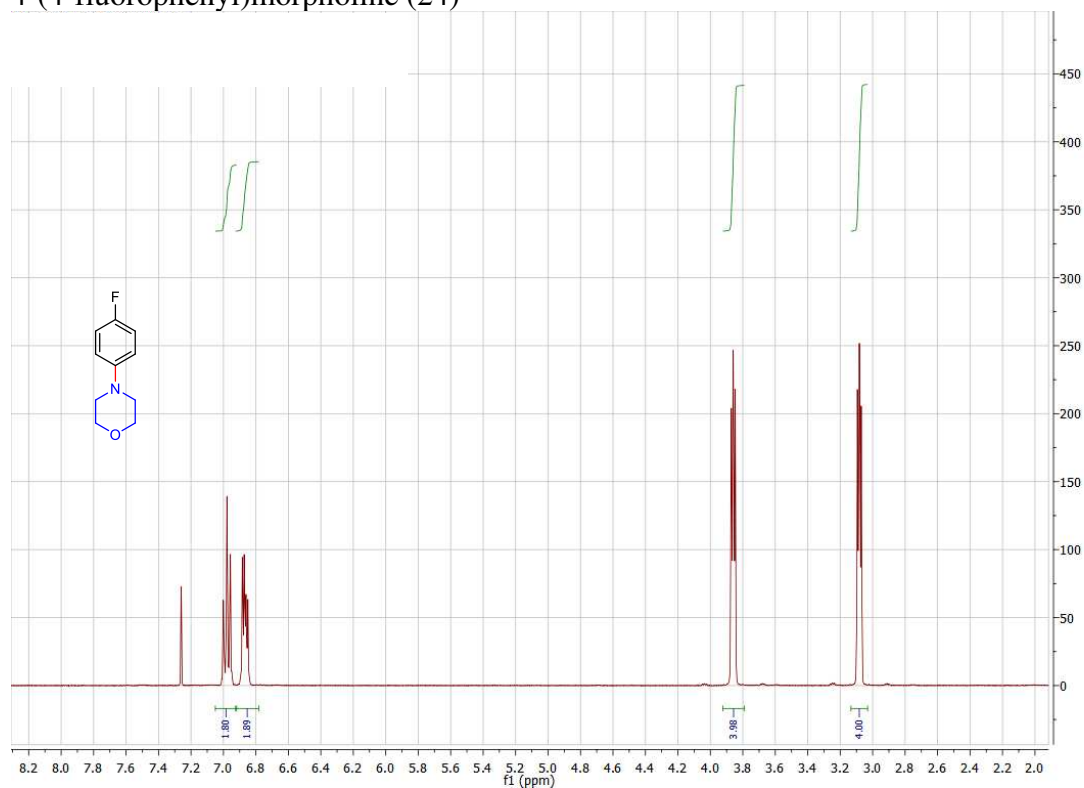


Figure S2.93.  $^{13}\text{C}$  NMR of N-(3,5-difluorophenyl)pyridin-3-amine (23)



4-(4-fluorophenyl)morpholine (24)



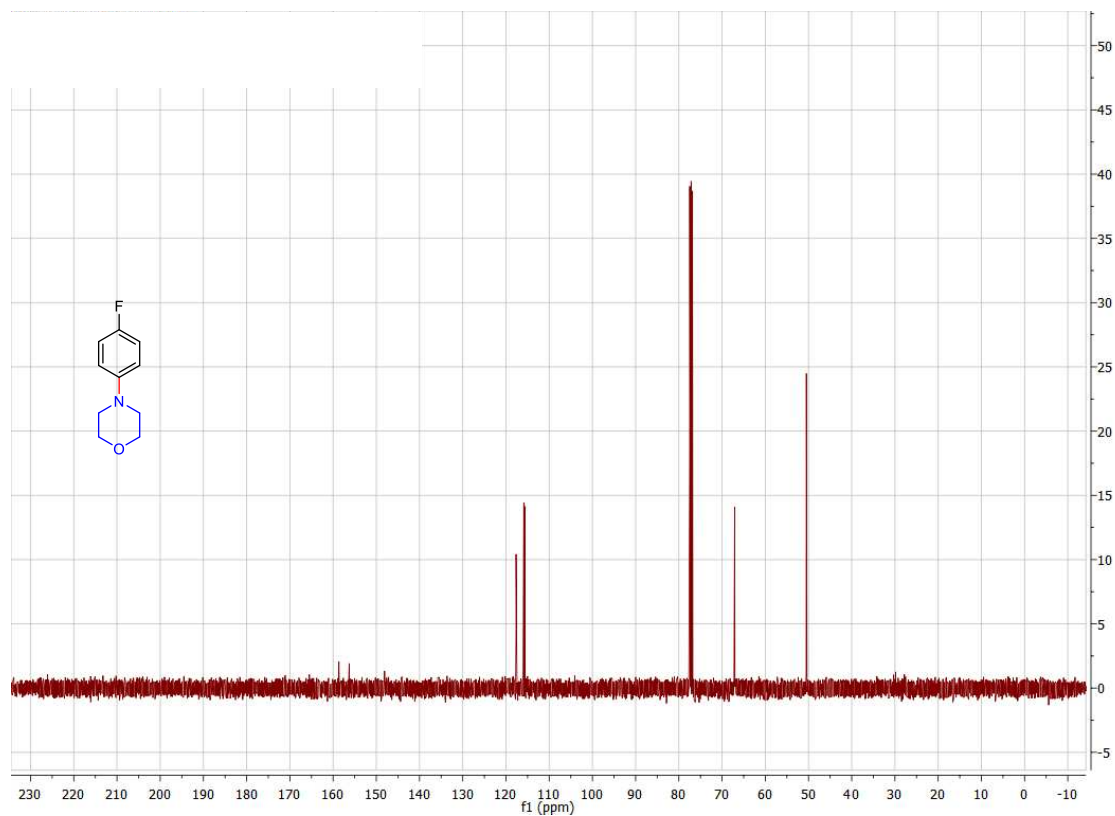


Figure S2.96.  $^{13}\text{C}$  NMR of 4-(4-fluorophenyl)morpholine (24)

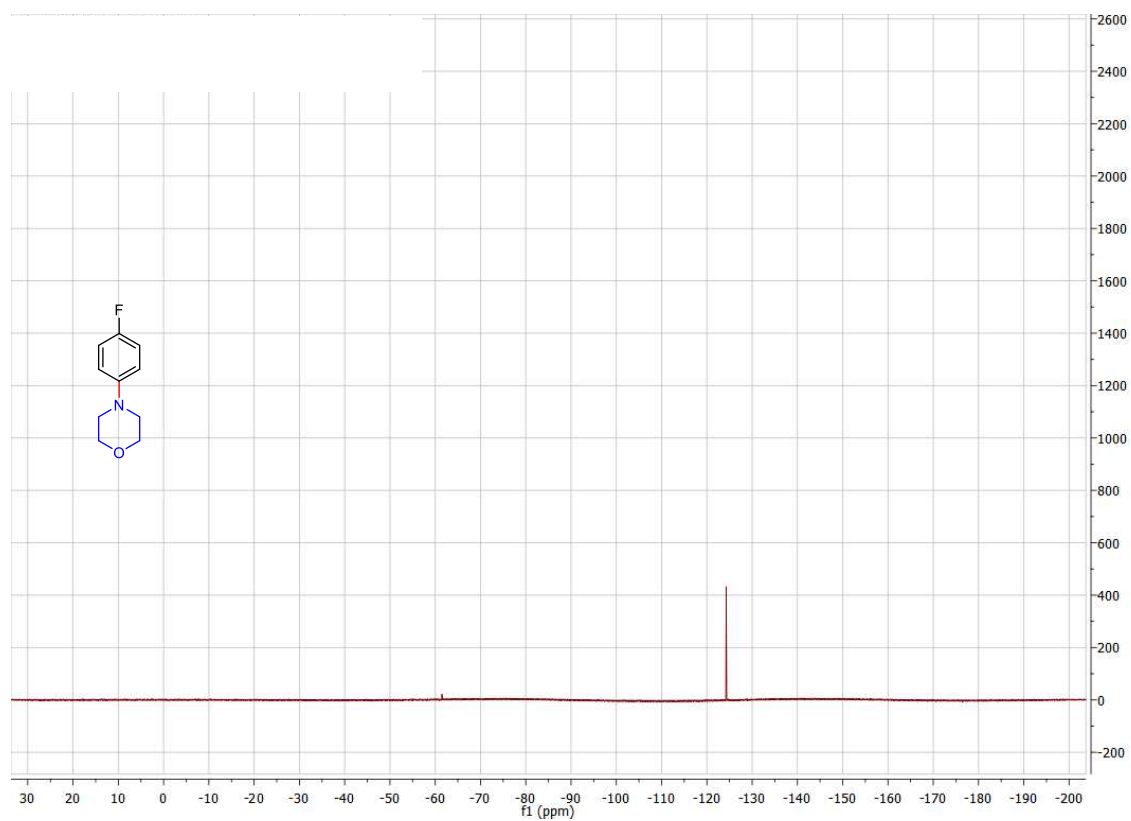
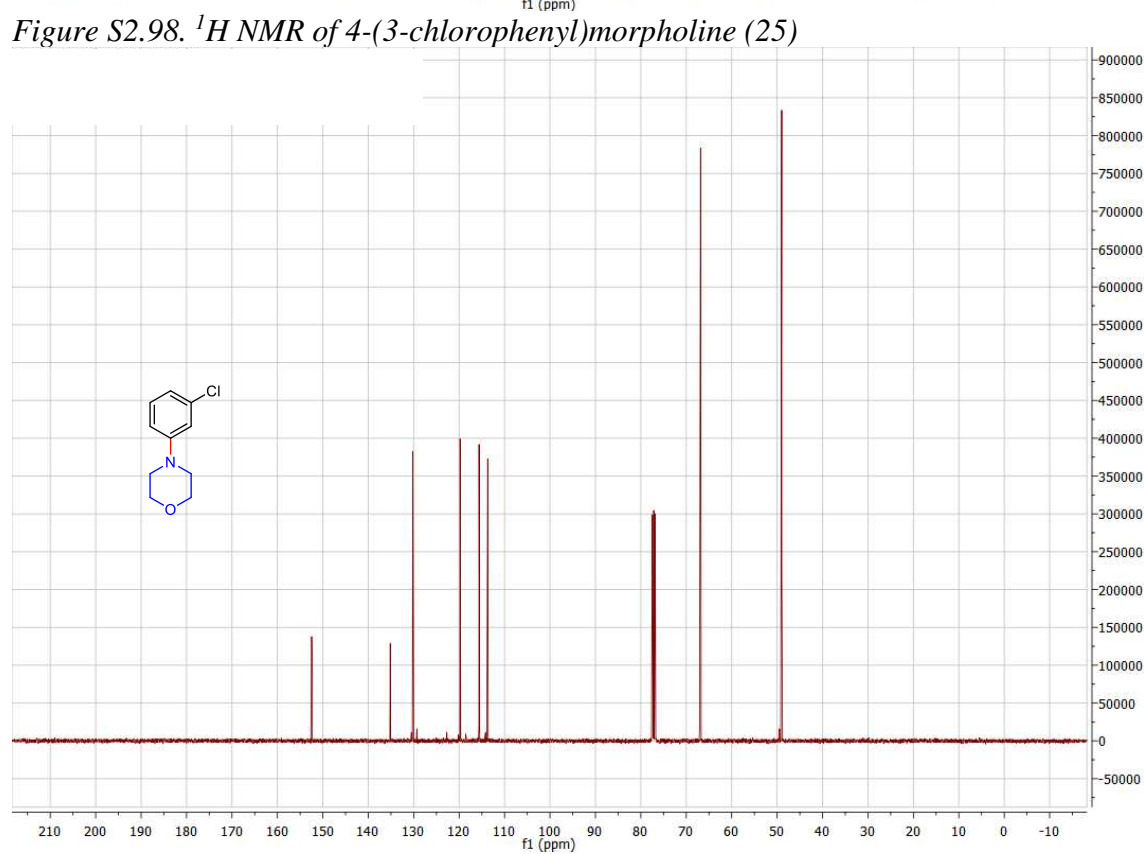
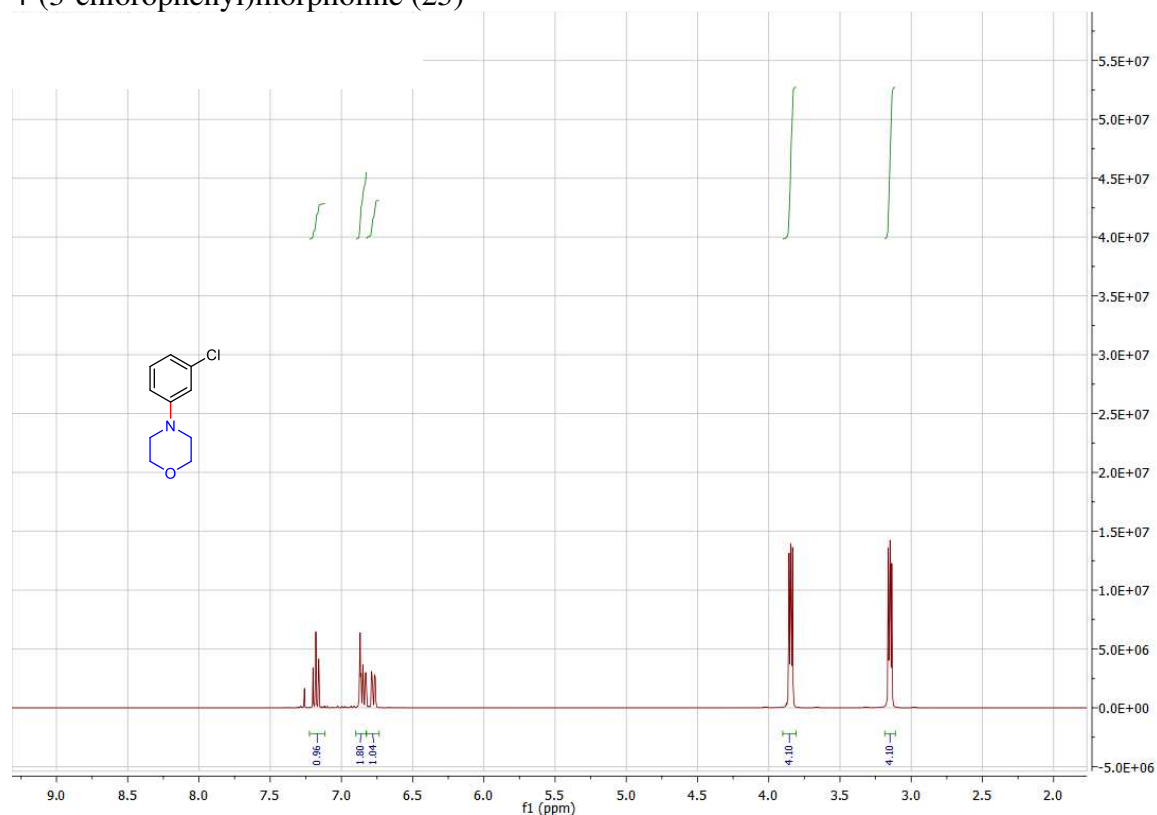


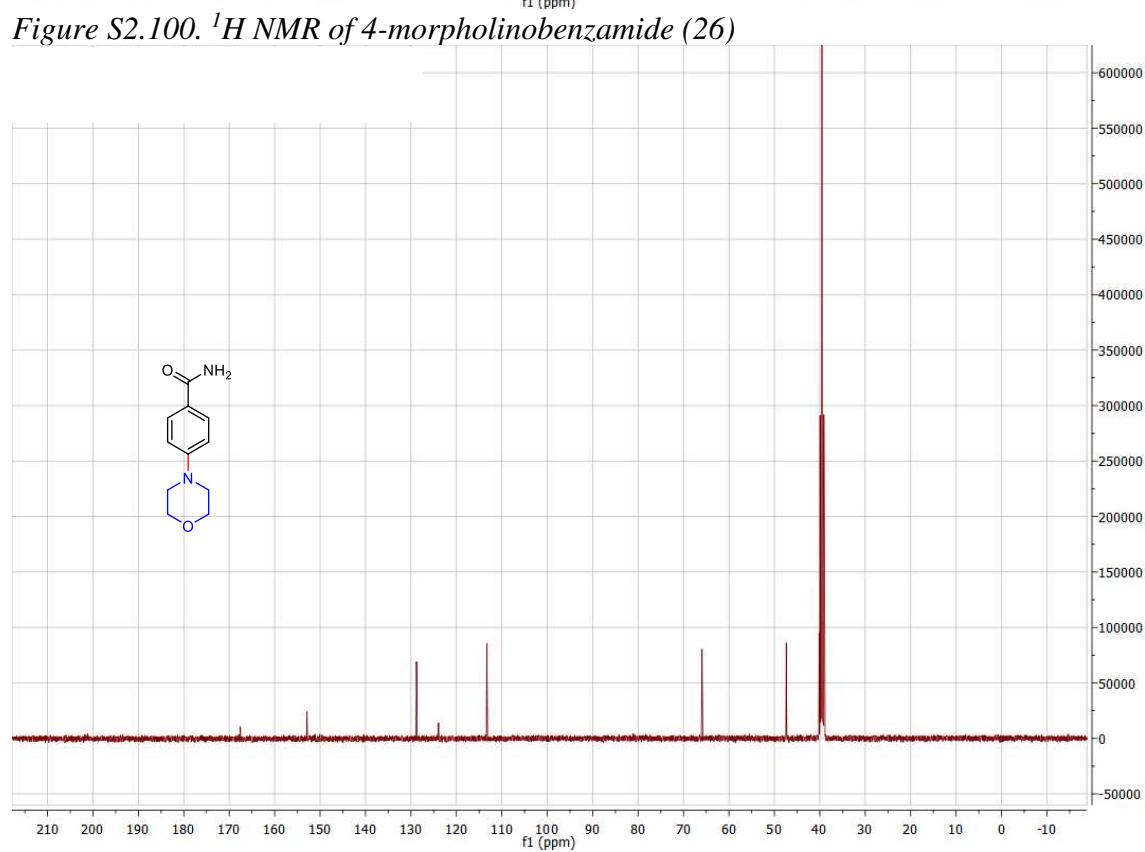
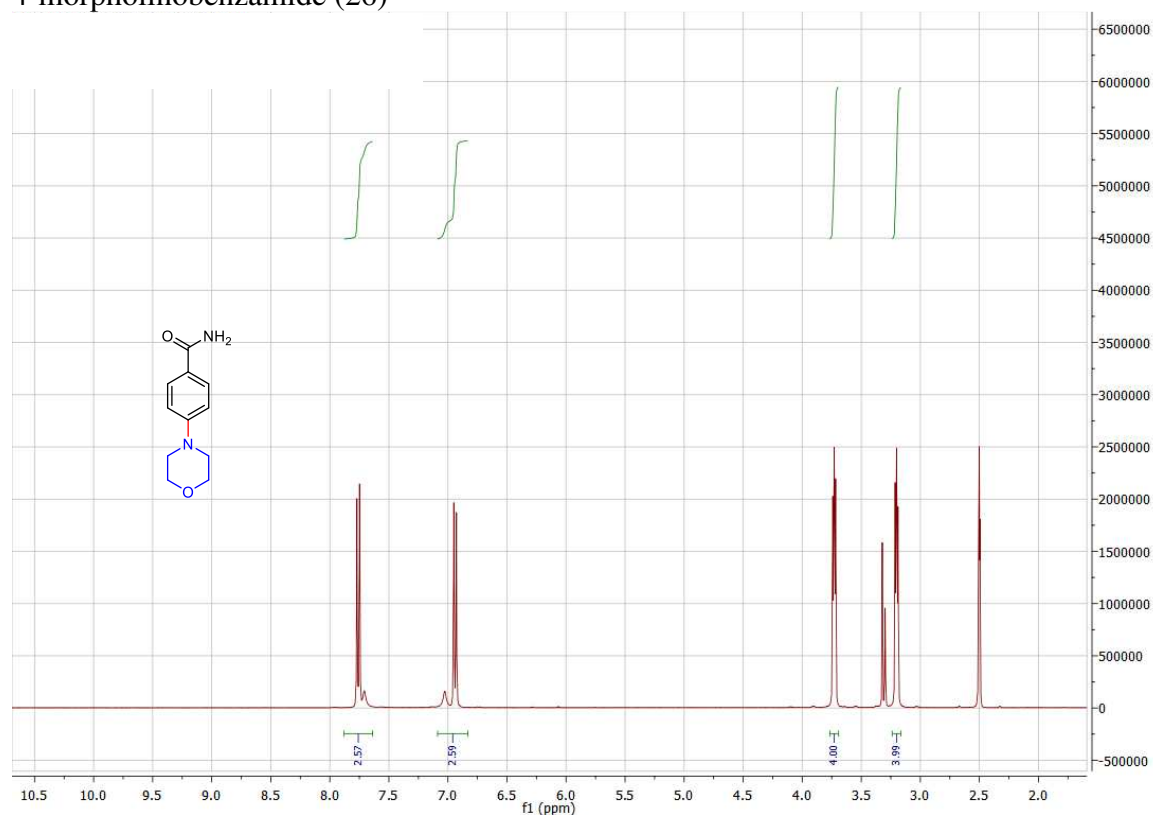
Figure S2.97.  $^{19}\text{F}$  NMR of 4-(4-fluorophenyl)morpholine (24)



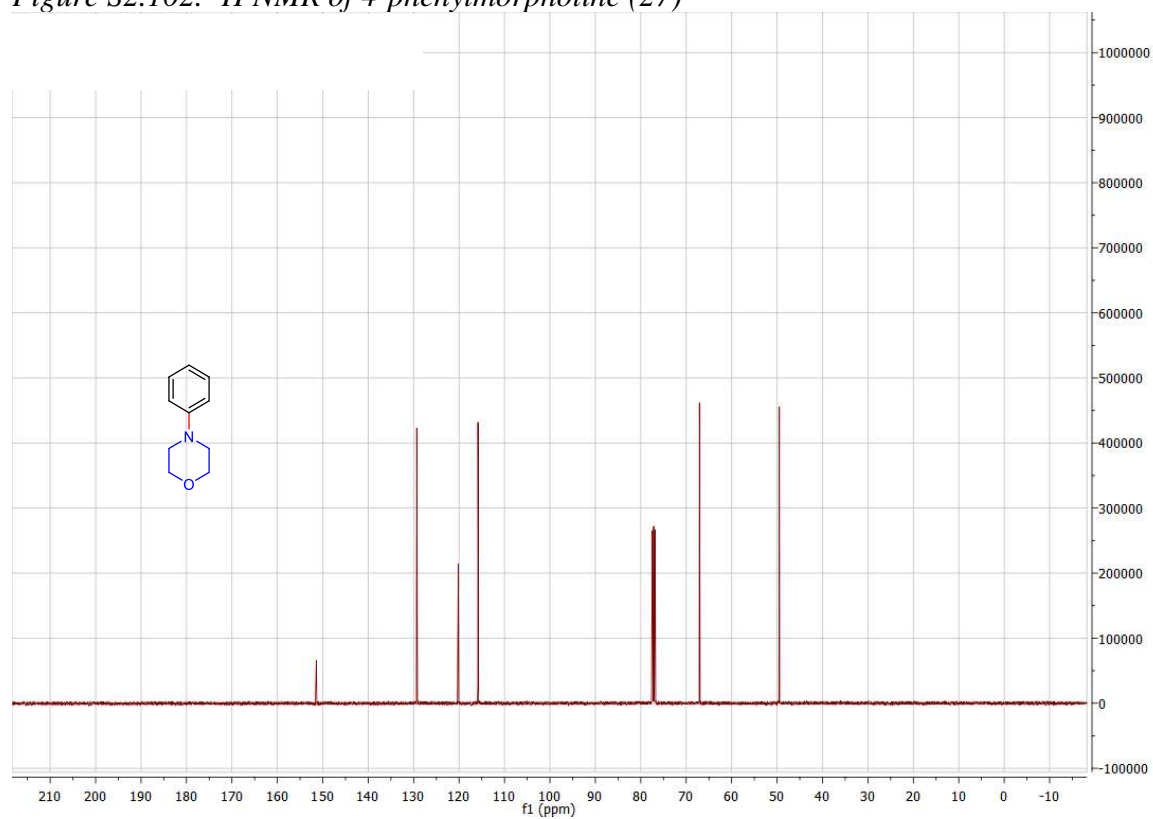
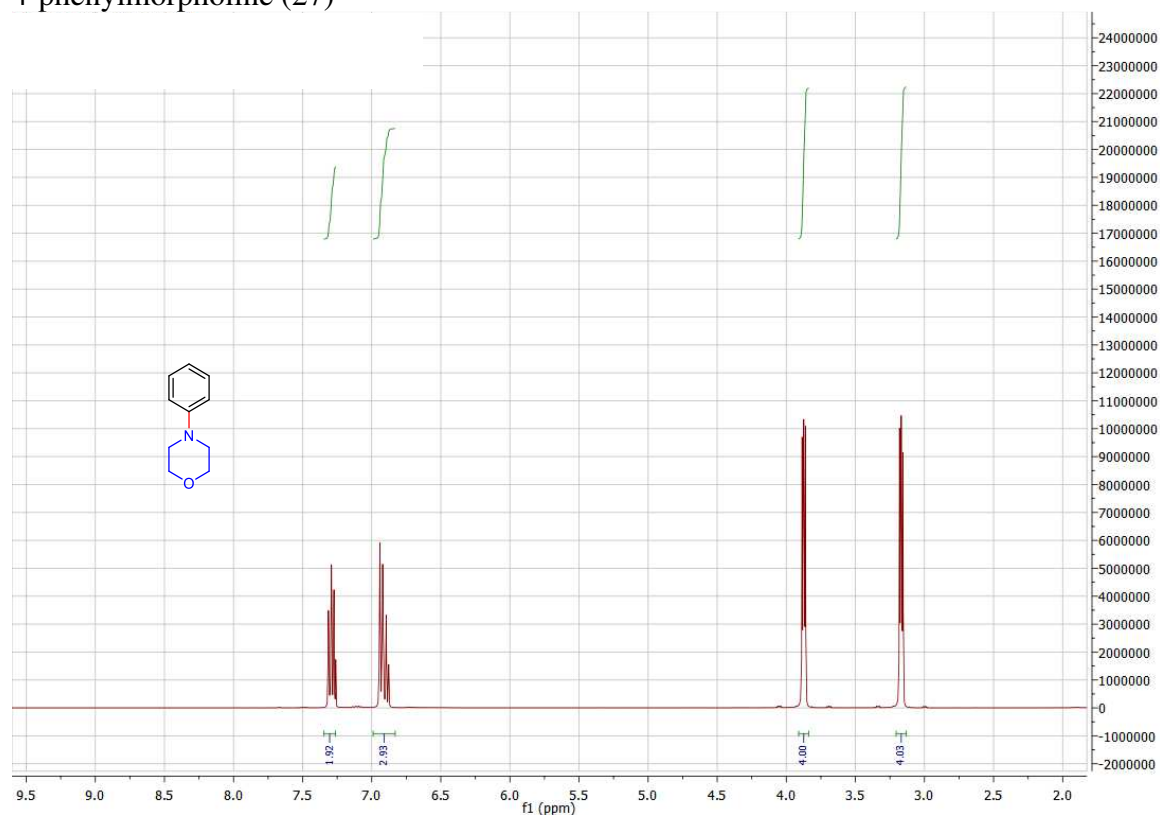
4-(3-chlorophenyl)morpholine (25)



4-morpholinobenzamide (26)



4-phenylmorpholine (27)



4-(p-tolyl)morpholine (28)

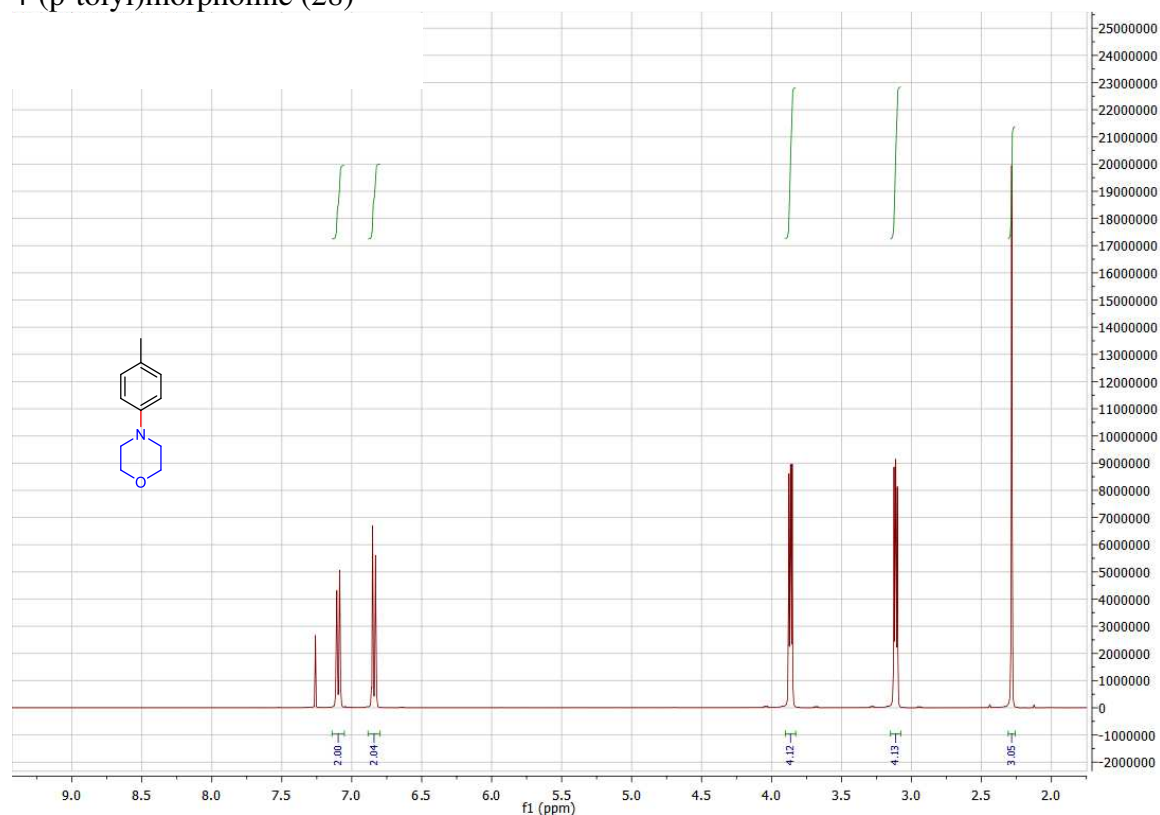


Figure S2.104.  $^1\text{H}$  NMR of 4-(p-tolyl)morpholine (28)

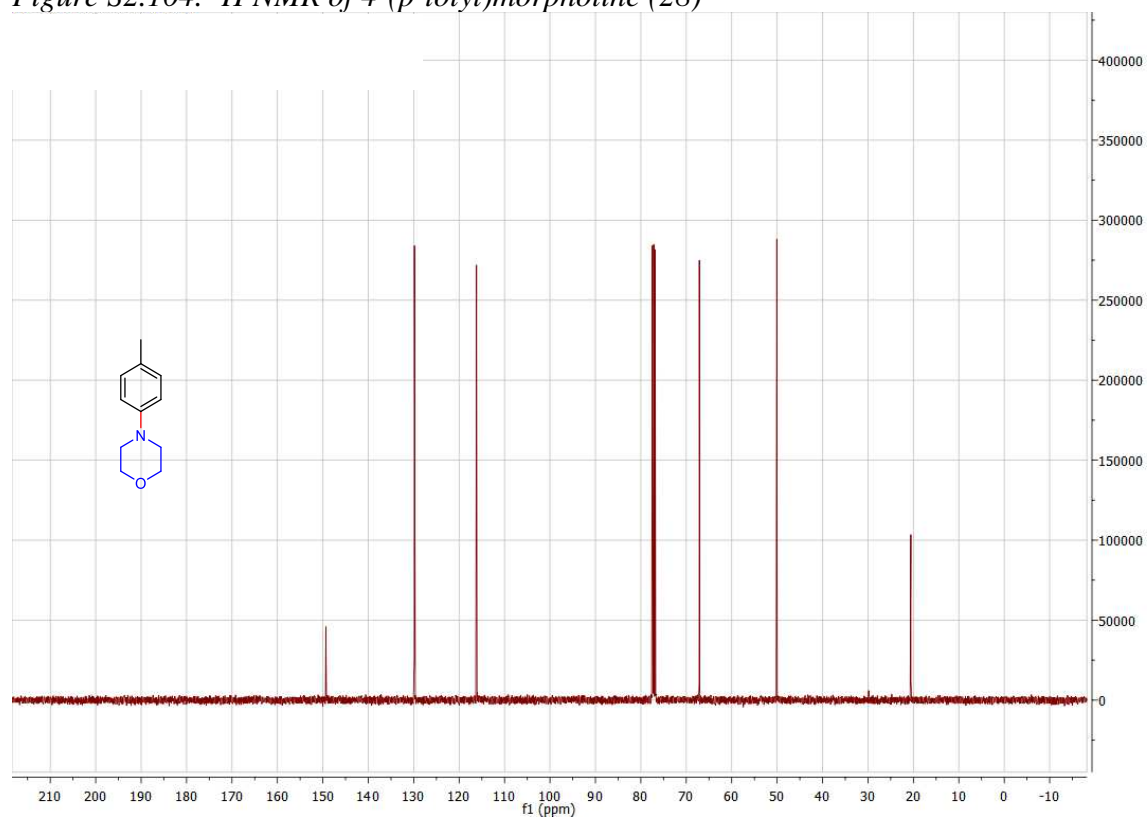
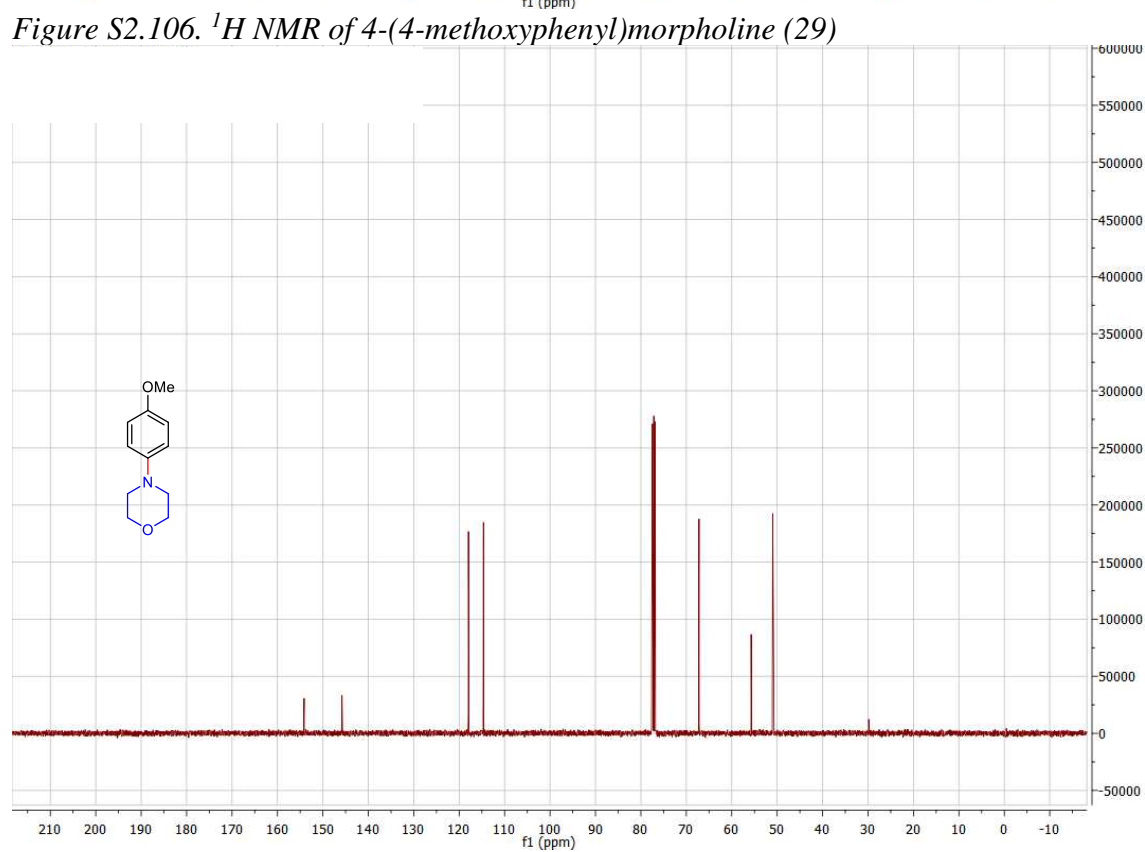
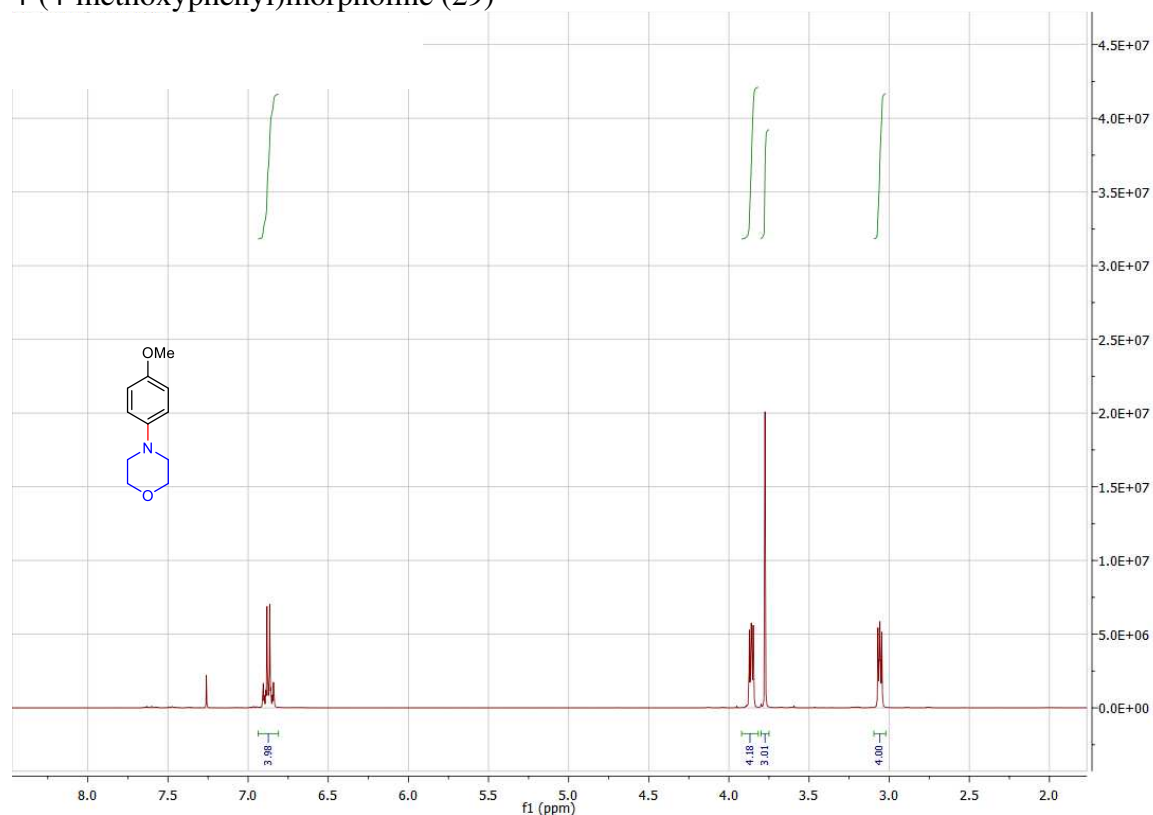


Figure S2.105.  $^{13}\text{C}$  NMR of 4-(p-tolyl)morpholine (28)

4-(4-methoxyphenyl)morpholine (29)



4-(3-methoxyphenyl)morpholine (30)

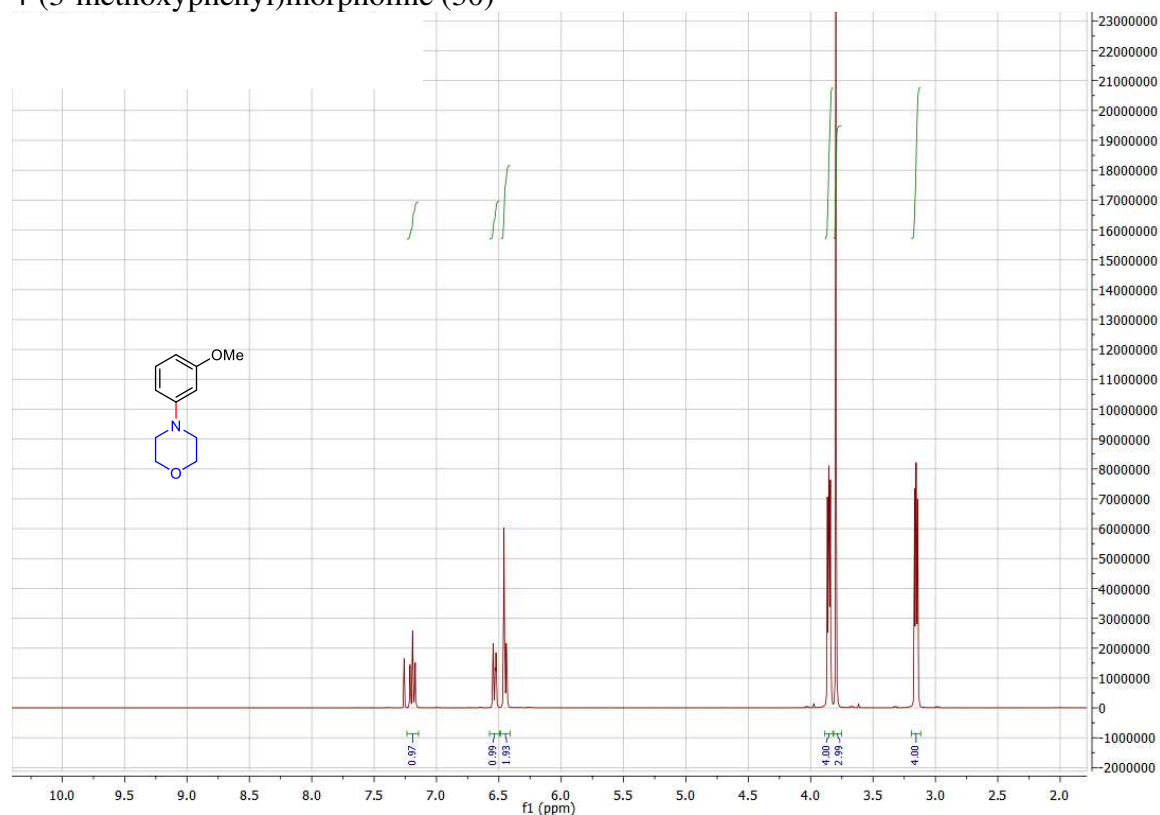


Figure S2.108.  $^1\text{H}$  NMR of 4-(3-methoxyphenyl)morpholine (30)

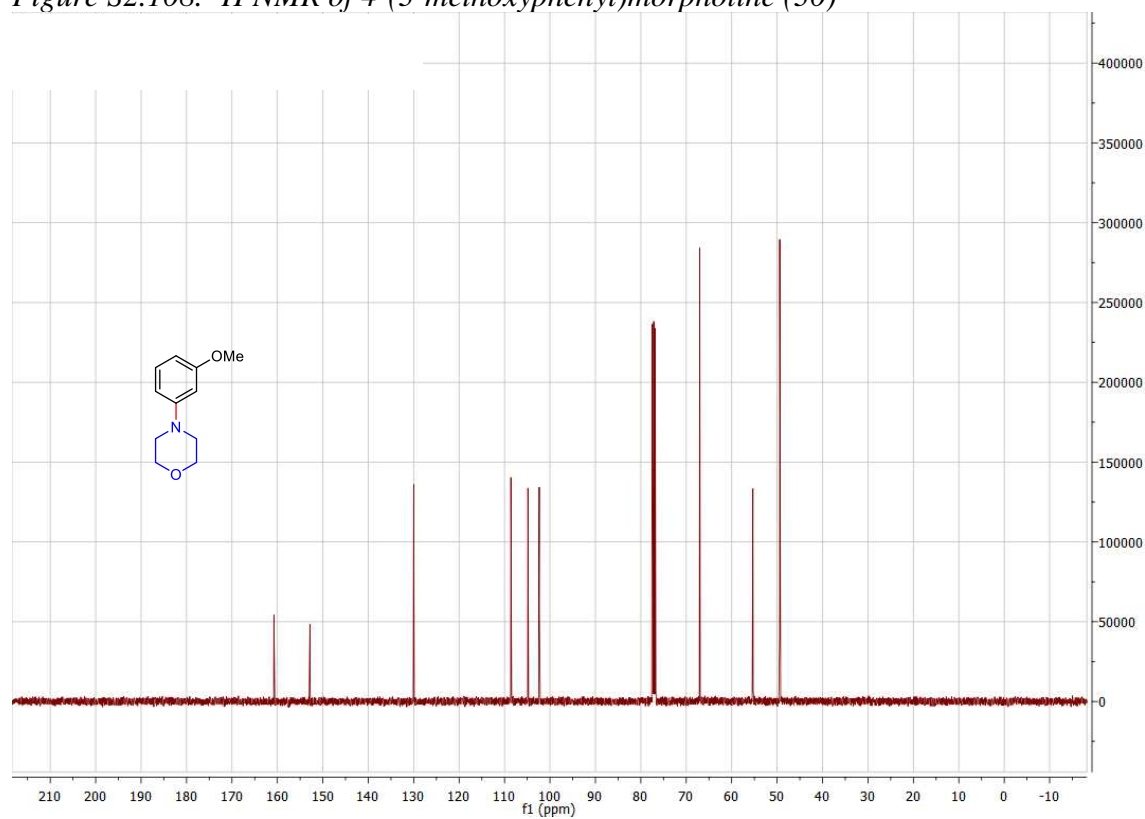


Figure S2.109.  $^{13}\text{C}$  NMR of 4-(3-methoxyphenyl)morpholine (30)

4-(3,5-dimethoxyphenyl)morpholine (31)

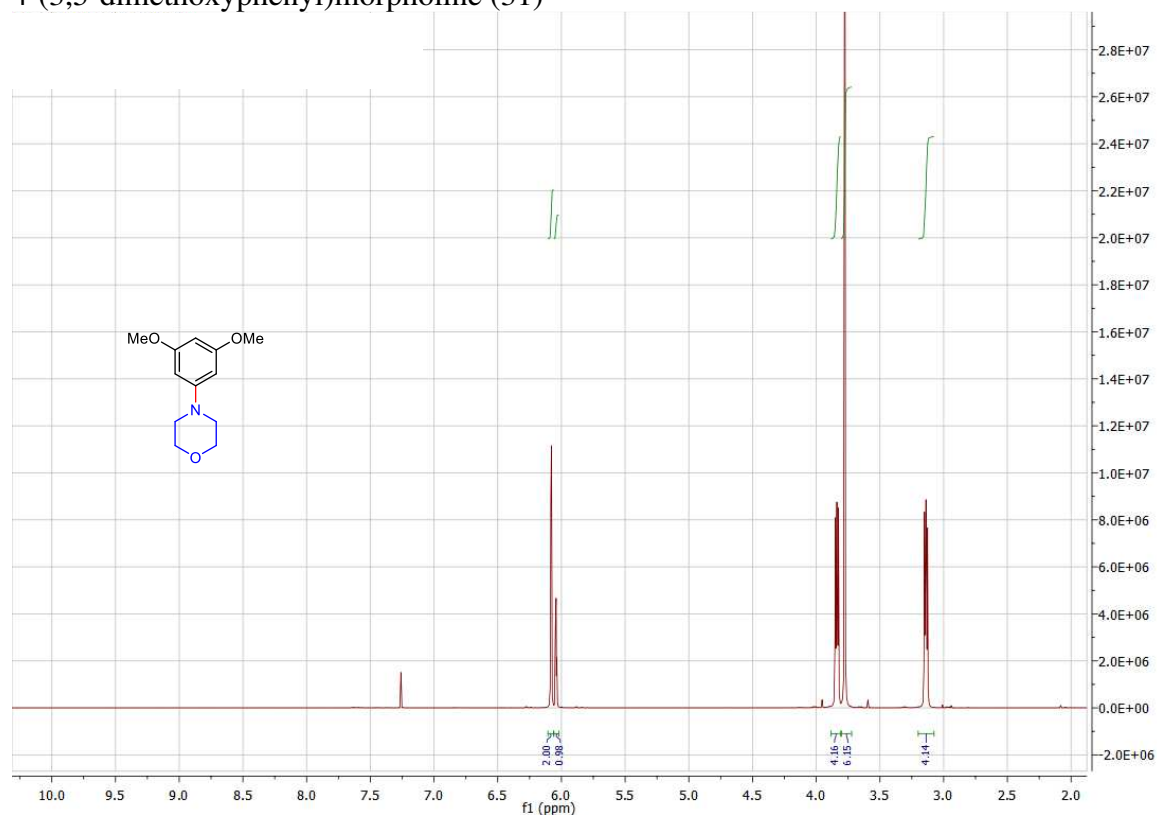


Figure S2.110. <sup>1</sup>H NMR of 4-(3,5-dimethoxyphenyl)morpholine (31)

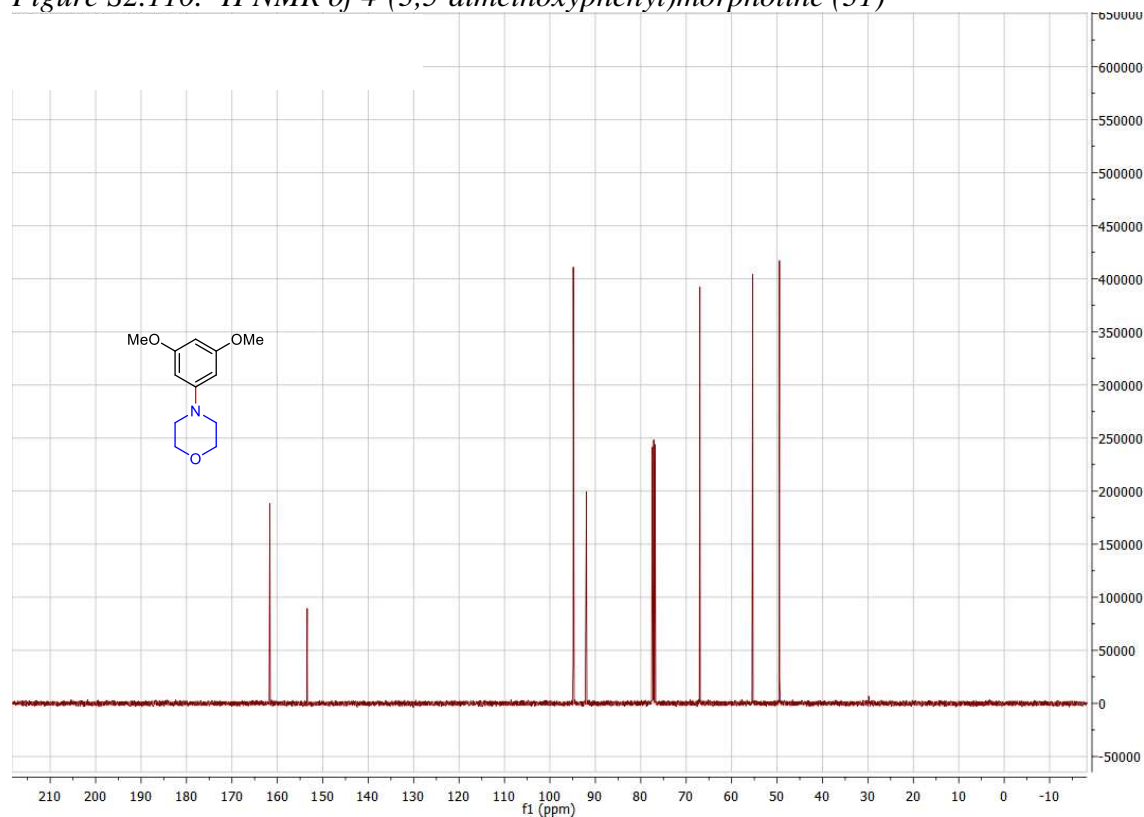


Figure S2.111. <sup>13</sup>C NMR of 4-(3,5-dimethoxyphenyl)morpholine (31)

4-morpholinobenzonitrile (32)

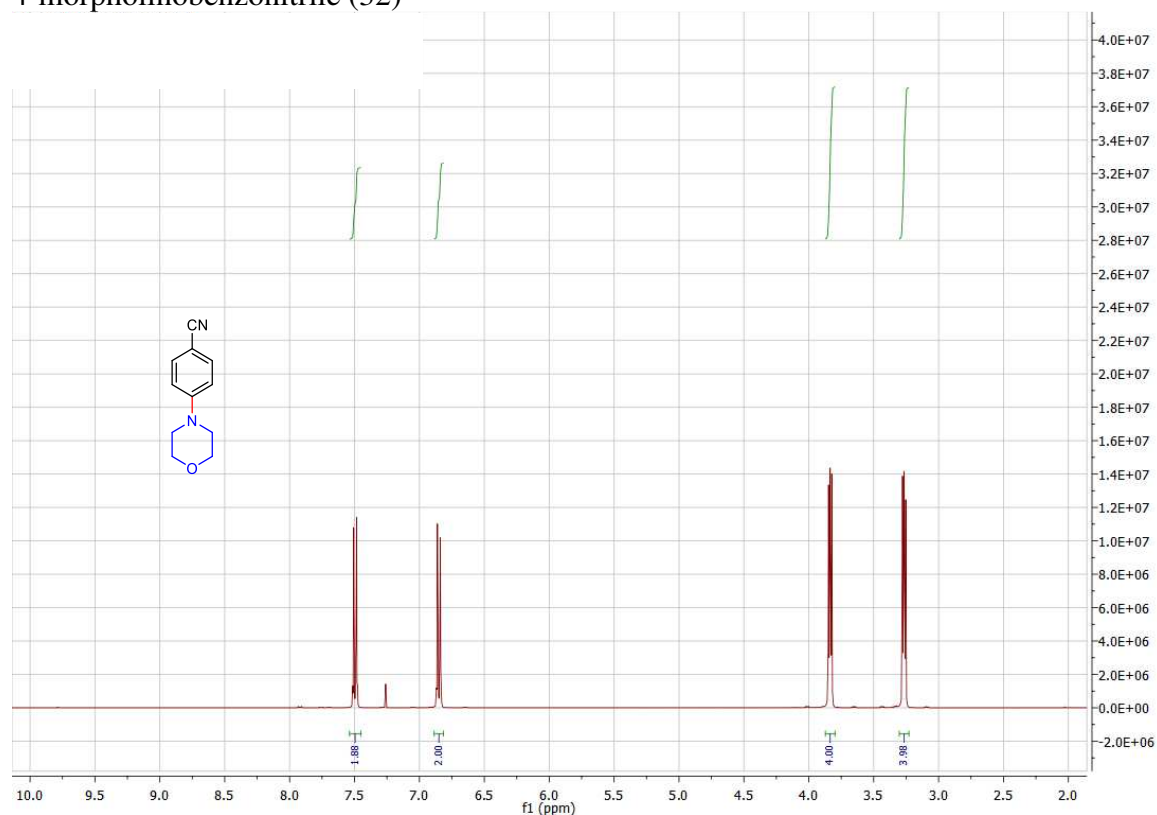


Figure S2.112. <sup>1</sup>H NMR of 4-morpholinobenzonitrile (32)

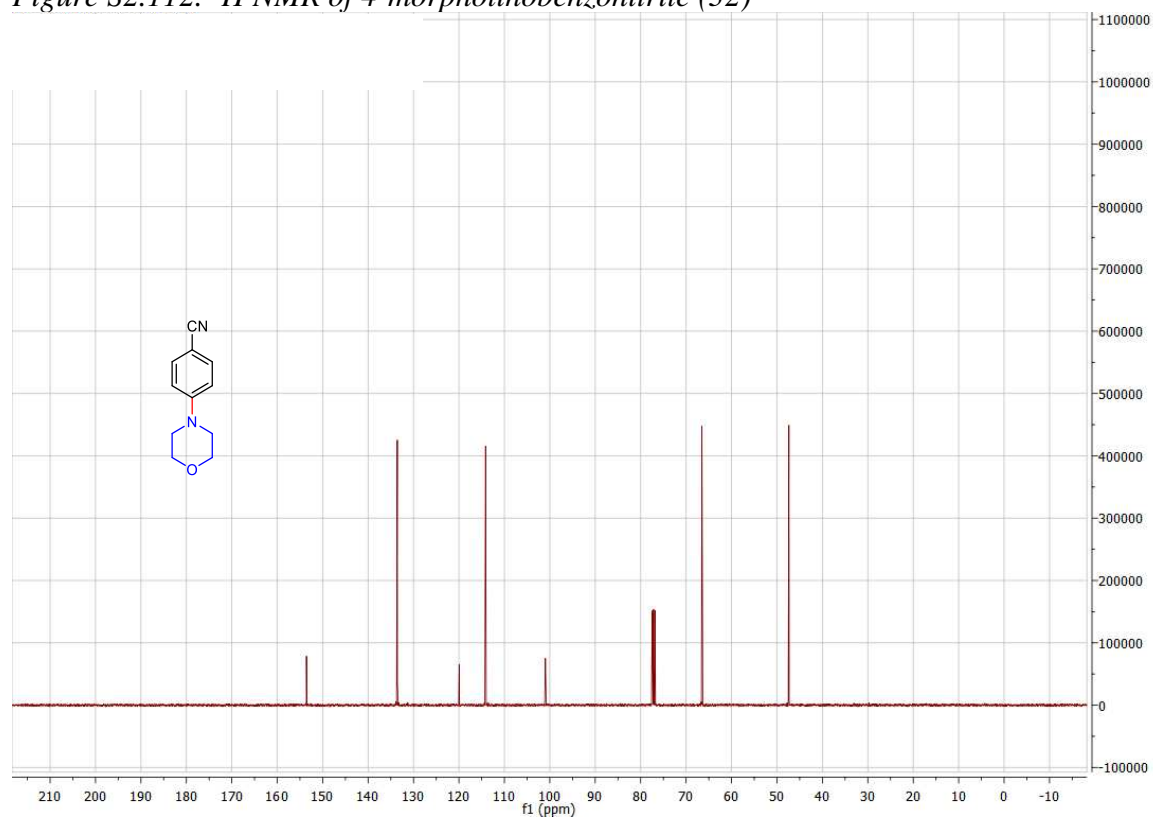


Figure S2.113. <sup>13</sup>C NMR of 4-morpholinobenzonitrile (32)



methyl 4-morpholinobenzoate (33)

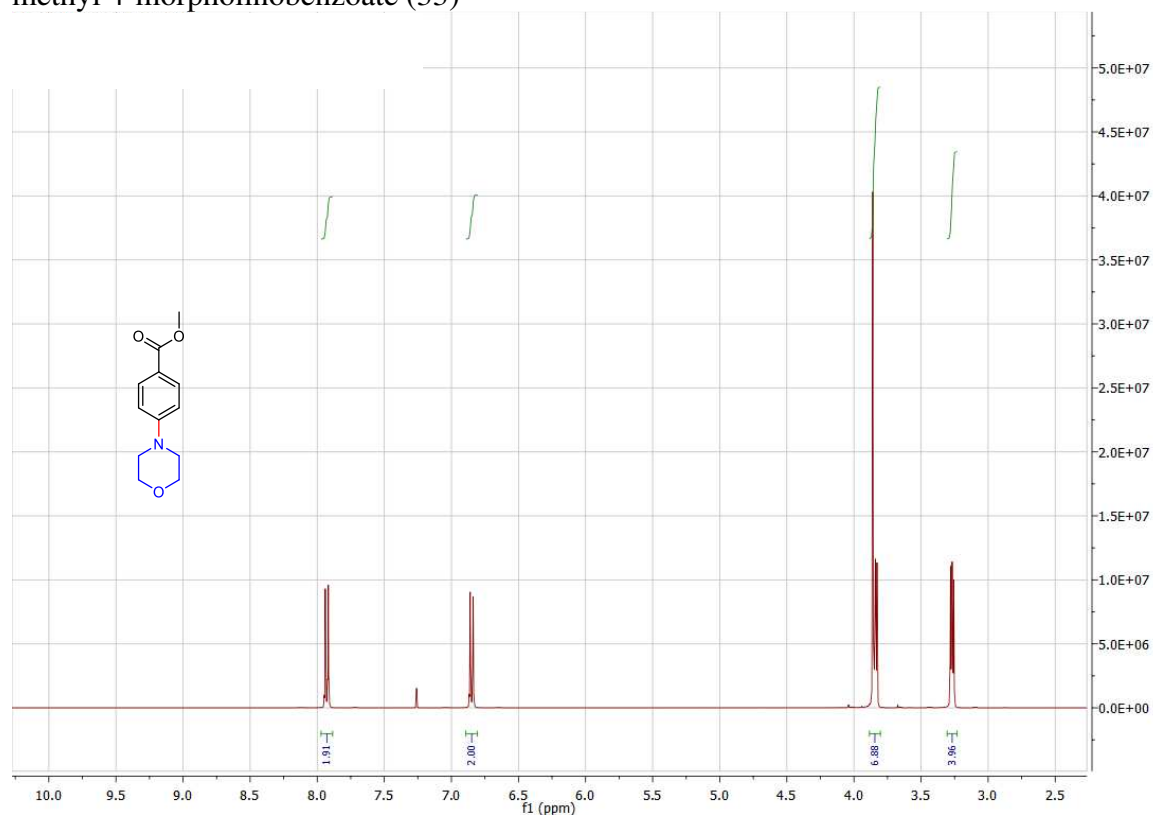


Figure S2.114.  $^1\text{H}$  NMR of methyl 4-morpholinobenzoate (33)

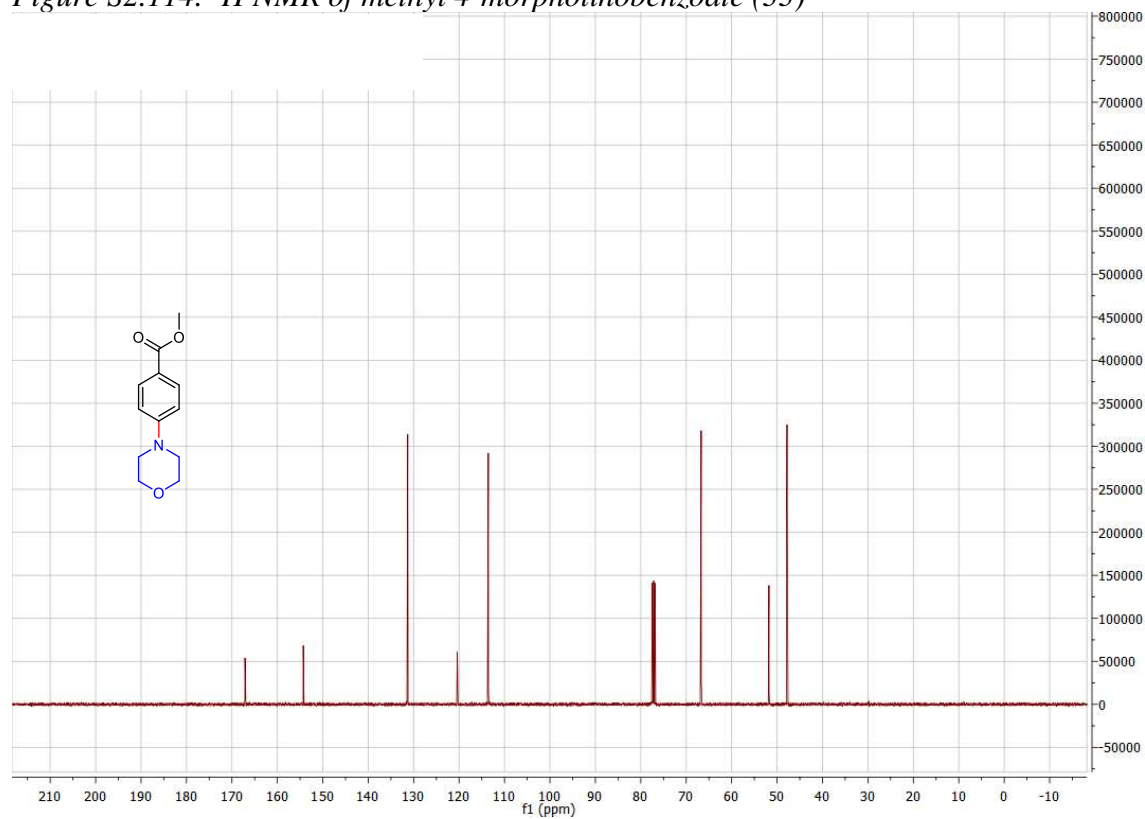


Figure S2.115.  $^{13}\text{C}$  NMR of methyl 4-morpholinobenzoate (33)

1-(4-morpholinophenyl)ethan-1-one (34)

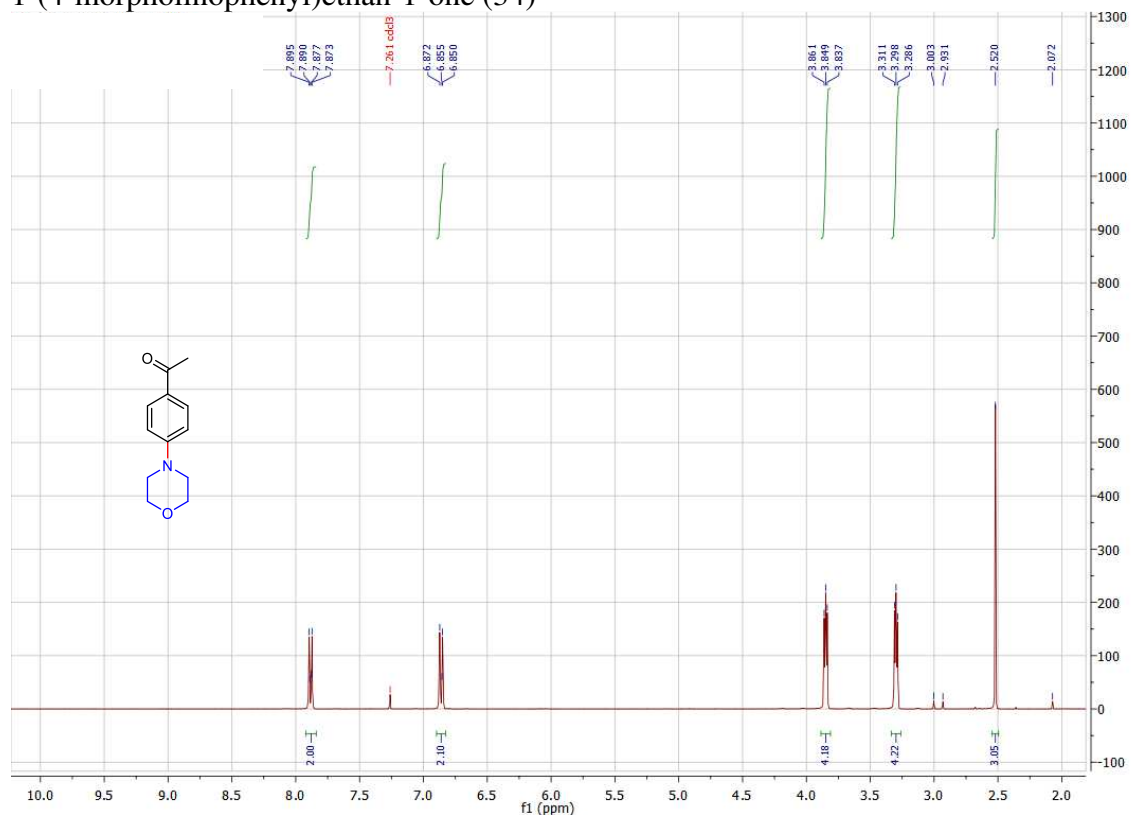


Figure S2.116.  $^1\text{H}$  NMR of 1-(4-morpholinophenyl)ethan-1-one (34)

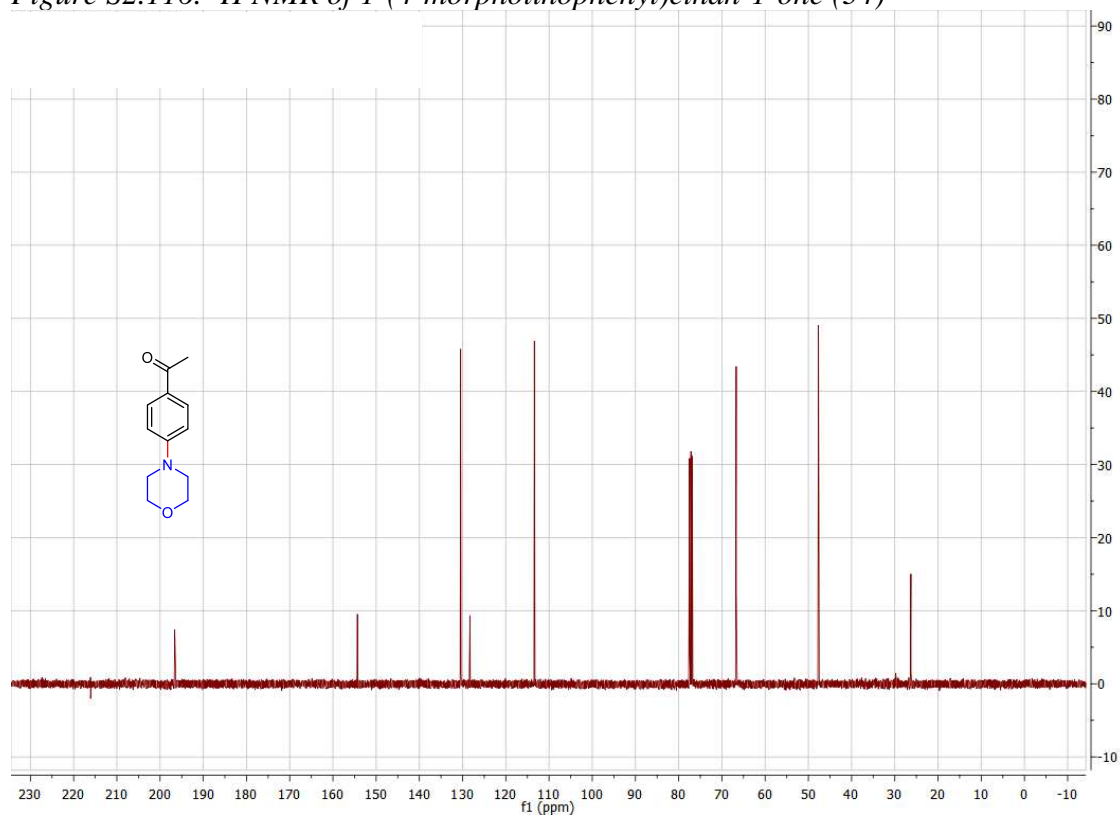


Figure S2.117.  $^{13}\text{C}$  NMR of 1-(4-morpholinophenyl)ethan-1-one (34)

4-(pyridin-3-yl)morpholine (35)

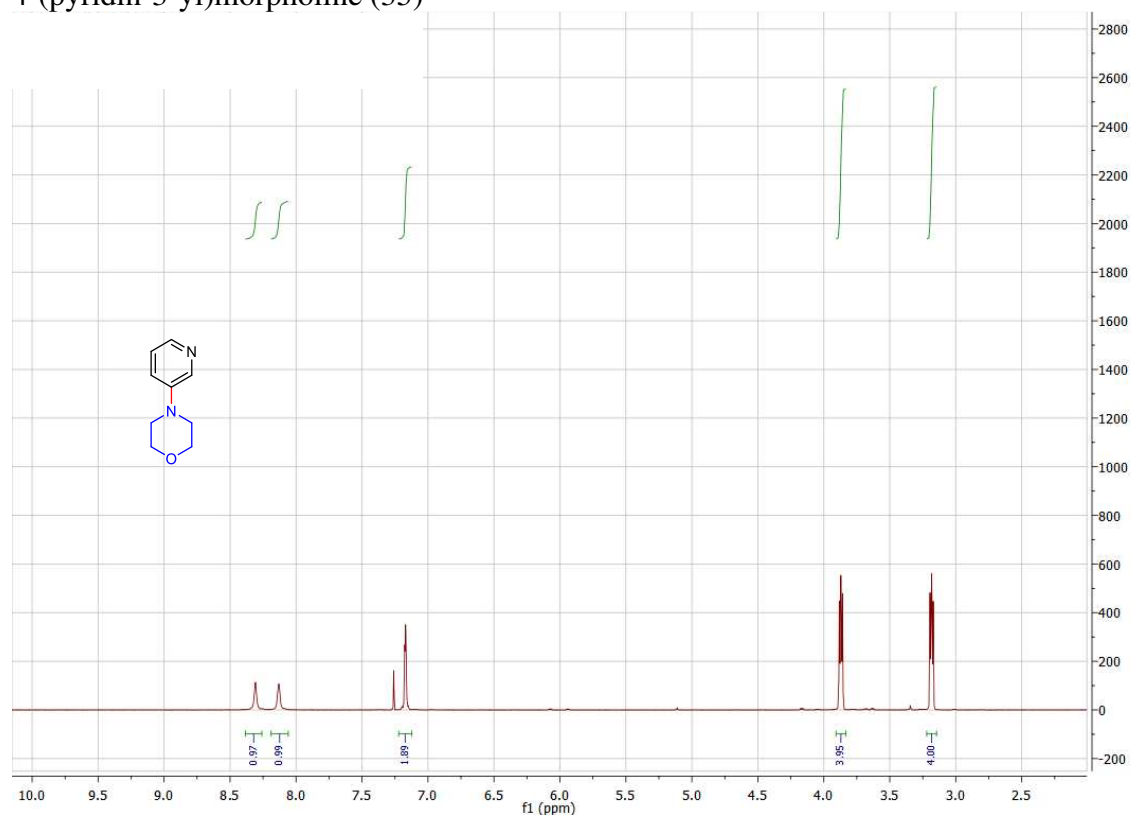


Figure S2.118.  $^1\text{H}$  NMR of 4-(pyridin-3-yl)morpholine (35)

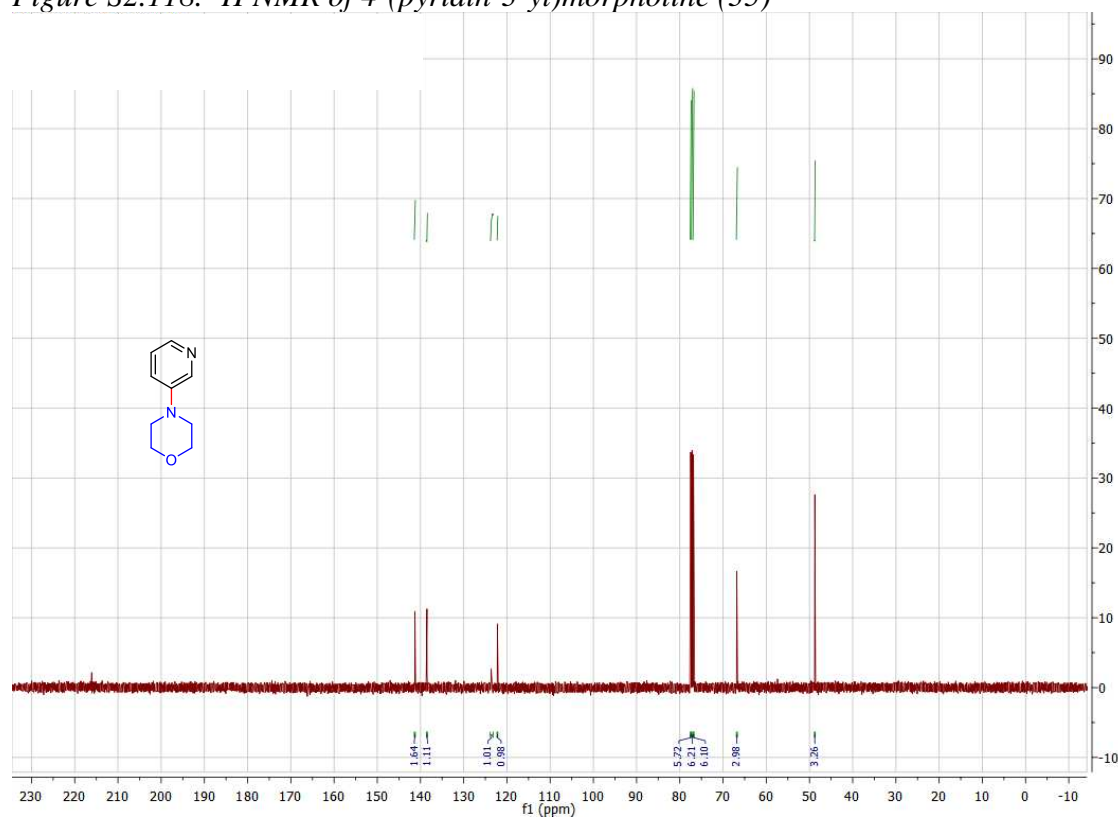


Figure S2.119.  $^{13}\text{C}$  NMR of 4-(pyridin-3-yl)morpholine (35)

4-(pyrimidin-5-yl)morpholine (36)

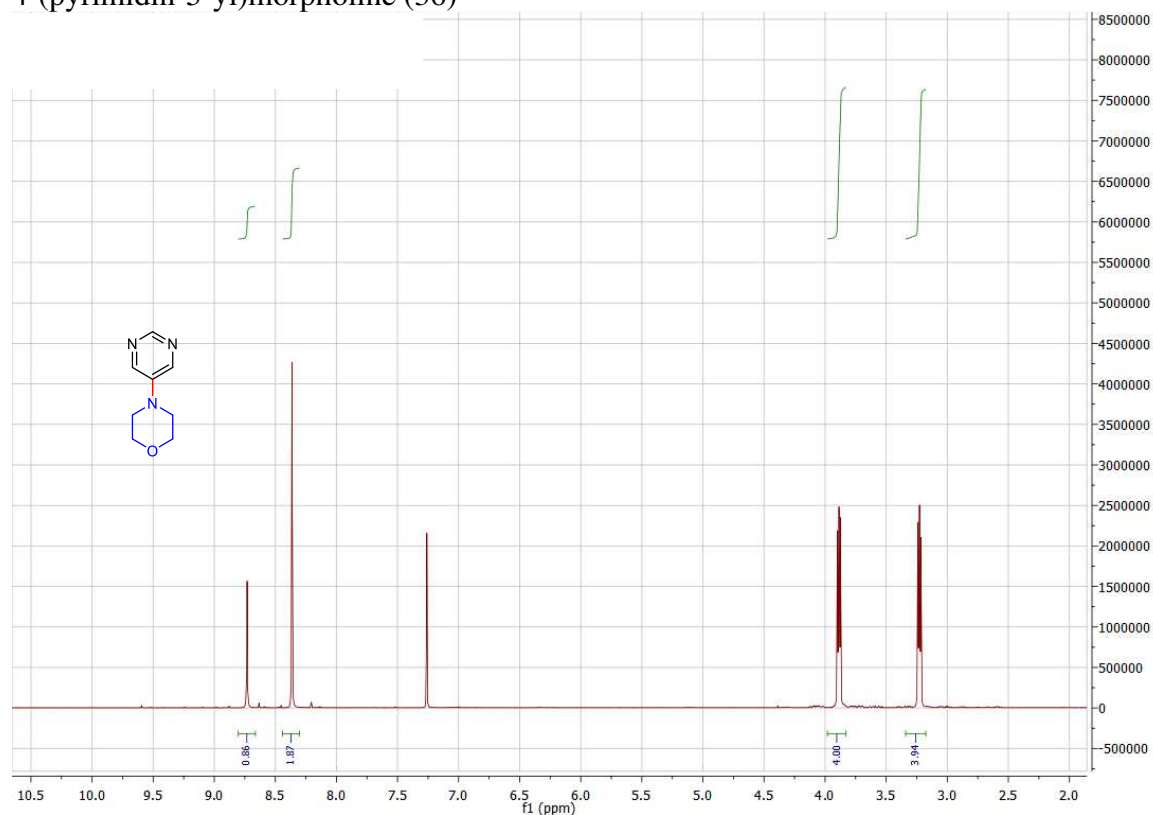


Figure S2.120.  $^1\text{H}$  NMR of 4-(pyrimidin-5-yl)morpholine (36)

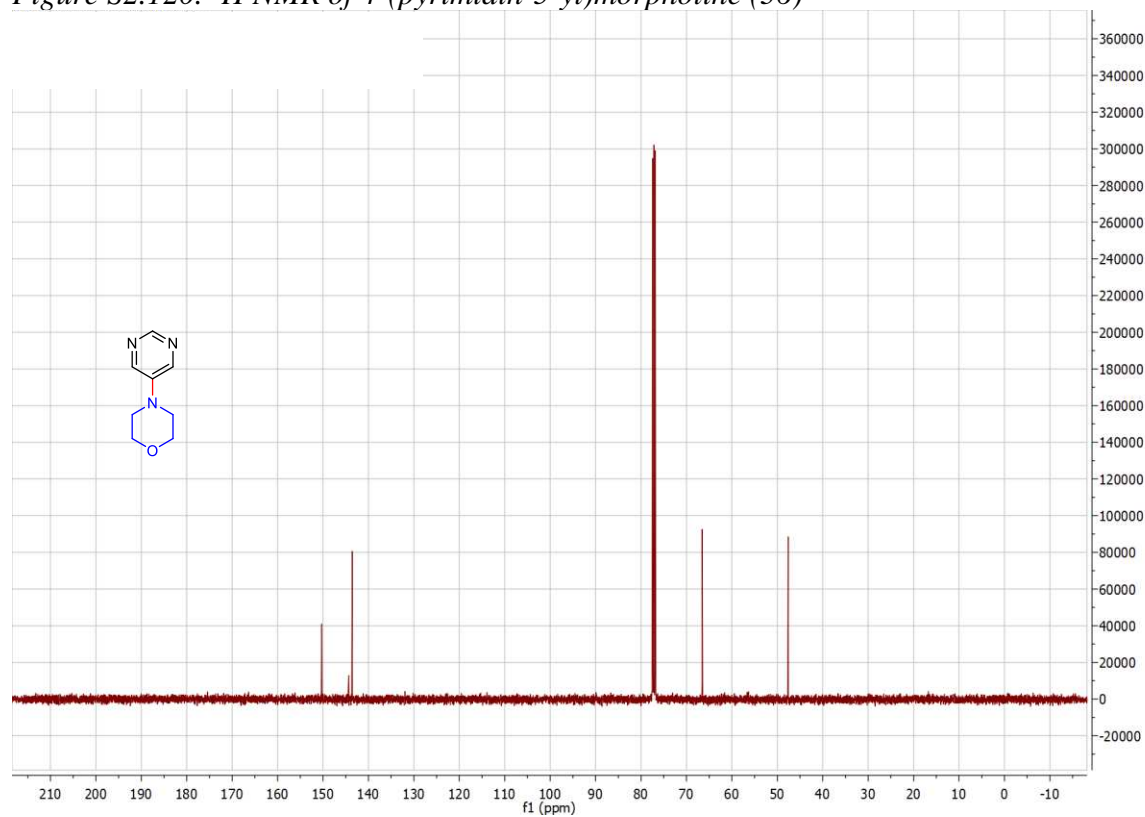


Figure S2.121.  $^{13}\text{C}$  NMR of 4-(pyrimidin-5-yl)morpholine (36)

1-(4-((3-bromophenyl)thio)phenyl)ethan-1-one (37)

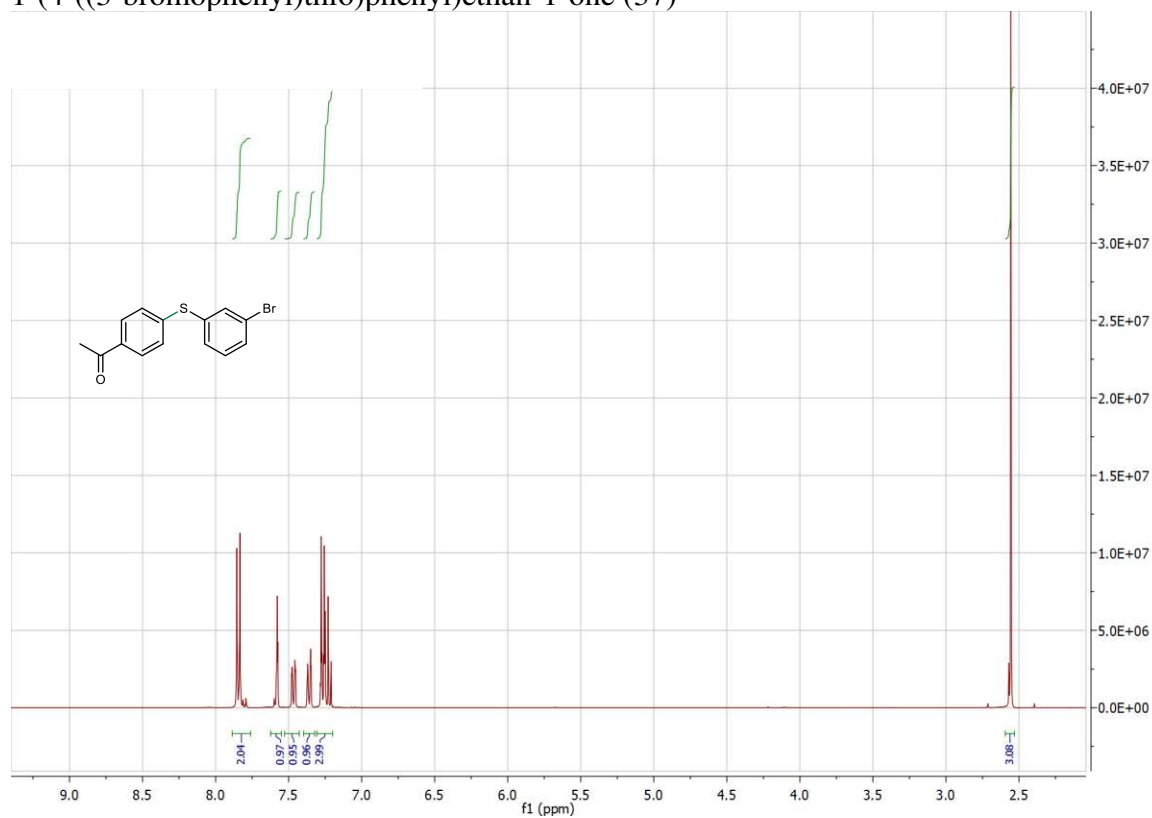


Figure S2.122.  $^1\text{H}$  NMR of 1-(4-((3-bromophenyl)thio)phenyl)ethan-1-one (37)

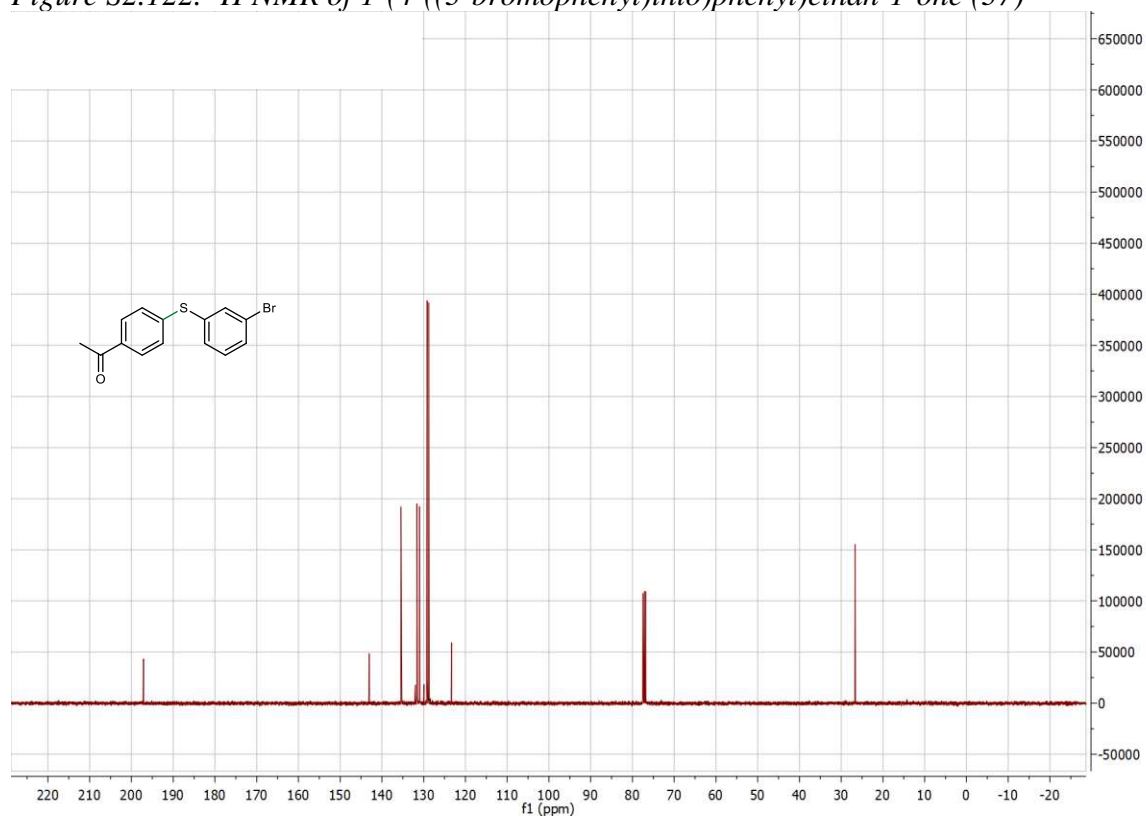


Figure S2.122.  $^{13}\text{C}$  NMR of 1-(4-((3-bromophenyl)thio)phenyl)ethan-1-one (37)

1-(4-((3-(pyridin-3-ylamino)phenyl)thio)phenyl)ethan-1-one (38)

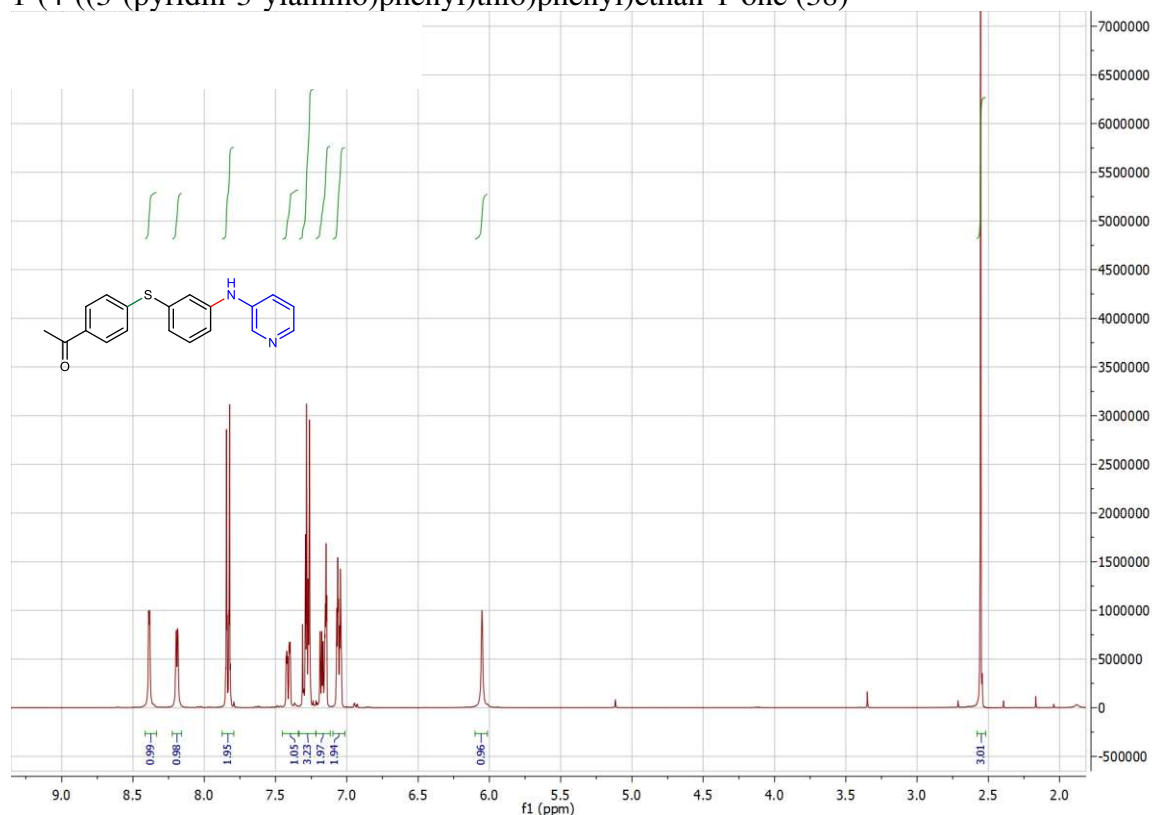


Figure S2.124.  $^1\text{H}$  NMR of 1-(4-((3-(pyridin-3-ylamino)phenyl)thio)phenyl)ethan-1-one (38)

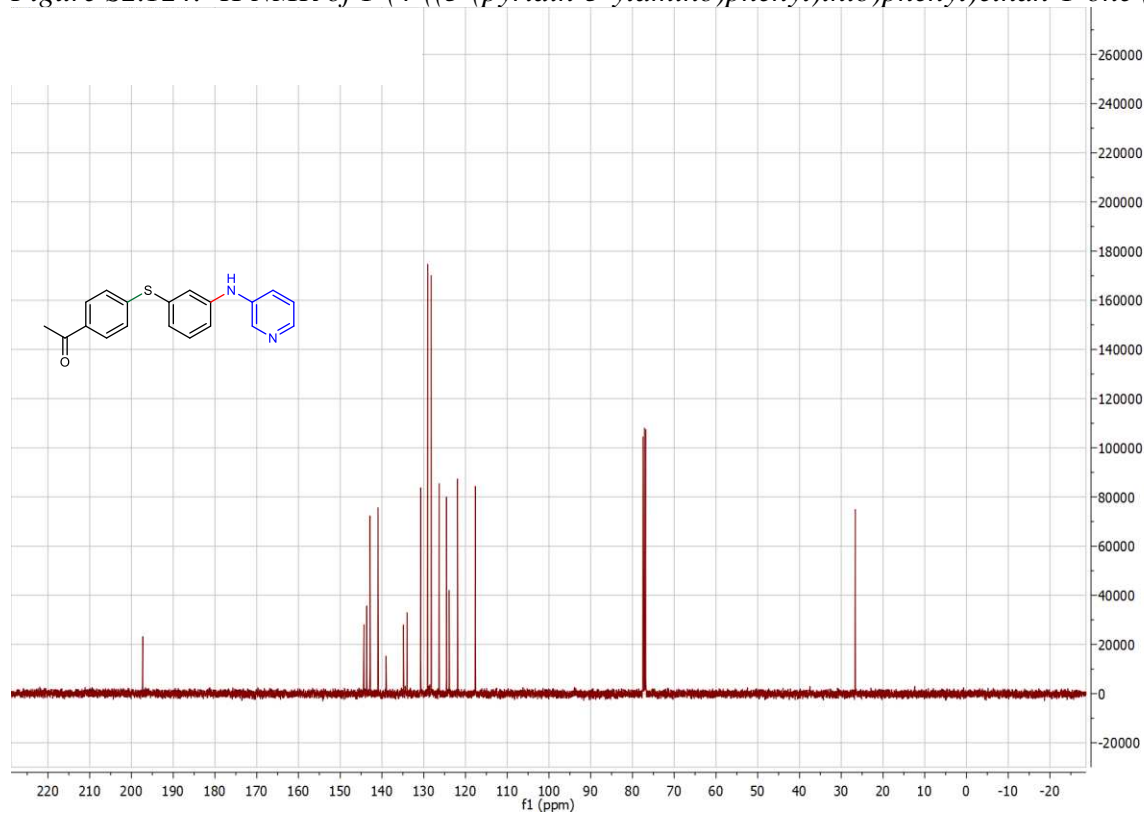


Figure S2.125.  $^{13}\text{C}$  NMR of 1-(4-((3-(pyridin-3-ylamino)phenyl)thio)phenyl)ethan-1-one (38)

1-(2-(4-(3-(trifluoromethyl)phenyl)piperazin-1-yl)ethyl)-1,3-dihydro-2H-benzo[d]imidazol-2-one (39, Flibanserin)

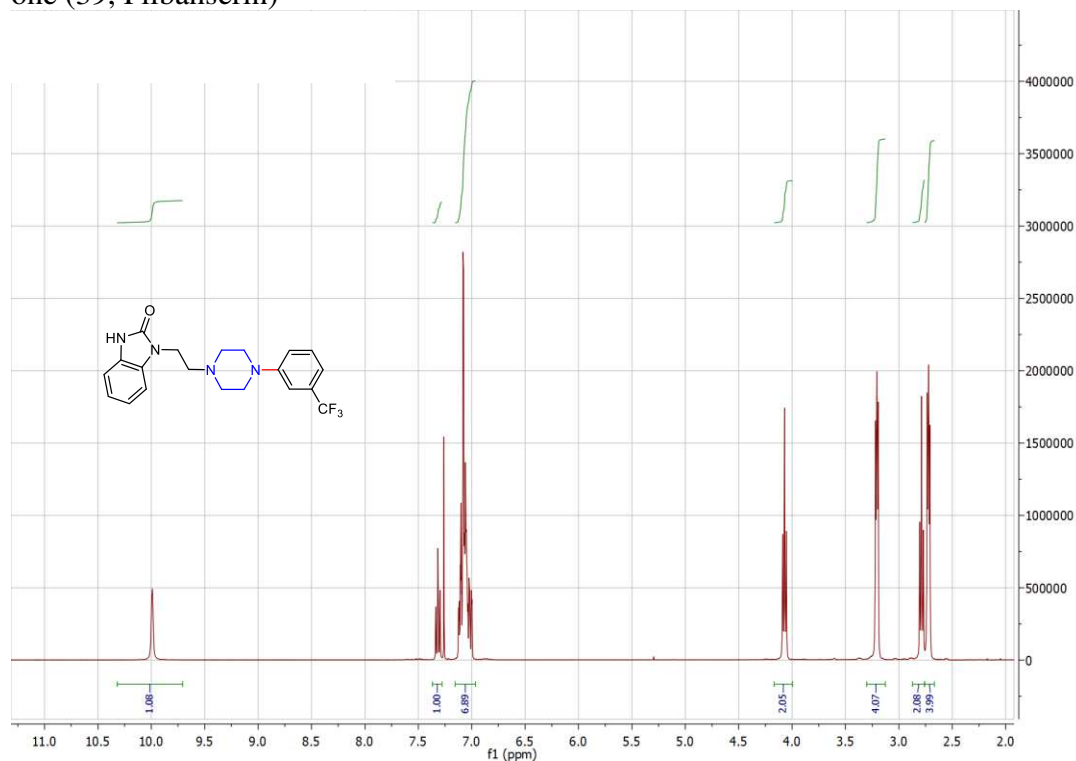


Figure S2.126. <sup>1</sup>H NMR of 1-(2-(4-(3-(trifluoromethyl)phenyl)piperazin-1-yl)ethyl)-1,3-dihydro-2H-benzo[d]imidazol-2-one (39, Flibanserin)

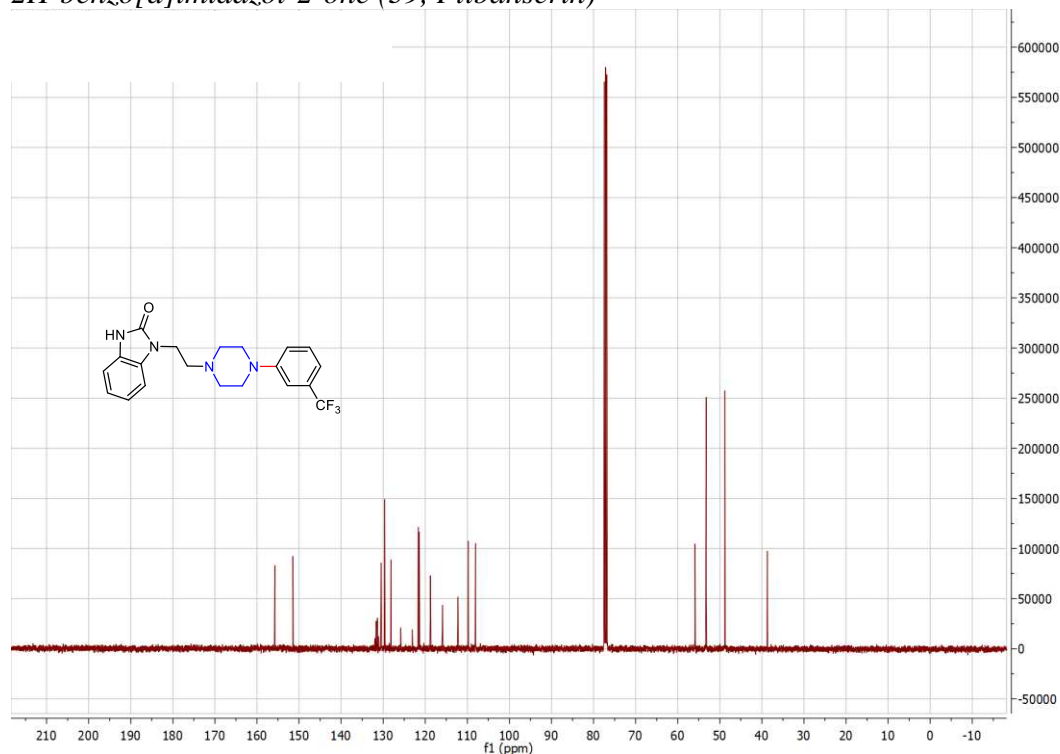


Figure S2.127. <sup>13</sup>C NMR of 1-(2-(4-(3-(trifluoromethyl)phenyl)piperazin-1-yl)ethyl)-1,3-dihydro-2H-benzo[d]imidazol-2-one (39, Flibanserin)

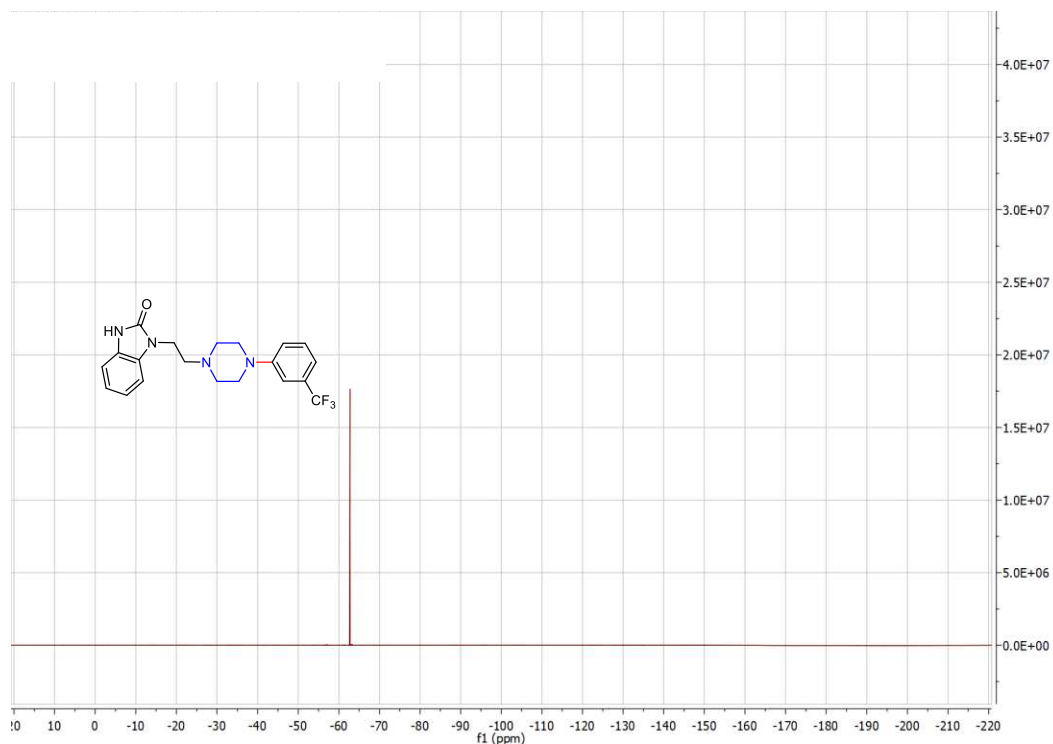


Figure S2.128.  $^{19}\text{F}$  NMR of 1-(2-(4-(3-(trifluoromethyl)phenyl)piperazin-1-yl)ethyl)-1,3-dihydro-2H-benzo[d]imidazol-2-one (39, Flibanserin)

1-(2-(4-(4-(trifluoromethyl)phenyl)piperazin-1-yl)ethyl)-1,3-dihydro-2H-benzo[d]imidazol-2-one (40)

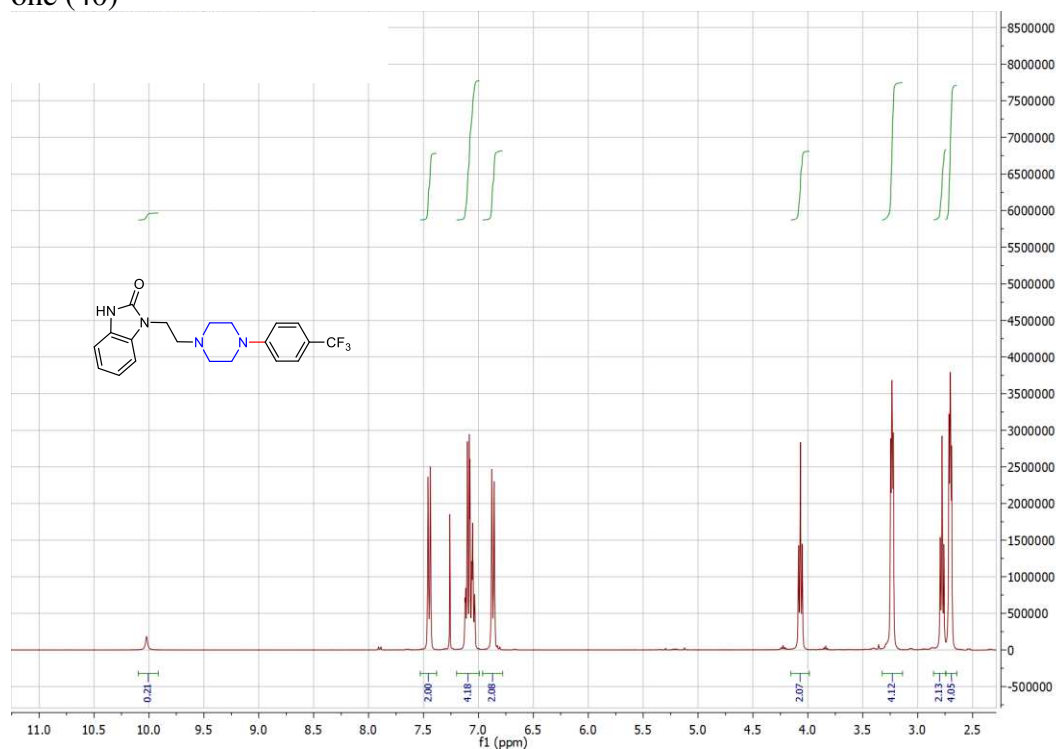


Figure S2.129.  $^1\text{H}$  NMR of 1-(2-(4-(4-(trifluoromethyl)phenyl)piperazin-1-yl)ethyl)-1,3-dihydro-2H-benzo[d]imidazol-2-one (40)



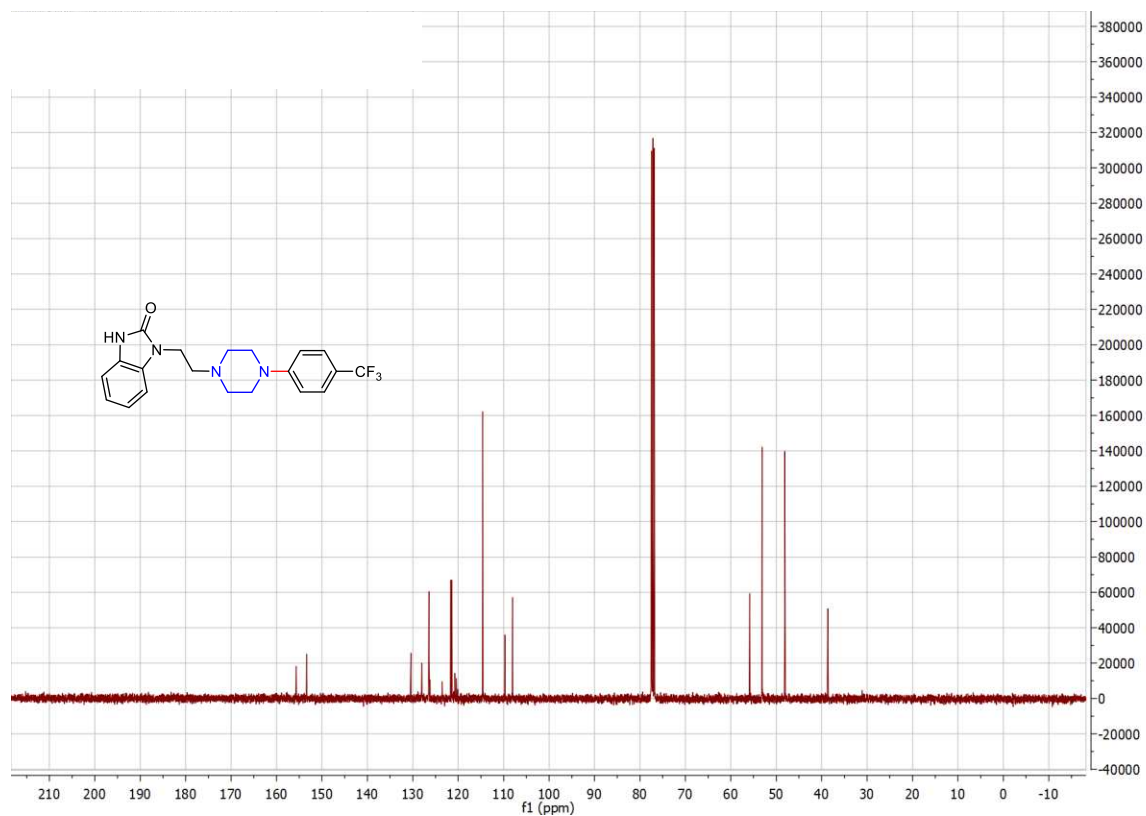


Figure S2.130.  $^{13}\text{C}$  NMR of 1-(2-(4-(4-(trifluoromethyl)phenyl)piperazin-1-yl)ethyl)-1,3-dihydro-2H-benzo[d]imidazol-2-one (40)

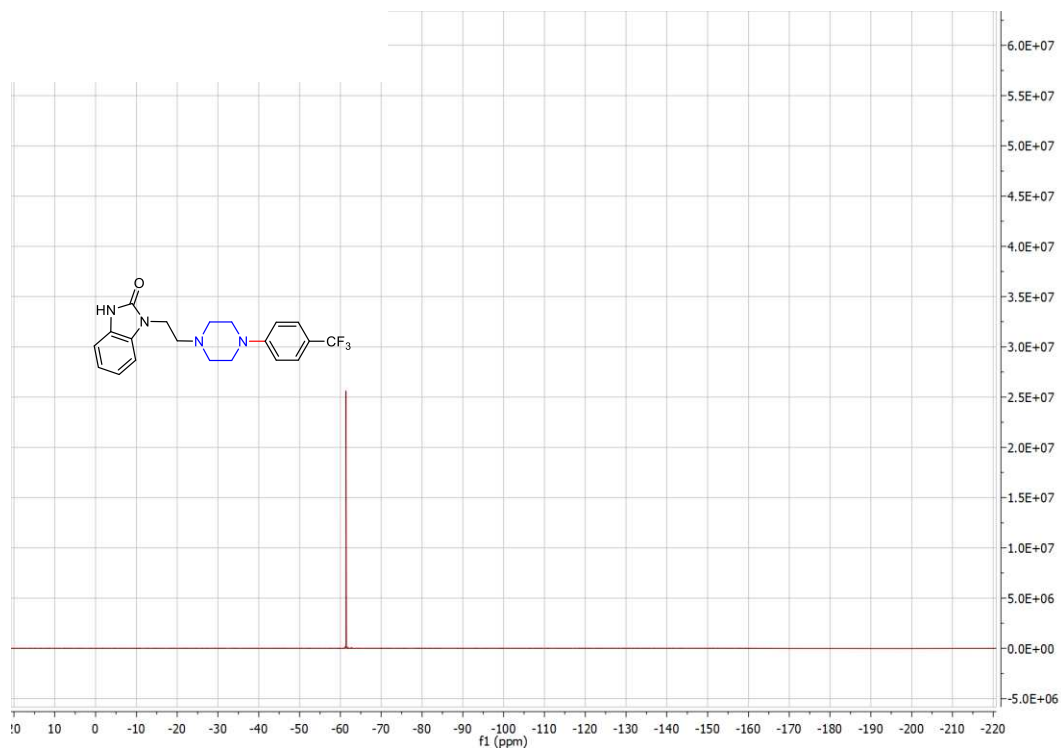


Figure S2.131.  $^{19}\text{F}$  NMR of 1-(2-(4-(4-(trifluoromethyl)phenyl)piperazin-1-yl)ethyl)-1,3-dihydro-2H-benzo[d]imidazol-2-one (40)

1-(2-(4-(3,5-difluorophenyl)piperazin-1-yl)ethyl)-1,3-dihydro-2H-benzo[d]imidazol-2-one (41)

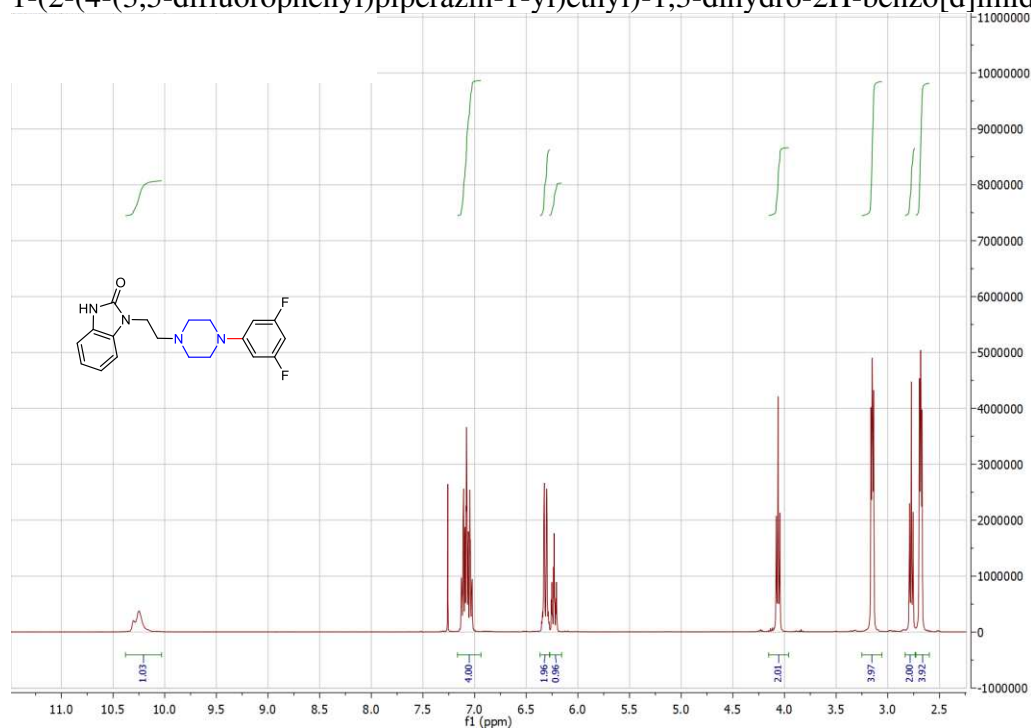


Figure S2.132. <sup>1</sup>H NMR of 1-(2-(4-(3,5-difluorophenyl)piperazin-1-yl)ethyl)-1,3-dihydro-2H-benzo[d]imidazol-2-one (41)

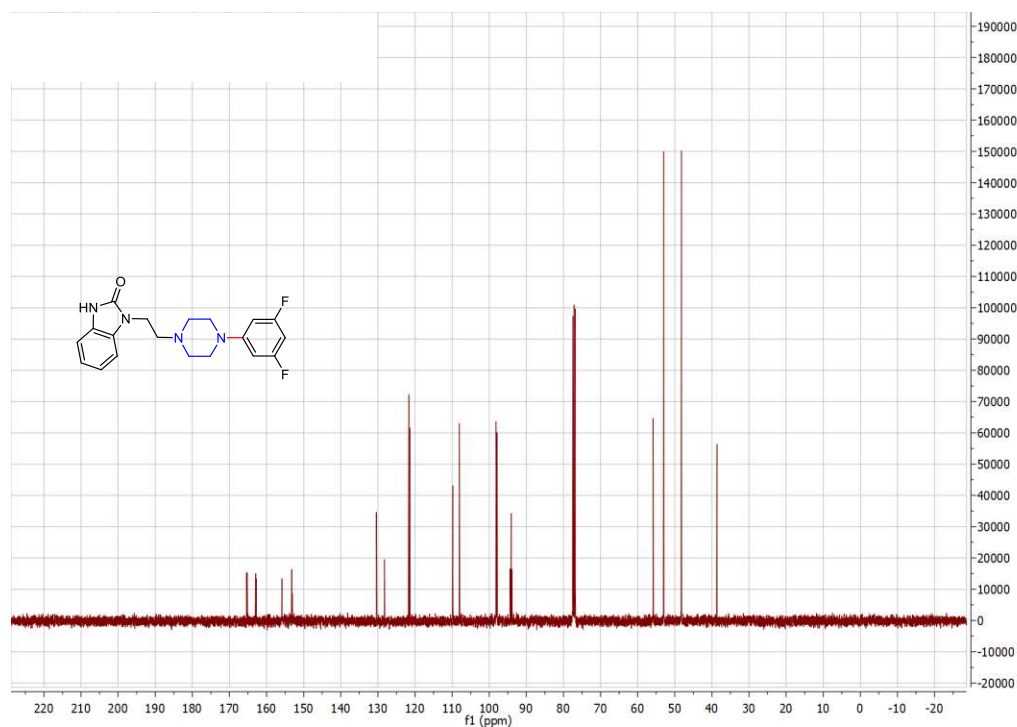


Figure S2.133. <sup>13</sup>C NMR of 1-(2-(4-(3,5-difluorophenyl)piperazin-1-yl)ethyl)-1,3-dihydro-2H-benzo[d]imidazol-2-one (41)

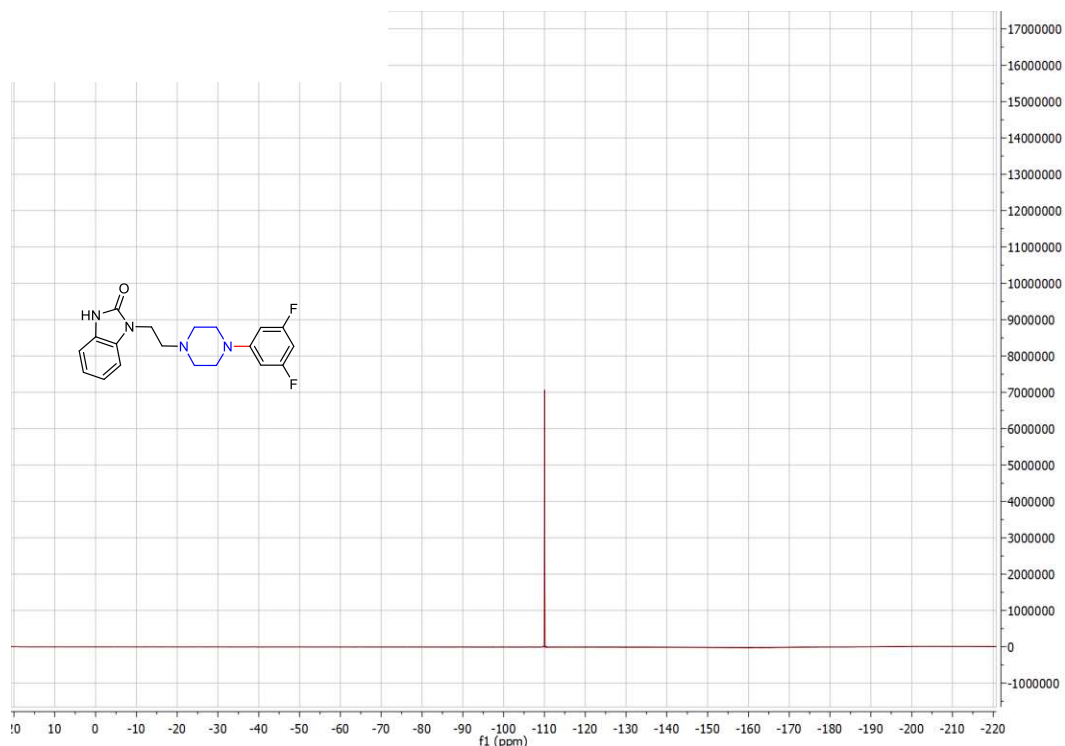


Figure S2.134.  $^{19}\text{F}$  NMR of 1-(2-(4-(3,5-difluorophenyl)piperazin-1-yl)ethyl)-1,3-dihydro-2H-benzod[e]imidazol-2-one (41)

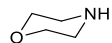
## 10. Coordinates of Molecular Structures

All coordinates are reported as XYZ Cartesian coordinates. Converged geometries were obtained from uM06/6-31+G\*\* level of theory in CPCM-described solvent DMAc. Single point energies computed at uM06/6-31+G\*\* level of theory (reported in parentheses) are arranged in the following order:  $E_{0K}$  (not ZPE and thermally corrected), H (298.15 K, 1 atm),  $G^{0*}$  (298.15 K, 1 atm), and  $G^0$  (298.15 K, 1 M). They are stated in Hartrees units. All energies reported were calculated using the GAUSSIAN 09 ver. D.01 computational chemistry package.

Br $\cdot$   
 (neutral radical, -2573.977116, -2573.974756, -2573.993946, -2573.990928)  
 Br    -0.72635    -0.03378    0.00000

H-O $\overset{\text{H}}{\curvearrowright}$   
 (neutral singlet, -76.4258868, -76.40059986, -76.42268086, -76.41966234)  
 O    0.43536    -0.63393    0.00000

H	1.39785	-0.59540	0.00000
H	0.15034	0.28627	0.00000



(neutral singlet, -287.6861675, -287.5454232, -287.5800572, -287.5770387)

C	-2.20285	-1.19488	0.03114
C	-0.68934	-1.22820	0.03839
C	-0.68800	0.89095	1.14902
C	-2.20135	0.87981	1.11703
H	0.82476	0.14605	-0.00876
H	-0.35288	-1.76891	0.94449
H	-0.32704	-1.77882	-0.83761
H	-2.56141	-0.74273	-0.91041
H	-2.62160	-2.20263	0.11703
H	-0.35144	0.45326	2.10905
H	-0.32371	1.92389	1.10282
H	-2.61987	1.38523	1.99310
H	-2.55796	1.39525	0.20778
O	-2.70126	-0.44955	1.13290
N	-0.19030	0.14257	-0.00072



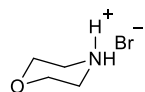
(cation radical, -287.468563, -287.3279498, -287.3634478, -287.3604293)

C	-2.19273	-1.17430	0.00632
C	-0.62494	-1.30141	0.14005
C	-0.62387	0.84902	1.26505
C	-2.19164	0.88899	1.08620
H	0.23164	0.46509	-0.61974
H	-0.42382	-1.84146	1.07150
H	-0.21144	-1.82689	-0.72117
H	-2.43120	-0.70249	-0.95567
H	-2.62409	-2.17553	0.06497
H	-0.42372	0.39134	2.23967
H	-0.20850	1.85532	1.20591
H	-2.62100	1.41165	1.94315
H	-2.43082	1.41192	0.15100
O	-2.65895	-0.42332	1.08296
N	-0.12917	0.02335	0.22506



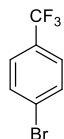
(neutral radical, -287.0275981, -286.9009658, -286.9363828, -286.9333642)

C	-2.17547	-0.64846	0.10330
C	-0.64102	-0.63892	0.10624
C	-0.63981	1.42547	1.18662
C	-2.17421	1.43430	1.19445
H	-0.26858	-1.16094	1.00352
H	-0.25286	-1.14664	-0.78156
H	-2.51172	-0.17754	-0.83794
H	-2.54145	-1.68130	0.12638
H	-0.26630	0.98645	2.12684
H	-0.25082	2.44397	1.09660
H	-2.53817	2.00388	2.05726
H	-2.51114	1.94050	0.27191
O	-0.15823	0.68782	0.08293
N	-2.66304	0.08328	1.24065



(neutral singlet, -2862.350059, -2862.1922, -2862.235191, -2862.232172)

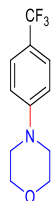
Br	-3.29026	-0.60111	-0.48400
C	-0.85911	-2.80788	1.40800
C	0.23144	-3.16340	2.39299
C	0.11581	-1.07208	3.42624
C	-0.98223	-0.60305	2.49856
H	-0.19782	-3.65770	3.28149
H	0.93863	-3.85504	1.92879
H	-0.44338	-2.35283	0.50225
H	-1.46388	-3.67394	1.12831
H	-0.31533	-1.51557	4.34017
H	0.73827	-0.22412	3.72194
H	-1.67411	0.08495	2.99032
H	-0.57097	-0.12038	1.60512
H	-2.30143	-2.19166	2.78134
H	-2.43804	-1.45253	1.27529
N	-1.75987	-1.78242	2.01446
O	0.95539	-2.01240	2.78335



(neutral singlet, -3142.571025, -3142.465352, -3142.511764, -3142.508745)

C	-0.08122	0.16040	0.00367
C	1.30734	0.15262	0.10060
C	1.98703	1.36195	0.09711

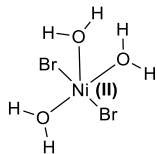
C	1.27553	2.55811	-0.00247
C	-0.11227	2.55393	-0.09729
C	-0.80053	1.34444	-0.09406
H	1.84883	-0.78548	0.17817
H	3.07202	1.37180	0.17203
H	-0.66232	3.48681	-0.17478
H	-1.88395	1.32823	-0.16747
C	2.04997	3.83745	-0.00491
F	1.27219	4.92203	-0.11569
F	2.77404	3.98569	1.12249
F	2.93411	3.88342	-1.02107
Br	-1.00562	-1.48756	0.00545



(neutral singlet, -855.6475516, -855.4136131, -855.4701661, -855.4671476)

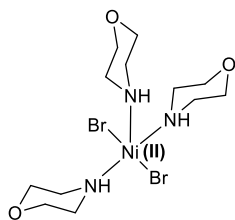
C	0.23250	-0.53250	2.26955
C	1.62064	-0.32627	2.15575
C	-0.56402	0.58090	2.61720
C	2.18403	0.92169	2.39090
H	2.28113	-1.13598	1.86551
C	0.00188	1.82080	2.84400
H	-1.63754	0.47548	2.73631
C	1.38336	2.00508	2.73379
H	3.25888	1.04340	2.28987
H	-0.63855	2.65765	3.11688
C	1.94652	3.36030	2.97353
F	1.65456	3.82521	4.20939
F	3.28188	3.40917	2.85022
F	1.44570	4.28040	2.11835
C	-1.65528	-1.85416	1.43352
C	0.51592	-2.89280	1.68221
C	-2.27717	-3.21854	1.62691
H	-1.54799	-1.64637	0.35316
H	-2.33156	-1.10627	1.85253
C	-0.20342	-4.21449	1.85288
H	0.84332	-2.77500	0.63226
H	1.40848	-2.91570	2.31602
H	-3.21612	-3.28527	1.06949
H	-2.48984	-3.38655	2.69701
H	0.41578	-5.02877	1.46517

H	-0.39303	-4.39829	2.92475
N	-0.34447	-1.78595	2.08387
O	-1.42802	-4.24303	1.14566



(neutral triplet, -6885.680612, -6885.589554, -6885.646443, -6885.643424)

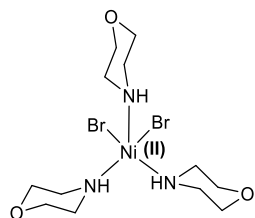
Ni	0.11804	-0.10548	-0.65494
Br	-1.64844	1.27260	0.19813
Br	2.17862	-1.24763	-1.11220
H	-0.51836	-1.19157	-2.95790
H	-1.78242	-0.47864	-2.40077
H	1.33105	1.21596	-2.61023
H	0.03969	2.02142	-2.25376
H	-1.35885	-1.60220	0.89417
H	-0.18383	-2.48962	0.38327
O	-1.00702	-0.99853	-2.14561
O	0.74576	1.47345	-1.88461
O	-0.40980	-1.60525	0.70468



(neutral triplet low energy configuration, -7519.51125, -7519.072274, -7519.153756, -7519.150738)

Ni	-0.24854	-0.30735	-0.97686
Br	-1.53752	1.36092	0.26651
Br	1.64298	-1.83653	-1.59336
C	0.00998	-1.45563	1.70527
C	-2.10403	-2.17012	0.77828
C	-0.09126	-2.57475	2.71830
H	-0.43954	-0.53742	2.10285
H	1.05872	-1.24351	1.45472
C	-2.14345	-3.26147	1.83080
H	-2.61977	-1.26954	1.13451
H	-2.60742	-2.51403	-0.13419
H	0.37993	-2.29015	3.66413
H	0.41386	-3.48175	2.33877

H	-3.17440	-3.48089	2.12498
H	-1.69536	-4.18816	1.42772
C	0.12784	2.32670	-2.64613
C	1.81688	1.74481	-1.02406
H	1.34172	0.67717	-2.69068
C	1.11877	3.28825	-3.26998
H	-0.47993	2.83021	-1.88455
H	-0.55189	1.93423	-3.41182
C	2.75488	2.72083	-1.70024
H	1.25680	2.24538	-0.22361
H	2.37009	0.90610	-0.58257
H	0.60361	4.15414	-3.69702
H	1.67448	2.78361	-4.08157
H	3.43982	3.17006	-0.97472
H	3.35671	2.19853	-2.46645
C	-2.87136	-0.34275	-2.45895
C	-0.98526	-1.03964	-3.81197
H	-1.68296	-1.97798	-2.15770
C	-3.78236	-0.96529	-3.49505
H	-2.70476	0.72001	-2.67625
H	-3.31687	-0.40567	-1.46067
C	-1.96953	-1.63236	-4.79758
H	-0.74851	-0.00892	-4.10588
H	-0.05329	-1.61372	-3.79061
H	-4.72885	-0.41930	-3.55153
H	-4.00490	-2.01322	-3.22046
H	-1.57268	-1.57535	-5.81555
H	-2.15172	-2.69580	-4.55812
O	-1.44951	-2.87073	3.00273
O	-3.19788	-0.92687	-4.78474
O	2.03339	3.78118	-2.30564
N	0.82296	1.20528	-1.98229
N	-1.54478	-1.00289	-2.44069
H	-0.24369	-2.60685	0.04612
N	-0.71320	-1.79512	0.45960

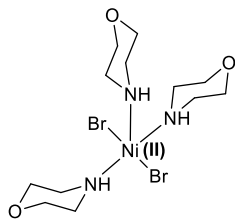


(neutral triplet high energy configuration, -7519.502094, -7519.063493, -7519.145703, -7519.142684)



Ni	-0.34395	-0.31491	-0.97220
Br	-1.36625	1.53341	0.31260
Br	1.01148	1.31421	-2.30257
C	-2.21083	-2.75280	0.15754
C	-0.62337	-1.74807	1.68530
C	-2.98582	-3.24119	1.36746
H	-1.51729	-3.53229	-0.18182
H	-2.91650	-2.54067	-0.65602
C	-1.45771	-2.26836	2.83610
H	0.15973	-2.48052	1.44715
H	-0.14057	-0.79929	1.95100
H	-3.48615	-4.18967	1.15047
H	-3.75551	-2.49713	1.64083
H	-0.82881	-2.50099	3.70052
H	-2.19837	-1.50634	3.14052
C	2.38277	-1.33783	-0.40696
C	1.03235	-3.10557	-1.35462
H	1.52126	-1.32660	-2.23882
C	3.61495	-2.12254	-0.80452
H	2.08761	-1.59613	0.61830
H	2.57388	-0.25978	-0.45247
C	2.31096	-3.83004	-1.72641
H	0.69966	-3.43503	-0.36190
H	0.23683	-3.33605	-2.07335
H	4.42713	-1.95614	-0.09083
H	3.96072	-1.79943	-1.80350
H	2.16693	-4.91383	-1.69087
H	2.61333	-3.55472	-2.75326
C	-2.67872	0.09055	-2.66104
C	-0.93185	-1.06739	-3.87771
H	-1.97299	-1.78841	-2.29008
C	-3.63292	-0.27319	-3.77825
H	-2.22283	1.07293	-2.84156
H	-3.20390	0.14247	-1.70019
C	-1.95912	-1.40683	-4.93701
H	-0.41536	-0.13251	-4.12208
H	-0.18047	-1.86353	-3.81042
H	-4.39079	0.50603	-3.90307
H	-4.15060	-1.22112	-3.54027
H	-1.48660	-1.47329	-5.92154
H	-2.43274	-2.38069	-4.71597
O	-2.12640	-3.46310	2.47032
O	-2.95503	-0.40235	-5.01480
O	3.35177	-3.51568	-0.81941
N	1.24320	-1.64579	-1.30454
N	-1.56791	-0.88568	-2.55112

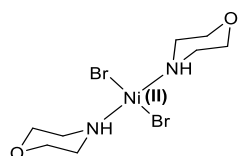
H	-2.11130	-0.79304	0.70577
N	-1.44100	-1.53312	0.47248



(neutral singlet, -7519.49154, -7519.052241, -7519.131422, -7519.128404)

Ni	-0.33085	-0.07389	-0.76722
Br	-2.02137	1.37884	-0.04258
Br	1.65444	-1.35390	-1.09589
C	-0.51628	-1.04125	1.88582
C	-2.27445	-1.97954	0.49838
C	-0.73421	-2.17867	2.85995
H	-1.13788	-0.17902	2.15070
H	0.53317	-0.72389	1.87749
C	-2.42668	-3.07826	1.53192
H	-2.95349	-1.14603	0.70654
H	-2.50253	-2.37106	-0.49944
H	-0.52598	-1.85180	3.88299
H	-0.06054	-3.02241	2.62396
H	-3.46545	-3.41867	1.57430
H	-1.79259	-3.94236	1.26230
C	-0.34862	2.13861	-2.79627
C	1.32720	2.19534	-1.05699
H	1.09996	0.74808	-2.46632
C	0.54997	3.02643	-3.63198
H	-1.03165	2.73719	-2.18505
H	-0.95052	1.48257	-3.43276
C	2.16570	3.08879	-1.94618
H	0.66415	2.78999	-0.41746
H	1.96216	1.57295	-0.41695
H	-0.04839	3.68102	-4.27248
H	1.19691	2.40726	-4.28130
H	2.75349	3.78873	-1.34527
H	2.86508	2.47417	-2.54243
C	-2.80610	-0.83338	-3.02931
C	-0.65256	-1.33897	-3.99061
H	-1.42314	-2.14723	-2.30702
C	-3.44470	-1.71581	-4.08261
H	-2.80077	0.20961	-3.37867
H	-3.38690	-0.85357	-2.09861
C	-1.35509	-2.20184	-5.02012

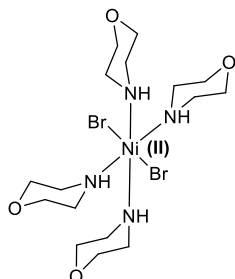
H	-0.51168	-0.32899	-4.40648
H	0.34006	-1.74362	-3.75716
H	-4.44233	-1.35698	-4.35653
H	-3.54081	-2.74842	-3.69754
H	-0.82431	-2.19359	-5.97786
H	-1.40677	-3.24626	-4.66092
O	-2.08038	-2.62049	2.82582
O	-2.66906	-1.72639	-5.27157
O	1.35222	3.85932	-2.81333
N	0.46929	1.30748	-1.88188
N	-1.42150	-1.22457	-2.74663
H	-0.26957	-2.22752	0.25435
N	-0.89002	-1.45088	0.50675



(neutral triplet, -7231.802134, -7231.507317, -7231.575001, -7231.571983)

Ni	-0.32641	-0.74928	-1.12014
Br	-0.40296	1.55968	-0.68726
Br	1.16540	-2.51743	-1.56627
C	-2.00500	-2.79492	0.27120
C	-0.73772	-1.29030	1.68638
C	-2.79752	-3.20858	1.49373
H	-1.13875	-3.45274	0.13313
H	-2.62935	-2.86284	-0.62674
C	-1.57201	-1.76344	2.85854
H	0.17059	-1.89988	1.58831
H	-0.43848	-0.24343	1.81025
H	-3.10996	-4.25372	1.41195
H	-3.70376	-2.58373	1.58917
H	-0.98371	-1.74597	3.78055
H	-2.44482	-1.09973	2.99269
C	-2.95767	-0.46625	-2.48155
C	-1.00006	-0.41939	-3.91247
H	-1.66019	-2.02125	-2.83254
C	-3.80684	-0.63018	-3.72496
H	-2.84984	0.59453	-2.22384
H	-3.42913	-0.97808	-1.63445
C	-1.92309	-0.57969	-5.10238
H	-0.82138	0.64400	-3.70578
H	-0.03263	-0.90240	-4.09279
H	-4.78421	-0.15851	-3.58713

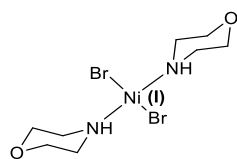
H	-3.96804	-1.70282	-3.93558
H	-1.51228	-0.06740	-5.97732
H	-2.04040	-1.64931	-5.35197
O	-2.01276	-3.09607	2.66736
O	-3.19404	-0.01045	-4.84071
N	-1.59692	-1.00902	-2.68941
H	-2.28222	-0.76662	0.46022
N	-1.48942	-1.41394	0.41342



(neutral triplet, -7807.205703, -7806.622537, -7806.716298, -7806.71328)

Ni	-0.08903	0.33546	-2.31985
Br	-1.80567	2.13113	-2.01562
Br	1.53258	-1.54716	-2.65100
C	-2.91188	-1.12421	-1.84936
C	-1.81891	-1.88124	-3.83464
H	-1.03911	-1.93043	-1.99587
C	-3.60775	-2.46779	-1.75677
H	-3.51137	-0.41157	-2.42884
H	-2.78765	-0.70024	-0.84620
C	-2.52326	-3.21348	-3.68642
H	-2.44476	-1.20626	-4.42965
H	-0.85144	-2.01165	-4.33326
H	-4.60614	-2.36025	-1.32136
H	-3.02091	-3.14499	-1.10810
H	-2.72447	-3.66094	-4.66469
H	-1.88577	-3.91192	-3.11202
N	-1.59951	-1.24887	-2.51745
O	-3.77214	-3.05931	-3.03362
C	1.11806	-0.49240	0.65790
C	-0.99331	0.62096	0.86385
H	-0.62518	-1.09637	-0.14220
C	0.88723	-1.11610	2.01829
H	1.66516	0.45276	0.78560
H	1.71810	-1.15803	0.02821
C	-1.16517	-0.03674	2.21628
H	-0.51387	1.60325	0.97641
H	-1.96636	0.79707	0.39586
H	1.83717	-1.26454	2.54129

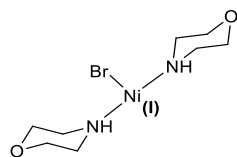
H	0.40175	-2.10264	1.90049
H	-1.73904	0.60632	2.89087
H	-1.71683	-0.98906	2.09809
N	-0.15182	-0.19448	-0.04076
O	0.08253	-0.28724	2.83808
C	2.88465	1.36293	-1.60901
C	1.49966	3.13164	-2.43211
H	1.09256	1.95825	-0.83552
C	3.72045	2.39935	-0.88700
H	3.29279	1.18003	-2.61147
H	2.91002	0.40821	-1.07861
C	2.36774	4.12250	-1.68497
H	1.90751	2.99778	-3.44478
H	0.47249	3.50662	-2.50565
H	4.76709	2.08399	-0.83432
H	3.34869	2.52816	0.14748
H	2.41578	5.07626	-2.21949
H	1.94025	4.30936	-0.68243
N	1.48316	1.80898	-1.77039
O	3.69574	3.64807	-1.55639
C	1.26482	0.67796	-5.17279
C	-1.10968	0.97494	-5.28022
H	0.15333	1.99922	-4.10581
C	1.39924	1.58692	-6.37940
H	1.17205	-0.36867	-5.48718
H	2.15298	0.74008	-4.53500
C	-0.91678	1.89631	-6.46609
H	-1.21615	-0.05230	-5.64465
H	-2.00398	1.24649	-4.70724
H	2.24737	1.28538	-7.00203
H	1.57173	2.62864	-6.04865
H	-1.76370	1.83238	-7.15620
H	-0.83106	2.94391	-6.12032
N	0.06360	1.01861	-4.38401
O	0.24377	1.53913	-7.19860



(anion radical, -7231.926212, -7231.632868, -7231.702509, -7231.69949)

Ni	-0.35732	-0.67021	-1.09591
Br	-0.29896	1.70418	-0.59596
Br	1.35794	-2.32294	-1.58790
C	-1.99992	-2.78396	0.32325

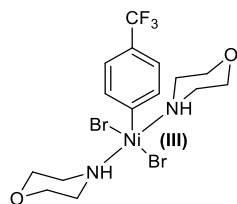
C	-0.80743	-1.24456	1.74507
C	-2.69732	-3.32664	1.55346
H	-1.09673	-3.37162	0.10603
H	-2.66282	-2.85890	-0.54755
C	-1.53809	-1.83515	2.93298
H	0.15236	-1.76165	1.59640
H	-0.59299	-0.18019	1.90020
H	-2.92189	-4.39265	1.44273
H	-3.64894	-2.78813	1.71869
H	-0.91444	-1.80977	3.83268
H	-2.46016	-1.25967	3.13644
C	-2.98840	-0.35499	-2.58244
C	-1.01810	-0.55188	-3.95215
H	-1.81966	-2.02588	-2.79850
C	-3.83223	-0.48844	-3.83390
H	-2.79209	0.70436	-2.36477
H	-3.52183	-0.77870	-1.72276
C	-1.91665	-0.68183	-5.16397
H	-0.74543	0.50227	-3.79472
H	-0.09030	-1.12219	-4.08106
H	-4.76151	0.08451	-3.74977
H	-4.09435	-1.54975	-4.00066
H	-1.44617	-0.25125	-6.05403
H	-2.12674	-1.74852	-5.36612
O	-1.87482	-3.19484	2.70252
O	-3.14104	0.00952	-4.96948
N	-1.68326	-1.01589	-2.72285
H	-2.40067	-0.78716	0.56128
N	-1.57561	-1.38663	0.49637



(neutral radical, -4657.723492, -4657.432192, -4657.495468, -4657.492449)

Ni	-2.04170	1.84086	-0.49747
Br	-4.33938	1.82767	-0.44783
C	-1.60848	-0.96100	0.17403
C	-1.57063	-0.50758	-2.20267
H	-0.17676	0.07558	-0.83649
C	-1.08659	-2.35151	-0.12345
H	-2.70632	-0.96437	0.19969
H	-1.24786	-0.60459	1.14597
C	-1.05281	-1.91431	-2.42221
H	-2.66731	-0.49329	-2.26155

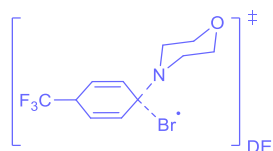
H	-1.18209	0.17838	-2.96511
H	-1.46485	-3.07599	0.60456
H	0.01773	-2.36163	-0.07854
H	-1.40730	-2.31805	-3.37578
H	0.05240	-1.91428	-2.43712
C	0.30325	3.26372	-1.46733
C	-0.65841	4.13587	0.57713
H	0.29569	2.34674	0.36018
C	1.49668	4.16890	-1.24212
H	-0.44386	3.77262	-2.09114
H	0.60294	2.34424	-1.98412
C	0.56678	5.01371	0.72827
H	-1.44661	4.67631	0.03414
H	-1.05920	3.84887	1.55545
H	1.92562	4.49285	-2.19538
H	2.27951	3.63229	-0.67570
H	0.31227	5.95690	1.22139
H	1.32888	4.49889	1.34113
O	-1.51168	-2.78969	-1.40421
O	1.11925	5.33929	-0.53636
N	-0.35864	2.90680	-0.19183
N	-1.19649	0.00429	-0.86777



(neutral radical, -7800.296693, -7799.897882, -7799.984819, -7799.981801)

Ni	-0.73235	0.10750	-0.57588
Br	-2.24864	0.79006	-2.32532
Br	-2.45485	-0.73597	0.77280
C	0.31722	-0.00791	1.04877
C	1.34939	-0.91313	1.25755
C	0.09409	1.01820	1.97134
C	2.15965	-0.80293	2.38964
H	1.56984	-1.71887	0.56226
C	0.89951	1.13193	3.09649
H	-0.72810	1.71963	1.83561
C	1.93292	0.21638	3.30451
H	2.96568	-1.51484	2.54161
H	0.71849	1.92852	3.81562
C	2.78673	0.37579	4.52023
F	3.37187	1.59011	4.56548
F	2.06816	0.27087	5.65710

F	3.76935	-0.53197	4.59585
C	-0.48694	-2.92141	-0.76763
C	-0.37705	-1.87985	-2.91827
H	0.95589	-1.63192	-1.40530
C	0.18504	-4.14381	-1.35748
H	-1.57576	-2.99409	-0.86554
H	-0.26171	-2.82951	0.29917
C	0.29787	-3.12633	-3.45131
H	-1.46563	-1.96477	-3.00737
H	-0.07112	-0.99821	-3.48675
H	-0.17111	-5.05108	-0.86050
H	1.28012	-4.08209	-1.21393
H	0.02920	-3.28484	-4.49999
H	1.39678	-3.01783	-3.39084
C	1.23900	1.15908	-2.62451
C	0.29390	2.77513	-1.09270
H	1.50601	1.20928	-0.61004
C	2.32946	2.16734	-2.93382
H	0.39746	1.27163	-3.31719
H	1.64475	0.14543	-2.71219
C	1.41818	3.72119	-1.45887
H	-0.57086	2.92564	-1.74718
H	-0.02248	2.93909	-0.05606
H	2.66492	2.05318	-3.96854
H	3.19727	2.00266	-2.27023
H	1.07177	4.75705	-1.40325
H	2.26440	3.60181	-0.75865
O	-0.10785	-4.27822	-2.73579
O	1.85859	3.49247	-2.78469
N	0.71996	1.35883	-1.24986
N	-0.06482	-1.68743	-1.47881

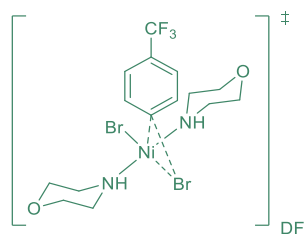


(neutral radical, 575.6 i cm<sup>-1</sup>, -3429.579196, -3429.346592, -3429.408194, -3429.405175)

C	1.04254	0.98497	-0.53004
C	2.07033	1.88644	-0.38704
C	1.83538	3.14949	0.18773
C	0.54386	3.51685	0.57565
C	-0.50361	2.62823	0.41907
H	1.21056	0.01010	-0.98060
H	3.06734	1.62573	-0.73671
H	0.35042	4.51061	0.96882



H	-1.51831	2.92425	0.67156
C	2.98444	4.09232	0.31211
F	2.65574	5.24417	0.91134
F	3.50453	4.41263	-0.89214
F	4.00095	3.55775	1.01970
C	-0.25111	1.30206	-0.02184
Br	-1.73477	0.41600	-0.88516
C	0.85328	0.39323	2.44742
C	-1.49338	0.61360	2.44361
C	0.74228	-0.55379	3.64432
H	0.97220	1.42631	2.82501
H	1.74103	0.12902	1.85995
C	-1.57777	-0.35777	3.61922
H	-1.40926	1.63347	2.85768
H	-2.40580	0.54480	1.83735
H	1.60853	-0.43492	4.30194
H	0.70916	-1.59599	3.28539
H	-2.42713	-0.10302	4.26031
H	-1.70806	-1.38767	3.24704
N	-0.34121	0.23006	1.65103
O	-0.41004	-0.26983	4.41044



(neutral radical,  $100.6 \text{ i cm}^{-1}$ , -7800.284282, -7799.886982, -7799.97292, -7799.969902)

Ni	-1.95423	1.59416	0.67489
Br	-3.57027	2.59359	-0.84232
Br	-3.32723	0.51542	2.35533
C	-1.37045	1.41137	2.58579
C	-0.29655	0.55553	2.86831
C	-1.46473	2.65757	3.23255
C	0.74414	1.00215	3.66897
H	-0.25094	-0.44437	2.44711
C	-0.42206	3.09368	4.03495
H	-2.34926	3.27574	3.08902
C	0.68960	2.27322	4.24448
H	1.59735	0.35446	3.85031
H	-0.47956	4.07148	4.50993
C	1.78937	2.77561	5.11734
F	2.28516	3.95181	4.67871
F	1.37028	3.00442	6.38035

F	2.82313	1.92635	5.20053
C	-1.67792	-1.46294	0.20019
C	-1.54944	-0.09015	-1.74881
H	-0.21577	-0.10542	-0.19556
C	-1.03955	-2.58877	-0.58642
H	-2.76982	-1.50188	0.09758
H	-1.44669	-1.56053	1.26515
C	-0.91868	-1.24829	-2.49118
H	-2.64185	-0.12387	-1.83869
H	-1.22329	0.86441	-2.16902
H	-1.41261	-3.55728	-0.23963
H	0.05684	-2.57300	-0.44772
H	-1.20503	-1.22854	-3.54708
H	0.18386	-1.18004	-2.43274
C	0.23657	2.77716	-1.16003
C	-0.73011	4.30335	0.41724
H	0.37255	2.64420	0.86778
C	1.38019	3.75437	-1.35036
H	-0.56357	2.97776	-1.88454
H	0.60466	1.75650	-1.31584
C	0.44512	5.22938	0.19582
H	-1.54352	4.53399	-0.28133
H	-1.11610	4.41622	1.43592
H	1.75711	3.70876	-2.37651
H	2.20983	3.49777	-0.66668
H	0.13975	6.27384	0.30983
H	1.23990	5.02029	0.93694
O	-1.34739	-2.49186	-1.96518
O	0.96500	5.08693	-1.11491
N	-0.35645	2.88723	0.18904
N	-1.23512	-0.13886	-0.29809

## 11. EXPERIMENTAL 1 References.

- (1) Corcoran, E. B.; Pirnot, M. T.; Lin, S.; Dreher, S. D.; DiRocco, D. A.; Davies, I. W.; Buchwald, S. L.; MacMillan, D. W. C. *Science* 2016, 353, 279.
- (2) Du, Y.; Pearson, R. M.; Lim, C.-H.; Sartor, S. M.; Ryan, M. D.; Yang, H.; Damrauer, N. H.; Miyake, G. M. *Chem. Eur. J.* 2017, 23, 10962.
- (3) Li, C.; Kawamata, Y.; Nakamura, H.; Vantourout, J. C.; Liu, Z.; Hou, Q.; Bao, D.; Starr, J. T.; Chen, J.; Yan, M.; Baran, P. S. *Angew. Chem. Int. Ed.* 2017, 56, 13088.

- (4) Reilly, S. W.; Mach, R. H. *Org. Lett.* 2016, 18, 5272.
- (5) Lui, E. K. J.; Schafer, L. L. *Adv. Synth. Cat.* 2016, 358, 713.
- (6) Mazu, T. K.; Etukala, J. R.; Jacob, M. R.; Khan, S. I.; Walker, L. A.; Ablordeppey, S. Y. *Eur. J. Med. Chem.* 2011, 46, 2378.
- (7) Li, J.; Cui, M.; Yu, A.; Wu, Y. *J. Organomet. Chem.* 2007, 692, 3732.
- (8) Yong, F.-F.; Teo, Y.-C.; Tan, K.-N. *Tetrahedron Lett.* 2013, 54, 5332.
- (9) Chen, M.; Buchwald, S. L. *Angew. Chem. Int. Ed.* 2013, 52, 11628.
- (10) Demory, E.; Devaraj, K.; Orthaber, A.; Gates, P. J.; Pilarski, L. T. *Angew. Chem.* 2015, 127, 11931.
- (11) Li, J.; Wang, Z.-X. *Org. Lett.* 2017, 19, 3723.
- (12) Guo, D.; Huang, H.; Xu, J.; Jiang, H.; Liu, H. *Org. Lett.* 2008, 10, 4513.
- (13) Richardson, J.; Ruble, J. C.; Love, E. A.; Berritt, S. *J. Org. Chem.* 2017, 82, 3741.
- (14) Lü, B.; Li, P.; Fu, C.; Xue, L.; Lin, Z.; Ma, S. *Adv. Synth. Cat.* 2011, 353, 100.
- (15) Reddy, C. V.; Kingston, J. V.; Verkade, J. G. *J. Org. Chem.* 2008, 73, 3047.
- (16) Mochizuki, A.; Nagata, T.; Kanno, H.; Suzuki, M.; Ohta, T. *Bioorganic Med. Chem.* 2011, 19, 1623.
- (17) Doherty, S.; Knight, J. G.; McGrady, J. P.; Ferguson, A. M.; Ward, N. A. B.; Harrington, R. W.; Clegg, W. *Adv. Synth. Cat.* 2010, 352, 201.
- (18) Charles, M. D.; Schultz, P.; Buchwald, S. L. *Org. Lett.* 2005, 7, 3965.
- (19) Yang, F.; Wu, C.; Li, Z.; Tian, G.; Wu, J.; Zhu, F.; Zhang, J.; He, Y.; Shen, J. *Org. Process Res. Dev.* 2016, 20, 1576.

## REFERENCES

- (1) Bariwal, J.; Van der Eycken, E. *Chem. Soc. Rev.* 2013, 42, 9283.
- (2) Ruiz-Castillo, P.; Buchwald, S. L. *Chem. Rev.* 2016, 116, 12564.
- (3) Brown, D. G.; Boström, J. *J. Med. Chem.* 2016, 59, 4443.
- (4) Ullmann, F. *Ber. Dtsch. Chem. Ges.* 1903, 36, 2382.
- (5) Monnier, F.; Taillefer, M. *Angew. Chem., Int. Ed.* 2009, 48, 6954.
- (6) Beletskaya, I. P.; Cheprakov, A. V. *Coord. Chem. Rev.* 2004, 248, 2337.
- (7) Ley, S. V.; Thomas, A. W. *Angew. Chem., Int. Ed.* 2003, 42, 5400.
- (8) Hartwig, J. F. *Angew. Chem., Int. Ed.* 1998, 37, 2046.
- (9) Wolfe, J. P.; Buchwald, S. L. *J. Org. Chem.* 1996, 61, 1133.
- (10) Wolfe, J. P.; Buchwald, S. L. *J. Am. Chem. Soc.* 1997, 119, 6054.
- (11) Ramgren, S. D.; Silberstein, A. L.; Yang, Y.; Garg, N. K. *Angew. Chem., Int. Ed.* 2011, 50, 2171.
- (12) Lavoie, C. M.; MacQueen, P. M.; Rotta-Loria, N. L.; Sawatzky, R. S.; Borzenko, A.; Chisholm, A. J.; Hargreaves, B. K. V.; McDonald, R.; Ferguson, M. J.; Stradiotto, M. *Nat. Commun.* 2016, 7, 11073.
- (13) Green, R. A.; Hartwig, J. F. *Angew. Chem., Int. Ed.* 2015, 54, 3768.
- (14) Marín, M.; Rama, R. J.; Nicasio, M. C. *Chem. Rec.* 2016, 16, 1819.
- (15) Brenner, E.; Fort, Y. *Tetrahedron Lett.* 1998, 39, 5359.
- (16) Chen; Yang, L.-M. *Org. Lett.* 2005, 7, 2209.
- (17) Li, C.; Kawamata, Y.; Nakamura, H.; Vantourout, J. C.; Liu, Z.; Hou, Q.; Bao, D.; Starr, J. T.; Chen, J.; Yan, M.; Baran, P. S. *Angew. Chem., Int. Ed.* 2017, 56, 13088.
- (18) Creutz, S. E.; Lotito, K. J.; Fu, G. C.; Peters, J. C. *Science* 2012, 338, 647.

- (19) Ziegler, D. T.; Choi, J.; Muñoz-Molina, J. M.; Bissember, A. C.; Peters, J. C.; Fu, G. C. *J. Am. Chem. Soc.* 2013, *135*, 13107.
- (20) Oderinde, M. S.; Jones, N. H.; Juneau, A.; Frenette, M.; Aquila, B.; Tentarelli, S.; Robbins, D. W.; Johannes, J. W. *Angew. Chem., Int. Ed.* 2016, *55*, 13219.
- (21) Corcoran, E. B.; Pirnot, M. T.; Lin, S.; Dreher, S. D.; DiRocco, D. A.; Davies, I. W.; Buchwald, S. L.; MacMillan, D. W. C. *Science* 2016, *353*, 279.
- (22) Theriot, J. C.; Lim, C.-H.; Yang, H.; Ryan, M. D.; Musgrave, C. B.; Miyake, G. M. *Science* 2016, *352*, 1082.
- (23) Pearson, R. M.; Lim, C.-H.; McCarthy, B. G.; Musgrave, C. B.; Miyake, G. M. *J. Am. Chem. Soc.* 2016, *138*, 11399.
- (24) Du, Y.; Pearson, R. M.; Lim, C.-H.; Sartor, S. M.; Ryan, M. D.; Yang, H.; Damrauer, N. H.; Miyake, G. M. *Chem. Eur. J.* 2017, *23*, 10962.
- (25) Theriot, J. C.; McCarthy, B. G.; Lim, C.-H.; Miyake, G. M. *Macromol. Rapid Commun.* 2017, *38*, 1700040.
- (26) Lim, C.-H.; Ryan, M. D.; McCarthy, B. G.; Theriot, J. C.; Sartor, S. M.; Damrauer, N. H.; Musgrave, C. B.; Miyake, G. M. *J. Am. Chem. Soc.* 2017, *139*, 348.
- (27) Arias-Rotondo, D. M.; McCusker, J. K. *Chem. Soc. Rev.* 2016, *45*, 5803.
- (28) Romero, N. A.; Nicewicz, D. A. *Chem. Rev.* 2016, *116*, 10075.
- (29) Twilton, J.; Le, C.; Zhang, P.; Shaw, M. H.; Evans, R. W.; MacMillan, D. W. *Nat. Rev. Chem.* 2017, *1*, 0052.
- (30) Oderinde, M. S.; Frenette, M.; Robbins, D. W.; Aquila, B.; Johannes, J. W. *J. Am. Chem. Soc.* 2016, *138*, 1760.

- (31) Terrett, J. A.; Cuthbertson, J. D.; Shurtleff, V. W.; MacMillan, D. W. C. *Nature* 2015, 524, 330.
- (32) Tellis, J. C.; Primer, D. N.; Molander, G. A. *Science* 2014, 345, 433.
- (33) Qi, Z.-H.; Ma, J. *ACS Catal.* 2018, 8, 1456.
- (34) Ishida, N.; Masuda, Y.; Ishikawa, N.; Murakami, M. *Asian J. Org. Chem.* 2017, 6, 669.
- (35) Shields, B. J.; Kudisch, B.; Scholes, G. D.; Doyle, A. G. *J. Am. Chem. Soc.* 2018, 140, 3035.
- (36) Morris, S. A.; Wang, J.; Zheng, N. *Acc. Chem. Res.* 2016, 49, 1957.
- (37) Xiong, T.; Zhang, Q. *Chem. Soc. Rev.* 2016, 45, 3069.
- (38) Tasker, S. Z.; Standley, E. A.; Jamison, T. F. *Nature* 2014, 509, 299.
- (39) Reilly, S. W.; Mach, R. H. *Org. Lett.* 2016, 18, 5272.
- (40) Vitaku, E.; Smith, D. T.; Njardarson, J. T. *J. Med. Chem.* 2014, 57, 10257.
- (41) Dean, B. V.; Stellpflug, S. J.; Burnett, A. M.; Engebretsen, K. M. *J. Med. Toxicol.* 2013, 9, 172.
- (42) Mazu, T. K.; Etukala, J. R.; Jacob, M. R.; Khan, S. I.; Walker, L. A.; Ablordeppey, S. Y. *Eur. J. Med. Chem.* 2011, 46, 2378.
- (43) Liu, B.; Lim, C.-H.; Miyake, G. M. *J. Am. Chem. Soc.* 2017, 139, 13616.
- (44) Yang, F.; Wu, C.; Li, Z.; Tian, G.; Wu, J.; Zhu, F.; Zhang, J.; He, Y.; Shen, J. *Org. Process Res. Dev.* 2016, 20, 1576.
- (45) Lim, C.-H.; Holder, A. M.; Hynes, J. T.; Musgrave, C. B. *J. Am. Chem. Soc.* 2014, 136, 16081.
- (46) Palazón, J.; Gálvez, J.; García, G.; Lopez, G. *Polyhedron* 1983, 2, 1353.
- (47) Huang, D.; Makhlynets, O. V.; Tan, L. L.; Lee, S. C.; Rybak-Akimova, E. V.; Holm, R. H. *Proc. Natl. Acad. Sci. U. S. A.* 2011, 108, 1222.
- (48) Liang, Y.; Liu, S.; Xia, Y.; Li, Y.; Yu, Z.-X. *Chem. Eur. J.* 2008, 14, 4361.

(49) Wiberg, K. B. *Chem. Rev.* 1955, 55, 713.

(50) Westheimer, F. H. *Chem. Rev.* 1961, 61, 265.

(51) Gómez-Gallego, M.; Sierra, M. A. *Chem. Rev.* 2011, 111, 4857.

## CHAPTER 3 | ENERGY TRANSFER TO NI-AMINE COMPLEXES IN DUAL CATALYTIC, LIGHT-DRIVEN C–N CROSS COUPLING REACTIONS

### OVERVIEW

Dual catalytic light-driven cross-coupling methodologies utilizing a Ni(II) salt with a photocatalyst (PC) have emerged as promising methodologies to forge aryl C–N bonds under mild conditions. The recent discovery that the PC can be omitted and the Ni(II) complex directly photoexcited suggests that the PC may perform energy transfer (EnT) to the Ni(II) complex, a mechanistic possibility that has recently been proposed in other systems across dual Ni photocatalysis. Here, we report the first studies in this field capable of distinguishing EnT from electron transfer (ET), and the results are consistent with Förster-type EnT from the excited state [Ru(bpy)<sub>3</sub>]Cl<sub>2</sub> PC to Ni-amine complexes. The structure and speciation of Ni-amine complexes that are the proposed EnT acceptors were elucidated by crystallography and spectroscopic binding studies. With the acceptors known, quantitative Förster theory was utilized to predict the ratio of quenching rate constants upon changing the PC, enabling selection of an organic phenoxazine PC that proved to be more effective in catalyzing C–N cross-coupling reactions with a diverse selection of amines and aryl halides.

### INTRODUCTION

Dual catalytic, light-driven C–N,<sup>1,2</sup> C–O,<sup>3</sup> C–C,<sup>4</sup> C–P,<sup>5</sup> and C–S<sup>6</sup> cross-coupling methodologies utilizing a Ni(II) catalyst along with a photocatalyst (PC) have recently emerged as promising systems for synthetic chemistry with advantages over traditional Pd catalysis in terms of sustainability, cost, and mildness of reaction conditions.<sup>7</sup> As such, mechanistic understanding



of these reactions is essential in order to rationally design effective catalysts and unlock new reactivity.

In 2016, two dual catalytic, C–N cross-coupling systems were independently developed. In both cases, a wide range of amines and aryl halides were coupled under blue light irradiation employing the same Ni(II) precatalyst (i.e., NiBr<sub>2</sub>·glyme) and Ir(III) PC (Figure 3.1A).<sup>1,2</sup> The

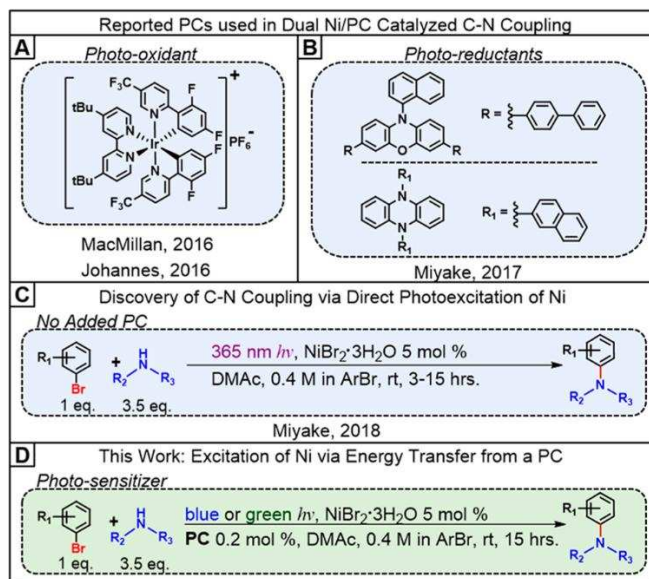


Figure 3.1. Reported C–N cross-coupling systems utilizing (A) a photo-oxidant, (B) photoreductants, or (C) no added PC. This work (D) on C–N bond formation promoted by energy transfer from a PC to the Ni-amine complex. In (A), the Ir PC used was [Ir(dF(CF<sub>3</sub>)ppy)<sub>2</sub>(dtbbpy)]PF<sub>6</sub>, where dF(CF<sub>3</sub>)ppy = 2-(2,4-difluorophenyl)-5-(trifluoromethyl)pyridine and dtbbpy = 4,4'-di-tert-butyl-2,2'-bipyridine. The organic PCs used in (B) were 3,7-di([1,1'-biphenyl]-4-yl)-10-(naphthalen-1-yl)-10H-phenoxazine and 5,10-di(naphthalen-2-yl)-5,10-dihydrophenazine. PC = photocatalyst; DMAc = N,N-dimethylacetamide. ArBr = aryl bromide.

Ir(III) PC used was [Ir(dF(CF<sub>3</sub>)ppy)<sub>2</sub>(dtbbpy)]PF<sub>6</sub>, which is a strong photo-oxidant. In contrast, our group recently found that organic PCs (e.g., dihydrophenazines<sup>8</sup> and phenoxazines<sup>9</sup>) that are strong photoreductants also functioned efficiently for dual catalytic C–N cross-coupling under similar conditions (Figure 3.1B).<sup>10</sup> These results suggest two potential scenarios. In one case, the Ni(II) precatalyst is sufficiently robust that C–N cross-coupling can occur through both reductive and oxidative electron transfer (ET) cycles utilizing a photo-oxidant and a photoreductant,

respectively. Alternatively, the Ni(II) precatalyst might be activated via energy transfer (EnT) from the PC; notably, the possibility of an EnT cycle has seldom been considered to date in C–N cross-coupling, with only one reported example describing the coupling of sulfonamides with aryl halides.<sup>11</sup>

Furthermore, we recently discovered that a PC can be omitted from the dual catalytic C–N cross-coupling system. Specifically, upon amine addition to a solution containing Ni(II) and aryl halide, we observed in situ formation of Ni-amine complexes that can be directly photoexcited with 365 nm LEDs for the formation of the desired aryl C–N product (Figure 3.1C).<sup>12</sup> The existence of a direct Ni(II) irradiation route supports the possibility of an EnT quenching mechanism as elucidated herein (Figure 3.1D). In the absence of an added PC, the Ni excited state is accessed directly through photoexcitation. Similarly, in a dual catalytic system, an analogous (but possibly distinct) Ni excited state can be accessed through EnT from a PC.

This discovery is complemented by the finding that a PC can be omitted for dual catalytic C–O<sup>13</sup> or C–C<sup>14</sup> systems, as the Ni complex can similarly be directly photoexcited, suggesting the possibility of an EnT pathway. More broadly, methods across photocatalysis that involve the direct excitation of transition metal complexes<sup>15–19</sup> suggest systems that may be conducive to EnT upon addition of a PC. Importantly, EnT pathways have been proposed to be operative with Ni(II) or Cu(I) complexes serving as the acceptor in several systems across light-driven dual catalysis.<sup>20–23</sup> However, to date, no study has utilized time-resolved techniques capable of distinguishing between electron and energy transfer to support that the excited state PC does indeed react via energy transfer in these systems.

Notably, obtaining spectroscopic evidence of an EnT pathway can unlock pivotal practical advances for a methodology as illustrated by the C–S cross-coupling of alkenes/alkynes with

disulfides in which replacement of the precious metal Ir(III) PC with an organic PC of higher triplet energy both accelerated the rate of product formation and alleviated sustainability concerns.<sup>24</sup> Furthermore, dual catalysis enables mild visible light irradiation, while 365 nm light was required previously to directly excite the Ni complex. Thus, addition of a PC can enable use of UV-sensitive substrates.

Herein, we provide spectroscopic evidence in support of EnT from an excited state PC to Ni-amine complexes under conditions relevant for dual catalytic C–N cross-coupling driven by visible light (Figure 3.1D). In particular, using nanosecond transient absorption (TA) spectroscopy, we observed the excited state of [Ru(bpy)<sub>3</sub>]Cl<sub>2</sub> (bpy = 2,2'-bipyridine) reacting with Ni-amine complexes formed in situ in C–N cross-coupling reaction mixtures. The spectral data are consistent with an EnT pathway proceeding primarily through a Förster-type mechanism, a result that is notably distinct from the Dexter-type pathway typically invoked in the literature in catalytic cycles involving EnT that results in substrate sensitization.<sup>25</sup> Next, speciation studies elucidated the Ni-amine complexes that serve as EnT acceptors (or as light absorbers in the direct excitation method).<sup>12</sup> Finally, these mechanistic insights were utilized in conjunction with quantitative Förster theory to select an organic phenoxazine PC (the same shown in Figure 3.1B) that proved to be more effective than [Ru(bpy)<sub>3</sub>]Cl<sub>2</sub> in the C–N coupling of 13 substrate pairs.

## RESULTS AND DISCUSSION

[Ru(bpy)<sub>3</sub>]Cl<sub>2</sub> was chosen as the PC for spectroscopic studies due to the extensive body of photophysical literature describing its spectral changes upon EnT or ET<sup>26,27</sup> and the precedence for its use as a PC in related dual catalytic C–N cross-coupling systems.<sup>1,28</sup> Here, we initially confirmed that [Ru(bpy)<sub>3</sub>]Cl<sub>2</sub> (PC 1) is an effective PC for C–N cross coupling involving 4-

bromobenzotrifluoride and morpholine, achieving 88% conversion as measured by  $^{19}\text{F}$  NMR after 22 h of irradiation with a green (i.e.,  $\lambda_{\text{max}} = 523 \text{ nm}$ ) LED (Figure 3.2A). Importantly, no product

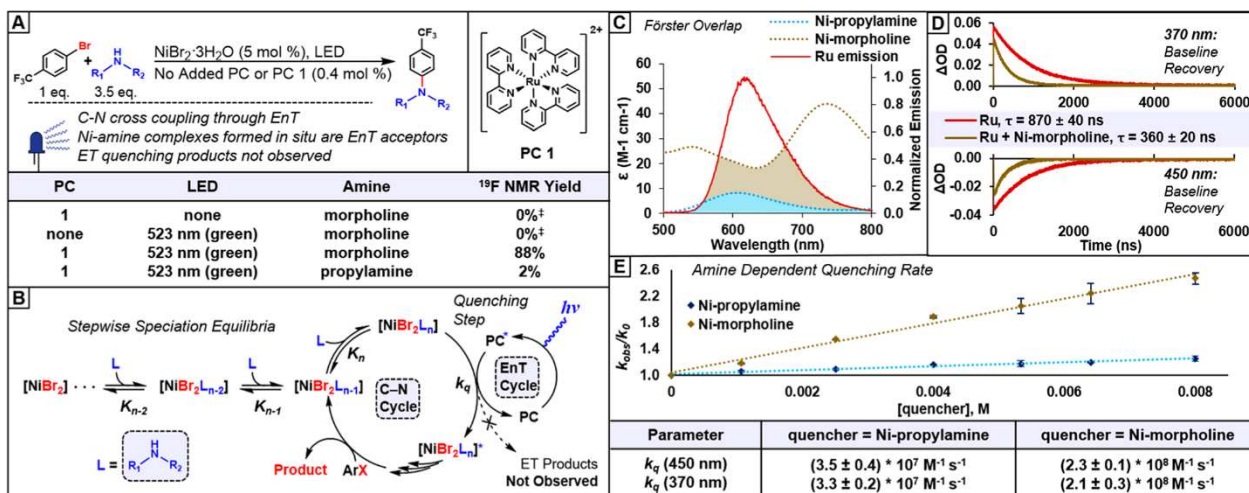


Figure 3.2. (A) Dual catalytic C–N cross-coupling control reactions. Reaction details: 0.4 mmol in aryl bromide in DMAc, 22 h reaction time. (B) Simplified catalytic cycle highlighting the focus of this work: the PC quenching step probed by transient absorption (TA) experiments and the speciation of the Ni catalyst. For the full proposed cycle, see EXPERIMENTAL 2, Figure S3.71. (C) Förster EnT efficiency approximated by overlap between PC 1 emission and Ni-amine complex absorption. (D) TA single wavelength kinetic traces acquired with  $\lambda_{\text{pump}} = 532 \text{ nm}$  and  $\lambda_{\text{probe}} = 450$  or 370 nm for PC 1 and a mixture (80:1 molar ratio of Ni:PC) containing PC 1 (0.1 mM) with Ni-morpholine complexes. (E) Stern–Volmer plot and extracted quenching rate constants. Quenchers are mixtures of Ni-amine complexes formed in situ. The species formed are determined later in this work.  $\ddagger$ We note that debromination was not observed (See EXPERIMENTAL 2, Figure S3.72); only unreacted aryl bromide was detected by  $^{19}\text{F}$  NMR. EnT = energy transfer. ET = electron transfer.  $k_q$  = quenching rate constant.  $k_0$  = decay rate constant of PC 1.  $k_{\text{obs}}$  = observed decay rate constant in the presence of quencher.  $K_n$  = equilibrium binding constant. See EXPERIMENTAL 2, Section 2, for TA experimental details and spectra.

was observed either in the absence of light or PC under these conditions, indicating that the direct excitation of the Ni complex was not a significant pathway, and thus the observed reactivity can be completely ascribed to the role of PC 1. The bimolecular quenching step (Figure 3.2B) between the excited state of PC 1 and the Ni-amine complex was further elucidated via nanosecond TA experiments. We note that the speciation of the Ni-amine complexes formed in situ is detailed later in this work. Laser irradiation at  $\lambda_{\text{pump}} = 532 \text{ nm}$  in N,N-dimethylacetamide (DMAc) solvent

containing PC 1 produced the long-lived (i.e.,  $870 \pm 40$  ns in DMAc, see EXPERIMENTAL 2, Figure S3.4) metal-to-ligand charge-transfer (MLCT) triplet excited state characterized by an excited state absorption (ESA) feature at  $\lambda = 370$  nm and a prominent ground state bleach (GSB) at  $\lambda = 450$  nm (see EXPERIMENTAL 2, Figure S3.3). The MLCT excited state lifetime measured here is consistent with previous reported values ranging from 800 to 1000 ns in polar, aprotic solvents.<sup>29</sup>

We note that the MLCT state can be approximated as a formal reduction of one bpy ligand to the radical anion along with formal oxidation of the Ru center to Ru(III). As such, the ESA at  $\lambda = 370$  nm has been previously assigned to a transition involving the radical anion of one bpy ligand on the basis of comparison to spectroelectrochemical measurement of the radical anion of free bpy and is thus diagnostic of MLCT state formation.<sup>26</sup> In addition, the GSB at  $\lambda = 450$  nm was attributed to the presence of Ru(III) in the MLCT state, which lacks a transition in this region. As such, quenching through ET is characterized by persistence of the ESA at  $\lambda = 370$  nm in the case of reductive quenching since  $[\text{Ru}(\text{bpy})_3]\text{Cl}_2$  is formally reduced, while oxidative quenching leads to persistence of the GSB at  $\lambda = 450$  nm.<sup>27</sup> However, in the case of EnT, both signals fully return to baseline since the ground state is recovered, and a decrease in the excited state lifetime is observed.<sup>27</sup>

In a C–N cross-coupling reaction mixture consisting of the same molar ratio of components detailed in Figure 3.2A, we monitored excited state quenching of PC 1 using  $\lambda_{\text{pump}} = 532$  nm, consistent with the green LED used in cross-coupling reactions. We note that under these conditions Ni-morpholine complexes are formed in situ (*vide infra*) and are active in quenching PC 1's excited state. Importantly, consistent with an EnT pathway, signals corresponding to PC 1's excited state return fully to the baseline at all wavelengths from  $\lambda = 300$ –800 nm (Figure

S3.11), indicative of recovery of the ground state of PC 1. In particular, kinetic traces of PC 1 at both  $\lambda_{\text{probe}} = 370 \text{ nm}$  and  $\lambda_{\text{probe}} = 450 \text{ nm}$  returned fully to baseline (Figure 3.2D), and thus neither oxidized nor reduced PC 1 indicative of an ET mechanism was observed.

We further note that cyclic voltammetry experiments suggest that an ET quenching mechanism (either oxidative or reductive) is unlikely to occur (EXPERIMENTAL 2, Section 4). Specifically,  $E^{0*}([\text{Ru}(\text{bpy})_3]^{*2+}/[\text{Ru}(\text{bpy})_3]^{3+}) = -1.19 \text{ V vs Fc/Fc}^+ (-0.74 \text{ V vs SCE})$  as measured in this work in DMAc, while the first reduction of a Ni-morpholine complex occurs at  $E_p = -1.71 \text{ V vs Fc/Fc}^+ (-1.26 \text{ V vs SCE})$ ; thus, an oxidative quenching pathway is thermodynamically unfavorable. Similarly, reductive quenching is unlikely as  $E^{0*}([\text{Ru}(\text{bpy})_3]^{*2+}/[\text{Ru}(\text{bpy})_3]^+) = 0.27 \text{ V vs Fc/Fc}^+ (0.72 \text{ V vs SCE})$ , and the first oxidation of a Ni-morpholine complex occurs at  $E_p/2 \approx 0.48 \text{ V vs Fc/Fc}^+ (0.93 \text{ V vs SCE})$ .

Furthermore, the presence of Ni-morpholine complexes led to significant reduction in the excited state lifetime of PC 1 from  $870 \pm 40 \text{ ns}$  to  $360 \pm 20 \text{ ns}$ , while free morpholine did not lead to quenching (Figures S3.5 and S3.6). Further control experiments showed that electron transfer products were not observed even under high laser power (Figures S3.9 and S3.10). We note that subtraction of spectra did not yield any signals that could be assigned to an excited state Ni complex, likely due to the excited state lifetime being too short to measure (Figure S3.12); for example, a square planar Ni(II) aryl halide complex was observed to have a  $4.2 \text{ ns}$  lifetime,<sup>13</sup> too short to be detectable with our setup. Overall, these results suggest that C–N cross-coupling reactivity is derived from excited Ni-amine complexes, which can be accessed through either EnT from a PC as in this work or through direct photoexcitation as in our previous work.<sup>12</sup> As such, we propose that mechanistic steps following the EnT step will mirror those we proposed previously (Figure S3.71, for the catalytic cycle).

Next, we observed that when using different types of amines and the Ni:amine ratio is held at 1:70, the same molar ratio used in C–N reactions, PC 1 was quenched to different degrees. To explore this relationship, a Stern–Volmer quenching study was performed with ratios of Ni:PC 1 increasing from 10:1 to 80:1. Notably, use of morpholine gives  $k_q = (2.3 \pm 0.1) \times 10^8 \text{ M}^{-1} \text{ s}^{-1}$  at  $\lambda_{\text{probe}} = 450 \text{ nm}$ , while propylamine quenched with a significantly reduced rate constant of  $k_q = (3.5 \pm 0.4) \times 10^7 \text{ M}^{-1} \text{ s}^{-1}$  (Figure 3.2E), consistent with the lower cross-coupling performance of primary amines relative to secondary amines observed herein and previously under direct excitation with 365 nm irradiation.<sup>12</sup> Since the same PC was used throughout and none of the other reaction components were suitable ET or EnT quenchers (Figures S3.5–S3.8), this variation in  $k_q$  must arise from changes in electronic structure of the Ni-amine complex, and thus the speciation of the complexes formed must be determined.

Unlike typical organic substrates for which the contribution of Förster-type EnT can be deduced to be minimal *a priori* on account of lacking significant spectral overlap with the excited PC,<sup>27</sup> Ni-amine complexes absorb significantly in the wavelength range of PC 1 phosphorescence (Figure 3.2C). Further, the overlap area for absorption of Ni-morpholine and Ni-propylamine mixtures appears correlated with the rate of quenching, supporting the hypothesis of Förster-type EnT. However, the components of the quenching mixture must be elucidated in order to determine the identity and molar absorptivity of the EnT acceptor(s) to utilize Förster theory quantitatively in examining this hypothesis. Turning to classic reports<sup>30–35</sup> describing monodentate primary and secondary amine ligands binding to Ni(II), the available information is insufficient due to the lack of both crystallographic characterization and speciation studies in DMAc solution.

To address this challenge, we first grew single crystals from concentrated Ni-amine mixtures, and analysis by single crystal X-ray diffraction (XRD) revealed for the first time that

propylamine, morpholine, and quinuclidine form 6-, 5-, and 4-coordinate Ni(II) bromide complexes, respectively (Figure 3.3A). Importantly, these complexes are likely the EnT acceptors,

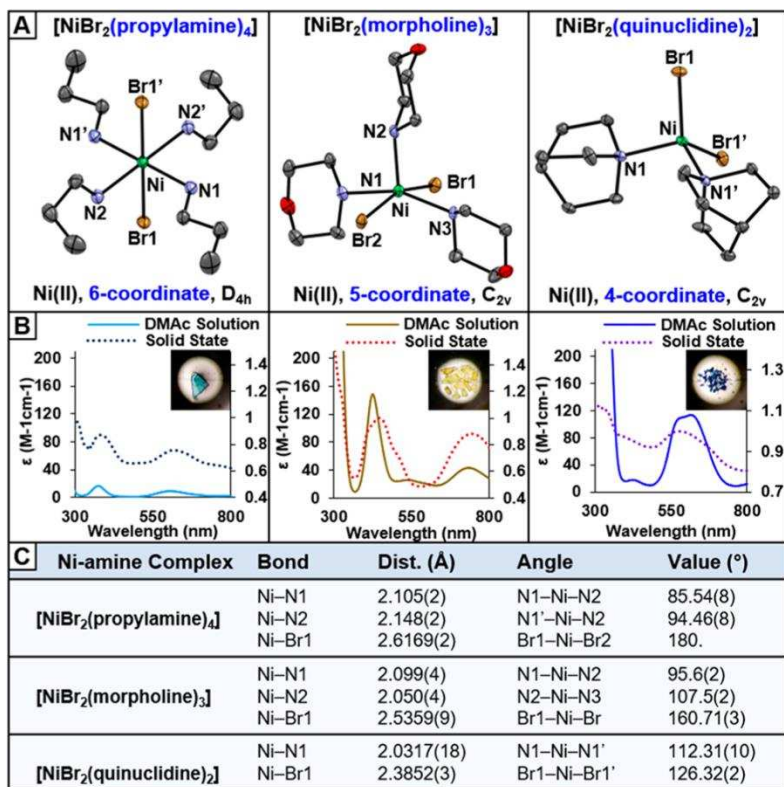


Figure 3.3. (A) Crystal structures of  $[\text{NiBr}_2(\text{propylamine})_4]$ ,  $[\text{NiBr}_2(\text{morpholine})_3]$ , and  $[\text{NiBr}_2(\text{quinuclidine})_2]$  shown at 50% thermal ellipsoids with hydrogens omitted for clarity. (B) Left axis: molar absorptivity of Ni-amine complexes in DMAC solution. Right axis: solid-state UV–visible absorption spectra of single crystals of complexes shown in (A). Inset: photographs of crystals of each complex at  $40\times$  magnification. (C) Selected bond distances and angles. See EXPERIMENTAL 2, Section 5, for further experimental details.

but it must be confirmed that the structures obtained in solid state can serve as reasonable approximations of the geometry of complexes formed in situ in DMAC solution. To confirm that this assumption is reasonable, single crystals were examined through solid-state UV–visible absorption spectroscopy (Figure 3.3B; see EXPERIMENTAL 2, Section 8, for details). Qualitatively, similar absorption features are observed in solution to those found in the single crystals for all complexes, suggesting that structures obtained from XRD are not changed significantly upon DMAC solvation. Further, a control UV–vis experiment supports that the same



complexes also exist in the full C–N coupling reaction mixtures (i.e., with aryl halide and PC added; Figure S3.58). As such, some bands in the UV–vis spectra of the quenching mixtures used in TA experiments can now be assigned to specific complexes, namely,  $[\text{NiBr}_2(\text{morpholine})_3]$  (i.e.,  $\lambda_{\text{max},1} = 427 \text{ nm}$ ,  $\lambda_{\text{max},2} = \sim 740 \text{ nm}$ ) and  $[\text{NiBr}_2(\text{propylamine})_4]$  ( $\lambda_{\text{max},1} = 379 \text{ nm}$ ,  $\lambda_{\text{max},2} = \sim 620 \text{ nm}$ ).

Notably, the structure obtained for  $[\text{NiBr}_2(\text{morpholine})_3]$  closely matches the density functional theory (DFT)-optimized ground state geometry in DMAc solution described in our previous work,<sup>12</sup> supporting this assignment as well as the accuracy of our reported DFT calculations. Further, the formation of  $[\text{NiBr}_2(\text{propylamine})_4]$  suggests the general trend that primary amines form six-coordinate  $\text{NiBr}_2$  complexes as supported by the isolation of  $[\text{NiBr}_2(\text{aniline})_4]$  and  $[\text{NiBr}_2(\text{cyclohexylamine})_4]$  (Figures S3.48 and S3.49). Ni-amine complexes of the type characterized here are proposed to form across Ni catalysis in systems lacking exogenous ligand and employing amines in conjunction with  $\text{NiBr}_2$ , regardless of the  $\text{NiBr}_2$  source used (e.g.,  $\text{NiBr}_2 \cdot \text{glyme}$ ,  $\text{NiBr}_2 \cdot 3\text{H}_2\text{O}$ , or anhydrous  $\text{NiBr}_2$ ; Figure S3.57). The same complexes also form in the presence of all PCs used in C–N coupling reactions (Ir(III), Ru(II), and phenoxazine; Figures S3.54–S3.56), suggesting they may more broadly serve as mechanistically relevant species in many dual catalytic Ni(II) cross-coupling systems.

Reported magnetic moment measurements of identical<sup>34</sup> or related<sup>36–38</sup> Ni(II) complexes, as well as our previous DFT calculations, are consistent with  $[\text{NiBr}_2(\text{propylamine})_4]$  and  $[\text{NiBr}_2(\text{morpholine})_3]$  possessing triplet ground states in DMAc solution, suggesting that the d–d absorptions in the region of Förster overlap are of triplet-to-triplet nature. As such, Förster EnT is allowed based on the conservation of spin angular momenta<sup>39</sup> from the triplet excited state of PC 1 as the donor to form a triplet excited state Ni-amine complex. In order to employ Förster theory

in modeling this excited state reactivity, the molar absorptivity of each acceptor complex overlapping with PC 1 emission must be known. However, UV–vis absorption peaks are observed in the Ni-amine solutions which remain to be assigned (e.g., the feature at  $\sim 550$  nm in the Ni-morpholine DMAc solution, Figure 3.2C) that might belong to viable EnT acceptors. We hypothesized that these features must originate from other Ni-amine complexes with fewer amine ligands, since a stepwise series of amine additions is required in the formation of the observed complexes from the  $\text{NiBr}_2 \cdot 3\text{H}_2\text{O}$  precatalyst. These binding equilibria were directly observed through UV–vis isothermal titrations in which mixtures were analyzed with increasing ratios of the amine ligand:Ni. UV–vis of these mixtures shows the evolution and demise of species with increasing numbers of amine ligands in the Ni-morpholine mixture (Figure 3.4A). Initially, we note that the DMAc solvent forms the salt  $[\text{Ni}(\text{DMAc})_6][\text{NiBr}_4]$  prior to amine addition (Figure S3.51) and that multiple pathways exist for the first two amine additions (Figures S3.69 and S3.70). However, all pathways converge to form the tetrahedral  $[\text{NiBr}_2(\text{morpholine})_2]$  as the product of  $K_2$ , which can be assigned to the signal with  $\lambda_{\text{max},1} = \sim 550$  nm and  $\lambda_{\text{max},2} = \sim 850$  nm. To precisely determine the ratio of these species in the Ni-morpholine quenching mixture, the titration data were fitted to four variants (flavors)<sup>40</sup> of a 1:3 (metal:ligand or host:guest) binding model. This analysis was performed using a Matlab code based on the analytical solution to the system of equations for the 1:3 equilibria, similar to that described in a NMR study on a 3:1 complexation of a bis-antimony receptor with halide anions.<sup>41</sup> In our work we performed a global analysis<sup>42</sup> using the UV–vis binding isotherms from  $\lambda = 395$  to 1200 nm (see EXPERIMENTAL 2, Section 7, for details). Comparing how the various flavors of the 1:3 binding model fitted the data<sup>40,43</sup> clearly showed that the “full” 1:3 model, which assumes (i) cooperativity and (ii) that the 1:1, 1:2,

and 1:3 stepwise complexes have distinct spectra, gave a significantly better fit to the data than the other binding models (flavors) considered. The full model allowed us to extract not only the

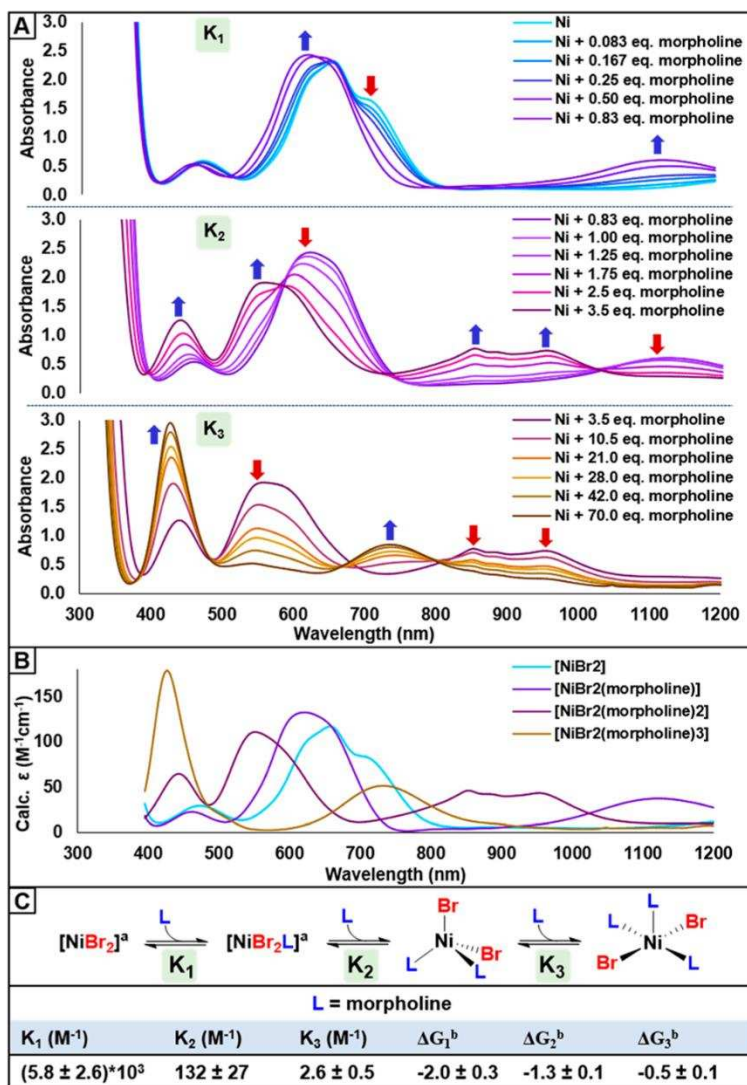


Figure 3.4. (A) Selected UV-vis traces from one replicate titration experiment showing equilibria between Ni-morpholine complexes. Arrows indicate features that rise or fall in the forward direction of each equilibrium. A 70 equiv. amount of amine ligand added (relative to Ni) corresponds to the exact conditions used in C–N cross coupling reactions. (B) Calculated average molar absorptivity ( $n = 3$  replicates) of Ni-morpholine complexes. (C) Scheme defining stepwise series of equilibria upon addition of amine ligands. Equilibrium constants and molar absorptivities were extracted from titration data via a global analysis fitting procedure (Figures S3.62–S3.65 for details). <sup>a</sup>We note that the  $\text{NiBr}_2$  precatalyst forms a tetrabromonickelate salt in DMAc solution from which multiple amine addition pathways are possible for  $K_1$  and  $K_2$ . <sup>b</sup>Values in  $\text{kcal mol}^{-1}$ . See EXPERIMENTAL 2 for details.

stepwise equilibrium binding constants but also the molar absorptivity (Figure 3.4B) of each species, giving  $K_1 = (6 \pm 3) \times 10^3 \text{ M}^{-1}$ ,  $K_2 = 130 \pm 30 \text{ M}^{-1}$ , and  $K_3 = 2.6 \pm 0.5 \text{ M}^{-1}$  with the corresponding free energies (after correcting for statistical factors)  $\Delta G_1 = -2.0 \pm 0.3 \text{ kcal mol}^{-1}$ ,  $\Delta G_2 = -1.3 \pm 0.1 \text{ kcal mol}^{-1}$ , and  $\Delta G_3 = -0.5 \pm 0.1 \text{ kcal mol}^{-1}$ , respectively (Figure 3.4C). The increasing  $\Delta G$  values indicate negative binding cooperativity or less favorable addition of morpholine to Ni with each successive association. Notably,  $\Delta G_3 = -0.5 \text{ kcal mol}^{-1}$  is reasonably close to the value of  $\Delta G_3 = -1.1 \text{ kcal mol}^{-1}$  calculated by DFT in our previous work.<sup>12</sup>

Furthermore, we calculate that under C–N coupling conditions (i.e., 70:1 amine:Ni molar ratio), the Ni-morpholine quenching mixture consists of 73%  $[\text{NiBr}_2(\text{morpholine})_3]$ , 27%  $[\text{NiBr}_2(\text{morpholine})_2]$ , and <0.3% other complexes. As shown in Figure 3.2C, both  $[\text{NiBr}_2(\text{morpholine})_2]$  and  $[\text{NiBr}_2(\text{morpholine})_3]$  demonstrate absorptions that overlap significantly with PC 1's emission. While  $[\text{NiBr}_2(\text{morpholine})_2]$  shows the largest overlap, it is present in lower concentration. Interestingly,  $[\text{NiBr}_2(\text{morpholine})_3]$  contains a morpholine bound in the apical position (Figure 3.3A) with a significantly shortened Ni–N bond of 2.050(4) Å compared to the other morpholines (i.e., 2.099(4) and 2.101(4) Å); thus, this morpholine is the strongest donor and may facilitate the subsequent proposed mechanistic step, intramolecular ET to generate a Ni(I) center and a morpholino radical cation (Figure S3.71, for our proposed mechanism). As such, both  $[\text{NiBr}_2(\text{morpholine})_2]$  and  $[\text{NiBr}_2(\text{morpholine})_3]$  show positive features for EnT catalysis, and we conclude that both are the EnT acceptors.

With the acceptors and their respective molar absorptivities known, we turned to classical Förster theory, in which the theoretical energy transfer rate constant,  $k_{\text{EnT}}$ , can be calculated as follows:<sup>27</sup>

$$k_{\text{EnT}} = k_{r,D} \left( \frac{R_0}{R} \right)^6 \text{ where} \quad (\text{Eq. 3.1})$$

$$R_0^6 = \frac{8.79 \cdot 10^{-25} \kappa^2 J}{\eta^4} \text{ and} \quad (\text{Eq. 3.2})$$

$$J = \int_0^\infty \frac{F_D(\nu) \epsilon_A(\nu)}{\nu^4} d\nu \quad (\text{Eq. 3.3})$$

In these equations,  $R$  is the donor–acceptor distance,  $R_0$  is the critical Förster distance defined in eq. 3.2,  $k_{r,D}$  is the radiative decay constant of the donor in the absence of acceptor,  $\kappa$  is the dipolar orientation factor,  $\eta$  is the refractive index of the solvent, and  $J$  is the spectral overlap integral defined in eq. 3.3, which involves  $F_D$ , the area-normalized emission spectrum of the donor, and  $\epsilon_A$ , the molar absorptivity of the acceptor as a function of frequency. In order to apply this equation to the reaction between excited state PC 1 and a Ni-amine complex, we needed to eliminate variables  $R$  and  $\kappa$ , which are difficult to measure in solution with freely tumbling donors and acceptors.

Utilizing an approach similar to that first demonstrated in the study of a system involving intramolecular EnT from a Re donor to a transition metal acceptor,<sup>44,45</sup> an expression was derived (see EXPERIMENTAL 2, Section 3, for details) to evaluate the ratio of quenching rate constants ( $k_{EnT,1}/k_{EnT,2}$ ) as the donor, PC 1, was held constant but the acceptor was changed, from the Ni-morpholine quenching mixture to the Ni-propylamine quenching mixture, according to the following equation:

$$\frac{k_{EnT,A1}}{k_{EnT,A2}} = \frac{J_1}{J_2} \quad (\text{Eq. 3.4})$$

Using eq 4, the ratio for PC 1 was calculated as  $k_{EnT,A1}/k_{EnT,A2} = 4.6$ , which compares favorably with the experimental value of 6.5 obtained from the TA experiments described above (Table S3.5, for  $J$  integrals used in the calculation). This level of agreement compares very well with that obtained for similar calculations in the literature,<sup>44</sup> supporting our assignment of the EnT quenching step as a Förster-type EnT process. Thus, based on equations 3.1–3.3, it can be seen

that selection of a PC with higher radiative rate constant  $k_{r,D}$  and higher overlap integral  $J$  will result in a higher EnT rate.

As such, we hypothesized that changing the donor PC from PC 1 to the organic phenoxazine PC 2 would impart improved performance in C–N cross-coupling reactions given that PC 2 covers an increased spectral range in its emission compared to PC 1 (Figure S3.33) and has a radiative rate constant reported<sup>46</sup> to be  $(4 \pm 1) \times 10^6 \text{ s}^{-1}$ , which is significantly higher than that of PC 1 (i.e.,  $7 \times 10^4 \text{ s}^{-1}$ ).<sup>29</sup> First, we confirmed that PC 2 also reacts via EnT as opposed to ET through spectroscopic (Figures S3.24–S3.32) and electrochemical (see EXPERIMENTAL 2, Section 4) control experiments. To theoretically probe the hypothesis that PC 2 will increase the rate of EnT, a second equation was derived (see SI, Section 3) to predict the ratio of quenching rate constants as the PC is changed but the Ni-morpholine mixture is kept constant as the acceptor:

$$\frac{k_{EnT,D1}}{k_{EnT,D2}} = \frac{k_{r,D1}J_{D1}}{k_{r,D2}J_{D2}} \quad (\text{Eq 5})$$

We note that the photophysics of PC 2 are more complicated than those of PC 1 in that both singlet and triplet excited states are populated. The triplet state is unlikely to react at a kinetically significant rate via a Förster-type pathway given the extremely low phosphorescence radiative decay rates of organic PCs in solution, typically on the order of  $10^0$ – $10^3 \text{ s}^{-1}$ .<sup>47</sup> Thus, the fluorescence spectrum and fluorescence radiative decay constant were used in conjunction with eq. 3.5 to calculate the ratio of  $k_{EnT,PC2}:k_{EnT,PC1} = 20.4$ , which is within a factor of 3 of the value of 12.7 determined experimentally from quenching studies (see above for PC 1 and EXPERIMENTAL 2, Section 3, for PC 2). Agreement between these values suggests that the observed EnT occurs through primarily a Förster-type pathway in the case of both PCs and with a much higher rate constant for PC 2 of  $(2.9 \pm 0.2) \times 10^9 \text{ M}^{-1} \text{ s}^{-1}$  (Figure S3.36) as compared to that for PC 1 of  $(2.3 \pm 0.1) \times 10^8 \text{ M}^{-1} \text{ s}^{-1}$ .

With these results in hand, we compared the performance of PCs 1 and 2 in C–N cross-coupling reactions (Figure 3.5; see EXPERIMENTAL 2, Section 9, for experimental details and product characterization). In order to directly compare the PCs, we chose to use the exact same conditions for all reactions. In particular, blue 457 nm light irradiation was chosen since PC 2 cannot absorb

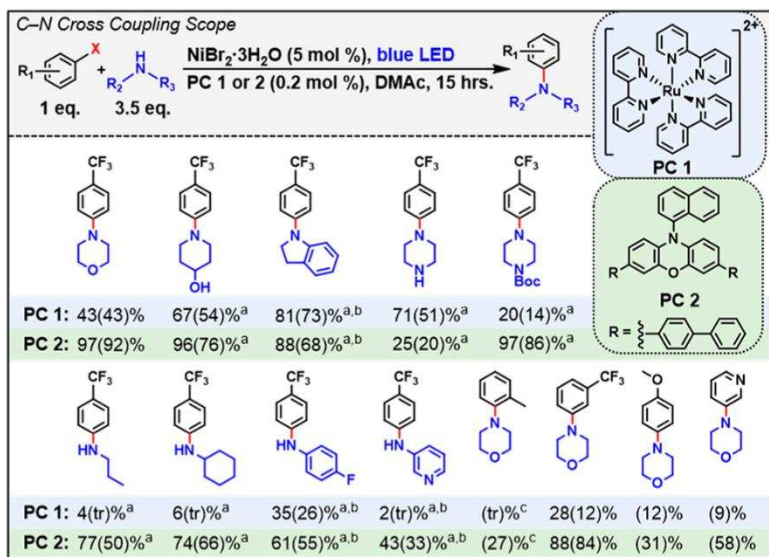


Figure 3.5. Scope of C–N coupling reactions using PC 1 and PC 2; PC 1 =  $[\text{Ru}(\text{bpy})_3]\text{Cl}_2$  and PC 2 = 3,7-di([1,1'-biphenyl]-4-yl)-10-(naphthalen-1-yl)-10H-phenoxazine. Yields were determined using  $^{19}\text{F}$  NMR for products containing fluorine. Isolated yields are reported in parentheses. X = Br unless otherwise indicated. <sup>a</sup>One equiv of KBr was used as an additive; <sup>b</sup>1.5 equiv. of the amine was used with 1.5 equiv. of added quinuclidine. <sup>c</sup>An aryl iodide was used. tr = trace product isolated. Reactions were performed with 0.4 mmol of aryl halide at room temperature. See EXPERIMENTAL 2, Section 9, for details and characterizations. The blue LED emission  $\lambda_{\text{max}} = 457 \text{ nm}$ .

green light. Further, an irradiation time of 15 h was chosen to allow for direct comparison with our previous work.<sup>12</sup> Control reactions confirmed that no product is formed in the absence of PC under blue irradiation (Table S3.9), and we further note that for PC 1 blue LED irradiation accesses the same absorption band as green irradiation, forming the same lowest MLCT excited state that we propose reacts via EnT.

Under these conditions, the performance with PC 1 and morpholine is significantly worsened (e.g., 43% conversion vs 88% in Figure 3.2A), and this can be attributed to a combination of factors, namely, the lower catalyst loading, which leads to a loss of 23% conversion (Table S3.9), a lower luminous flux of the blue LED as compared with the green LED (1:4.4, blue:green; Table S3.1), and the inner-filter effect resulting from increased unproductive absorption of blue vs green excitation light by the Ni-morpholine complexes (3:1, blue:green; Figure S3.33). Despite these worsened conditions, PC 1 is effective for coupling of secondary aliphatic amines with 4-bromobenzotrifluoride, highlighted by coupling of unprotected piperazine (51%) and indoline (73%), nitrogen heterocycles that are among those most frequently used in medicinal chemistry.<sup>48</sup>

On the other hand, PC 2 is more broadly effective, achieving higher yields than PC 1 with almost all substrates (Figure 3.5). Notably, PC 2 is effective in coupling difficult aliphatic (e.g., propylamine, 50%) and aromatic primary amines such as 4-fluoroaniline (55%) and 3-aminopyridine (33%) with 4-bromobenzotrifluoride, while PC 1 is ineffective, achieving only trace product formation with primary aliphatic amines. PC 2's emission extends ~100 nm further into the blue than PC 1, overlapping an absorption band of  $[\text{NiBr}_2(\text{propylamine})_4]$  that PC 1 cannot access (Figure S3.33). Since the efficiency of EnT has been shown to depend on specific electronic transitions,<sup>45</sup> we hypothesize that this blue-shifted band may facilitate EnT and thus might explain PC 2's increased performance.

With aromatic amines (e.g., 4-fluoroaniline), quinuclidine was employed as a base additive based on a beneficial effect on yield observed in our previous work.<sup>12</sup> The effect of quinuclidine is likely due at least in part to its role in controlling the speciation of the Ni catalyst; investigation by UV-vis revealed that quinuclidine binds more strongly than aniline to  $\text{NiBr}_2$  (Figure S3.59),



forming  $[\text{NiBr}_2(\text{quinuclidine})_2]$ , which has good overlap between its absorption and PC 2's emission (Figure S3.33). In addition, the use of 1 equiv of KBr as an additive improved the performance of some amines such as propylamine and unprotected piperazine (14% and 26% increase, respectively; Table S3.10, and following supplemental discussion). With propylamine, we hypothesize that KBr improves reactivity by inhibiting the speciation equilibria as observed by UV-vis (Figures S3.60 and S3.61); this inhibition increases the concentration of  $[\text{NiBr}_2(\text{propylamine})_3]$ , which has better overlap with PC 2 than  $[\text{NiBr}_2(\text{propylamine})_4]$ .

With regard to the aryl halide coupling partner, PC 2 successfully promotes coupling of morpholine with aryl halides containing electron-withdrawing groups (EWGs, e.g., 4-bromobenzotrifluoride, 92%) as well as electron-donating groups (EDGs, e.g., 4-bromoanisole, 31%). Notably, a heterocyclic aryl bromide, 3-bromopyridine, could be coupled in good yield (58%). In addition, the difficult ortho-substituted aryl halide 2-iodotoluene could be coupled with morpholine in moderate yield (27%), constituting the first example of C–N bond formation with this substrate pair in light-driven Ni catalysis.

Trends in reactivity for both PCs mirror those observed in our previous work with secondary > primary > primary aromatic amines in terms of yield. Similarly, aryl halides containing EWGs gave greater yields than those containing EDGs. Overall, the similarity in these trends across both PCs to trends obtained in our previous work<sup>12</sup> supports that a similar Ni-amine excited state intermediate forms in both cases that can be accessed either via EnT from a PC under visible light or via direct excitation under 365 nm irradiation.

## CONCLUSION

In sum, spectroscopic evidence supports an EnT quenching mechanism in dual catalytic C–N cross-coupling that proceeds via a Förster-type pathway. In addition, the EnT acceptors have

been identified via single-crystal XRD and spectroscopic binding studies as a series of  $[\text{Ni}(\text{II})\text{Br}_2(\text{amine})_x]$  complexes formed in situ in C–N cross-coupling reaction mixtures. These complexes are proposed to form more broadly across catalytic systems utilizing  $\text{NiBr}_2$  and amines and thus constitute mechanistically significant intermediates across Ni catalysis. Elucidating the speciation enabled the use of quantitative Förster theory to calculate EnT rate constant ratios that agreed with values determined experimentally from spectroscopic studies. Employment of this mechanistic knowledge through selection of phenoxazine PC 2 led to increased performance relative to  $[\text{Ru}(\text{bpy})_3]\text{Cl}_2$  PC 1 in catalyzing C–N bond formation between diverse amines and aryl halides under mild conditions. Ultimately, future work utilizing quantitative Förster theory has the potential to both predict and discover new reactivity in energy transfer systems across light-driven Ni catalysis.

## EXPERIMENTAL 2: SUPPLEMENTARY INFORMATION FOR CHAPTER 3

### 1. General Information

N,N-dimethylacetamide (DMAc) solvent, aryl halides, amines,  $\text{Bu}_4\text{NPF}_6$ ,  $\text{AgNO}_3$ , and ferrocene were purchased from Sigma-Aldrich, TCI or Alfa Aesar and used as received. For all spectral studies, DMAc HPLC grade > 99.5 % purity was used. Anhydrous toluene was purified and dried using an MB-SPS solvent purification system (MBraun). All commercially available solvents and reagents were degassed and used without further purifications except for morpholine and aniline. Morpholine and aniline were dried over  $\text{CaH}_2$  with stirring for 24 hours, followed by vacuum distillation, according to a published procedure.<sup>1</sup> The dried and degassed amines were stored under  $\text{N}_2$  in a sealed Schlenk flask until use. For aniline, the flask was wrapped in aluminum foil to protect from light. All Ni precatalysts (e.g.,  $\text{NiBr}_2 \cdot 3\text{H}_2\text{O}$ ,  $\text{NiBr}_2 \cdot \text{glyme}$ , and anhydrous  $\text{NiBr}_2$ ) were purchased from Sigma-Aldrich or Alfa Aesar, stored in a  $\text{N}_2$  filled glove box upon receipt, and used without further purification. All substrates used in C–N cross coupling reactions were purchased from Sigma-Aldrich or Alfa Aesar and used as received, with the exception of morpholine which was purified as mentioned above.

The photoreactor used was custom designed and built-in house and the specifications have been published previously.<sup>2</sup> All LEDs used were purchased from LED Engin and full emission spectra, as well as peak wavelength shift vs. temperature data, are available online in the respective manufacturer datasheets (see below). In the photoreactor, blue and green LEDs are run at 700mA and a forward voltage of 13.5V.

Table S3.1. LED Information

LED color and peak wavelength	Luminous Flux	Model #	URL
Green, $\lambda_{\text{max}} = 523$ nm	640 lm, 700mA	LZ4-00G108	<a href="http://www.ledengin.com/files/products/LZ4/LZ4-00G108.pdf">http://www.ledengin.com/files/products/LZ4/LZ4-00G108.pdf</a>
Blue, $\lambda_{\text{max}} = 457$ nm	145 lm, 700mA	LZ4-00B208	<a href="http://www.ledengin.com/files/products/LZ4/LZ4-00B208.pdf">http://www.ledengin.com/files/products/LZ4/LZ4-00B208.pdf</a>
Amber, $\lambda_{\text{max}} = 590$ nm	400 lm, 700mA	LZ4-00A108	<a href="http://www.ledengin.com/files/products/LZ4/LZ4-00A108.pdf">http://www.ledengin.com/files/products/LZ4/LZ4-00A108.pdf</a>
Far Red, $\lambda_{\text{max}} = 740$ nm	2.1 W, 700mA	LZ4-00R308	<a href="http://www.ledengin.com/files/products/LZ4/LZ4-00R308.pdf">http://www.ledengin.com/files/products/LZ4/LZ4-00R308.pdf</a>

The  $^1\text{H}$ ,  $^{13}\text{C}$ , and  $^{19}\text{F}$  NMR spectra were recorded on a Bruker US400 instrument at (400, 101, or 376 MHz, respectively) in the Colorado State University Central Instrument Facility. Deuterated chloroform was purchased from Cambridge Isotope Laboratories (Andover, MA) and used as received. All  $^1\text{H}$  NMR experiments are reported in  $\delta$  units, parts per million (ppm), and were measured relative to the signals for residual chloroform (7.26 ppm) or dimethylsulfoxide (2.50 ppm) in the deuterated solvents. Data for  $^1\text{H}$  NMR are reported as follows: chemical shift ( $\delta$  ppm), multiplicity (s = singlet, d = doublet, t = triplet, q = quartet, h = heptet, br = broad), coupling constant (Hz) and integration. All  $^{13}\text{C}$  NMR spectra are reported in ppm relative to  $\text{CDCl}_3$  (77.16 ppm) or  $\text{DMSO-}d_6$  (39.52 ppm).

Reactions were analyzed by thin layer chromatography (TLC) using TLC silica gel F254 250  $\mu\text{m}$  pre-coated-plates from Merck. Developed chromatograms were observed using a UV lamp with emission at 255 nm or 365 nm. Accurate mass measurements were obtained using an Agilent 6224 Time of Flight (TOF) mass spectrometer interfaced to a direct analysis in real time (DART) ionization source (IonSense DART-SVP).

## 2. Transient Absorption Spectroscopy

Nanosecond transient absorption spectra were acquired with an LP980KS spectrometer (Edinburgh Instruments) with a Minilite Nd:YAG Q-switched laser (Continuum Lasers) configured to deliver a 532 nm or 355 nm excitation pulse. Spectral data was acquired from 300-

800 nm at the indicated time delay through use of an iStar ICCD camera (Andor) as the detector. Kinetic data was recorded on the same instrument utilizing a photomultiplier tube (included in the LP980) interfaced with an MD03022 mixed domain oscilloscope (Tektronix) as the detector. Time zero was set on the instrument using the emission of  $[\text{Ru}(\text{bpy})_3]\text{Cl}_2$  to locate the pump pulse with 1 ns resolution.

Stock solutions of 0.3 mM  $[\text{Ru}(\text{bpy})_3]\text{Cl}_2$  were prepared by weighing out  $[\text{Ru}(\text{bpy})_3]\text{Cl}_2 \cdot 6\text{H}_2\text{O}$  (5.6 mg, 2.5  $\mu\text{mol}$ ) into a 20 mL scintillation vial. After fully dissolving in 10 mL N,N-dimethylacetamide (DMAc) in a 40°C water bath, the solution was transferred to a 25 mL volumetric flask and the vial was rinsed with DMAc to recover any remaining  $[\text{Ru}(\text{bpy})_3]\text{Cl}_2$ . The solution was diluted with DMAc to complete the 25 mL stock solution. In the following experiments, 1 mL of stock solution was added to a scintillation vial along with the appropriate amount of quencher, and the resulting mixture was diluted to 3 mL total with DMAc to produce all mixtures 0.1 mM in  $[\text{Ru}(\text{bpy})_3]\text{Cl}_2$ . At this concentration, OD = 0.156 at 532 nm.

All Ni-amine mixtures were prepared as follows: An appropriate amount of  $\text{NiBr}_2 \cdot 3\text{H}_2\text{O}$  was weighed out in a  $\text{N}_2$ -filled glovebox into a scintillation vial. The vial was then removed from the glovebox and immediately the Ni was dissolved in spectral grade DMAc (>99.5 %) with heating at 40°C in a water bath to make a 0.048 M stock solution. 500  $\mu\text{L}$  of this stock solution was then added for every 3 mL of desired final concentration 0.008 M Ni solution. An appropriate amount of morpholine or propylamine was then added via pipette to complete the Ni-amine mixture (70:1 molar ratio amine:Ni, 0.56 M in amine). All mixtures to be analyzed via TA spectroscopy were degassed by sparging for 15 minutes with Ar in a sidearm-equipped, 1 cm path length quartz screw cap cuvette. All kinetic traces shown were acquired with 25 or 50 averages and laser power between 3-15  $\text{mW}/\text{cm}^2$  at 1 Hz repetition rate.

[Ru(bpy)<sub>3</sub>]Cl<sub>2</sub> in DMAc without quencher.

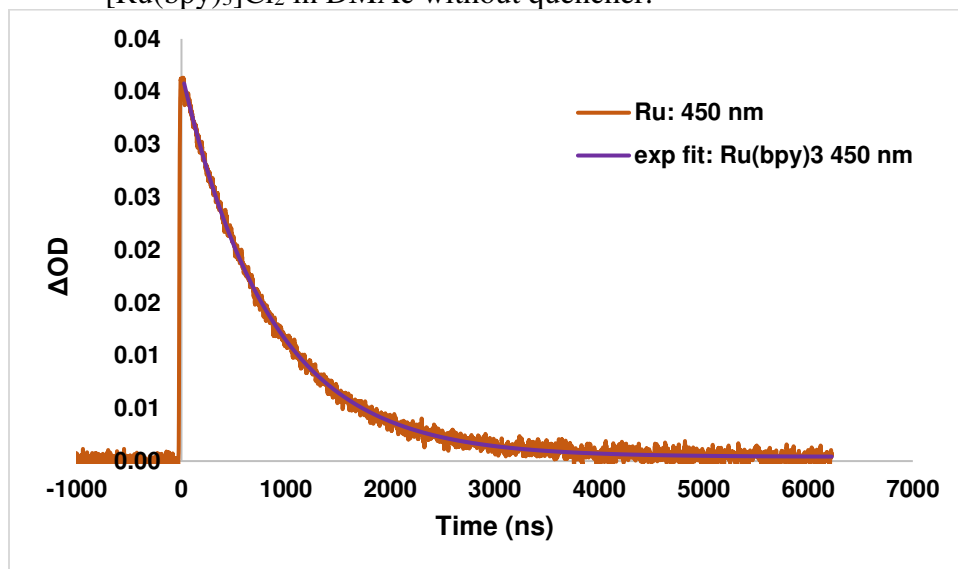


Figure S3.1. Kinetic trace of [Ru(bpy)<sub>3</sub>]Cl<sub>2</sub> 0.1 mM in DMAc with  $\lambda_{pump} = 532$  nm and  $\lambda_{probe} = 450$  nm. Data was scaled by -1 to accommodate an exponential tail fit.

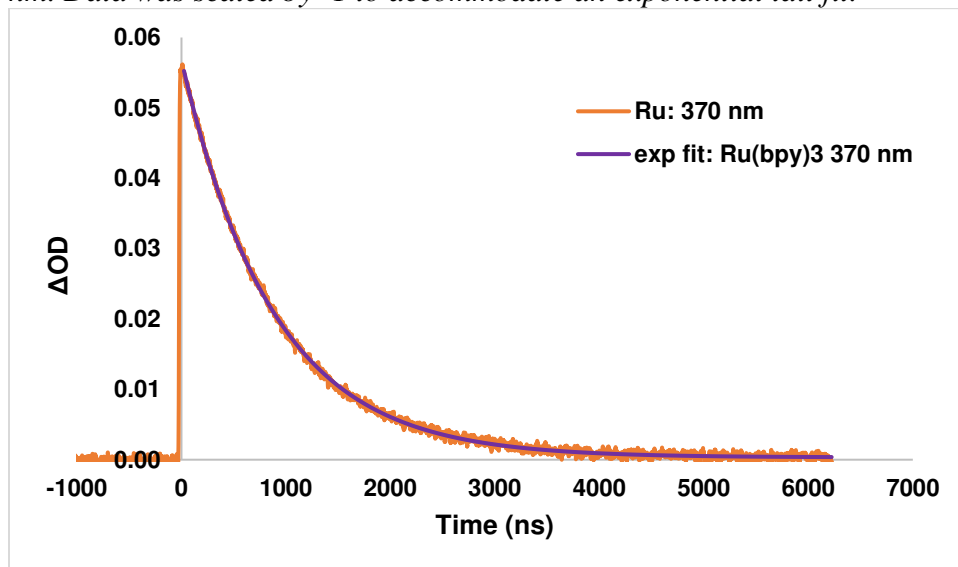


Figure S3.2. Kinetic trace of [Ru(bpy)<sub>3</sub>]Cl<sub>2</sub> 0.1 mM in DMAc with  $\lambda_{pump} = 532$  nm and  $\lambda_{probe} = 370$  nm.

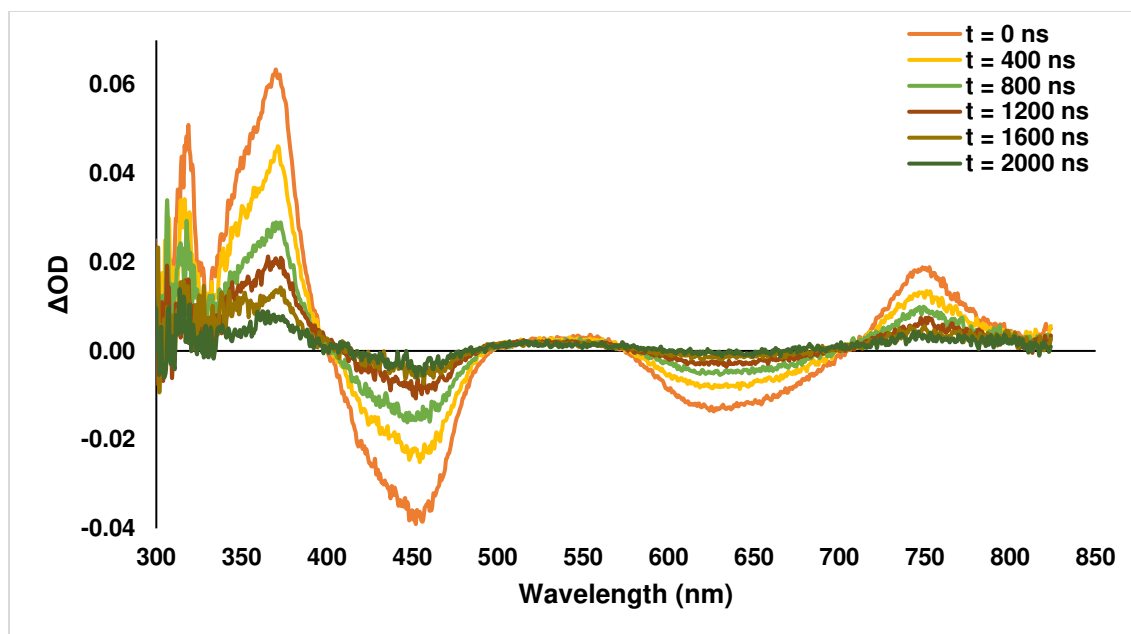


Figure S3.3. Absorption map of  $[\text{Ru}(\text{bpy})_3]\text{Cl}_2$  0.1 mM in DMAc at various time delays with  $\lambda_{\text{pump}} = 532$  nm. Clear excited state absorption (ESA) features can be seen at  $\lambda_{\text{max}} = 370$  nm and  $\lambda_{\text{max}} = 746$  nm. A ground state bleach (GSB) can be seen at  $\lambda_{\text{max}} = 450$  nm as well as a stimulated emission (SE) signal at  $\lambda_{\text{max}} = 617$  nm.

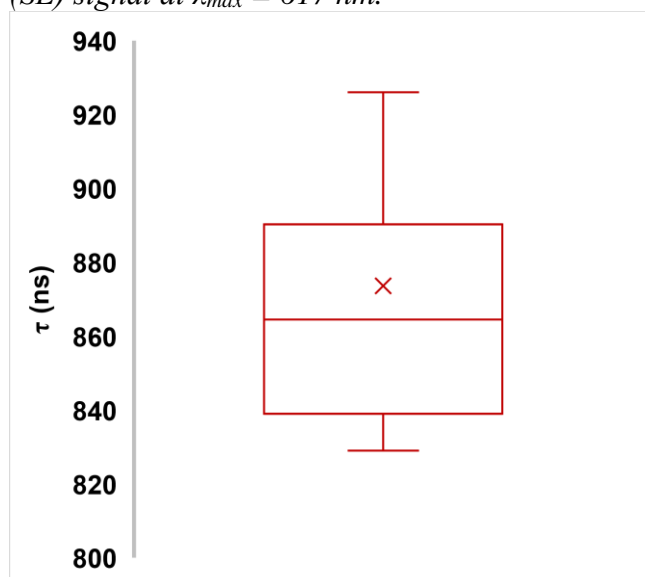


Figure S3.4. Boxplot of  $[\text{Ru}(\text{bpy})_3]\text{Cl}_2$  excited state lifetime 0.1 mM in DMAc. The mean lifetime was  $870 \pm 40$  ns (standard deviation),  $n = 16$  measurements. "X" marks the sample mean.

### Reactivity of $[\text{Ru}(\text{bpy})_3]\text{Cl}_2$ in the presence of quenchers.

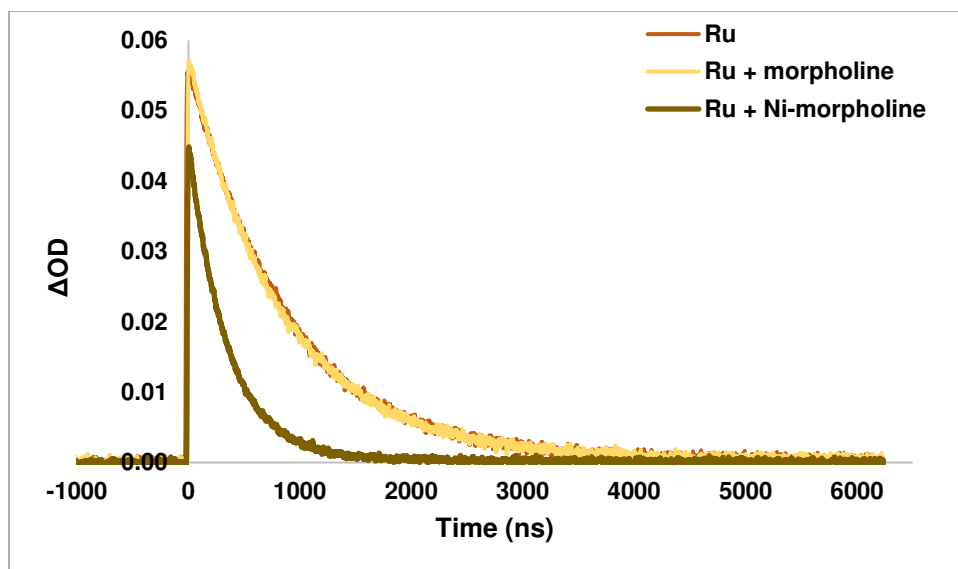


Figure S3.5. Kinetic traces of  $[Ru(bpy)_3]Cl_2$  0.1 mM in DMAc with  $\lambda_{pump} = 532$  nm and  $\lambda_{probe} = 370$  nm alone and in the presence of morpholine (5600 eq. relative to  $Ru(bpy)_3$ , 0.56 M) and a Ni-morpholine solution (0.008 M in  $NiBr_2 \cdot 3H_2O$ , 0.56 M in morpholine). Note:  $[NiBr_2(morpholine)_3]$  and  $[NiBr_2(morpholine)_2]$  make up >99% of this mixture and are formed in situ upon mixing morpholine with a DMAc solution of  $NiBr_2 \cdot 3H_2O$ . See UV-visible spectroscopy section for characterization of this mixture.

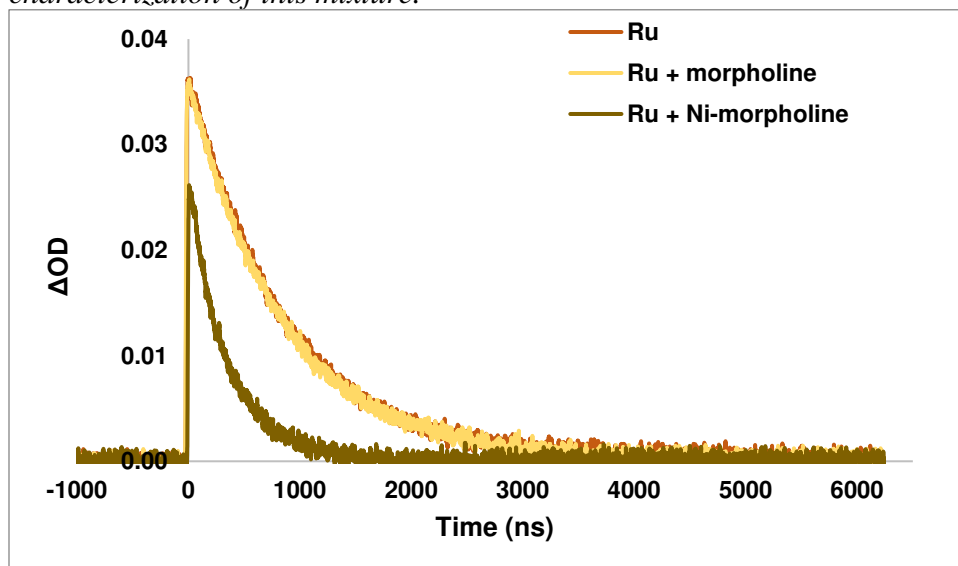


Figure S3.6. Kinetic traces of  $[Ru(bpy)_3]Cl_2$  0.1 mM in DMAc with  $\lambda_{pump} = 532$  nm and  $\lambda_{probe} = 450$  nm alone and in the presence of morpholine (5600 eq. relative to  $Ru(bpy)_3$ , 0.56 M) and a Ni-morpholine solution (0.008 M in  $NiBr_2 \cdot 3H_2O$ , 0.56 M in morpholine). Data was scaled by -1 to accommodate an exponential tail fit.



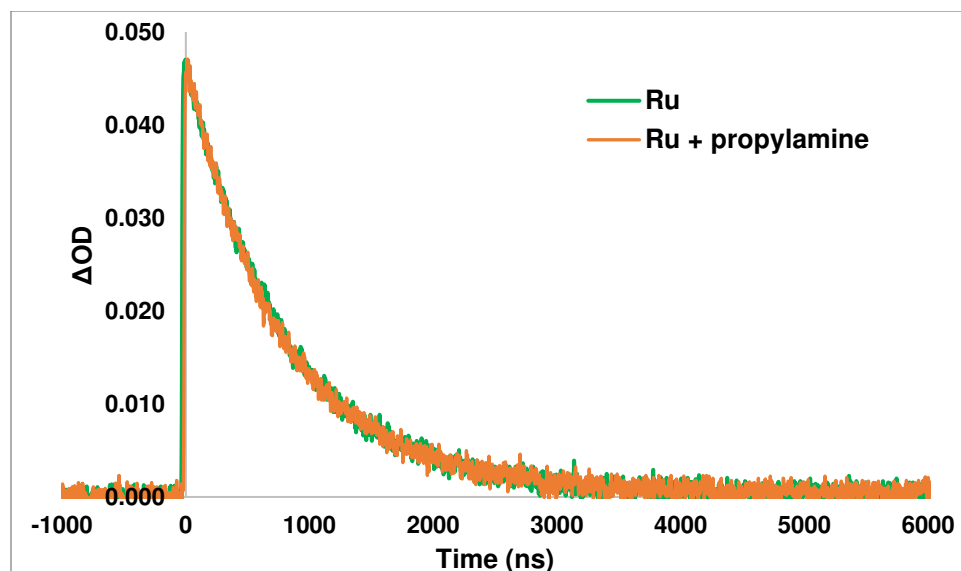


Figure S3.7. Kinetic traces of  $[\text{Ru}(\text{bpy})_3]\text{Cl}_2$  0.1 mM in DMAc with  $\lambda_{\text{pump}} = 532$  nm and  $\lambda_{\text{probe}} = 450$  nm alone and in the presence of propylamine (5600 eq. relative to  $\text{Ru}(\text{bpy})_3$ , 0.56 M). Data was scaled by -1 to accommodate an exponential tail fit.

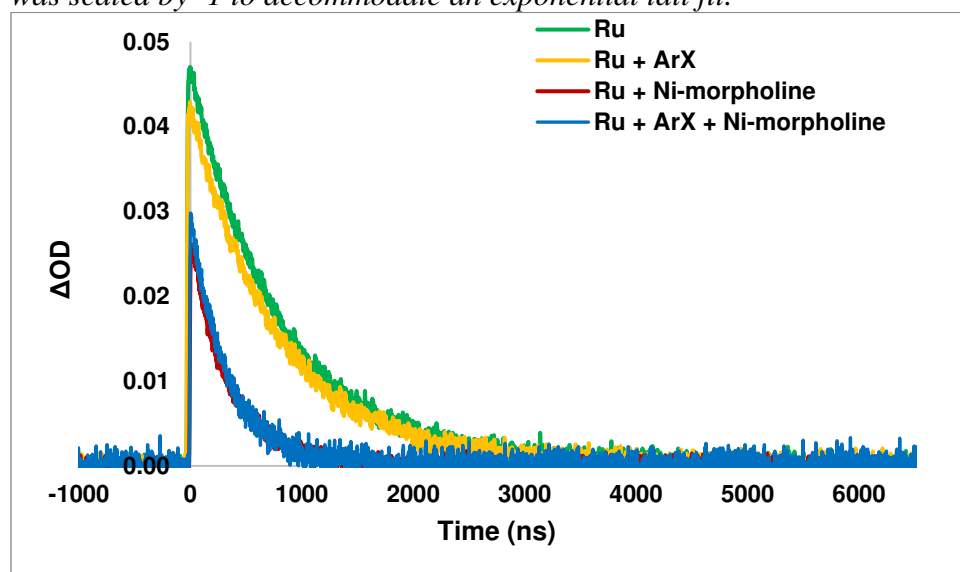


Figure S3.8. Kinetic traces of  $[\text{Ru}(\text{bpy})_3]\text{Cl}_2$  0.1 mM in DMAc with  $\lambda_{\text{pump}} = 532$  nm and  $\lambda_{\text{probe}} = 450$  nm alone and in the presence of 4-bromobenzotrifluoride (1600 eq. relative to  $\text{Ru}(\text{bpy})_3$ , 0.16 M, "ArX") and a Ni-morpholine mixture. The traces were scaled by -1 to accommodate an exponential fit.

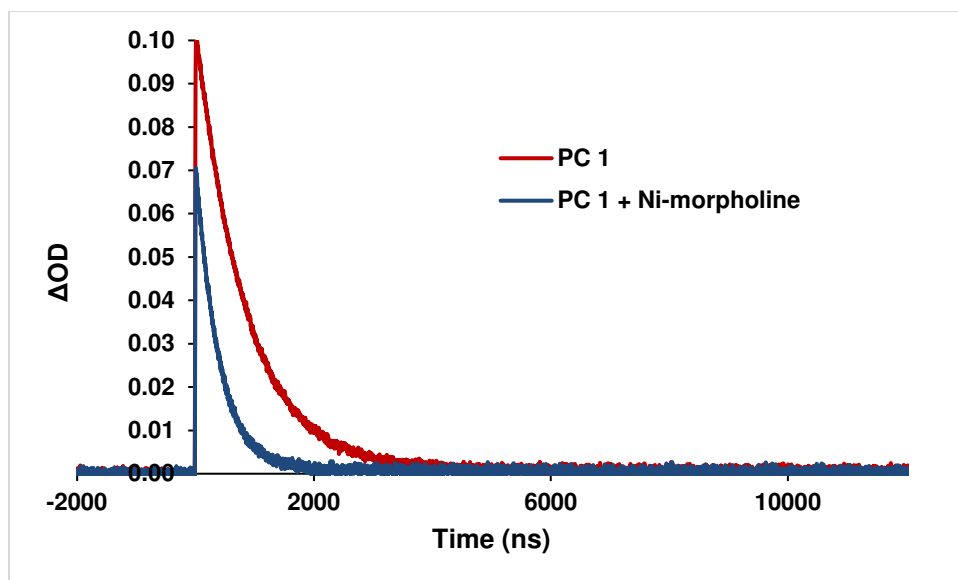


Figure S3.9. High power quenching experiment. Kinetic traces of  $[\text{Ru}(\text{bpy})_3]\text{Cl}_2$  0.1 mM in DMAc with  $\lambda_{\text{pump}} = 532$  nm and  $\lambda_{\text{probe}} = 370$  nm alone and in the presence of a Ni-morpholine mixture (5 mM in Ni, 50:1 Ni:Ru; 70:1 morpholine:Ni). The experiment was performed at 13-15 mW laser power.

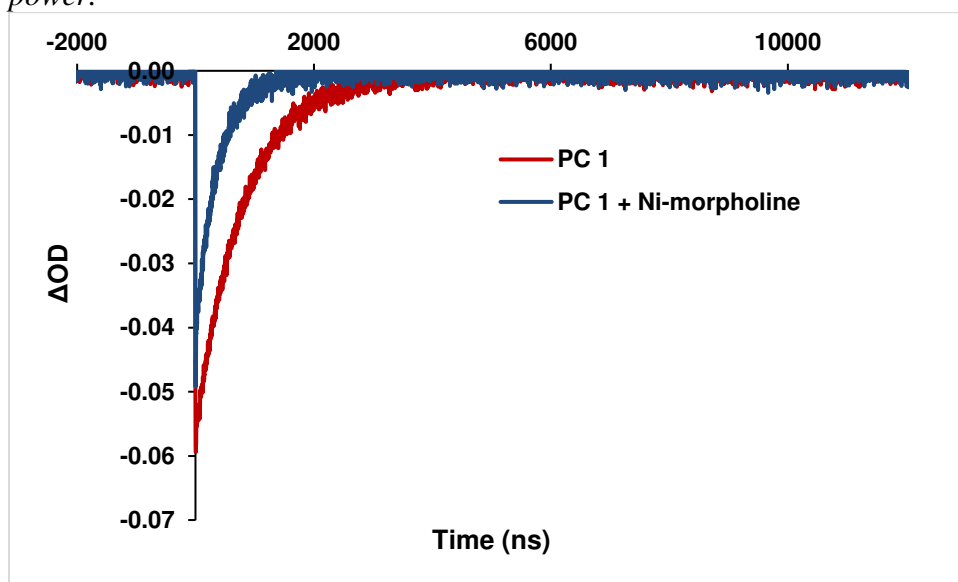


Figure S3.10. High power quenching experiment. Kinetic traces of  $[\text{Ru}(\text{bpy})_3]\text{Cl}_2$  0.1 mM in DMAc with  $\lambda_{\text{pump}} = 532$  nm and  $\lambda_{\text{probe}} = 450$  nm alone and in the presence of a Ni-morpholine mixture (5 mM in Ni, 50:1 Ni:Ru; 70:1 morpholine:Ni). The experiment was performed at 13-15 mW laser power.

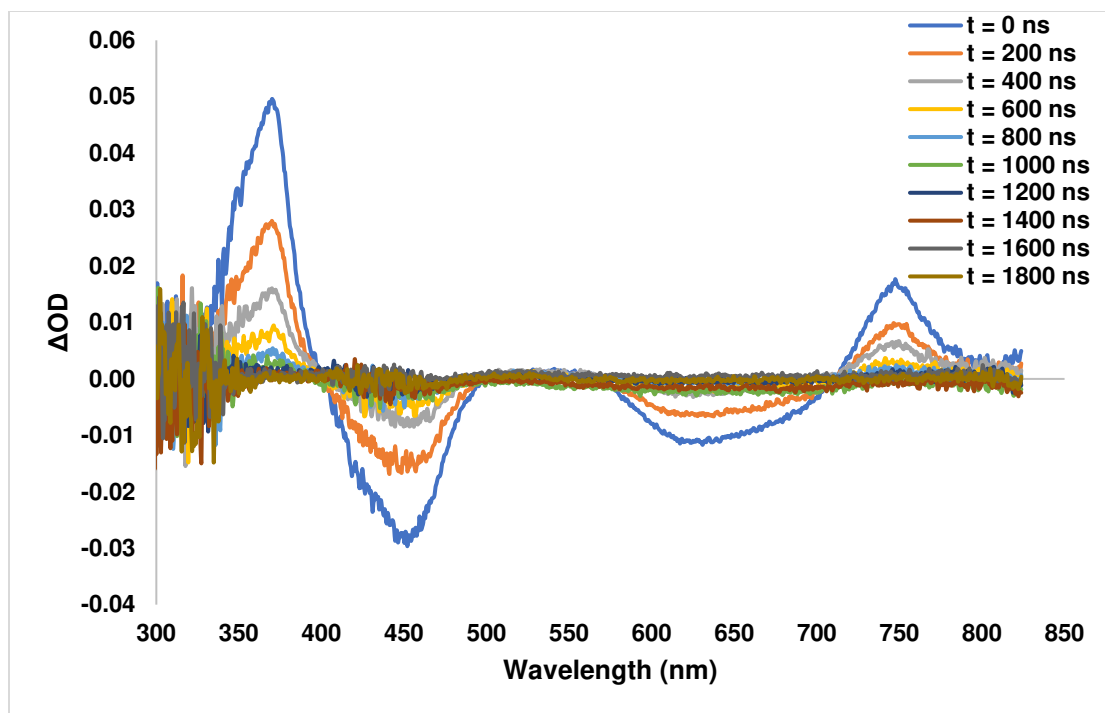


Figure S3.11. Spectral absorption map of  $[Ru(bpy)_3]Cl_2$  (0.1 mM) with  $\lambda_{pump} = 532$  nm in the presence of Ni-morpholine complexes (8 mM in Ni) at various time delays, demonstrating the complete recovery of the ground state photocatalyst at all wavelengths.

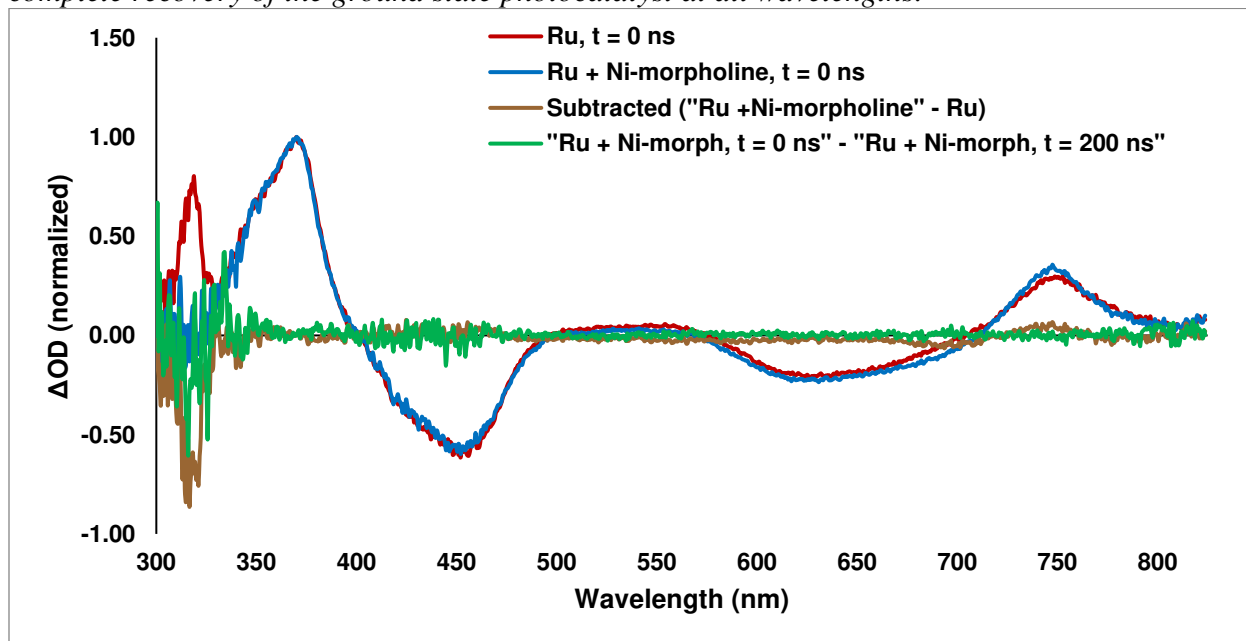


Figure S3.12. Spectra of  $[Ru(bpy)_3]Cl_2$  (0.1 mM) with  $\lambda_{pump} = 532$  nm in the absence and presence of a Ni-morpholine quenching mixture (8 mM in Ni), normalized to the largest peak. The brown trace results from subtraction of the Ru signal from the Ru + Ni-morpholine mixture to isolate the spectrum of Ni-morpholine complexes. The green trace results from subtraction of the  $t = 200$  ns trace from the  $t = 0$  trace to isolate the spectrum of a short-lived species. The noisy feature at  $\lambda = 315$  nm appears in both subtracted spectra but is due to increased absorption of the probe by Ni

and resultant loss of resolution in that region. We hypothesize that the excited state Ni complex has a lifetime shorter than 5-6 ns, the limit in time resolution of this setup.

### Stern-Volmer Quenching Experiments.

A stock solution of  $[\text{Ru}(\text{bpy})_3]\text{Cl}_2$  0.3 mM in DMAc was prepared as above. This solution was used to make two working stock solutions both 0.1 mM in  $[\text{Ru}(\text{bpy})_3]\text{Cl}_2$ , either with or without a Ni-amine solution. In all cases the Ni-amine solution has a final concentration in the working stock solution of 0.008 M in  $\text{NiBr}_2 \cdot 3\text{H}_2\text{O}$  and 0.56 M in amine. These two working solutions were then mixed in various ratios to produce 3 mL mixtures for TA analysis according to the following table.

Table S3.2. Stern-Volmer solutions.

Solution #	mL Ru stock	mL Ni + Ru stock	Ni:Ru molar ratio
1	3.000	0	0
2	2.600	0.400	10.7
3	2.060	0.940	25.1
4	1.500	1.500	40.0
5	1.000	2.000	53.3
6	0.600	2.400	64.0
7	0	3.000	80.0

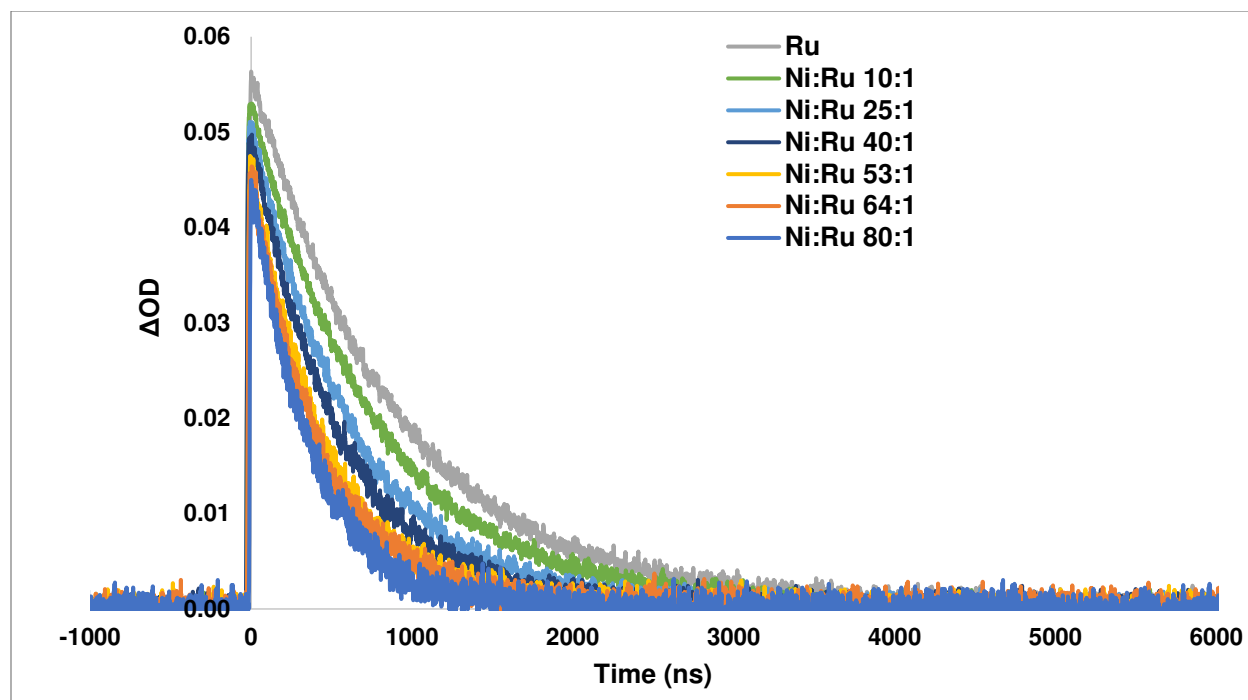


Figure S3.13. Raw kinetic traces of  $[\text{Ru}(\text{bpy})_3]\text{Cl}_2$  0.1 mM in DMAc with  $\lambda_{\text{pump}} = 532$  nm and  $\lambda_{\text{probe}} = 450$  nm alone and in the presence of increasing molar ratios of a Ni-morpholine quencher solution (0.008 M in  $\text{NiBr}_2 \cdot 3\text{H}_2\text{O}$ , 0.56 M in morpholine). This data is from a single representative replicate of 3 total repeated experiments.

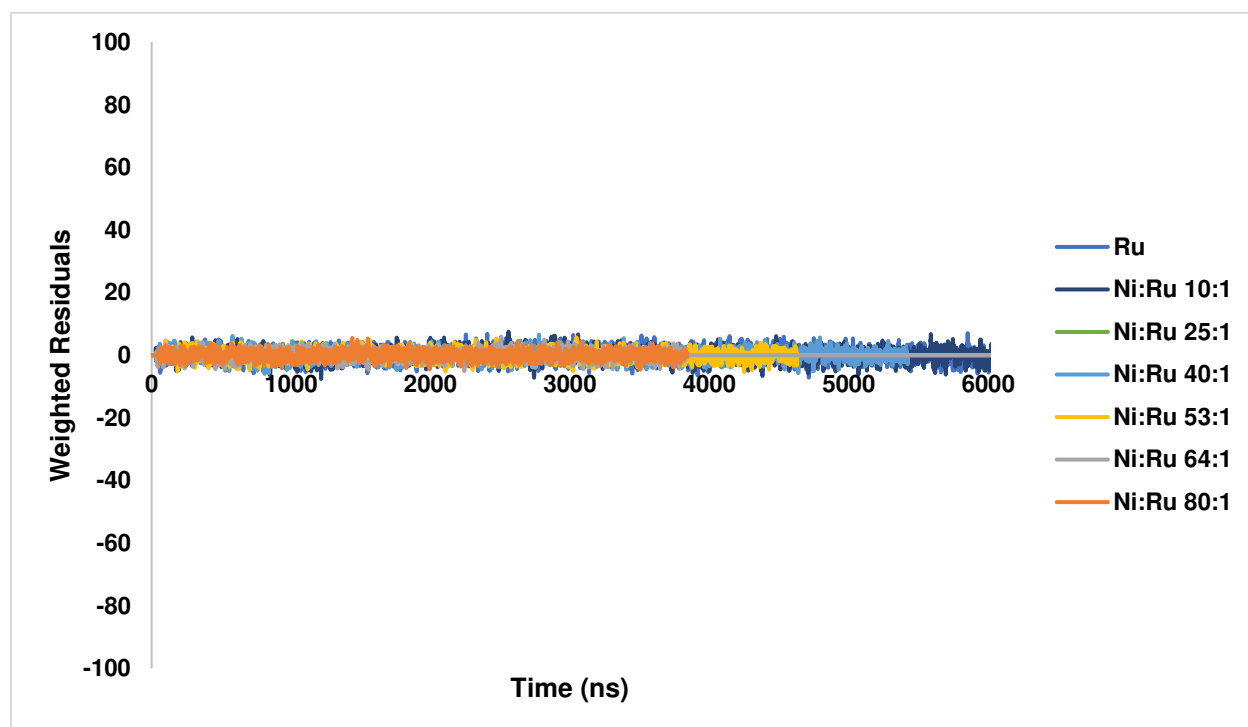


Figure S3.14. Weighted residuals for exponential tail fits of kinetic traces at 450 nm. This data is from a single representative replicate of 3 total repeated experiments.

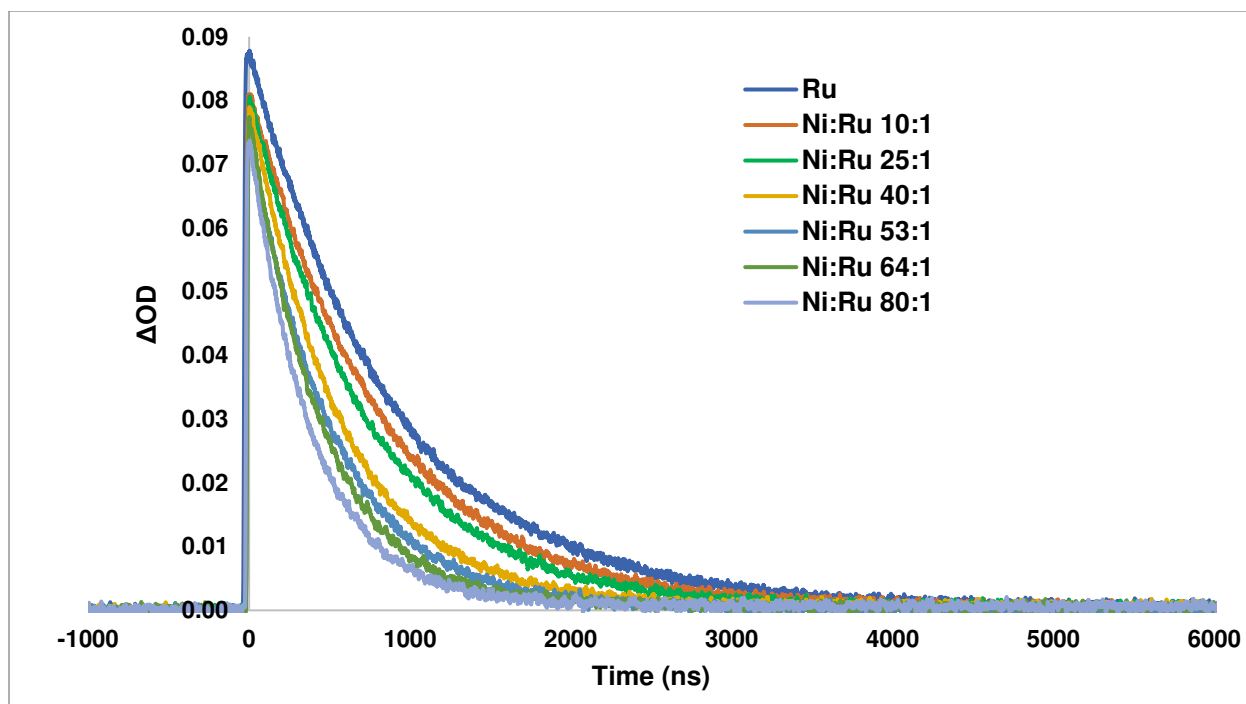


Figure S3.15. Raw kinetic traces of  $[\text{Ru}(\text{bpy})_3]\text{Cl}_2$  0.1 mM in DMAc with  $\lambda_{\text{pump}} = 532$  nm and  $\lambda_{\text{probe}} = 370$  nm alone and in the presence of increasing molar ratios of a Ni-morpholine quencher solution (0.008 M in  $\text{NiBr}_2 \cdot 3\text{H}_2\text{O}$ , 0.56 M in morpholine). This data is from a single representative replicate of 3 total repeated experiments.

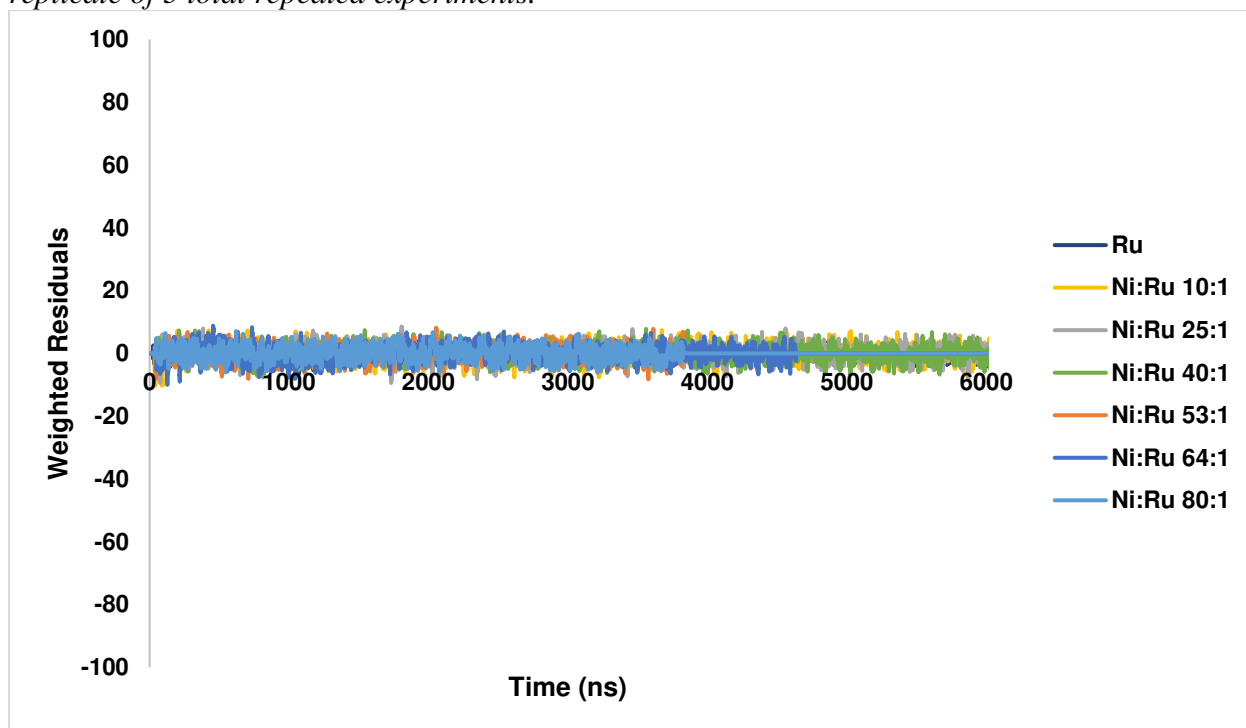


Figure S3.16. Weighted residuals for exponential tail fits of kinetic traces at 370 nm. This data is from a single representative replicate of 3 total repeated experiments.

Table S3.3. Excited state lifetimes of  $[Ru(bpy)_3]Cl_2$  in the presence of different ratios of Ni-morpholine quenching solutions.

Run	Quencher Concentration (M)	Ni:Ru ratio	Tau 450 nm	Tau 370 nm
1	0.0011	10.7:1	710	786
1	0.0025	25.1:1	541	579
1	0.0040	40.0:1	441	508
1	0.0053	53.3:1	422	416
1	0.0064	64.0:1	388	413
1	0.0080	80.0:1	327	341
2	0.0011	10.7:1	707	745
2	0.0025	25.1:1	543	648
2	0.0040	40.0:1	447	470
2	0.0053	53.3:1	382	460
2	0.0064	64.0:1	346	378
2	0.0080	80.0:1	341	373
3	0.0011	10.7:1	683	730
3	0.0025	25.1:1	522	561
3	0.0040	40.0:1	426	450
3	0.0053	53.3:1	403	409
3	0.0064	64.0:1	375	360
3	0.0080	80.0:1	335	730

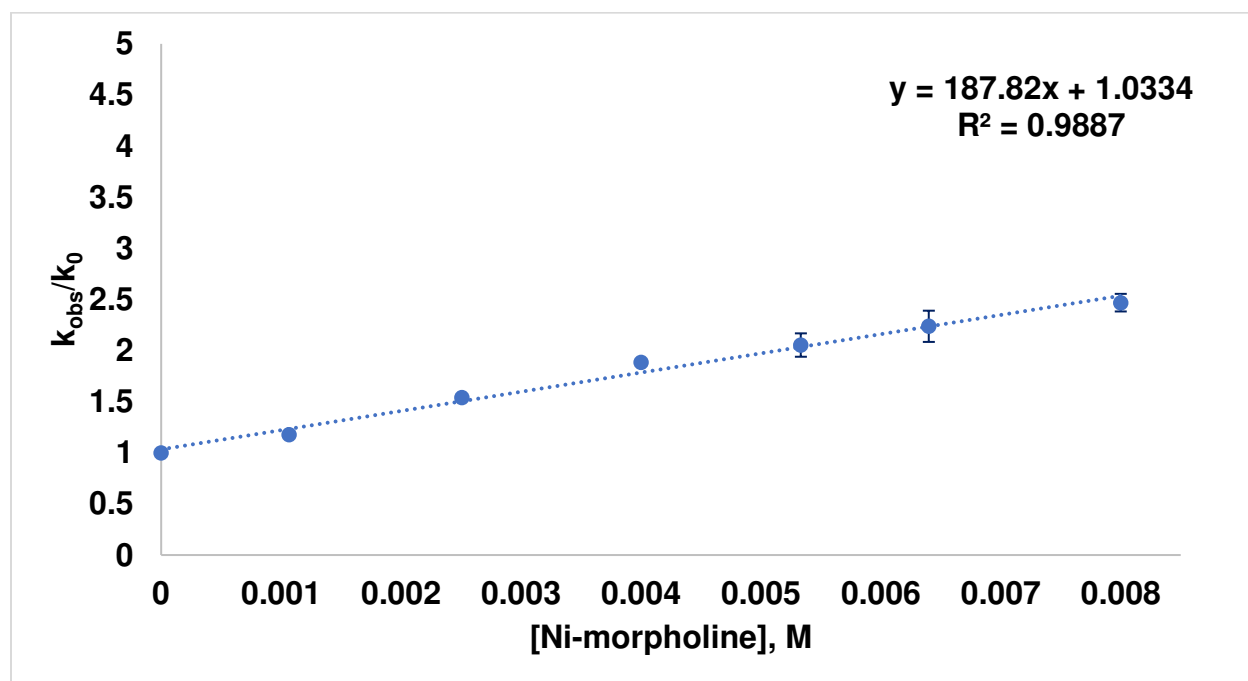


Figure S3.17. Stern-Volmer plot  $k_{obs}/k_0$  data at  $\lambda_{probe} = 450$  nm, where  $k_{obs}$  is the observed rate constant ( $1/\tau_{obs}$ ) in the presence of quencher and  $k_0$  is the excited state decay rate constant ( $1/\tau_0$ ) of  $[Ru(bpy)_3]Cl_2$  in absence of quencher. Excited state lifetimes used for the plot are given in Table S3. Each plotted data point is the average of 3 replicates and error bars are  $\pm$  standard deviation.

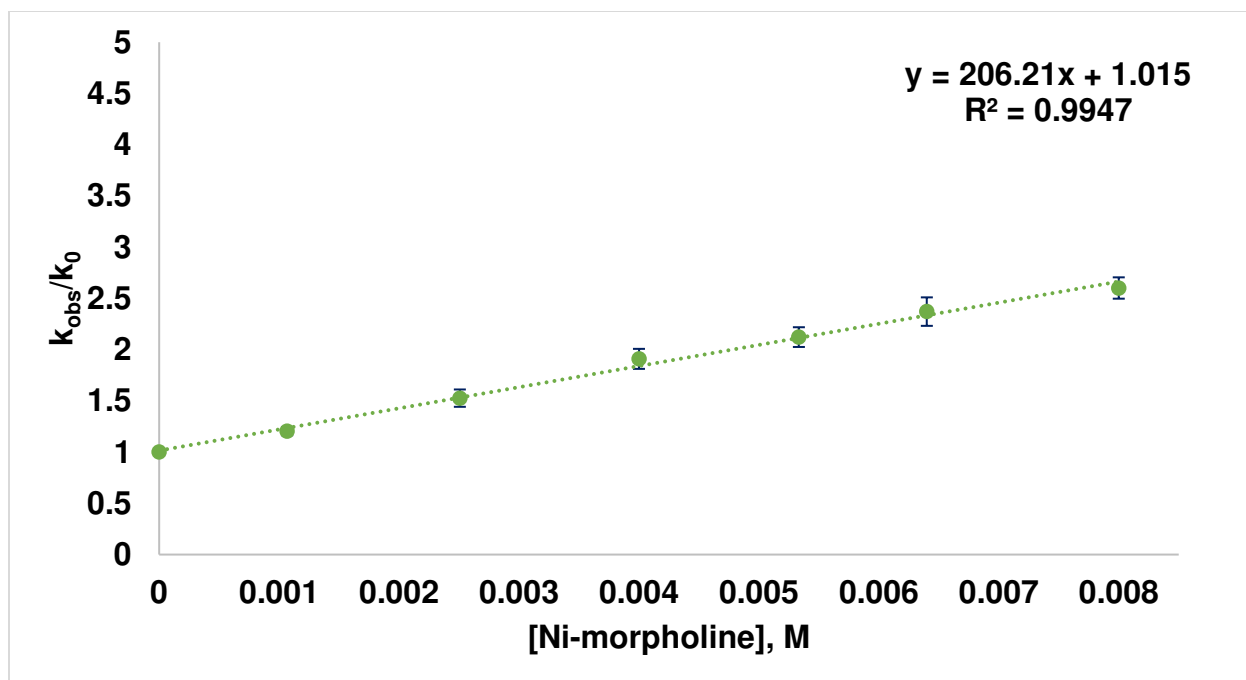


Figure S3.18. Stern-Volmer plot of  $k_{obs}/k_0$  data at  $\lambda_{probe} = 370$  nm, where  $k_{obs}$  is the observed rate constant ( $1/\tau_{obs}$ ) in the presence of quencher and  $k_0$  is the excited state decay rate constant ( $1/\tau_0$ ) of  $[Ru(bpy)_3]Cl_2$  in absence of quencher. Excited state lifetimes used for the plot are given in Table S3. Each plotted data point is the average of 3 replicates and error bars are  $\pm$  standard deviation.

#### Calculation of $k_q$ , the quenching rate constant, for Q = Ni-morpholine mixture.

From the above Stern-Volmer plots (Fig S3.9, S3.10),  $k_q = b/\tau_0$ , (see literature for kinetic derivation of the Stern-Volmer relationship in this context)<sup>3</sup> where  $b$  is the slope of the linear regression line. Thus, for Ni-morpholine quenching mixtures:

$$k_q(450 \text{ nm}) = 2.3 \pm 0.1 * 10^8 \text{ M}^{-1} \text{ s}^{-1}, k_q(370 \text{ nm}) = (2.1 \pm 0.3) * 10^8 \text{ M}^{-1} \text{ s}^{-1}.$$

where the reported error is the standard error in the regression coefficient  $b$ .<sup>4</sup>

We note that the lowest molar ratio of 10:1 of Ni:PC 1 used lies at the lower limit that can be assumed to establish pseudo first order conditions.<sup>5</sup> However, based on the  $R^2$  values calculated for the linear regressions and the fact that the first data point lies on the regression line, this assumption appears to be reasonable.



Ni-propylamine quenching experiments.

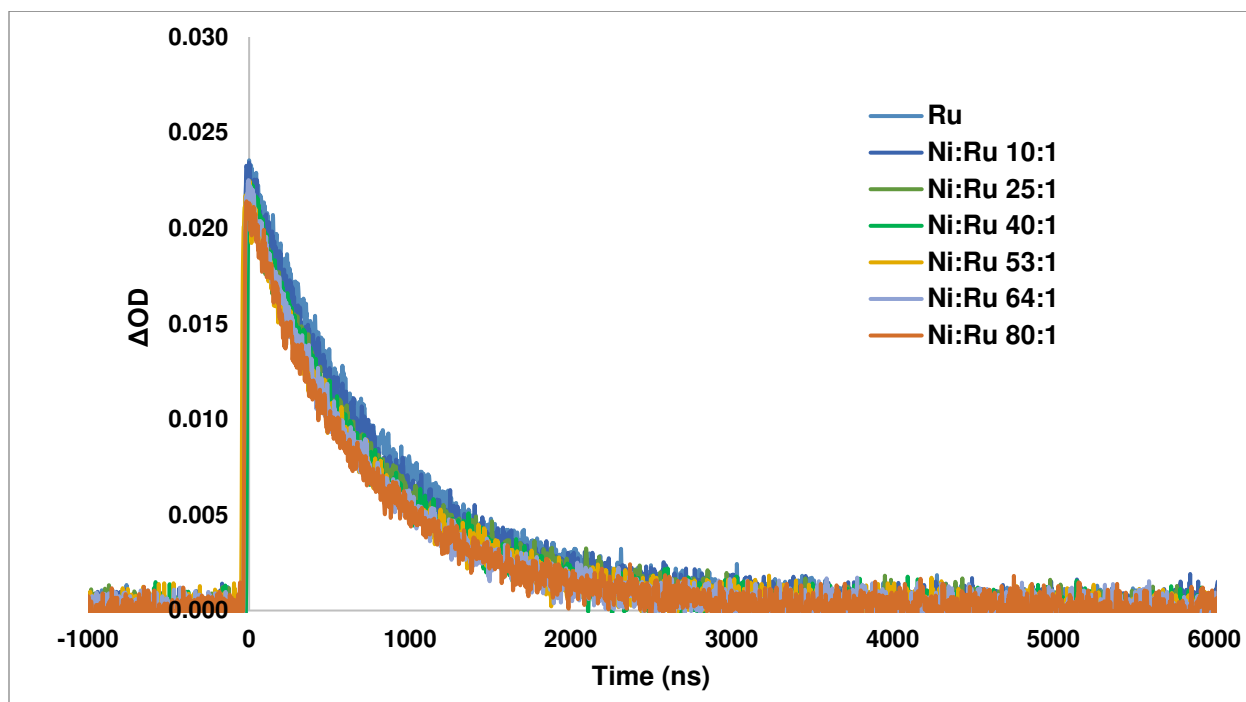


Figure S3.19. Raw kinetic traces of  $[Ru(bpy)_3]Cl_2$  0.1 mM in DMAc with  $\lambda_{pump} = 532$  nm and  $\lambda_{probe} = 450$  nm alone and in the presence of increasing molar ratios of a Ni-propylamine quencher solution (0.008 M in  $NiBr_2 \cdot 3H_2O$ , 0.56 M in propylamine). This data is from a single representative replicate of 3 total repeated experiments.

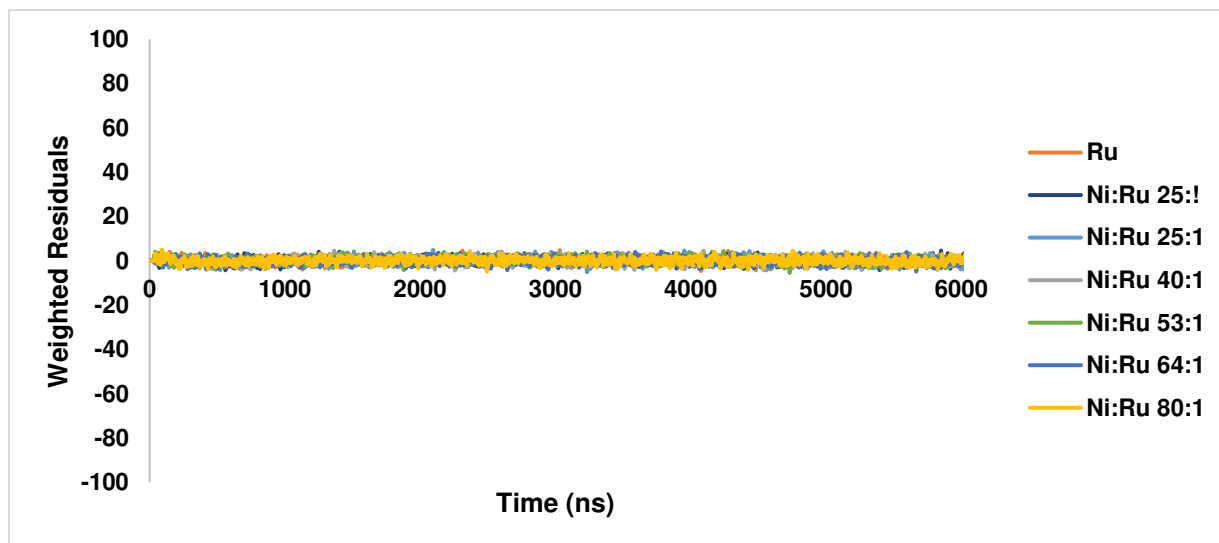


Figure S3.20. Weighted residuals for exponential tail fits of kinetic traces at 450 nm. This data is from a single representative replicate of 3 total repeated experiments.

Table S3.4. Excited state lifetimes of  $[Ru(bpy)_3]Cl_2$  in the presence of different ratios of Ni-propylamine quenching solutions.

Run	Quencher Concentration (M)	Ni:Ru ratio	Tau 450 nm	Tau 370 nm
1	0.0011	10.7:1	774	824
1	0.0025	25.1:1	725	812
1	0.0040	40.0:1	702	746
1	0.0053	53.3:1	660	744
1	0.0064	64.0:1	672	696
1	0.0080	80.0:1	635	714
2	0.0011	10.7:1	790	856
2	0.0025	25.1:1	793	797
2	0.0040	40.0:1	733	815
2	0.0053	53.3:1	746	738
2	0.0064	64.0:1	705	758
2	0.0080	80.0:1	707	703
3	0.0011	10.7:1	836	855
3	0.0025	25.1:1	801	837
3	0.0040	40.0:1	753	781
3	0.0053	53.3:1	752	786
3	0.0064	64.0:1	738	738
3	0.0080	80.0:1	684	737

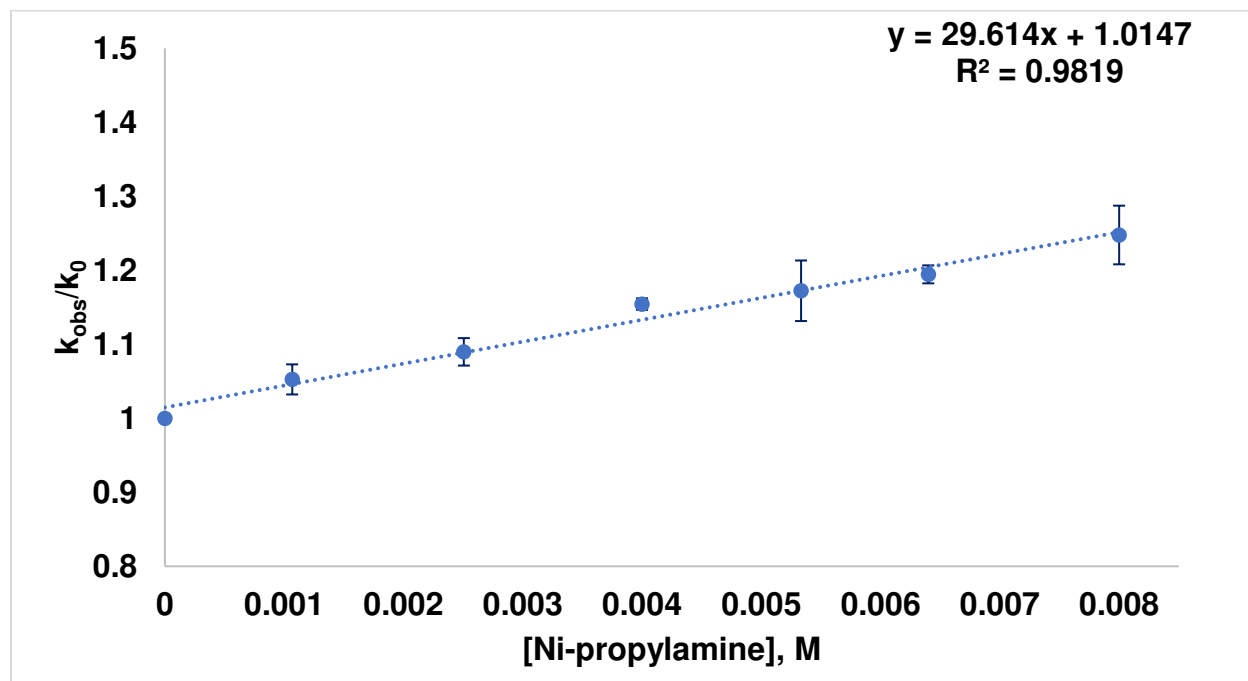


Figure S3.21. Stern-Volmer plot of  $k_{obs}/k_0$  data at  $\lambda_{probe} = 450$  nm, where  $k_{obs}$  is the observed rate constant ( $1/\tau_{obs}$ ) in the presence of quencher and  $k_0$  is the excited state decay rate constant ( $1/\tau_0$ )

of  $[Ru(bpy)_3]Cl_2$  in absence of quencher. Excited state lifetimes used for the plot are given in Table S3. Each plotted data point is the average of 3 replicates and error bars are  $\pm$  standard deviation.

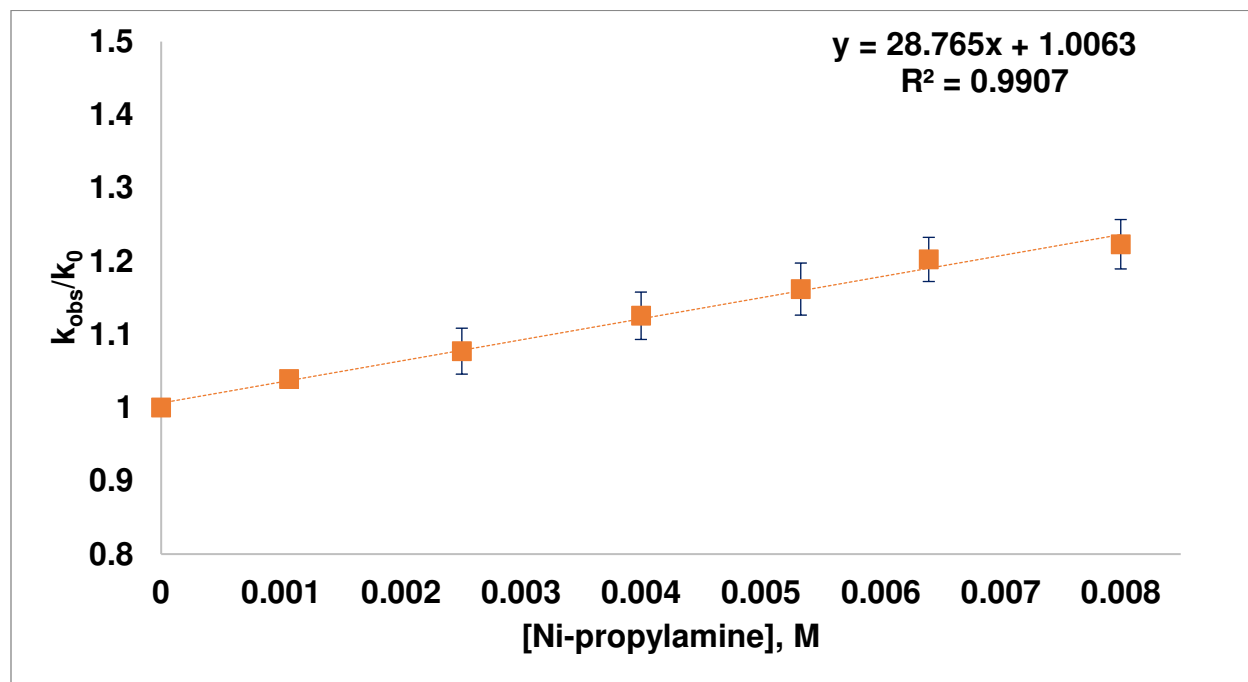


Figure S3.22. Stern-Volmer plot of  $k_{obs}/k_0$  data at  $\lambda_{probe} = 370$  nm, where  $k_{obs}$  is the observed rate constant ( $1/\tau_{obs}$ ) in the presence of quencher and  $k_0$  is the excited state decay rate constant ( $1/\tau_0$ ) of  $[Ru(bpy)_3]Cl_2$  in absence of quencher. Excited state lifetimes used for the plot are given in Table S3. Each plotted data point is the average of 3 replicates and error bars are  $\pm$  standard deviation.

#### Calculation of $k_q$ , the quenching rate constant, for Q = Ni-propylamine mixture.

From the above Stern-Volmer plots (Fig S3.15, S3.16),  $k_q = b/\tau_0$ , (see literature for kinetic derivation of the Stern-Volmer relationship in this context)<sup>3</sup> where b is the slope of the linear regression line. Thus, for Ni-propylamine quenching mixtures:

$$k_q (450 \text{ nm}) = (3.5 \pm 0.4) * 10^7 \text{ M}^{-1} \text{ s}^{-1}, k_q (370 \text{ nm}) = (3.3 \pm 0.2) * 10^7 \text{ M}^{-1} \text{ s}^{-1}.$$

where the reported error is the standard error in the regression coefficient b.<sup>4</sup>

**Controls for PC 2: 3,7-di([1,1'-biphenyl]-4-yl)-10-(naphthalen-1-yl)-10H-phenoxazine**

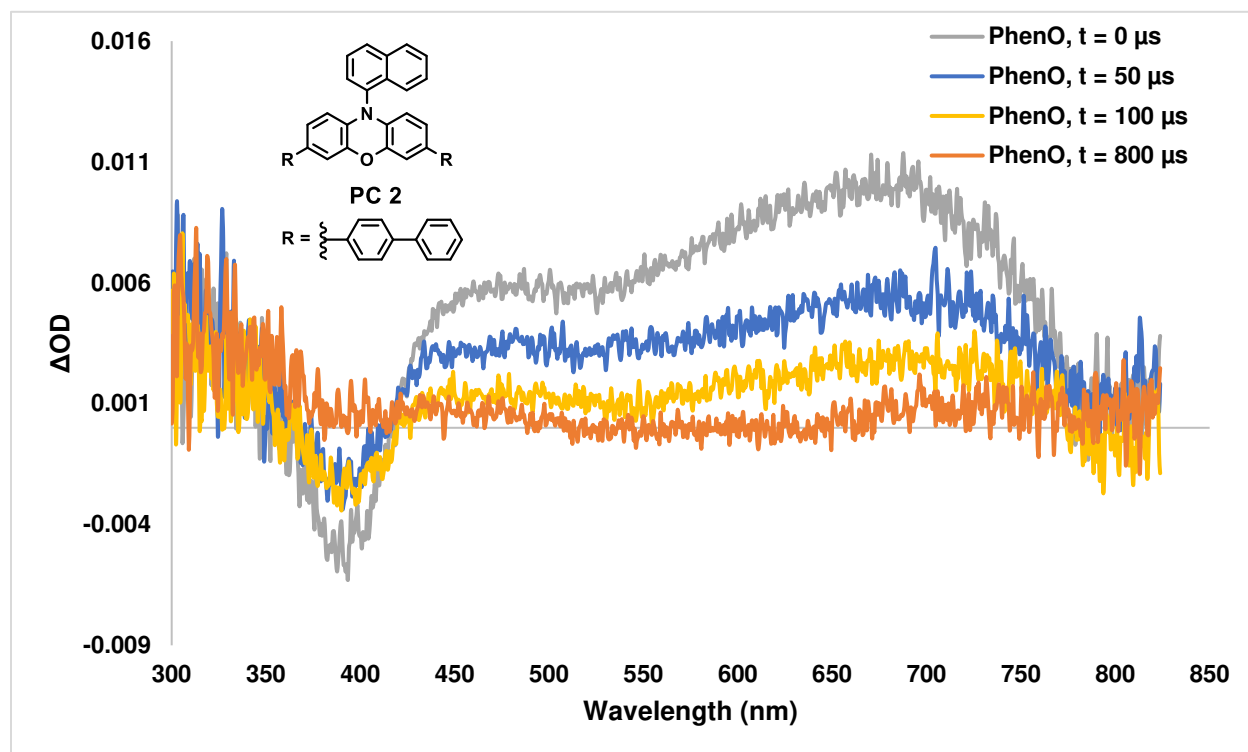


Figure S3.23. Spectral traces acquired for PC 2 ( $10 \mu M$  in DMAc) at various time delays with  $\lambda_{pump} = 355$  nm. The ground state bleach is observed at  $\lambda = 390$  nm along with a broad excited state absorption feature at  $\lambda = 660$  nm. This spectral data matches previously published transient absorption data for PC 2.<sup>6-7</sup> As such, we elected to measure PC 2 in single wavelength kinetics at  $\lambda = 390$  nm and  $\lambda = 660$  nm.

### Single Wavelength Kinetic Data.

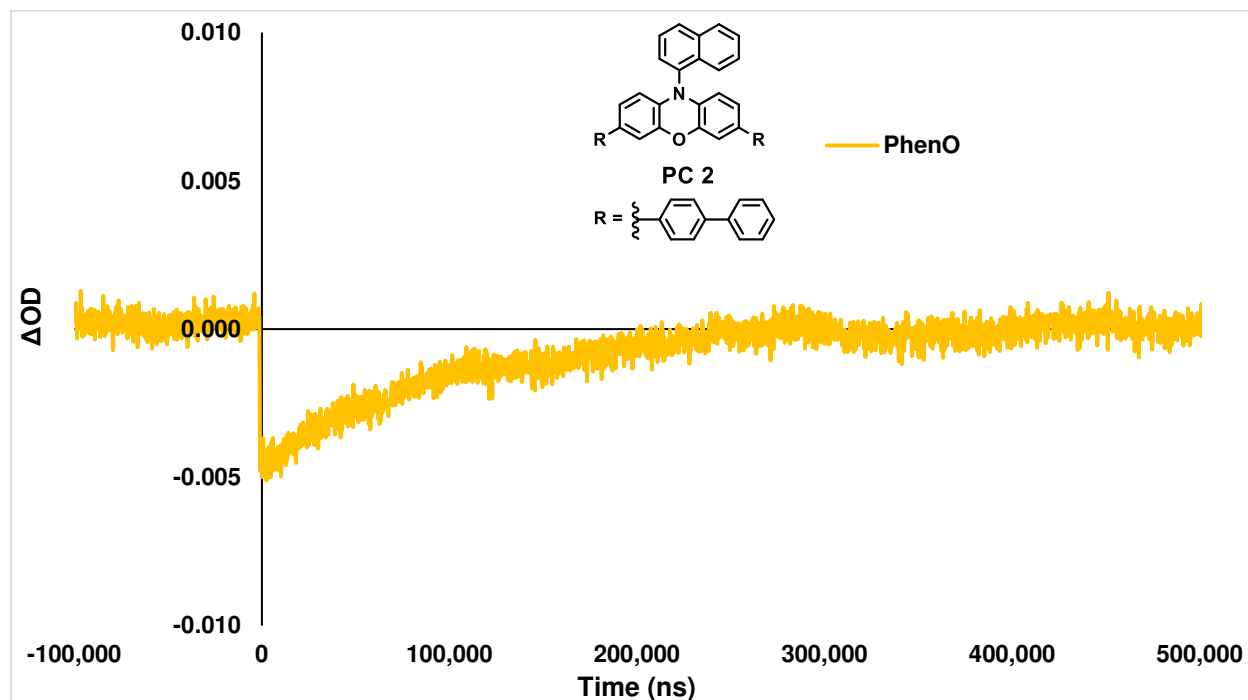


Figure S3.24. Kinetic trace of PC 2 ( $10 \mu\text{M}$  in DMAc) at  $\lambda_{\text{pump}} = 355 \text{ nm}$  and  $\lambda_{\text{probe}} = 390 \text{ nm}$  in absence of quencher.

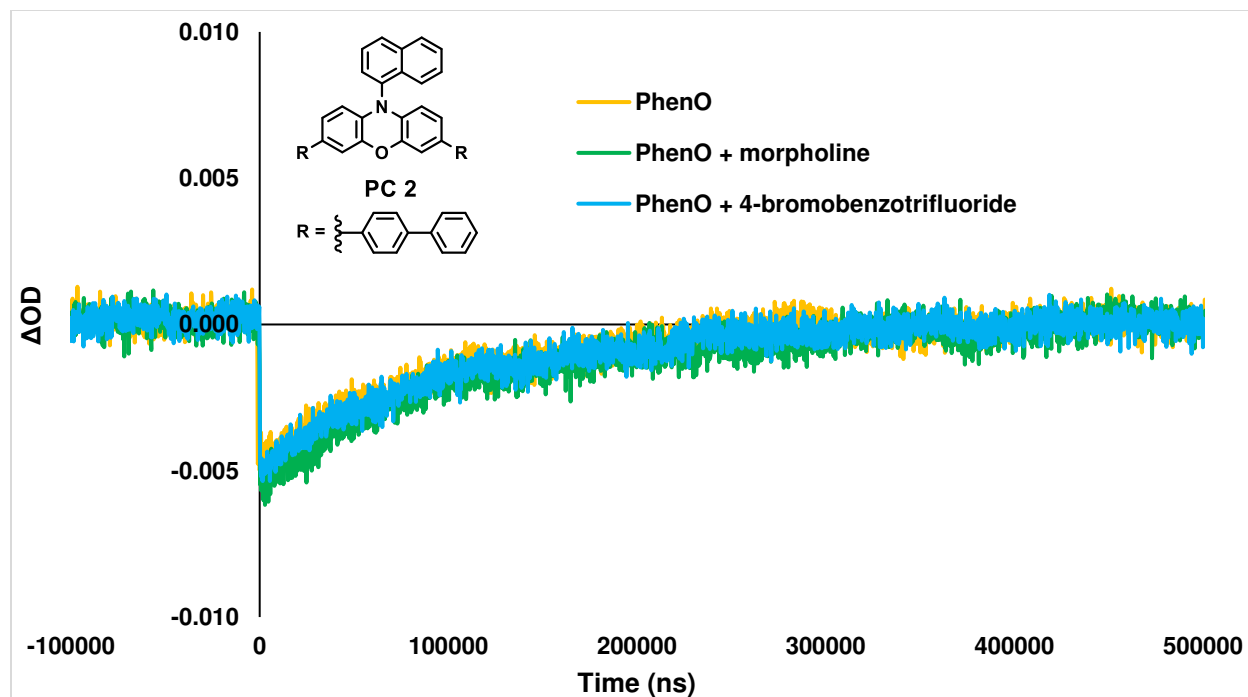


Figure S3.25. Kinetic trace of PC 2 ( $10 \mu\text{M}$  in DMAc) at  $\lambda_{\text{pump}} = 355 \text{ nm}$  and  $\lambda_{\text{probe}} = 390 \text{ nm}$  in the presence of free morpholine as quencher ( $0.056 \text{ M}$ ; 5600:1 morpholine:PhenO) or 4-bromobenzotrifluoride as quencher ( $0.8 \text{ mM}$ ; 80:1 4-bromobenzotrifluoride:PhenO).

Thus, neither 4-bromobenzotrifluoride nor free morpholine quench PC 2.

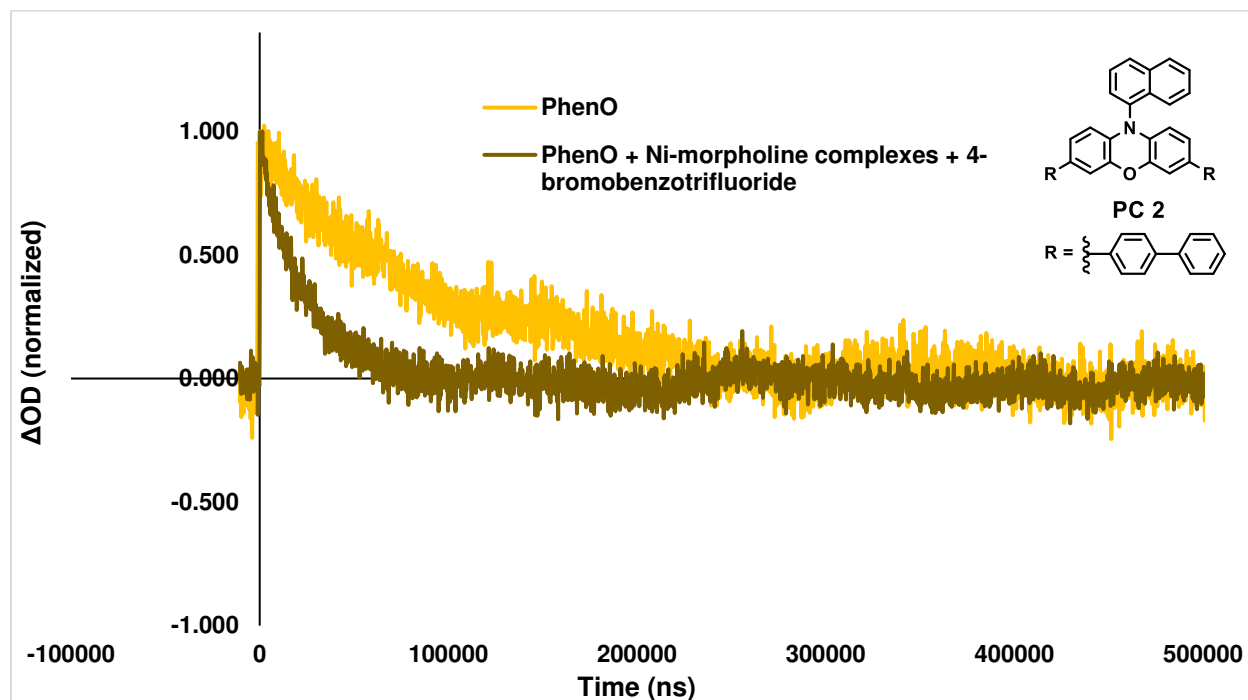


Figure S3.26. Kinetic trace of PC 2 ( $10 \mu\text{M}$  in DMAc) at  $\lambda_{\text{pump}} = 355 \text{ nm}$  and  $\lambda_{\text{probe}} = 390 \text{ nm}$  in the presence of a Ni-morpholine mixture as quencher ( $0.8 \text{ mM}$  in Ni; 80:1 Ni:PhenO) and 4-bromobenzotrifluoride ( $0.8 \text{ mM}$ ; 80:1 4-bromobenzotrifluoride:PhenO). The traces are normalized to signal at  $t = 0$  due to the fact that a slightly higher laser power was needed for the run with quencher (due to absorption by the quencher). Data scaled by  $-1$  to accommodate an exponential fit.

Thus, PC 2 is significantly quenched in the presence of Ni-morpholine complexes and the signal fully returns to baseline at  $\lambda_{\text{probe}} = 390 \text{ nm}$ .

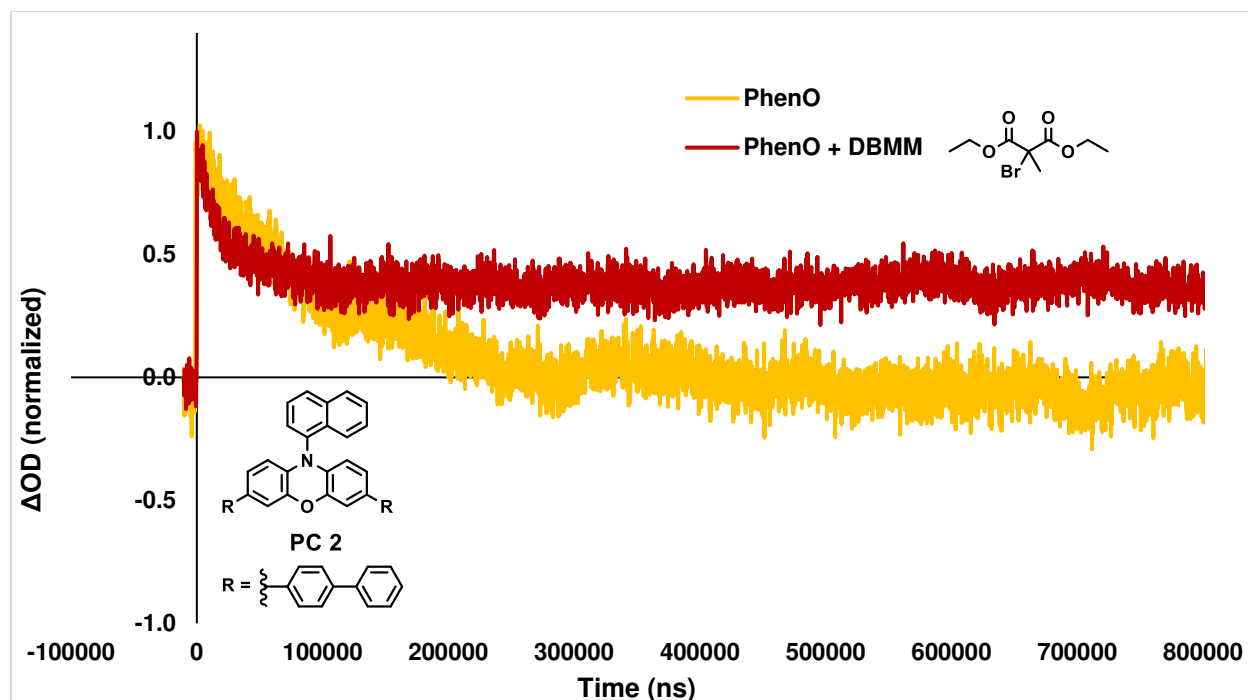


Figure S3.27. Kinetic trace of PC 2 (10  $\mu\text{M}$  in DMAc) at  $\lambda_{\text{pump}} = 355 \text{ nm}$  and  $\lambda_{\text{probe}} = 390 \text{ nm}$  in the presence of diethyl 2-bromo-2-methylmalonate (DBMM) as quencher (0.8 mM; 80:1 DBMM:PhenO). The traces are normalized to signal at  $t = 0$  due to the fact that a slightly higher laser power was needed for the run with DBMM. Data scaled by  $-1$  to accommodate an exponential fit.

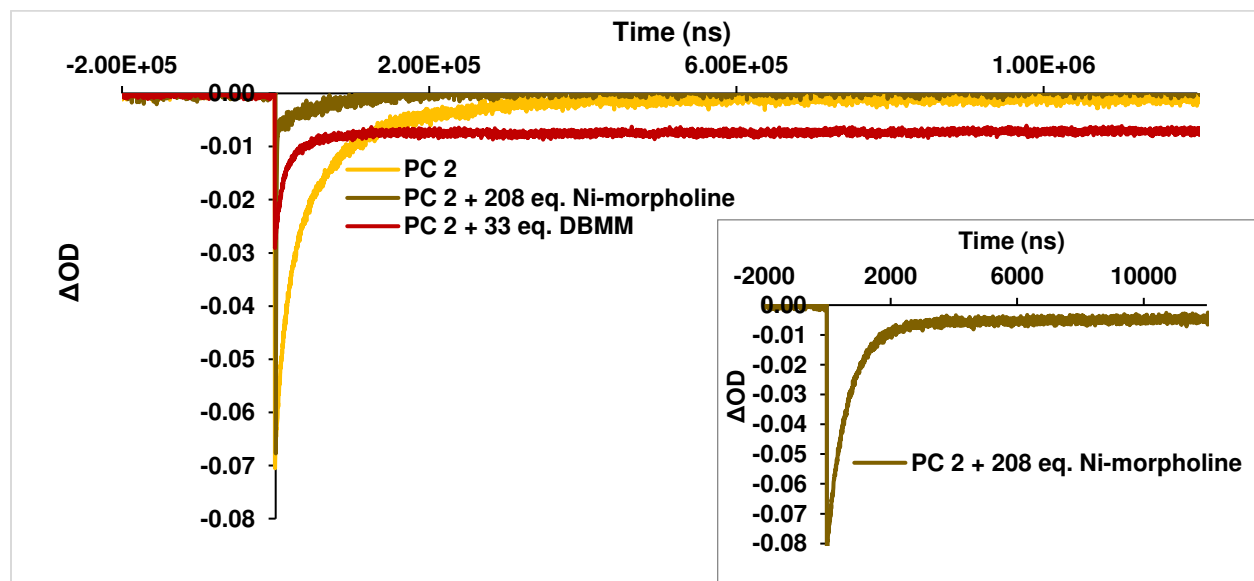


Figure S3.28. High power quenching experiments. Kinetic trace of PC 2 (24  $\mu\text{M}$  in DMAc) at  $\lambda_{\text{pump}} = 355 \text{ nm}$  and  $\lambda_{\text{probe}} = 390 \text{ nm}$  in the presence of diethyl 2-bromo-2-methylmalonate (DBMM) as quencher (0.8 mM; 33:1 DBMM:PhenO) and a Ni-morpholine mixture (5 mM in Ni; 208:1 Ni:PC 2) as quencher. Inset: PC 2 + Ni-morpholine mixture at a shorter timescale at which the initial decay can be observed. Laser power was 5-7 mW.

The runs with DBMM serves as a positive control for electron transfer. Formation of the long-lived radical cation of PC 2 leads to persistence of the GSB signal at  $\lambda = 390$  nm as marked by the failure to return to baseline in 800  $\mu$ s. As such, the full return to baseline in the presence of Ni-morpholine complexes above, in conjunction with significant quenching, is consistent with EnT from the triplet excited state of PC 2 to the Ni complex. We note that the singlet excited state of PC 2 also must be quenched by EnT given the full return to baseline. Even though the singlet is too short-lived to observe in this setup, quenching by ET would lead to the radical cation which is long-lived and therefore can be observed with this setup; this scenario would be marked by a failure to return to the baseline in this experiment. We note that in the high laser power experiment, the second component in the decay of the PC 2 + Ni-morpholine experiment can be assigned to triplet-triplet annihilation, consistent with the full return to baseline in  $\sim 500$   $\mu$ s. Thus, even with a much stronger signal up to 70 mOD, the quenching data is consistent with EnT and ET products were not observed.

#### Kinetic traces at $\lambda = 660$ nm:

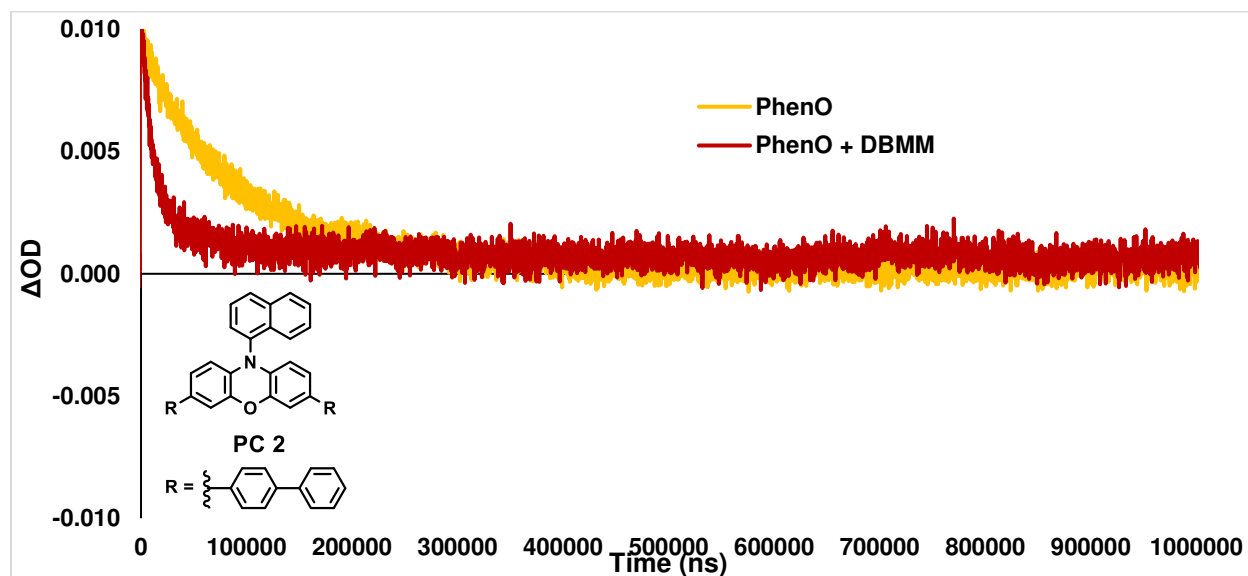


Figure S3.29. Kinetic traces of PC 2 ( $10 \mu\text{M}$  in DMAc) at  $\lambda_{\text{pump}} = 355$  nm and  $\lambda_{\text{probe}} = 660$  nm in the presence of diethyl 2-bromo-2-methylmalonate (DBMM) as quencher ( $0.8$  mM; 80:1 DBMM:PhenO).



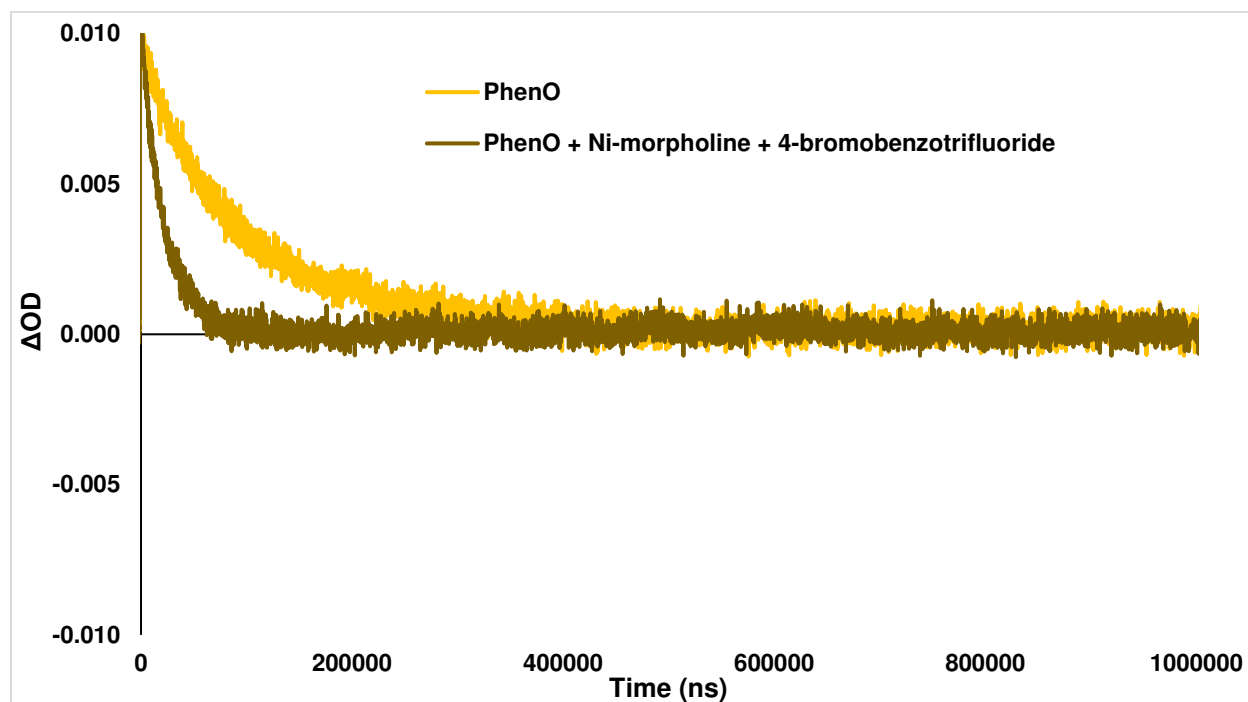


Figure S3.30. Kinetic trace of PC 2 ( $10 \mu\text{M}$  in DMAc) at  $\lambda_{\text{pump}} = 355 \text{ nm}$  and  $\lambda_{\text{probe}} = 660 \text{ nm}$  in the presence of a Ni-morpholine mixture as quencher ( $0.8 \text{ mM}$  in Ni; 80:1 Ni:PhenO) and 4-bromobenzotrifluoride ( $0.8 \text{ mM}$ ; 80:1 4-bromobenzotrifluoride:PhenO).

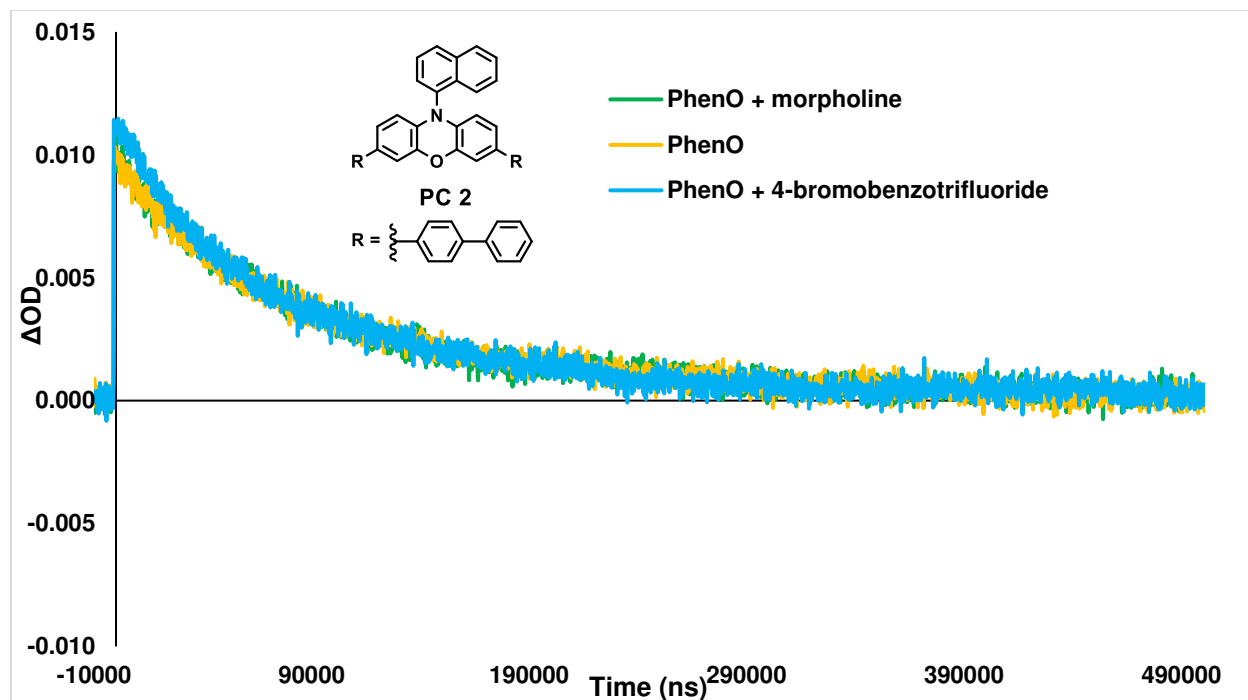


Figure S3.31. Kinetic trace of PC 2 ( $10 \mu\text{M}$  in DMAc) at  $\lambda_{\text{pump}} = 355 \text{ nm}$  and  $\lambda_{\text{probe}} = 660 \text{ nm}$  in the presence of free morpholine as quencher ( $0.056 \text{ M}$ ; 5600:1 morpholine:PhenO) or 4-bromobenzotrifluoride as quencher ( $0.8 \text{ mM}$ ; 80:1 4-bromobenzotrifluoride:PhenO).

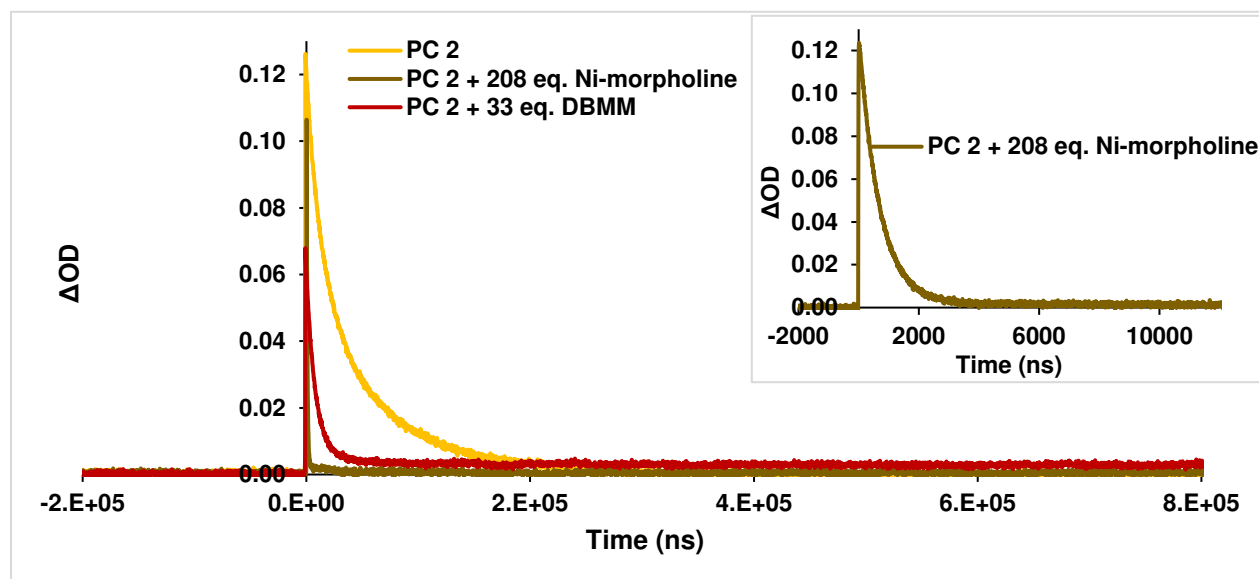


Figure S3.32. High power quenching experiments. Kinetic trace of PC 2 ( $24 \mu\text{M}$  in DMAc) at  $\lambda_{\text{pump}} = 355 \text{ nm}$  and  $\lambda_{\text{probe}} = 660 \text{ nm}$  in the presence of diethyl 2-bromo-2-methylmalonate (DBMM) as quencher ( $0.8 \text{ mM}$ ; 33:1 DBMM:PhenO) and a Ni-morpholine mixture ( $5 \text{ mM}$  in Ni; 208:1 Ni:PC 2) as quencher. Inset: PC 2 + Ni-morpholine mixture at a shorter timescale at which the initial decay can be observed. Laser power was 5-7 mW.

The long-lived component of the spectra is due to competing triplet-triplet annihilation. This component decays to baseline within the 2 ms experimental window and thus cannot belong to a radical cation of PC 2. In the presence of DBMM (known electron transfer quencher of PC 2), the spectra do not return to baseline within this window. Thus, these spectra, in combination with the data at  $\lambda_{\text{probe}} = 390 \text{ nm}$ , are consistent with an EnT quenching event.

### 3. Förster Theory Calculations and Steady State Emission Spectroscopy

If the observed quenching occurs via a Förster type process, then the theoretical rate constant of energy transfer can be obtained from Förster theory:<sup>3</sup>

$$k_{EnT} = k_{r,D} \left( \frac{R_0}{R} \right)^6 \text{ where} \quad (\text{Eq. S3.1})$$

$$R_0^6 = \frac{8.79 \times 10^{-25} \kappa^2 J}{\eta^4} \text{ and} \quad (\text{Eq. S3.2})$$

$$J = \int_0^\infty \frac{F_D(\nu) \epsilon_A(\nu)}{\nu^4} d\nu \quad (\text{Eq. S3.3})$$

In these equations,  $R$  is the donor-acceptor distance,  $R_0$  is the critical Förster distance defined in Eq. S3.2,  $k_{r,D}$  is the radiative decay constant of the donor in absence of acceptor,  $\kappa$  is the dipolar orientation factor,  $\eta$  is the refractive index of the solvent, and  $J$  is the spectral overlap integral defined in Eq. S3.3 which involves  $F_D$ , the area-normalized emission spectrum of the donor, and  $\epsilon_A$ , the molar absorptivity of the acceptor as a function of frequency. These values can be determined experimentally or are known except for  $R$ , since the donor and acceptor are freely tumbling in solution. However, if one considers the case where the donor remains fixed but the acceptor is changed, for example from a Ni-morpholine complex to a Ni-propylamine complex, it can be assumed that  $R_{A1} \approx R_{A2}$ . This assumption appears reasonable since, statistically, the donor and acceptor will diffuse into sufficiently close contact for EnT at about the same distribution of donor-acceptor distances considering that the only structural change is the geometry of the acceptor complex. With this assumption,  $R$  cancels out if we write an expression comparing the energy transfer rates for both acceptors. Further,  $k_{r,D}$  cancels out since the donor is the same in both cases, and we are left with Eq. S3.4.

$$\frac{k_{EnT,A1}}{k_{EnT,A2}} = \frac{k_{r,D} \left( \frac{R_{0,A1}}{R_{A1}} \right)^6}{k_{r,D} \left( \frac{R_{0,A2}}{R_{A2}} \right)^6} = \frac{R_{0,A1}}{R_{0,A2}} \quad (\text{Eq. S3.4})$$

If it is further assumed that the orientation factor for the relevant transition dipoles  $\kappa = 2/3$  in both cases as is commonly done for a freely diffusing donor and acceptor in solution,<sup>3</sup> Eq. S3.4 simplifies to:

$$\frac{R_{0,A1}}{R_{0,A2}} = \frac{\frac{8.79 \times 10^{-25} \kappa^2 J_{A1}}{\eta_{A1}^4}}{\frac{8.79 \times 10^{-25} \kappa^2 J_{A2}}{\eta_{A2}^4}} = \frac{\eta_{A2}^4 J_1}{\eta_{A1}^4 J_2} \quad (\text{Eq. S3.5})$$

A final assumption is made that the free amine only has a minimal impact on the overall refractive index of the solvent such that  $\eta_{A1} = \eta_{A2}$ , and we arrive at the expression:

$$\frac{k_{EnT,A1}}{k_{EnT,A2}} = \frac{J_1}{J_2} \quad (\text{Eq. S3.6})$$

Freely available software, a|e,<sup>8</sup> was used to evaluate the overlap integral  $J$  using spectra shown below. The emission spectrum of the donor is input raw (not normalized) and the software normalizes it to an area = 1. The molar absorptivity spectrum of the acceptor is input in units of  $M^{-1} \text{ cm}^{-1}$ . The software outputs the computed value of  $J$  in units of  $\text{nm}^4 M^{-1} \text{ cm}^{-1}$  which can be converted to units of  $\text{cm}^3 M^{-1}$ . Values used in computed energy transfer rate constant ratios are reported below in Table S3.5.

Alternatively, one can employ a similar derivation in the scenario in which the acceptor remains constant but the donor changes. The assumptions made are the same, except now the rate of radiative decay cannot be cancelled, giving the following expression:

$$\frac{k_{EnT,D1}}{k_{EnT,D2}} = \frac{k_{r,D1} J_1}{k_{r,D2} J_2} \quad (\text{Eq. S3.7})$$

Employing Eq. S6 or Eq. S7, the following values in Table S5 were calculated and compared with results taken from Section 2 (Transient absorption spectroscopy) or the steady state emission quenching experiments in this section.

Table S3.5. Calculated energy transfer rate constant ratios from either Eq. S3.6 or Eq. S3.7 compared with experimental ratios. Experimental values were determined from Stern-Volmer plots by either transient absorption (Ru) or steady-state fluorescence quenching (PhenO). <sup>a</sup>the singlet excited state, <sup>1</sup>[PC 2]\*, serves as the donor given that experimental values were determined from emission quenching, and the emissive state has previously been identified<sup>7</sup> as a singlet with lifetime  $\tau = 5.2$  ns in DMAc at room temperature. <sup>b</sup>The values of the radiative rate constant were obtained from the literature<sup>6</sup> for PC 2,  $k_{r,D1} = 4 * 10^6$  s<sup>-1</sup> or, for PC 1, calculated from the published radiative quantum yield<sup>9</sup> of  $\Phi = 0.095$  using the excited state lifetime data in Section 2.

Parameter	Donor	Acceptor	Value (calc.)	Value (exp.)
$J_1$	<sup>3</sup> [Ru(bpy) <sub>3</sub> ]Cl <sub>2</sub> *	Ni-morpholine	$4.4 * 10^{-16}$ cm <sup>3</sup> M <sup>-1</sup>	N/A
$J_2$	<sup>3</sup> [Ru(bpy) <sub>3</sub> ]Cl <sub>2</sub> *	Ni-propylamine	$9.4 * 10^{-17}$ cm <sup>3</sup> M <sup>-1</sup>	N/A
$J_1$	<sup>1</sup> PhenO-1N-Biph* <sup>a</sup>	Ni-morpholine	$2.4 * 10^{-16}$ cm <sup>3</sup> M <sup>-1</sup>	N/A
$k_{r,D1}$	<sup>1</sup> PhenO-1N-Biph* <sup>a</sup>	N/A	$4 * 10^6$ s <sup>-1</sup>	N/A
$k_{r,D2}$	<sup>3</sup> [Ru(bpy) <sub>3</sub> ]Cl <sub>2</sub> *	N/A	$1 * 10^5$ s <sup>-1</sup>	N/A
$k_{EnT,A1}/k_{EnT,A2}$	<sup>3</sup> [Ru(bpy) <sub>3</sub> ]Cl <sub>2</sub> *	A1: Ni-morpholine A2: Ni-propylamine	4.6	6.5
$k_{EnT,D1}/k_{EnT,D2}$	D1: <sup>1</sup> PhenO-1N-Biph* <sup>a</sup> D2: <sup>3</sup> [Ru(bpy) <sub>3</sub> ]Cl <sub>2</sub> *	Ni-morpholine	20.4 <sup>b</sup>	12.7

Notably, these ratios match the experimental values reasonably well (within a factor of 3 in both cases). This agreement supports a Förster type energy transfer quenching event and is consistent with agreement to Förster theory reported in other systems. For example, agreement to theoretical values that was within a factor of 3 was reported in a system involving a multinuclear transition metal complex performing intramolecular energy transfer.<sup>10</sup> We speculate that the larger difference between calculated and experimental values in the calculation comparing PhenO and Ru may be due to a difference in the dipolar orientation factors between the two PCs and the Ni-morpholine complexes.

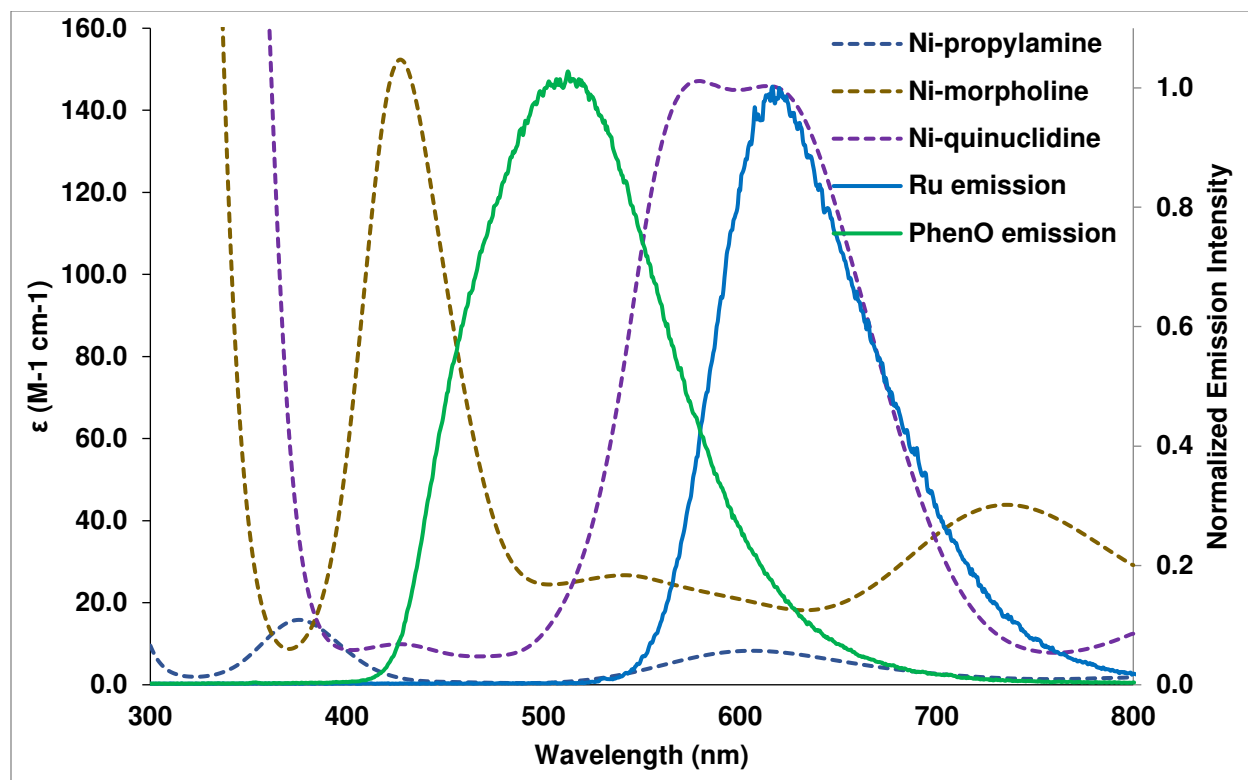


Figure S3.33. Spectral overlap between Ru and PhenO PCs and either Ni-morpholine, Ni-quinuclidine, or Ni-propylamine at concentration used in C–N cross coupling reactions (e.g., 20 mM in Ni). Normalized (to highest peak) emission spectra were acquired via time-resolved emission scans at  $t = 0$  utilizing the transient absorption spectrometer setup described above with the ICCD camera as detector. Molar absorptivities were calculated point by point from absorbance spectra using Beer's law. Ru PC =  $[\text{Ru}(\text{bpy})_3]\text{Cl}_2$ ; PhenO PC = 3,7-di([1,1'-biphenyl]-4-yl)-10-(naphthalen-1-yl)-10H-phenoxazine.

### Steady-State Emission Spectroscopy.

A Spectrofluorometer FS5 (Edinburgh Instruments) was used for all measurements. Corrected emission spectra were recorded with the same excitation and emission slit sizes of 4.5 and 3.5 nm, respectively, and an integration time of 0.25 seconds was used for all quenching measurements.

Stern-Volmer Quenching Experiments. Stock solutions were prepared as follows. For the Ni + PC stock solution,  $\text{NiBr}_2 \cdot 3\text{H}_2\text{O}$  (54.5 mg, 0.2 mmol) was weighed out in the glove box into a 10 mL volumetric flask, removed, and 2 mL of DMAc was immediately added. After stirring for 30 minutes in a water bath at 40°C, morpholine (1.208 mL, 1.4 mmol) was then added to the

volumetric flask containing the fully dissolved Ni solution. A solution containing the phenoxazine PC dissolved in DMAc (9.8 mg, 0.8 mM, 10 mL) was prepared. After stirring for 30 minutes in a water bath at 40°C, 5 mL of this solution was added to the volumetric flask containing the Ni-morpholine mixture and 5 mL was added to a second empty volumetric flask. Both flasks were then filled to the line with DMAc to complete the stock solutions. Stock solutions were then mixed to produce 3 mL of the following 6 mixtures which were then analyzed by UV-vis and emission spectroscopy:

Mixture #	Ni-morpholine + PhenO Stock (mL)	PhenO Stock (mL)
1	0	3
2	0.6	2.4
3	1.2	1.8
4	1.8	1.2
5	2.4	0.6
6	3	0

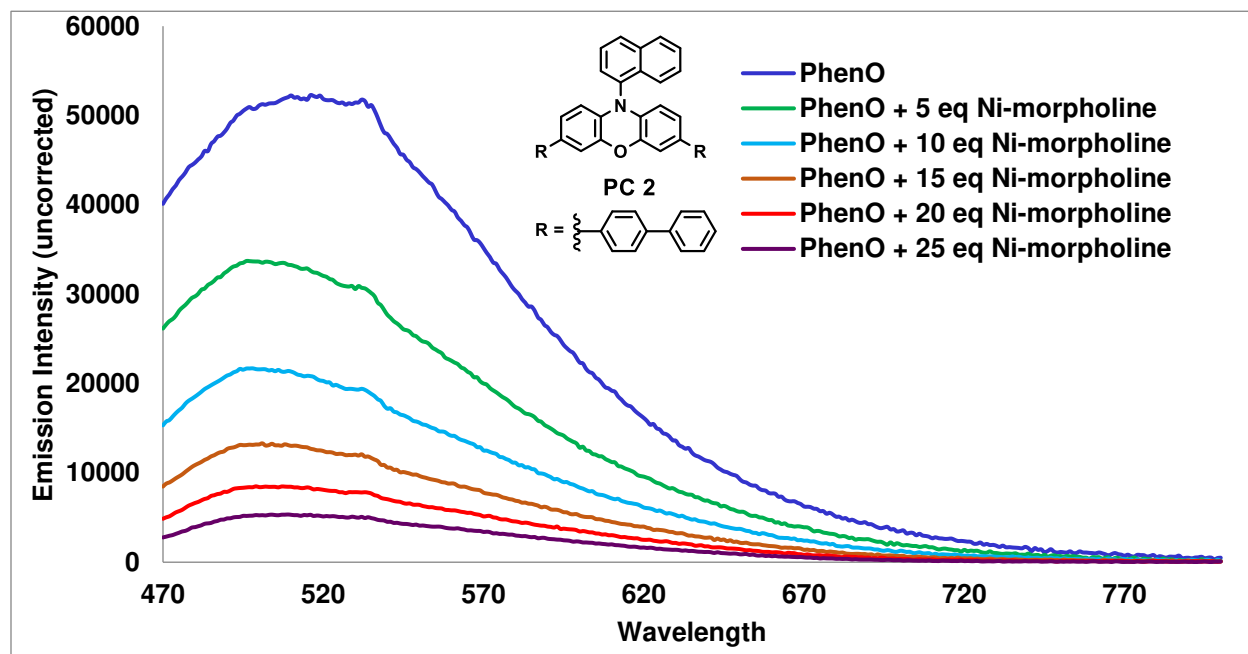


Figure S3.34. Example of one replicate of the raw emission data for the Stern-Volmer quenching of PhenO PC 2 by Ni-morpholine complexes. Sample mixtures were made as described above and

the emission wavelength was scanned while keeping the excitation wavelength constant at 460 nm to be consistent with the blue light excitation used in C-N cross coupling reactions.

Since Ni-amine complexes can absorb excitation light as well as emitted light, a correction for primary and secondary inner-filter effects was. The mathematical correction given by Lakowicz<sup>11</sup> was applied:  $I_{corr} = I_{raw} * 10^{\left(\frac{A_{ex} + A_{em}}{2}\right)}$ , where  $I_{corr}$  is the corrected emission intensity,  $I_{raw}$  is the raw emission intensity,  $A_{ex}$  is the absorption of the sample at the excitation wavelength, and  $A_{em}$  is the absorption of the sample at the emission wavelength. This correction was applied to intensity data for all wavelengths scanned.

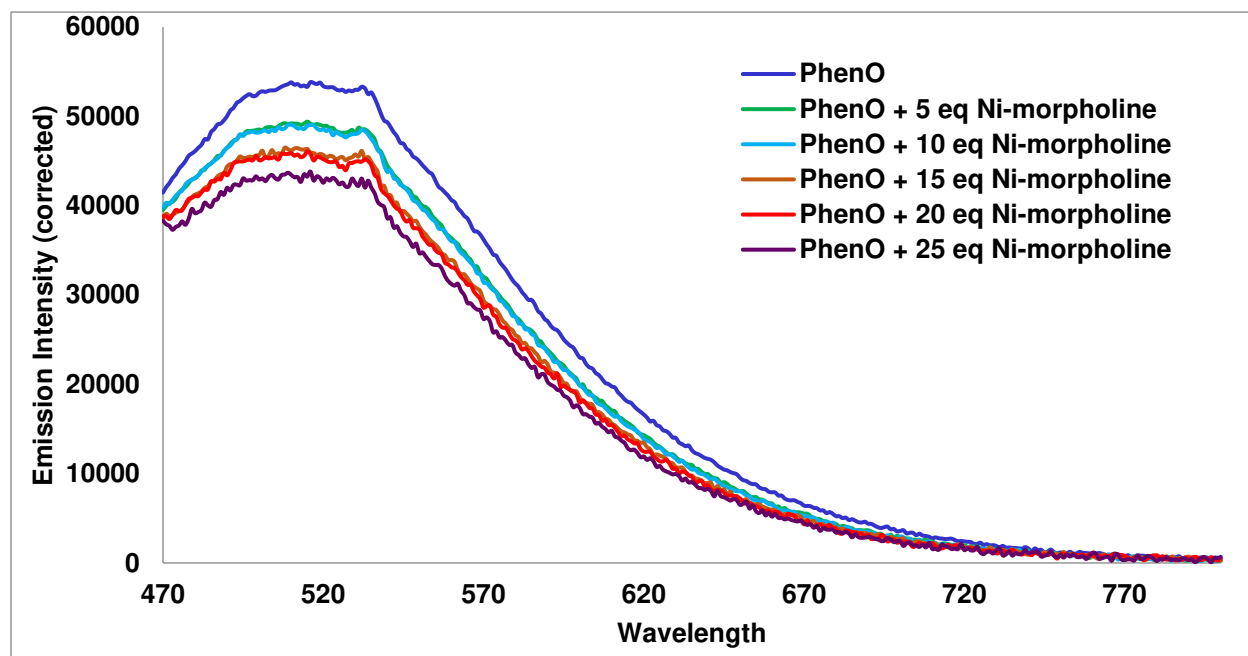


Figure S3.35. Emission spectra for the same replicate shown above, corrected for inner-filter effects.

A Stern-Volmer plot was created by repeating the experiment 3 times and plotting the average corrected emission intensity ( $I_{0,corr}$ ) of the PC divided by the average emission intensity of the PC in the presence of quencher ( $I_{corr}$ ) vs. the concentration of the quencher.



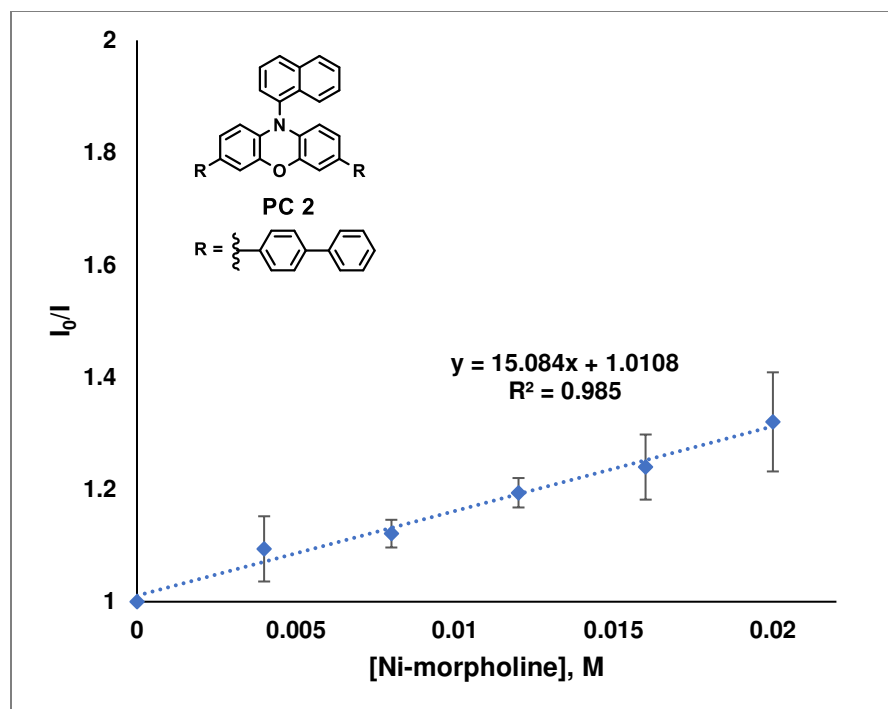


Figure S3.36. Stern-Volmer plot for quenching of the phenoxazine PC (3,7-di([1,1'-biphenyl]-4-yl)-10-(naphthalen-1-yl)-10H-phenoxazine) by Ni-morpholine complexes. Error bars are standard deviation of 3 replicates.

The quenching rate constant was calculated as follows:

$$k_q = \frac{b}{\tau_{\text{PhenO}}} = (2.9 \pm 0.2) * 10^9 \text{ M}^{-1} \text{ s}^{-1}, \text{ where } b \text{ is the slope of the Stern-Volmer plot}$$

linear regression line,  $\tau_{\text{PhenO}}$  is the singlet excited state lifetime of the PhenO PC, and the reported error is the standard error in the regression coefficient  $b$ .<sup>4</sup>

#### 4. Cyclic Voltammetry

General procedure. In an electrochemical cell consisting of a Pt working electrode, a Pt wire counter electrode, and an Ag/AgNO<sub>3</sub> reference electrode (silver wire, Vycor frit, 0.01 M AgNO<sub>3</sub> in DMAc), an analyte solution in DMAc containing dissolved Bu<sub>4</sub>NPF<sub>6</sub> (0.1 M) electrolyte was probed utilizing a potentiostat (Gamry Instruments) to perform cyclic voltammetry. All reported experiments were performed at a 100 mV/s scan rate. Where viable, ferrocene was utilized as an internal standard. In the case of Ni-amine mixtures and free amines, presence of amine

prohibited internal use of ferrocene, so ferrocene was also evaluated separately. Potentials in figures below are vs. Ag/AgNO<sub>3</sub>.

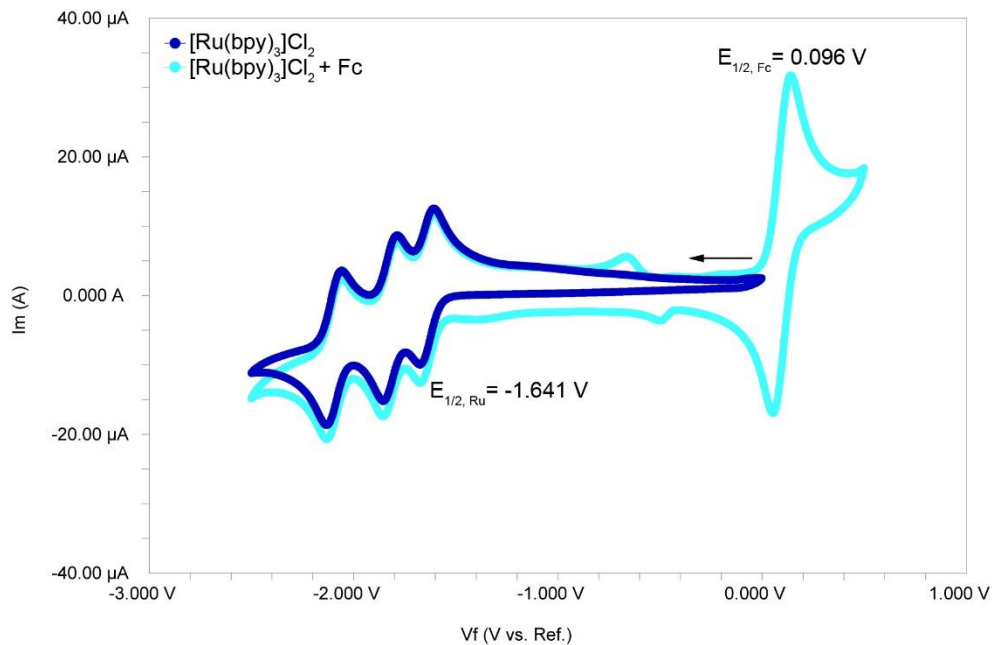


Figure S3.37. CV of  $[Ru(bpy)_3]Cl_2$  (1 mM in DMAc) and  $[Ru(bpy)_3]Cl_2$  + ferrocene (1 mM in DMAc). Potentials vs. Ag/AgNO<sub>3</sub>.

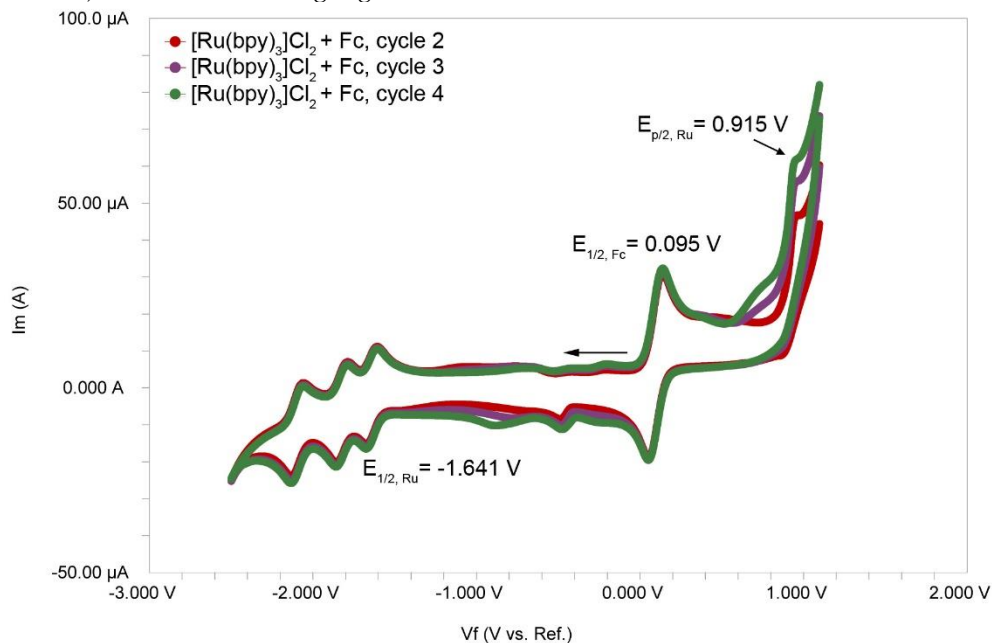


Figure S3.38. CV of  $[Ru(bpy)_3]Cl_2$  (1 mM in DMAc) + ferrocene (1 mM in DMAc) over several cycles. Potentials vs. Ag/AgNO<sub>3</sub>.

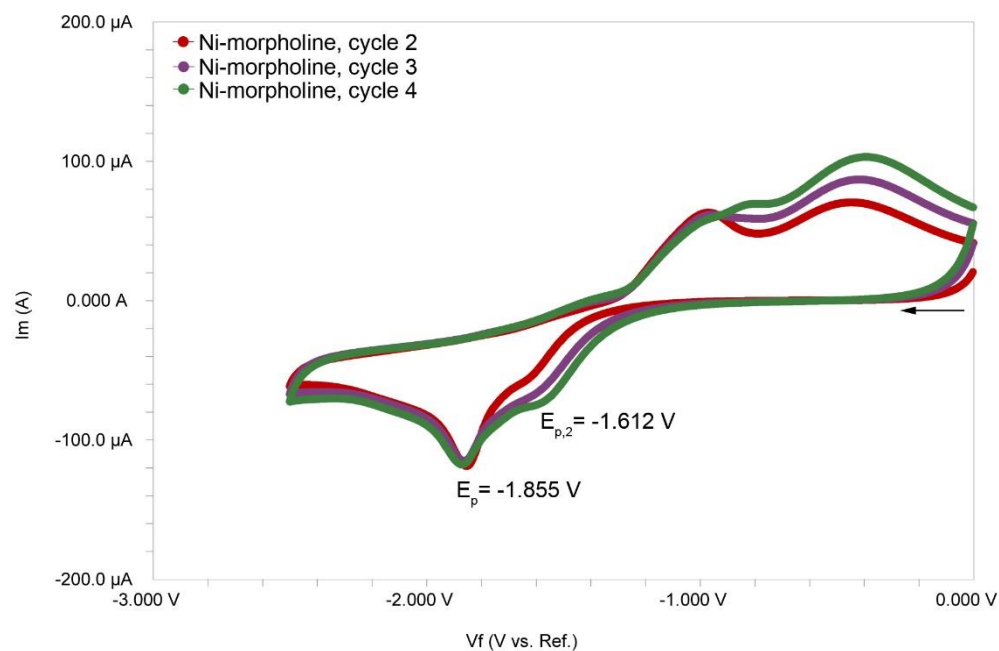


Figure S3.39. CV of a Ni-morpholine mixture in DMAc (8 mM in Ni, 0.56 M in morpholine) over several cycles at 100 mV/s. Potentials vs. Ag/AgNO<sub>3</sub>.

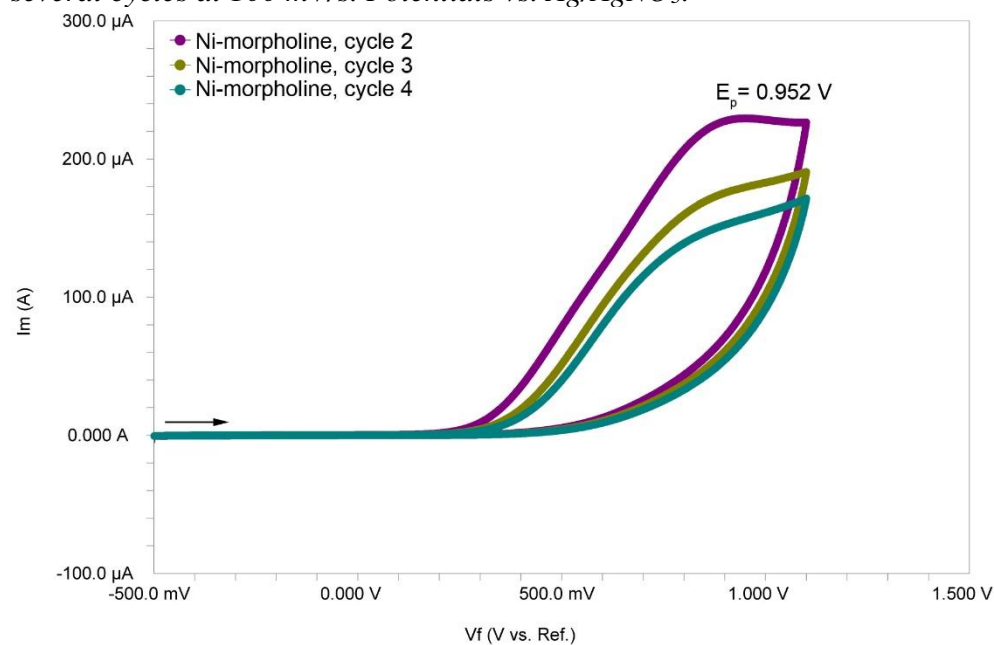


Figure S3.40. CV of a Ni-morpholine mixture in DMAc (8 mM in Ni, 0.56 M in morpholine) over several cycles at 100 mV/s. Potentials vs. Ag/AgNO<sub>3</sub>.

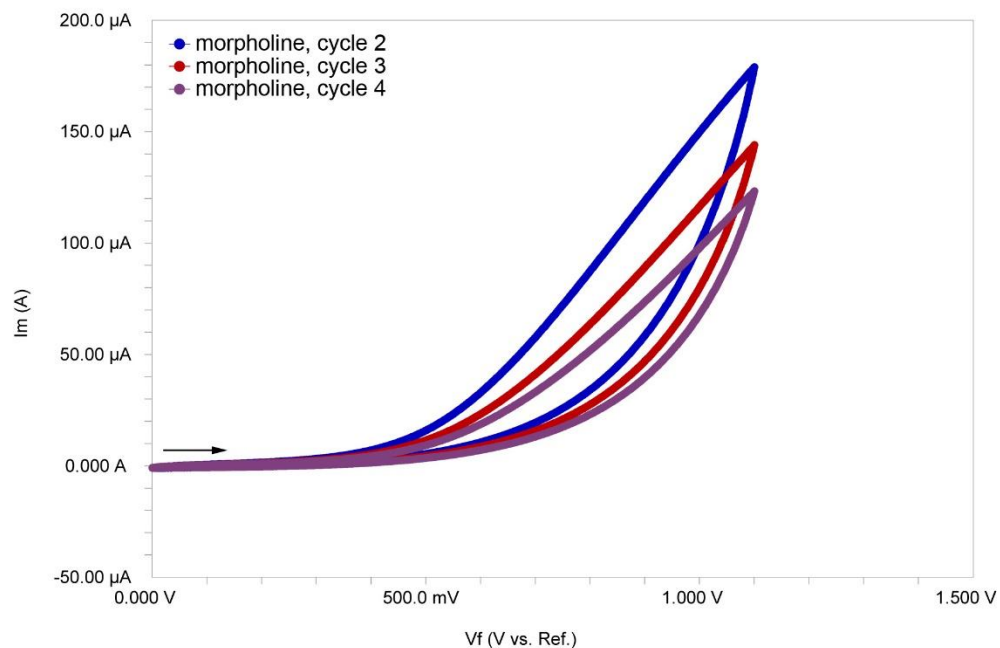


Figure S3.41. CV of morpholine (0.56 M) over several cycles at 100 mV/s. Potentials vs. Ag/AgNO<sub>3</sub>.

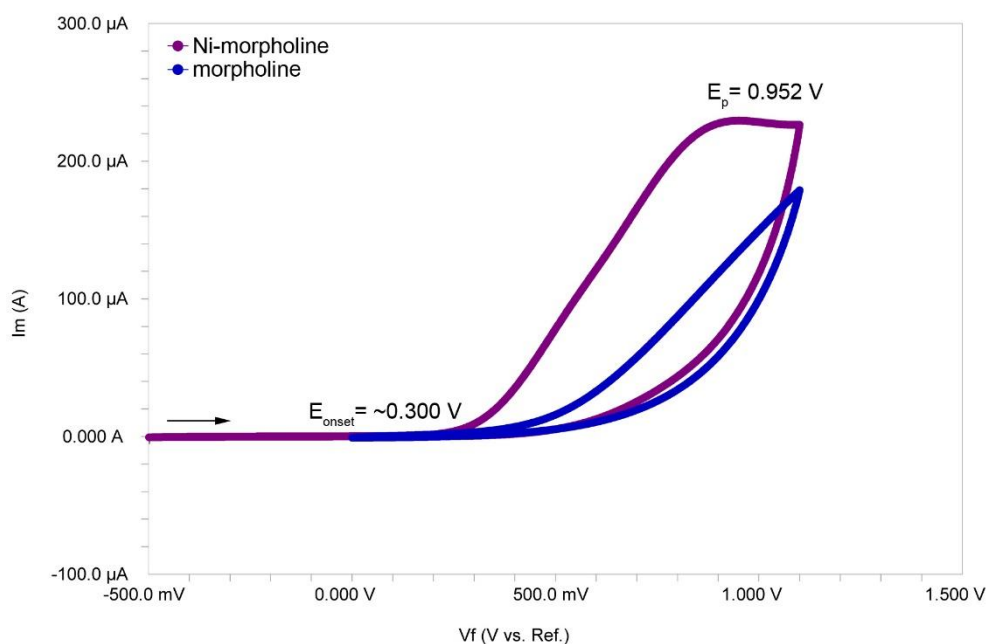


Figure S3.42. Traces from above 2 plots overlaid for the Ni-morpholine mixture and free morpholine in DMAc. Potentials vs. Ag/AgNO<sub>3</sub>.

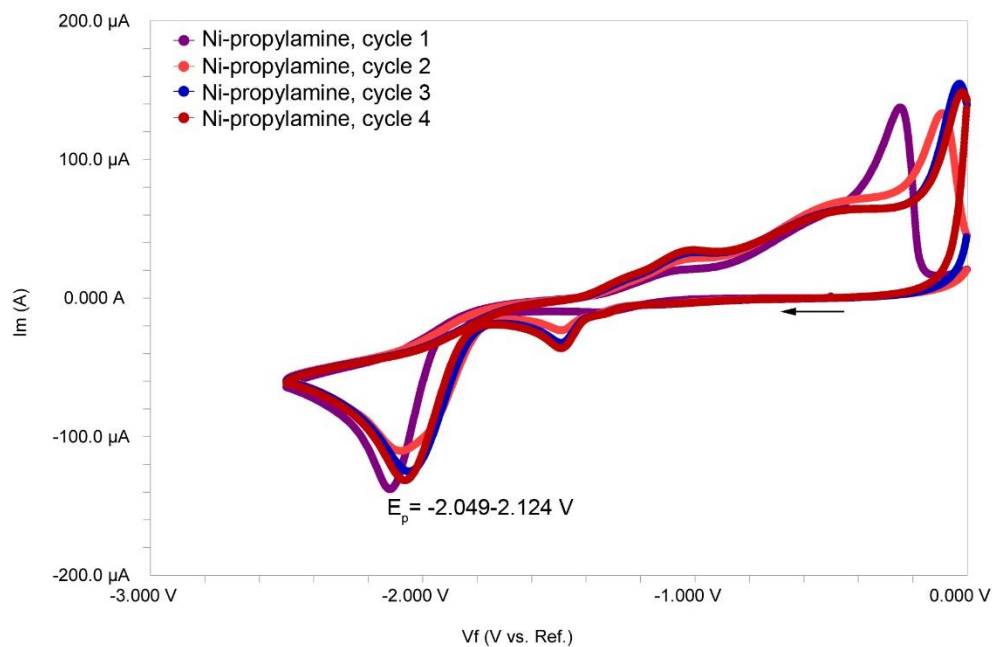


Figure S3.43. CV of a Ni-propylamine mixture in DMAc (8 mM in Ni, 0.56 M in propylamine) over several cycles at 100 mV/s. Potentials vs. Ag/AgNO<sub>3</sub>.

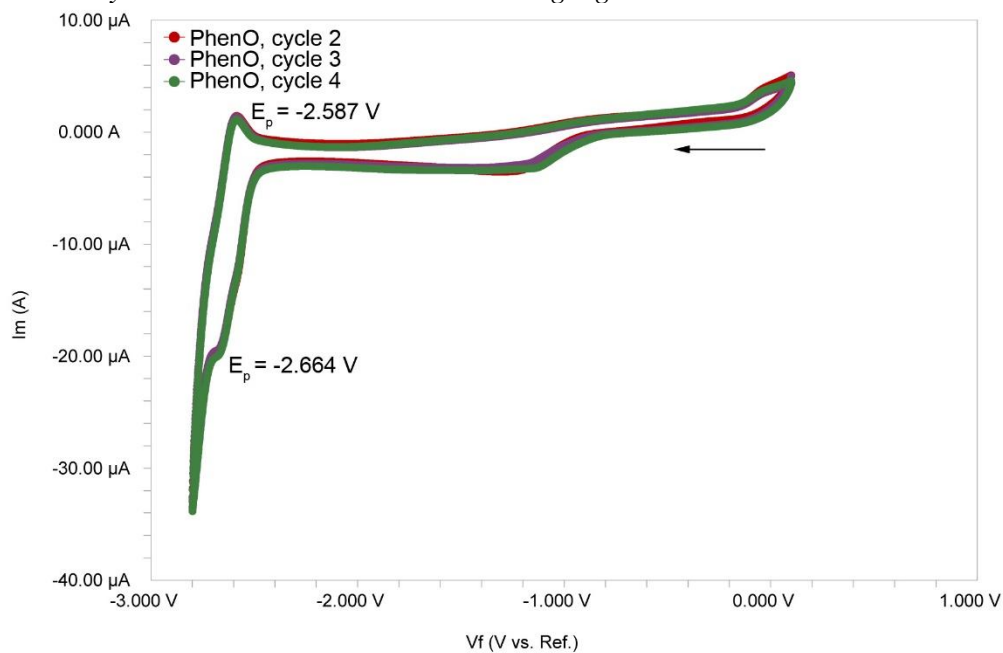


Figure S3.44. CV of phenoxazine PC 2 in DMAc (1 mM). Potentials vs. Ag/AgNO<sub>3</sub>.

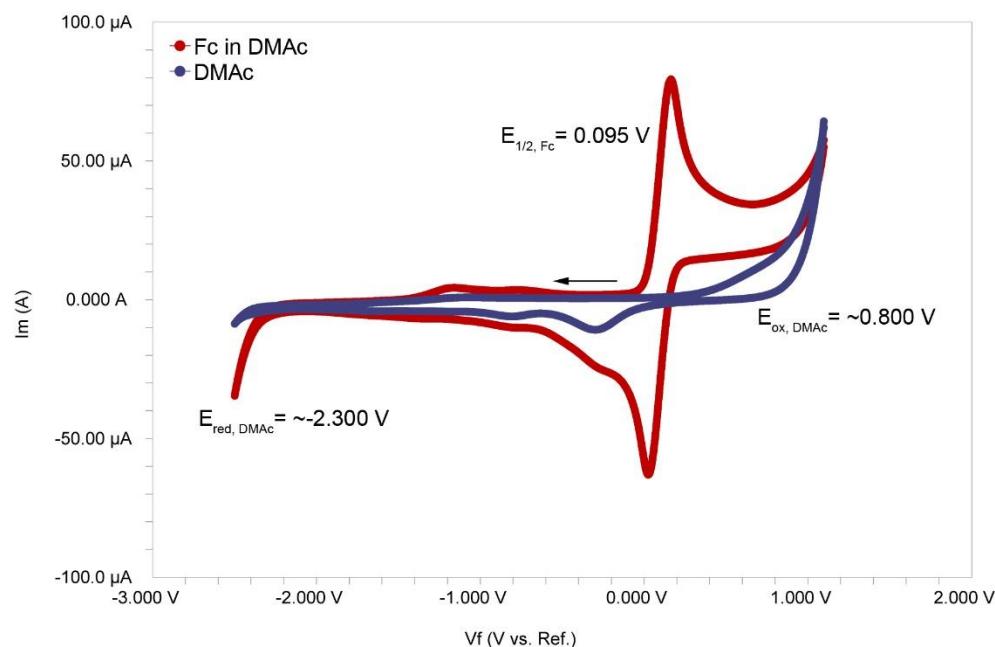


Figure S3.45. Solvent window of DMAc and CV of ferrocenium (5 mM in DMAc). Potentials vs. Ag/AgNO<sub>3</sub>.

Table S3.6. Measured potentials of various species in DMAc. <sup>a</sup>literature conversion value<sup>12</sup> used for Fc/Fc<sup>+</sup> vs. SCE in DMF. <sup>b</sup>calculated from phosphorescence  $\lambda_{max} = 617$  nm in DMAc. <sup>c</sup>Not observed within the DMAc + electrolyte window. Ref = referenced value. <sup>d</sup>calculated from fluorescence  $\lambda_{max} = 510$  nm in DMAc.

Redox Couple	Potential (V vs. Fc/Fc <sup>+</sup> )	Potential (V vs. SCE) <sup>a</sup>
[Ru(bpy) <sub>3</sub> ] <sup>2+</sup> /[Ru(bpy) <sub>3</sub> ] <sup>+</sup>	$E_{1/2} = -1.74$	-1.29; Ref: -1.33 (MeCN) <sup>13</sup>
[Ru(bpy) <sub>3</sub> ] <sup>2+</sup> /[Ru(bpy) <sub>3</sub> ] <sup>3+</sup>	$E_{1/2} = 0.82$	1.27; Ref: 1.29 (MeCN) <sup>13</sup>
[Ru(bpy) <sub>3</sub> ] <sup>*2+</sup> /[Ru(bpy) <sub>3</sub> ] <sup>+</sup>	0.27 <sup>b</sup>	0.72; Ref: 0.77 (MeCN) <sup>13</sup>
[Ru(bpy) <sub>3</sub> ] <sup>*2+</sup> /[Ru(bpy) <sub>3</sub> ] <sup>3+</sup>	-1.19 <sup>b</sup>	-0.74; Ref: -0.81 (MeCN) <sup>13</sup>
PhenO/PhenO <sup>-</sup>	$E_{p/2} = -2.71$	$E_{p/2} = -2.26$
<sup>1</sup> PhenO*/PhenO <sup>-</sup>	-0.28 <sup>d</sup>	0.17 <sup>d</sup>
<sup>1</sup> PhenO*/PhenO <sup>+</sup>	-2.18 <sup>6</sup>	-1.73 <sup>6</sup>
morpholine/morpholine <sup>-</sup>	Not observed <sup>c</sup>	Not observed <sup>c</sup>
morpholine/morpholine <sup>+</sup>	Onset at ~-0.40	Onset at ~-0.85
[NiBr <sub>2</sub> (morpholine) <sub>n</sub> ]/[NiBr <sub>2</sub> (morpholine) <sub>n</sub> ] <sup>-</sup> n = 2 or 3	$E_p = -1.95$ $E_p = -1.71$	$E_p = -1.50$ $E_p = -1.26$
[NiBr <sub>2</sub> (morpholine) <sub>n</sub> ]/[NiBr <sub>2</sub> (morpholine) <sub>n</sub> ] <sup>+</sup> n = 2 or 3	$E_p \approx 0.86$ $E_{p/2} \approx 0.48$	$E_p \approx 1.31$ $E_{p/2} \approx 0.93$
[NiBr <sub>2</sub> (propylamine) <sub>4</sub> ]/[NiBr <sub>2</sub> (propylamine) <sub>4</sub> ] <sup>-</sup>	$E_p = -2.05$	$E_p = -1.65$
[NiBr <sub>2</sub> (propylamine) <sub>4</sub> ]/[NiBr <sub>2</sub> (propylamine) <sub>4</sub> ] <sup>+</sup>	Not observed <sup>c</sup>	Not observed <sup>c</sup>

## Redox Argument, PC 1.

Based on the measured potentials in DMAc, two possible ET quenching scenarios can be explored. In the first, the excited state PC,  $[\text{Ru}(\text{bpy})_3]^{1*2+}$ , reduces a component of the Ni-morpholine quenching mixture to produce the oxidized PC,  $\text{Ru}(\text{bpy})_3^{3+}$ . From UV-vis titration studies of the Ni-morpholine mixture (See section below), the only species available in appreciable concentration are  $[\text{NiBr}_2(\text{morpholine})_3]$ ,  $[\text{NiBr}_2(\text{morpholine})_2]$ , and free morpholine. The least negative reduction potential of these species was observed at  $-1.71 \text{ V vs. Fc/Fc}^+$ , while  $E^{0*}([\text{Ru}(\text{bpy})_3]^{*2+}/[\text{Ru}(\text{bpy})_3]^{3+}) = -1.19 \text{ V vs. Fc/Fc}^+$  was measured in this work for oxidative quenching of the PC. Thus, oxidative quenching is highly unlikely on thermodynamic grounds.

Alternatively, in the case of reductive quenching,  $[\text{Ru}(\text{bpy})_3]^{*2+}$  is reduced to  $[\text{Ru}(\text{bpy})_3]^+$ , with a potential measured in this work as  $E^{0*}([\text{Ru}(\text{bpy})_3]^{*2+}/[\text{Ru}(\text{bpy})_3]^+) = 0.27 \text{ V vs. Fc/Fc}^+$ . The most concentrated species in the mixture is free morpholine (e.g., 0.56 M) and its oxidation is observed at  $E_{\text{onset}} \approx 0.40 \text{ V vs. Fc/Fc}^+$ . Further, free morpholine did not quench  $[\text{Ru}(\text{bpy})_3]^{*2+}$  in TA spectroscopy experiments (See section 2). The first Ni-amine complex oxidation occurs at  $E_{p/2} \approx 0.48 \text{ V vs. Fc/Fc}^+$ . Therefore, based on the observed potentials,  $[\text{Ru}(\text{bpy})_3]^{*2+}$  is unlikely to oxidize the Ni-morpholine complex, the species in the mixture with the lowest oxidation potential.

Further,  $[\text{Ru}(\text{bpy})_3]^+$  would be characterized by persistence of the  $\lambda_{\text{pump}} = 370 \text{ nm}$  signal. We observed a high signal:noise ratio at that detection wavelength, and the signal did not persist and fully decayed to baseline (See section 2 for details). As such, while we cannot exclude the possibility of a contribution from a reductive quenching pathway with a fast back ET, the observed potentials suggest that an ET pathway is unlikely. As such, we conclude that the scenario most

supported by the spectral and electrochemical data is quenching of  $[\text{Ru}(\text{bpy})_3]^{*2+}$  by energy transfer to a Ni-amine complex.

### **Redox Argument, PC 2.**

PC 2 is a potent excited state reductant with  $E^{0*}({}^1\text{PhenO}^*/\text{PhenO}^{*\cdot}) = -1.73 \text{ V vs. SCE}$ . Thus, while single electron reduction of a Ni-morpholine complex (easiest to reduce =  $-1.26 \text{ V vs. SCE}$ ) is feasible thermodynamically, the resultant radical cation was not observed spectroscopically in TA experiments. The radical cation is stable and long-lived and can be detected in our setup as indicated by the positive control reaction in which PC 2 reduces diethyl 2-bromo-2-methylmalonate (DBMM). As such, if quenching by ET does occur with Ni-morpholine complexes, it must be a minor enough contributor to avoid detection.

Alternatively, reductive quenching is thermodynamically unfavorable. Reduction of the ground state PC 2 occurs at  $E_{\text{red}}({}^1\text{PhenO}/\text{PhenO}^{\cdot-}) = -2.26 \text{ V vs. SCE}$ . Thus, the excited state oxidation potential is  $E^{0*}({}^1\text{PhenO}/\text{PhenO}^{\cdot-}) = 0.17 \text{ V vs. SCE}$ . As such, PC 2 is extremely unlikely to oxidize any species present from its excited state by a large margin.

Based on the electrochemical data herein, the only probable ET event is that of oxidative quenching to form the radical cation of PC 2 which was not observed in TA experiments. Therefore, we conclude that the most likely mechanistic quenching step is EnT from excited state PC 2 to a Ni-amine complex.



## 5. Single Crystal X-ray Diffraction

Crystals were stored in mother liquor until the time of mounting. Crystals grown under air were removed from the mother liquor using high vacuum grease or Paratone-N oil and placed into a drop of Paratone-N oil on a glass slide. Vacuum grease was removed by physical manipulation within the Paratone-N oil and a single crystal was selected and attached to the goniometer head with the aid of a dissection microscope (Leica) at 45X magnification or a polarizing microscope (Zeiss) at 80X magnification. The crystal was placed into a stream of N<sub>2</sub> gas precooled to 100-130 K. Data were collected at this temperature using a Bruker D8 Quest ECO with Mo k<sub>α</sub> radiation and a Photon 50<sup>TM</sup> CMOS detector. Crystals grown under N<sub>2</sub> were removed from the crystallization vessel in the glove box or on Schlenk lines under N<sub>2</sub> using a spatula with Paratone-N oil on the tip and placed into a drop of Paratone-N oil on a glass slide. The glass slide was removed from the glove box and data collection proceeded as above. In all cases, data analysis was performed using Bruker APEX 3 software. Please see attached .cif files for crystallographic details. Each of the following procedures has been repeated at least 1 additional time, and the identity of new batches of crystals was verified by XRD analysis through solving a 1 hour phi scan ( $2\theta = 20^\circ$ , Sweep =  $180^\circ$ ). Crystals used for solid-state UV-vis were also verified in this way.

### **[NiBr<sub>2</sub>(morpholine)<sub>3</sub>].**

A flame-dried 50 mL Schlenk flask equipped with a stir bar was brought into the glove box. 100 mg (0.324 mmol) of NiBr<sub>2</sub>.glyme was weighed out and transferred to the flask. This red-orange powder was dissolved in 3 mL of anhydrous DMAc to form a dark teal solution and the flask was sealed with a septum and brought out of the glove box. 70 eq anhydrous morpholine (relative to Ni, 22.68 mmol, 1.957 mL) was added under N<sub>2</sub> on Schlenk lines via a degassed syringe to form a dark brown solution. 15 mL of anhydrous toluene was then layered on top of the solution

with a degassed syringe. The flask was sealed with a septum, the puncture holes were sealed with electrical tape, and it was placed in the freezer at  $-20\text{ }^{\circ}\text{C}$ . After 4 months, dark yellow-brown crystals were observed. The crystal structure includes a disordered toluene molecule which was omitted in the main text for clarity.

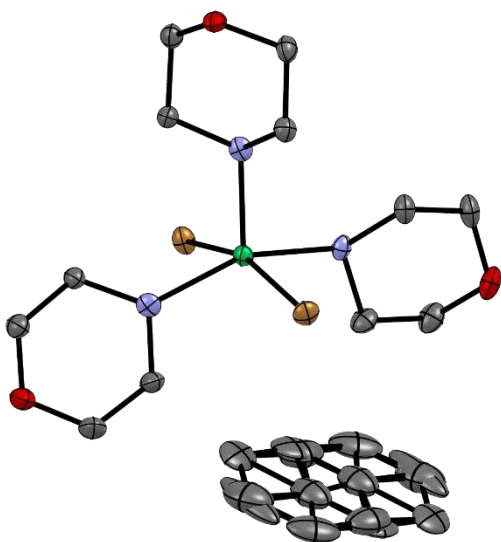


*Figure S3.46. Crystal structure of  $[\text{NiBr}_2(\text{morpholine})_3]$  shown at 50% thermal ellipsoids. Hydrogens omitted for clarity. See .cif file for crystallographic details.*

### **$[\text{NiBr}_2(\text{quinuclidine})_2]$ .**

In the glovebox, 200 mg of  $\text{NiBr}_2$  (anhydrous, 1.012 mmol) was weighed out into a 20 mL scintillation vial charged with a stir bar. 2 mL DMAc (anhydrous) was added to the vial. Quinuclidine (228.9 mg, 2.059 mmol) was weighed into another scintillation vial. After stirring overnight, both vials were capped with septa, sealed with electrical tape, and removed from the glove box. The Ni solution was sonicated for 30 minutes. Caps were removed and the Ni solution was syringe filtered through a  $0.45\text{ }\mu\text{m}$  filter. 1.5 mL of this solution was added by micropipette to the quinuclidine under air. Immediately, a royal blue solution formed and very small royal blue crystals formed in the vial that were suitable for XRD.

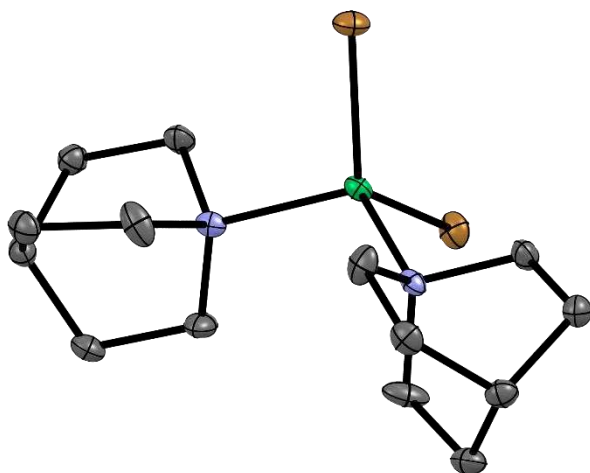


Figure S3.47. Crystal structure of  $[\text{NiBr}_2(\text{quinuclidine})_2]$  shown at 50% thermal ellipsoids. Hydrogens omitted for clarity. See .cif file for crystallographic details.

#### **$[\text{NiBr}_2(\text{cyclohexylamine})_4]$ .**

A C–N cross coupling reaction was performed in which 5.4 mg  $\text{NiBr}_2 \cdot 3\text{H}_2\text{O}$  (0.02 mmol) was dissolved in 0.323 mL DMAc in the glove box in a 0.5 dram vial charged with a stir bar. To this solution was added 0.500 mL of a solution of 3,7-Di(4-biphenyl) 1-naphthalene-10-phenoxazine (0.008 mmol) in DMAc. 0.056 mL 4-bromobenzotrifluoride was added (0.4 mmol). The vial was sealed with electrical tape, brought out of the glove box, and 0.160 mL cyclohexylamine (degassed, 1.4 mmol) was added through the septum cap with a degassed Hamilton syringe. The completed mixture was irradiated with a 457 nm blue LED for 22 hours and the reaction went to 84% yield by  $^{19}\text{F}$  NMR. 3 days later, light green transparent plate-like crystals were observed in the crude reaction mixture that were suitable for X-ray diffraction.

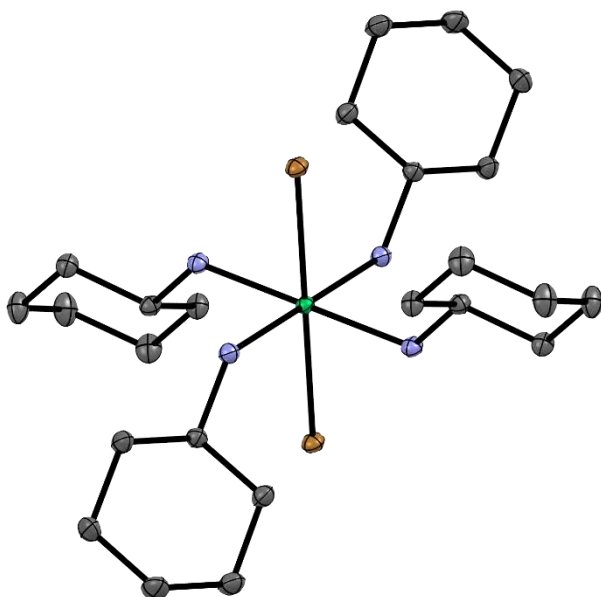


Figure S48. Crystal structure of  $[\text{NiBr}_2(\text{cyclohexylamine})_4]$  shown at 50% thermal ellipsoids. Hydrogens omitted for clarity. See .cif file for crystallographic details.

#### **$[\text{NiBr}_2(\text{aniline})_4]$ .**

In the glove box, 100 mg of  $\text{NiBr}_2 \cdot 3\text{H}_2\text{O}$  (0.367 mmol) was weighed out into a 20 mL scintillation vial containing a stir bar and dissolved in 1 mL anhydrous DMAc to form a dark teal solution. This solution was sealed with a septum, wrapped in electrical tape, and removed from the glove box. Aniline (25.68 mmol, 2.34 mL, degassed by sparging with  $\text{N}_2$ ) was added via degassed syringe and stirred to form a dark green solution. Toluene (8 mL, anhydrous) was layered on top of the aniline solution via syringe. Punctures were sealed with electrical tape. After several days at room temperature, emerald green crystals were obtained. This complex was also grown from  $\text{NiBr}_2 \cdot \text{glyme}$  and its identity was confirmed by solving a 1 hour XRD phi scan.

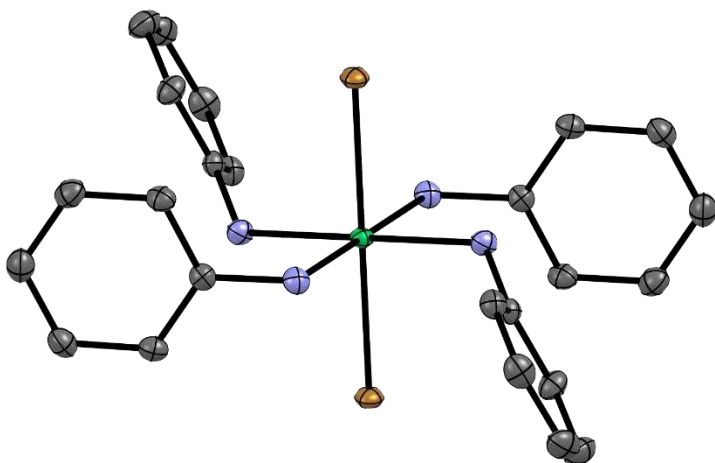


Figure S49. Crystal structure of  $[\text{NiBr}_2(\text{aniline})_4]$  shown at 50% thermal ellipsoids. Hydrogens omitted for clarity. See .cif file for crystallographic details.

#### **$[\text{NiBr}_2(\text{propylamine})_4]$ .**

In the glove box, 100 mg  $\text{NiBr}_2 \cdot 3\text{H}_2\text{O}$  (0.367 mmol) was weighed out into a 20 mL scintillation vial equipped with a stir bar. Outside the glove box, the Ni was dissolved in 1 mL DMAc to form a dark teal solution. Propylamine (25.68 mmol, 2.11 mL) was then added with stirring. Stirring was stopped and 8 mL toluene was carefully added via a 1 mL micropipette. Due to the low density of propylamine, the toluene layered underneath, causing mixing. A blue powder crashed out overnight, was filtered, dried, and 95 mg of teal powder was recovered. The 95 mg of teal powder was wetted with propylamine, restoring a dark blue color, dissolved in 1 mL DMAc, and 1 mL toluene was layered on top. This mixture was kept at room temperature. After 4 days, it had fully mixed and no crystals formed. 2 more mL of toluene was layered on top on day 5. 2 more mL toluene was layered on top on day 8 and day 10. On day 12, 3 more mL toluene was added for a total of 10 mL toluene. Large transparent teal crystals formed that were suitable for XRD.

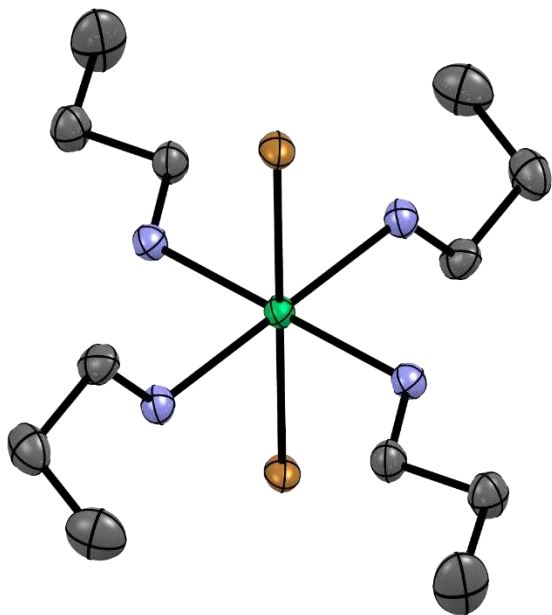


Figure S3.50. Crystal structure of  $[\text{NiBr}_2(\text{propylamine})_4]$  shown at 50% thermal ellipsoids. Hydrogens omitted for clarity. See .cif file for crystallographic details.

**$[\text{Ni}(\text{DMAc})_6][\text{NiBr}_4]$ . DMAc = N,N-dimethylacetamide.**

In the glove box, 100 mg  $\text{NiBr}_2 \cdot 3\text{H}_2\text{O}$  (0.367 mmol) was dissolved in 1 mL anhydrous DMAc in a scintillation vial. The vial was capped with a septum, sealed with electrical tape, and removed from the glove box. Anhydrous toluene (8 mL) was layered via degassed syringe on the DMAc solution. The puncture was sealed with electrical tape and the vial was stored at room temperature. Large dark blue/teal crystals formed after 3 days.

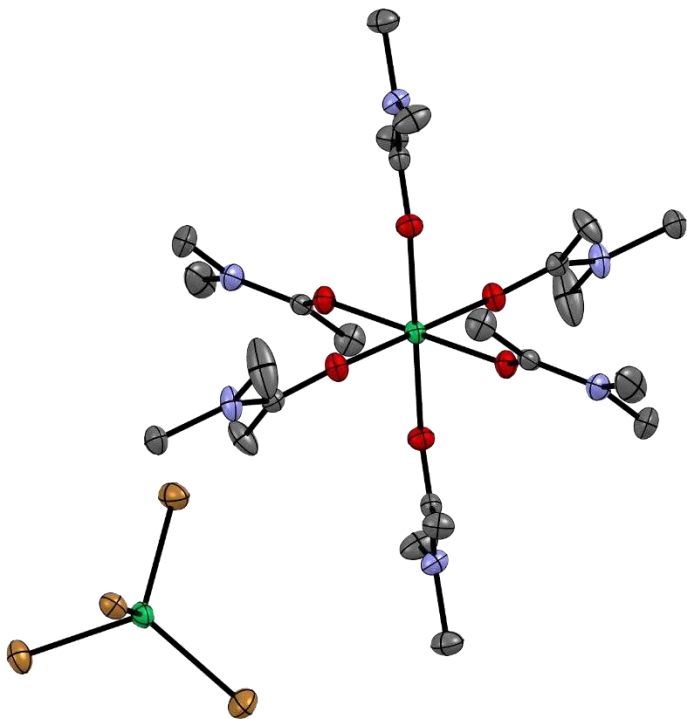


Figure S3.51. Crystal structure of  $[\text{Ni}(\text{DMAC})_6][\text{NiBr}_4]$  shown at 50% thermal ellipsoids . Hydrogens omitted for clarity. See .cif file for crystallographic details.

## 6. UV-Visible Spectroscopy in Solution

UV-visible spectroscopy was performed on a Cary 5000 instrument (Agilent) with either the standard liquid cell holder and a 1 cm path length quartz cuvette or the standard solid sample holder. In all cases, the ultraviolet, visible, and near infrared lamps were allowed to warm up for 30 minutes before recording data. Background correction was performed for all runs utilizing a solvent blank (> 99.5 % purity DMAc) in the case of liquid samples. For solids, a glass microscope slide was used as the blank.

TA before/after control spectra.

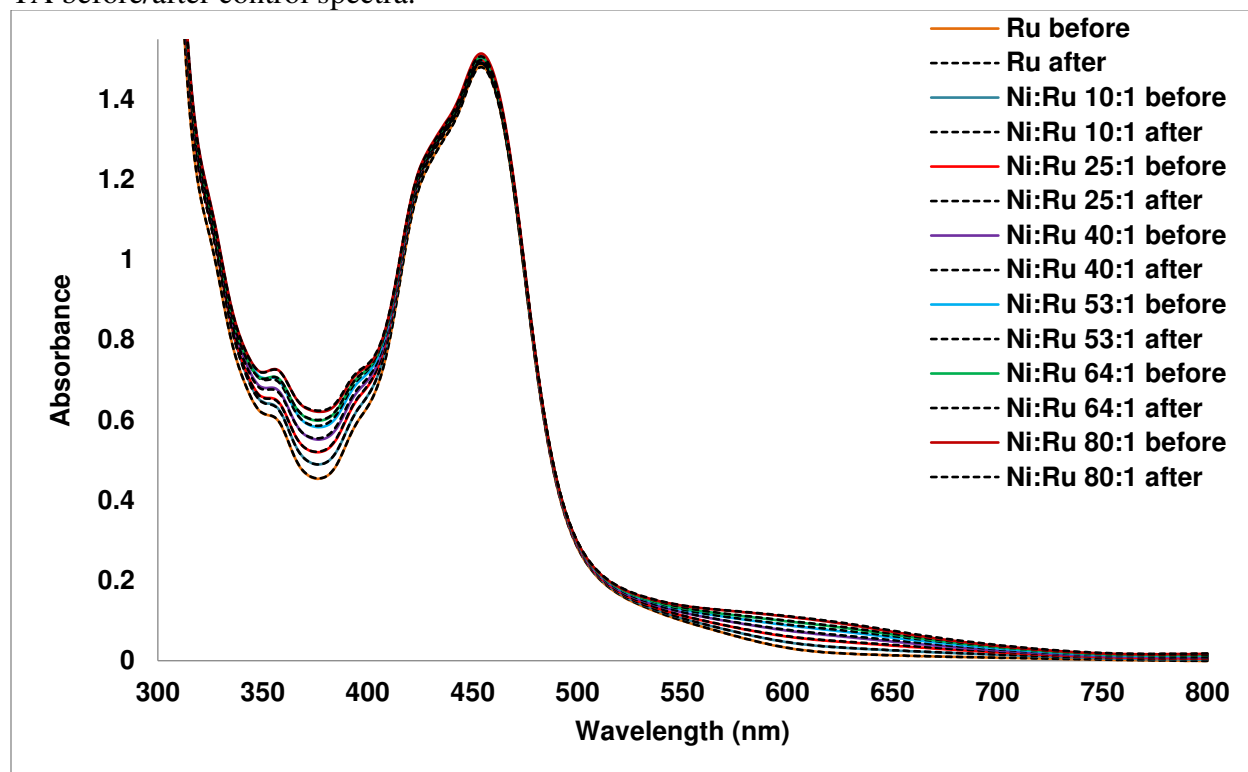


Figure S3.52. UV-vis of Ni-propylamine + [Ru(bpy)<sub>3</sub>]Cl<sub>2</sub> (0.1 mM) mixtures before and after TA experiments.



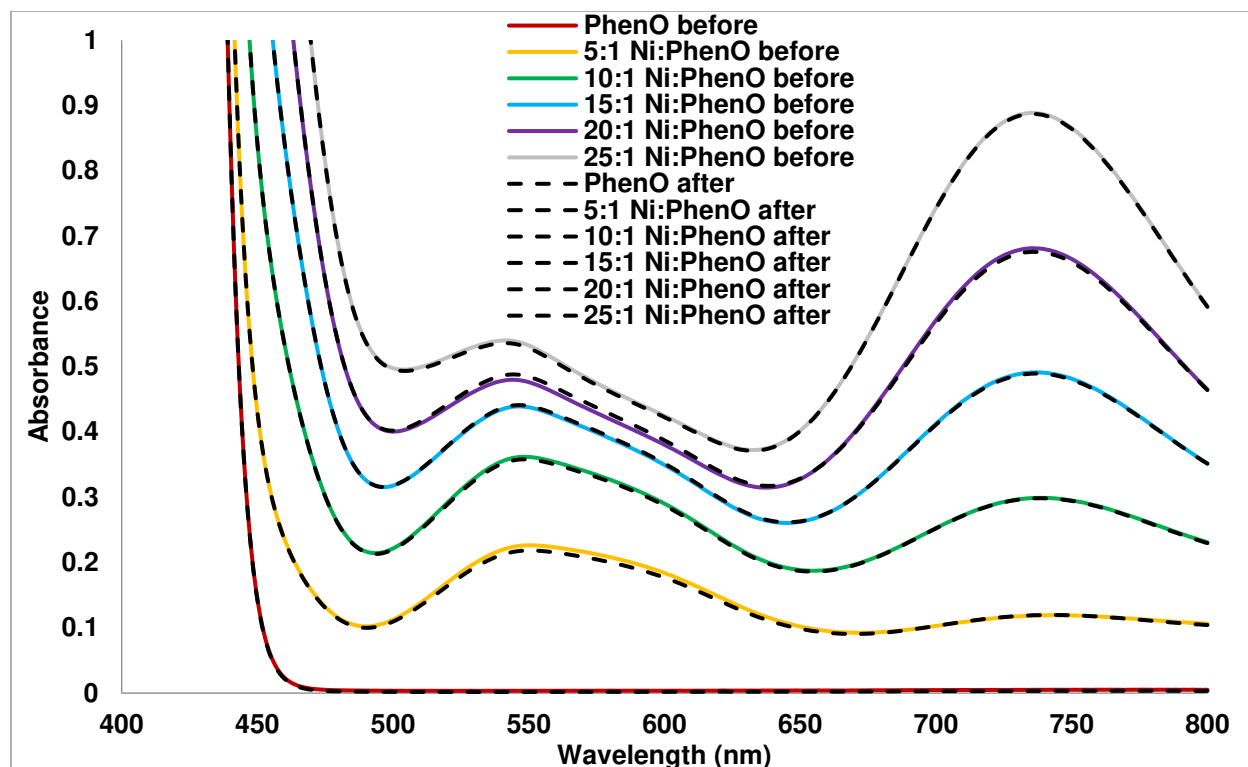


Figure S3.53. UV-vis of Ni-morpholine + PhenO PC 2 (0.8 mM) mixtures before and after steady state emission quenching experiments. Ratios in the figure are molar ratios.

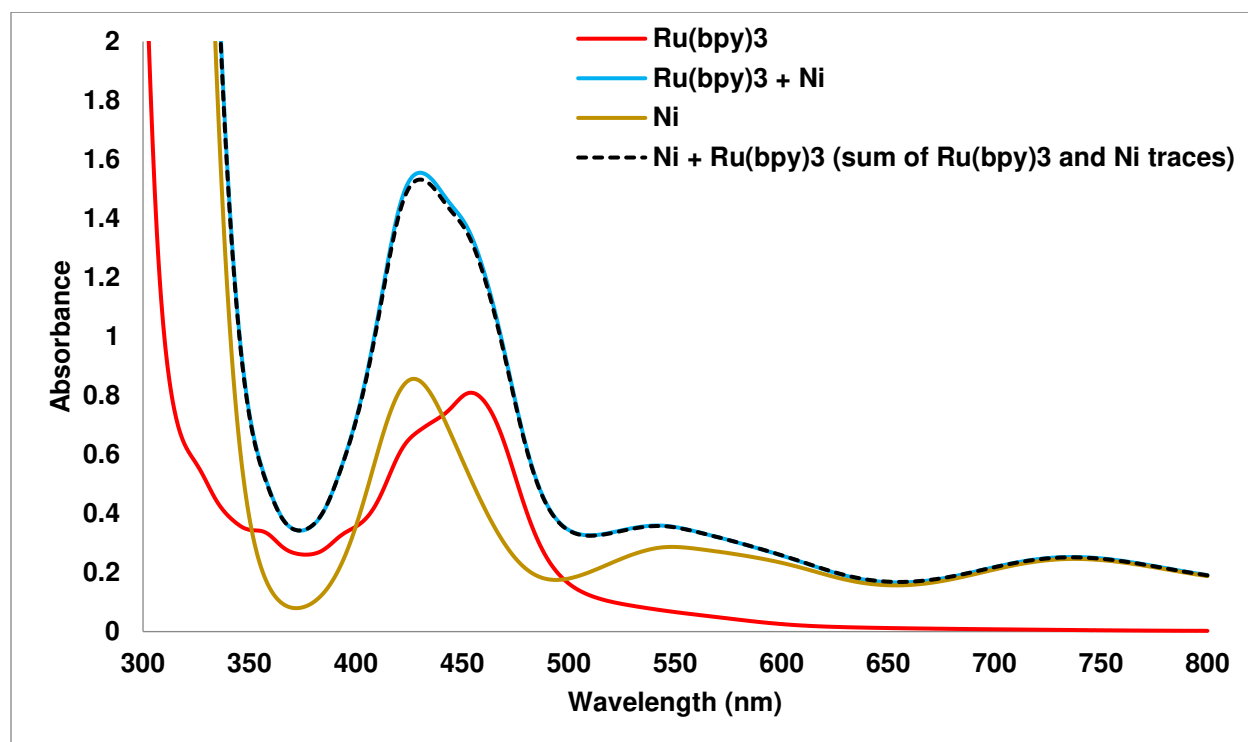


Figure S3.54. Traces of  $[Ru(bpy)_3]Cl_2$  (0.1 mM) and a Ni-morpholine quenching mixture (8 mM in Ni) separate and combined. The dashed trace is the sum of the absorption data for the two

separate solutions.  $[Ru(bpy)_3]Cl_2$  and Ni-morpholine quenchers demonstrate additive absorptions and therefore evidence of ground state aggregation or reactivity between these species is not observed.

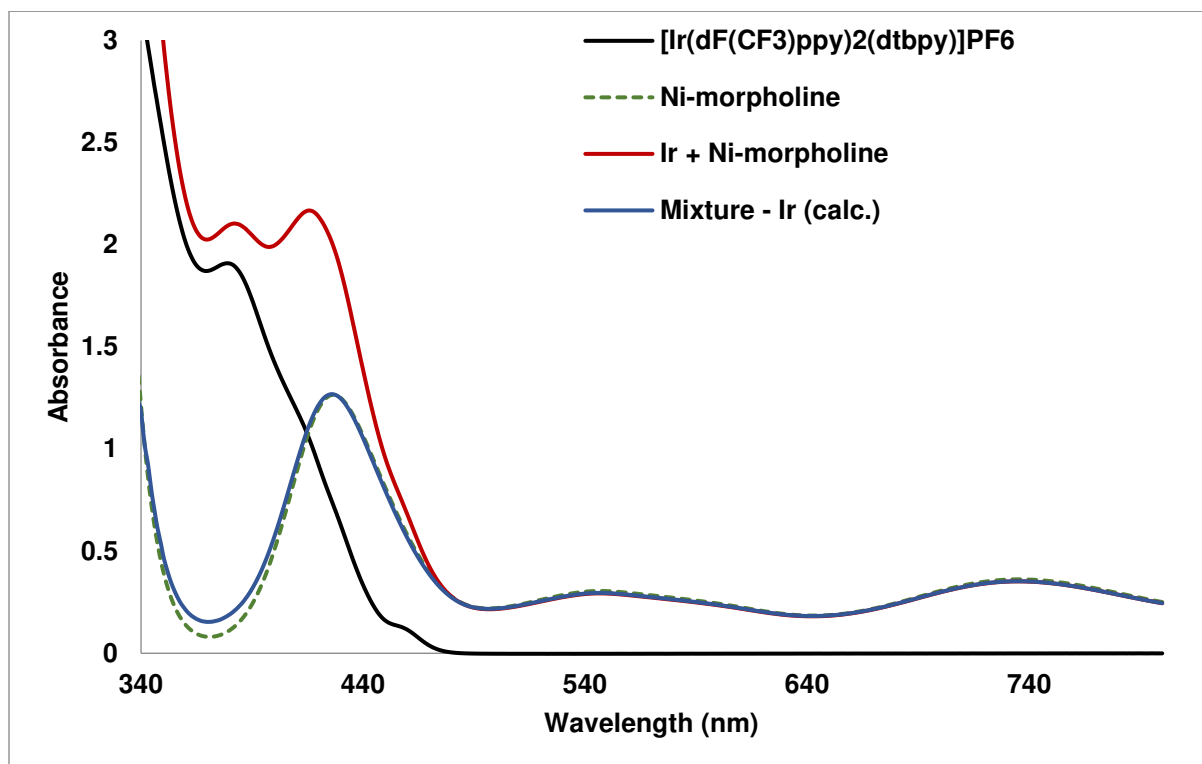


Figure S3.55. Traces of  $[Ir(dF(CF_3)ppy)_2(dtbbpy)]PF_6$  (0.38 mM in DMAc) and a Ni-morpholine quenching mixture (9.43 mM in DMAc) separate and combined. The dashed trace is the absorption of the mixture – the absorption of the Ir complex. These species therefore demonstrate additive absorptions and thus evidence of ground state aggregation or reactivity between these species is not observed. This data suggests that Ni-morpholine complexes also form in systems that use this Ir PC (without an additional ligand additive).

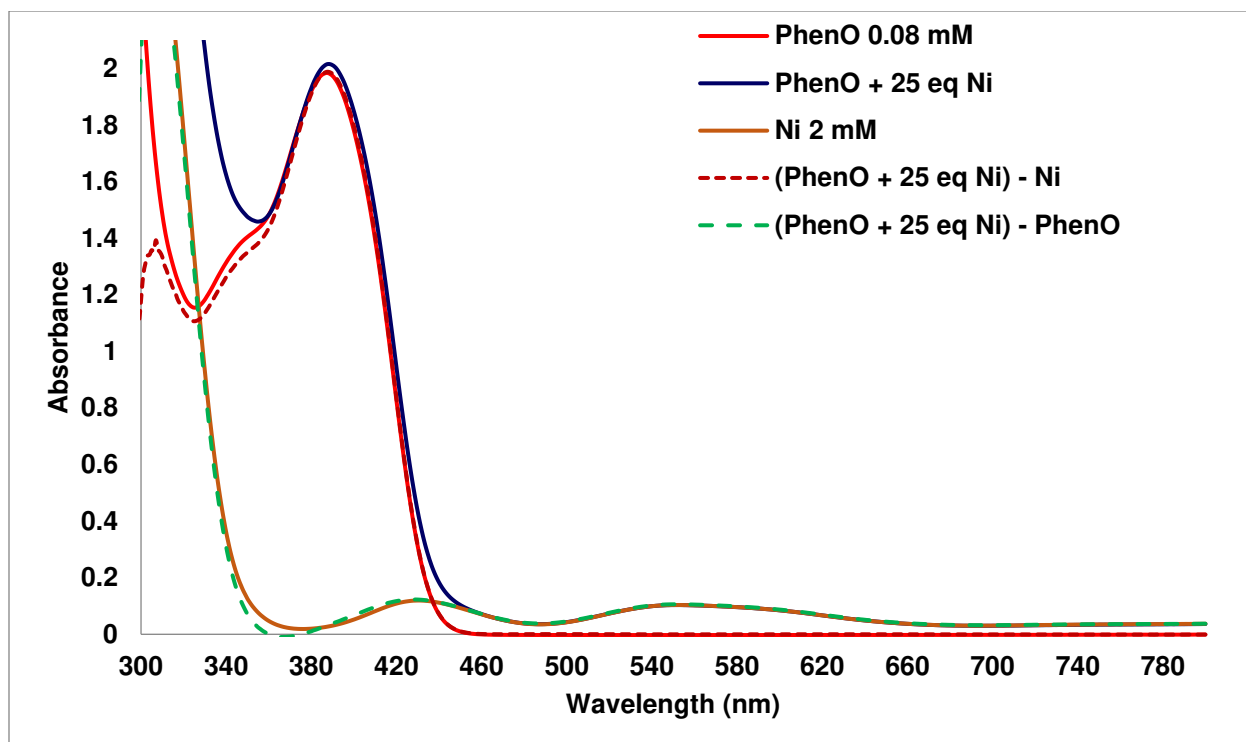


Figure S3.56. Traces of the phenoxazine PC, 3,7-di([1,1'-biphenyl]-4-yl)-10-(naphthalen-1-yl)-10H-phenoxazine, and a Ni-morpholine quenching mixture separate and combined. The dashed traces are the absorption of the mixture – the absorption of either component. These species therefore demonstrate additive absorptions and thus do not show evidence of ground state aggregation or reactivity.

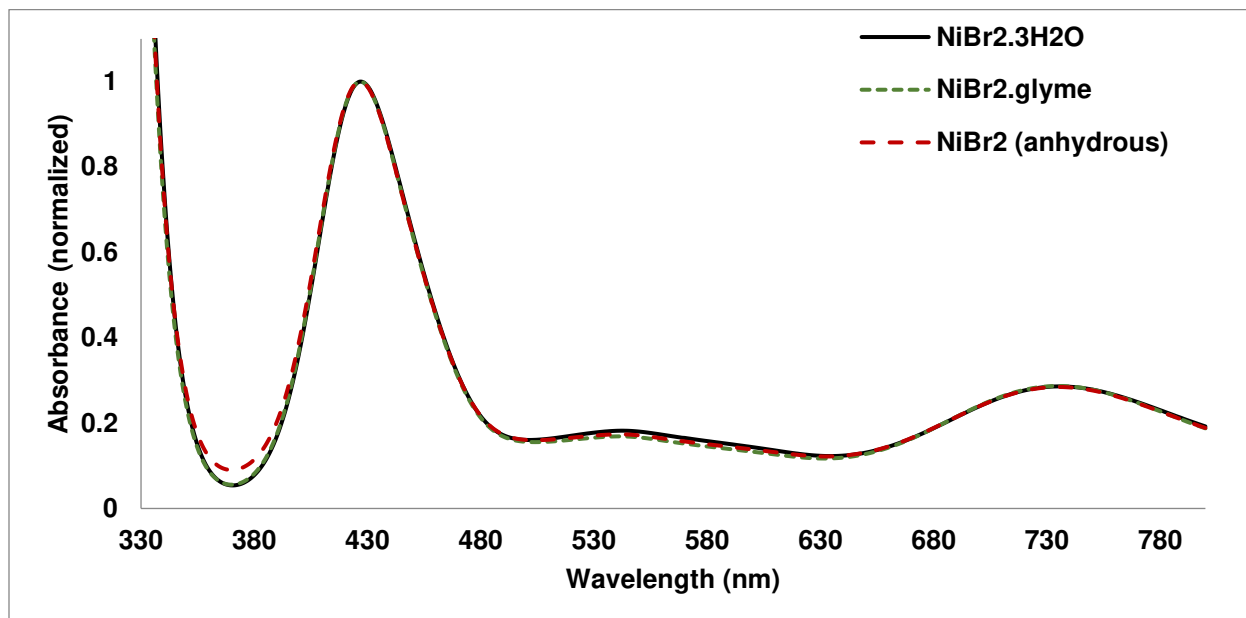


Figure S3.57. UV-vis of the Ni-morpholine mixture starting from  $\text{NiBr}_2 \cdot 3\text{H}_2\text{O}$ ,  $\text{NiBr}_2 \cdot \text{glyme}$ , and anhydrous  $\text{NiBr}_2$ . Regardless of  $\text{Ni(II)}$  bromide source, it can be seen that the same mixture of

complexes form. Anhydrous  $\text{NiBr}_2$  is significantly less soluble than the glyme or hydrate salts, so the same concentration could not be achieved. However, upon normalization, the spectra overlap well.

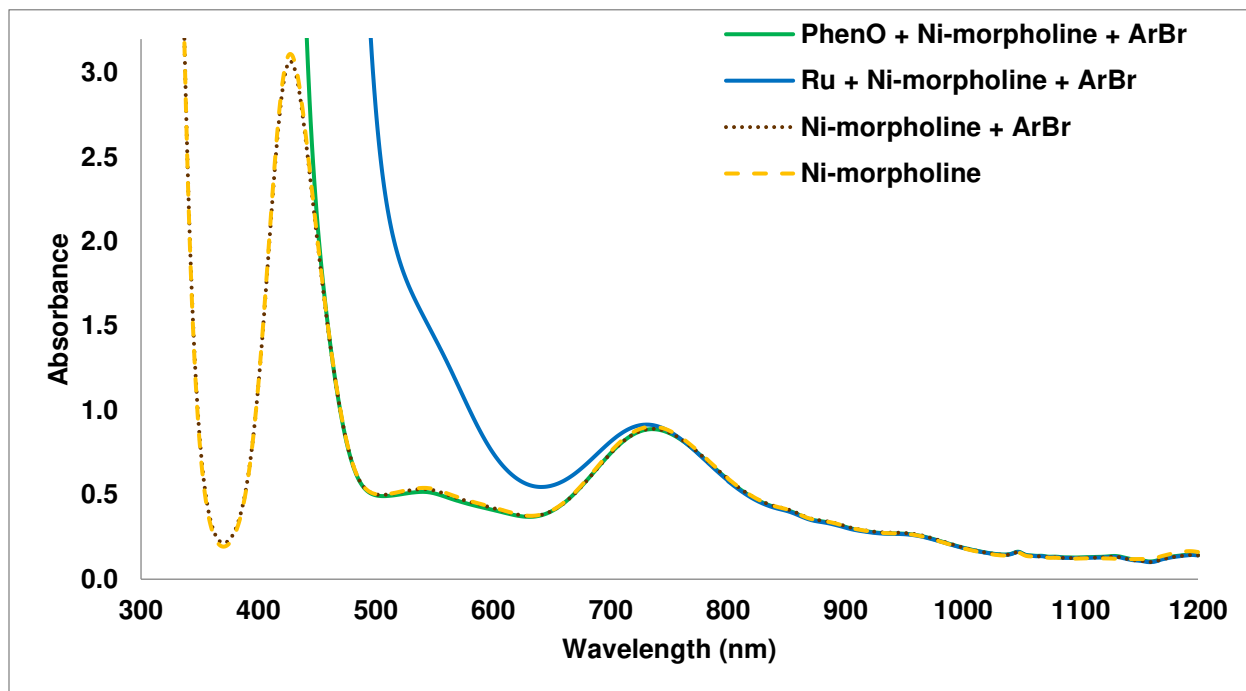


Figure S3.58. UV-vis of C–N coupling reaction mixtures with/without PCs 1 and 2 (0.8 mM), with/without 4-bromobenzotrifluoride (0.4 M), and containing Ni-morpholine complexes (20 mM in Ni and 1.4 M in morpholine).

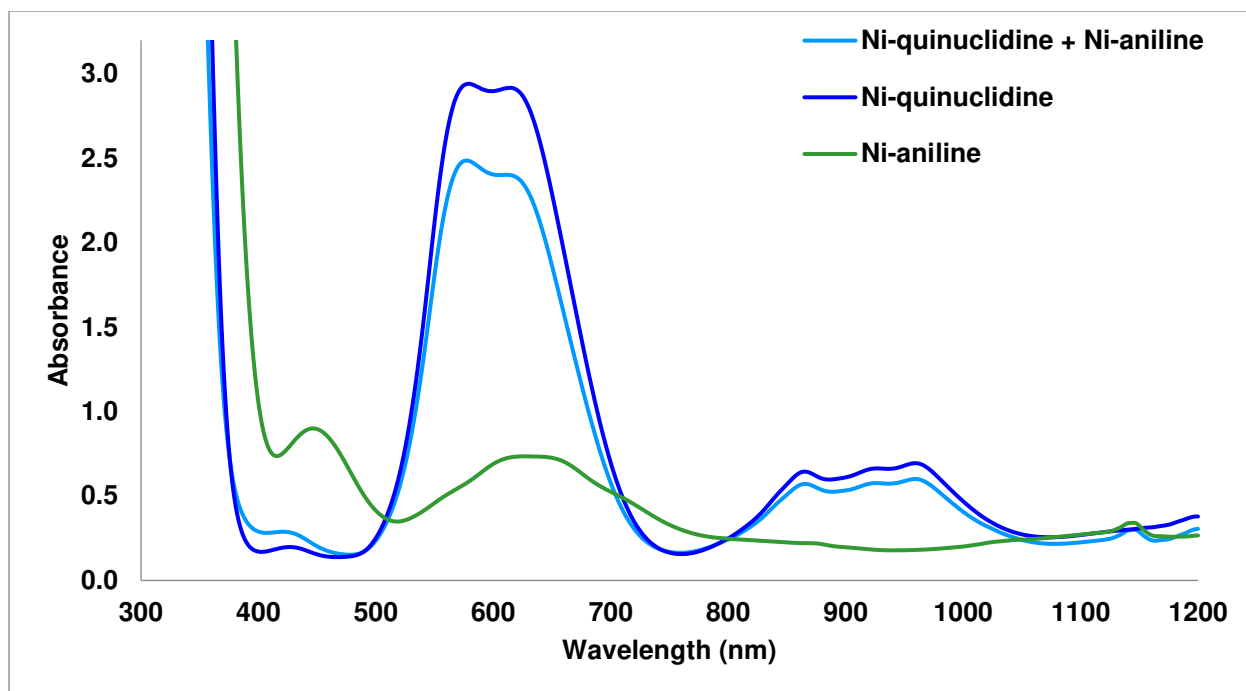


Figure S3.59. UV-vis of Ni-quinuclidine complexes (0.02 M in Ni and 0.6 M in quinuclidine), Ni-aniline complexes (0.02 M in Ni and 1.4 M in aniline), and a mixture containing the same concentrations of Ni, quinuclidine, and aniline.

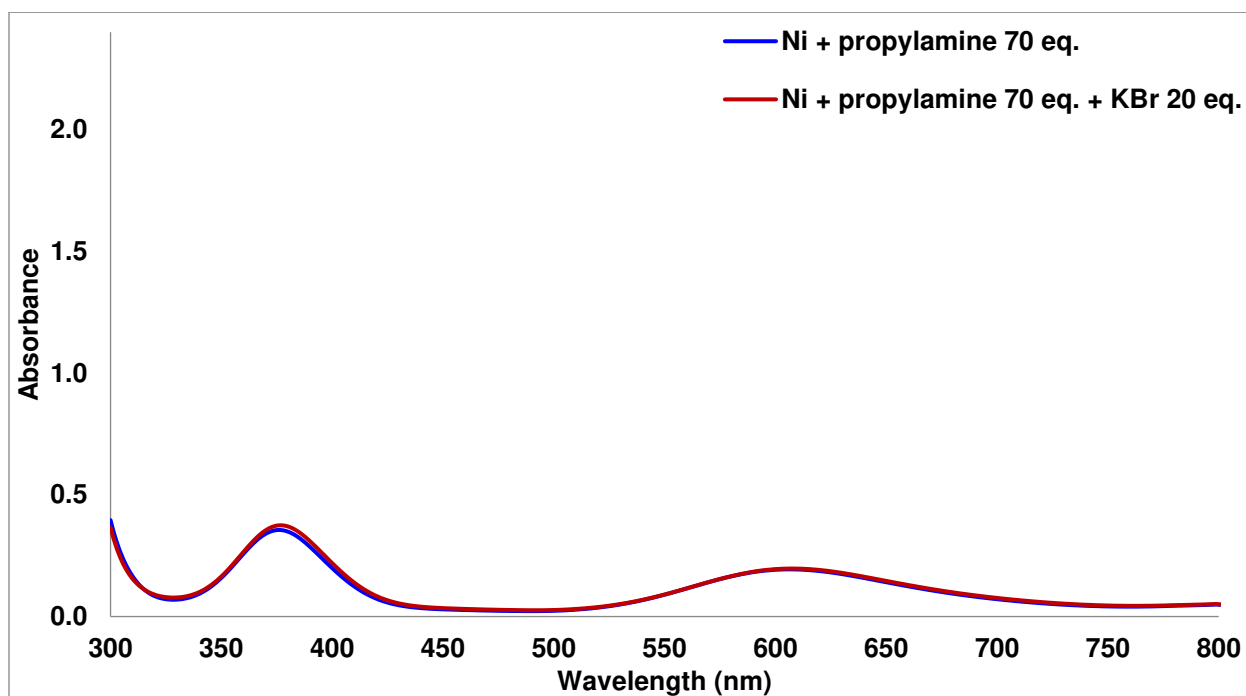


Figure S3.60. UV-vis of Ni-propylamine complexes (0.02 M in Ni and 1.4 M in propylamine) with and without KBr (0.4 M).

A small red-shift is observed with KBr addition that is significant considering the binding strength of propylamine (explored in the next figure).

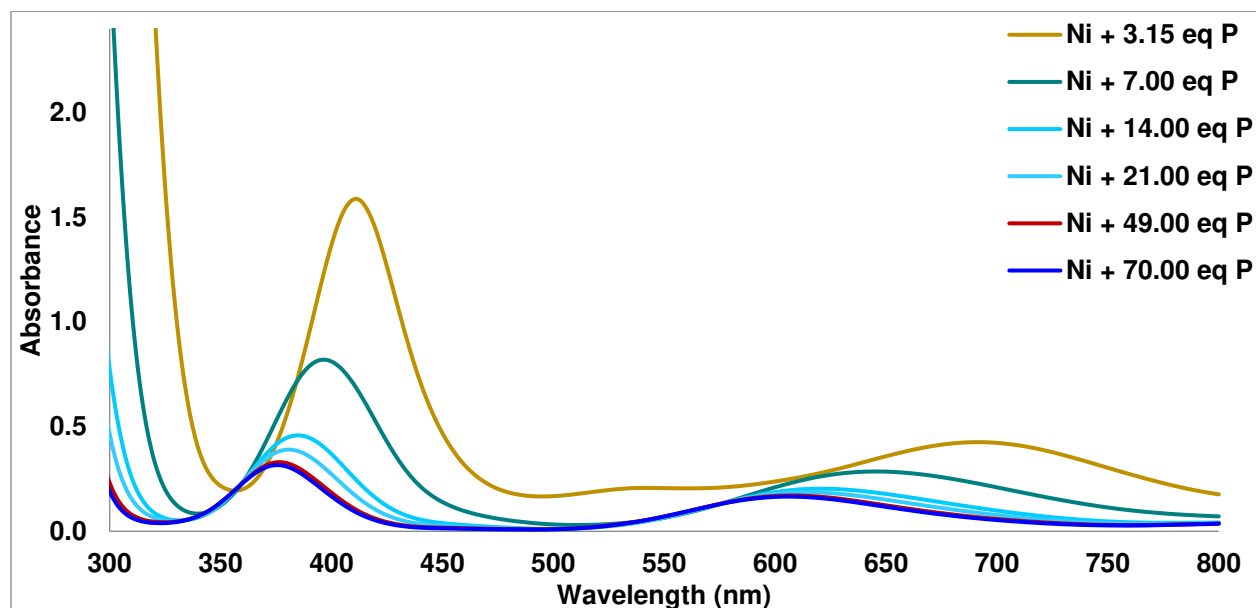


Figure S3.61. UV-vis of Ni-propylamine complexes with increasing ratios of propylamine:Ni (0.02 M in Ni and 0.063-1.4 M in propylamine). P = propylamine.

The feature at  $\lambda_{\text{max}} = 416$  nm can be assigned to  $[\text{NiBr}_2(\text{propylamine})_3]$  based on its similarity to the absorption profile of  $[\text{NiBr}_2(\text{morpholine})_3]$ . Thus, KBr inhibits the series of 4 stepwise equilibria to the extent that the same concentration of  $[\text{NiBr}_2(\text{propylamine})_3]$  is present as if 21-49 eq. propylamine had been added instead of 70 eq. While the spectral change is small,  $[\text{NiBr}_2(\text{propylamine})_3]$  has better spectral overlap with PCs 1 and 2. Further, if the reaction goes through the oxidative addition pathway (see Fig. S3.71), then an open coordination site is necessary. Thus, increasing the concentration of  $[\text{NiBr}_2(\text{propylamine})_3]$  likely both increases the energy transfer rate (by increasing spectral overlap) and facilitates the subsequent oxidative addition step. Future work will explore the stepwise equilibria of propylamine binding to Ni in greater detail; we note that a series of 4 equilibria results in a quintic system of equations which we have not yet developed a fitting procedure to deconvolute as we have done for systems of 3 stepwise equilibria (as detailed in the next section).

## 7. UV-Visible titration experiments and equilibrium constants

### Titration Binding Experiments and Equilibrium Constant Calculation.

Titration experiments were performed by mixing stock solutions containing the same total Ni concentration and varying amine molar ratio. Ni concentration was held constant by including amine volume when making stock solutions. Each stock solution was prepared as follows: NiBr<sub>2</sub>·3H<sub>2</sub>O (136.3 mg, 0.5 mmol) was weighed out in a N<sub>2</sub> filled glove box into each of 5 20 mL scintillation vials. The vials were removed from the glovebox and 10 mL N,N-dimethylacetamide (DMAc) solvent was added immediately under air. Vials were capped, sealed with electrical tape, and heated at 40.0 °C in a water bath for 30 minutes. The solutions were then transferred one at a time to a 25 mL volumetric flask. To make the 1<sup>st</sup> stock solution, “Ni + 70 eq. morpholine”, morpholine (3.019 mL, 35 mmol) was added and the resulting yellow-brown solution was diluted to 25 mL with DMAc. To make the 2<sup>nd</sup> stock solution, “Ni + 7 eq. morpholine”, morpholine (0.3019 mL, 3.5 mmol) was added. To make the 3<sup>rd</sup> stock solution, “Ni + 2.5 eq. morpholine”, morpholine (0.1078 mL, 1.25 mmol) was added. To make the final two “Ni” stock solutions, no morpholine was added. Each 25 mL stock solution was filtered through a 45 µm syringe filter to ensure homogeneity. No change was observed by UV-vis before/after filtration. The free morpholine is UV-vis silent (i.e. absorption < 0.005 at wavelengths > 365 nm at highest concentration used).

Mixtures totaling 3 mL were prepared in a quartz cuvette for UV-vis analysis by varying the ratio of the 2 stock solutions according to the following table. Before analysis, each cuvette was placed in a 25.0 °C water bath for 5 – 15 minutes to mitigate laboratory temperature fluctuations. The temperature inside the cuvette was monitored with a type K thermocouple

immediately after each run. The average temperature was  $23.0 \pm 0.3$  °C (n = 28). These titration experiments were carried out three times (triplicate repeat).

*Table S7. Preparation of mixtures for UV-vis titration experiments.*

Mixture #	Ni (mL)	Ni + 2.5 eq. morph (mL)	Ni + 7.0 eq. morph (mL)	Ni + 70 eq. morph
1	3	0	0	0
2	2.9	0.1	0	0
3	2.8	0.2	0	0
4	2.7	0.3	0	0
5	2.4	0.6	0	0
6	2	1	0	0
7	1.8	1.2	0	0
8	1.5	1.5	0	0
9	1.2	1.8	0	0
10	0.9	2.1	0	0
11	0.6	2.4	0	0
12	0.3	2.7	0	0
13	0	3	0	0
14	1.8	0	1.2	0
15	1.5	0	1.5	0
16	1.2	0	1.8	0
17	0.9	0	2.1	0
18	0.6	0	2.4	0
19	0.3	0	2.7	0
20	0	0	3	0
21	2.55	0	0	0.45
22	2.4	0	0	0.6
23	2.1	0	0	0.9
24	1.8	0	0	1.2
25	1.2	0	0	1.8
26	0.6	0	0	2.4
27	0.3	0	0	2.7
28	0	0	0	3



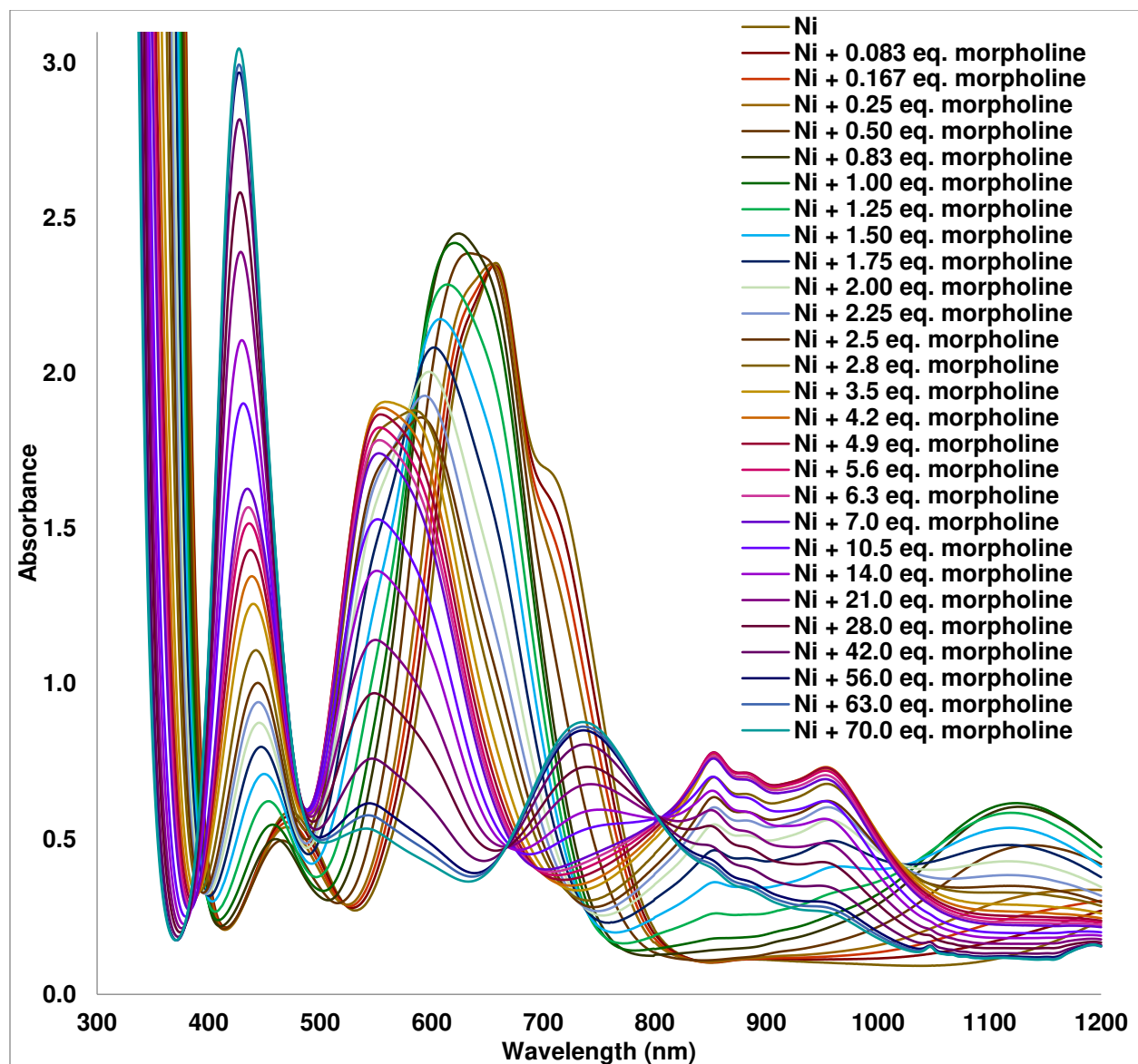


Figure S3.62. Representative titration plot from one of the three experiments that were carried out by varying Ni:morpholine mole ratio from 1:0 – 1:70. Solvent = DMAc, Temperature =  $23.0 \pm 0.3$  °C

The titration data was then fitted to various binding models:

i) Attempts to fit the data to models simpler than the 1:3 binding model.

The UV-Vis titration data was fitted to 1:1, 2:1 and 1:2 binding models using the bindfit program.<sup>14</sup> In short, these model did not yield a good fit to the experimental data, compared to the 1:3 model (*vide supra*).

For a representation of these attempts, the results from fitting the (full) 1:2 model can be accessed via the [www.supramolecular.org](http://www.supramolecular.org)<sup>14</sup> database through the unique URL below for the three experiments carried out: (copy-paste into a web-browser – this is one way to access the raw data used for the 1:3 calculations)

*Experiment 1 (MK-2-95) as a 1:2 complex*

<http://app.supramolecular.org/bindfit/view/593176a0-85aa-4264-941c-84dbad9fb584>

*Experiment 2 (MK-2-99) as a 1:2 complex*

<http://app.supramolecular.org/bindfit/view/f1565dff-0ab7-42f3-9d0d-992471b9d27e>

*Experiment 3 (MK-2-114) as a 1:2 complex*

<http://app.supramolecular.org/bindfit/view/49c5f203-3fe0-47cb-ad8e-5c2731d25b64>

Fitting the experimental data to a 1:3 binding model:

The data was fitted to 1:3 using a similar approach to that described by Cozzolino and co-workers in their NMR study on a 3:1 complexation of a bis-antimony receptor with halide anions.<sup>15</sup> Here, the system of equations has been solved using the Wolfram Mathematica – see a file in the attached zip (see list of included files below).

Full details on the terminology used here (H = host, G = guest,  $[X]_0$  total concentration of species X, and  $K$  = association constants) for the binding models have been published previously.<sup>16</sup>

Below the most important equations referred to in this paper are summarized:

For 1:3 H:G<sub>3</sub> complexation occurs according to equations S3.8-S3.10. Here, the stepwise association constants ( $K_1$ ,  $K_2$  and  $K_3$ ) can be expressed in terms of the free energy changes ( $\Delta G_1$ ,  $\Delta G_2$  and  $\Delta G_3$ ) according to equations S11-S13 after correcting for statistical factors. If the binding was non-cooperative,  $\Delta G_1$ ,  $\Delta G_2$  and  $\Delta G_3$  would be expected to be the same, hence any difference between these are an indication of cooperativity.

$$K_1 = \frac{[\mathbf{HG}]}{[\mathbf{H}][\mathbf{G}]} \quad \text{Eq. (S3.8)} \quad K_2 = \frac{[\mathbf{HG}_2]}{[\mathbf{HG}][\mathbf{G}]} \quad \text{Eq. (S3.9)} \quad K_3$$

$$= \frac{[\mathbf{HG}_3]}{[\mathbf{HG}_2][\mathbf{G}]} \quad \text{Eq. (S3.10)}$$

$$\Delta G_1 = -RT \ln\left(\frac{K_1}{3}\right) \quad \text{Eq. (S3.11)}$$

$$\Delta G_2 = -RT \ln(K_2) \quad \text{Eq. (S3.12)}$$

$$\Delta G_3 = -RT \ln(3K_3) \quad \text{Eq. (S3.13)}$$

Equations S3.8 to S3.10, together with the corresponding mass-balance equations form the system of equations that is then solved using the Wolfram Mathematica program as mentioned above. This yields a quartic (fourth-order) equation S3.14 for the concentration of the free guest [G]:

$$\begin{aligned} & [\mathbf{G}]^4(K_1K_2K_3) + [\mathbf{G}]^3\{(K_1K_2)\} - (K_1K_2K_3[\mathbf{G}]_0) + (3K_1K_2K_3[\mathbf{H}]_0) + [\mathbf{G}]^2\{(K_1)\} \\ & - (K_1K_2[\mathbf{G}]_0) + (2K_1K_2[\mathbf{H}]_0) + [\mathbf{G}]\{1 - (K_1[\mathbf{G}]_0) + (K_1[\mathbf{H}]_0)\} - [\mathbf{G}]_0 \\ & = 0 \end{aligned}$$

Eq. (S3.14)

### Binding models:

In the analysis below, four different binding models or “flavors”<sup>17</sup> are compared. The first one is the stepwise (non-degenerate) “full 1:3” binding model. This model assumes three non-identical binding sites per molecule of host 1 that allows for cooperativity (negative or positive). Using a similar approach to the previously described 1:2 full model for NMR data, we first define  $\varepsilon_{\Delta\mathbf{HG}}$ ,  $\varepsilon_{\Delta\mathbf{HG}_2}$  and  $\varepsilon_{\Delta\mathbf{HG}_3}$  as the difference between the UV-Vis molar absorptivities ( $\varepsilon$ ) between the 1:1, 1:2 and 1:3 host-guest complexes, respectively and the molar absorptivity of the pure host

( $\varepsilon_H$ ), e.g., for  $\varepsilon_{\Delta HG_3} = \varepsilon_{HG_3} - \varepsilon_H$ . This, together with Equations S3.8-S3.10 and the mass balance equations yields S15 (with  $\Delta A$  = change in absorption upon performing the titration).

$$\Delta A = [H_0] \left( \frac{\Delta \varepsilon_{HG} K_1 [G] + \Delta \varepsilon_{HG_2} K_1 K_2 [G]^2 + \Delta \varepsilon_{HG_3} K_1 K_2 K_3 [G]^3}{1 + K_1 [G] + K_1 K_2 [G]^2 + K_1 K_2 K_3 [G]^3} \right) \quad \text{Eq. (S3.15)}$$

Here the guest [G] concentration is obtained from the quartic equation S3.14 above.

We note also here that in practice, this is done in the matlab program in two steps; in the first step the concentrations of the 1:1, 1:2 and 1:3 complex are calculated and then a matrix division is performed to solve the system of linear equations that yields the molar absorptivities in S3.15. The matlab program includes a calculation loop that ensures that none of the molar absorptivities are negative (if they are found, they are set to zero).

The second model (flavor) considered is the stepwise (non-degenerate) “additive 1:3” binding model. To reduce the number of fitted parameters we note that in many circumstances it can be assumed that the spectra of the 1:1, 1:2 and 1:3 are simply additive, i.e. for the absorption at any given wavelength, the change in absorptivity on going on from the free host to the 1:1 complex is simply 1/2 of the change between the 1:2 complex and the free host and 1/3 of the change between the 1:3 complex and the free host. It then follows that  $\varepsilon_{\Delta HG} = 2\varepsilon_{\Delta HG_2} = 3\varepsilon_{\Delta HG_3}$  and we can simplify equation S3.15 to yield equation S3.16.

$$\Delta A = [H_0] \left( \frac{\Delta \varepsilon_{HG} \{K_1 [G] + 2K_1 K_2 [G]^2 + 3K_1 K_2 K_3 [G]^3\}}{1 + K_1 [G] + K_1 K_2 [G]^2 + K_1 K_2 K_3 [G]^3} \right) \quad \text{Eq. (S3.16)}$$

It should be noted here that although the additive model is not an unreasonable assumption when analyzing data based on NMR titrations, it seems rather unlikely that UV-Vis molar absorptivities for multi-step ligand binding should be (perfectly) additive.

The third model (flavor) considered is the stepwise “non-cooperative 1:3” model. Here we revert back to noting that the molar absorptivities may not be correlated (see equation S3.14). However, instead we now make the assumption that the 1:3 complexation is non-cooperative and, hence, after considering statistical factors, that  $K_1 = 3K_2 = 9K_3$ . If we define  $K_{1n} = K_1 = 3K_2 = 9K_3$ , from equation S3.14 we can simplify to obtain equation S3.17:

$$\Delta A = [H_0] \left( \frac{\Delta \varepsilon_{HG} K_{1n} [G] + \Delta \varepsilon_{HG_2} K_{1n}^2 K_1 K_2 [G]^2 + \Delta \varepsilon_{HG_3} K_{1n}^3 [G]^3}{1 + K_{1n} [G] + K_{1n}^2 [G]^2 + K_{1n}^3 [G]^3} \right) \quad \text{Eq. (S3.17)}$$

Here,  $K_{1n}$  replaces the need to fit 3 parameters (one for each step-wise binding constants) and once the data has been fitted to S3.17, the three step-wise non-cooperative binding constants can be readily obtained  $K_{1n} = K_1 = 3K_2 = 9K_3$ .

The fourth and last model (flavor) is the “statistical 1:3” model. Here we not only make the assumption that the binding is non-cooperative ( $K_1 = 3K_2 = 9K_3$ ) but also that the molar absorptivities are all additive ( $\varepsilon_{\Delta HG} = 2\varepsilon_{\Delta HG_2} = 3\varepsilon_{\Delta HG_3}$ ). We can now combine the approached used for S3.13 and S3.17 to get equation S3.18:

$$\Delta A = [H_0] \left( \frac{\Delta \varepsilon_{HG} (K_{1n} [G] + 2K_{1n}^2 K_1 K_2 [G]^2 + 3K_{1n}^3 [G]^3)}{1 + K_{1n} [G] + K_{1n}^2 [G]^2 + K_{1n}^3 [G]^3} \right) \quad \text{Eq. (S3.18)}$$

Compared to the “full” model which has 3 binding constants and 3 molar absorptivities per wavelength point (which could be many for a global fit) we have now a much simpler model with only one binding constant  $K_{1n}$  and one molar absorptivity change  $\varepsilon_{\Delta HG}$  (per wavelength point) to fit to our data.

### **How we fit the models:**

Using equations S3.15-S3.18 we wrote a code in the Matlab program similar to that described in our earlier work.<sup>16-17</sup> The program files are all provided in a zip-file named:

*Matlabprogramfiles1to3Eq.zip*

This package includes one file that solves the quartic equation S14 – this file is named:

*uv1to3bbb.m*

And then a pair of files with the prefixes (file extension is the matlab .m extension):

*Runfitbinding1to3uv*            and            *uv1to3fitbind*

With the former starting the program, the latter is then called upon from that program for the iteration process. The suffix of these file names then varies depending on which of the four models / equations above they refer to:

Suffix = (none)	“full model”	Equation S3.15
Suffix = agg	“additive model”	Equation S3.16
Suffix = noncoop	“non-cooperative model”	Equation S3.17
Suffix = stat	“statistical model”	Equation S3.18

After fitting the data to these models, a matlab data file (.mat) with all the inputs was generated. These files have been aggregated in a separate zip-file included named:

*FitteddatafromMatlab.zip*

This package includes a total of 12 files, 4 for each of the 4 models x 3 for each of the repeat experiments, which are named *mk2x95*, *mk2x99* and *mk2x114*. The names of these file are created using this system:

Prefix = *fitted1to3*

Center = experimental replicate name, i.e., *mk2x95*, *mk2x99* or *mk2x114*

Suffix = which model, i.e. *full*, *agg*, *noncoop* and *stat*

Where full = full model, agg = additive model, noncoop = non-cooperative and stat = statistical model.

As an example, the file name:

*fitted1to3mk2x99noncoop.mat*

corresponds to the data file from experiment mk2x99 fitted to the non-cooperative binding model (equation S17).

### **Comparing the models:**

To analyze and compare the model used we used two indicators for the quality of the fit; the covariance of the fit ( $\text{cov}_{\text{fit}}$ ) as in our previous work,<sup>16-17</sup> and the Bayesian Information Criteria (BIC)<sup>18</sup> as another robust method for model comparison. The challenge is that the more complicated the model (= higher number of parameters), the better the fit is likely to be. However, generally we should only pick a more complicated model if the fit is significantly better when compared to a simpler model. As discussed previously, the  $\text{cov}_{\text{fit}}$  is relatively insensitive to the number of parameters used and if there is a more than 2-3-fold reduction in  $\text{cov}_{\text{fit}}$  then the more complicated model (flavor) is a reasonable one. The BIC is a different type of measure of fit and is based on the calculated log-likelihood, the number of parameters, and the number of data points, whereby an increase in the number of parameters leads to a penalty (increase) in the BIC value. A low BIC is generally better and when comparing two models, and a difference of more than 6-10 is usually considered as a strong evidence that there is a significant difference between the two models being compared.

In this study, the “full” 1:3 model (flavor) always appeared to fit the experimental data considerably better than any of the other models (flavors). This comparison is shown in detail in 3 excel files, one for each repeat experiment, that have been included in the zip-file named:

*ExcelSummaryAndMathematicaFile.zip*

Which contains four files:

<i>summaryMax2x95.xlsx</i>	Summary from experiment 1 (MK-2-95)
<i>summaryMax2x99.xlsx</i>	Summary from experiment 2 (MK-2-99)
<i>summaryMax2x114.xlsx</i>	Summary from experiment 3 (MK-2-114)
<i>eqfor1to3.nb</i>	Mathematica derivation of Equation S14

As an example, we can look at the comparison of the four models (flavors) for experiment 2 (MK-2-99):

Model (flavor) for the 1:3 complexation	cov <sub>fit</sub>	Ratio compared to full model <sup>a</sup>	BIC <sup>b</sup>	□ BIC compared to full model <sup>c</sup>
Full	13.9	n/a	-78555	n/a
Additive	1384	100	9162	87718
Non-cooperative	117	8.5	-30349	48206
Statistical	1385	100	9145	87701

<sup>a</sup>This is the cov<sub>fit</sub>(for X model) / cov<sub>fit</sub>(for full model). <sup>b</sup>The lower, the better. BIC can be negative and if so, the more negative the better. <sup>c</sup>Defined here as BIC(X model)-BIC(full model). A ΔBIC > 6-10 is usually considered as a strong evidence in favor of the model with a lower (more negative) BIC.

Based on these calculations, the full 1:3 model fits much better to the experimental data than any of the other models (flavors).

### Overall results for the full 1:3 binding model:

After fitting all three experiments (repeats) to the full 1:3 model, we then obtained the following binding constants (uncertainties are based on the calculated standard deviation from the three experiments).

$$K_1 = (6 \pm 3) \times 10^3 \text{ M}^{-1} \quad \Delta G_1 = -8.2 \pm 1.1 \text{ kJ mol}^{-1}$$

$$K_2 = 130 \pm 30 \text{ M}^{-1} \quad \Delta G_2 = -5.3 \pm 0.5 \text{ kJ mol}^{-1}$$

$$K_3 = 2.6 \pm 0.5 \text{ M}^{-1} \quad \Delta G_3 = -2.2 \pm 0.5 \text{ kJ mol}^{-1}$$



(note that the free energies, DG's, have all been corrected for statistical factors according to Equations S11-S13).

We can also calculate the overall binding constant  $\beta_{13} = K_1K_2K_3$  as:

Overall binding constant  $\beta_{13} = (1.83 \pm 0.08) \times 10^6 \text{ M}^{-3}$ ,  $\Delta G = -15.5 \pm 0.1 \text{ kJ mol}^{-1}$

Calculating the spectra for the complexes formed:

The raw titration data was fit in the region from 395–1200 nm utilizing a MATLAB code as discussed above. At each wavelength point, the program therefore obtains an estimate of the differences between the free host spectra and that of the three complexes. A non-negative constraint was employed during the optimization process, however, only a small region of the  $[\text{NiBr}_2(\text{morpholine})_3]$  spectrum around 550 nm was forced to have molar absorptivity = 0.

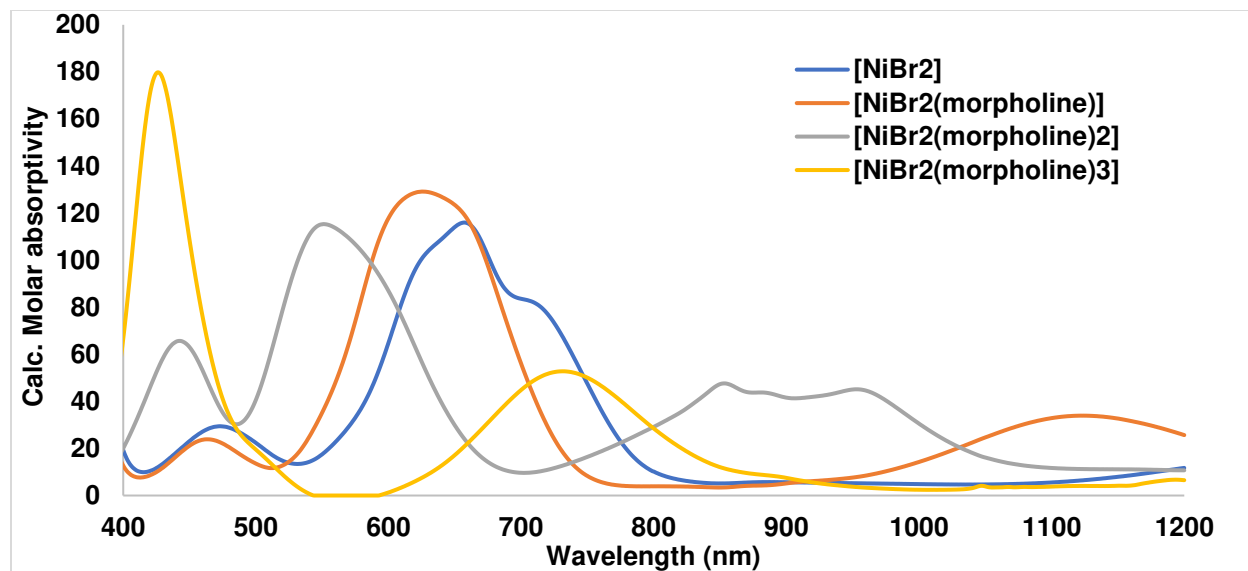


Figure S3.63. A representative (from experimental repeat 1 – MK-2-95) calculated molar absorptivity for each species output from global analysis of titration data for the Ni-morpholine mixture.

The Matlab program also yields an estimate of the changes in concentration of the free host and the three complexes (1:1, 1:2 and 1:3) as the titration experiments proceed:

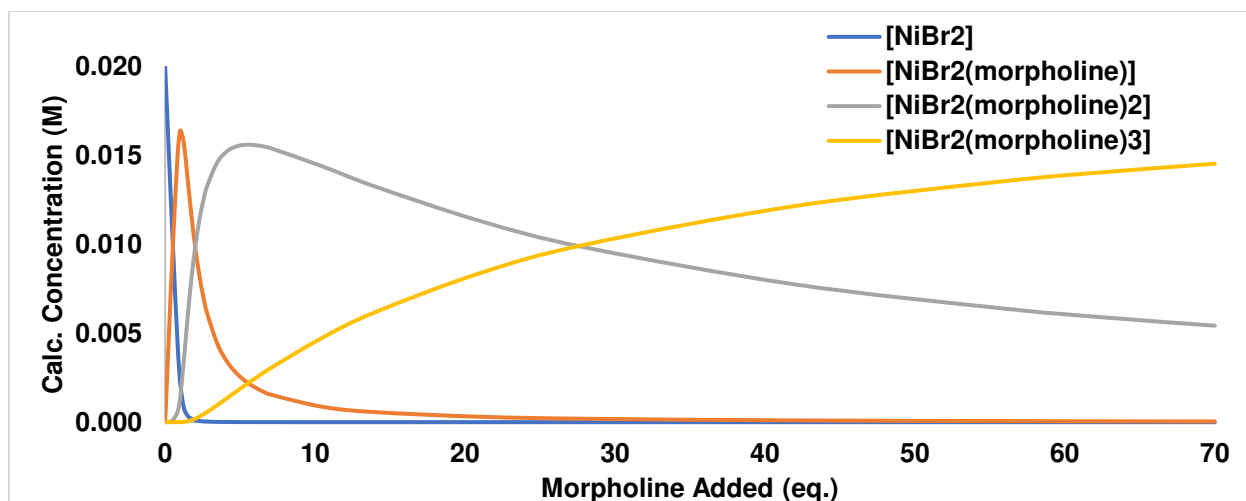


Figure S3.64. A representative (from experimental repeat 1 – MK-2-95) calculated concentration of each species as a function of equivalents of added morpholine output from global analysis of titration data for the Ni-morpholine mixture.

We can also analyze the residuals from the fits, i.e., the calculated overall spectra – the experimental spectra. For a model that gives a good fit to experimental data, the residuals should be relatively small and randomly distributed.

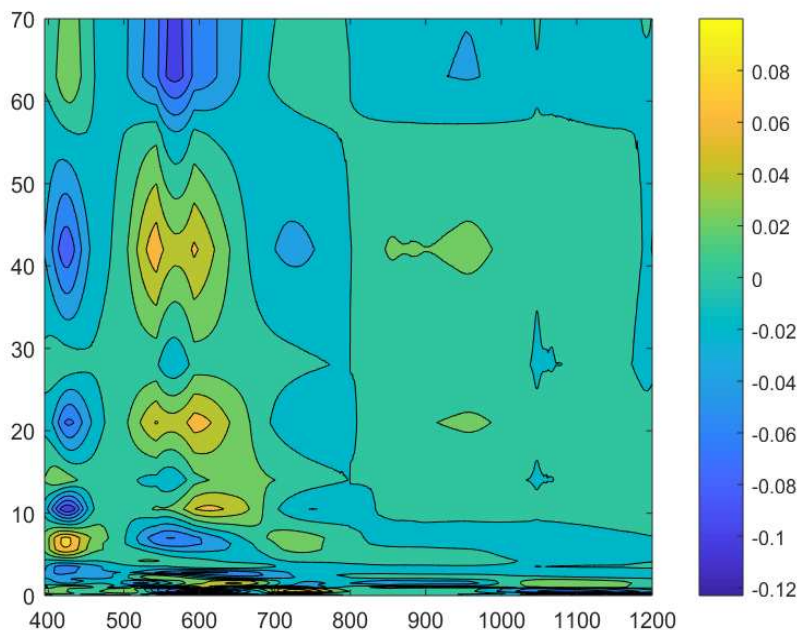


Fig. S3.65. A representative (from experimental repeat 1 – MK-2-95) fit residuals (absorbance units) plotted as a function of morpholine:Ni molar ratio (left axis) and wavelength (nm, x-axis). Notably, residuals are  $< \pm 0.12$  absorbance across all ratios and wavelengths.

## 8. Solid-state UV-Visible Spectroscopy

Solid-state UV-visible Transmittance Spectroscopy.

Single crystals were suspended in Nujol (IR spectroscopy grade, Alfa Aesar) on glass slides. Slides were mounted in the instrument using the standard solid sample slide holder equipped with a 1 mm aperture. A 1 mm aperture was also placed on an identical slide holder in the reference position. Data were recorded with background correction to a blank glass slide.

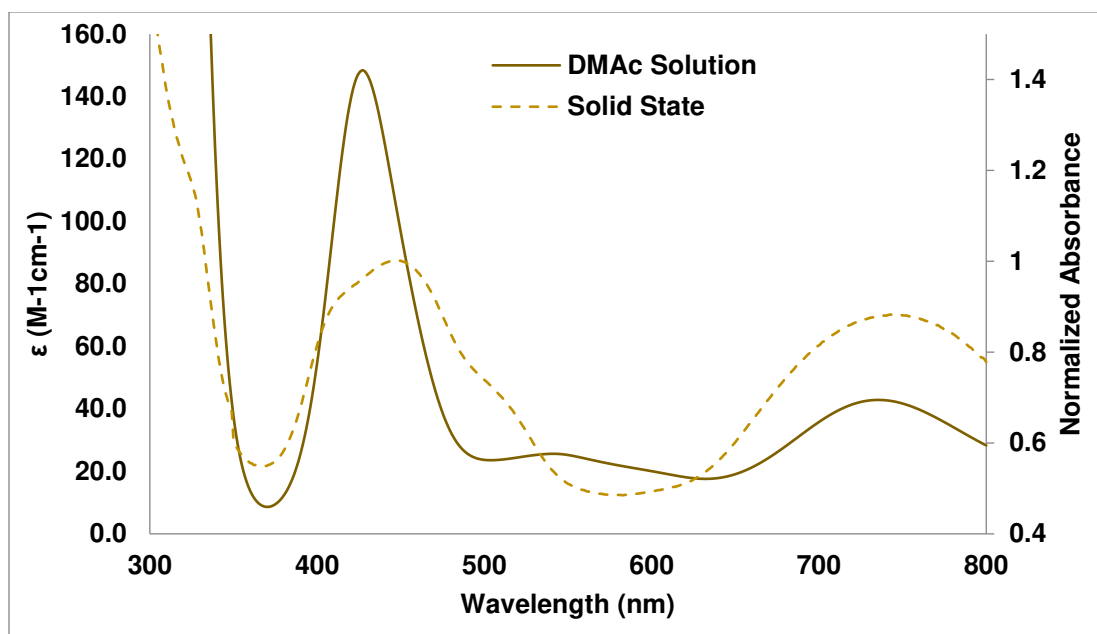


Figure S3.66. Solid-state UV-vis spectrum for single crystals of  $[\text{NiBr}_2(\text{morpholine})_3]$  plotted with solution-state UV-vis spectrum of the Ni-morpholine DMAc mixture (0.02 M in Ni, 1.4 M in morpholine).

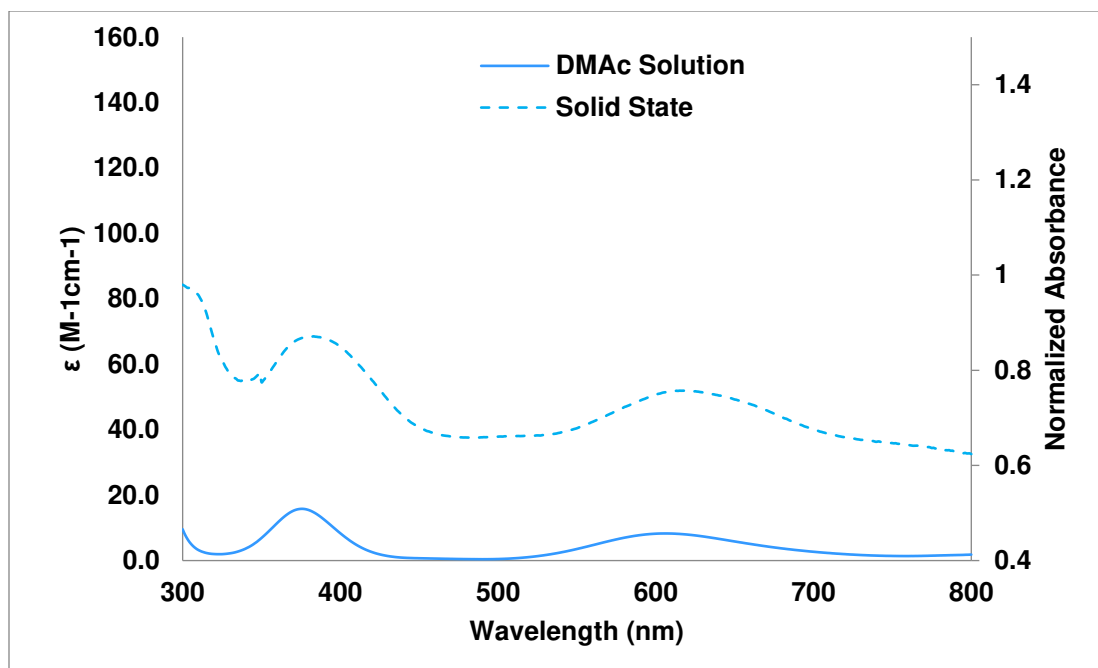


Figure S3.67. Solid-state UV-vis spectrum for single crystals of  $[\text{NiBr}_2(\text{propylamine})_4]$  plotted with solution-state UV-vis spectrum of the Ni-propylamine DMAC mixture (0.02 M in Ni, 1.4 M in propylamine).

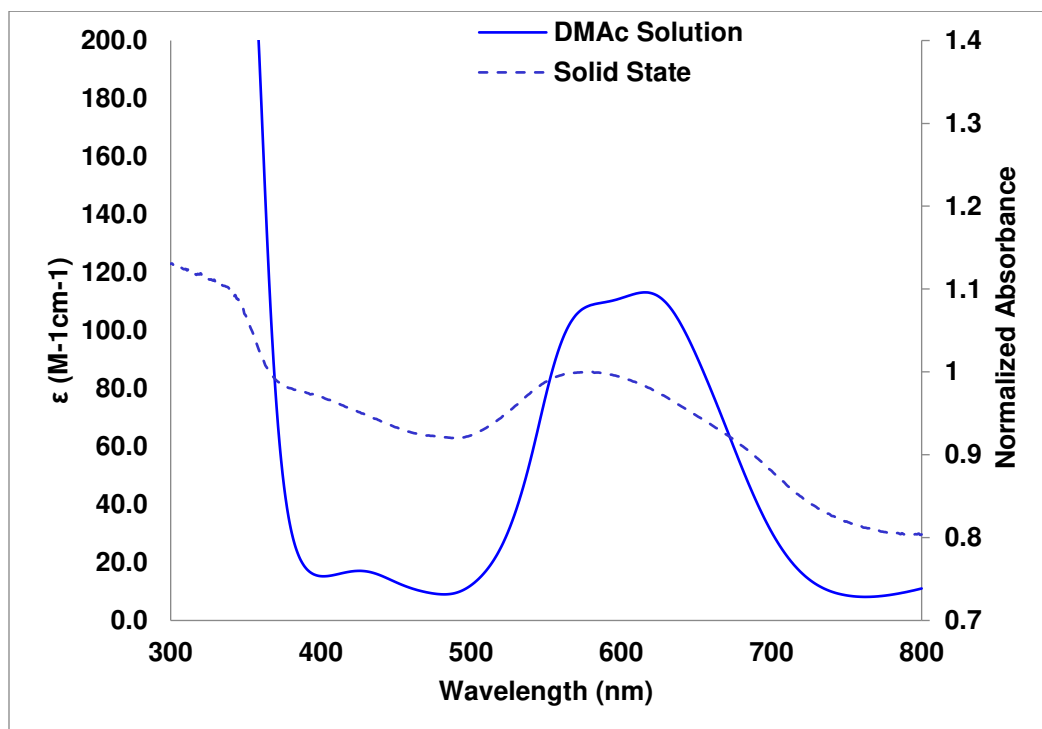


Figure S3.68. Solid-state UV-vis spectrum for single crystals of  $[\text{NiBr}_2(\text{quinuclidine})_2]$  plotted with solution-state UV-vis spectrum of the Ni-quinuclidine DMAC mixture (0.02 M in Ni, 0.6 M in quinuclidine).

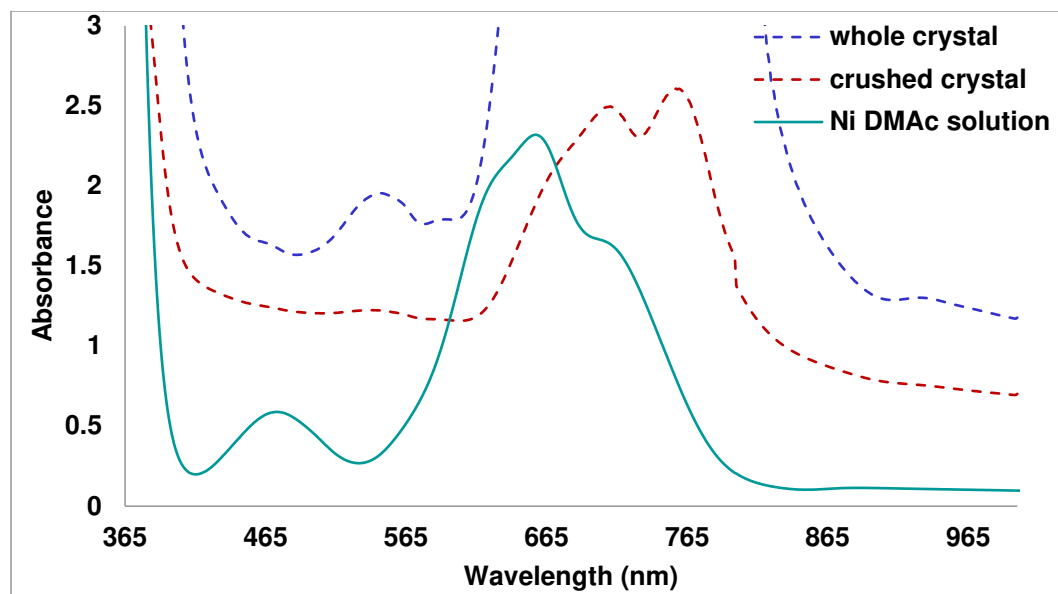


Figure S3.69. Solid-state UV-vis spectrum for single crystals of  $[\text{Ni}(\text{DMAc})_6][\text{NiBr}_4]$  plotted with solution-state UV-vis spectrum of  $\text{NiBr}_2 \cdot 3\text{H}_2\text{O}$  (0.02 M in DMAc) with no amine added.

This spectrum suggests that  $[\text{Ni}(\text{DMAc})_6][\text{NiBr}_4]$  exists in solution. Therefore, several possible pathways of attack exist for amine ligand substitution reactions.

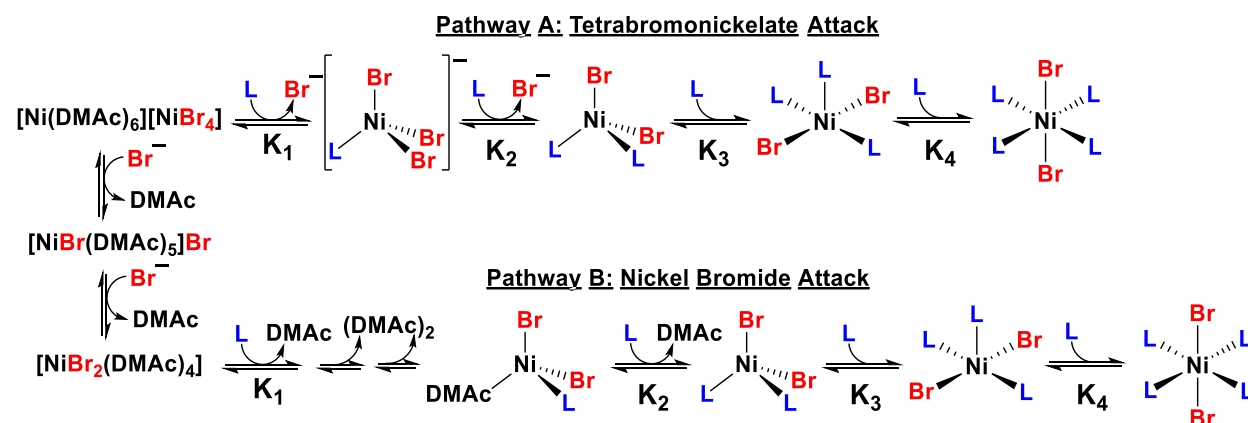


Figure S3.70. Two hypothesized pathways for stepwise equilibria to form Ni-amine complexes.

The dominant observed solution-state UV-vis signals (e.g., ~600 nm, 653 nm, and ~710 nm) of  $[\text{Ni}(\text{DMAc})_6][\text{NiBr}_4]$  can be assigned to  $[\text{NiBr}_4]^{2-}$  on the basis of similarity to spectral data acquired for other tetrabromonickelate salts.<sup>19</sup> In order to form,  $[\text{Ni}(\text{DMAc})_6][\text{NiBr}_4]$  must be related to  $[\text{NiBr}_2(\text{DMAc})_4]$  through a series of bromide substitution equilibria. Either the  $[\text{NiBr}_4]^{2-}$ ,  $[\text{NiBr}(\text{DMAc})_5]\text{Br}$ , or  $[\text{NiBr}_2(\text{DMAc})_4]$  could be attacked by the amine ligand “L” once it is

introduced. Two of these possible pathways are shown in Fig. S3.36. In all cases, the spectral data obtained above (Fig. S3.28-S3.30) suggests pseudotetrahedral geometry for the product of  $K_1$  based on the characteristic UV-visible absorption spectra previously observed in the mixed ligand  $NiBr_3(PPh_3)$  complex examined by Cotton et. al.<sup>20</sup> Further, we assign pseudotetrahedral geometry to the  $K_2$  product,  $[NiBr_2L_2]$ , based on 2 lines of evidence. First, the absorptions observed when  $L =$  morpholine match reasonably well with those observed when  $L =$  quinuclidine, and this complex  $[NiBr_2(quinuclidine)_2]$  was crystallographically characterized in this work and observed to have pseudotetrahedral geometry. In addition, Cotton and Goodgame examined a related  $NiBr_2L_2$  complex where  $L = Ph_3PO$  and found absorptions which closely match those observed herein.<sup>21</sup> Based on the equilibrium data and single-crystal UV-vis, we can now assign the signals in Ni-amine reaction mixtures and quenching mixtures as follows:

*Table S3.8. DMAc solution peak assignments to Ni(II) complexes. ss = solid-state.*

Mixture	Peak $\lambda_{max}$ (nm)	Assignment	Evidence
Ni-morpholine	~550	$[NiBr_2(morpholine)_2]$	$[NiBr_2(quinuclidine)_2]$ ssUV-vis, UV-vis titration fit, references <sup>21-22</sup>
Ni-morpholine	868	$[NiBr_2(morpholine)_2]$	UV-vis titration fit
Ni-morpholine	~970	$[NiBr_2(morpholine)_2]$	UV-vis titration fit
Ni-morpholine	427	$[NiBr_2(morpholine)_3]$	$[NiBr_2(morpholine)_3]$ ssUV-vis, UV-vis titration fit, reference <sup>22</sup>
Ni-morpholine	~740	$[NiBr_2(morpholine)_3]$	$[NiBr_2(morpholine)_3]$ ssUV-vis, UV-vis titration fit
Ni-propylamine	379	$[NiBr_2(propylamine)_4]$	$[NiBr_2(propylamine)_4]$ ssUV-vis
Ni-propylamine	~620	$[NiBr_2(propylamine)_4]$	$[NiBr_2(propylamine)_4]$ ssUV-vis
Ni (no amine)	~600	$[Ni(DMAc)_6][NiBr_4]$	$[Ni(DMAc)_6][NiBr_4]$ ssUV-vis, reference <sup>19</sup>
Ni (no amine)	653	$[Ni(DMAc)_6][NiBr_4]$	$[Ni(DMAc)_6][NiBr_4]$ ssUV-vis, reference <sup>19</sup>
Ni (no amine)	~710	$[Ni(DMAc)_6][NiBr_4]$	$[Ni(DMAc)_6][NiBr_4]$ ssUV-vis, reference <sup>19</sup>

## 9. Characterizations and Proposed Mechanism

Proposed Mechanism:

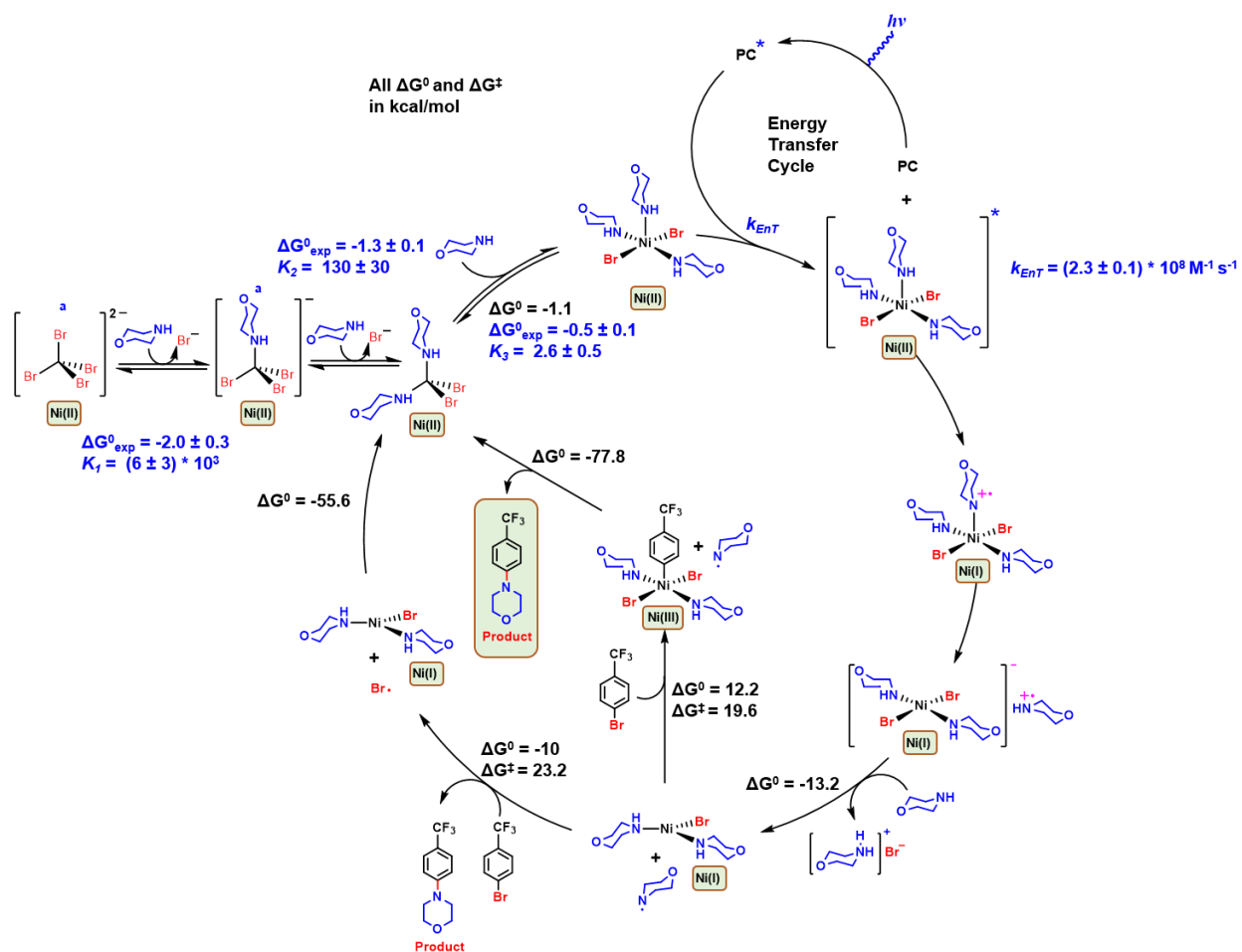


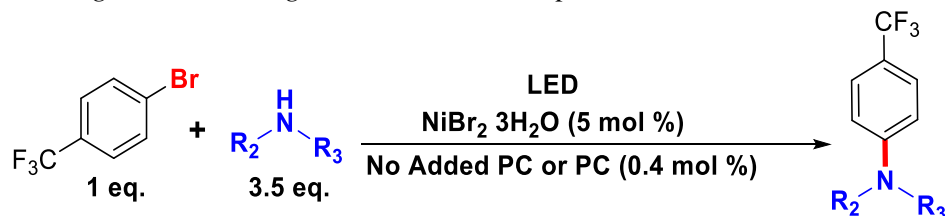
Fig. S3.71. Proposed Mechanism. Values in black were calculated by density functional theory in our previous work.<sup>2</sup> Values shown in blue were measured experimentally in this work. <sup>a</sup>We note that multiple pathways are possible for the first 2 additions of morpholine. The most likely hypothesized pathway is shown here involving ligand substitution of the tetrabromonickelate anion. See Fig. S3.70 for further details.

### General Procedure A:

C–N cross coupling reactions were performed according to the following procedure. Under a nitrogen atmosphere in a glovebox, a DMAc solution containing dissolved NiBr<sub>2</sub>•3H<sub>2</sub>O (0.323 mL, 0.02 mmol, 0.05 eq., 5.5 mg) was added to a 0.5 dram glass vial charged with a stir bar. This vial was removed from the glove box. If present, 500  $\mu$ L photocatalyst (0.0016 mmol, 0.004 eq.)

dissolved in DMAc was added under air. If not, 500  $\mu$ L DMAc was added. Aryl halide (56  $\mu$ L, 0.4 mmol, 1.0 eq.) and amine (1.40 mmol, 3.5 eq.) was added by micropipette. The glass vial was then capped using a screw cap equipped with a PTFE/silicone septum and sealed with a strip of electrical tape. The vial was then sparged through the septum with Ar for 15 minutes. After sparging, the puncture was sealed with electrical tape and the capped glass vial containing the reaction mixture was then placed in a 3D-printed vial holder and subjected to LED irradiation with fan cooling to maintain the vial at room temperature using a setup described previously.<sup>2</sup> After 22 hours, the reaction was stopped by turning off the reactor and a 15  $\mu$ L aliquot was removed for <sup>19</sup>F NMR. This procedure was utilized for reactions reported in Figure 2 in the main text and Table S3.9.

Table S3.9. C-N cross coupling reaction controls. Scale = 0.4 mmol in aryl halide. % DH = % dehalogenated starting material. <sup>a</sup>General procedure B was used.



Amine	Time	Lights	Solvent	PC	% Conv.	% DH
morpholine	22 hrs	457 nm LED	DMAc	none	0%	0%
morpholine	22 hrs	523 nm LED	DMAc	none	0%	0%
morpholine	22 hrs	590 nm LED	DMAc	none	0%	0%
morpholine	22 hrs	740 nm LED	DMAc	none	0%	0%
morpholine	22 hrs	523 nm LED	DMAc	Ru(bpy) <sub>3</sub> ]Cl <sub>2</sub> (PC 1)	88%	0%
morpholine	22 hrs	523 nm LED	DMAc	PC 1, 0.2 mol %	65%	0%
morpholine	15 hrs	523 nm LED	DMAc	PC 1, 0.2 mol %	59% <sup>a</sup>	0%
morpholine	22 hrs	none	DMAc	PC 1	0%	0%
propylamine	22 hrs	523 nm LED	DMAc	PC 1	2%	0%



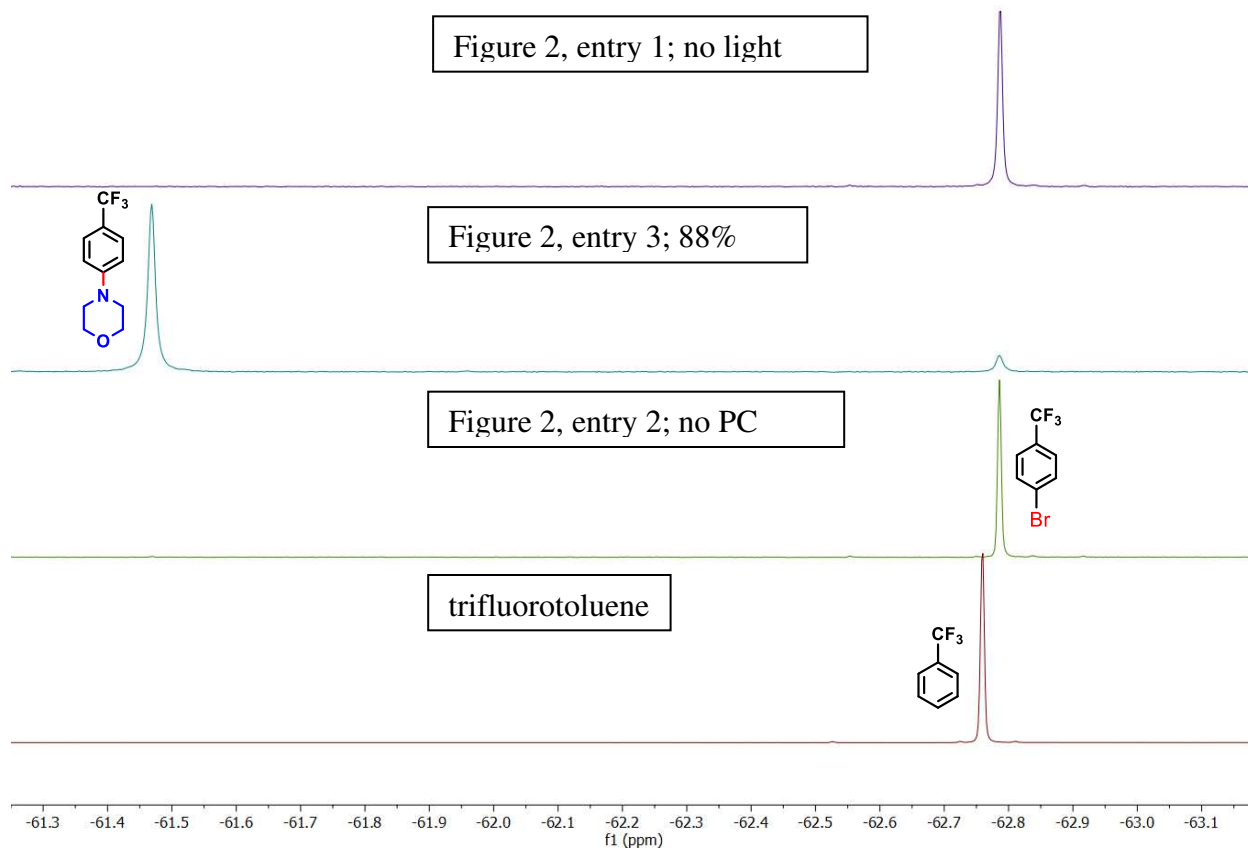
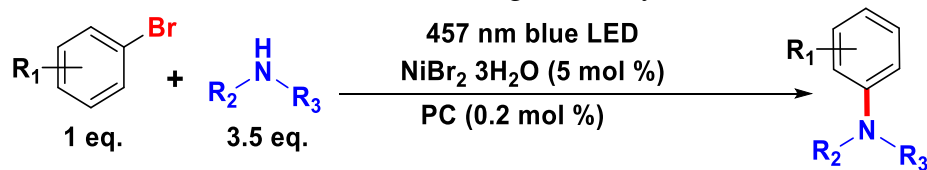


Figure S3.72. Overlaid NMRs of controls in the main text in Figure 2 with authentic trifluorotoluene (dehalogenated 4-bromobenzotrifluoride).

Table S3.10. C-N cross coupling reactions. Effect of KBr. 4-BrBzCF<sub>3</sub> = 4-bromobenzotrifluoride; 3-BrBzCF<sub>3</sub> = 3-bromobenzotrifluoride; 4-IBzCF<sub>3</sub> = 4-iodobenzotrifluoride. %DH = % dehalogenated aryl halide.



Amine	Substrate	Additive	Base	PC	% DH	% Conv. <sup>19</sup> F NMR
morpholine	4-BrBzCF <sub>3</sub>	none	none	1	0%	43%
morpholine	4-BrBzCF <sub>3</sub>	KBr, 1 eq	none	1	0%	36%
propylamine	4-BrBzCF <sub>3</sub>	none	none	2	13%	63%
propylamine	4-BrBzCF <sub>3</sub>	KBr, 1 eq	none	2	13%	77%
piperazine	4-BrBzCF <sub>3</sub>	none	none	1	6%	45%
piperazine	4-BrBzCF <sub>3</sub>	KBr, 1 eq	none	1	9%	71%
morpholine	3-IBzCF <sub>3</sub>	none	none	1	0%	99%
morpholine	3-IBzCF <sub>3</sub>	KBr, 1 eq	none	1	0%	89%
morpholine	3-BrBzCF <sub>3</sub>	none	none	1	<1%	28%
morpholine	3-BrBzCF <sub>3</sub>	KBr, 1 eq	none	1	<1%	28%

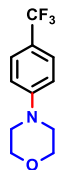
Thus, for reactions involving morpholine, KBr was determined to be ineffective. However, with propylamine and piperazine, use of KBr led to higher yields. Many potential effects could be at the root of this improvement, such as the inhibition of the competing dehalogenation reaction or inhibition of bromide displacement (leading to inhibition of the stepwise equilibria and blue-shifting of Ni-amine complex absorption). Inhibition of dehalogenation appears unlikely since the amount of trifluorotoluene did not change significantly with/without KBr in any of the entries of Table S3.10. UV-vis studies suggest that KBr inhibits binding of propylamine to Ni (See Fig. S3.60-S3.61), supporting the former hypothesis.

### General Procedure B:

C-N cross coupling reactions were performed according to the following procedure. Under a nitrogen atmosphere in a glovebox, aryl halide (1.0 eq., 0.4 mmol) was added to a 0.5 dram glass vial charged with a stir bar and, if applicable, solid amine (1.5 eq. or 3.5 eq.) and/or KBr (1 eq., 0.4 mmol, 47.6 mg). A DMAc solution containing dissolved NiBr<sub>2</sub>·3H<sub>2</sub>O (0.500 mL, 0.02 mmol,

0.05 eq., 5.5 mg) was then added to the vial via micropipette. For reactions containing quinuclidine, the Ni solution was first added to a vial containing weighed out quinuclidine (1.5 eq., 0.6 mmol, 66.7 mg). Once fully dissolved, the solution containing Ni and quinuclidine was added to the 0.5 dram vial. A solution of photocatalyst (0.0008 mmol, 0.002 eq.) dissolved in DMAc (0.500 mL) was added via micropipette. The glass vial was then capped using a screw cap equipped with a PTFE/silicone septum and sealed with Parafilm®. The vial was removed from the glovebox and amine (1.40 mmol, 3.5 eq., degassed) was added by using a degassed Hamilton syringe. The capped glass vial containing the reaction mixture was then placed in a 3D-printed vial holder and subjected to LED irradiation with fan cooling to maintain the vial at room temperature using a setup described previously.<sup>2</sup> After 15 hours, the reaction was stopped by turning off the reactor and a 10  $\mu$ L aliquot was removed for <sup>19</sup>F NMR if the product contains fluorine. The crude reaction mixture was then transferred to a 100 mL column for separation by flash chromatography. The photocatalyst used is indicated prior to each reported yield. PhenO = 3,7-di([1,1'-biphenyl]-4-yl)-10-(naphthalen-1-yl)-10*H*-phenoxazine. Ru = [Ru(bpy)<sub>3</sub>]Cl<sub>2</sub>, where bpy = 2,2-bipyridine.

### Product Characterization:



4-(4-(trifluoromethyl)phenyl)morpholine

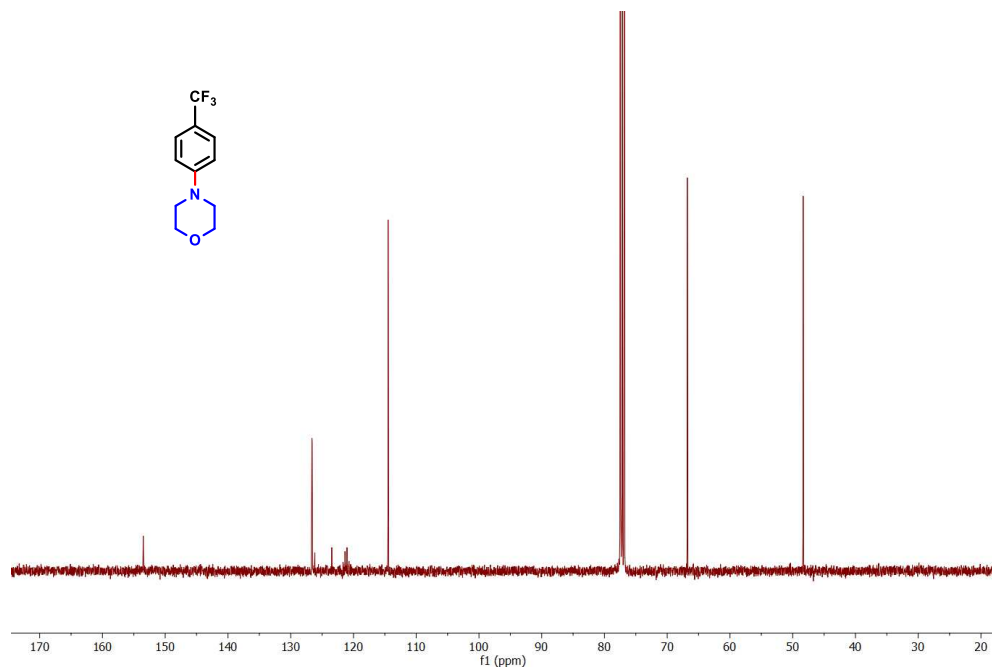
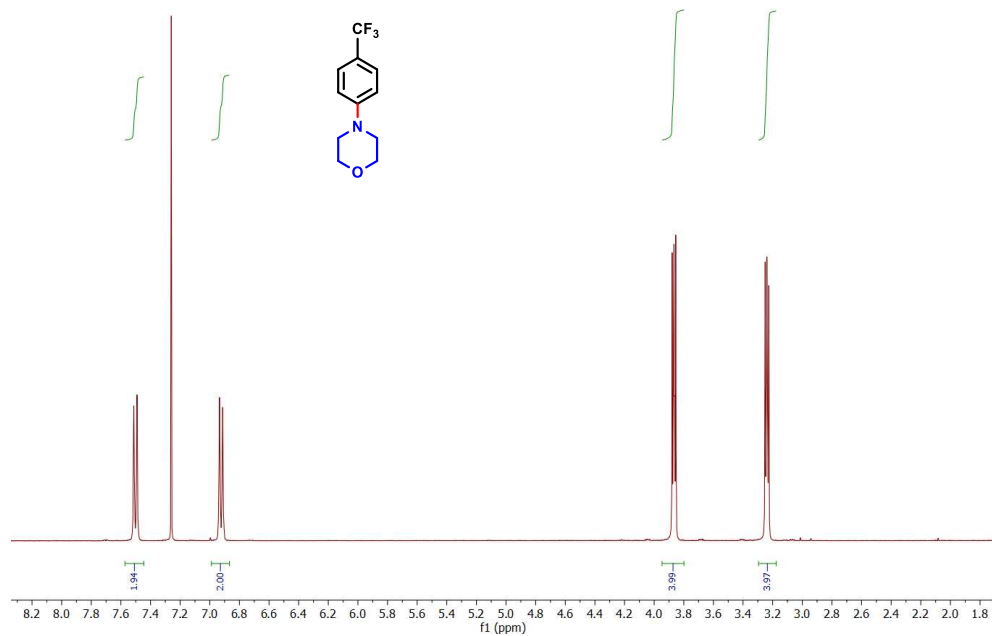
General procedure B was used with morpholine as the amine and 4-bromobenzotrifluoride as the aryl halide. The product was purified by flash chromatography on silica gel in a 100 mL column. The solvent system for product elution was 20% EtOAc/80% hexanes to obtain the product as a white solid (PhenO: 85 mg, 92%; Ru: 40 mg, 43%). NMR spectra matched spectra reported previously.<sup>2</sup>

<sup>1</sup>H NMR (400 MHz, Chloroform-*d*)  $\delta$  7.50 (d,  $J$  = 8.4 Hz, 2H), 6.92 (d,  $J$  = 8.4 Hz, 2H), 3.87 (t,  $J$  = 4.8 Hz, 4H), 3.24 (t,  $J$  = 10.0 Hz, 4H).

<sup>13</sup>C NMR (101 MHz, Chloroform-*d*)  $\delta$  153.5, 126.6 (q,  $J_{C-F}$  = 3.7 Hz), 124.9 (q,  $J_{C-F}$  = 302.2 Hz), 121.2 (q,  $J_{C-F}$  = 33.0 Hz), 114.5, 66.8, 48.3.

<sup>19</sup>F NMR (376 MHz, Chloroform-*d*)  $\delta$  -61.5 (s, 3F).

HRMS (DART-TOF): calculated for C<sub>11</sub>H<sub>13</sub>F<sub>3</sub>NO ([M+H]<sup>+</sup>) 232.0944, found 232.0942.



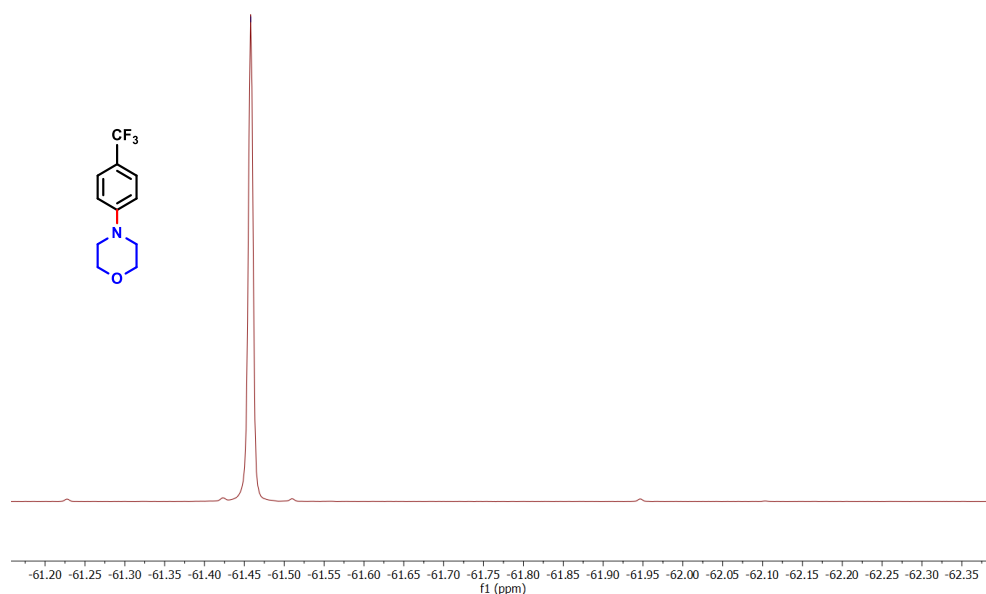
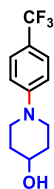


Figure S3.75.  $^{19}\text{F}$  NMR of 4-(4-(trifluoromethyl)phenyl)morpholine



#### 1-(4-(trifluoromethyl)phenyl)piperidin-4-ol

General procedure B was used with 4-hydroxypiperidine as the amine and 4-bromobenzotrifluoride as the aryl halide. The product was purified by flash chromatography on silica gel in a 100 mL column. The solvent system for product elution was 50% EtOAc/50% hexanes and a white solid (PhenO: 75 mg, 76%; Ru: 53 mg, 54%) was recovered. NMR spectra matched those previously reported.<sup>2</sup>

$^1\text{H}$  NMR (400 MHz, Chloroform-*d*)  $\delta$  7.47 (d,  $J = 8.6$  Hz, 2H), 6.94 (d,  $J = 8.7$  Hz, 2H), 3.92 (tt,  $J = 8.6, 4.1$  Hz, 1H), 3.67 (m, 2H), 3.05 (ddd,  $J = 13.0, 9.7, 3.3$  Hz, 2H), 2.01 (m, 2H), 1.67 (m, 2H) 1.50 (s, 1H).

$^{13}\text{C}$  NMR (101 MHz, Chloroform-*d*)  $\delta$  153.2, 126.6 (q,  $J_{\text{C-F}} = 3.8$  Hz), 124.9 (q,  $J_{\text{C-F}} = 271.5$  Hz), 120.2 (q,  $J_{\text{C-F}} = 32.8$  Hz), 114.9, 67.7, 46.1, 33.8, 29.9.

$^{19}\text{F}$  NMR (376 MHz, Chloroform-*d*)  $\delta$  -61.3 (s, 3F).

HRMS (DART-TOF): calculated for  $\text{C}_{12}\text{H}_{15}\text{F}_3\text{NO}$  ( $[\text{M}+\text{H}]^+$ ) 246.1100, found 246.1116.

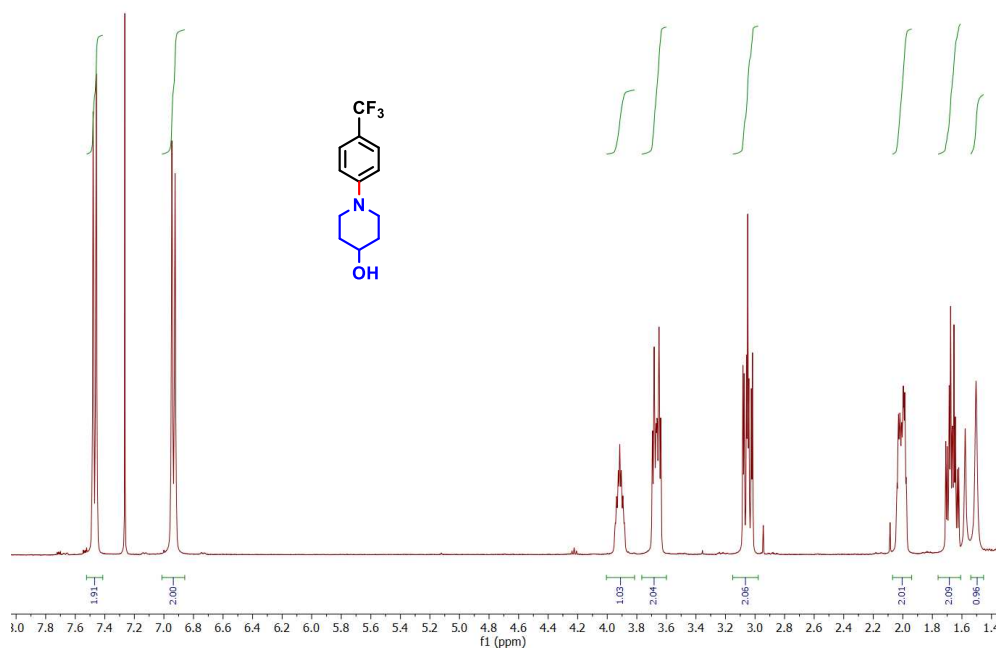


Figure S3.76. <sup>1</sup>H NMR of 1-(4-(trifluoromethyl)phenyl)piperidin-4-ol

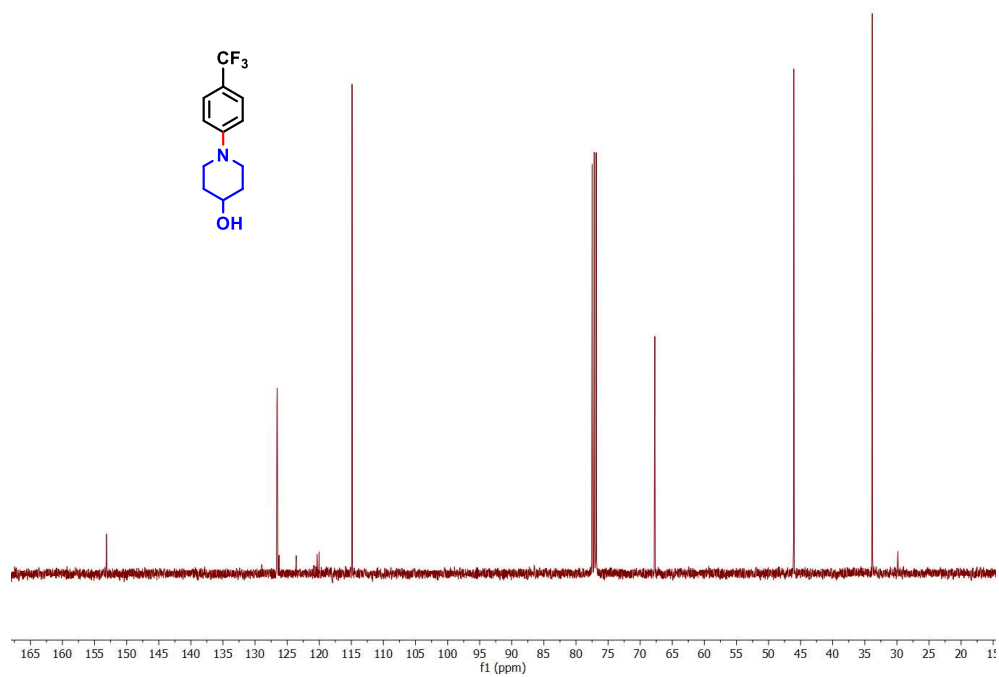


Figure S3.77. <sup>13</sup>C NMR of 1-(4-(trifluoromethyl)phenyl)piperidin-4-ol

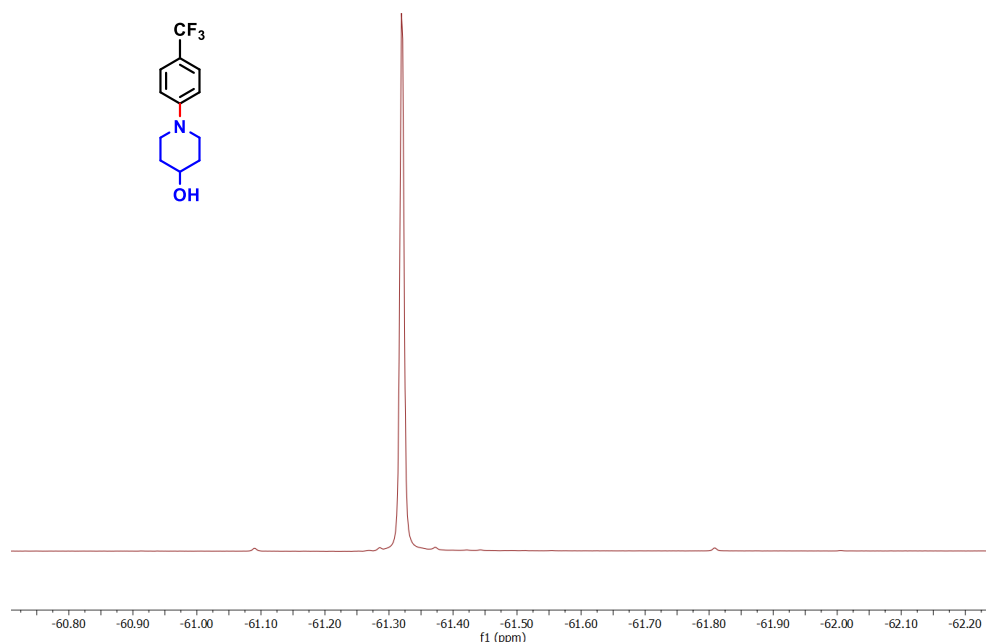
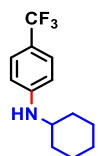


Figure S3.78.  $^{19}\text{F}$  NMR of 1-(4-(trifluoromethyl)phenyl)piperidin-4-ol



#### N-cyclohexyl-4-(trifluoromethyl)aniline

General procedure B was used with cyclohexylamine as the amine and 4-bromobenzotrifluoride as the aryl halide. Flash chromatography was performed on silica gel with 10% EtOAc/90% hexanes to give the product as a pale yellow solid (PhenO: 64 mg, 66%; Ru: <2 mg, trace). NMR spectra matched those previously reported.<sup>2</sup>

$^1\text{H}$  NMR (400 MHz, Chloroform-*d*)  $\delta$  7.37 (d,  $J = 8.4$  Hz, 2H), 6.57 (d,  $J = 8.6$  Hz, 2H), 3.88 (s, 1H), 3.37 – 3.20 (m, 1H), 2.14 – 1.95 (m, 2H), 1.85 – 1.71 (m, 2H), 1.72 – 1.61 (m, 1H), 1.46 – 1.31 (m, 2H), 1.30 – 1.10 (m, 3H).

$^{13}\text{C}$  NMR (101 MHz, Chloroform-*d*)  $\delta$  149.9, 126.8 (q,  $J_{\text{C-F}} = 3.8$  Hz), 125.2 (q,  $J_{\text{C-F}} = 271.1$  Hz), 118.2 (q,  $J_{\text{C-F}} = 32.7$  Hz), 112.1, 51.5, 33.3, 25.9, 25.0.

$^{19}\text{F}$  NMR (376 MHz, Chloroform-*d*)  $\delta$  -60.9 (s, 3F).

HRMS (DART-TOF): calculated for  $\text{C}_{13}\text{H}_{17}\text{F}_3\text{N}$  ( $[\text{M}+\text{H}]^+$ ) 244.1308, found 244.1325.

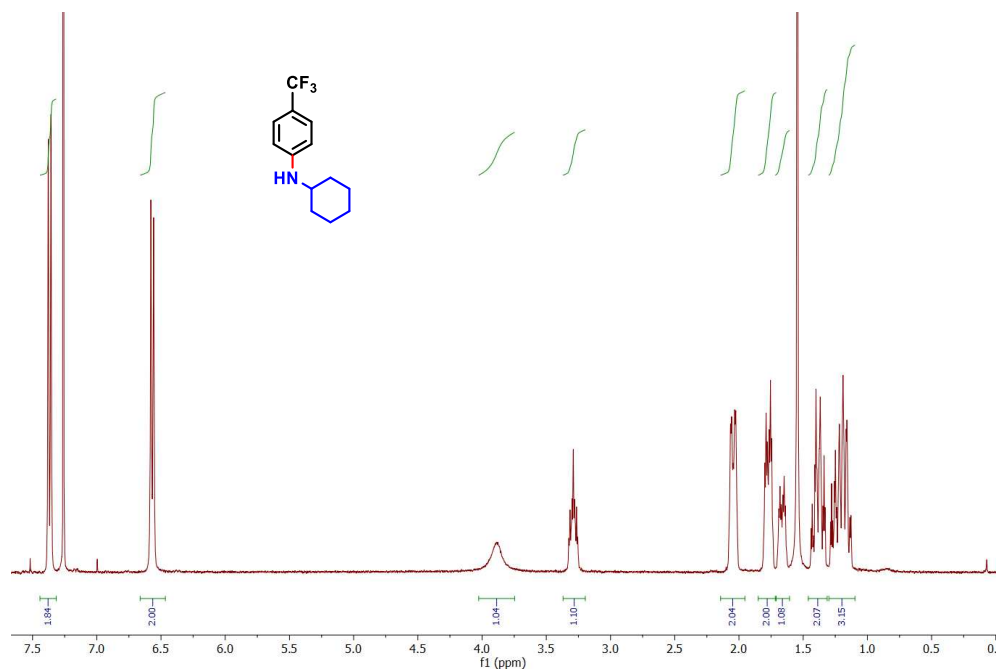


Figure S3.79.  $^1\text{H}$  NMR of *N*-cyclohexyl-4-(trifluoromethyl)aniline

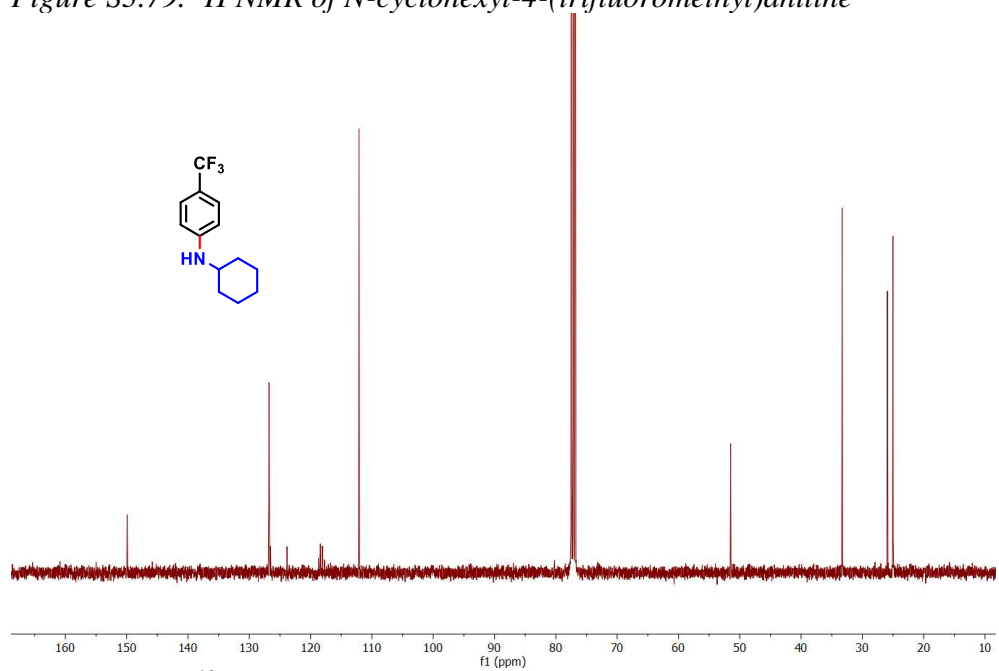


Figure S3.80.  $^{13}\text{C}$  NMR of *N*-cyclohexyl-4-(trifluoromethyl)aniline



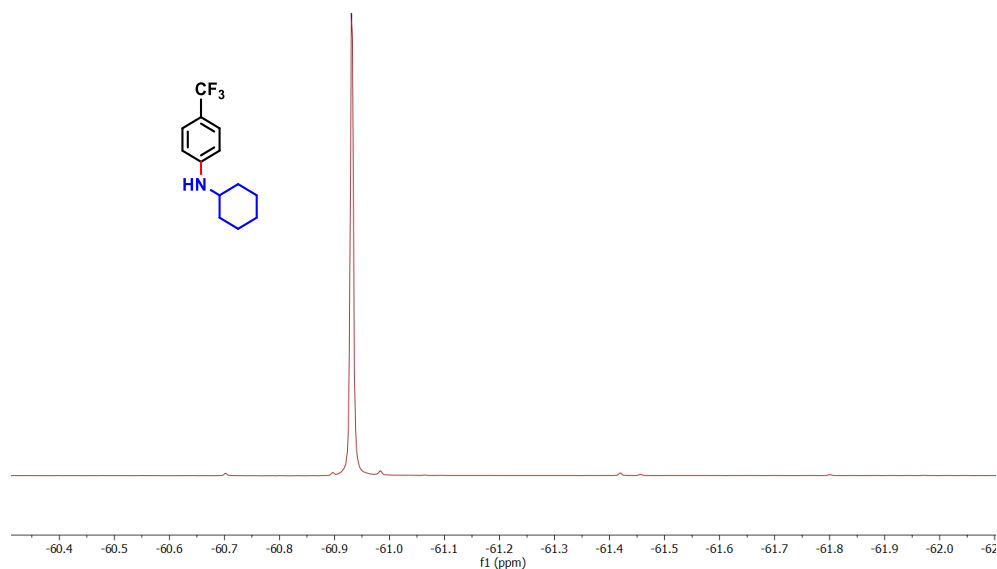
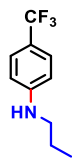


Figure S3.81.  $^{19}\text{F}$  NMR of *N*-cyclohexyl-4-(trifluoromethyl)aniline



#### *N*-propyl-4-(trifluoromethyl)aniline

General procedure B was used with propylamine as the amine and 4-bromobenzotrifluoride as the aryl halide. Flash chromatography was performed on silica gel with 20% EtOAc/80% hexanes to give the product as a pale yellow oil (PhenO: 41 mg, 50%; Ru: <2 mg, trace). NMR spectra matched those previously reported.<sup>2</sup>

$^1\text{H}$  NMR (400 MHz, Chloroform-*d*)  $\delta$  7.39 (d,  $J = 8.3$  Hz, 2H), 6.59 (d,  $J = 8.4$  Hz, 2H), 4.01 (s, 1H), 3.11 (t,  $J = 7.1$  Hz, 2H), 1.67 (dt,  $J = 14.4$  Hz, 7.3 Hz, 2H), 1.01 (t,  $J = 7.4$  Hz, 3H).

$^{13}\text{C}$  NMR (101 MHz, Chloroform-*d*)  $\delta$  151.0, 126.7 (q,  $J_{\text{C-F}} = 3.8$  Hz), 125.2 (q,  $J_{\text{C-F}} = 271.2$  Hz), 118.6 (q,  $J_{\text{C-F}} = 32.7$  Hz), 111.8, 45.4, 22.6, 11.7.

$^{19}\text{F}$  NMR (376 MHz, Chloroform-*d*)  $\delta$  -60.9 (s, 3F).

HRMS (DART-TOF): calculated for  $\text{C}_{10}\text{H}_{13}\text{F}_3\text{N}$  ( $[\text{M}+\text{H}]^+$ ) 204.0995, found 204.1009.

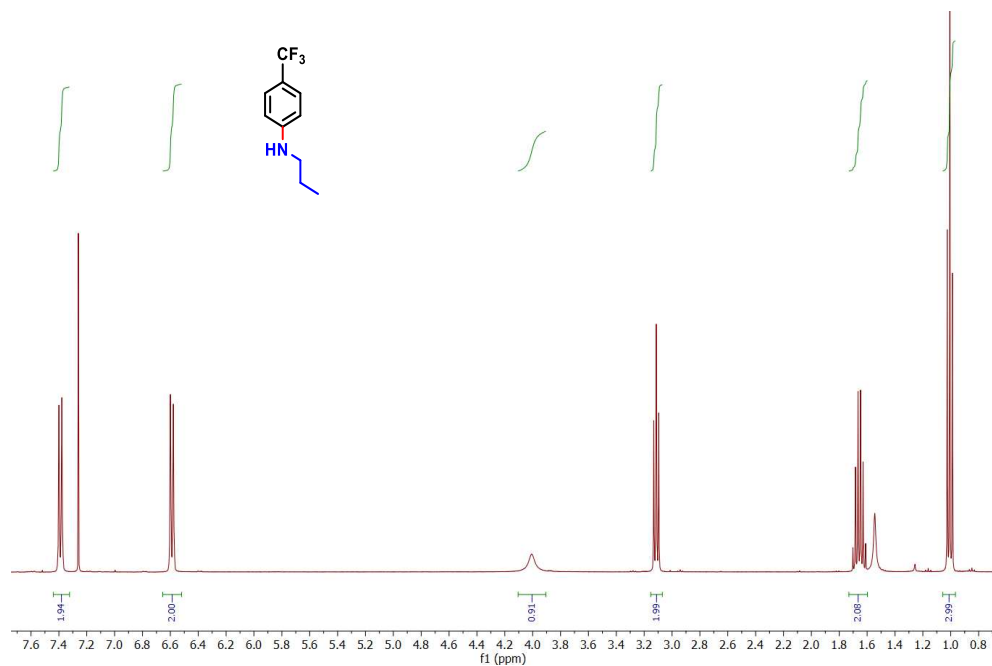


Figure S3.82.  $^1\text{H}$  NMR of *N*-propyl-4-(trifluoromethyl)aniline

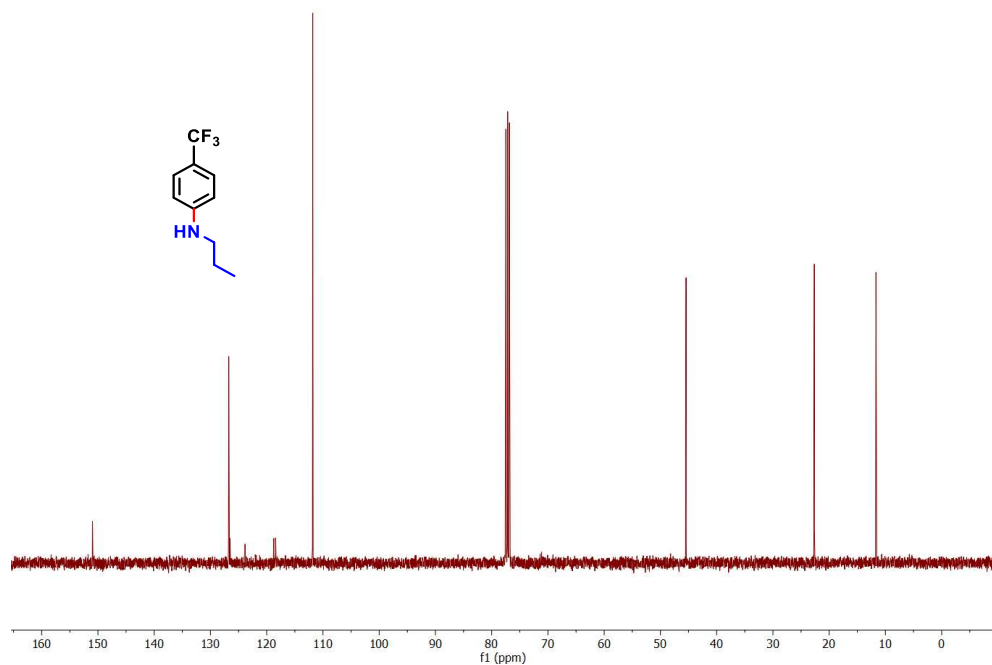


Figure S3.83.  $^{13}\text{C}$  NMR of *N*-propyl-4-(trifluoromethyl)aniline

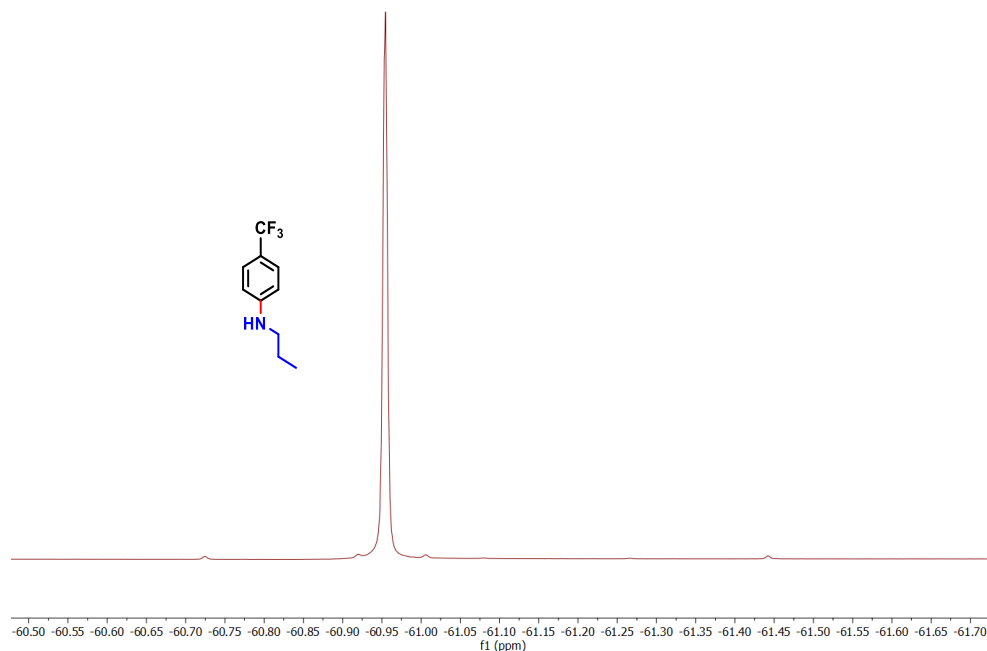
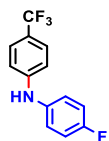


Figure S3.84.  $^{19}\text{F}$  NMR of *N*-propyl-4-(trifluoromethyl)aniline



#### 4-fluoro-*N*-(4-(trifluoromethyl)phenyl)aniline

General procedure B was followed with 4-fluoroaniline as the amine and 4-bromobenzotrifluoride as the aryl halide. Flash chromatography was performed on silica gel, eluting with 20% EtOAc/80% hexanes to give the product as a yellow solid (PhenO: 56 mg, 55%; Ru: 27 mg, 26%). NMR spectra matched those previously reported.<sup>2</sup>

$^1\text{H}$  NMR (400 MHz, Chloroform-*d*)  $\delta$  7.45 (d,  $J = 8.4$  Hz, 2H), 7.18 – 7.09 (m, 2H), 7.09 – 6.98 (m, 2H), 6.93 (d,  $J = 8.4$  Hz, 2H), 5.79 (s, 1H).

$^{13}\text{C}$  NMR (101 MHz, Chloroform-*d*)  $\delta$  159.3 (d,  $J_{\text{C-F}} = 242.5$  Hz), 147.7, 137.1 (d,  $J_{\text{C-F}} = 2.8$  Hz), 126.9 (q,  $J_{\text{C-F}} = 3.8$  Hz), 124.8 (q,  $J_{\text{C-F}} = 270.6$  Hz), 123.2 (d,  $J_{\text{C-F}} = 8.0$  Hz), 121.6 (q,  $J_{\text{C-F}} = 32.8$  Hz), 116.4 (d,  $J_{\text{C-F}} = 22.6$  Hz), 114.7.

$^{19}\text{F}$  NMR (376 MHz, Chloroform-*d*)  $\delta$  -61.5 (s, 3F), -119.2 (hept,  $J = 5.1, 5.1, 4.5, 4.5, 3.5, 3.2$  Hz, 1F).

HRMS (DART-TOF): calculated for  $\text{C}_{13}\text{H}_{10}\text{F}_4\text{N}$  ( $[\text{M}+\text{H}]^+$ ) 256.0744, found 256.0698.

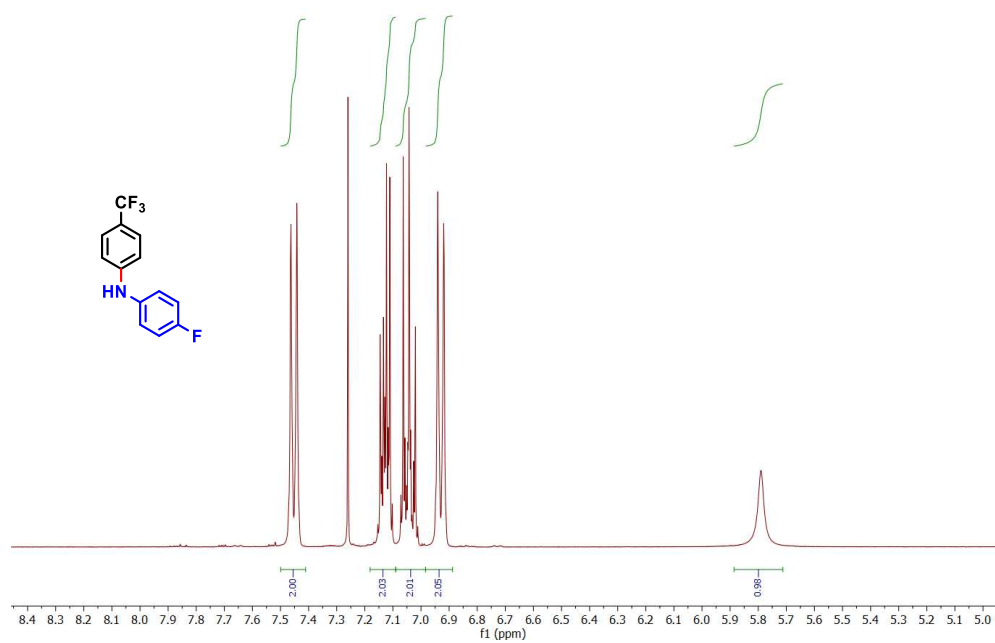


Figure S3.85. <sup>1</sup>H NMR of 4-fluoro-N-(4-(trifluoromethyl)phenyl)aniline

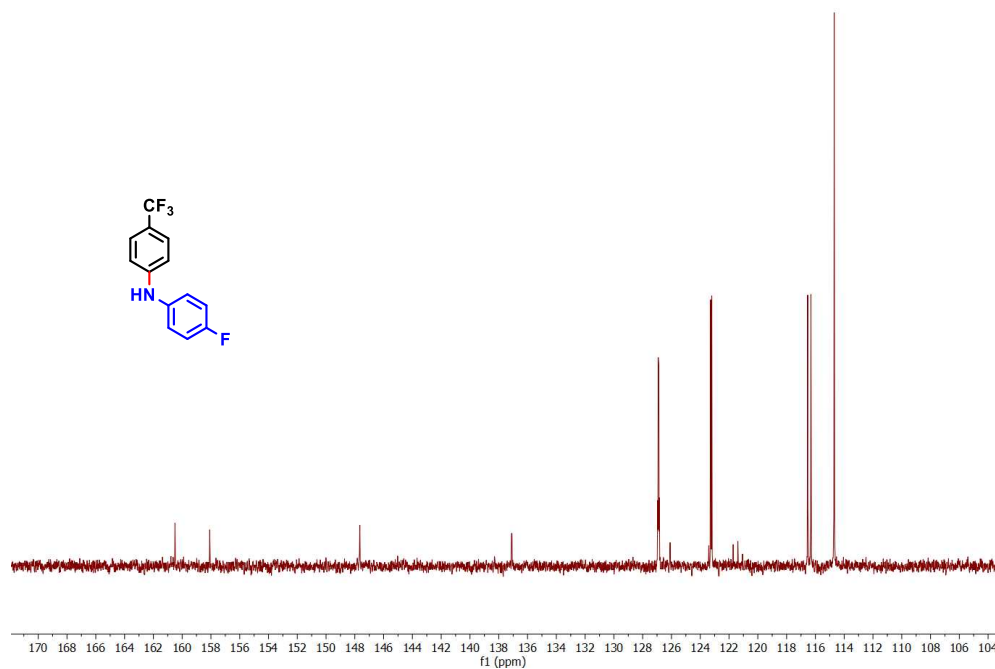


Figure S3.86. <sup>13</sup>C NMR of 4-fluoro-N-(4-(trifluoromethyl)phenyl)aniline

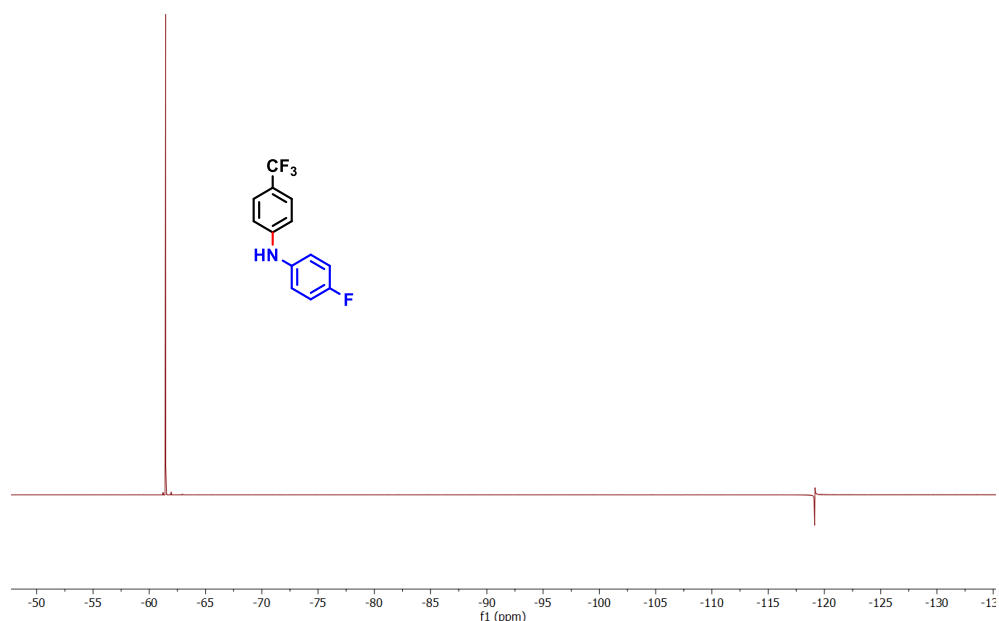
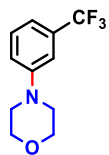


Figure S3.87.  $^{19}\text{F}$  NMR of 4-fluoro-*N*-(4-(trifluoromethyl)phenyl)aniline



#### 4-(3-(trifluoromethyl)phenyl)morpholine

General procedure B was used with morpholine as the amine and 3-bromobenzotrifluoride as the aryl halide. Flash chromatography was performed on silica gel with 15% EtOAc/ 85% hexanes to give the product as a pale yellow oil (PhenO: 78 mg, 84%; Ru: 11 mg, 12%). NMR spectra matched those previously reported.<sup>2</sup>

$^1\text{H}$  NMR (400 MHz, Chloroform-*d*)  $\delta$  7.44 – 7.31 (m, 1H), 7.17 – 7.00 (m, 3H), 3.87 (t,  $J = 4.8$ , 4H), 3.20 (t,  $J = 4.9$ , 4H).

$^{13}\text{C}$  NMR (101 MHz, Chloroform-*d*)  $\delta$  151.6, 131.7 (q,  $J_{\text{C-F}} = 31.9$  Hz), 129.8, 124.9 (q,  $J_{\text{C-F}} = 374.5$  Hz), 118.6, 116.4 (q,  $J_{\text{C-F}} = 3.9$  Hz), 112.0 (q,  $J_{\text{C-F}} = 3.9$  Hz), 66.9, 49.0.

$^{19}\text{F}$  NMR (376 MHz, Chloroform-*d*)  $\delta$  -62.76 (s, 3F).

HRMS (DART-TOF): calculated for  $\text{C}_{11}\text{H}_{13}\text{F}_3\text{NO}$  ( $[\text{M}+\text{H}]^+$ ) 232.0944, found 232.0960.

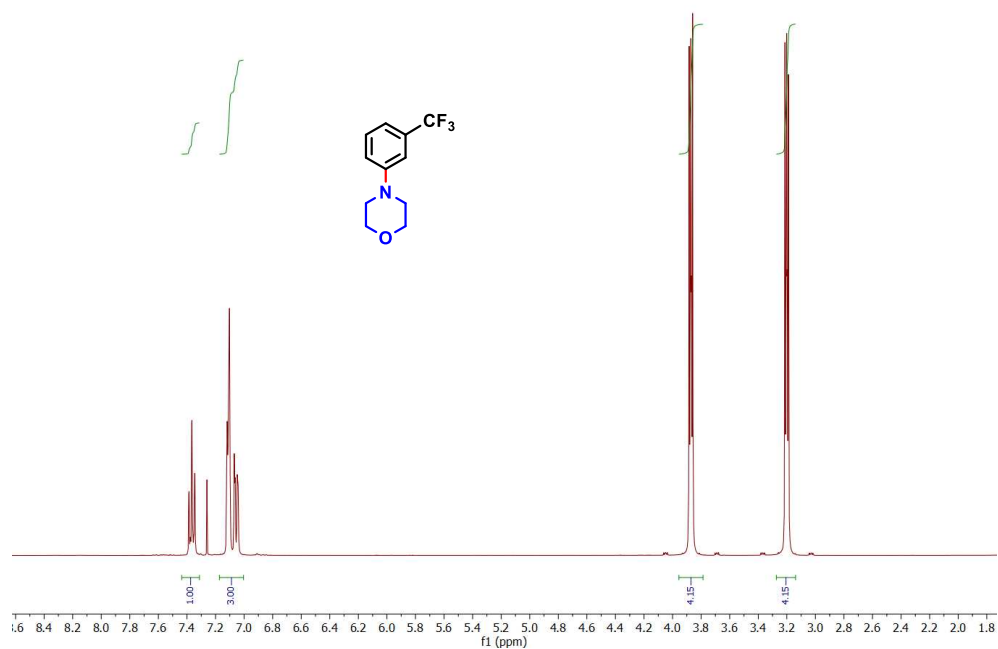


Figure S3.88.  $^1\text{H}$  NMR of 4-(3-(trifluoromethyl)phenyl)morpholine

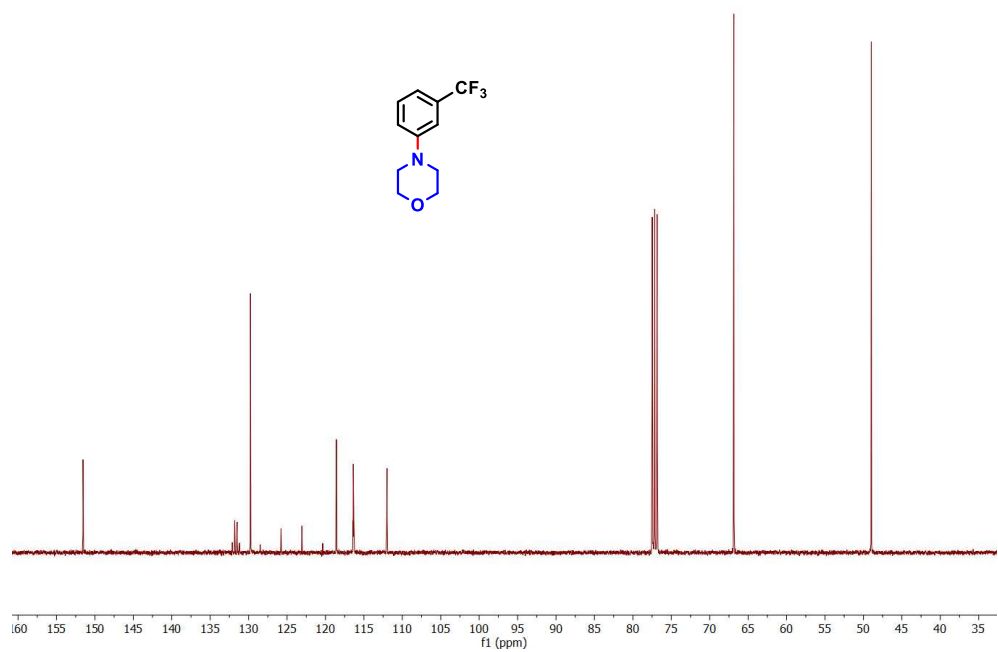


Figure S3.89.  $^{13}\text{C}$  NMR of 4-(3-(trifluoromethyl)phenyl)morpholine

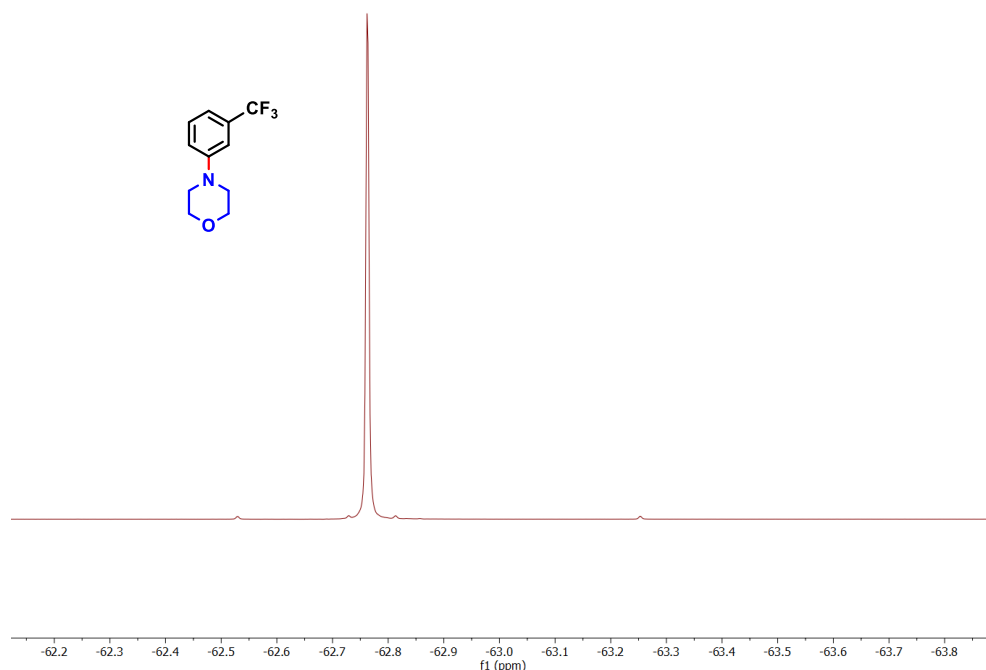
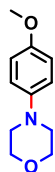


Figure S3.90.  $^{19}\text{F}$  NMR of 4-(3-(trifluoromethyl)phenyl)morpholine



#### 4-(4-methoxyphenyl)morpholine

General procedure B was used with morpholine as the amine and 4-bromoanisole as the aryl halide. Flash chromatography was performed on silica gel, eluting with 20% EtOAc/ 80% hexanes to give the product as a white solid (PhenO: 24 mg, 33%; Ru: 10 mg, 13%). NMR spectra matched those previously reported.<sup>2</sup>

$^1\text{H}$  NMR (400 MHz, Chloroform-*d*)  $\delta$  7.00 – 6.79 (m, 4H), 3.86 (t,  $J = 4.7$  Hz, 4H), 3.77 (s, 3H), 3.06 (t,  $J = 4.8$  Hz, 4H).

$^{13}\text{C}$  NMR (101 MHz, Chloroform-*d*)  $\delta$  154.1, 145.8, 118.0, 114.7, 67.2, 55.7, 51.0, 29.9.

HRMS (DART-TOF): calculated for  $\text{C}_{11}\text{H}_{16}\text{NO}_2$  ( $[\text{M}+\text{H}]^+$ ) 194.1176, found 194.1192.

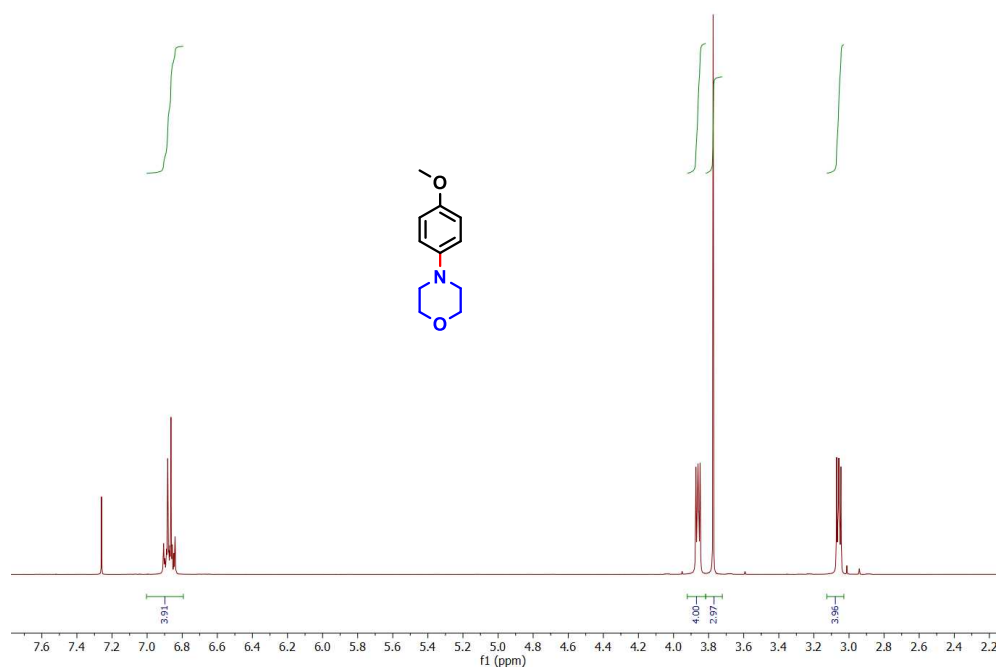


Figure S3.91.  $^1\text{H}$  NMR of 4-(4-methoxyphenyl)morpholine

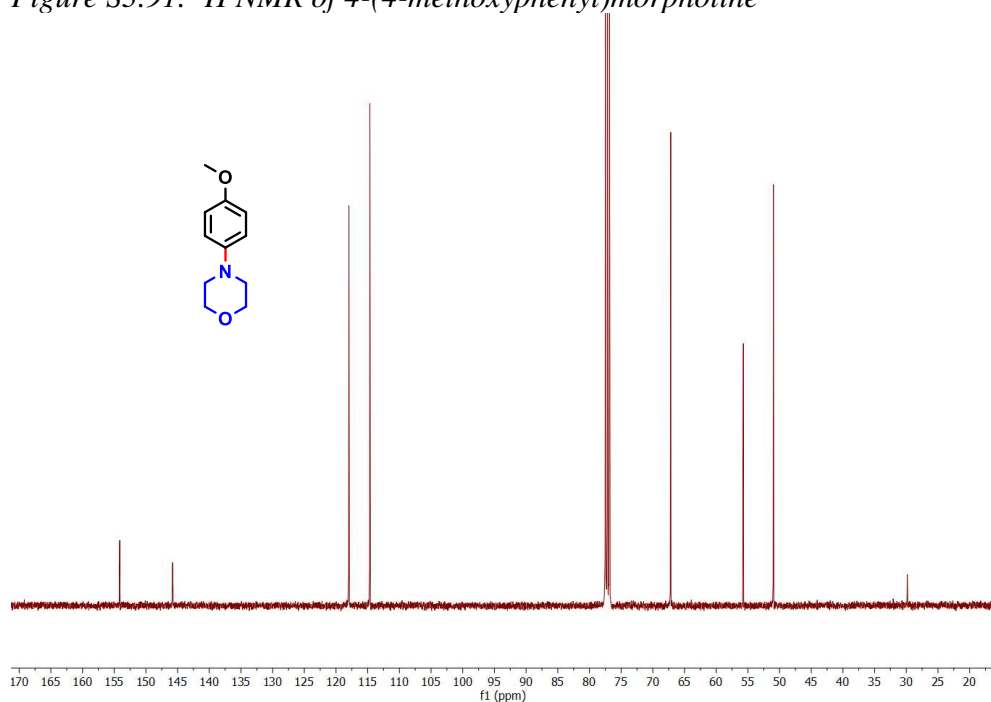
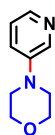


Figure S3.92.  $^{13}\text{C}$  NMR of 4-(4-methoxyphenyl)morpholine



#### 4-(pyridin-3-yl)morpholine

General procedure B was used with morpholine as the amine and 3-bromopyridine as the aryl halide. Flash chromatography was performed on silica gel with 50% EtOAc/50% hexanes to give



the product as a pale yellow oil (PhenO: 38 mg, 58%; Ru: 6 mg, 9%). NMR spectra matched those previously reported.<sup>2</sup>

<sup>1</sup>H NMR (400 MHz, Chloroform-*d*) δ 8.30 (s, 1H), 8.12 (t, *J* = 2.8 Hz, 1H), 7.16 (d, *J* = 2.5 Hz, 2H), 3.86 (t, *J* = 4.8 Hz, 4H), 3.17 (t, *J* = 5.3 Hz, 4H).

<sup>13</sup>C NMR (101 MHz, Chloroform-*d*) δ 147.0, 141.3, 138.4, 123.6, 122.2, 66.8, 48.7.

HRMS (DART-TOF): calculated for C<sub>9</sub>H<sub>13</sub>N<sub>2</sub>O ([M+H]<sup>+</sup>) 165.1022, found 165.1036.

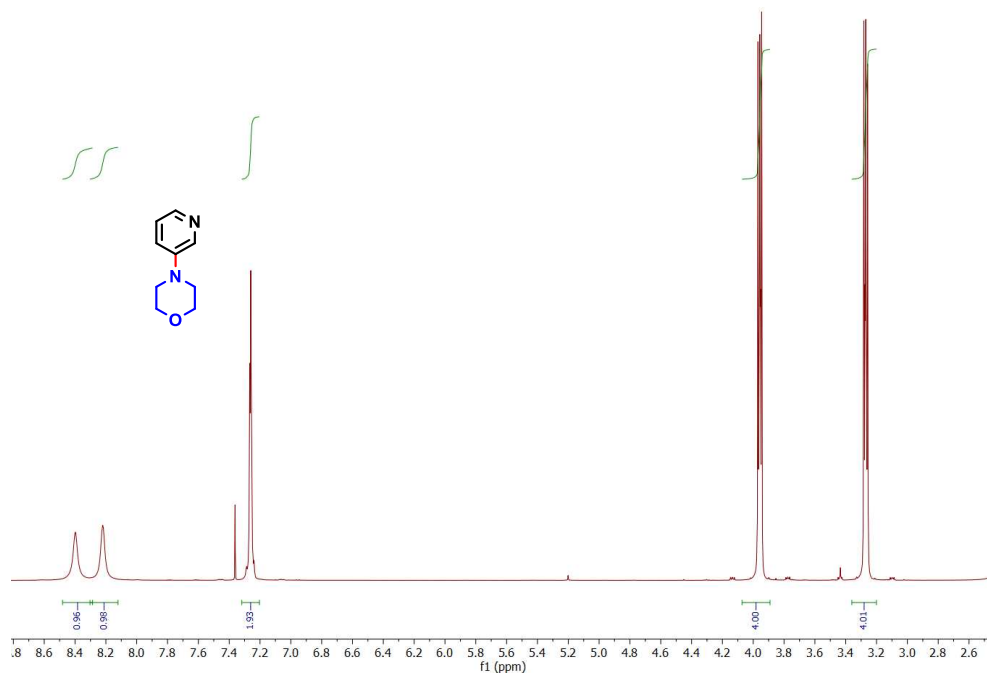


Figure S3.93. <sup>1</sup>H NMR of 4-(pyridin-3-yl)morpholine

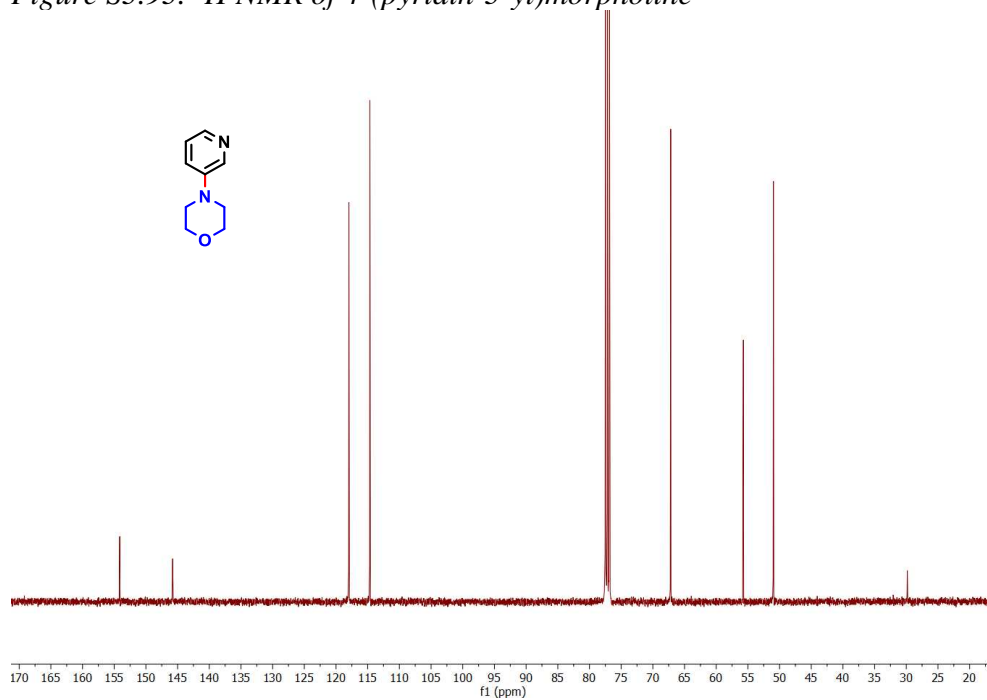
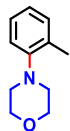


Figure S3.94. <sup>13</sup>C NMR of 4-(pyridin-3-yl)morpholine



#### 4-(*o*-tolyl)morpholine

General procedure B was used with morpholine as the amine and 2-iodotoluene as the aryl halide. Flash chromatography was performed on silica gel with 10% EtOAc/ 90% hexanes to give the product as a pale yellow (PhenO: 19 mg, 27%; Ru: < 2 mg, trace). NMR data matched previously reported spectra.<sup>23</sup>

<sup>1</sup>H NMR (400 MHz, Chloroform-*d*)  $\delta$  7.23 – 7.13 (m, 2H), 7.07 – 6.94 (m, 2H), 3.86 (t,  $J = 4.5$  Hz, 4H), 2.92 (t,  $J = 4.5$  Hz, 4H), 2.33 (s, 3H).

<sup>13</sup>C NMR (101 MHz, Chloroform-*d*)  $\delta$  151.4, 132.8, 131.3, 126.8, 123.6, 119.1, 67.6, 52.4, 29.9, 18.0.

HRMS (DART-TOF): calculated for C<sub>11</sub>H<sub>16</sub>NO ( $[M+H]^+$ ) 178.1226, found 178.1213.

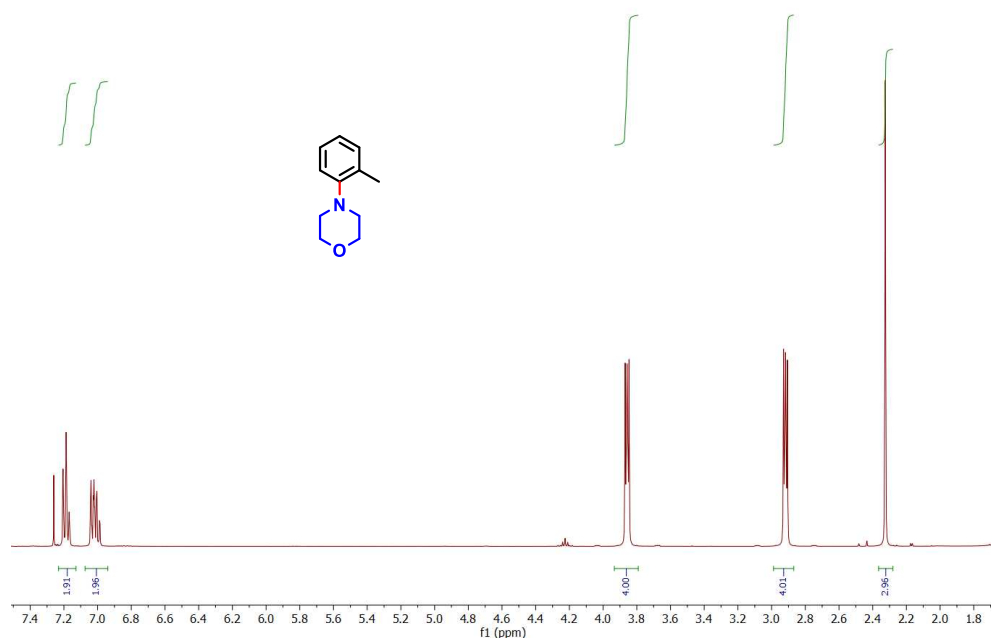


Figure S3.95. <sup>1</sup>H NMR of 4-(*o*-tolyl)morpholine

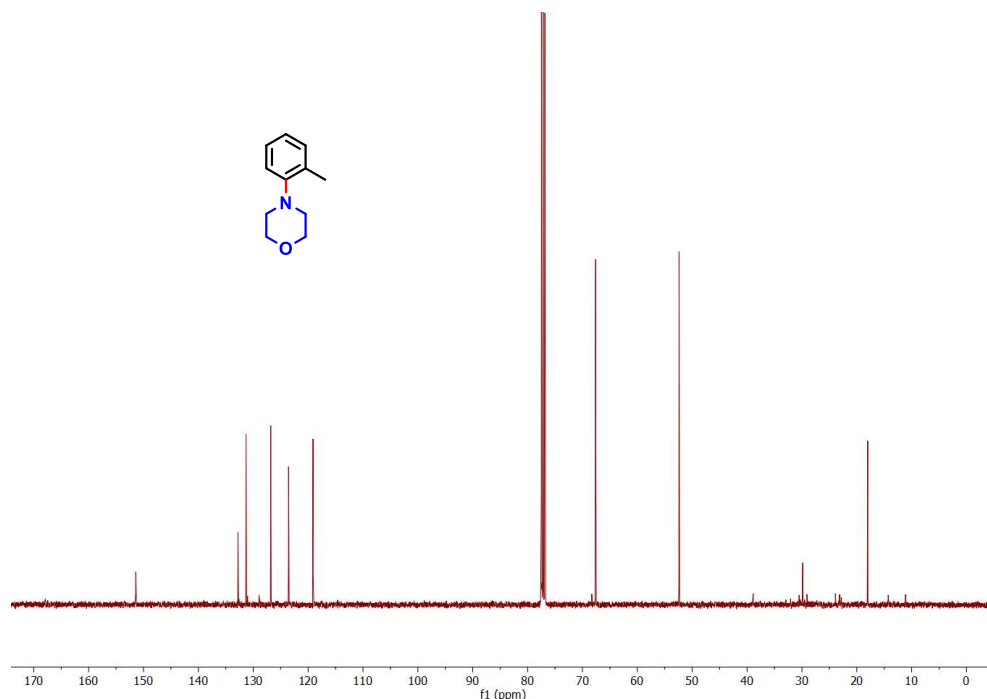
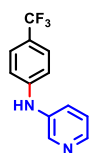


Figure S3.96.  $^{13}\text{C}$  NMR of 4-(*o*-tolyl)morpholine



N-(4-(trifluoromethyl)phenyl)pyridin-3-amine

General procedure B was used with 3-aminopyridine as the amine and 4-bromobenzotrifluoride as the aryl halide. Flash chromatography was performed on silica gel with 90% EtOAc/10% hexanes to give the product as a yellow solid (PhenO: 32 mg, 33%; Ru: < 2 mg, trace). NMR spectra matched those previously reported.<sup>2</sup>

$^1\text{H}$  NMR (400 MHz,  $\text{DMSO-}d_6$ )  $\delta$  8.85 (s, 1H), 8.42 (d,  $J = 2.5$  Hz, 1H), 8.17 (dd,  $J = 4.6, 1.4$  Hz, 1H), 7.60 (dq,  $J = 8.3, 1.4$  Hz, 1H), 7.55 (d,  $J = 8.6$  Hz, 2H), 7.33 (dd,  $J = 4.7, 3.6$  Hz, 1H), 7.17 (d,  $J = 8.5$  Hz, 2H).

$^{13}\text{C}$  NMR (101 MHz,  $\text{DMSO-}d_6$ )  $\delta$  146.8, 142.5, 141.1, 138.2, 126.7 (q,  $J_{\text{C-F}} = 3.8$  Hz), 125.1, 124.8 (q,  $J_{\text{C-F}} = 270.8$  Hz), 124.0, 119.3 (q,  $J_{\text{C-F}} = 32.2$  Hz), 115.1.

$^{19}\text{F}$  NMR (376 MHz,  $\text{DMSO-}d_6$ )  $\delta$  -59.7 (s, 3F).

HRMS (DART-TOF): calculated for  $C_{12}H_{10}F_3N_2$  ( $[M+H]^+$ ) 239.0791, found 239.0803.

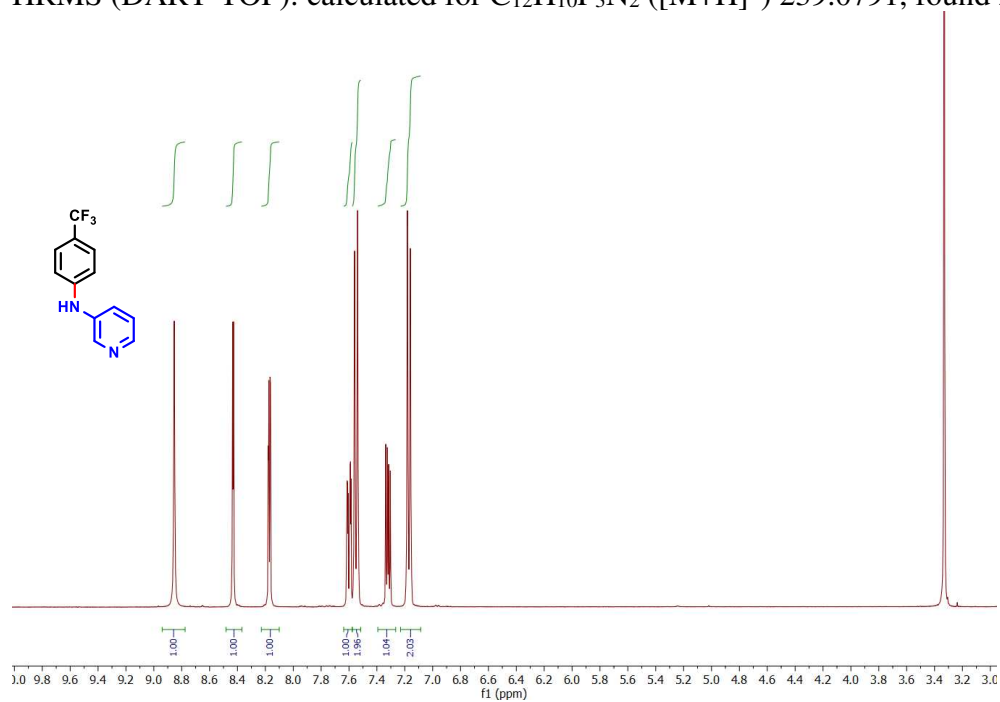


Figure S3.97.  $^1H$  NMR of *N*-(4-(trifluoromethyl)phenyl)pyridin-3-amine

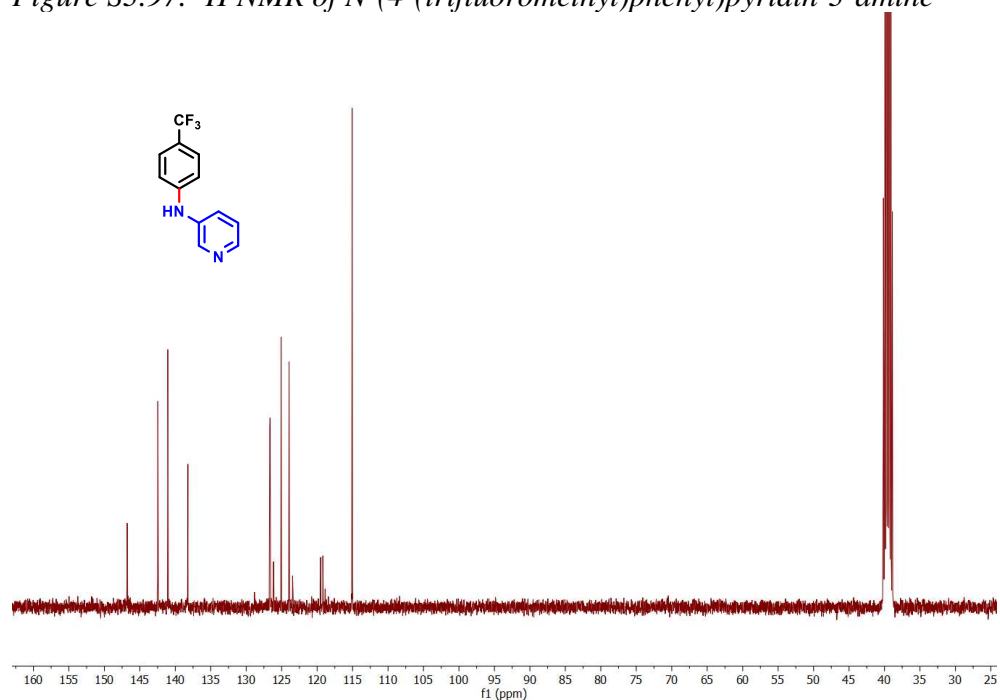


Figure S3.98.  $^{13}C$  NMR of *N*-(4-(trifluoromethyl)phenyl)pyridin-3-amine

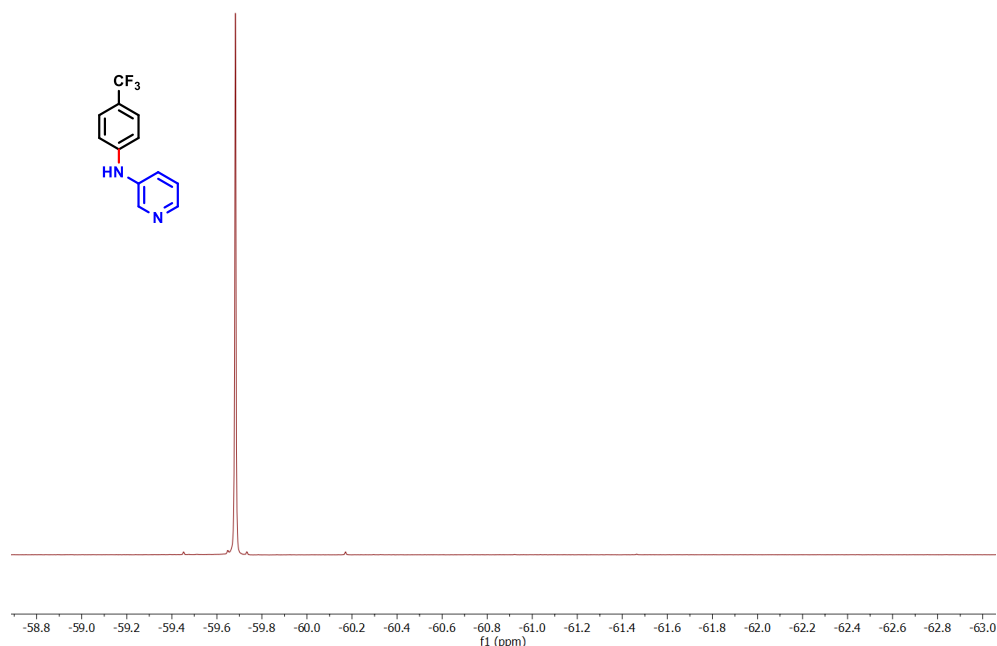
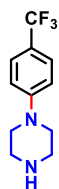


Figure S3.99.  $^{19}\text{F}$  NMR of *N*-(4-(trifluoromethyl)phenyl)pyridin-3-amine



#### 1-(4-(trifluoromethyl)phenyl)piperazine

General procedure B was used with piperazine as the amine and 4-bromobenzotrifluoride as the aryl halide. Flash chromatography was performed on silica gel with 30% MeOH/85% DCM to give the product as a yellow solid (PhenO: 18 mg, 20%; Ru: 47 mg, 51%). NMR spectra matched those previously reported.<sup>2</sup>

$^1\text{H}$  NMR (400 MHz, Chloroform-*d*)  $\delta$  7.53 (d,  $J = 8.5$  Hz, 2H), 6.95 (d,  $J = 8.6$  Hz, 2H), 3.56 (t,  $J = 3.8$  Hz, 4H), 3.36 (t,  $J = 5.2$  Hz, 4H), 1.25 (s, 1H)

$^{13}\text{C}$  NMR (101 MHz, DMSO-*d*<sub>6</sub>)  $\delta$  152.5, 126.3 (q,  $J = 3.6$  Hz), 124.8 (q,  $J = 271.2$  Hz), 118.9 (q,  $J = 32.1$  Hz), 114.8, 44.7, 42.7.

$^{19}\text{F}$  NMR (376 MHz, Chloroform-*d*)  $\delta$  -61.8 (s, 3F).

HRMS (DART-TOF): calculated for  $C_{11}H_{14}F_3N_2$  ( $[M+H]^+$ ) 231.1104, found 231.1117.

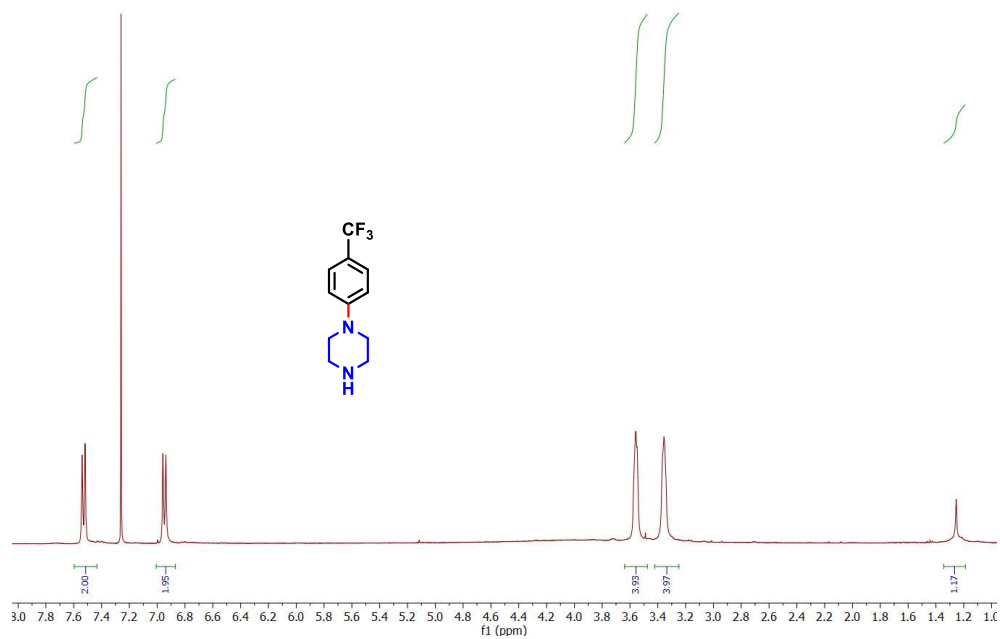


Figure S3.100.  $^1H$  NMR of 1-(4-(trifluoromethyl)phenyl)piperazine

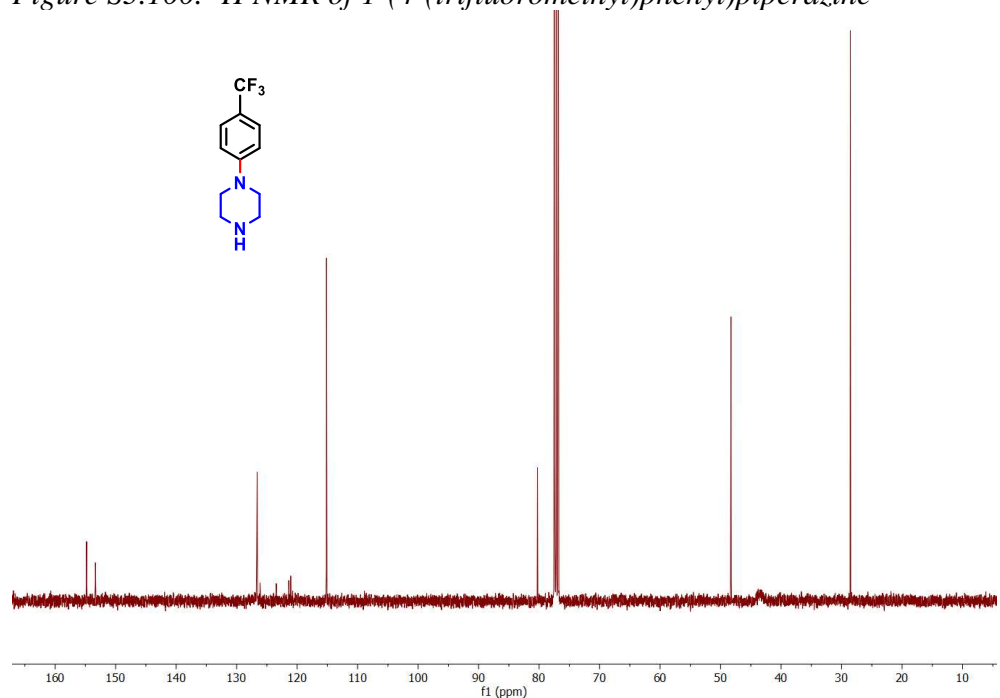


Figure S3.101.  $^{13}C$  NMR of 1-(4-(trifluoromethyl)phenyl)piperazine

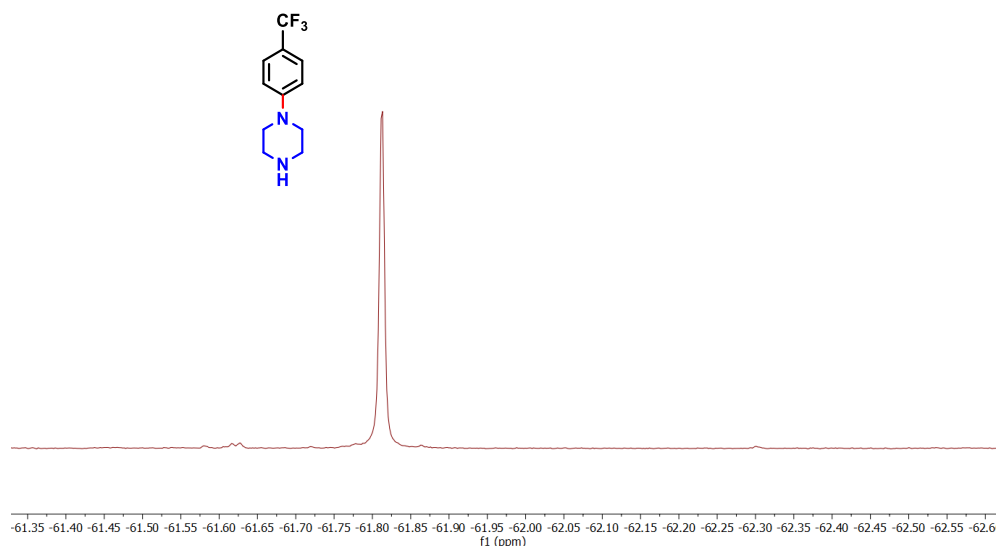
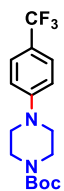


Figure S3.102.  $^{19}\text{F}$  NMR of 1-(4-(trifluoromethyl)phenyl)piperazine



*tert*-butyl 4-(3-(trifluoromethyl)phenyl)piperazine-1-carboxylate

General procedure B was used with *tert*-butyl piperazine-1-carboxylate as the amine and 4-bromobenzotrifluoride as the aryl halide. Flash chromatography was performed on silica gel with 15% EtOAc/85% hexanes to give the product as a white solid (PhenO: 114 mg, 86%; Ru: 19 mg, 14%). NMR spectra matched those previously reported.<sup>2</sup>

$^1\text{H}$  NMR (400 MHz, Chloroform-*d*)  $\delta$  7.49 (d,  $J = 8.2$  Hz, 2H), 6.92 (d,  $J = 8.7$  Hz, 2H), 3.59 (t,  $J = 5.1$  Hz, 4H), 3.24 (t,  $J = 5.2$  Hz, 4H), 1.49 (s, 9H).

$^{13}\text{C}$  NMR (101 MHz, Chloroform-*d*)  $\delta$  154.8, 153.3, 126.6 (q,  $J = 3.8$  Hz), 124.8 (q,  $J = 271.6$  Hz), 121.2 (q,  $J = 33.2$  Hz), 115.1, 80.3, 48.3, 28.6.

$^{19}\text{F}$  NMR (376 MHz, Chloroform-*d*)  $\delta$  -61.5 (s, 3F).

HRMS (DART-TOF): calculated for  $\text{C}_{16}\text{H}_{22}\text{F}_3\text{N}_2\text{O}_2$  ( $[\text{M}+\text{H}]^+$ ) 331.1628, found 331.1644.

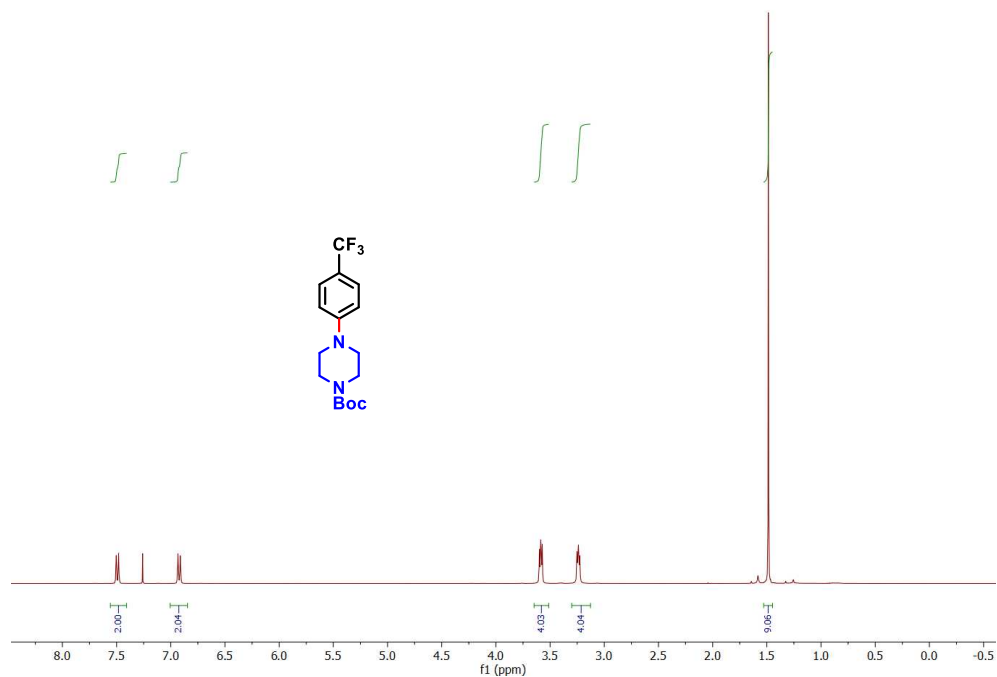


Figure S3.103.  $^1\text{H}$  NMR of tert-butyl 4-(3-(trifluoromethyl)phenyl)piperazine-1-carboxylate

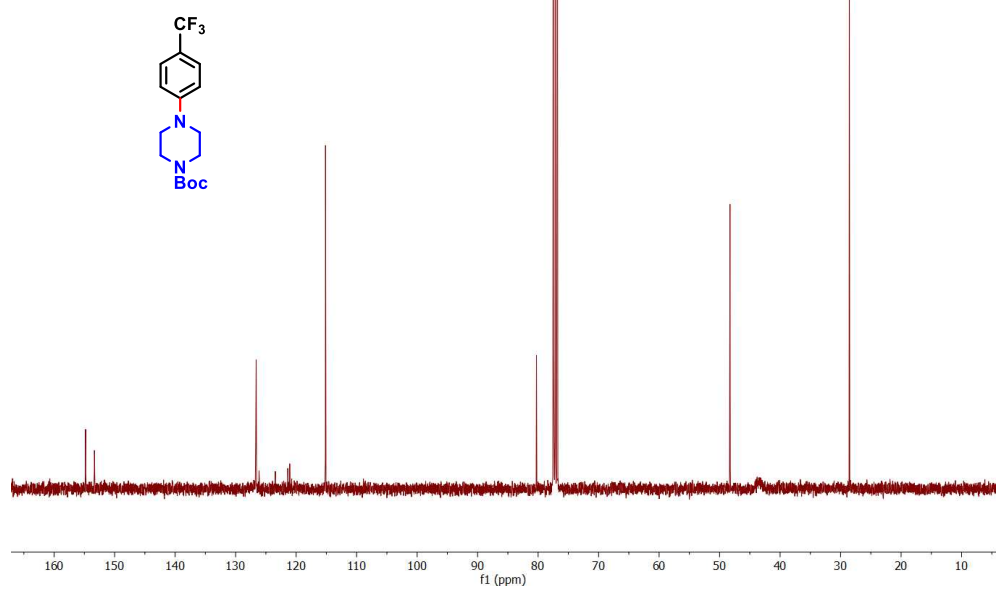


Figure S3.104.  $^{13}\text{C}$  NMR of tert-butyl 4-(3-(trifluoromethyl)phenyl)piperazine-1-carboxylate



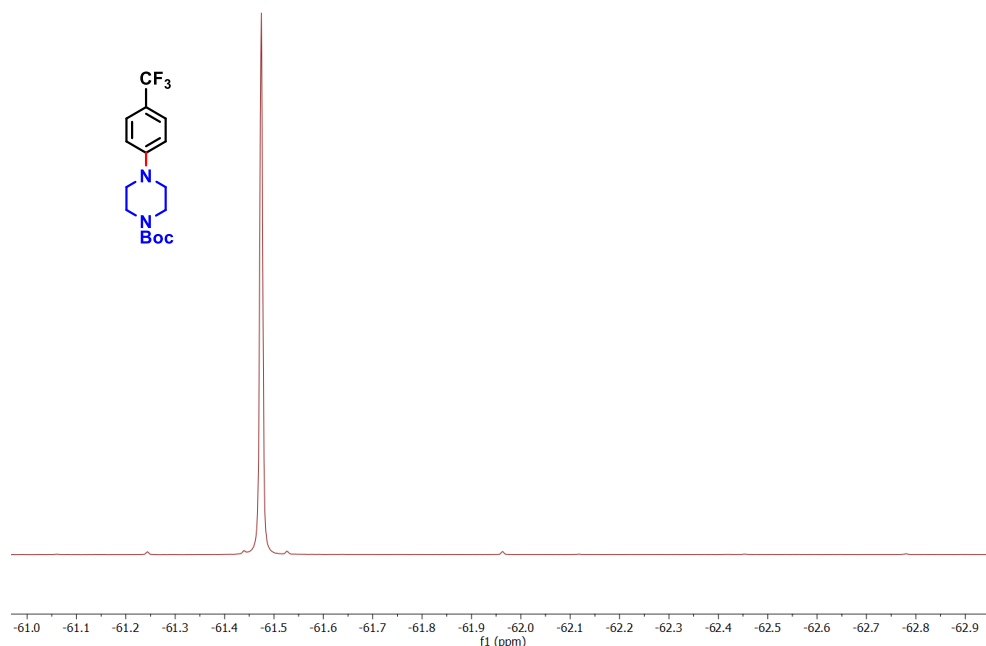
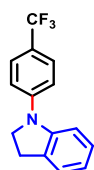


Figure S3.105.  $^{19}\text{F}$  NMR of *tert*-butyl 4-(3-(trifluoromethyl)phenyl)piperazine-1-carboxylate



#### 1-(4-(trifluoromethyl)phenyl)indoline

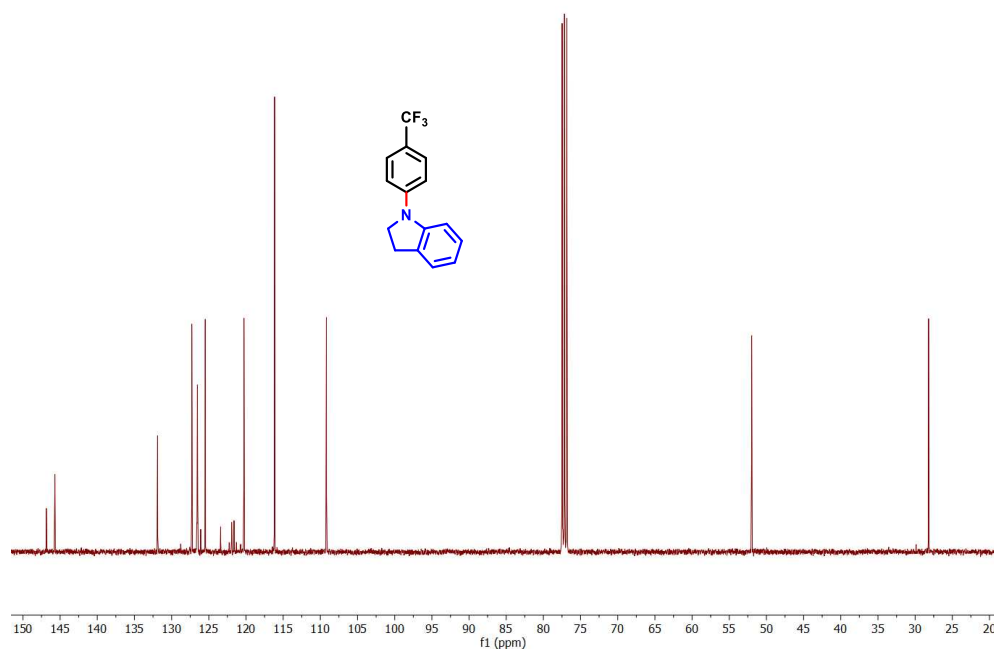
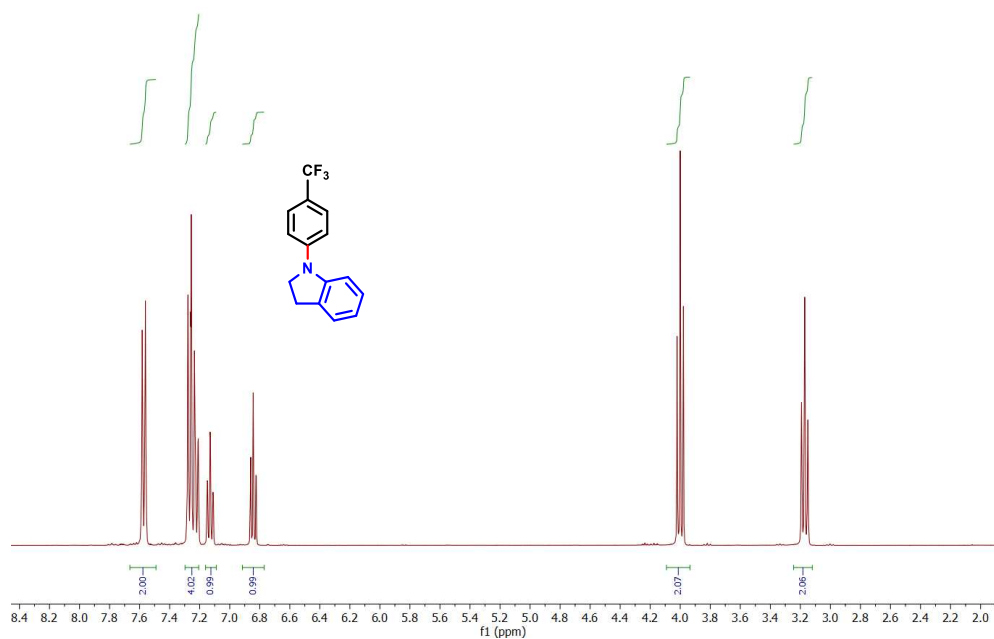
General procedure B was used with indoline as the amine and 4-bromobenzotrifluoride as the aryl halide. Flash chromatography was performed on silica gel with 10% EtOAc/90% hexanes to give the product as a white solid (PhenO: 72 mg, 68%; Ru: 77 mg, 73%). NMR spectra matched those previously reported.<sup>24</sup>

$^1\text{H}$  NMR (400 MHz, Chloroform-*d*)  $\delta$  7.57 (d,  $J$  = 8.9 Hz, 2H), 7.30 – 7.21 (m, 4H), 7.13 (t,  $J$  = 7.9 Hz, 1H), 6.84 (td,  $J$  = 7.4, 1.0 Hz, 1H), 4.00 (t,  $J$  = 8.4 Hz, 2H), 3.17 (t,  $J$  = 8.4 Hz, 2H).

$^{13}\text{C}$  NMR (101 MHz, Chloroform-*d*)  $\delta$  146.9, 145.7, 131.9, 127.3, 126.5 (q,  $J$  = 3.8 Hz), 125.5, 124.7 (q,  $J$  = 270.5 Hz), 121.8 (q,  $J$  = 32.7 Hz), 120.3, 116.2, 109.2, 52.0, 28.2.

$^{19}\text{F}$  NMR (376 MHz, Chloroform-*d*)  $\delta$  -61.5 (s, 3F).

HRMS (DART-TOF): calculated for  $\text{C}_{15}\text{H}_{13}\text{F}_3\text{N}$  ( $[\text{M}+\text{H}]^+$ ) 264.0995, found 264.1011



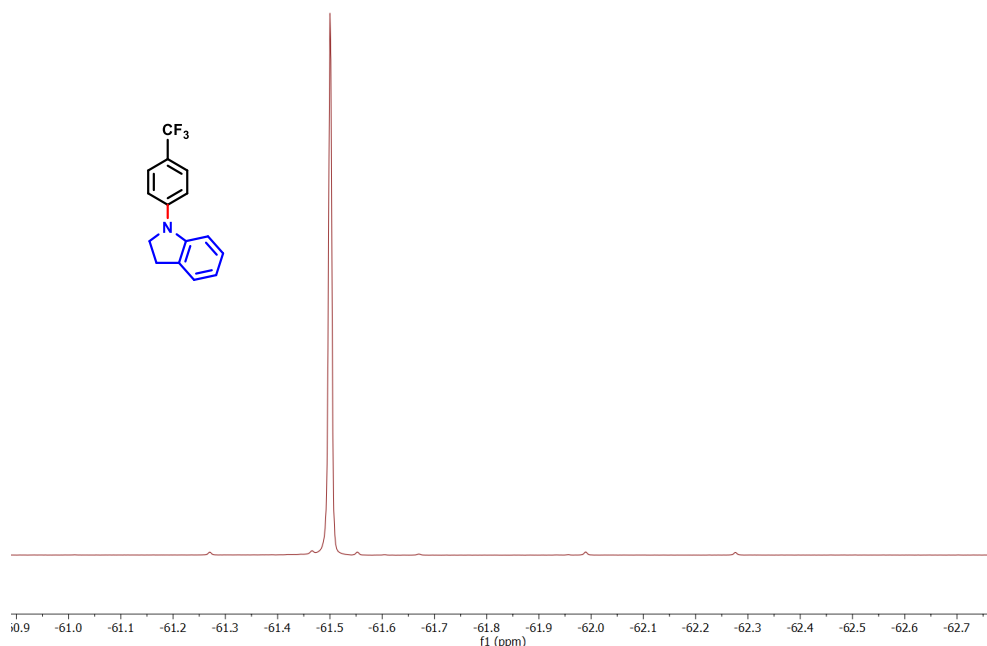


Figure S3.108.  $^{19}\text{F}$  NMR of 1-(4-(trifluoromethyl)phenyl)indoline

## 10. References – EXPERIMENTAL 2.

- (1) Armarego, W. L. F.; Chai, C. L. L., Chapter 4 - Purification of Organic Chemicals. In *Purification of Laboratory Chemicals (Sixth Edition)*, Armarego, W. L. F.; Chai, C. L. L., Eds. Butterworth-Heinemann: Oxford, 2009, 88.
- (2) Lim, C.-H.; Kudisch, M.; Liu, B.; Miyake, G. M., *J. Am. Chem. Soc.* 2018, *140*, 7667.
- (3) Arias-Rotondo, D. M.; McCusker, J. K., *Chem. Soc. Rev.* 2016, *45*, 5803.
- (4) Weisstein, E. W. <http://mathworld.wolfram.com/LeastSquaresFitting.html>.
- (5) Espenson, J. H., 2-7: Rate Expressions and the Method of Flooding. In *Chemical Kinetics and Reaction Mechanisms*, McGraw-Hill, Inc.: New York, 1981.
- (6) Du, Y.; Pearson, R. M.; Lim, C.-H.; Sartor, S. M.; Ryan, M. D.; Yang, H.; Damrauer, N. H.; Miyake, G. M., *Chem. Eur. J.* 2017, *23*, 10962.
- (7) Sartor, S. M.; McCarthy, B. G.; Pearson, R. M.; Miyake, G. M.; Damrauer, N. H., *J. Am. Chem. Soc.* 2018, *140*, 4778.

- (8) Preus, S. a|e - UV-Vis-IR Spectral Software 1.2, FluorTools. [www.fluortools.com](http://www.fluortools.com).
- (9) Suzuki, K.; Kobayashi, A.; Kaneko, S.; Takehira, K.; Yoshihara, T.; Ishida, H.; Shiina, Y.; Oishi, S.; Tobita, S., *Phys. Chem. Chem. Phys.* 2009, *11*, 9850.
- (10) Knight, T. E.; Guo, D.; Claude, J. P.; McCusker, J. K., *Inorg. Chem.* 2008, *47*, 7249.
- (11) Instrumentation for Fluorescence Spectroscopy. In *Principles of Fluorescence Spectroscopy*, Lakowicz, J. R., Ed. Springer US: Boston, MA, 2006; 27.
- (12) Connelly, N. G.; Geiger, W. E., *Chem. Rev.* 1996, *96*, 877.
- (13) Prier, C. K.; Rankic, D. A.; MacMillan, D. W. C., *Chem. Rev.* 2013, *113*, 5322.
- (14) supramolecular.org. <http://supramolecular.org> (accessed 2019).
- (15) Qiu, J.; Song, B.; Li, X.; Cozzolino, A. F., *Phys. Chem. Chem. Phys.* 2018, *20*, 46.
- (16) Thordarson, P., *Chem. Soc. Rev.* 2011, *40*, 1305.
- (17) Howe, E. N. W.; Bhadbhade, M.; Thordarson, P., *J. Am. Chem. Soc.* 2014, *136*, 7505.
- (18) Schwarz, G., Estimating the Dimension of a Model. *Ann. Stat.* 1978, *6*, 461.
- (19) Goodgame, D. M. L.; Goodgame, M.; Cotton, F. A., *J. Am. Chem. Soc.* 1961, *83*, 4161.
- (20) Cotton, F. A.; Faut, O. D.; Goodgame, D. M. L., *J. Am. Chem. Soc.* 1961, *83*, 344.
- (21) Cotton, F. A.; Goodgame, D. M. L., *J. Am. Chem. Soc.* 1960, *82*, 5771.
- (22) Palazón, J.; Gálvez, J.; García, G.; Lopez, G., *Polyhedron* 1983, *2*, 1353.
- (23) Kim, M.; Shin, T.; Lee, A.; Kim, H., *Organometallics* 2018, *37* (19), 3253-3258.
- (24) Corcoran, E. B.; Pirnot, M. T.; Lin, S.; Dreher, S. D.; DiRocco, D. A.; Davies, I. W.; Buchwald, S. L.; MacMillan, D. W. C., *Science* 2016, *353*, 279.

## REFERENCES

- (1) Corcoran, E. B.; Pirnot, M. T.; Lin, S.; Dreher, S. D.; DiRocco, D. A.; Davies, I. W.; Buchwald, S. L.; MacMillan, D. W. C. *Science* 2016, *353*, 279.
- (2) Oderinde, M. S.; Jones, N. H.; Juneau, A.; Frenette, M.; Aquila, B.; Tentarelli, S.; Robbins, D. W.; Johannes, J. W. *Angew. Chem., Int. Ed.* 2016, *55*, 13219.
- (3) Terrett, J. A.; Cuthbertson, J. D.; Shurtleff, V. W.; MacMillan, D. W. C. *Nature* 2015, *524*, 330.
- (4) Zuo, Z.; Ahneman, D. T.; Chu, L.; Terrett, J. A.; Doyle, A. G.; MacMillan, D. W. C. *Science* 2014, *345*, 437.
- (5) Xuan, J.; Zeng, T.-T.; Chen, J.-R.; Lu, L.-Q.; Xiao, W.-J. *Chem. Eur. J.* 2015, *21*, 4962.
- (6) Oderinde, M. S.; Frenette, M.; Robbins, D. W.; Aquila, B.; Johannes, J. W. *J. Am. Chem. Soc.* 2016, *138*, 1760.
- (7) Butters, M.; Catterick, D.; Craig, A.; Curzons, A.; Dale, D.; Gillmore, A.; Green, S. P.; Marziano, I.; Sherlock, J.-P.; White, W. *Chem. Rev.* 2006, *106*, 3002.
- (8) Lim, C.-H.; Ryan, M. D.; McCarthy, B. G.; Theriot, J. C.; Sartor, S. M.; Damrauer, N. H.; Musgrave, C. B.; Miyake, G. M. *J. Am. Chem. Soc.* 2017, *139*, 348.
- (9) Pearson, R. M.; Lim, C.-H.; McCarthy, B. G.; Musgrave, C. B.; Miyake, G. M. *J. Am. Chem. Soc.* 2016, *138*, 11399.
- (10) Du, Y.; Pearson, R. M.; Lim, C.-H.; Sartor, S. M.; Ryan, M. D.; Yang, H.; Damrauer, N. H.; Miyake, G. M. Strongly Reducing, *Chem. Eur. J.* 2017, *23*, 10962.
- (11) Kim, T.; McCarver, S. J.; Lee, C.; MacMillan, D. W. C. *Angew. Chem., Int. Ed.* 2018, *57*, 3488.
- (12) Lim, C.-H.; Kudisch, M.; Liu, B.; Miyake, G. M. *J. Am. Chem. Soc.* 2018, *140*, 7667.

- (13) Shields, B. J.; Kudisch, B.; Scholes, G. D.; Doyle, A. G. *J. Am. Chem. Soc.* 2018, *140*, 3035.
- (14) Ishida, N.; Masuda, Y.; Ishikawa, N.; Murakami, M. *Asian J. Org. Chem.* 2017, *6*, 669.
- (15) Creutz, S. E.; Lotito, K. J.; Fu, G. C.; Peters, J. C. *Science* 2012, *338*, 647.
- (16) Ziegler, D. T.; Choi, J.; Muñoz-Molina, J. M.; Bissember, A. C.; Peters, J. C.; Fu, G. C. *J. Am. Chem. Soc.* 2013, *135*, 13107.
- (17) Shields, B. J.; Doyle, A. G. *J. Am. Chem. Soc.* 2016, *138*, 12719.
- (18) Hwang, S. J.; Powers, D. C.; Maher, A. G.; Anderson, B. L.; Hadt, R. G.; Zheng, S.-L.; Chen, Y.-S.; Nocera, D. G. *J. Am. Chem. Soc.* 2015, *137*, 6472.
- (19) Kainz, Q. M.; Matier, C. D.; Bartoszewicz, A.; Zultanski, S. L.; Peters, J. C.; Fu, G. C. *Science* 2016, *351*, 681.
- (20) Heitz, D. R.; Tellis, J. C.; Molander, G. A. *J. Am. Chem. Soc.* 2016, *138*, 12715.
- (21) Dewanji, A.; Krach, P. E.; Rueping, M. *Angew. Chem., Int. Ed.* 2019, *58*, 3566.
- (22) Yoo, W.-J.; Tsukamoto, T.; Kobayashi, S. *Org. Lett.* 2015, *17*, 3640.
- (23) Welin, E. R.; Le, C.; Arias-Rotondo, D. M.; McCusker, J. K.; MacMillan, D. W. C. *Science* 2017, *355*, 380.
- (24) Teders, M.; Henkel, C.; Anhäuser, L.; Strieth-Kalthoff, F.; Gómez-Suárez, A.; Kleinmans, R.; Kahnt, A.; Rentmeister, A.; Guldi, D.; Glorius, F. *Nat. Chem.* 2018, *10*, 981.
- (25) Strieth-Kalthoff, F.; James, M. J.; Teders, M.; Pitzer, L.; Glorius, F. *Chem. Soc. Rev.* 2018, *47*, 7190.
- (26) Brown, A. M.; McCusker, C. E.; McCusker, J. K. *Dalton Trans.* 2014, *43*, 17635.
- (27) Arias-Rotondo, D. M.; McCusker, J. K. *Chem. Soc. Rev.* 2016, *45*, 5803.
- (28) Le, C. C.; Wismer, M. K.; Shi, Z.-C.; Zhang, R.; Conway, D. V.; Li, G.; Vachal, P.; Davies, I. W.; MacMillan, D. W. C. *ACS Cent. Sci.* 2017, *3*, 647.

- (29) Caspar, J. V.; Meyer, T. J. *J. Am. Chem. Soc.* 1983, *105*, 5583.
- (30) Shukla, P.; Narain, G. *J. Prakt. Chem.* 1968, *38*, 289.
- (31) Pavkovic, S. F.; Rapp, B. *Inorg. Chem.* 1970, *9*, 2800.
- (32) Lee-Thorp, J. A.; Rüede, J. E.; Thornton, D. A. *J. Mol. Struct.* 1978, *50*, 65.
- (33) Jansky, M. T.; Yoke, J. T. *J. Inorg. Nucl. Chem.* 1979, *41*, 1707.
- (34) Palazón, J.; Gálvez, J.; García, G.; Lopez, G. *Polyhedron* 1983, *2*, 1353.
- (35) Kenessey, G.; Carson, B. R.; Allan, J. R.; Wadsten, T.; Liptay, G. *J. Therm. Anal.* 1997, *50*, 167.
- (36) Drago, R. S.; Meek, D. W.; Longhi, R.; Joesten, M. D. *Inorg. Chem.* 1963, *2*, 1056.
- (37) Cotton, F. A.; Goodgame, D. M. L. *J. Am. Chem. Soc.* 1960, *82*, 5771.
- (38) Goodgame, D. M. L.; Goodgame, M.; Cotton, F. A. *J. Am. Chem. Soc.* 1961, *83*, 4161.
- (39) Guo, D.; Knight, T. E.; McCusker, J. K. *Science* 2011, *334*, 1684.
- (40) Howe, E. N. W.; Bhadbhade, M.; Thordarson, P. *J. Am. Chem. Soc.* 2014, *136*, 7505.
- (41) Qiu, J.; Song, B.; Li, X.; Cozzolino, A. F. *Phys. Chem. Chem. Phys.* 2018, *20*, 46.
- (42) Thordarson, P. *Chem. Soc. Rev.* 2011, *40*, 1305.
- (43) Brynn Hibbert, D.; Thordarson, P. *Chem. Commun.* 2016, *52*, 12792.
- (44) Knight, T. E.; Guo, D.; Claude, J. P.; McCusker, J. K. *Inorg. Chem.* 2008, *47*, 7249.
- (45) Knight, T. E.; McCusker, J. K. *J. Am. Chem. Soc.* 2010, *132*, 2208.
- (46) Sartor, S. M.; McCarthy, B. G.; Pearson, R. M.; Miyake, G. M.; Damrauer, N. H. *J. Am. Chem. Soc.* 2018, *140*, 4778.
- (47) Introduction to Fluorescence. In *Principles of Fluorescence Spectroscopy*; Lakowicz, J. R., Ed.; Springer US: Boston, MA, 2006; 1–26.
- (48) Vitaku, E.; Smith, D. T.; Njardarson, J. T. *J. Med. Chem.* 2014, *57*, 10257.

## PART 2: ORGANOCATALYZED BIRCH REDUCTION DRIVEN BY VISIBLE LIGHT



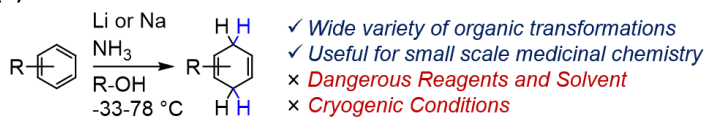
## CHAPTER 4 | INTRODUCTION TO PART 2

The Birch reduction reaction, first developed by Arthur Birch in the 1940's,<sup>1</sup> is pivotal for the selective reduction of aromatic feedstocks such as benzene to produce cyclohexadienes that are extremely useful starting materials for building molecular complexity *en route* to the synthesis of pharmaceutical compounds or chemical products. For example, in an analysis of medicinal compounds that became approved drugs as compared with those in phase I-III trials or the discovery phase, it was found that successful drugs contained a significantly higher fraction of  $sp^3$  carbon centers which serve to break planarity and facilitate enzymatic binding.<sup>2</sup> Birch reduction serves as a critical tool in this regard, producing two new  $sp^3$  centers in a manner which is difficult to achieve by other means. Historically, Birch reduction has been an indispensable tool in medicinal chemistry as exemplified by its use in the development of the first synthetic hormone and the first oral contraceptive.<sup>3</sup> Given the utility of this chemistry, it is strongly desirable to achieve Birch type reductions under the most sustainable and environmentally benign conditions.

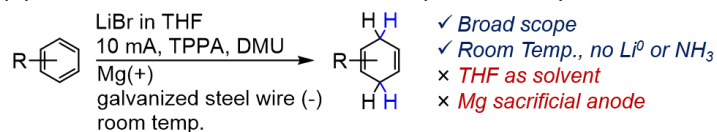
Unfortunately, the current state-of-the-art process suffers from multiple drawbacks in that it requires the use of stoichiometric quantities of alkali metals in liquid ammonia at cryogenic temperatures (Fig. 4.1A). When scaling up this chemistry for industrial use, these reagents present extreme challenges.<sup>4</sup> Specifically, alkali metals such as lithium, sodium, or potassium are pyrophoric, producing  $H_2$  gas in an exothermic reaction upon contact with  $H_2O$ , presenting considerable safety concerns. In addition, alkali metal hydroxide salts are produced as stoichiometric waste upon quenching of the excess metal. Further, ammonia is used in a solvent quantity near its boiling point of  $-33\text{ }^\circ\text{C}$ , presenting challenges related to its toxicity, volatility, and pressurization of the reaction vessel upon loss of temperature control. The energy required to maintain a reaction vessel at such a low temperature is considerable and does not directly facilitate

## Development of Light-Driven Birch Reduction

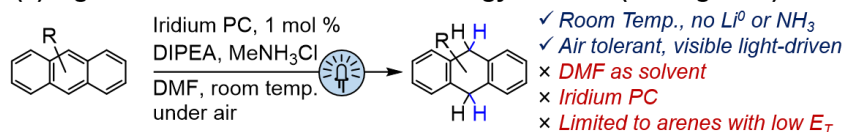
### (a) Traditional Birch reduction conditions



### (b) Electrochemical Birch reduction (Baran 2019)



### (c) Light-driven Birch reduction via Energy Transfer (Koenig 2019)



### (d) Photocatalytic Birch reduction catalyzed by BPIs (This Work)

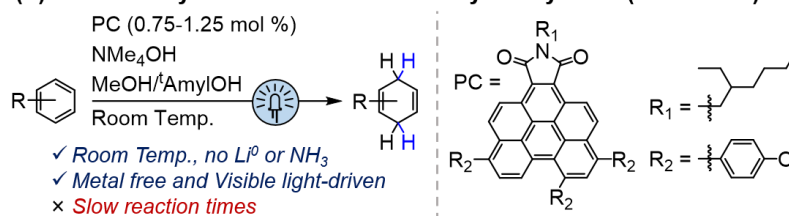


Figure 4.1. Development of light-driven Birch reduction reactions.

formation of the product. These drawbacks constitute significant motivation for the development of more sustainable methods for Birch type reductions of aromatic compounds.

Recent research has attacked this problem from multiple fronts. Although ammonia-free Birch reduction has been developed,<sup>5</sup> alkali metals are still required and reactions are not catalytic, among other drawbacks. More recently, a significant advance was made in the discovery of an electrochemical Birch reduction that operates with a wide substrate scope at room temperature without either alkali metals or liquid ammonia (Fig. 4.1b).<sup>6</sup> The method employs a sacrificial Mg anode with a galvanized steel wire cathode, and a phosphoramidate anti-plating agent (to avoid formation of  $\text{Li}(0)$  on the electrode) with dimethylurea as the proton source. While this method constitutes a significant advance, the breakdown of the Mg anode produces stoichiometric Mg waste which could lead to metal contamination of a medicinal product, a prospect that could lead

to hypermagnesia upon use of the product.<sup>7</sup> In addition, use of THF as solvent presents concerns due to its instability and air quality impacts.<sup>8</sup> Therefore, development of a metal free system that operates in a solvent with lessened environmental impacts is desirable.

Only one prior example of a photochemical Birch type reduction has been reported, involving the use of an iridium photocatalyst (PC) to generate the triplet excited state of an aromatic substrate via energy transfer, thus activating it for subsequent reduction (Fig. 4.1c).<sup>9</sup> However, this strategy is only viable for arenes possessing triplet energies lower than that of the iridium PC. Important arene feedstocks such as benzene and benzene derivatives have high triplet energies (e.g., 3.6 eV for benzene)<sup>10</sup> and are thus inaccessible by this approach. In addition, the use of an iridium PC raises sustainability concerns due to its rarity as a precious metal.

The goal of the following work to be discussed in Chapter 5 is the development of a photochemical Birch reduction reaction capable of utilizing challenging arenes such as benzene as substrates. While a method has been reported in which arenes are directly photolyzed in the presence of hydroxide to achieve Birch type reductions,<sup>11</sup> a high intensity ultraviolet arc lamp was required, and benzoic acid was the only challenging arene that was demonstrated in low yield. Since the types of medicinal substrates that this type of transformation is useful for often absorb high energy UV light, a method that can operate under visible light is highly desirable to avoid direct excitation of substrates. However, this need for visible light imposes a thermodynamic limitation – the energy of a single photon of violet light is not enough to reduce benzene (Fig. 4.2a-4.2b) as benzene reduction occurs at  $-3.42$  V vs. SCE.<sup>12</sup> Further, the total photon energy cannot be utilized in a light-driven transformation due to losses from excited state relaxation processes.

As such, a number of strategies have now been developed to harness the energy from more than one visible photon of light to perform challenging photoreductions that require large energy

Super-reductant Catalytic Cycles: Concepts

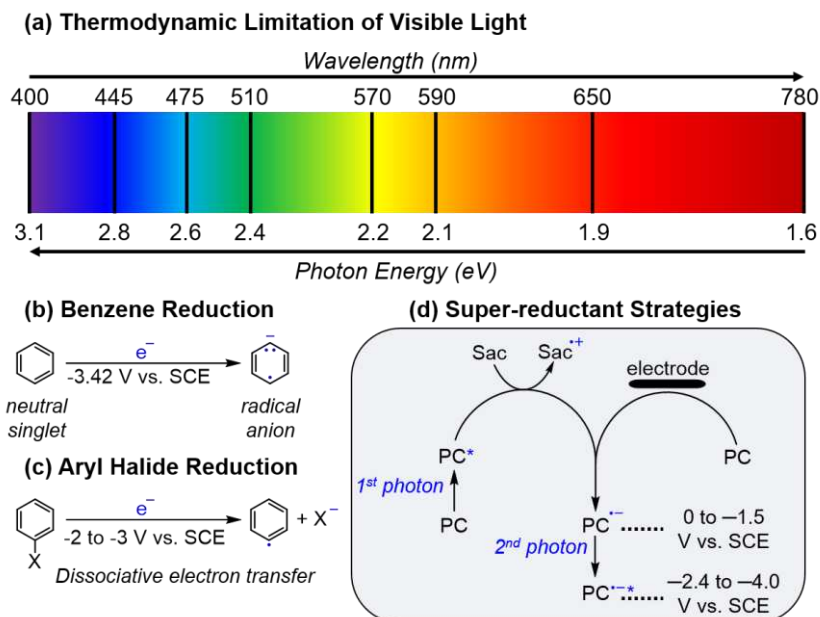


Figure 4.2. Conceptual representation of challenges and strategies in reductions of aromatic substrates. Sac = sacrificial electron donor.

input. Most of these methods involve a PET step to form a radical ion which can then be excited to form a state reducing enough to perform the desired substrate reduction. An additional strategy involves generating a radical anion electrochemically and photoexciting that species. These strategies are summarized schematically in Figure 4.2d. Several recent works have emerged that involve multiple photon absorption steps that are not included in Chapter 5, including a method that involves excitation of semiquinone radicals to perform aryl dehalogenation,<sup>13</sup> the excitation of phenothiazine radical cation to perform challenging oxidations,<sup>14</sup> and the photoinduced degradation of  $\text{Ir}[(\text{ppy})_2(\text{dtbpy})]^+$  to form a more reducing, neutral Ir PC that can be photoexcited to achieve the reduction of aryl halides and activated alkenes.<sup>15-16</sup> Further, this nascent field of multi-photon excitation strategies has recently been reviewed,<sup>17</sup> and the reader is directed there for additional information.

In addition, the development of our Birch reduction system described in Chapter 5 is also based on the chemistry of aromatic imides. Aromatic diimides exhibit a rich chemistry through the

formation of pi-anion complexes or through undergoing reduction with anions as the electron donor (e.g.,  $\text{OH}^-$ ,  $\text{CN}^-$ ,  $\text{F}^-$ ,  $\text{Cl}^-$ ,  $\text{I}^-$ ).<sup>18-21</sup> In some cases, the reduction can be photoinduced if it does not occur thermally at room temperature. These reactions have been studied in some detail and provide context for the role of hydroxide as a sacrificial electron donor in the work described in Chapter 5.

Ultimately, the first photocatalytic reaction system capable of reducing benzene to 1,4-cyclohexadiene (Fig. 4.1d) was developed.<sup>22</sup> An organic benzo[ghi]perylene imide (BPI) PC was synthesized that catalyzes the transformation at a low loading (i.e. 0.75 – 1.25 mol % relative to the arene) at ambient temperature and pressure under visible light irradiation with  $\text{OH}^-$  as the sacrificial electron donor in mixed methanol/tert-amyl alcohol which serves as solvent and proton source. The versatility of this reaction and potential for organic synthesis was demonstrated through the reduction of 21 arenes possessing diverse functional groups, including alcohols, carboxylic acids, amides, carbamates, and cyclic ethers. In addition, selectivity between Birch reduction and other reactions such as alkene reduction could be controlled by tuning the reaction conditions. Finally, hydrodechlorination of late-stage pharmaceutical compounds was demonstrated.

Mechanistic studies are consistent with a catalytic cycle in which the PC reversibly forms an addition adduct with hydroxide. This adduct is photolyzed to form the radical anion of the PC which is then photoexcited in a second photon absorption step to form a highly reducing excited state. This reducing state is ionized to release a solvated electron which reduces the arene to the corresponding diene through a series of protonation and reduction steps. More detailed mechanistic studies and PC design work is ongoing in our laboratory with the primary aim of improving the reaction time and substrate scope, as well as determining the pathway of PC degradation.

## REFERENCES

- (1) Birch, A. J., 117. *J. Chem. Soc.* 1944, 430.
- (2) Lovering, F.; Bikker, J.; Humblet, C., *J. Med. Chem.* 2009, 52, 6752.
- (3) Birch, A. J., *Pure Appl. Chem.* 1996, 68, 553.
- (4) Joshi, D. K.; Sutton, J. W.; Carver, S.; Blanchard, J. P., *Org. Process Res. Dev.* 2005, 9, 997.
- (5) Lei, P.; Ding, Y.; Zhang, X.; Adijiang, A.; Li, H.; Ling, Y.; An, J., *Org. Lett.* 2018, 20, 3439.
- (6) Peters, B. K.; Rodriguez, K. X.; Reisberg, S. H.; Beil, S. B.; Hickey, D. P.; Kawamata, Y.; Collins, M.; Starr, J.; Chen, L.; Udyavara, S.; Klunder, K.; Gorey, T. J.; Anderson, S. L.; Neurock, M.; Minter, S. D.; Baran, P. S., *Science* 2019, 363, 838.
- (7) Swaminathan, R., *Clin. Biochem. Rev.* 2003, 24, 47.
- (8) Alder, C. M.; Hayler, J. D.; Henderson, R. K.; Redman, A. M.; Shukla, L.; Shuster, L. E.; Sneddon, H. F., *Green Chem.* 2016, 18, 3879.
- (9) Chatterjee, A.; König, B., *Angew. Chem. Int. Ed.* 2019, 58, 14289.
- (10) Ishikawa, H.; Noyes, W. A., *J. Am. Chem. Soc.* 1962, 84, 1502.
- (11) Yoshimi, Y.; Ishise, A.; Oda, H.; Moriguchi, Y.; Kanezaki, H.; Nakaya, Y.; Katsuno, K.; Itou, T.; Inagaki, S.; Morita, T.; Hatanaka, M., *Tetrahedron Lett.* 2008, 49, 3400.
- (12) Mortensen, J.; Heinze, J. *Angew. Chem., Int. Ed. Engl.* 1984, 23, 84.
- (13) Graml, A.; Neveselý, T.; Jan Kutta, R.; Cibulka, R.; König, B., *Nat. Commun.* 2020, 11, 3174.
- (14) Targos, K.; Williams, O. P.; Wickens, Z. K., *J. Am. Chem. Soc.* 2021, 143, 4125.
- (15) Connell, T. U.; Fraser, C. L.; Czyz, M. L.; Smith, Z. M.; Hayne, D. J.; Doeven, E. H.; Agugiaro, J.; Wilson, D. J. D.; Adcock, J. L.; Scully, A. D.; Gómez, D. E.; Barnett, N. W.; Polyzos, A.; Francis, P. S., *J. Am. Chem. Soc.* 2019, 141, 17646.

- (16) Czyz, M. L.; Taylor, M. S.; Horngren, T. H.; Polyzos, A., Reductive Activation and Hydrofunctionalization of Olefins by Multiphoton Tandem Photoredox Catalysis. *ACS Catal.* 2021, *11*, 5472.
- (17) Glaser, F.; Kerzig, C.; Wenger, O. S., *Angew. Chem. Int. Ed.* 2020, *59*, 10266.
- (18) Guha, S.; Goodson, F. S.; Roy, S.; Corson, L. J.; Gravenmier, C. A.; Saha, S., *J. Am. Chem. Soc.* 2011, *133*, 15256.
- (19) Guha, S.; Goodson, F. S.; Corson, L. J.; Saha, S., *J. Am. Chem. Soc.* 2012, *134*, 13679.
- (20) Goodson, F. S.; Panda, D. K.; Ray, S.; Mitra, A.; Guha, S.; Saha, S., *Org. Biomol. Chem.* 2013, *11*, 4797.
- (21) Saha, S., *Acc. Chem. Res.* 2018, *51*, 2225.
- (22) Cole, J. P.; Chen, D.-F.; Kudisch, M.; Pearson, R. M.; Lim, C.-H.; Miyake, G. M., *J. Am. Chem. Soc.* 2020, *142*, 13573.

## CHAPTER 5 | ORGANOCATALYZED BIRCH REDUCTION DRIVEN BY VISIBLE LIGHT

### OVERVIEW

The Birch reduction is a powerful synthetic methodology that uses solvated electrons to convert inert arenes to 1,4-cyclohexadienes – valuable intermediates for building molecular complexity. Birch reductions traditionally employ alkali metals dissolved in ammonia to produce a solvated electron for the reduction of unactivated arenes such as benzene ( $E_{red} < -3.42$  V vs SCE). Photoredox catalysts have been gaining popularity in highly reducing applications, but none have been reported to demonstrate reduction potentials powerful enough to reduce benzene. Here, we introduce benzo[ghi]perylene imides as new organic photoredox catalysts for Birch reductions performed at ambient temperature and driven by visible light from commercially available LEDs. Using low catalyst loadings (<1 mol percent), benzene and other functionalized arenes were selectively transformed to 1,4-cyclohexadienes in moderate to good yields in a completely metal-free reaction. Mechanistic studies support that this unprecedented visible-light-induced reactivity is enabled by the ability of the organic photoredox catalyst to harness the energy from two visible-light photons to affect a single, high-energy chemical transformation.

### INTRODUCTION

Visible-light photoredox catalysis has transformed the synthesis of small molecules and materials through the conversion of photochemical energy to chemical potentials enabling unique reactivity under mild conditions.<sup>1-4</sup> However, the scope of accessible chemical transformations using these catalytic platforms is fundamentally confined by the energetics of a



visible photon. For example, a 400 nm photon provides 3.1 eV of energy, defining the upper limit or the thermodynamic driving force for transformations using visible light. Thus, the low electron affinity of inert substrates such as benzene render it unreactive and difficult to reduce by single electron transfer, requiring a reduction potential of  $-3.42$  V vs SCE,<sup>5</sup> while the high triplet energy of benzene (3.6 eV) prevents triplet energy sensitization.<sup>6</sup> As such, the reduction of benzene requires harsher conditions than accessible by current visible-light photoredox catalyst systems. The Birch reduction — the prototypical example being the overall  $2e^-/2H^+$  reduction of benzene to 1,4-cyclohexadiene — represents one of the most demanding reductions in organic synthesis and traditionally employs solvated electrons as the reductant, generated using lithium or sodium metal under cryogenic liquid ammonia conditions (Figure 5.1a and 5.1b).<sup>7,8</sup> Several variations of Birch

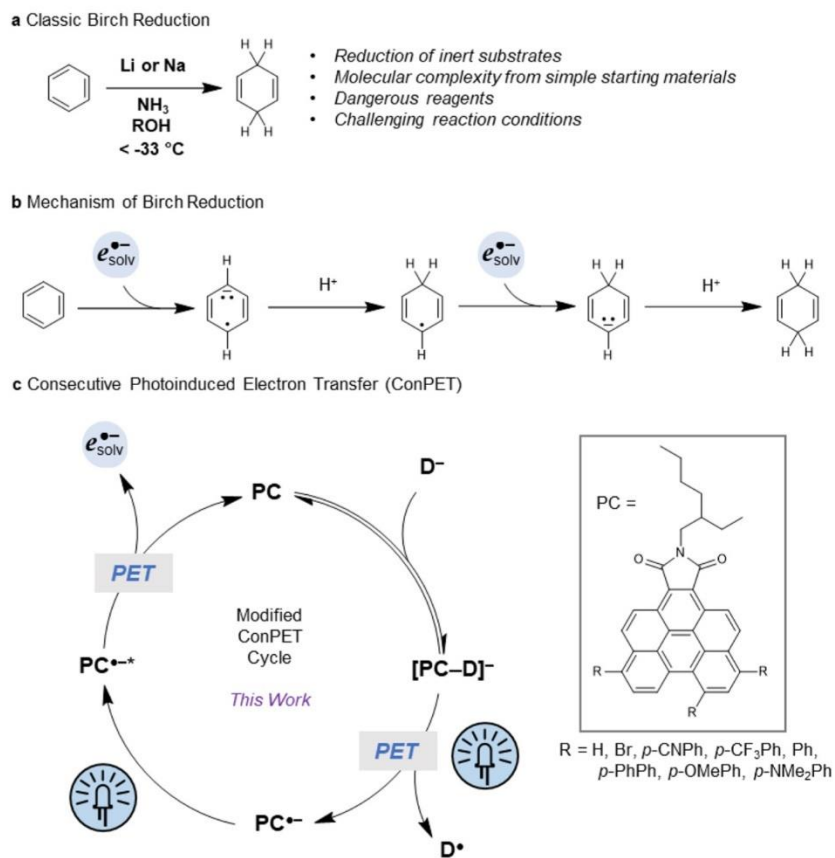


Figure 5.1. Background and plausible mechanism of a visible-light-driven Birch reduction. (a) Reaction conditions and considerations for traditional Birch reduction. (b) Mechanism of  $2e^-/2H^+$  reduction of benzene to afford 1,4-cyclohexadiene. (c) Plausible consecutive photoinduced

*electron transfer (ConPET) catalytic cycle to merge the energetics of two photons to generate a highly reducing solvated electron. D = electron donor (OH<sup>-</sup> or F<sup>-</sup> in this work).*

reductions have been developed, including ammonia free,<sup>9</sup> electrochemical,<sup>10,11</sup> and photochemical,<sup>12</sup> each of which has increased the safety of performing Birch reductions. Despite these advances, the development of a mild, metal-free, visible light-driven Birch reduction is highly desirable.

To overcome the energetic constraints of a visible-light photon, approaches to harness the energetics of two photons into a single chemical event and access more challenging reactivity have been developed.<sup>13</sup> For example, under high photon flux conditions using a laser, an iridium(III) complex underwent two successive photoexcitations, allowing ionization to iridium(IV) and a solvated electron;<sup>14</sup> while promising, the practicality and utility of this system for Birch reductions remain unknown. Efforts toward a Birch reduction driven by visible light utilized an iridium complex that served as both a triplet sensitizer of the arene as well as a photoreductant in conjunction with a sacrificial electron donor.<sup>15</sup> However, this system was unable to reduce benzene due to the high triplet energy of benzene, and reactivity was restricted to arenes possessing a lower triplet energy.

In another approach to accessing more reducing power, the concept of consecutive photoinduced electron transfer (ConPET) was applied with a perylene diimide (PDI) system.<sup>16,17</sup> Here, the first photon generates an excited-state PDI that is reduced by a sacrificial electron donor to yield a radical anion. Subsequently, the radical anion is photoexcited by a second photon, generating a much stronger reducing species. This catalytic system was employed in the reduction of aryl halides to generate aryl radicals that could be coupled with an appropriate trapping agent. Similarly, reductive quenching of an acridinium PC was found to generate an acridine radical that

could be photoexcited for the reduction of aryl chlorides and the reductive desosylation of amines.<sup>18</sup> However, reduction of the aromatic ring was not observed in any of these systems.

Recently, replacing the first photoinduced electron transfer (PET) step to generate the radical anion, electrochemical reduction of naphthalene imides<sup>19</sup> or dicyanoanthracene<sup>20</sup> catalysts was reported. Electrochemical reduction of the catalyst afforded a stable radical anion that can be subsequently photoexcited to a strongly reducing species capable of reducing aryl halides, including aryl chlorides, to aryl radicals for subsequent coupling reactions. Although these systems generate catalyst species with reactivity near Li(0) and excited state reduction potentials  $< -3$  V vs SCE, reduction of the arene ring was not observed. Thus, Birch reduction reactivity by a visible-light photoredox catalyst (PC) system remains elusive.

Our interest in photoredox catalysis originated with the motivation to develop strongly reducing organic PCs for organocatalyzed atom transfer radical polymerization (OATRP). Using computationally accelerated discovery we identified N,N-diaryl dihydrophenazines,<sup>21</sup> N-aryl phenoxazines,<sup>22</sup> and N-aryl dimethyl-dihydroacridines<sup>23</sup> as classes of strongly reducing organic PCs. The most successful O-ATRP catalysts have impressively strong excited-state reduction potentials, some possessing  $E^\circ(\text{PC}^{\bullet+}/\text{PC}^*) < -2$  V vs SCE, representing some of the strongest single-photon visible-light PC reductants known. This work has motivated us to identify even more strongly reducing PC systems targeting the reduction of benzene and other arenes. Acknowledging the limitations of single-photon photoredox catalysis, we envisioned that through exploiting a ConPET process we could realize a catalyst system for the reduction of benzene (Figure 5.1c).

## RESULTS AND DISCUSSION

Our pursuit of a visible-light photoredox-catalyzed Birch reduction led to the investigation of benzo[ghi]perylene monoimides (BPIs) as potential PCs.<sup>24</sup> This class of molecules possesses a

computationally predicted high-energy lowest unoccupied molecular orbital (LUMO) [or in equivalence, relatively low electron affinity at  $E_{0,\text{comp}}(\text{PC}/\text{PC}^{\bullet-}) \approx -1.3$  V vs SCE].<sup>25</sup> This reduction potential is significantly more negative than that reported for a PDI [ $E_{1/2}(\text{PDI}/\text{PDI}^{\bullet-}) = -0.43$  V vs SCE] that is structurally very similar to the PC used in the ConPET system above.<sup>26</sup> Thus, we hypothesized that by utilizing the more strongly reducing  $\text{PC}^{\bullet-}$  accessible with BPIs, photoexcitation to  $\text{PC}^{\bullet-*}$  would access an even more reducing excited state that might be competent for the reduction of benzene. To test this hypothesis, we synthesized a family of targeted PCs in 2–4 steps from commercial reagents, resulting in a series of BPI molecules possessing electron-neutral, -withdrawing, and -donating core substituents on the 6-, 8-, and 11-core positions of the BPI (Figure 5.1c). All of these molecules exhibited strong visible-light absorption (wavelength of maximum absorption  $\lambda_{\text{max}} > 400$  nm and molar absorptivity  $\epsilon_{\text{max}} > 20,000$   $\text{M}^{-1}\text{cm}^{-1}$ ), high-lying LUMOs [ $E_{1/2,\text{exp}}(\text{PC}/\text{PC}^{\bullet-}) < -1.2$  V vs SCE], and redox reversibility for single electron transfers as determined by cyclic voltammetry (Table S5.5).

To investigate the ability of these molecules to serve as PCs in a ConPET mechanism, we first examined the light-induced reduction of the BPI by an electron donor to generate the PC radical anion ( $\text{PC}^{\bullet-}$ ). While commonly employed trialkyl amine electron donors failed to generate the  $\text{PC}^{\bullet-}$ , we found that  $\text{OH}^-$  and  $\text{F}^-$  ions could reduce the PC upon light irradiation through taking advantage of an association reaction analogous to that observed in the light-gated reduction of naphthalene diimides (NDIs) with  $\text{Cl}^-$  as the reductant (we note that the association reaction observed here resulted in a different type of complexation; see below for a mechanistic discussion).<sup>27</sup> The lack of reactivity of trialkylamines likely results from both their inability to associate with the PC and the lack of driving force for the electron transfer ( $E^{0*}_{\text{comp}}[\text{}^3\text{PC}^*/\text{}^2\text{PC}^{\bullet-}] = 0.38$  V vs SCE;  $E_{p/2}[\text{Et}_3\text{N}/\text{Et}_3\text{N}^{*+}] = 0.83$  V vs SCE).<sup>28</sup> Our initial survey of the targeted

photoredox-catalyzed Birch reduction implemented 2-phenylethanol as the substrate to produce the cyclohexadiene product 2-(cyclohexa-1,4-dien-1-yl)ethan-1-ol (1). Gratifyingly, using the various BPI PCs (0.25 mol %), NBu<sub>4</sub>OH (2 equiv) as the electron source,<sup>29</sup> in mixed methanol and tert-amyl alcohol as the solvent and H<sup>+</sup> source, and irradiated with a 405 nm LED resulted in conversion of the arene to the target product, albeit in low conversions (Table S5.2). The BPI derivative possessing *p*-OMePh core substituents outperformed the other PCs, resulting in 17% conversion after 16 h. Surveying potential reductants revealed that using the less sterically hindered NMe<sub>4</sub>OH and increasing the loading to 10 equivalents resulted in an increase in conversion to 42% after 48 h.

The reaction still proceeded using a lower catalyst loading (0.1 mol %), but conversion did not improve with increased catalyst loading (e.g., 1 mol %), presumably because of quenching of the photoexcited PC (PC\*) or the catalyst decomposing as an aromatic substrate in the reaction (Table S5.2). We found that conversion slowed dramatically after 48 h, so catalyst was added to the reaction at intervals in order to drive the reaction to higher conversions. Excitingly, it was found that 88% conversion (70% isolated yield, 1 in Figure 5.2b) could be achieved by adding a total of 0.75 mol % of catalyst divided over three additions during the course of the reaction (96 h). Control experiments revealed that the reaction did not proceed or resulted in minimal conversion with omission of any single component (PC, OH<sup>-</sup>, H<sup>+</sup> source, or light). While the reaction was not oxygen tolerant (PC<sup>\*-</sup> can be quenched by O<sub>2</sub>, E<sup>0</sup>(O<sub>2</sub>/O<sub>2</sub><sup>\*-</sup>) ≈ -1.0 V vs SCE),<sup>30</sup> it was tolerant to water.

With these reaction conditions established, we explored the general applicability of this photoinduced Birch reduction (Figure 5.2). The reduction of structurally similar 1-phenyl-2-propanol (a secondary alcohol) also proceeded well to afford product 2 in 62% yield. Notably,

additional substituents on the phenyl ring affected reaction efficiency. For example, meta- and para-methylphenylethanol exhibited reduced reactivity, and products 3 and 4 were isolated in 51%

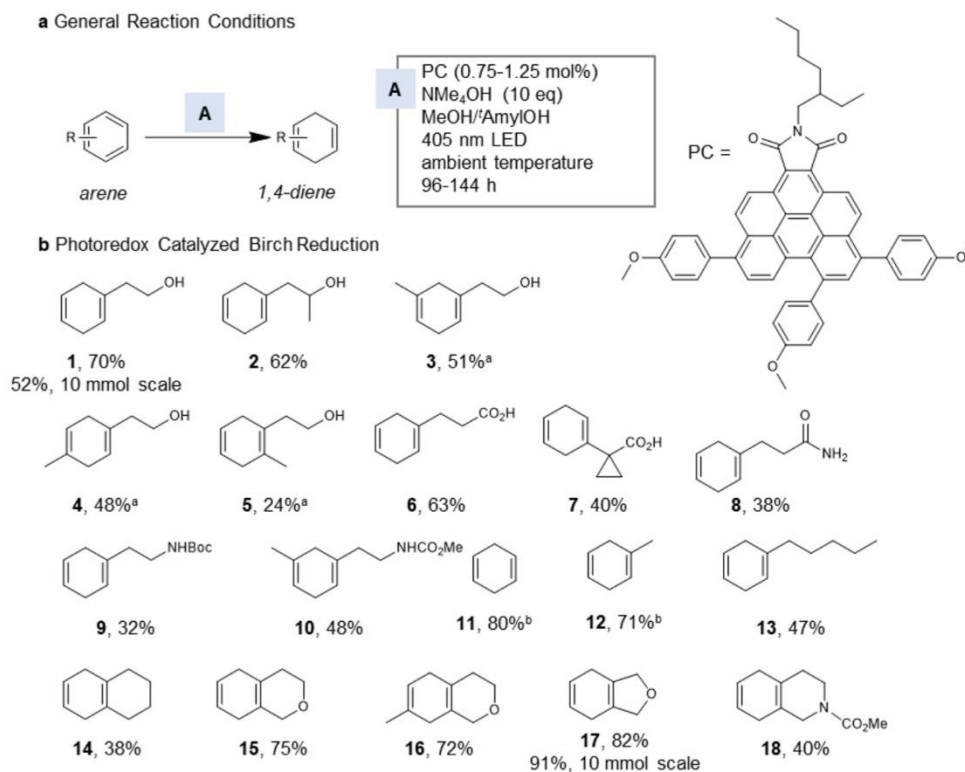
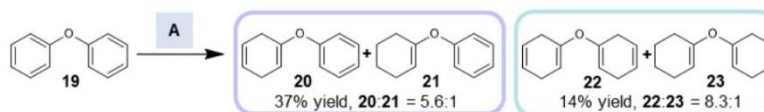


*Figure 5.2. Synthesis of 1,4-cyclohexadienes by visible-light-driven Birch reduction of arenes. (a) General reaction conditions. (b) Substrate scope; isolated yields are reported unless otherwise indicated. <sup>a</sup>144 h reaction, otherwise 96 h. <sup>b</sup>Yield determined by <sup>1</sup>H NMR using 1,3,5-trimethoxybenzene as the internal standard. <sup>c</sup>See EXPERIMENTAL 3 for details. Scale: 0.5 mmol in arene unless otherwise indicated.*

and 48% yield, respectively. Introduction of a methyl group at the ortho position significantly inhibited the reactivity (5, 24% yield). Functional groups, such as carboxylic acid (6 and 7), amide (8), carbamate (9 and 10), and strained cyclopropane (7), are well tolerated. The reduction of feedstocks benzene, toluene, and other simple mono- or disubstituted alkyl benzene derivatives were successful as well, affording 11–14 in moderate to high yields (38–80%). Remarkably, the cyclic ether motif was preserved in the high-yielding reduction of isochroman derivatives (15 and 16), while exclusive benzyl C–O bond cleavage occurs under conventional Birch conditions using

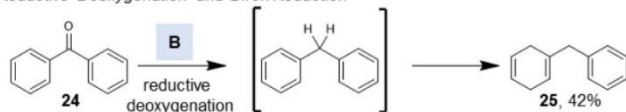
lithium.<sup>31</sup> Similarly, 1,3-dihydroisobenzofuran and 1,2,3,4-tetrahydroisoquinoline were transformed to 17 and 18 in 82% and 40% yield, respectively. We also demonstrated that this Birch reduction methodology was capable of generating products 1 and 17 on a larger scale. Performing the reaction at 10 mmol (1.2 g) scale, we achieved 70% conversion (52% isolated yield) to product 1 and 98% conversion (91% isolated yield) to product 17. Scale up required minimal optimization as the same reactant stoichiometry was used in a larger reactor with using four 405 nm LEDs. Under these prescribed reaction conditions this methodology proved less successful or ineffective in the reduction of electron-rich arenes as well as with substrates possessing alkenes, alkynes, alkyl halides, unprotected amines, or nitrogen-containing heterocycles (Figure S5.1).

#### Reduction of Aryl Ethers



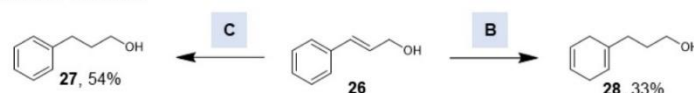
**A** PC (0.25 mol% x 6), NMe<sub>2</sub>OH (5 eq x 3), MeOH/AmylOH, 405 nm, rt, 168 h

#### Reductive Deoxygenation and Birch Reduction



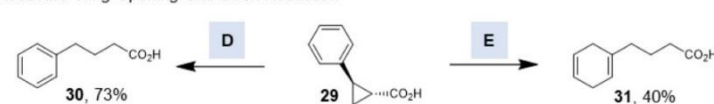
**B** PC (0.25 mol% x 3), NMe<sub>2</sub>OH (5 eq x 3), MeOH/AmylOH, 405 nm, rt, 96 h

#### Selective Reduction



**C** PC (0.25 mol%), NMe<sub>2</sub>OH (5 eq), MeOH/AmylOH, 405 nm, rt, 24 h

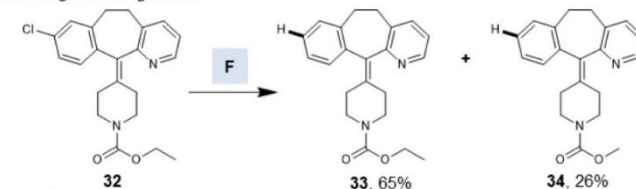
#### Reductive Ring-Opening and Birch Reduction



**D** PC (0.25 mol% x 2), NMe<sub>2</sub>OH (10 eq), MeOH/AmylOH, 405 nm, rt, 72 h

**E** PC (0.25 mol% x 5), NMe<sub>2</sub>OH (15 eq), MeOH/AmylOH, 405 nm, rt, 144 h

#### Late-Stage Dehalogenation



**F** PC (0.25 mol%), NMe<sub>2</sub>OH (10 eq), MeOH/AmylOH/THF, 405 nm, rt, 48 h

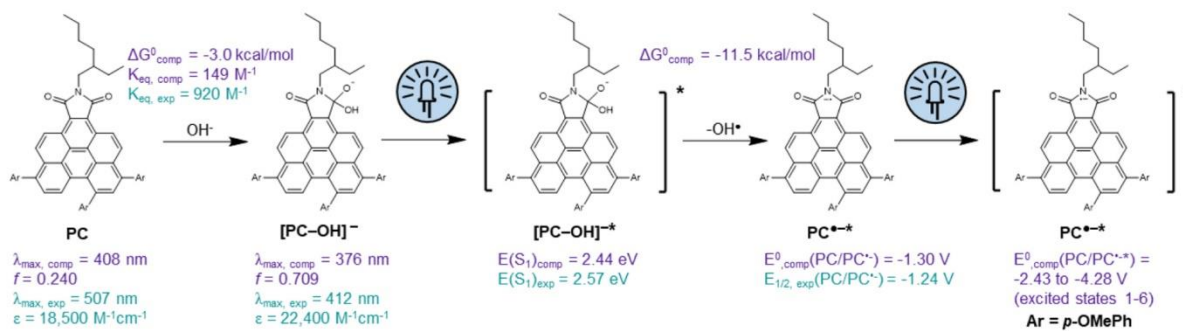
*Figure 5.3. Selective reductions. Modulation of the reaction conditions enables selective reduction.*

Selective reduction of arenes containing multiple reactive unsaturated functional groups could be achieved through modulation of the reaction conditions (Figure 5.3). Interestingly, reduction of one or both phenyl rings of diphenyl ether were observed (20 and 22) as well as the over-reduction to afford vinyl ethers 21 and 23. Employing optimized conditions, benzophenone proceeded through the tandem reductive deoxygenation and Birch reduction to afford 1-benzyl-1,4-cyclohexadiene 25 in 42% yield. By manipulating the equivalents of  $\text{NMe}_4\text{OH}$  and reaction time, cinnamyl alcohol could be converted to either phenyl propanol 27 through alkene reduction or 28 via both alkene and aromatic reductions. Similarly, *trans*-2-phenylcyclopropane-1-carboxylic acid underwent a reductive ring-opening process to give 30 in 73% yield, while further reduction provided 31 in 40% yield. In addition, dehalogenation of the pharmaceutical loratadine was facile (33, 65% yield), although significant transesterification also occurred with the solvent (34).

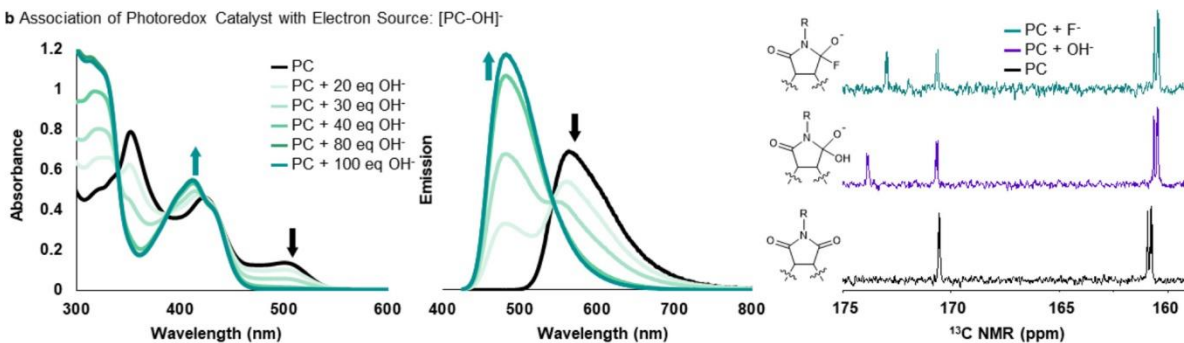
To investigate the mechanism underlying this reactivity, spectroscopic studies and density functional theory (DFT) calculations were performed (Figure 5.4). Overall, these results support a catalytic cycle involving two photon absorption steps in this photoredox-catalyzed Birch reduction (Figure 5.4a). Prior to irradiation, a color change from orange to yellow was observed upon  $\text{OH}^-$  addition to an orange solution of the PC, suggesting dark reactivity between the PC and  $\text{OH}^-$  (Figure 5.4b). To further investigate the nature of this interaction, a series of solutions was



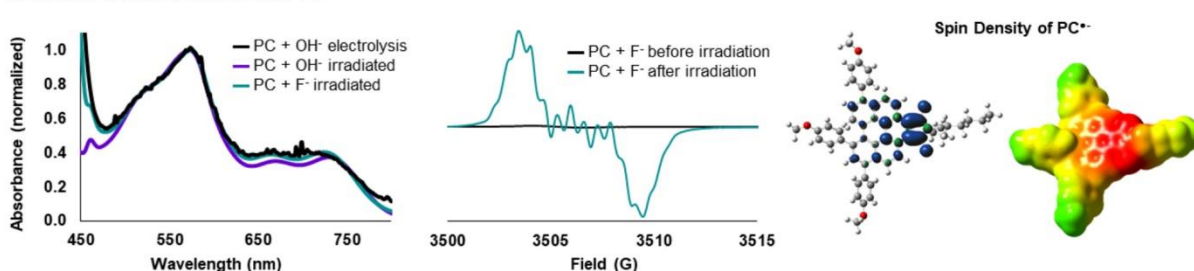
**a Plausible Mechanism for Consecutive Photoinduced Electron Transfer**



**b Association of Photoredox Catalyst with Electron Source: [PC-OH]<sup>-</sup>**



**c Generation of a Stable Radical Anion: PC<sup>•-</sup>**



**d Photoexcited Radical Anion: PC<sup>•-\bullet</sup>**

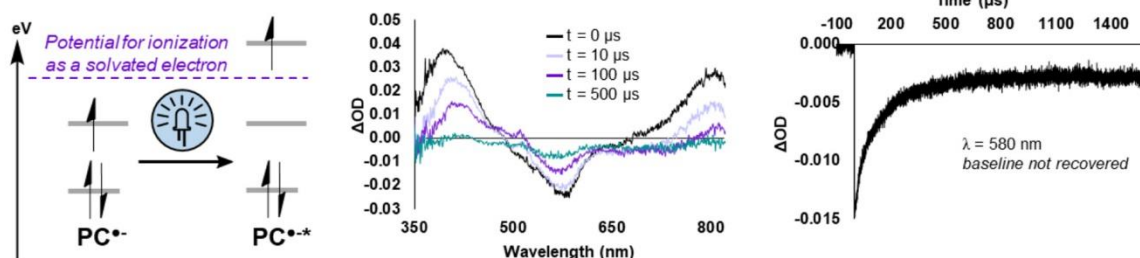


**Figure 5.4. Mechanistic studies.** (a) Proposed mechanism of ConPET proceeds through a covalent [PC–OH]<sup>–</sup> complex; DFT-predicted values are shown in purple and experimentally measured values in turquoise. Electrochemical reference in Volts vs SCE; Ar = *p*-OMePh. (b) Association of the PC and OH<sup>–</sup> can be observed by absorption (left), fluorescence (middle), and <sup>13</sup>C NMR (right) spectroscopy; R = 2-ethylhexyl. (c) PC<sup>•–</sup> is stable and can be observed by absorption (left) and EPR (middle) spectroscopy. Computational characterization of PC<sup>•–</sup> by visualization of spin density and electrostatic potential (ESP)-mapped electron density depicting electron-rich “red” and electron-poor “green” regions (right). (d) Nanosecond transient absorption spectroscopy of PC<sup>•–</sup>; irradiation performed with a 405 nm LED (middle and right).

analyzed by UV–visible spectroscopy (UV–vis) in which the molar ratio of  $\text{OH}^-$  was increased while the total volume of each solution was held constant. In this titration experiment, absorption bands assigned to the PC ( $\lambda_{\text{abs,max}} = 353, 423, \text{ and } 507 \text{ nm}$ ) decrease with increasing  $[\text{OH}^-]$  in conjunction with the appearance of new absorbance features ( $\lambda_{\text{abs,max}} = 312 \text{ and } 412 \text{ nm}$ ). Monitoring the emission of these same mixtures shows a progressive decrease in the intensity of the PC fluorescence ( $\lambda_{\text{em,max}} = 563 \text{ nm}$ ) with the appearance of emission from a new species ( $\lambda_{\text{em,max}} = 481 \text{ nm}$ ), supporting assignment of a 1:1 equilibrium binding model.<sup>32</sup> Fitting the UV–vis data to this 1:1 model yields the equilibrium constant for  $\text{OH}^-$  association ( $K_{\text{eq}} = 920 \text{ M}^{-1}$ ). It is relevant to note that in formation of a charge-transfer anion– $\pi$  complex between iodide and NDIs a red shift was reported, as opposed to the blue shift observed here, suggesting a fundamentally different mode of complexation in this system.<sup>33</sup> Interestingly,  $^{13}\text{C}$  NMR supports formation of a covalent hydroxide adduct  $[\text{PC-OH}]^-$  (Figure 5.4b, SI Figures S5.114–S5.116) rather than an anion– $\pi$  type complex.<sup>27</sup> A new signal emerges after addition of 100 equiv of either  $\text{OH}^-$  ( $\delta = 173.9 \text{ ppm}$ ) or  $\text{F}^-$  ( $\delta = 173.0 \text{ ppm}$ ), which suggests a new covalent bond is formed in the proximity of the imide moiety. Formation of  $[\text{PC-OH}]^-$  is further supported by DFT calculations (Figure 5.4a), which predict complex formation to be exergonic by  $3.0 \text{ kcal mol}^{-1}$  ( $K_{\text{eq,comp}} = 150 \text{ M}^{-1}$ ) along with a qualitative blue shift in the predicted lowest energy UV–vis absorption ( $\lambda_{\text{abs,max,comp}}$  from 408 to 376 nm). Thus, spectroscopic data and DFT computations support that  $\text{OH}^-$  attacks the PC reversibly to form  $[\text{PC-OH}]^-$ , which comprises the majority species in the equilibrium mixture under the reaction conditions (i.e.,  $\text{OH}^-$ :PC molar ratio of 800–1333:1 in the reactions performed to determine scope (Figures 5.2 and 5.3)). Further,  $[\text{PC-OH}]^-$  is stable in the dark, such that thermally induced electron transfer does not occur and is predicted to be endergonic by  $44.8 \text{ kcal mol}^{-1}$ , although such ground-state reactivity was observed with the structurally related PDIs and

NDIs.<sup>34,35</sup> Finally, control experiments reveal that in the absence of  $\text{OH}^-$ , the  $\text{PC}^*$  is not quenched by either benzene or alcohols, supporting that the catalytic cycle proceeds through  $[\text{PC-OH}]^-$  (Figure S5.18).

With the dark speciation of the  $\text{PC/OH}^-$  mixture driven toward  $[\text{PC-OH}]^-$ , we next investigated its reactivity under the influence of light (Figure 5.4c). Upon photon absorption, we propose that PET occurs intramolecularly from  $\text{OH}^-$  to the imide moiety to form the radical anion  $\text{PC}^{\bullet-}$  and  $\text{OH}^{\bullet}$ . While the fate of  $\text{OH}^{\bullet}$  (primarily  $\text{O}^{\bullet-}$  under basic conditions)<sup>36</sup> is currently unknown, we hypothesize that it may react with the methanol solvent to produce a hydroxymethyl radical and  $\text{OH}^-$ ;<sup>37</sup> further studies to elucidate the ultimate fate of these reactive species are ongoing in our laboratory. This PET step is predicted by DFT to be exergonic by 11.5 kcal/mol and thermodynamically driven by the lowest singlet excited state of the  $[\text{PC-OH}]^-$  [ $E_{(\text{S1})\text{exp}} = 2.57$  eV;  $E_{(\text{S1})\text{comp}} = 2.44$  eV] (Figure 5.4a). Time-dependent DFT calculations suggest that the relevant absorption for  $[\text{PC-OH}]^-$  under 405 nm LED irradiation is the HOMO-LUMO transition ( $E_{\text{comp}} = 3.29$  eV, 376 nm,  $f = 0.709$ ), which is of  $\pi-\pi^*$  nature (Figure S5.118).

Formation of  $\text{PC}^{\bullet-}$  is further supported by multiple independent experiments. First, upon irradiation of  $[\text{PC-OH}]^-$  with a 405 nm LED a color change from yellow to purple is observed along with the appearance of several new absorption bands ( $\lambda_{\text{abs,max}} = 580$  nm). In support that this new species is the persistent radical  $\text{PC}^{\bullet-}$ ; the same absorbance spectrum could be observed when using  $\text{F}^-$  as the electron source or through bulk electrolysis at an applied potential ( $E_{\text{app}} = -2.26$  V vs SCE) (Figure 5.4c). In addition, electron paramagnetic resonance (EPR) spectroscopy was used to characterize the photogenerated  $\text{PC}^{\bullet-}$ . The experimental EPR spectrum could be reasonably simulated<sup>38</sup> and demonstrated delocalization of the unpaired electron on the benzo[ghi]-perylene monoimide core as indicated by its interactions with N ( $a = 1.985$  G), two equivalent methylene

Hs adjacent to the N ( $a = 0.540$  G), and seven nondegenerate Hs on the aromatic core ( $a = 0.611$ ,  $0.612$ ,  $0.639$ ,  $0.644$ ,  $0.644$ ,  $0.645$ , and  $0.645$  G); other parameters used in the simulation include  $g_{\text{isotropic}} = 2.00171$ , line width =  $0.666$  G, and line shape = Gaussian (Figure S5.42).  $\text{PC}^{\bullet-}$  was further characterized by visualization of the DFT-predicted spin density in which the unpaired electron is localized on the imide moiety and to a lesser extent delocalized over the methylene group adjacent to nitrogen and the aromatic system on the BPI core.

Although  $\text{PC}^{\bullet-}$  is a relatively strong reductant [ $E_{1/2,\text{exp}}(\text{PC}/\text{PC}^{\bullet-}) = -1.24$  V vs SCE;  $E_{\text{comp}}^0(\text{PC}/\text{PC}^{\bullet-}) = -1.30$  V vs SCE], this reducing power is insufficient for a Birch reduction and reactivity is not observed in the absence of light. Thus, we hypothesized that  $\text{PC}^{\bullet-}$  absorbs a second photon to generate  $\text{PC}^{\bullet-*}$ , a much stronger reductant that can engage in Birch reduction (Figure 5.4d). Notably,  $\text{PC}^{\bullet-}$  is a persistent radical with sufficient lifetime for reversible CV and EPR analysis. This long lifetime allows  $\text{PC}^{\bullet-}$  to absorb a photon using a practical LED setup as opposed to requiring laser irradiation.<sup>14</sup> The excited-state properties of the  $\text{PC}^{\bullet-*}$  were predicted using time-dependent DFT calculations to evaluate the thermodynamic feasibility of generating a solvated electron or directly reducing the substrate. We determined that the first six doublet excited states of  $\text{PC}^{\bullet-*}$  can be accessed with a 405 nm photon (3.06 eV) used in this study (Figure S5.117). Excited states 2–6 have enough energy for ionization of  $\text{PC}^{\bullet-*}$  by an electron transfer to the solvent ( $k_{\text{ET},1}$ ) to form a solvated electron and the ground-state PC. For efficient generation of a solvated electron,  $k_{\text{ET},1}$  must be competitive with the internal conversion process ( $k_{\text{IC}}$ ), deactivating high-lying excited states to the lowest doublet excited state of  $\text{PC}^{\bullet-*}$ , which is below the energy threshold for both solvated electron formation and direct PET to benzene. Solvated electron formation has been observed to occur in as little as  $11 \pm 1$  ps in methanol, supporting the feasibility of this competition.<sup>39</sup> Further, electron transfer from the solvated electron to an aromatic substrate

( $k_{\text{ET},2}$ ) for Birch reduction reactivity must also be facile relative to the unproductive back electron transfer to the lowest excited state of  $\text{PC}^{\bullet-*$  ( $k_{\text{ET},3}$ ).

The photoexcitation of  $\text{PC}^{\bullet-}$  was investigated using nanosecond transient absorption spectroscopy (Figure 5.4d). Selective excitation of  $\text{PC}^{\bullet-}$  could be achieved through irradiation at 532 nm due to the minimal spectral overlap with PC or  $[\text{PC-OH}]^-$ . Laser excitation produces a ground state bleach feature ( $\lambda_{\text{min}} = 580$  nm) that matches the absorption of  $\text{PC}^{\bullet-}$  and thus can be assigned to  $\text{PC}^{\bullet-*$ . Kinetic monitoring of this signal reveals that the baseline is not recovered on the millisecond time scale, indicating that  $\text{PC}^{\bullet-*$  decomposes. Decomposition is consistent with either direct PET to the substrate or production of a solvated electron as both processes yield the neutral, closed-shell PC which lacks an absorption at  $\lambda = 580$  nm. Since the photoionization event to release a solvated electron is likely orders of magnitude faster than the time resolution of our TA setup (*vide supra*), the absorption signal of the solvated electron would be expected to appear in the TA spectrum immediately following the laser pulse at  $t = 0$  ns. However, we note that in THF the solvated electron has been observed at  $\lambda_{\text{max}} = 2120$  nm, which is outside the range of our detector.<sup>40</sup> Our attempts at measurement in MeOH where this absorption would fall within the visible spectrum so far have been without success, likely due to the low solubility of the PC in MeOH and the resulting challenge of generating high-enough concentrations of  $\text{PC}^{\bullet-}$  for spectroscopic study.

Interestingly, the observed excited-state  $\text{PC}^{\bullet-*$  is several orders of magnitude longer lived than the doublet excited states of other aromatic imides and diimides.<sup>26</sup> This observation suggests that the signal followed by TA can be tentatively assigned to the lowest quartet excited state  $^4\text{PC}^{\bullet-*$  produced via intersystem crossing (ISC) from the doublet manifold, as observed to occur upon excitation of other persistent organic radicals such as the enzyme DNA photolyase.<sup>41,42</sup> Comparing

the kinetic traces at  $\lambda_{\text{probe}} = 580$  nm with and without the benzene substrate present as a potential quencher does not reveal a significant change in the lifetime of  ${}^4\text{PC}^{*-}$  (Figure S5.15), suggesting that  ${}^4\text{PC}^{*-}$  does not react efficiently with the substrate. Considering that the computed lowest doublet state  ${}^2\text{PC}^{*-}$  is also unlikely to reduce benzene (insufficient by  $\sim 1.0$  V vs SCE, Figure S5.117), direct PET to the substrate appears to be thermodynamically unfavorable. One possibility to achieve increased driving force involves the occurrence of PET from a higher lying excited state in an anti-Kasha fashion, an unlikely prospect that is typically observed only in systems in which intramolecular PET is possible.<sup>43</sup> Although we do not see evidence by UV-vis for association of  $[\text{PC-OH}]^-$  or  $\text{PC}^{*-}$  with benzene (Figure S5.13), we are actively investigating the alternate hypothesis that  $\text{PC}^{*-}$  may form ground-state  $\pi$ -stacking complexes or exciplexes with benzene to enable intramolecular PET, potentially through an anti-Kasha process. These considerations taken together suggest the working hypothesis that  $\text{PC}^{*-}$  photoionizes with  $k_{\text{ET},1}$  competitive with  $k_{\text{IC}}$ , releasing a solvated electron that subsequently reduces the substrate. Overall, the initial mechanistic experiments herein support formation of  $[\text{PC-OH}]^-$  and subsequent photodissociation to form  $\text{PC}^{*-}$ . Further experiments are currently ongoing to elucidate the role of  ${}^2\text{PC}^{*-}$ ,  ${}^4\text{PC}^{*-}$ , and the competition between  $k_{\text{ET},1}$  and  $k_{\text{IC}}$ .

## CONCLUSION

In summary, a class of organic benzo[ghi]perylene imide photoredox catalysts was developed for Birch reductions under mild benchtop conditions and visible-light LED irradiation. This work represents the first visible-light photoredox catalysis system that is capable of engaging arenes such as benzene that were previously out of reach due to their high triplet energies and extremely negative reduction potentials. Despite this unprecedented reactivity, this platform requires further development to realize its full synthetic potential. Initial mechanistic experiments

support formation of the hydroxide adduct  $[\text{PC-OH}]^-$  and its subsequent photodissociation to  $\text{PC}^{\bullet-}$ , which we posit undergoes absorption of a second photon to release a solvated electron as the active reductant. Future mechanistic studies are ongoing to test this hypothesis and to identify mechanistically guided PC design principles for more robust and active PCs to improve the scope of photocatalyzed Birch reductions.

## EXPERIMENTAL 3 – SUPPLEMENTARY INFORMATION FOR CHAPTER 5

### 1. Materials and Methods

#### General Methods

All purchased reagents were used without further purification. NMR spectra were recorded on a Varian 300 MHz, 400 MHz, or 500 MHz NMR Spectrometer as noted for all characterizations. All  $^1\text{H}$  NMR are reported in  $\delta$  units (parts per million – ppm) and were measured relative to the signals found in residual chloroform (7.26 ppm). All  $^{13}\text{C}$  NMR were measured relative to  $\text{CDCl}_3$  (77.16 ppm).

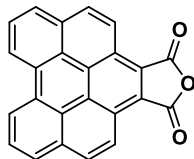
The photoreactors used were custom designed and built in-house and the specifications have been published previously <sup>1</sup>. All LEDs were purchased from LED Engin and full emission spectra, as well as peak wavelength shift vs. temperature data, are available online in the respective manufacturer datasheets (see below). In the photoreactor, 405 nm, 457 nm, cool white, 523 nm, and 590 nm LEDs were run at 700mA and a forward voltage of 13.5 V, while 365 nm and 395 nm LEDs were run at 700 mA and a forward voltage of 15.5 V. For 10 mmol scale reduction, the reactors were modified so that 4 of the LEDs could be arranged around a 100 mL storage tube.

*Table S5.1: LED Information*

LED Peak Wavelength	Luminous Flux	Model #	URL
405 nm	4.1 W @ 700 mA	LZ4-40UB00-00U8	<a href="https://media.osram.info/media/img/osram-dam-5412925//LED_Engin_Datasheet_LuxiGen_LZ4-00UB00_rev1.pdf">https://media.osram.info/media/img/osram-dam-5412925//LED_Engin_Datasheet_LuxiGen_LZ4-00UB00_rev1.pdf</a>

#### Catalyst Synthesis

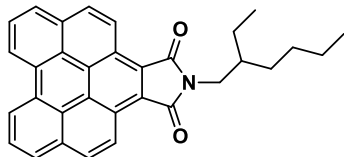
##### *Benzo[ghi]perylene-1,2-dicarboxylic Anhydride*





*Benzo[ghi]perylene-1,2-dicarboxylic anhydride* was synthesized according to literature procedure.<sup>2</sup> Perylene (5.1 g, 20 mmol, 1.0 eq.) was dissolved in molten maleic anhydride (80.0 g, 0.80 mol, 40 eq.) at 240 °C. p-chloranil (11.2 g, 45.6 mmol, 2.3 eq.) was then slowly added and the mixture was refluxed for 10 minutes. Xylenes (100 mL) was then added and the flask was cooled to room temperature. The red solids were collected by filtration and then refluxed in 2:1 EtOAc:CHCl<sub>3</sub> overnight before being filtered while hot. The product was used without further purification or characterization because of its insolubility.

*2-(2-ethylhexyl)-1H-peryleno[1,12-efg]isoindole-1,3(2H)-dione* (PC 1)

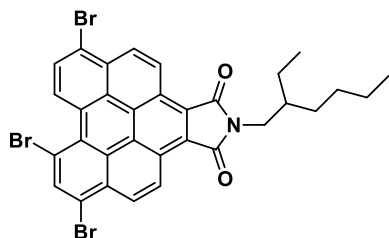


Benzo[ghi]perylene-1,2-dicarboxylic Anhydride (0.9 g, 2.6 mmol, 1.0 eq) and a stir bar were added to a 250 mL round bottom flask followed by 150 mL of DMF. 2-Ethyl-1-hexylamine (0.6 mL, 3.9 mmol, 1.5 eq.) was added and the reaction was heated to 125 °C for 16 hours. The reaction was cooled down and 60 mL of concentrated HCl was added to the solution and a yellow-brown solid precipitated from solution. The solid was filtered and then washed with 300 mL of 1M KOH solution, followed by deionized water until a neutral pH was obtained to give an orange powder. The orange powder was recrystallized using DCM/MeOH. Yield: 0.86 g, 72% yield.

<sup>1</sup>H NMR (300 MHz, Chloroform-*d*)  $\delta$  = 8.23-8.16 (m, 4H), 7.61-7.55 (m, 4H), 7.34 (d, *J* = 9.0 Hz, 2H), 3.60 (d, *J* = 7.1 Hz, 2H), 1.97-1.85 (m, 1H), 1.55-1.35 (m, 8H), 1.05 (t, *J* = 7.3 Hz, 3H), 0.98 (t, *J* = 6.7 Hz, 3H). <sup>13</sup>C NMR (300 MHz, Chloroform-*d*)  $\delta$  = 169.3, 130.6, 128.5, 128.2, 126.2, 124.4, 122.4, 122.2, 121.8, 121.4, 120.2, 41.6, 39.1, 30.9, 28.9, 24.2, 23.3, 14.4, 10.71

DART: Calcd. for C<sub>32</sub>H<sub>27</sub>NO<sub>2</sub> [M+H]<sup>+</sup> 458.2115, found 458.2118.

*6,8,11-tribromo-2-(2-ethylhexyl)-1H-peryleno[1,12-efg]isoindole -1,3(2H)-dione* (PC 2)



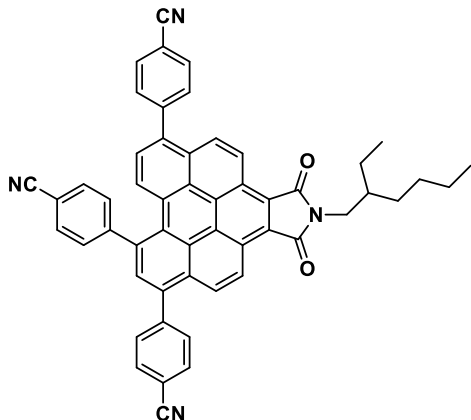
To a 100 mL thick walled flask was added 1 (0.6 g, 1.3 mmol, 1.0 eq.) and stir bar. DCM was added to the solids then heated up to 60 °C until the solid was fully dissolved (~40 mL). After which bromine (2.0 mL, 39 mmol, 30 eq.) was added quickly. The bomb flask was capped and the reaction went from orange to a dark red. After 4 days, the reaction was concentrated and the

bromine blown off. The product was recrystallized in DCM and filtered and washed further with hexanes to give a yellow solid. Yield: 0.82 g, 91%.

$^1\text{H}$  NMR (300 MHz, Chloroform-*d*)  $\delta$  = 8.42 (d,  $J$  = 8.7 Hz, 1H), 8.01 (d,  $J$  = 8.9 Hz, 1H), 7.98 (d,  $J$  = 8.9, 1H), 7.66 (s, Hz, 1H), 7.45 (d,  $J$  = 9.0 Hz, 1H), 7.30 (d,  $J$  = 9.0 Hz, 1H), 7.24 (d,  $J$  = 8.8 Hz, 1H), 3.56 (d,  $J$  = 7.1 Hz, 2H), 1.93-1.77 (m, 1H), 1.55-1.33 (m, 8H), 1.07-0.93 (m, 6H).  $^{13}\text{C}$  NMR (75 MHz, Chloroform-*d*)  $\delta$  = 168.3, 168.2, 138.1, 129.1, 127.4, 127.3, 127.2, 126.6, 124.8, 124.4, 124.3, 123.9, 123.0, 122.8, 122.7, 122.6, 122.5, 122.2, 122.0, 121.7, 121.6, 121.0, 116.3, 42.1, 38.9, 30.9, 28.8, 24.1, 23.4, 14.4, 10.7. HRMS (ESI): Calcd. for  $\text{C}_{32}\text{H}_{24}\text{Br}_3\text{NO}_2$   $[\text{M}]^+$  694.9321, found 694.9332.

General Procedure for the Synthesis of TriAryl Substituted BPIs: To a 100 mL storage flask was added 2 (0.23 g, 0.32 mmol, 1.0 eq.) and boronic acid (2.0 mmol, 6.0 eq.). The storage flask was then moved into a  $\text{N}_2$  filled glovebox where  $\text{Pd}(\text{PPh}_3)_4$  (0.06 g, 0.005 mmol, 15 mol%) was added. 25 mL of THF was then added and the storage tube was removed from the glovebox. 6.2 mL of 2M aqueous  $\text{K}_2\text{CO}_3$  was then added. The reaction was then heated to 100 °C for 24 hours. DCM was added to the mixture and washed with water 3 times, then brine, and dried with  $\text{MgSO}_4$ . All compounds were purified by column chromatography using a gradient of hexanes:toluene as an eluent.

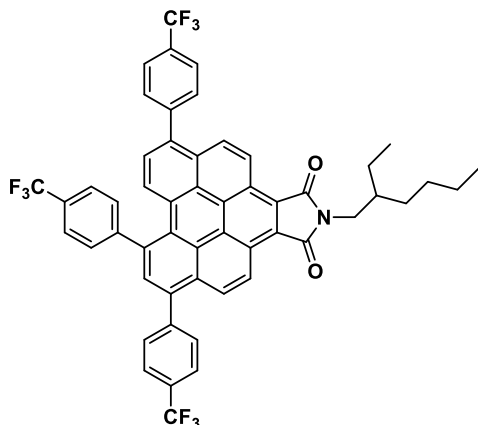
*4,4',4''-(2-(2-ethylhexyl)-1,3-dioxo-2,3-dihydro-1H-perylene[1,12-efg]isoindole-6,8,11-triyl)tribenzonitrile* (PC 3)



The general procedure was followed exactly using 4-cyanophenylboronic acid (0.29 g, 6.0 eq.). Yield: 0.23 g, 95%.

$^1\text{H}$  NMR (300 MHz, Chloroform-*d*)  $\delta$  = 9.37 (d,  $J$  = 9.3 Hz, 1H), 9.30 (d,  $J$  = 9.4 Hz, 1H), 8.31-8.25 (m, 3H), 7.95 (s, 1H), 7.93-7.71 (m, 12H), 7.61 (d,  $J$  = 8.3 Hz, 1H), 3.73 (d,  $J$  = 7.2 Hz, 2H), 1.98 (m, 1H), 1.41 (m, 8H), 0.98 (t,  $J$  = 7.4 Hz, 3H), 0.90 (t,  $J$  = 6.8 Hz, 3H).  $^{13}\text{C}$  NMR (75 MHz, Chloroform-*d*)  $\delta$  = 169.9, 169.8, 149.3, 144.6, 144.3, 138.1, 137.6, 137.1, 133.8, 132.6, 132.4, 131.2, 131.1, 130.1, 129.4, 129.2, 129.1, 129.1, 128.4, 127.5, 127.4, 127.1, 126.5, 124.8, 124.6, 124.5, 124.4, 123.7, 118.6, 118.5, 112.2, 112.0, 111.8, 42.1, 38.6, 30.7, 28.6, 24.0, 23.0, 14.1, 10.5. HRMS (ESI): Calcd. for  $\text{C}_{53}\text{H}_{36}\text{N}_4\text{O}_2$   $[\text{M}]^+$  760.2833, found 760.2822.

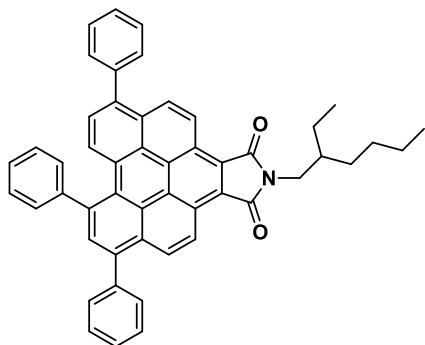
2-(2-ethylhexyl)-6,8,11-tris(4-(trifluoromethyl)phenyl)-1H-peryleno[1,12-efg]isoindole-1,3(2H)-dione (PC 4)



The general procedure was followed exactly using 4-(trifluoromethyl)phenylboronic acid (0.24 g, 6.0 eq.). The compound was purified by column chromatography using silica as the stationary phase and eluting with 10% hexanes in DCM. It was then recrystallized in DCM/Methanol, the product was filtered and washed sparingly with methanol to give yellow orange solid. Yield: 0.17g, 60%.

$^1\text{H}$  NMR (300 MHz, Chloroform-*d*)  $\delta$  = 9.10 (d,  $J$  = 9.3 Hz, 1H), 8.97 (d,  $J$  = 9.3 Hz, 1H), 8.23 (d,  $J$  = 8.4 Hz, 1H), 8.20 (d,  $J$  = 9.3 Hz, 1H), 8.14 (d,  $J$  = 9.3 Hz, 1H), 7.95 (s, 1H), 7.92-7.66 (m, 12H), 7.56 (d,  $J$  = 8.3 Hz, 1H), 3.58 (d,  $J$  = 7.3 Hz, 2H), 1.97-1.83 (m, 1H), 1.50-1.27 (m, 8H), 0.96 (t,  $J$  = 7.4, 3H), 0.89 (t,  $J$  = 7.0 Hz, 3H).  $^{13}\text{C}$  NMR (101 MHz, Chloroform-*d*)  $\delta$  = 169.8, 169.7, 148.6, 143.7, 143.5, 138.4, 138.1, 137.7, 133.4, 130.9, 130.7, 130.6, 130.4, 130.3, 130.1, 130.0, 129.7, 129.4, 129.2, 129.1, 128.9, 128.1, 127.7, 127.6, 127.6, 127.5, 127.3, 127.1, 127.1, 126.8, 126.3, 125.9, 125.9, 125.8, 125.7, 125.7, 124.4, 124.2, 124.2, 124.0, 123.9, 123.2, 123.0, 42.0, 38.7, 30.8, 28.8, 24.1, 23.2, 14.2, 10.7.  $^{19}\text{F}$  NMR (282 MHz, Chloroform-*d*)  $\delta$  = -62.40 (3F), -62.43(3F), -62.45(3F). HRMS (ESI): Calcd. for  $\text{C}_{53}\text{H}_{36}\text{F}_9\text{NO}_2$  [ $\text{M}$ ] $^+$  775.3298, found 775.3287.

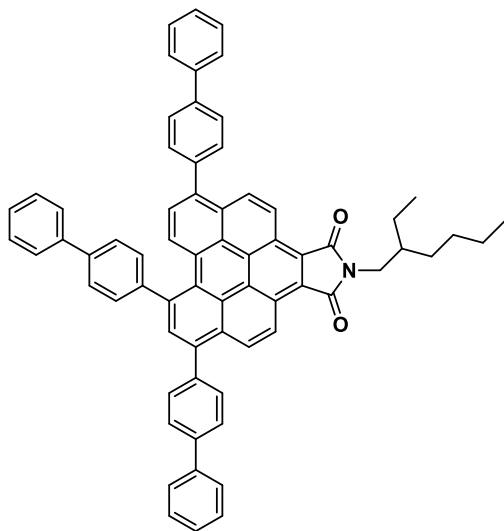
2-(2-ethylhexyl)-6,8,11-triphenyl-1H-peryleno[1,12-efg]isoindole-1,3(2H)-dione (PC 5)



The general procedure was followed exactly using phenylboronic acid (0.24 g, 6.0 eq.). Yield: 0.17 g, 78%.

$^1\text{H}$  NMR (300 MHz, Chloroform- $d$ )  $\delta$  = 9.16 (d,  $J$  = 9.3 Hz, 1H), 9.07 (d,  $J$  = 9.4 Hz, 1H), 8.34 (d,  $J$  = 9.2 Hz, 1H), 8.31 (d,  $J$  = 8.1 Hz 1H), 8.29 (d,  $J$  = 9.4 Hz, 1H), 8.02 (s, 1H), 7.77-7.65 (m, 2H), 7.64-7.36 (m, 14H), 3.68 (d,  $J$  = 7.2 Hz, 2H), 2.09-1.78 (m, 1H), 1.52-1.21 (m, 8H), 0.98 (t,  $J$  = 7.4 Hz, 3H), 0.90 (t,  $J$  = 6.8 Hz, 3H).  $^{13}\text{C}$  NMR (75 MHz, Chloroform- $d$ )  $\delta$  = 169.9, 169.8, 145.3, 140.3, 140.2, 139.2, 139.1, 139.0, 133.8, 130.7, 130.6, 129.9, 129.3, 129.0, 128.9, 128.7, 128.6, 128.0, 127.9, 127.8, 127.7, 127.6, 127.5, 127.5, 127.5, 127.4, 126.6, 126.1, 124.2, 123.7, 123.6, 123.5, 122.8, 122.3, 41.9, 38.7, 30.8, 28.8, 24.1, 23.2, 14.3, 10.7. HRMS (ESI): Calcd. for  $\text{C}_{50}\text{H}_{39}\text{NO}_2$   $[\text{M}]^+$  685.291, found 685.2967.

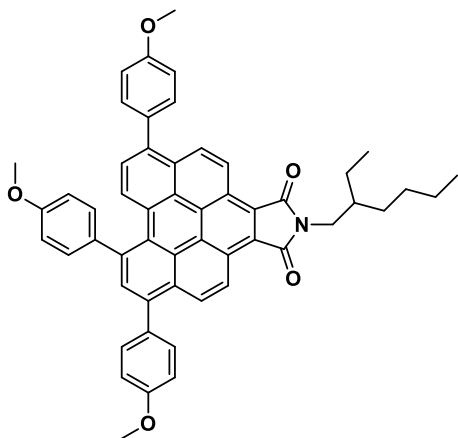
*6,8,11-tri([1,1'-biphenyl]-4-yl)-2-(2-ethylhexyl)-1H-peryleno [1,12-efg]isoindole-1,3(2H)-dione*  
(PC 6)



The general procedure was followed exactly using 4-biphenylboronic acid (0.39 g, 6.0 eq.). Yield: 0.26 g, 89%.

$^1\text{H}$  NMR (400 MHz, Chloroform- $d$ )  $\delta$  = 9.19 (d,  $J$  = 9.3 Hz, 1H), 9.09 (d,  $J$  = 9.3 Hz, 1H), 8.44 (d,  $J$  = 8.4 Hz, 1H), 8.43 (d,  $J$  = 9.3 Hz, 1H), 8.38 (d,  $J$  = 9.3 Hz, 1H), 8.11 (s, 1H), 7.89-7.63 (m, 18H), 7.59 (d,  $J$  = 8.4 Hz, 1H), 7.55-7.46 (m, 6H), 7.46-7.37 (m, 3H), 3.70 (d,  $J$  = 7.3 Hz, 2H), 2.03-1.93 (m, 1H), 1.50-1.30 (m, 8H), 0.99 (t,  $J$  = 7.4 Hz, 3H), 0.90 (t,  $J$  = 7.1 Hz, 3H).  $^{13}\text{C}$  NMR (75 MHz, Chloroform- $d$ )  $\delta$  = 170.3, 170.2, 144.2, 140.8, 140.7, 140.6, 140.4, 139.2, 139.1, 138.9, 138.8, 133.8, 131.1, 131.1, 129.8, 129.3, 129.2, 129.1, 129.1, 128.9, 128.6, 128.3, 128.1, 127.8, 127.7, 127.5, 127.4, 127.3, 127.3, 127.2, 127.0, 126.5, 124.6, 124.1, 124.0, 123.2, 122.7, 42.0, 38.7, 30.8, 28.8, 24.1, 23.2, 14.3, 10.7. HRMS (ESI): Calcd. for  $\text{C}_{68}\text{H}_{51}\text{NO}_2$   $[\text{M}]^+$  913.3920, found 913.3920.

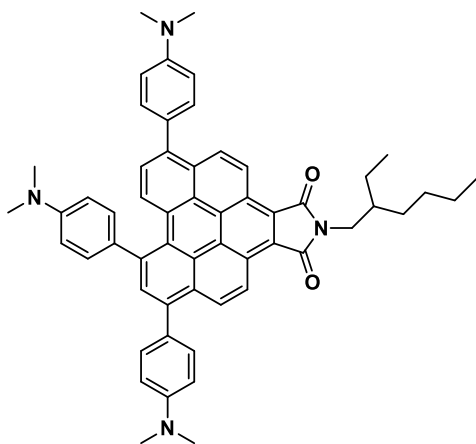
*2-(2-ethylhexyl)-6,8,11-tris(4-methoxyphenyl)-1H-peryleno [1,12-efg]isoindole-1,3(2H)-dione*  
(PC 7)



The general procedure was followed exactly using 4-methoxyphenylboronic acid (0.30 g, 6.0 eq.). Yield: 0.22 mg, 89%.

$^1\text{H}$  NMR (300 MHz, Chloroform-*d*)  $\delta$  = 8.85 (d,  $J$  = 9.3 Hz, 1H), 8.73 (d,  $J$  = 9.3 Hz, 1H), 8.21 (d,  $J$  = 8.4 Hz, 1H), 8.18 (d,  $J$  = 9.3 Hz, 1H), 8.11 (d,  $J$  = 9.4 Hz, 1H), 7.90 (s, 1H), 7.56 (d,  $J$  = 8.6 Hz, 2H), 7.53-7.36 (m, 5H), 7.12 (d,  $J$  = 8.7 Hz, 2H), 7.09 (d,  $J$  = 8.6 Hz, 2H), 7.02 (d,  $J$  = 8.7 Hz, 2H), 3.98 (s, 3H), 3.96 (s, 3H), 3.91 (s, 3H), 3.53 (d,  $J$  = 7.2, 2H), 1.97-1.82 (m, 1H), 1.50-1.26 (m, 8H), 0.96 (t,  $J$  = 7.2 Hz, 3H), 0.91 (t,  $J$  = 6.8 Hz, 3H).  $^{13}\text{C}$  NMR (75 MHz, Chloroform-*d*)  $\delta$  = 170.0, 169.9, 159.4, 159.3, 159.2, 138.7, 138.6, 138.6, 133.9, 132.7, 132.5, 131.8, 131.7, 130.3, 129.0, 128.9, 128.8, 128.3, 128.0, 127.8, 127.6, 127.5, 127.2, 126.7, 126.1, 124.1, 123.6, 123.3, 123.3, 122.4, 122.0, 115.3, 114.2, 114.1, 55.6, 55.5, 55.5, 55.5, 41.8, 38.7, 30.8, 28.8, 24.1, 23.2, 14.3, 10.6. HRMS (ESI): Calcd. for  $\text{C}_{53}\text{H}_{45}\text{NO}_5$   $[\text{M}]^+$  775.3298, found 775.3287.

*6,8,11-tris(4-(dimethylamino)phenyl)-2-(2-ethylhexyl)-1H-peryleno[1,12-efg]isoindole-1,3(2H)-dione* (PC 8)



The general procedure was followed exactly using 4-(dimethylamino)phenylboronic acid (0.43 g, 6.0 eq.). Yield: 0.27 g, 77%.

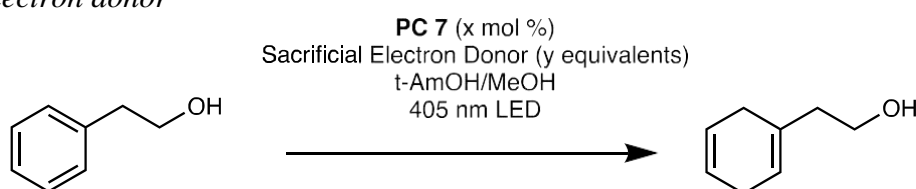
$^1\text{H}$  NMR (400 MHz, Chloroform-*d*)  $\delta$  = 9.25 (d,  $J$  = 9.3 Hz, 1H), 9.21 (d,  $J$  = 9.4 Hz, 1H), 8.57 (d,  $J$  = 8.4 Hz, 1H), 8.53-8.48 (m, 2H), 8.07 (s, 1H), 7.62 (s, 1H), 7.59 (d,  $J$  = 8.9 Hz, 2H), 7.52

(d,  $J = 8.7$  Hz, 2H), 7.48 (d,  $J = 8.7$ , 2H), 6.93 (dd,  $J = 11.8, 8.3$ , 4H), 6.87 (d,  $J = 8.2$  Hz, 2H), 3.76 (d,  $J = 7.3$  Hz, 2H), 3.09 (d,  $J = 6.9$  Hz, 12H), 3.05 (s, 6H), 2.01 (m, 1H), 1.58-1.18(m, 8Hz), 0.99 (t,  $J = 7.4$  Hz, 3H), 0.90 (t,  $J = 7.1$  Hz, 3H).  $^{13}\text{C}$  NMR (75 MHz, Chloroform- $d$ )  $\delta = 170.7, 170.7, 150.0, 139.2, 133.9, 131.6, 131.5, 130.1, 129.3, 128.8, 128.7, 128.7, 128.5, 128.5, 127.7, 127.4, 127.2, 126.8, 124.8, 124.2, 123.7, 122.3, 122.2, 114.0, 112.8, 42.0, 40.9, 38.8, 30.9, 28.8, 24.2, 23.2, 14.3, 10.7$ . HRMS (ESI): Calcd. for  $\text{C}_{56}\text{H}_{55}\text{N}_4\text{O}_2$   $[\text{M}]^+$  815.4320, found 815.4305.

Single crystals for SCXRD were grown by slow diffusion of benzene against hexanes.

### Birch Reduction Optimization

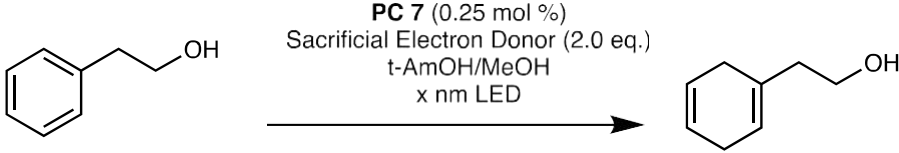
Table S5.2: Optimization of Photoredox Birch Reduction of Phenylethanol using hydroxide as a sacrificial electron donor<sup>a</sup>



Entry	PC	x	Sacrificial Electron Donor	y	Time (hr)	Conv. % <sup>b</sup>
1	1	0.25	Bu <sub>4</sub> NOH	2.0	16	3
2	3	0.25	Bu <sub>4</sub> NOH	2.0	16	5
3	4	0.25	Bu <sub>4</sub> NOH	2.0	16	8
4	5	0.25	Bu <sub>4</sub> NOH	2.0	16	12
5	6	0.25	Bu <sub>4</sub> NOH	2.0	16	2
6	7	0.25	Bu <sub>4</sub> NOH	2.0	16	17
7	8	0.25	Bu <sub>4</sub> NOH	2.0	16	3
8	7	0.25	Et <sub>4</sub> NOH	2.0	16	9
9	7	0.25	Me <sub>4</sub> NOH	2.0	16	25
10	7	0.25	Hex <sub>4</sub> NOH	2.0	16	1
11	7	0.25	Me <sub>4</sub> NOH	5.0	48	33
12 <sup>c</sup>	7	0.25	Me <sub>4</sub> NOH	10.0	48	42
13	7	0.10	Me <sub>4</sub> NOH	10.0	48	20
14	7	0.50	Me <sub>4</sub> NOH	10.0	48	43
15	7	1.0	Me <sub>4</sub> NOH	10.0	48	33
16	7	0.25×3 <sup>d</sup>	Me <sub>4</sub> NOH	10.0	96	88 (70 <sup>e</sup> )

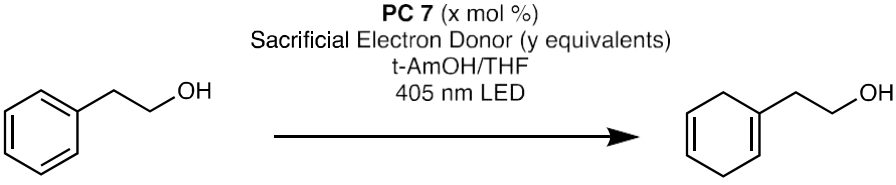
<sup>a</sup>Conditions: A mixture of PC 7, phenylethanol (0.50 mmol), sacrificial electron source, and solvent were irradiated with 405 nm LEDs for indicated time at room temperature. <sup>b</sup>Determined by crude <sup>1</sup>H NMR. <sup>c</sup>No conversion was observed in the absence of PC 7, Me<sub>4</sub>NOH, or light. <sup>d</sup>BPI was added in three portions at *t* = 0 hr, 48 hr, and 72 hr. <sup>e</sup>Isolated yield.

Table S5.3: Varying Light Sources



Conditions:	Mass	Moles	Equivalents
PC 7	1.0 mg	0.001 mmol	0.25 mol %
PhEtOH	0.06 mL	0.5 mmol	1 eq
Me <sub>4</sub> NOH/MeOH	1.0 mL	1.0 mmol	2 eq
tAmOH	0.45 mL	4.0 mmol	8 eq
Lights	Conv. @ 20 hr		
365 nm	14%		
395 nm	20%		
405 nm	20%		
457 nm	8%		
Cool White	2%		
523 nm	0%		
590 nm	0%		
740 nm	0%		

Table S4: Photoredox Birch Reduction of Phenylethanol Using Fluoride as the Sacrificial Electron Donor<sup>a</sup>



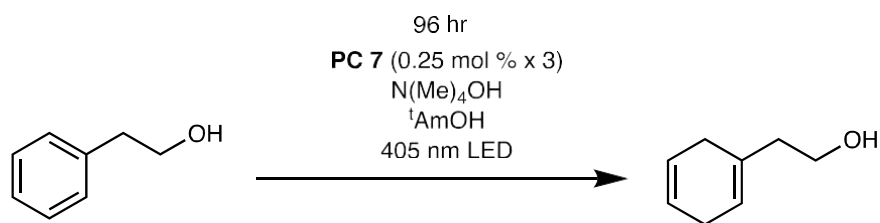
Entry	PC	x	Sacrificial Electron Donor	y	Time (hr)	Conv. % <sup>b</sup>
1	7	0.75	Bu <sub>4</sub> NF	5.0	24	14
2 <sup>c</sup>	7	0.75	Bu <sub>4</sub> NF	5.0	24	1

<sup>a</sup>Conditions: A mixture of PC 7, phenylethanol (0.50 mmol), 2.5 mL of Bu<sub>4</sub>NF (1.0 M in THF), and *t*-AmOH (0.45 mL) were irradiated with 405 nm LEDs for indicated time at room temperature. <sup>b</sup>Determined by crude <sup>1</sup>H NMR. <sup>c</sup>No *t*-AmOH.

## Substrate Scope

General Procedure for Photoredox Organocatalyzed Birch Reduction: A 1.5-dram scintillation vial was loaded with a Teflon-coated stir bar and catalyst (1.0 mg, 0.25 mol %). The vial was transferred to an N<sub>2</sub> filled glovebox where substrate (0.50 mmol), *t*-amyl alcohol (0.45 mL, 8.0 eq.), and N(Me)<sub>4</sub>OH (2.0 mL, 10 eq. (25% solution in MeOH)) were added. The vial was then sealed using a septum cap, removed from the glovebox, and placed into the light reactor. After 48 hours, the reaction was moved back into the glovebox, where more catalyst (1.0 mg, 0.25 mol %) was added. The vial was then removed from the glovebox and placed back into the light reactor. This catalyst addition was repeated at 24-hour intervals. The reaction was stopped the indicated time and worked up according to the details below.

*2-(cyclohexa-1,4-dien-1-yl)ethan-1-ol* (1)



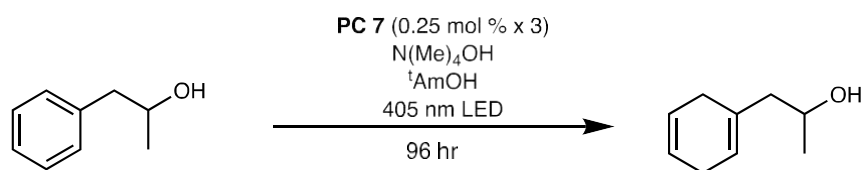
The general procedure was followed using *2-phenyl ethanol*. After the reaction, volatiles were removed using a rotary evaporator and the residue was flashed through a plug of silica. The eluent was then concentrated and purified by silica gel flash column chromatography (gradient of 0-10% EtOAc in Hexanes) resulting in a colorless oil. Yield: 43.5 mg, 70%.

<sup>1</sup>H NMR (400 MHz, CDCl<sub>3</sub>) δ = 5.68-5.60 (m, 2H), 5.50-5.46 (m, 1H), 3.63 (t, *J* = 6.27 Hz, 2H), 2.69-2.61 (m, 2H), 2.59-2.51 (m, 2H), 2.21-2.16 (m, 2H), 1.76 (br s, 1H). <sup>13</sup>C NMR (101 MHz, CDCl<sub>3</sub>) δ = 131.4, 124.2, 124.0, 121.4, 60.0, 40.5, 28.7, 26.8. This data matches reported literature values <sup>3</sup>.



10 mmol scale: A 100 mL storage tube was loaded with a glass stir bar and catalyst (20.0 mg, 0.25 mol %). The storage tube was transferred to an N<sub>2</sub> filled glovebox where *2-phenyl ethanol* (1.2 mL, 10.0 mmol), *t*-amyl alcohol (9.0 mL, 8.0 eq.), and N(Me)<sub>4</sub>OH (40.0 mL, 10 eq. (25% solution in MeOH)) were added. The storage tube was then sealed, removed from the glovebox, and placed into the light reactor. After 72 hours, the reaction was moved back into the glovebox, where more catalyst (20.0 mg, 0.25 mol %) was added. The storage tube was then removed from the glovebox and placed back into the light reactor. This catalyst addition was repeated at 48-hour intervals. The reaction was stopped after 216 h (4 catalyst additions) and worked up according to the details above. Yield: 0.63 g, 52%.

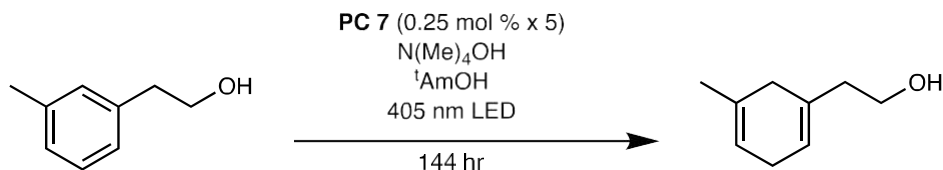
*1-(cyclohexa-1,4-dien-1-yl)propan-2-ol* (2)



The general procedure was followed using *1-phenyl-2-propanol*. After the reaction, volatiles were removed using a rotary evaporator and the residue was flashed through a plug of silica. The eluent was then concentrated and purified by silica gel flash column chromatography (gradient of 0-10% EtOAc in Hexanes) resulting in a colorless oil. Yield: 42.7 mg, 62%.

<sup>1</sup>H NMR (400 MHz, CDCl<sub>3</sub>) δ = 5.72-5.56 (m, 2H), 5.50-5.40 (m, 1H), 3.84 (dq, *J* = 8.4 Hz, 6.1 Hz, 4.6 Hz, 1H), 2.71-2.41 (m, 4H), 2.09-1.95 (m, 2H), 1.74 (br s, 1H), 1.13 (d, 6.1 Hz) <sup>13</sup>C NMR (101 MHz, CDCl<sub>3</sub>) δ = 132.1, 124.1, 124.0, 122.1, 64.8, 47.7, 29.0, 26.8, 22.9. DART: Calcd. for C<sub>9</sub>H<sub>15</sub>O [M+H]<sup>+</sup> 139.1123, found 139.1127.

*2-(5-methylcyclohexa-1,4-dien-1-yl)ethan-1-ol* (3)

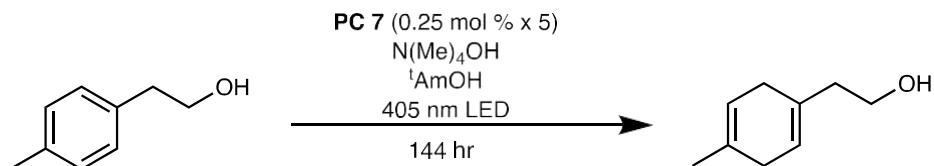


The general procedure was followed using *2-(3-methylphenyl)ethanol*. After the reaction, volatiles were removed using a rotary evaporator and the residue was flashed through a plug of silica. The eluent was then concentrated and purified by silica gel flash column chromatography (gradient of 0-10% EtOAc in Hexanes) resulting in a colorless oil. Yield: 34.9 mg, 51%.

<sup>1</sup>H NMR (400 MHz, CDCl<sub>3</sub>) δ = 5.55-5.49 (m, 1H), 5.41-5.36 (m, 1H), 3.68 (t, *J* = 6.34 Hz, 2H), 2.73-2.63 (m, 2H), 2.53-2.45 (m, 2H), 2.24 (t, *J* = 6.18 Hz, 2H), 1.78 (s, 1H), 1.66 (s, 3H)

$^{13}\text{C}$  NMR (101 MHz,  $\text{CDCl}_3$ )  $\delta = 131.3, 131.0, 121.3, 118.4, 60.0, 40.3, 33.7, 27.7, 23.1$ . This data matches reported literature values <sup>3</sup>.

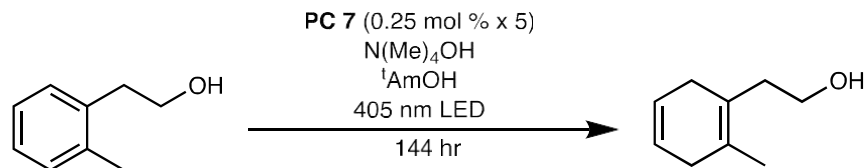
*2-(4-methylcyclohexa-1,4-dien-1-yl)ethan-1-ol* (4)



The general procedure was followed using *2-(4-methylphenyl)ethanol*. After the reaction, volatiles were removed using a rotary evaporator and the residue was flashed through a plug of silica. The eluent was then concentrated and purified by silica gel flash column chromatography (gradient of 0-10% EtOAc in Hexanes) resulting in a colorless oil. Yield: 33.0 mg, 48%.

$^1\text{H}$  NMR (400 MHz,  $\text{CDCl}_3$ )  $\delta = 5.56\text{-}5.49$  (m, 1H), 5.43-5.36 (m, 1H), 3.68 (t,  $J = 6.31$  Hz, 2H), 2.65-2.55 (m, 4H), 2.24 (t,  $J = 6.28$  Hz, 2H), 1.66 (s, 3H), 1.58 (s, 1H).  $^{13}\text{C}$  NMR (101 MHz,  $\text{CDCl}_3$ )  $\delta = 131.3, 131.2, 121.5, 118.3, 60.1, 40.2, 31.6, 29.7, 23.0$ . DART: Calcd. for  $\text{C}_9\text{H}_{15}\text{O}$   $[\text{M}+\text{H}]^+$  139.1123, found 139.1123.

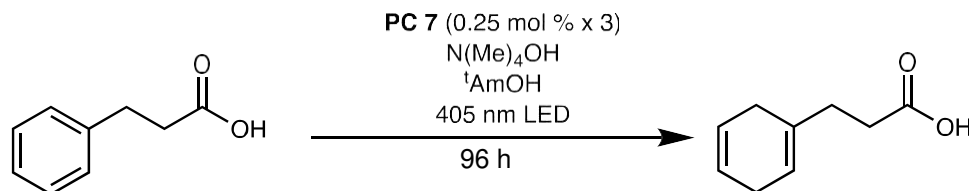
*2-(2-methylcyclohexa-1,4-dien-1-yl)ethan-1-ol* (5)



The general procedure was followed using *2-(4-methylphenyl)ethanol*. After the reaction, volatiles were removed using a rotary evaporator and the residue was flashed through a plug of silica. The eluent was then concentrated and purified by silica gel flash column chromatography (gradient of 0-10% EtOAc in Hexanes) resulting in a colorless oil. Yield: 16.7 mg, 24%.

$^1\text{H}$  NMR (400 MHz,  $\text{CDCl}_3$ )  $\delta = 5.73\text{-}5.63$  (m, 2H), 3.67 (t,  $J = 6.83$  Hz, 2H), 2.69-2.57 (m, 4H), 2.35 (t,  $J = 6.81$  Hz, 2H), 1.69 (s, 3H), 1.48 (s, 1H).  $^{13}\text{C}$  NMR (101 MHz,  $\text{CDCl}_3$ )  $\delta = 127.1, 124.4, 124.4, 123.4, 60.8, 36.0, 33.0, 30.7, 30.7, 18.7$ . DART: Calcd. for  $\text{C}_9\text{H}_{15}\text{O}$   $[\text{M}+\text{H}]^+$  139.1123, found 139.1125.

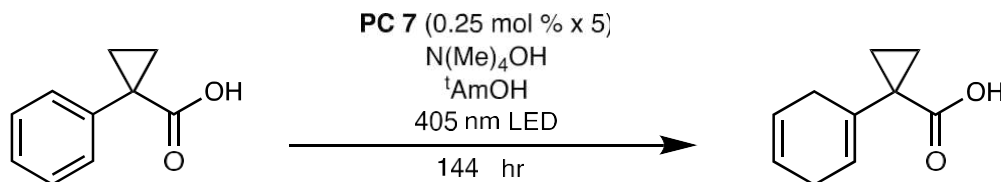
*3-(cyclohexa-1,4-dien-1-yl)propanoic acid (6)*



The general procedure was followed using *hydrocinnamic acid*. After the reaction, volatiles were removed using a rotary evaporator and the residue was flashed through a plug of silica. The eluent was then concentrated and purified by silica gel flash column chromatography (gradient of 5-20% EtOAc in Hexanes) resulting in a white solid. Yield: 47 mg, 63%.

<sup>1</sup>H NMR (400 MHz, CDCl<sub>3</sub>)  $\delta$  = 11.57 (br s, 1H), 5.67-5.58 (m, 2H), 5.42-5.37 (m, 1H), 2.66-2.57 (m, 2H), 2.57-2.49 (m, 2H), 2.47-2.38 (m, 2H), 2.22 (br t,  $J$  = 7.6 Hz, 2H) <sup>13</sup>C NMR (101 MHz, CDCl<sub>3</sub>)  $\delta$  = 179.9, 133.0, 124.2, 124.0, 119.2, 32.2, 31.9, 28.9, 26.7. This data matches reported literature values <sup>3</sup>.

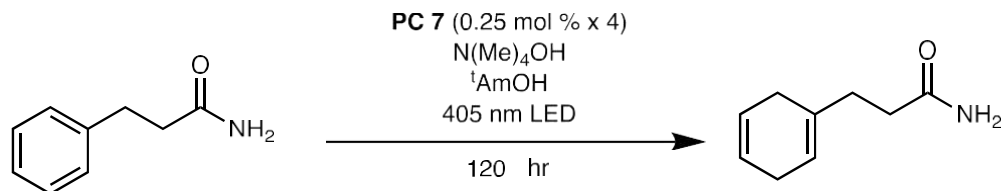
*1-(cyclohexa-1,4-dien-1-yl)cyclopropane-1-carboxylic acid (7)*



The general procedure was followed using *1-phenylcyclopropane-1-carboxylic acid*. After the reaction, volatiles were removed using a rotary evaporator and the residue was flashed through a plug of silica. The eluent was then concentrated and purified by silica gel flash column chromatography (gradient of 5-20% EtOAc in Hexanes) resulting in a white solid. Yield: 32.5 mg, 40%.

<sup>1</sup>H NMR (400 MHz, CDCl<sub>3</sub>)  $\delta$  = 11.81 (br s, 1H), 5.94-5.30 (m, 3H), 2.92-2.62 (m, 4H), 1.43-1.35 (m, 2H), 1.05-0.96 (m, 2H). <sup>13</sup>C NMR (101 MHz, CDCl<sub>3</sub>)  $\delta$  = 181.3, 132.8, 124.4, 123.8, 123.3, 29.7, 29.4, 28.7, 26.7, 16.4. DART: Calcd. for C<sub>10</sub>H<sub>13</sub>O<sub>2</sub> [M+H]<sup>+</sup> 165.0916, found 165.0915.

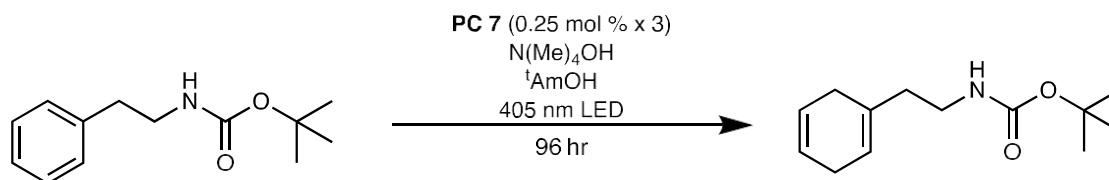
*3-(cyclohexa-1,4-dien-1-yl)propenamide (8)*



The general procedure was followed using *3-phenylpropanamide*. After the reaction, volatiles were removed using a rotary evaporator and the residue was flashed through a plug of silica. The eluent was then concentrated and purified by silica gel flash column chromatography (gradient of 10-30% EtOAc in Hexanes) resulting in a white solid. Yield: 28.5 mg, 38%.

$^1\text{H}$  NMR (400 MHz,  $\text{CDCl}_3$ )  $\delta$  = 5.95-5.31 (m, 5H), 2.78-2.50 (m, 4H), 2.42-2.22 (m, 4H).  $^{13}\text{C}$  NMR (101 MHz,  $\text{CDCl}_3$ )  $\delta$  = 175.3, 133.5, 124.2, 124.0, 119.3, 33.8, 32.8, 28.9, 26.7. DART: Calcd. for  $\text{C}_9\text{H}_{14}\text{NO}$   $[\text{M}+\text{H}]^+$  152.1075, found 152.1074.

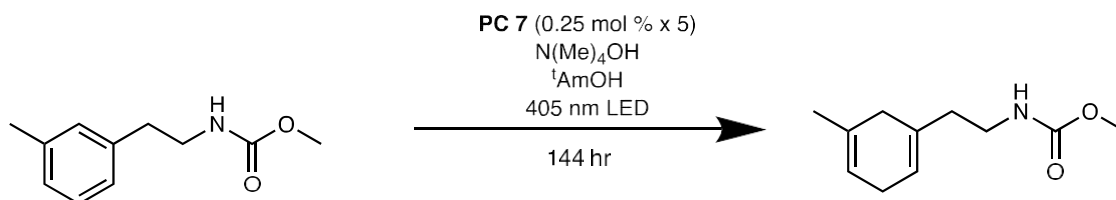
*tert-butyl (2-(cyclohexa-1,4-dien-1-yl)ethyl)carbamate* (9)



*tert-Butyl phenylethylcarbamate* was synthesized according to literature procedure <sup>4</sup>. The general procedure was followed using *tert-butyl phenylethyl carbamate*. After the reaction, volatiles were removed using a rotary evaporator and the residue was flashed through a plug of silica. The eluent was then concentrated and purified by silica gel flash column chromatography (gradient of 0-30% EtOAc in Hexanes) resulting in a colorless oil. Yield: 11.0 mg, 32%.

$^1\text{H}$  NMR (400 MHz,  $\text{CDCl}_3$ )  $\delta$  = 5.65-5.61 (m, 2H), 5.44-5.39 (m, 1H), 4.43 (br s, 1H), 3.15 (br t,  $J$  = 6.68 Hz, 2H), 2.68-2.59 (m, 2H), 2.57-2.48 (m, 2H), 2.08 (br t,  $J$  = 6.67 Hz, 2H), 1.37 (s, 9H).  $^{13}\text{C}$  NMR (101 MHz,  $\text{CDCl}_3$ )  $\delta$  = 155.9, 131.8, 124.1, 124.0, 120.8, 79.1, 38.1, 37.6, 28.6, 28.4, 26.7. DART: Calcd. for  $\text{C}_{13}\text{H}_{22}\text{NO}_2$   $[\text{M}+\text{H}]^+$  224.1651, found 224.1667.

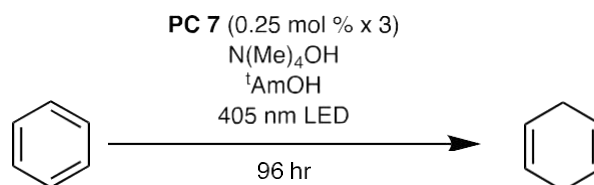
*methyl (2-(5-methylcyclohexa-1,4-dien-1-yl)ethyl)carbamate* (10)



*methyl (3-methylphenethyl)carbamate* was synthesized according to literature procedure <sup>5</sup>. The general procedure was followed using *methyl (3-methylphenethyl)carbamate*. After the reaction, volatiles were removed using a rotary evaporator and the residue was flashed through a plug of silica. The eluent was then concentrated and purified by silica gel flash column chromatography (gradient of 0-10% EtOAc in Hexanes) resulting in a colorless oil. Yield: 46.7 mg, 48%.

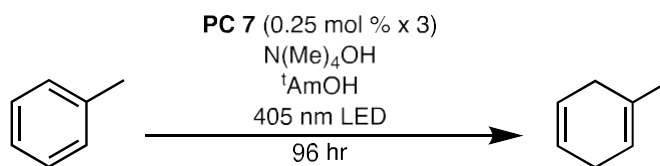
$^1\text{H}$  NMR(400 MHz,  $\text{CDCl}_3$ )  $\delta$  = 5.51-5.44 (m, 1H), 5.43-5.35 (m, 1H), 4.84-4.46 (m, 1H), 3.75-3.56 (m, 3H), 3.35-3.15 (m, 2H), 2.87-2.59 (m, 2H), 2.55-2.40 (m, 2H), 2.24-2.11 (m, 2H), 1.67 (s, 3H).  $^{13}\text{C}$  NMR (101 MHz,  $\text{CDCl}_3$ )  $\delta$  = 156.9, 131.6, 130.9, 120.8, 118.4, 52.0, 38.4, 37.2, 33.5, 27.7, 23.1. DART: Calcd. for  $\text{C}_{11}\text{H}_{18}\text{NO}_2$   $[\text{M}+\text{H}]^+$  196.1338, found 196.1336.

*1,4-cyclohexadiene* (11)



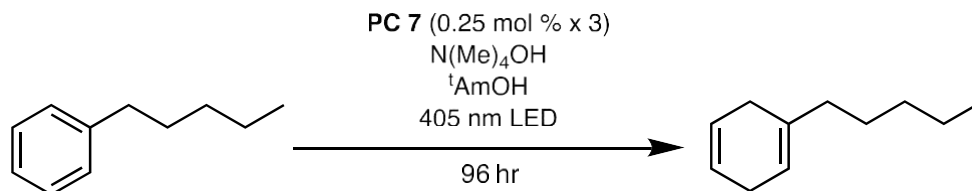
The general procedure was followed using *benzene*. After the reaction, 1,3,5-trimethoxybenzene (0.1 mmol, 16.8 mg, 0.1 eq.) was added as an internal standard, and an 0.1 mL aliquot was taken to measure yield by  $^1\text{H}$  NMR ( $\text{CD}_3\text{CN}$ ). Yield: 80% (NMR). Because of its volatility, 1,4- cyclohexadiene was not isolated.

*1-methylcyclohexa-1,4-diene* (12)



The general procedure was followed using *toluene*. After the reaction, 1,3,5-trimethoxybenzene (0.1 mmol, 16.8 mg, 0.1 eq.) was added as an internal standard, and an 0.1 mL aliquot was taken to measure yield by  $^1\text{H}$  NMR ( $\text{CD}_3\text{CN}$ ). Yield: 71% (NMR). Because of its volatility, 1-methylcyclohexa-1,4-diene was not isolated.

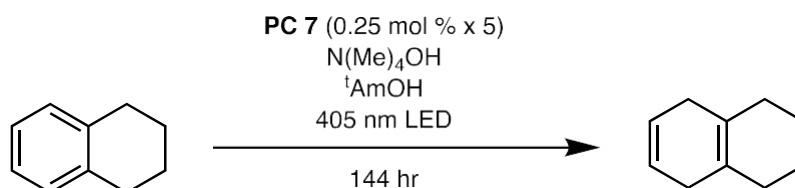
*1-pentylcyclohexa-1,4-diene* (13)



The general procedure was followed using *n-pentyl benzene*. After the reaction, volatiles were removed using a rotary evaporator and the residue was flashed through a plug of silica. The eluent was then concentrated and purified by silica gel flash column chromatography (gradient of hexanes) resulting in a colorless oil. Yield: 35.3 mg, 47%.

$^1\text{H}$  NMR (400 MHz,  $\text{CDCl}_3$ )  $\delta$  = 5.69-5.59 (m, 2H), 5.36-5.30 (m, 1H), 2.68-2.57 (m, 2H), 2.55-2.48 (m, 2H), 1.94-1.78 (m, 2H), 1.39-1.11 (m, 6H), 0.82, (t,  $J$  = 7.0 Hz, 3H)  $^{13}\text{C}$  NMR (101 MHz,  $\text{CDCl}_3$ )  $\delta$  = 135.3, 124.4, 124.3, 117.9, 37.5, 31.6, 28.9, 27.0, 26.8, 22.6, 14.1. This data matches reported literature values <sup>3</sup>.

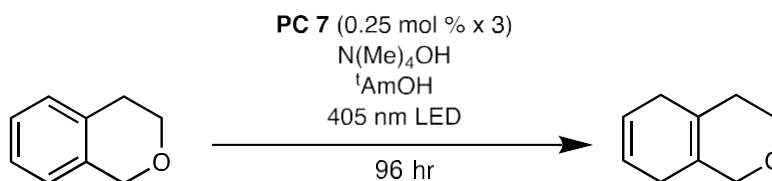
*1,2,3,4,5,8-hexahydronaphthalene* (14)



The general procedure was followed using *1,2,3,4-tetrahydronaphthalene*. After the reaction, volatiles were removed using a rotary evaporator and the residue was flashed through a plug of silica. The eluent was then concentrated and purified by silica gel flash column chromatography (hexanes) resulting in a colorless oil. Yield: 25.7 mg, 38%.

$^1\text{H}$  NMR (400 MHz,  $\text{CDCl}_3$ )  $\delta$  = 5.75-5.69 (m, 2H), 2.53 (app s, 4H), 1.92-1.82 (m, 2H), 1.69-1.60 (m, 2H)  $^{13}\text{C}$  NMR (101 MHz,  $\text{CDCl}_3$ )  $\delta$  = 125.6, 124.6, 31.6, 29.8, 23.2. DART: Calcd. for  $\text{C}_{10}\text{H}_{15}$   $[\text{M}+\text{H}]^+$  135.1174, found 135.1170.

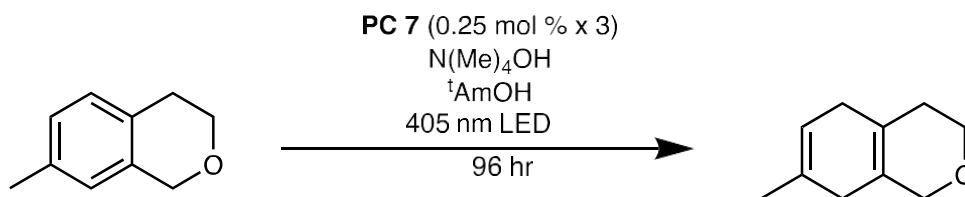
*3,4,5,8-tetrahydro-1H-isochromene* (15)



The general procedure was followed using *isochroman*. After the reaction, volatiles were removed using a rotary evaporator and the residue was flashed through a plug of silica. The eluent was then concentrated and purified by silica gel flash column chromatography (gradient of 0-5% EtOAc in Hexanes) resulting in a colorless oil. Yield: 51.4 mg, 75%.

$^1\text{H}$  NMR (400 MHz,  $\text{CDCl}_3$ )  $\delta$  = 5.78-5.68 (m, 2H), 3.97-3.90 (m, 2H), 3.83 (t,  $J$  = 5.57 Hz, 2H), 2.64-2.52 (m, 2H), 2.51-2.40 (m, 2H), 2.05-1.94 (m, 2H)  $^{13}\text{C}$  NMR (101 MHz,  $\text{CDCl}_3$ )  $\delta$  = 124.9, 124.3, 123.6, 123.6, 68.1, 64.9, 30.7, 29.1, 26.5. DART: Calcd. for  $\text{C}_9\text{H}_{13}\text{O}$   $[\text{M}+\text{H}]^+$  137.0966, found 137.0964.

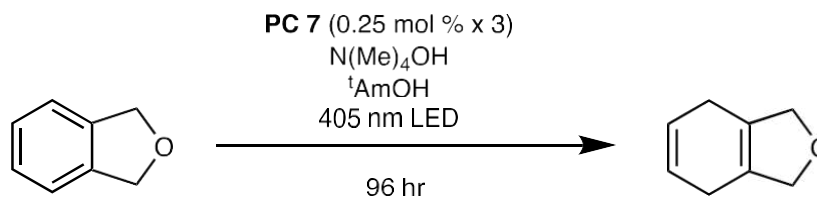
*7-methyl-3,4,5,8-tetrahydro-1H-isochromene* (16)



*7-methylisochromane* was synthesized according to literature procedure <sup>6</sup>. The general procedure was followed using *7-methylisochromane*. After the reaction, volatiles were removed using a rotary evaporator and the residue was flashed through a plug of silica. The eluent was then concentrated and purified by silica gel flash column chromatography (gradient of 0-5% EtOAc in Hexanes) resulting in a colorless oil. Yield: 54.4 mg, 72%.

<sup>1</sup>H NMR (400 MHz, CDCl<sub>3</sub>)  $\delta$  = 5.51-5.38 (m, 1H), 4.04-3.89 (m, 2H), 3.83 (t,  $J$  = 5.56 Hz, 2H), 2.64-2.50 (m, 2H), 2.41-2.27 (m, 2H), 2.07-1.95 (m, 2H), 1.69 (s, 3H). <sup>13</sup>C NMR (101 MHz, CDCl<sub>3</sub>)  $\delta$  = 130.7, 124.8, 123.5, 118.6, 68.0, 4.9, 31.8, 31.3, 28.9, 23.1. DART: Calcd. for C<sub>10</sub>H<sub>15</sub>O [M+H]<sup>+</sup> 151.1123, found 151.1120.

#### *1,3,4,7-tetrahydroisobenzofuran* (17)

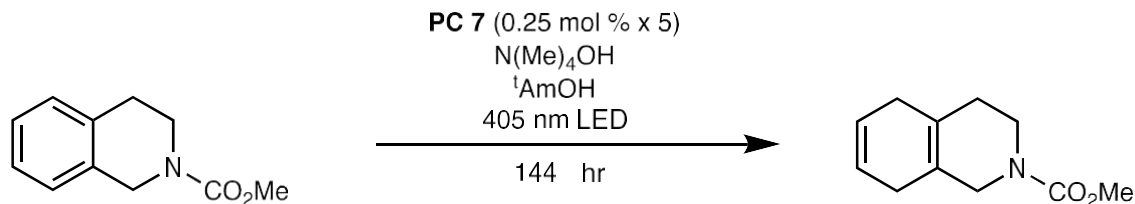


The general procedure was followed using *1,3-dihydroisobenzofuran*. After the reaction, volatiles were removed using a rotary evaporator and the residue was flashed through a plug of silica. The eluent was then concentrated and purified by silica gel flash column chromatography (gradient of 0-5% EtOAc in Hexanes) resulting in a colorless oil. Yield: 50.0 mg, 82%.

<sup>1</sup>H NMR (400 MHz, CDCl<sub>3</sub>)  $\delta$  = 5.76 (s, 2H), 4.53 (s, 4H), 2.56 (s, 4H). <sup>13</sup>C NMR (101 MHz, CDCl<sub>3</sub>)  $\delta$  = 128.5, 123.8, 77.2, 23.5. DART: Calcd. for C<sub>8</sub>H<sub>11</sub>O [M+H]<sup>+</sup> 123.0810, found 123.0813.

10 mmol scale: A 100 mL storage tube was loaded with a glass stir bar and catalyst (20.0 mg, 0.25 mol %). The storage tube was transferred to an N<sub>2</sub> filled glovebox where *1,3-dihydroisobenzofuran* (1.1 mL, 10.0 mmol), *t*-amyl alcohol (9.0 mL, 8.0 eq.), and N(Me)<sub>4</sub>OH (40.0 mL, 10 eq. (25% solution in MeOH)) were added. The storage tube was then sealed, removed from the glovebox, and placed into the light reactor. After 72 hours, the reaction was moved back into the glovebox, where more catalyst (20.0 mg, 0.25 mol %) was added. The storage tube was then removed from the glovebox and placed back into the light reactor. This catalyst addition was repeated at 48-hour intervals. The reaction was stopped after 168 h (3 catalyst additions) and worked up according to the details above. Yield: 1.11 g, 91%.

*methyl 3,4,5,8-tetrahydroisoquinoline-2(1H)-carboxylate* (18)



*methyl 3,4-dihydroisoquinoline-2(1H)-carboxylate* was synthesized according to literature procedure<sup>7</sup>. The general procedure was followed using *methyl 3,4-dihydroisoquinoline-2(1H)-carboxylate*. After the reaction, volatiles were removed using a rotary evaporator and the residue was flashed through a plug of silica. The eluent was then concentrated and purified by silica gel flash column chromatography (gradient of 0-10% EtOAc in Hexanes) resulting in a colorless oil. Yield: 38.4 mg, 40%.

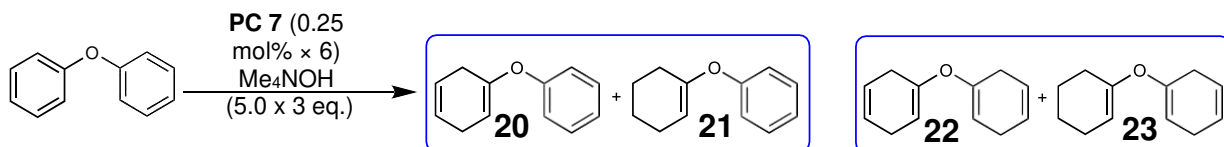
<sup>1</sup>H NMR (400 MHz, CDCl<sub>3</sub>)  $\delta$  = 5.79-5.65 (m, 2H), 3.82-3.65 (m, 5H), 3.63-3.48 (m, 2H), 2.62-2.47 (m, 4H), 2.05-1.94 (m, 2H). <sup>13</sup>C NMR (101 MHz, CDCl<sub>3</sub>)  $\delta$  = 156.0, 126.5, 126.3, 124.1, 123.6, 52.5, 46.3, 40.7, 30.9, 29.1, 28.3. DART: Calcd. for C<sub>11</sub>H<sub>16</sub>NO<sub>2</sub> [M+H]<sup>+</sup> 194.1181, found 194.1181.

(cyclohexa-1,4-dien-1-yloxy)benzene (20)

(cyclohex-1-en-1-yloxy)benzene (21)

1,1'-oxydicyclohexa-1,4-diene (22)

1-(cyclohex-1-en-1-yloxy)cyclohexa-1,4-diene (23)



The general procedure was followed using *diphenyl ether*, except catalyst was added 6 times at 24hr intervals and 5.0 eq. of Me<sub>4</sub>NOH was used and a further 5.0 eq. of Me<sub>4</sub>NOH was added at 48 hr intervals. After the reaction, volatiles were removed using a rotary evaporator and the residue was flashed through a plug of silica. The eluent was then concentrated and purified by silica gel flash column chromatography (gradient of 0-2% EtOAc in Hexanes) resulting in colorless oils. Because of the small differences in the R<sub>f</sub> the products were collected as two fractions, each being a mixture of two compounds in the ratios listed.

**Fraction 1:** a 5.6:1 mixture of (cyclohexa-1,4-dien-1-yloxy)benzene (20) and (cyclohex-1-en-1-yloxy)benzene (21) Yield: 32.1 mg, 37%.



(cyclohexa-1,4-dien-1-yloxy)benzene (20):  $^1\text{H}$  NMR (400 MHz,  $\text{CDCl}_3$ )  $\delta$  = 7.39-7.24 (m, 2H), 7.11-6.97 (m, 3H), 5.77-5.67 (m, 2H), 5.03-4.98 (m, 1.00H), 2.96-2.75 (m, 4H).  $^{13}\text{C}$  NMR (101 MHz,  $\text{CDCl}_3$ )  $\delta$  = 155.8, 150.9, 129.5, 124.3, 123.2, 123.0, 119.2, 103.4, 27.6, 26.6. DART: Calcd. for  $\text{C}_{12}\text{H}_{13}\text{O}$   $[\text{M}+\text{H}]^+$  173.0966, found 173.0965.

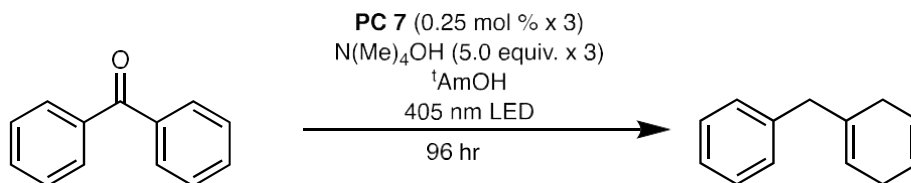
(cyclohex-1-en-1-yloxy)benzene (21):  $^1\text{H}$  NMR (400 MHz,  $\text{CDCl}_3$ )  $\delta$  = 7.39-7.24 (m, 0.36H), 7.11-6.97 (m, 0.54H), 5.11-5.04 (m, 0.18H), 2.24-2.15 (m, 0.36H), 2.13-2.04 (m, 0.36H), 1.82-1.71 (m, 0.36H), 1.67-1.57 (m, 0.36H).  $^{13}\text{C}$  NMR (101 MHz,  $\text{CDCl}_3$ )  $\delta$  = 156.3, 153.1, 129.4, 122.5, 118.7, 107.1, 26.6, 23.6, 22.9, 22.3. DART: Calcd. for  $\text{C}_{12}\text{H}_{13}\text{O}$   $[\text{M}+\text{H}]^+$  173.0966, found 173.0965. DART: Calcd. for  $\text{C}_{12}\text{H}_{15}\text{O}$   $[\text{M}+\text{H}]^+$  175.1123, found 175.1122.

**Fraction 2:** a 8.3:1 mixture of 1,1'-oxydicyclohexa-1,4-diene (22) and 1-(cyclohex-1-en-1-yloxy)cyclohexa-1,4-diene (23) (8.3:1) Yield: 11.8 mg, 14%.

1,1'-oxydicyclohexa-1,4-diene (22):  $^1\text{H}$  NMR (400 MHz,  $\text{CDCl}_3$ )  $\delta$  = 5.77-5.60 (m, 4H), 5.13-5.03 (m, 2H), 2.88-2.70 (m, 8H).  $^{13}\text{C}$  NMR (101 MHz,  $\text{CDCl}_3$ )  $\delta$  = 148.7, 124.2, 123.3, 103.0, 27.2, 26.6. DART: Calcd. for  $\text{C}_{12}\text{H}_{15}\text{O}$   $[\text{M}+\text{H}]^+$  175.1123, found 175.1123.

1-(cyclohex-1-en-1-yloxy)cyclohexa-1,4-diene (23):  $^1\text{H}$  NMR (400 MHz,  $\text{CDCl}_3$ )  $\delta$  = 5.77-5.60 (m, 0.48H), 5.13-5.03 (m, 0.24H), 5.03-4.95 (m, 0.24H), 2.88-2.70 (m, 0.96H), 2.13-2.01 (m, 0.96H), 2.75-2.64 (m, 0.48H), 1.63-1.52 (m, 0.48H).  $^{13}\text{C}$  NMR (101 MHz,  $\text{CDCl}_3$ )  $\delta$  = 151.1, 149.2, 124.3, 123.4, 106.7, 101.7, 29.7, 27.4, 26.3, 23.7, 22.9, 22.3. DART: Calcd. for  $\text{C}_{12}\text{H}_{17}\text{O}$   $[\text{M}+\text{H}]^+$  177.1279, found 177.1282.

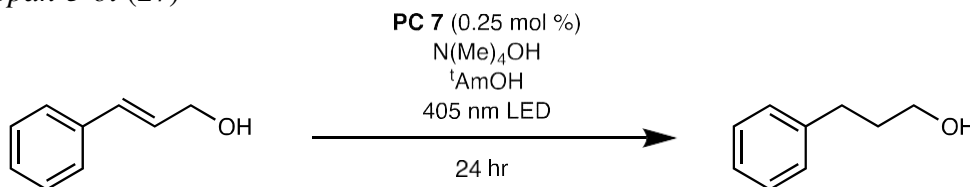
(cyclohexa-1,4-dien-1-ylmethyl)benzene (25)



The general procedure was followed using *benzophenone*, except both PC (0.25 mol%) and  $\text{Me}_4\text{NOH}$  (5.0 eq.) were added at 24 hr intervals. After the reaction, volatiles were removed using a rotary evaporator and the residue was flashed through a plug of silica. The eluent was then concentrated and purified by silica gel flash column chromatography (hexanes) resulting in a colorless oil. Yield: 36.0 mg, 42%.

$^1\text{H}$  NMR (400 MHz,  $\text{CDCl}_3$ )  $\delta$  = 7.34-7.27 (m, 2H), 7.25-7.17(m, 3H), 5.76-5.63 (m, 2H), 5.54-5.47 (m, 1H), 3.34-3.25 (s, 2H), 2.80-2.69 (m, 2H), 2.60-2.49 (m, 2H)  $^{13}\text{C}$  NMR (101 MHz,  $\text{CDCl}_3$ )  $\delta$  = 139.7, 134.5, 129.0, 128.3, 126.0, 124.3, 124.0, 120.3, 44.2, 28.9, 26.9. DART: Calcd. for  $\text{C}_{13}\text{H}_{15}$   $[\text{M}+\text{H}]^+$  171.1174, found 171.1178.

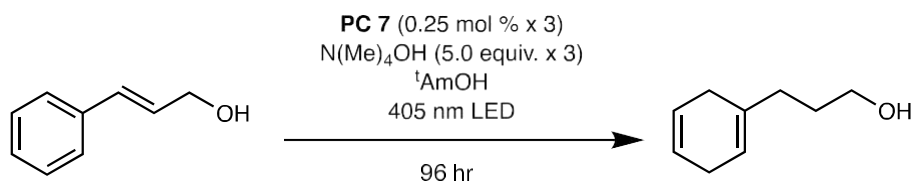
*phenylpropan-3-ol* (27)



The general procedure was followed using *cinnamyl alcohol*, except 5.0 eq. of  $\text{Me}_4\text{NOH}$  was used and the reaction was stopped at 24 hours with no further addition of catalyst. After the reaction, volatiles were removed using a rotary evaporator and the residue was flashed through a plug of silica. The eluent was then concentrated and purified by silica gel flash column chromatography (gradient of 0-10% EtOAc in Hexanes) resulting in a colorless oil. Yield: 36.6 mg, 54%.

$^1\text{H}$  NMR(400 MHz,  $\text{CDCl}_3$ )  $\delta$  = 7.34-7.27 (m, 2H), 7.25-7.17 (m, 3H), 3.68 (t,  $J$  = 6.5 Hz, 2H), 2.72 (br t,  $J$  = 7.5 Hz, 2H), 1.96-1.86 (m, 2H), 1.74 (br s, 1H)  $^{13}\text{C}$  NMR (101 MHz,  $\text{CDCl}_3$ )  $\delta$  = 141.8, 128.4, 128.4, 125.9, 62.21, 34.2, 32.1. This data matches reported literature values <sup>8</sup>.

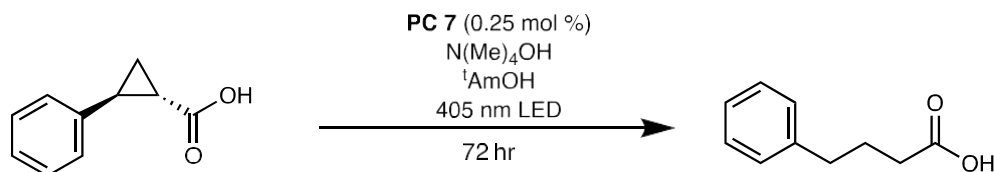
*3-(cyclohexa-1,4-dien-1-yl)propan-1-ol* (28)



The general procedure was followed using *cinnamyl alcohol*, except 5.0 eq. of  $\text{Me}_4\text{NOH}$  was used and a further 5.0 eq. of  $\text{Me}_4\text{NOH}$  was added with each catalyst addition. After the reaction, volatiles were removed using a rotary evaporator and the residue was flashed through a plug of silica. The eluent was then concentrated and purified by silica gel flash column chromatography (gradient of 0-10% EtOAc in Hexanes) resulting in a colorless oil. Yield: 22.7 mg, 33%.

$^1\text{H}$  NMR(400 MHz,  $\text{CDCl}_3$ )  $\delta$  = 5.76-5.60 (m, 2H), 5.49-5.39 (m, 1H), 3.63 (t,  $J$  = 6.5 Hz, 2H) 2.72-2.63 (m, 2H), 2.62-2.55 (m, 2H), 2.03 (br t,  $J$  = 7.6 Hz, 2H), 1.75 (br s, 1H), 1.72-1.64 (m, 2H)  $^{13}\text{C}$  NMR (101 MHz,  $\text{CDCl}_3$ )  $\delta$  = 134.5, 124.3, 124.2, 118.7, 62.7, 33.7, 30.2, 28.9, 26.7. DART: Calcd. for  $\text{C}_9\text{H}_{15}\text{O}$   $[\text{M}+\text{H}]^+$  139.1123, found 139.1122.

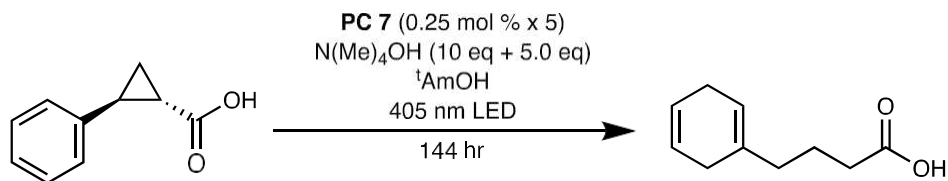
4-phenylbutanoic acid (30)



The general procedure was followed using *2-phenylcyclopropane-1-carboxylic acid*, except catalyst was only added one time at 48 hr and the reaction was stopped after 72 hr. After the reaction, volatiles were removed using a rotary evaporator and the residue was flashed through a plug of silica. The eluent was then concentrated and purified by silica gel flash column chromatography (gradient of 0-10% EtOAc in Hexanes) resulting in a white solid. Yield: 59 mg, 73%.

$^1\text{H}$  NMR (400 MHz,  $\text{CDCl}_3$ )  $\delta$  = 11.51 (br, s), 7.33-7.27 (m, 2H), 7.24-7.16 (m, 3H), 2.69 (t,  $J$  = 7.43 Hz, 2H), 2.39 (t,  $J$  = 7.42 Hz, 2H), 1.98 (dt,  $J$  = 7.61, 7.00 Hz, 2H)  $^{13}\text{C}$  NMR (101 MHz,  $\text{CDCl}_3$ )  $\delta$  = 180.0, 141.2, 128.5, 128.4, 126.1, 35.0, 33.3, 26.2. This data matches reported literature values <sup>9</sup>.

4-(cyclohexa-1,4-dien-1-yl)butanoic acid (31)

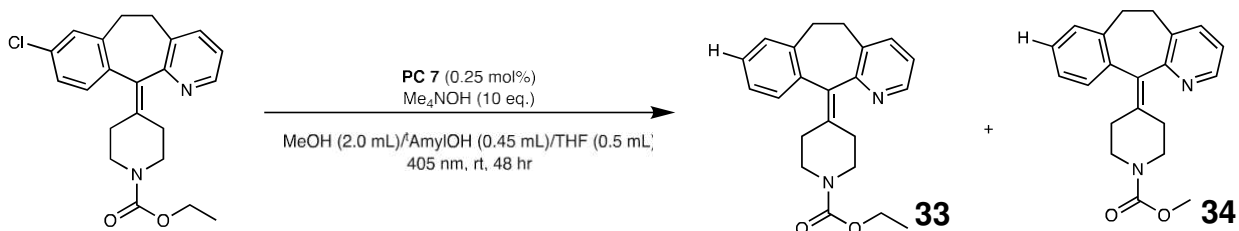


The general procedure was followed using *2-phenylcyclopropane-1-carboxylic acid*, except catalyst was added once more after 96 hours along with another 1 mL of TMAOH solution and the reaction was stopped after 144 hours. After the reaction, volatiles were removed using a rotary evaporator and the residue was flashed through a plug of silica. The eluent was then concentrated and purified by silica gel flash column chromatography (gradient of 0-10% EtOAc in Hexanes) resulting in a white solid. Yield: 33.1 mg, 40%.

$^1\text{H}$  NMR (400 MHz,  $\text{CDCl}_3$ )  $\delta$  = 11.56 (br s, 1H), 5.75-5.64 (m, 2H), 5.46-5.39 (m, 1H), 2.73-2.63 (m, 2H), 2.62-2.54 (m, 2H), 2.35 (t,  $J$  = 7.45 Hz, 2H), 2.02 (br t,  $J$  = 7.52 Hz, 2H), 1.77 (dt,  $J$  = 7.65, 7.39 Hz, 2H)  $^{13}\text{C}$  NMR (101 MHz,  $\text{CDCl}_3$ )  $\delta$  = 180.4, 133.7, 124.2, 124.2, 119.4, 36.6, 33.5, 28.7, 26.7, 22.2. DART: Calcd. for  $\text{C}_{10}\text{H}_{15}\text{O}_2$   $[\text{M}+\text{H}]^+$  167.1072, found 167.1071.

ethyl 4-(5,6-dihydro-11H-benzo[5,6]cyclohepta[1,2-b]pyridin-11-ylidene)piperidine-1-carboxylate (33)

methyl 4-(5,6-dihydro-11H-benzo[5,6]cyclohepta[1,2-b]pyridin-11-ylidene)piperidine-1-carboxylate (34)



The general procedure was followed using *loratadine* except the reaction was stopped at 48 hr and no further catalyst was added. After the reaction, volatiles were removed using a rotary evaporator and the residue was flashed through a plug of silica. The eluent was then concentrated and purified by silica gel flash column chromatography (gradient of 10-30% EtOAc in Hexanes) resulting in white solids.

ethyl 4-(5,6-dihydro-11H-benzo[5,6]cyclohepta[1,2-b]pyridin-11-ylidene)piperidine-1-carboxylate (33) Yield: 112.7 mg, 65%.

<sup>1</sup>H NMR (400 MHz, CDCl<sub>3</sub>) δ = 8.42-8.34 (m, 1H), 7.46-7.37 (m, 1H), 7.23-7.10 (m, 4H), 7.10-7.01 (m, 1H), 4.12 (q, J = 7.10 Hz, 2H), 3.91-3.72 (m, 2H), 3.48-3.28 (m, 2H), 3.19-3.07 (m, 2H), 2.90-2.74 (m, 2H), 2.55-2.25 (m, 4H), 1.24 (t, J = 7.10 Hz, 3H). <sup>13</sup>C NMR (101 MHz, CDCl<sub>3</sub>) δ = 157.3, 155.5, 146.4, 139.3, 137.7, 137.6, 136.8, 135.2, 133.7, 129.2, 129.0, 127.4, 126.0, 122.1, 61.3, 44.9, 44.8, 31.8, 31.8, 30.7, 30.5, 14.7. DART: Calcd. for C<sub>22</sub>H<sub>25</sub>N<sub>2</sub>O<sub>2</sub> [M+H]<sup>+</sup> 349.1916, found 349.1917.

methyl 4-(5,6-dihydro-11H-benzo[5,6]cyclohepta[1,2-b]pyridin-11-ylidene)piperidine-1-carboxylate (34) Yield: 44.0 mg, 26%.

<sup>1</sup>H NMR (400 MHz, CDCl<sub>3</sub>) δ = 8.46-8.31 (m, 1H), 7.50-7.36 (m, 1H), 7.22-7.04 (m, 5H), 3.92-3.72 (m, 2H), 3.68 (s, 3H), 3.48-3.29 (m, 2H), 3.16-3.09 (m, 2H), 2.90-2.75 (m, 2H), 2.55-2.24 (m, 4H). <sup>13</sup>C NMR (101 MHz, CDCl<sub>3</sub>) δ = 157.1, 155.9, 146.2, 139.2, 137.9, 137.6, 136.9, 135.0, 133.8, 129.2, 129.0, 127.5, 126.1, 122.2, 52.6, 44.9, 44.9, 31.8, 31.7, 30.7, 30.5. DART: Calcd. for C<sub>21</sub>H<sub>23</sub>N<sub>2</sub>O<sub>2</sub> [M+H]<sup>+</sup> 335.1760, found 335.1757.

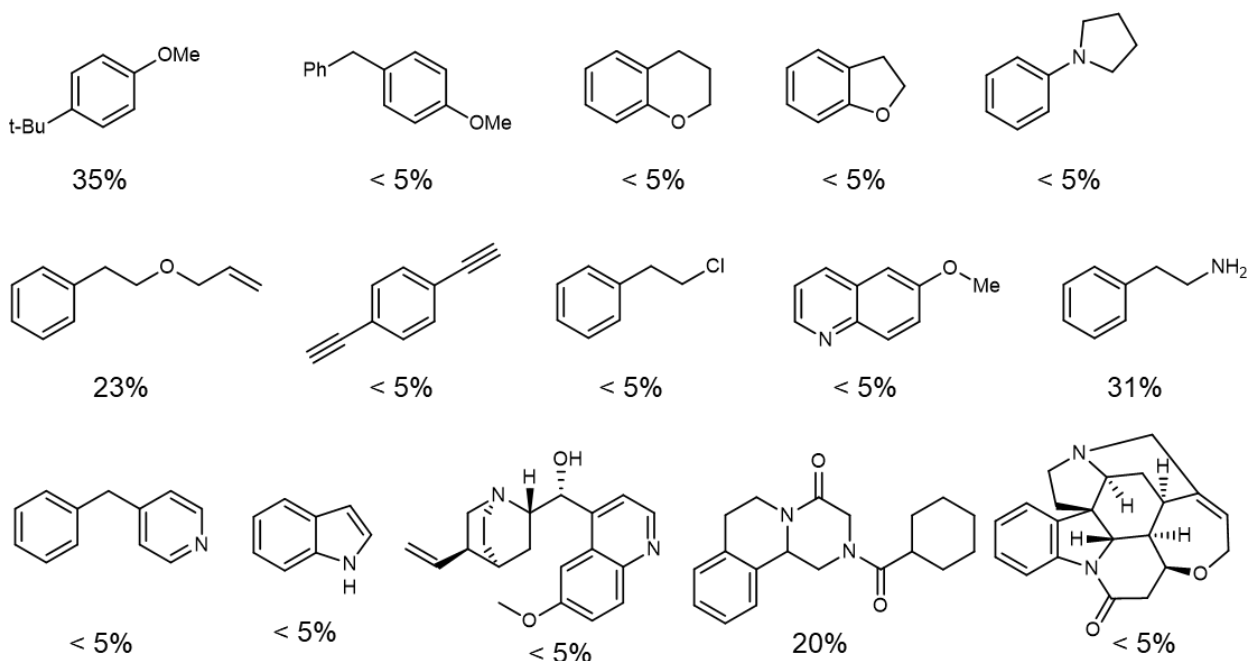


Fig. S5.1. List of substrates that were screened for Birch reduction but failed to reach high conversions.

## 2. Photophysical Characterization of Photocatalysts

Note about solvent choice: For most photophysical characterizations, THF was used as the solvent. Under optimized reaction conditions we found that MeOH/Me<sub>4</sub>NOH provided higher conversion, however, the ground state catalyst was not soluble in this system. THF did work as a solvent for the reaction (see Table S4), however resulted in lower yields. Because the reaction works in THF and each of the catalytic species was soluble in THF, we decided that using THF as the spectroscopy solvent was more representative than other solvent options. Further, Bu<sub>4</sub>NOH was selected over Me<sub>4</sub>NOH due to increased solubility in THF. Bu<sub>4</sub>NOH was used as received (1 M anhydrous solution in MeOH).

Mechanistic experiments were performed using THF with volume measurement using Hamilton glass syringes (25, 50, 250, 1000, or 5000 μL) or volumetric glassware (10 or 25 mL). All experiments involving PC 7 in the presence of Bu<sub>4</sub>NOH were performed using aluminum foil

to protect solutions from light exposure prior to measurements. Foil was removed from cuvettes under a black cloth while they were transferred to either the UV-vis or transient absorption spectrometer.

Ultraviolet-visible spectroscopy was performed on a Cary 5000 spectrophotometer scanning from 200-800 nm at a scan rate of 600 nm/min. Steady-state emission spectroscopy was performed on a SLM 8000C spectrofluorometer or an Edinburgh Instruments FS5 spectrometer. Emission data for compound characterization was collected by exciting the compounds near lambda max of 340 nm scanning 400-750 nm for hexanes and 400-800 nm for DMSO all with an integration time of 0.50 seconds. Fluorescence quantum yield in chloroform at 340 nm was determined by the direct method using an Edinburgh Instruments FS5 fluorescence spectrometer fitted with an SC30 integration sphere. The scattering peak was measured from 320 nm-360 nm using a 10% OD Filter. The excitation spectrum was measured from 360 nm-800 nm without a filter. The excitation bandwidth was 8.0 nm and the emission bandwidth was 0.6 nm. The step size was 0.7 nm and the dwell time was 0.5 sec. For the titration experiment, the FS5 was used to measure emission with  $\lambda_{\text{excitation}} = 416$  nm, 1 nm step size, a dwell time of 0.25 s, an excitation bandwidth of 1.2 nm and an emission bandwidth of 0.7 nm.  $\lambda_{\text{excitation}} = 416$  nm was chosen due to the isosbestic point in the absorption spectra of PC 7 and [PC-OH]<sup>-</sup> at that wavelength in order to minimize inner-filter effects.

Nanosecond transient absorption (TA) spectra were acquired with an LP980KS spectrometer (Edinburgh Instruments) with a Minilite Nd:YAG Q-switched laser (Continuum Lasers) configured to deliver a 532 nm excitation pulse. Spectral data was acquired from 300-800 nm at the indicated time delay through use of an iStar ICCD camera (Andor) as the detector. Kinetic data was recorded on the same instrument utilizing a photomultiplier tube (included in the

LP980) interfaced with an MD03022 mixed domain oscilloscope (Tektronix) as the detector. Time zero was set on the instrument using the emission of  $[\text{Ru}(\text{bpy})_3]\text{Cl}_2$  to locate the pump pulse with 1 ns resolution. For kinetic experiments, the laser power was  $4\text{--}6\text{ mW}/\text{cm}^2$  at a 1 Hz repetition rate. For spectral traces, a higher power of  $9\text{--}12\text{ mW}/\text{cm}^2$  was used. For TA experiments, samples were prepared in a  $\text{N}_2$ -filled glovebox by dissolving solid PC 7 in anhydrous THF. Solutions were transferred to a long necked, sidearm equipped screw cap cuvette wrapped in aluminum foil and the appropriate amount of  $\text{Bu}_4\text{NOH}$  (1 M solution in MeOH) was added to achieve the concentration mentioned in each figure caption. After tightly closing the cap, the cuvette was removed from the glovebox and irradiated with a high intensity 405 nm LED for 1 minute using a modified version of the same photoreactor used for Birch reductions. During irradiation, the cuvette was fan-cooled from below. After irradiation, samples were analyzed on the TA spectrometer, with UV-vis measured before and after analysis.

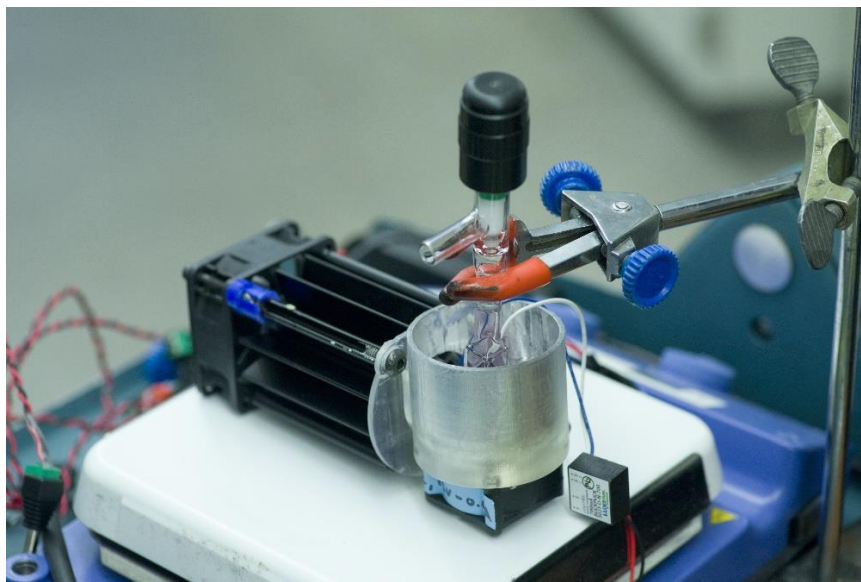


*Fig. S5.2. Modified 405 nm light reactor used to irradiate cuvettes for spectroscopic studies. A fancools the cuvette from below. The setup was shielded for safety in a box when in use (not shown).*

Table S5: Photophysical and electrochemical properties relevant to photocatalysis.

PC	$\lambda_{\text{Max}}$ Absorption (nm)	$\epsilon_{\text{Max}}$	$\lambda_{\text{Local Max}}$ Absorption (nm)	$\epsilon_{\text{Max}}$	$\lambda_{\text{Local Max}}$ Absorption (nm)	$\epsilon_{\text{Max}}$	$\lambda_{\text{Max}}$ Emission (nm) <sup>a</sup>	$\Phi_{\text{f}}$ <sup>b</sup>	$E_{1/2}$ (PC/ PC <sup>•+</sup> ) <sup>c</sup>
<b>1</b>	340	51,100	390	15,100	481	5,700	523	0.266	-1.25 V
<b>2</b>	347	53,600	406	22,200	485	5,500	----- <sup>d</sup>	----- <sup>d</sup>	----- <sup>e</sup>
<b>3</b>	352	53,400	419	26,000	489	7,500	539	0.654	-1.15
<b>4</b>	351	48,700	415	22,600	492	6,700	541	0.421	-1.16
<b>5</b>	352	43,800	417	20,500	501	7,000	566	0.372	-1.20
<b>6</b>	355	59,600	423	34,000	505	9,500	579	0.389	-1.20
<b>7</b>	355	40,400	425	23,300	507	7,700	595	0.391	-1.23
<b>8</b>	349	36,200	450	25,700	535	7,800	656	0.047	-1.25

<sup>a</sup>Emission data obtained from excitation with 350 nm light in chloroform. <sup>b</sup>Quantum yields obtained using the direct method in chloroform excited at 340nm. <sup>c</sup>Values reported are vs. SCE. Cyclic voltammetry of the photoredox catalysts were performed in a 3-compartment electrochemical cell with Ag/AgNO<sub>3</sub> (0.01 M) in MeCN as the reference electrode, TBAPF<sub>6</sub> in DMAc (0.100 M) as the electrolyte solution, and platinum for the working and counter electrodes. <sup>d</sup>PC 2 was non-emissive. <sup>e</sup>PC 2 did not have a reversible reduction.  $\epsilon_{\text{Max}}$  units: M<sup>-1</sup> cm<sup>-1</sup>

### 3. Supplemental Photophysical Characterization



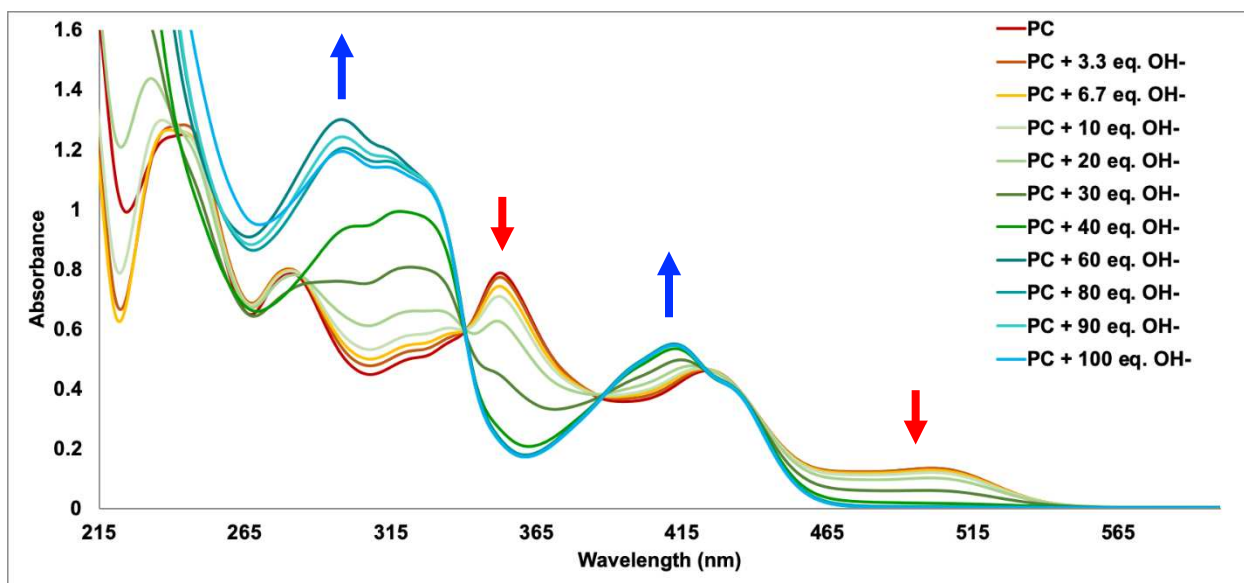


Fig. S5.3. UV-Vis spectroscopy of PC 7 (0.02 mM in THF) with increasing molar ratios of Bu<sub>4</sub>NOH relative to PC 7. Each solution was prepared by mixing two stock solutions, one of PC 7 alone and the other equimolar with 100 eq. Bu<sub>4</sub>NOH, in the appropriate ratios to make 11 analyte solutions. Each solution was equilibrated at 25 °C for 5 minutes in a temperature-controlled water bath before the measurement was taken.

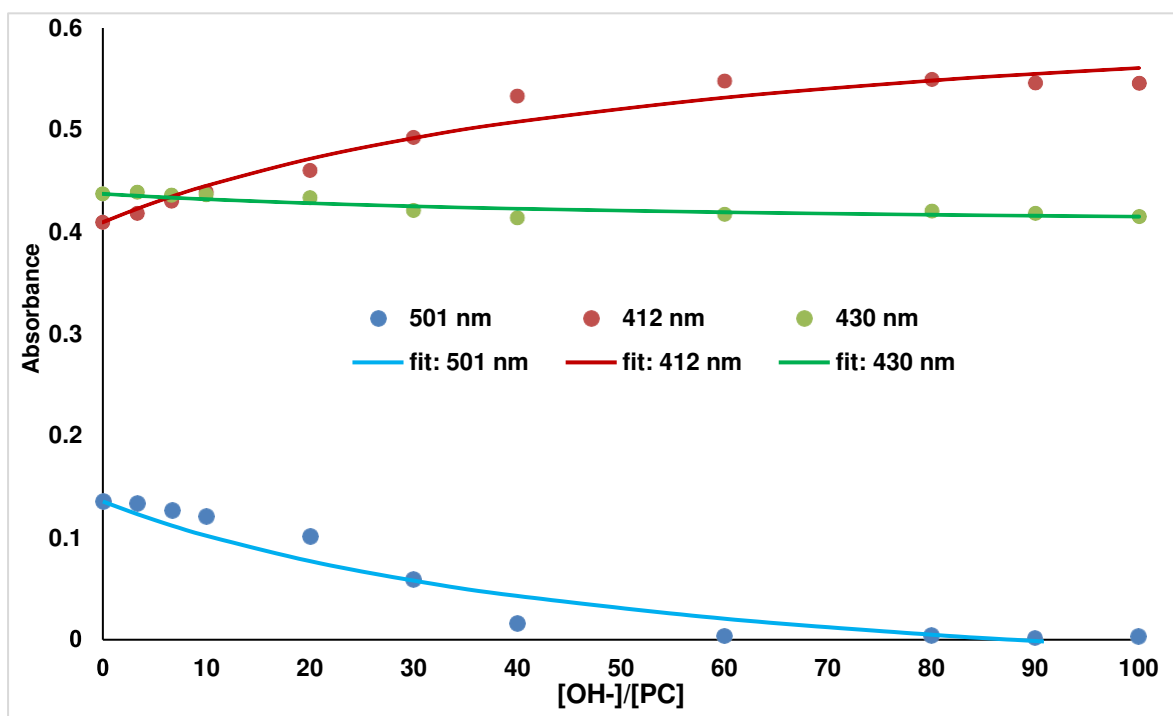


Fig. S5.4. Single wavelength absorption data and fit to the 1:1 binding model used to extract the equilibrium constant for hydroxide association. Fitting was done using BindFit<sup>10</sup> software which solves the system of equations derived in the literature previously for a 1:1 system<sup>11</sup>.

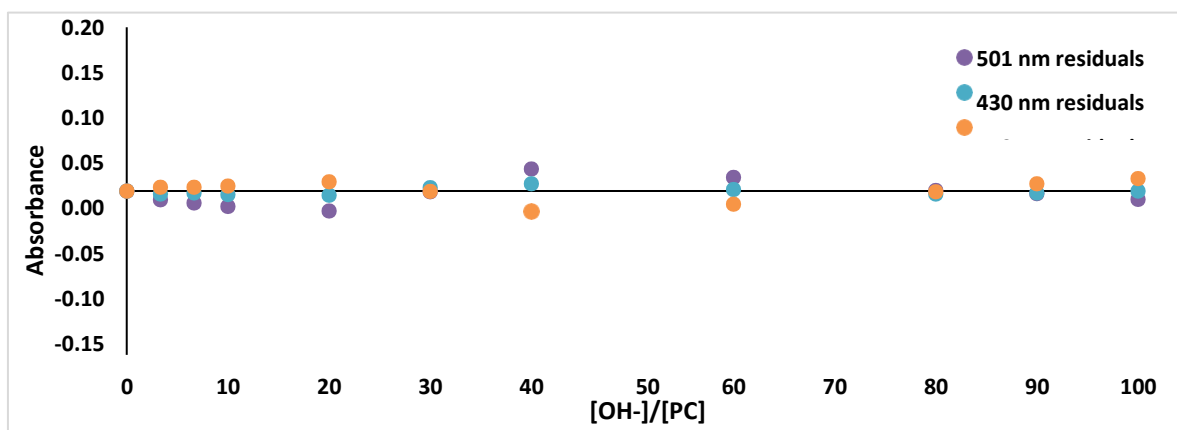


Fig. S5.5. Fitting residuals for the above data.

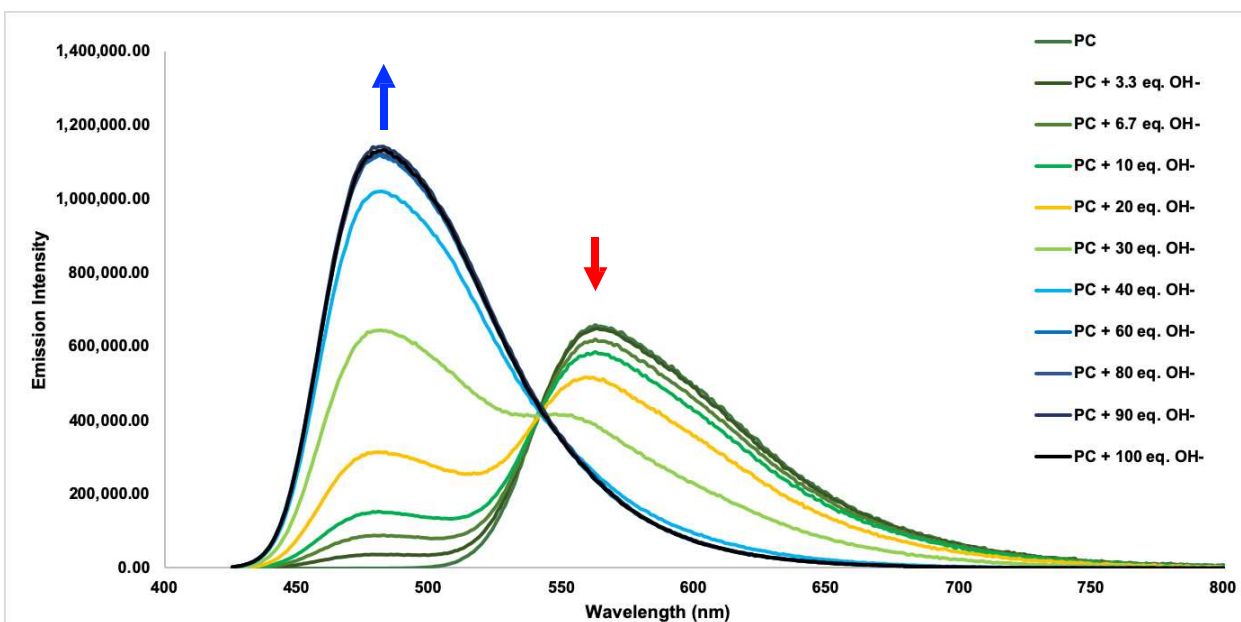


Fig. S5.6. Fluorescence spectroscopy of PC 7 (0.02 mM in THF) with increasing molar ratios of  $Bu_4NOH$  relative to PC 7. Each solution was prepared by mixing two stock solutions, one of PC 7 alone and the other equimolar with 100 eq.  $Bu_4NOH$ , in the appropriate ratios to make 11 analyte solutions. Each solution was equilibrated at 25° C for 5 minutes in a temperature-controlled water bath before the measurement was taken.

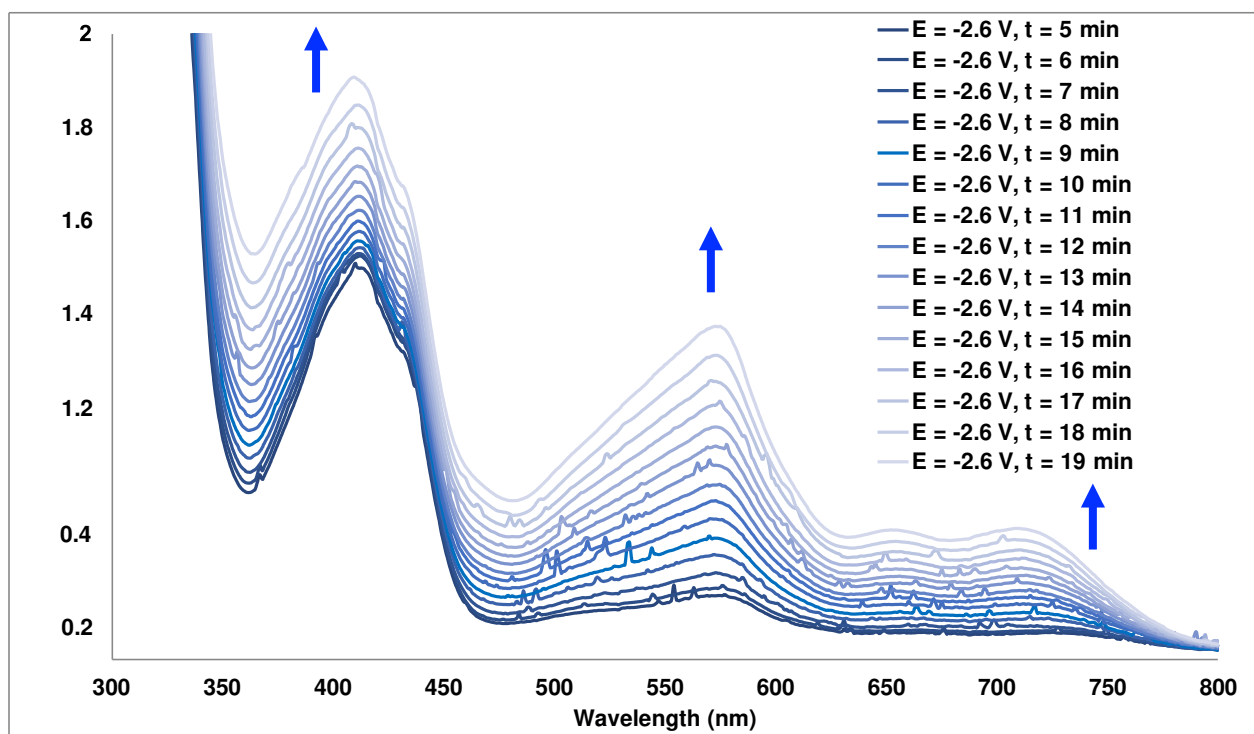


Fig. S5.7. Spectroelectrochemistry. UV-vis traces of PC 7 (0.02 mM in THF) with  $Bu_4NOH$  (100 eq., 2 mM) and  $TBAPF_6$  electrolyte (0.1 M) under  $E_{app} = -2.6$  V vs.  $Ag/AgNO_3$  in a 3 electrode electrochemical cell using a fiber optic probe setup. Cell configuration and setup is described in the next section: Electrochemistry.

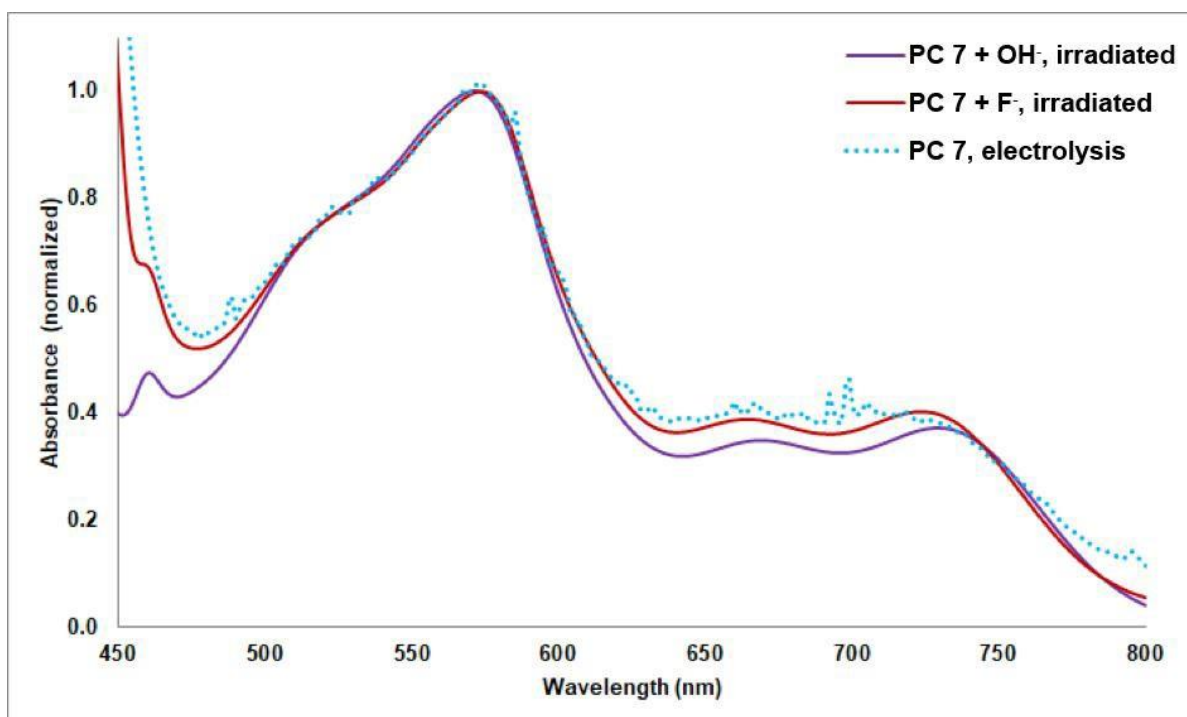


Fig. S5.8. Normalized UV-Vis traces comparing the photolysis and electrolysis of [PC-OH]- (PC 7) 0.2 mM + 100 eq. Bu<sub>4</sub>NOH) and [PC-F]- (PC 7 0.2 mM + 100 eq. Bu<sub>4</sub>NF). The [PC-OH]- mixture was irradiated for 1 min with 405 nm light in the setup described above, while the [PC-F]- mixture was irradiated for 10 s. The electrolysis trace was taken from the above experiment (Fig. S5.7, t = 7 min).

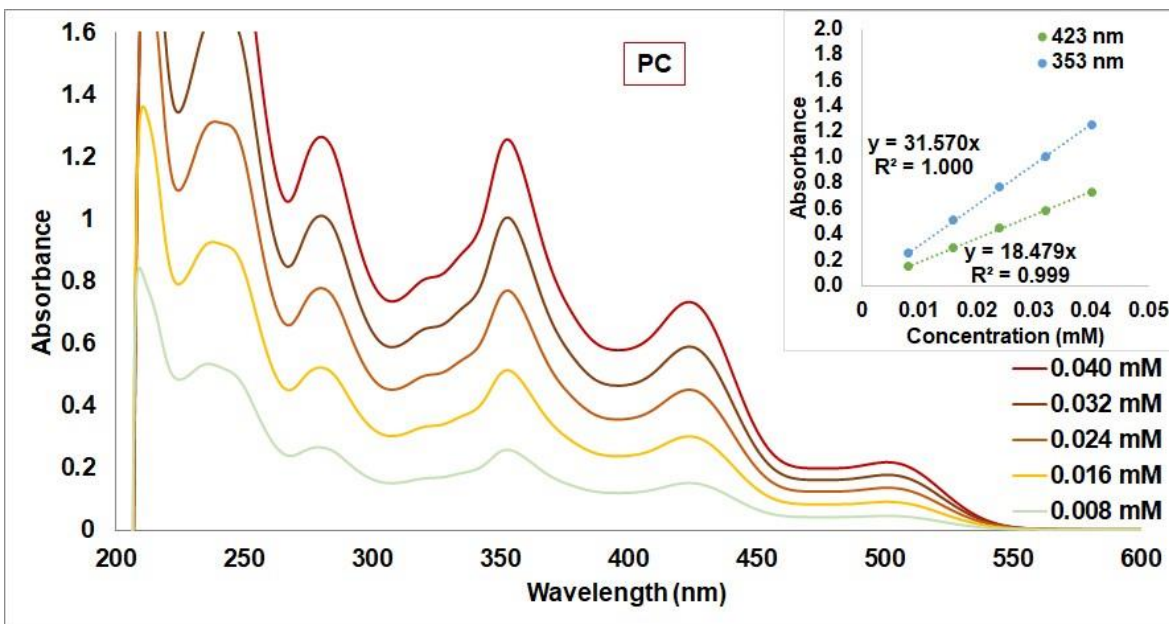


Fig. S5.9. UV-Vis spectroscopy of PC 7 at 0.0400 mM, 0.0320 mM, 0.0240 mM, 0.0160 mM, and 0.0080 mM. Extinction coefficients were derived from absorbance at 423 nm and 353 nm (inset).

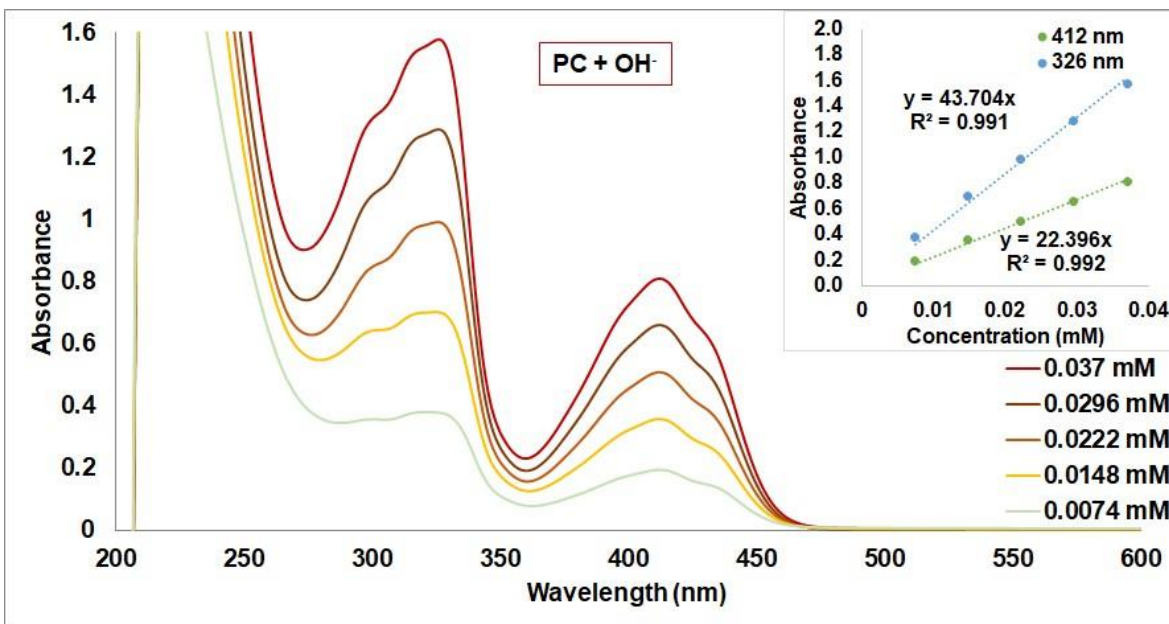


Fig. S5.10. UV-Vis spectroscopy of PC 7 with 200 eq. of  $Bu_4NOH$  H at 0.0370 mM, 0.0296 mM, 0.0222 mM, 0.0148 mM, and 0.0074 mM. Extinction coefficients were derived from absorbance at 412 nm and 326 nm (inset).

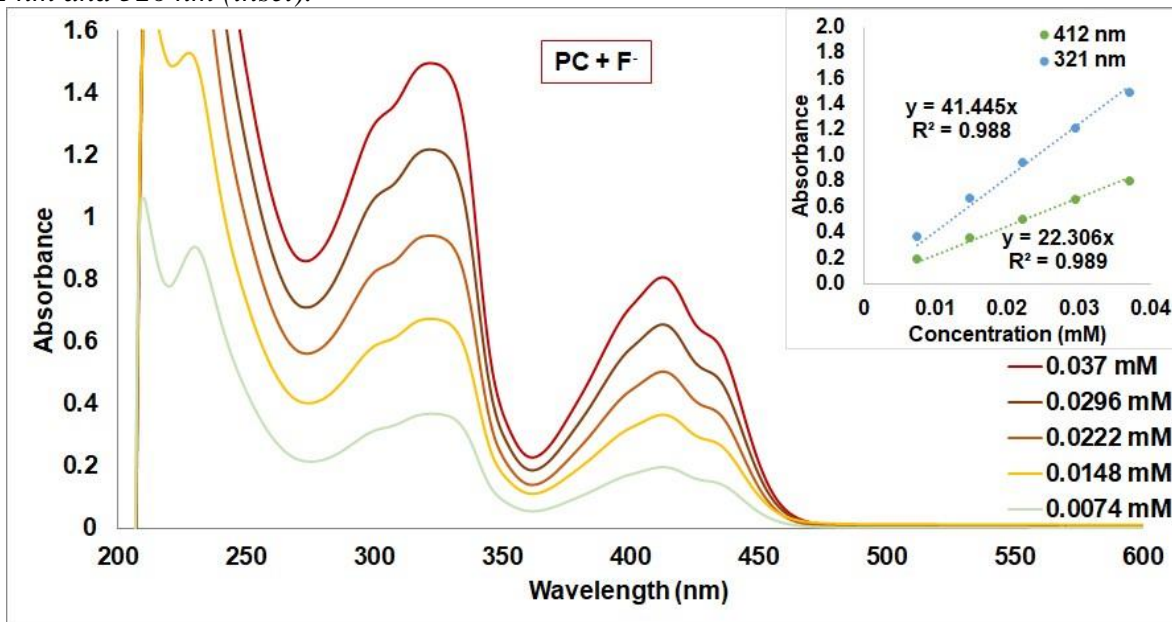


Fig. S5.11. UV-Vis spectroscopy of PC 7 with 200 eq. of  $Bu_4NF$  at 0.0370 mM, 0.0296 mM, 0.0222 mM, 0.0148 mM, and 0.0074 mM. Extinction coefficients were derived from absorbances at 412 nm and 321 nm (inset).

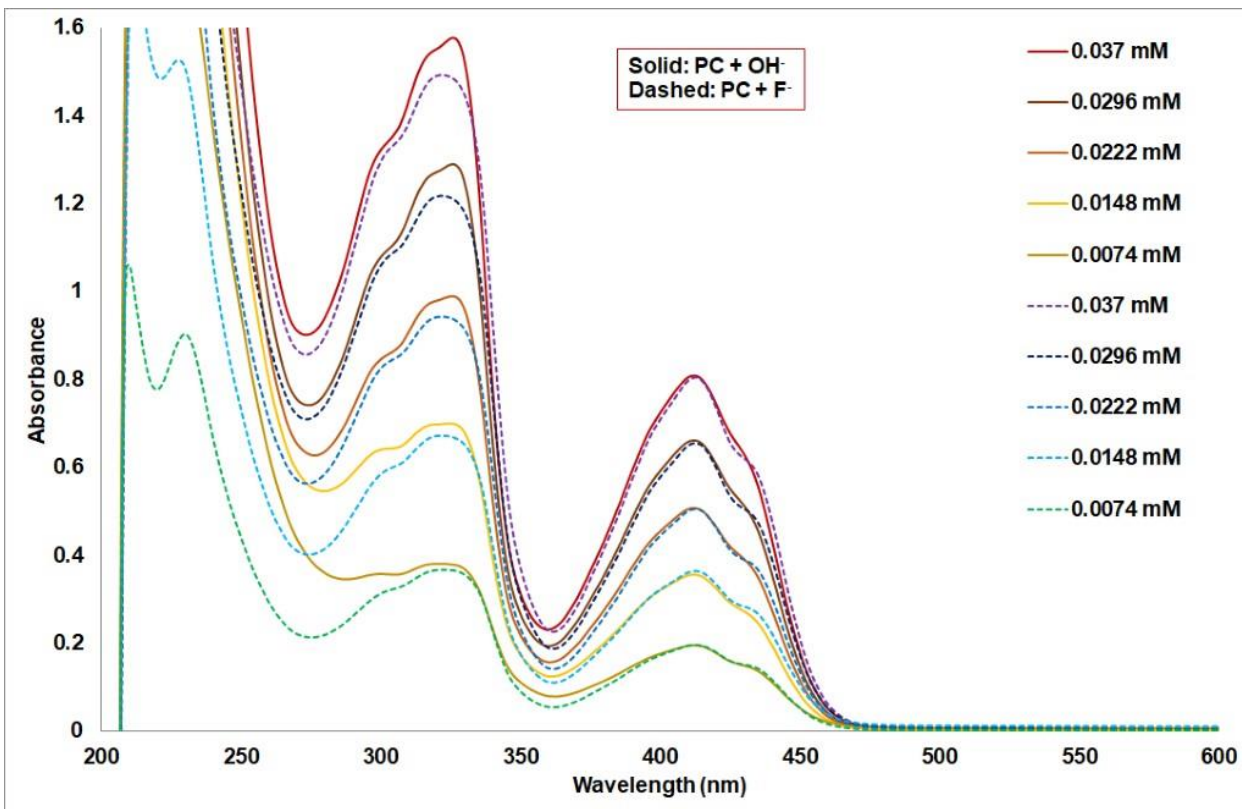


Fig. S5.12: Comparison of UV-Vis spectroscopy of PC 7 with 200 eq. of  $Bu_4NF$  (dashed lines) or  $Bu_4NOH$  (solid lines) at 0.0370 mM, 0.0296 mM, 0.0222 mM, 0.0148 mM, and 0.0074 mM.

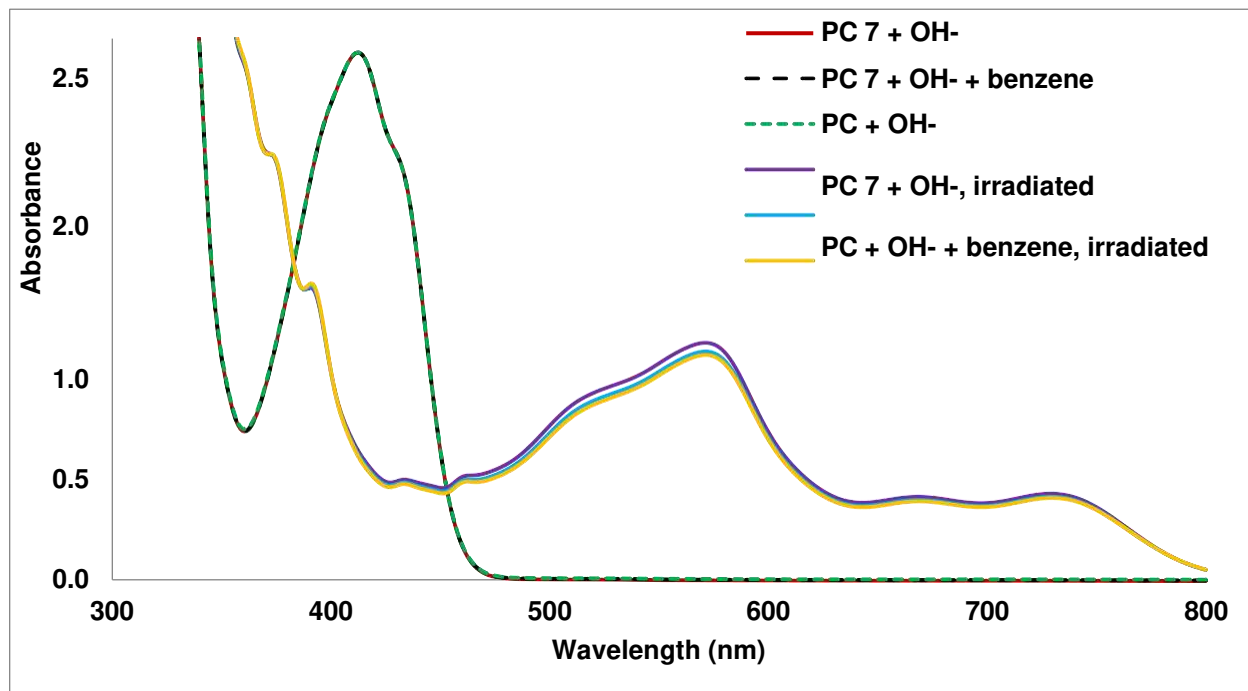


Fig. S5.13. UV-vis of PC 7 (0.1 mM in THF) + 20 eq.  $Bu_4NOH$  with or without 200 eq. benzene, before and after irradiation for 1 min with 405 nm light in the setup described above. All 3 samples overlap exactly prior to irradiation. The two samples without benzene were identical and samples were measured in the sequence: PC 7 + OH-, PC 7 + OH- + benzene, PC 7 + OH-. Thus, the small decrease in signal observed in the sample containing benzene cannot be attributed to an effect involving benzene, since the control measured afterwards shows a further decrease.

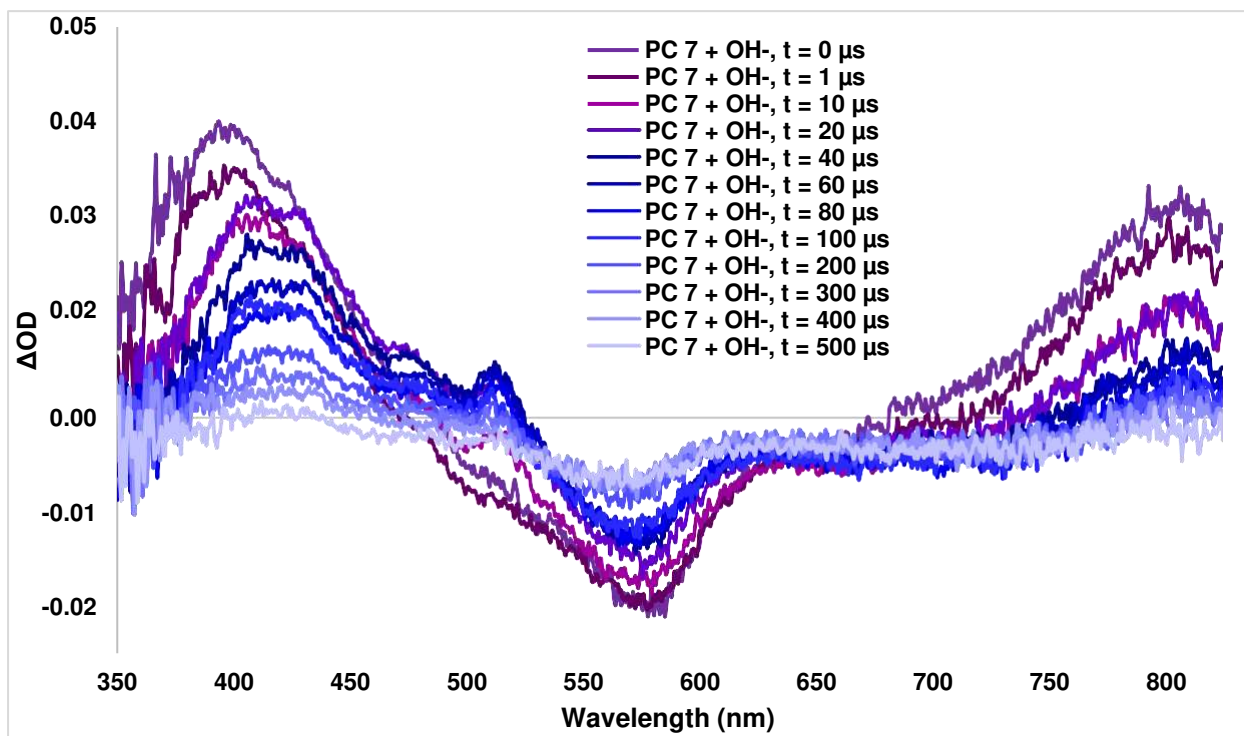


Fig. S5.14. TA spectral traces at  $\lambda_{\text{rump}} = 532 \text{ nm}$  with various time delays of PC 7 (0.1 mM in THF) + 100 eq. Bu<sup>4</sup>NOH, irradiated prior to TA measurement for 1 min with 405 nm light. See above for details on the irradiation setup.

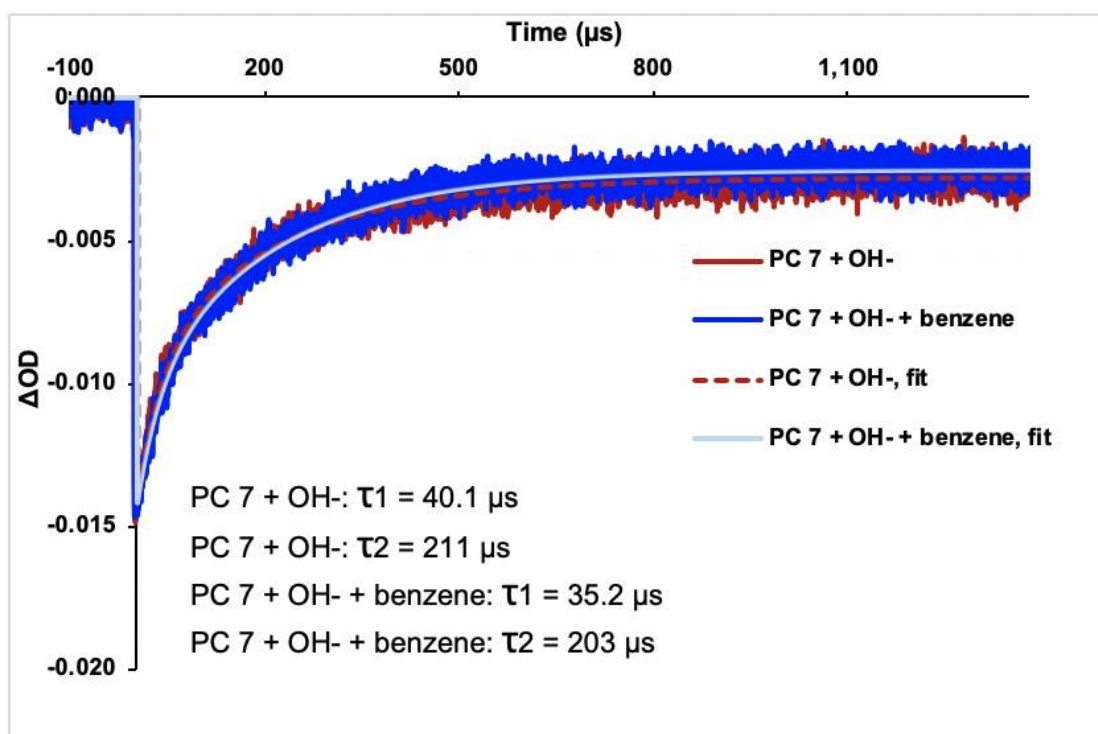


Fig. S5.15. Kinetic traces (125 averages) with emission background subtraction recorded at  $\lambda_{\text{pump}} = 532 \text{ nm}$  and  $\lambda_{\text{probe}} = 580 \text{ nm}$  for a mixture of PC 7 (0.1 mM in THF) + 20 eq. Bu<sub>4</sub>NOH with or without 100 eq. benzene. Biexponential fits are overlaid with each trace. Samples were prepared from a single mixture that was irradiated for 1 min with 405 nm light, brought into the glovebox, and divided equally into 2 screw cap cuvettes. At this point, benzene was added to 1 of the cuvettes. See above for details on the irradiation setup.

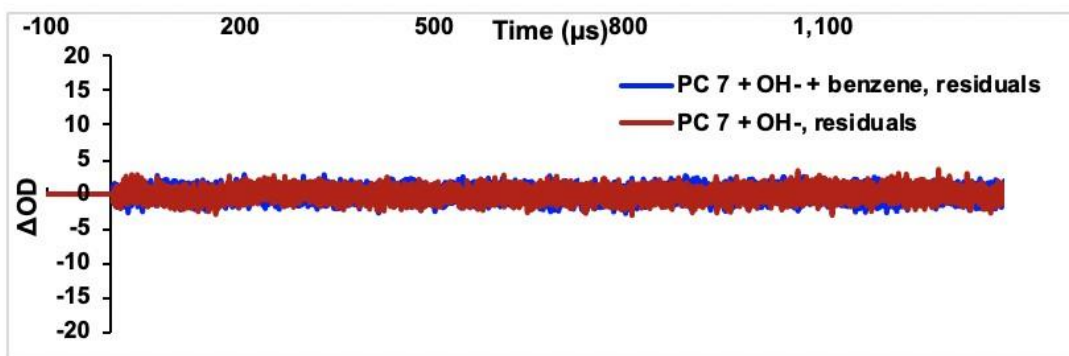


Fig. S5.16. Residuals of biexponential fits shown in the Fig S5.15.

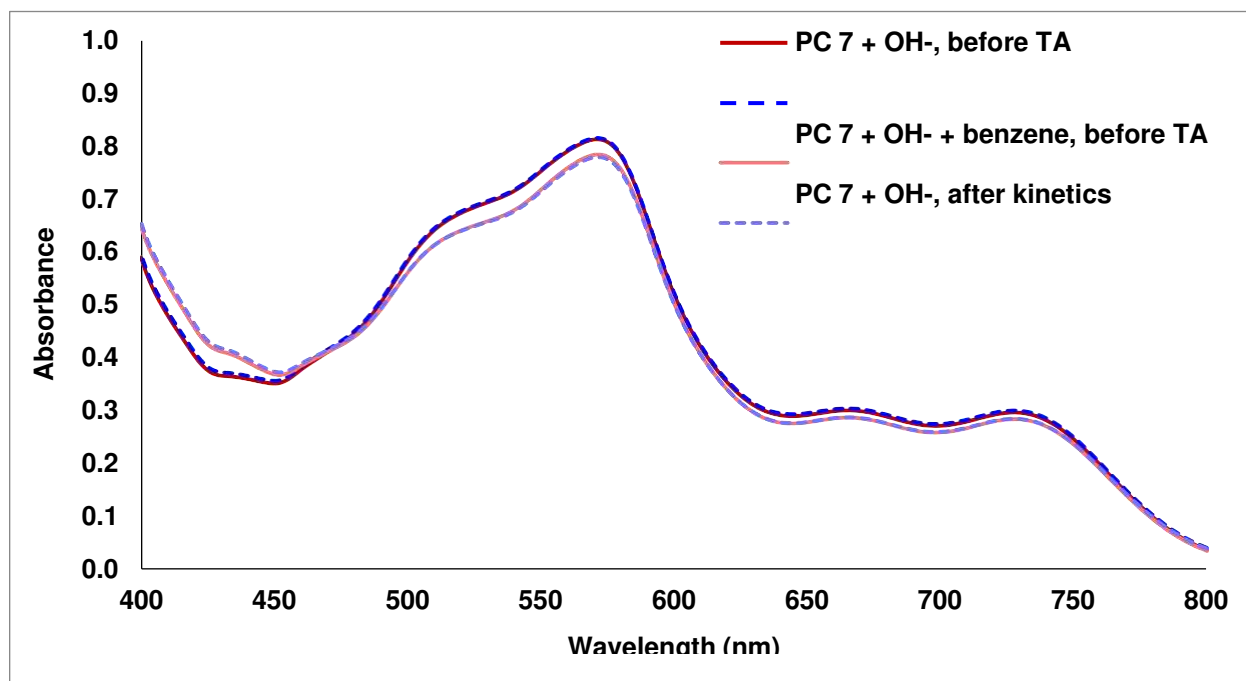


Fig. S5.17. UV-vis of above samples before/after recording kinetic traces.



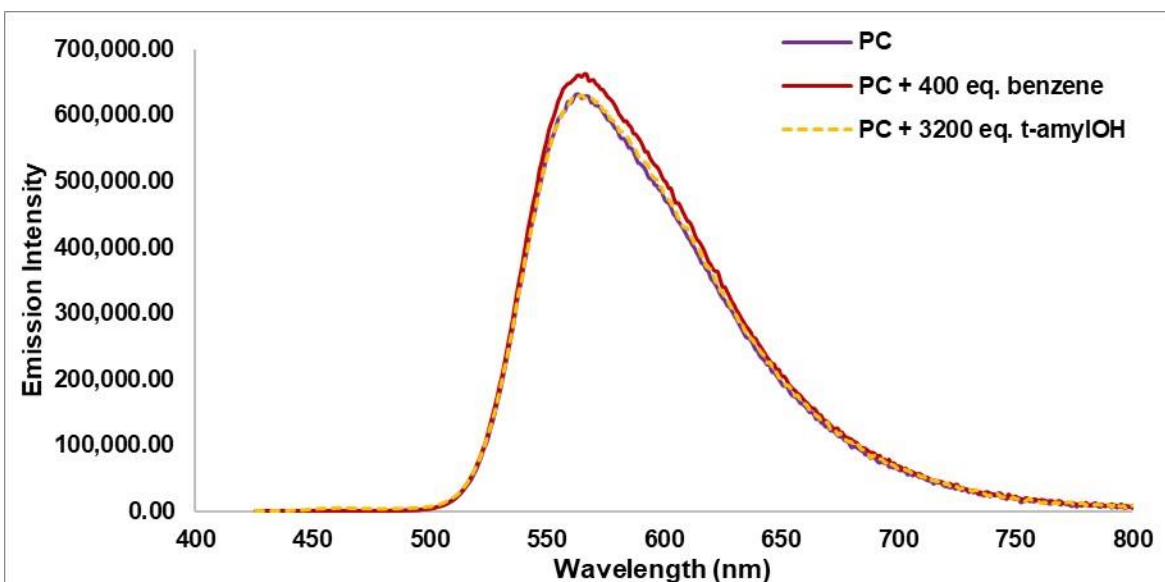


Fig. S5.18. Emission spectrum of PC 7 (0.02 mM) in THF in the presence of 400 eq. benzene, 3200 eq. *t*-amyl alcohol, or no quencher.  $\lambda_{excitation} = 416$  nm.

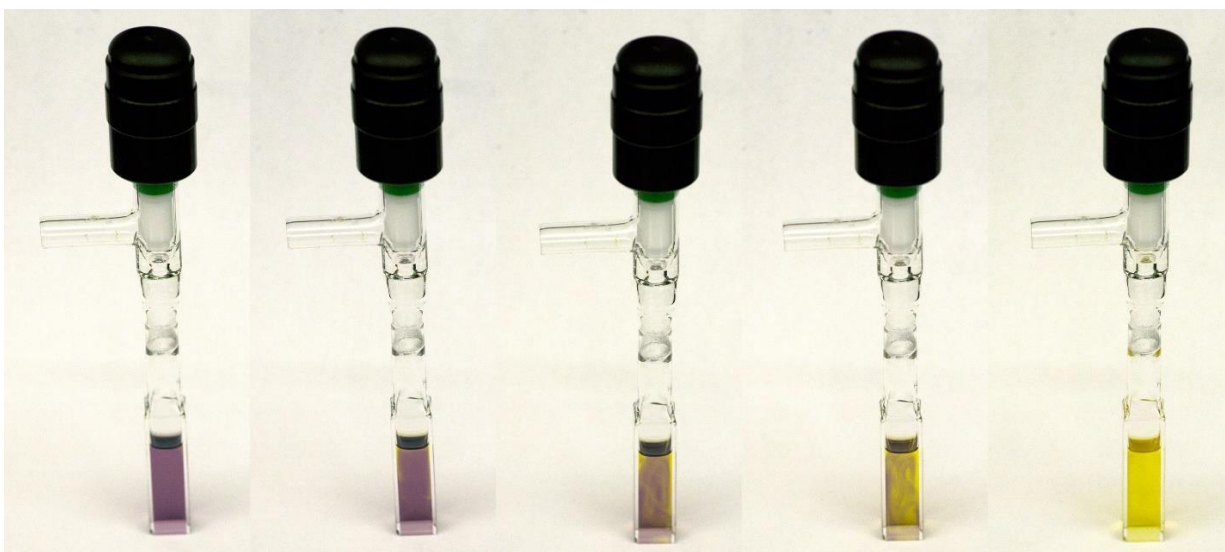


Fig. S5.19. Photographs of a mixture of PC 7 (0.1 mM in THF) with Bu<sub>4</sub>NOH (20 eq), irradiated for 1 min with 405 nm light. The mixture was initially under N<sub>2</sub> (left) and was exposed to air, turning yellow over a period of ~5 minutes.

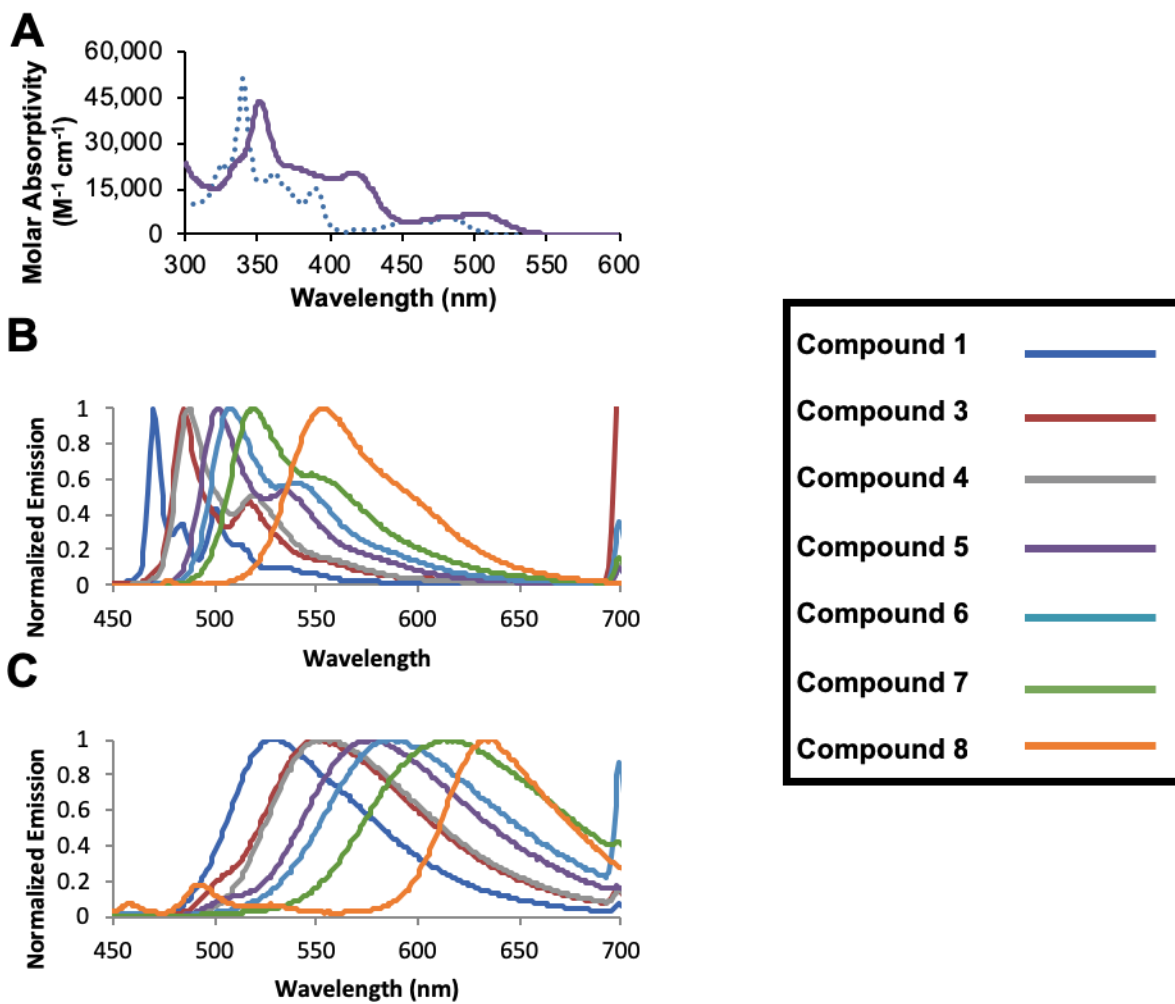


Fig. S5.20. (A) Molar absorptivity vs. wavelength for compounds 1 (dotted blue line) and 5 (solid purple line) taken in chloroform. Emission spectra of compounds 1 & 3-8 taken in hexanes with dielectric constant ( $\epsilon$ ) = 1.882 (B), and in DMSO,  $\epsilon$  = 46.70, (C) excited at 340 nm.

## Steady-State Absorbance of PCs

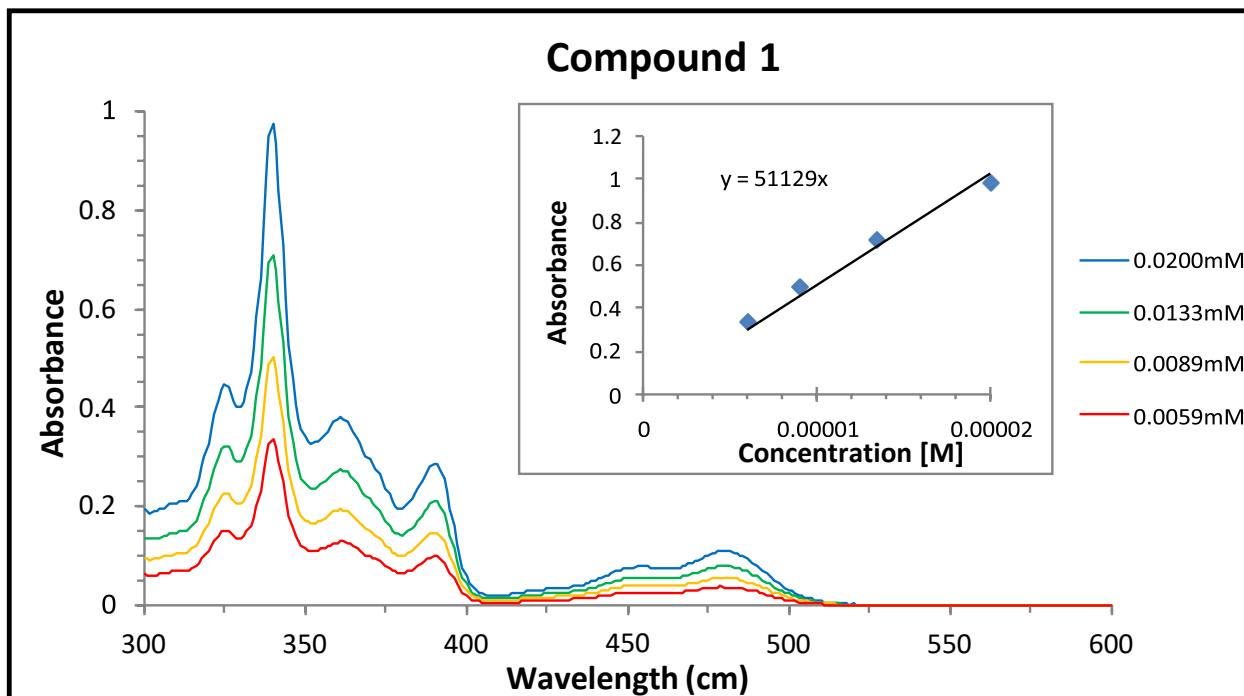


Fig. S5.21. UV-Vis absorption of Compound 1 taken at different concentrations in chloroform. Path length 1 cm.

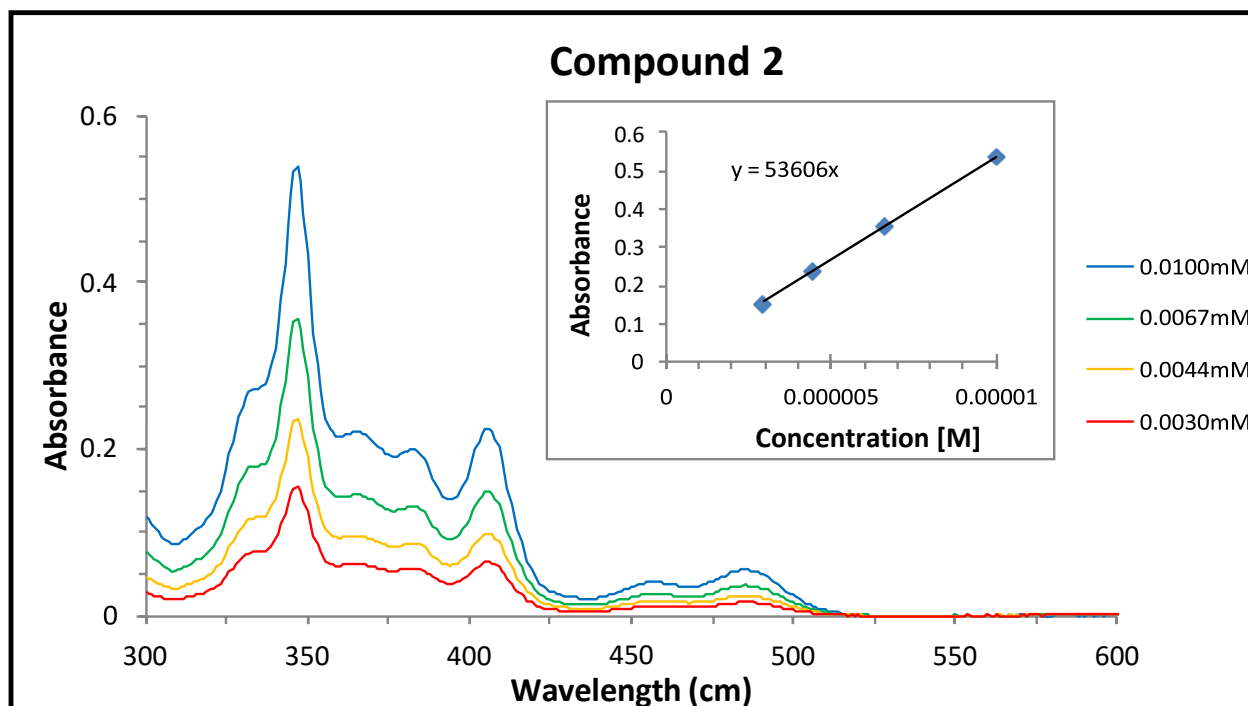


Fig. S5.22. UV-Vis absorption of Compound 2 taken at different concentrations in chloroform. Path length 1 cm.

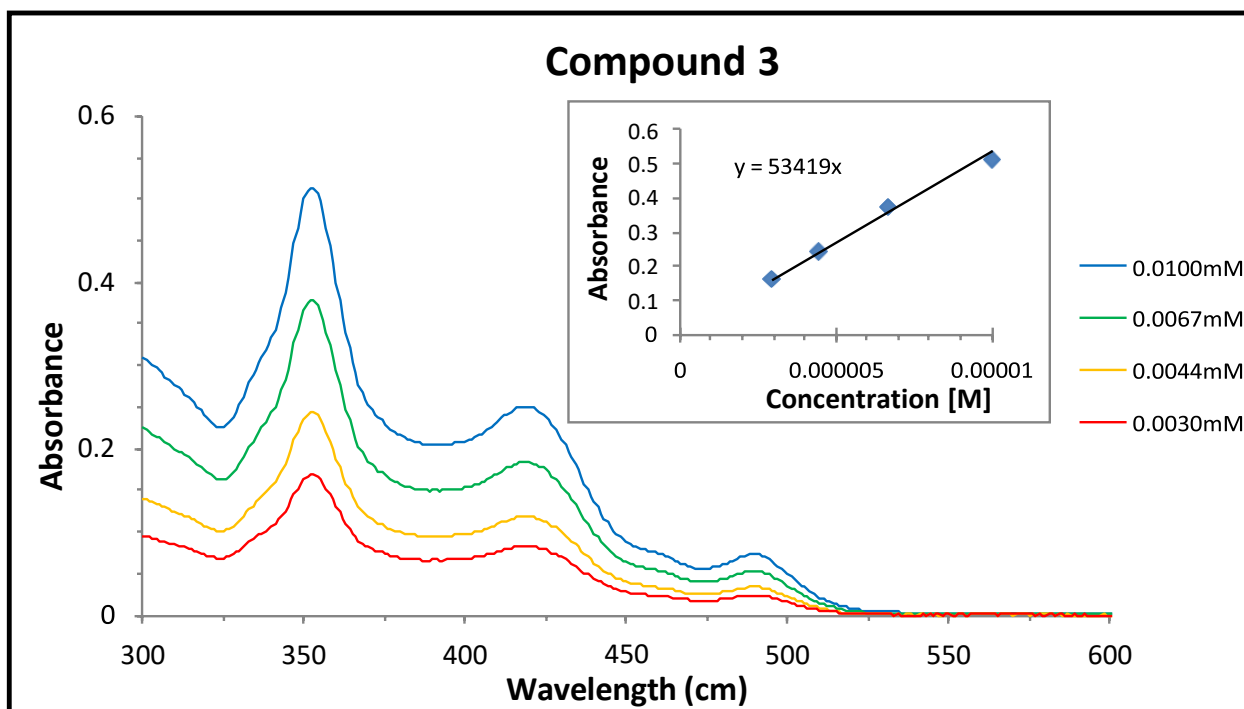


Fig. S5.23. UV-Vis absorption of Compound 3 taken at different concentrations in chloroform. Path length 1 cm.

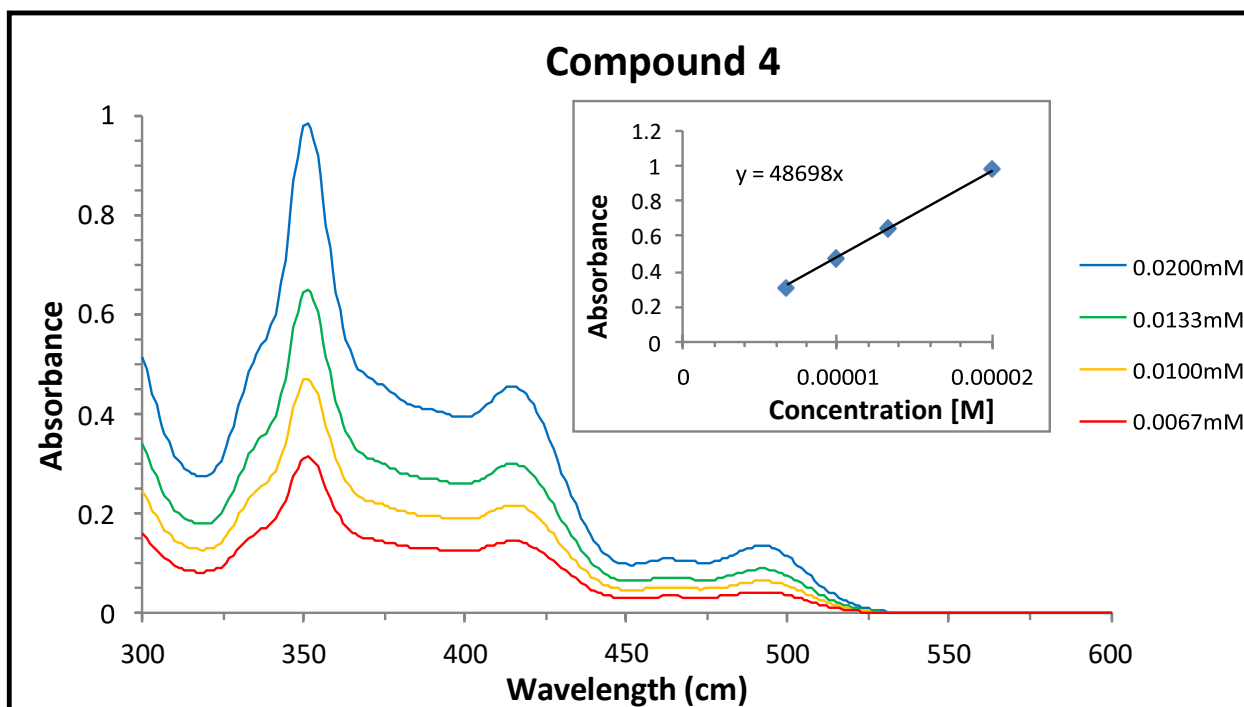


Fig. S5.24. UV-Vis absorption of Compound 4 taken at different concentrations in chloroform. Path length 1 cm.

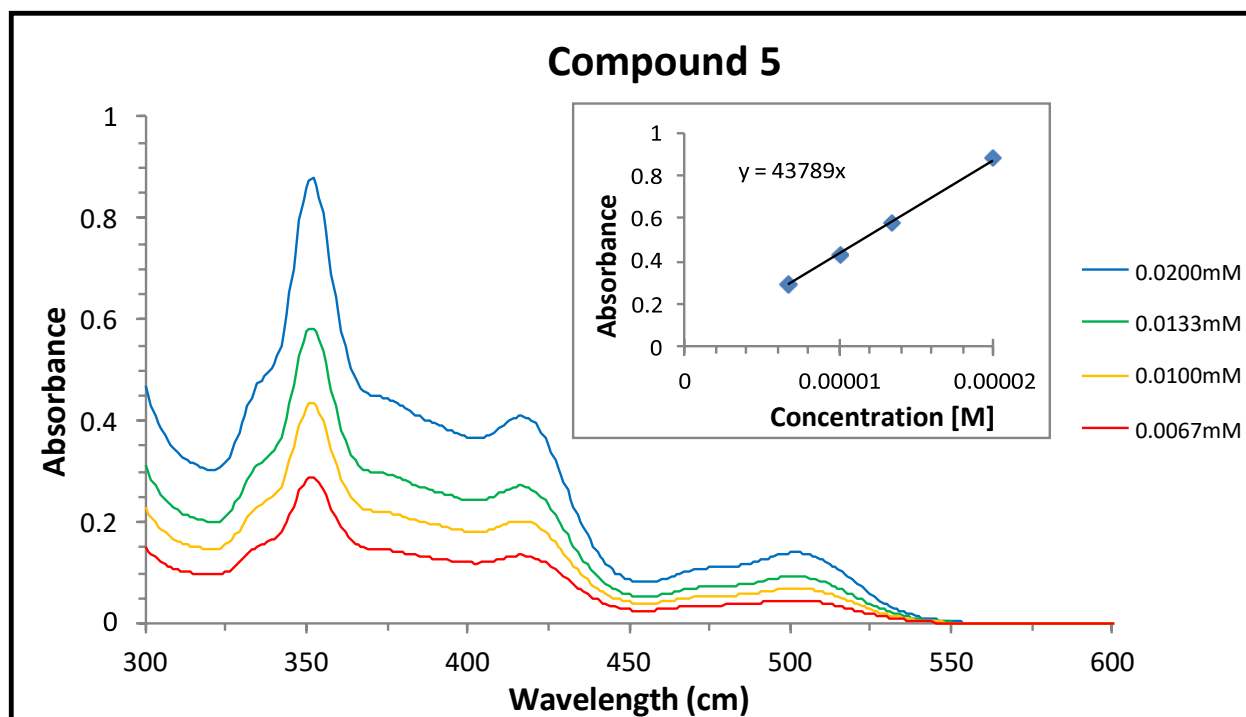


Fig. S5.25. UV-Vis absorption of Compound 5 taken at different concentrations in chloroform. Path length 1 cm.

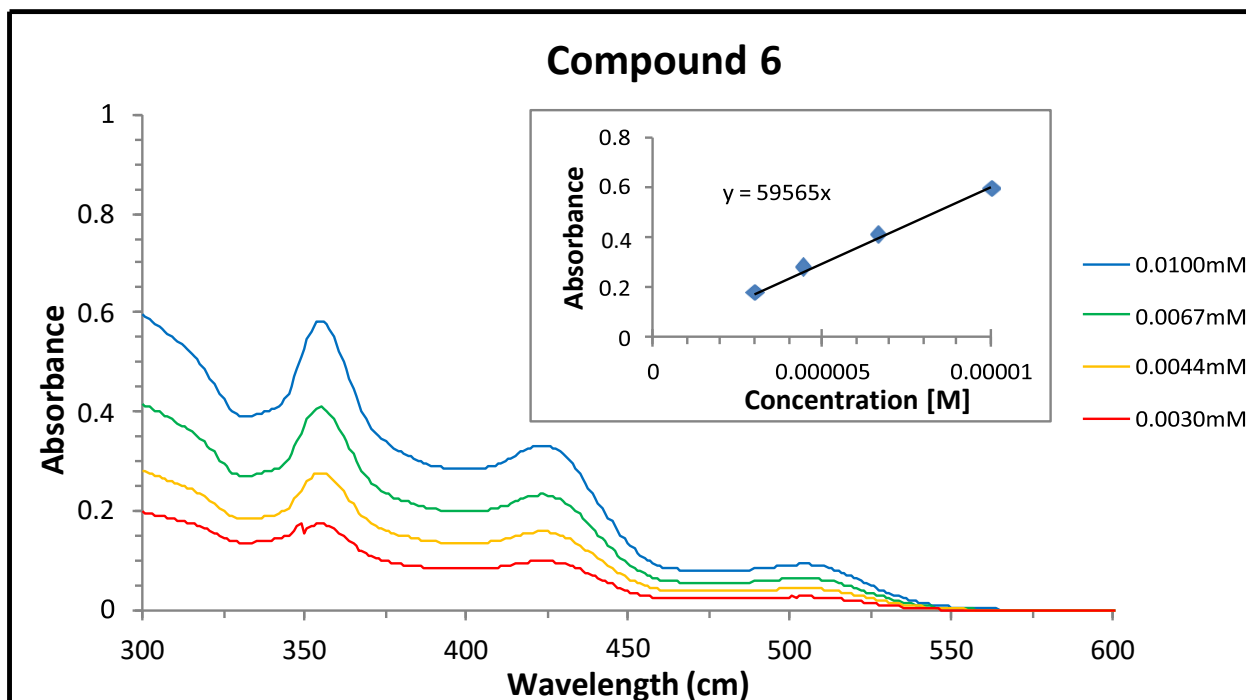


Fig. S5.26. UV-Vis absorption of Compound 6 taken at different concentrations in chloroform. Path length 1 cm.

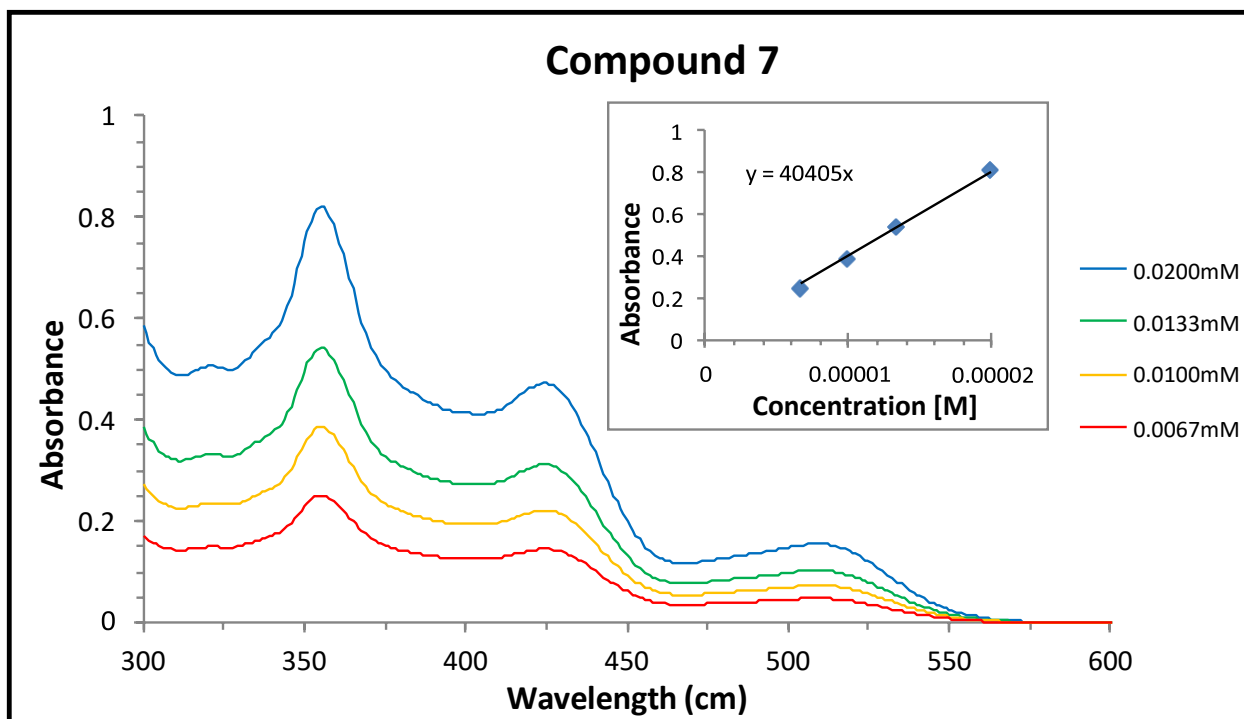


Fig. S5.27. UV-Vis absorption of Compound 7 taken at different concentrations in chloroform. Path length 1 cm.

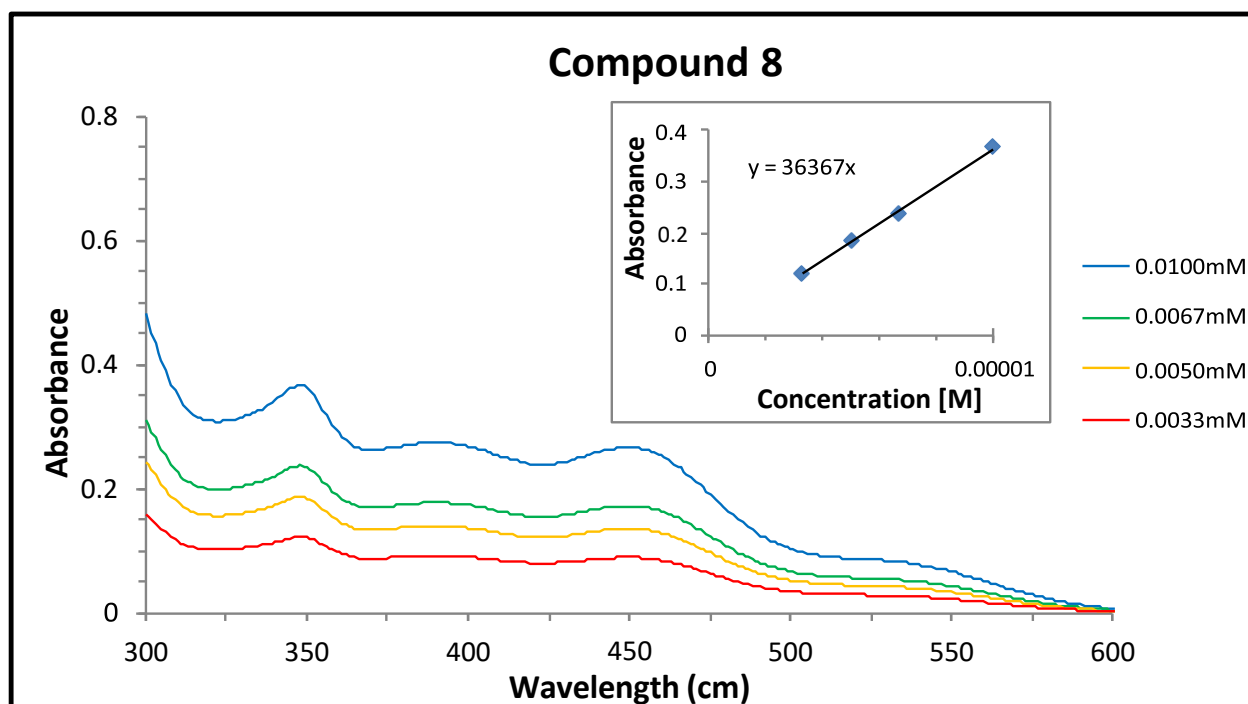


Fig. S5.28. UV-Vis absorption of Compound 8 taken at different concentrations in chloroform. Path length 1 cm.

#### 4. Electrochemical Characterization of Catalysts

Cyclic voltammetry (CV) was performed with a potentiostat (Gamry Instruments) using a 3- electrode electrochemical cell with a Ag/AgNO<sub>3</sub> reference electrode consisting of Ag wire and an AgNO<sub>3</sub> solution (0.01 M) in MeCN or DMAc with TBAPF<sub>6</sub> electrolyte (0.100 M), separated by a frit from the analyte solution. The counter electrode was a Pt wire and was separated from the analyte solution by a Vycor frit for bulk electrolysis in the spectroelectrochemistry experiment and for CVs performed in THF. For CV characterization of PCs 1-7, it was not separated. A Pt working electrode (Gamry Instruments) was used for CV characterization of catalysts. For spectroelectrochemistry, a 1 x 5 cm glassy carbon working electrode (IKA) was used. For other CVs in THF, a small glassy carbon working electrode (IKA) was used. TBAPF<sub>6</sub> in DMAc or THF (0.100 M) was used as the electrolyte in all analyte solutions. For spectroelectrochemistry, UV-vis spectra were recorded using the Cary 5000 equipped with a fiber optic coupler (Harrick Scientific FiberMate) and probe that was placed in the analyte solution in the electrochemical cell. The cell and probe assembly were placed on a stir plate inside a light-tight box. For all experiments, solutions were degassed by sparging with N<sub>2</sub> through a Teflon tube for at least 15 minutes prior to starting the potentiostat. CV was performed with the tube pulled out of the solution and without stirring. For spectroelectrochemistry, the solution was stirred and sparged throughout the measurement.

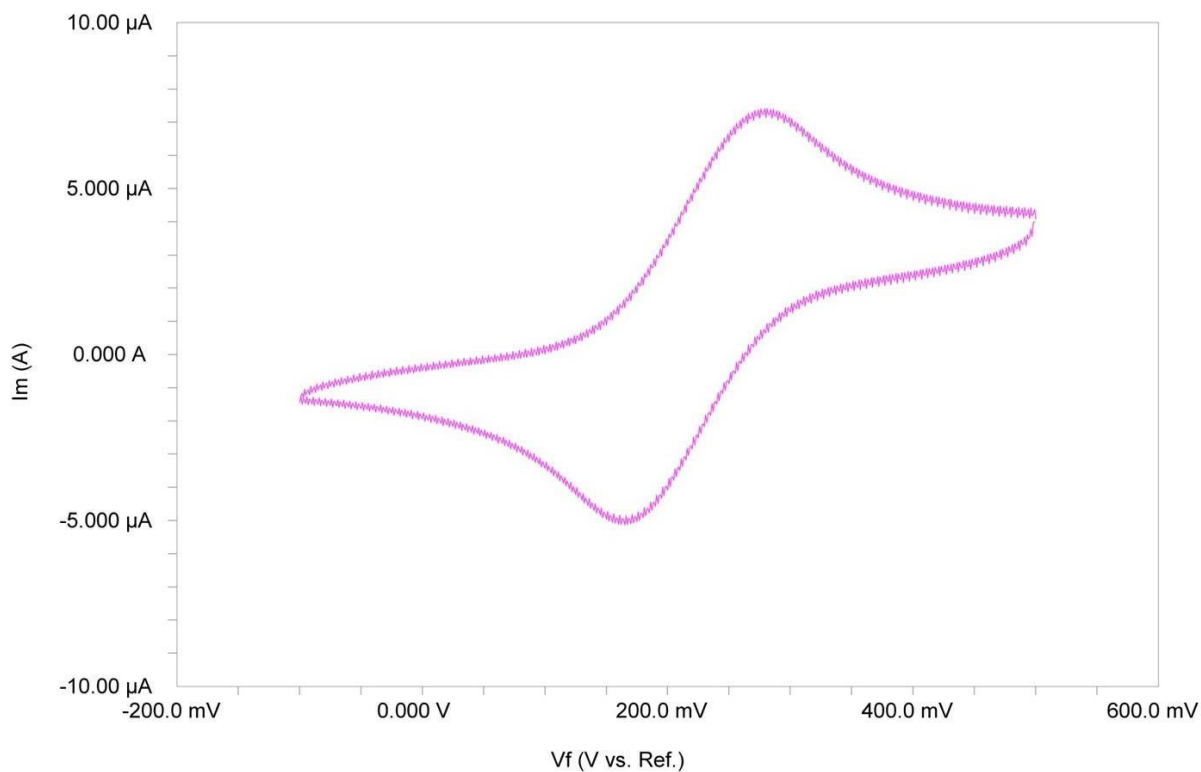


Fig. S5.29. Cyclic voltammogram of Fc/Fc<sup>+</sup> standard (1 mM in THF).

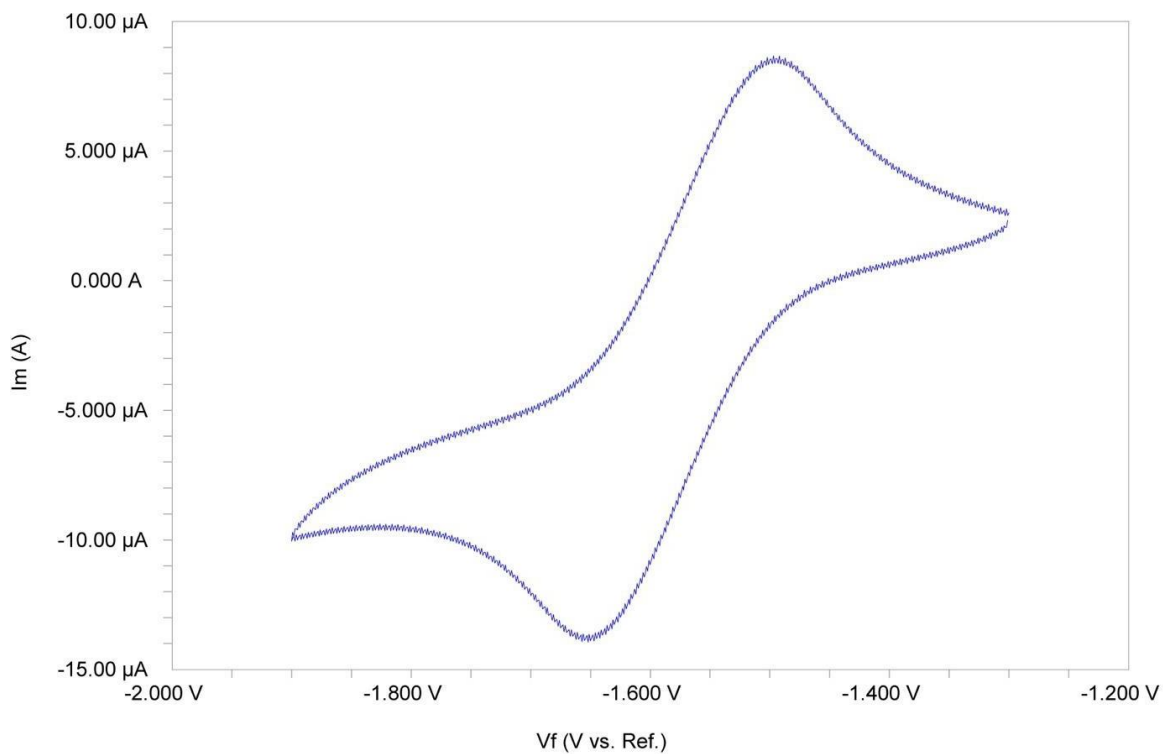


Fig. S5.30. Cyclic voltammogram of PC 7 (1 mM in THF) showing first reduction event is reversible.



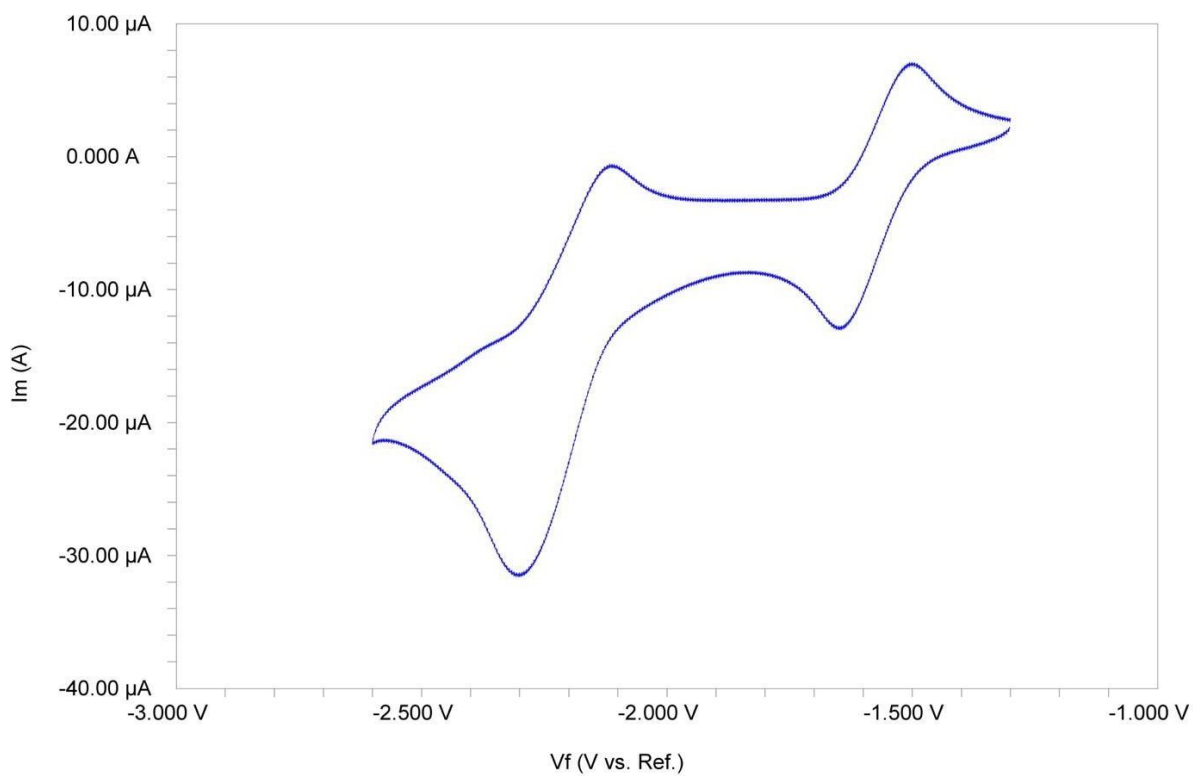


Fig. S5.31. Cyclic voltammogram of PC 7 (1 mM in THF) showing two reduction events.

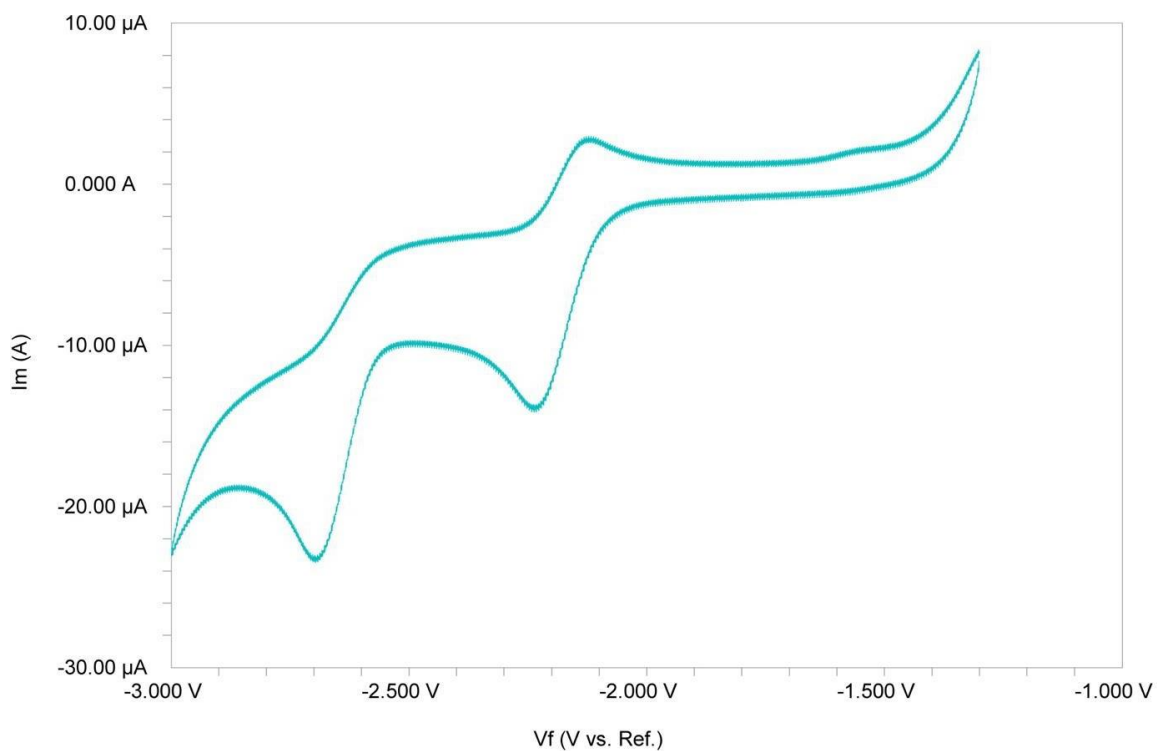


Fig. S5.32. Cyclic voltammogram of PC 7 (1 mM in THF) with 200 eq. Bu<sub>4</sub>NF showing two reduction events.

Table S5.6: Summarized Electrochemical data in THF in V.

Couple	E <sub>1/2</sub> or E <sub>p/2</sub> vs. Fc/Fc <sup>+</sup>		E <sub>1/2</sub> or E <sub>p/2</sub> vs. SCE <sup>a</sup>	
PC/PC <sup>-</sup>	-1.80	-2.43	-1.24	-1.87
[PC + F] <sup>-</sup> / [PC + F] <sup>2-</sup>	-2.40	-2.85	-1.84	-2.29
[PC + OH] <sup>-</sup> / [PC + OH] <sup>2-</sup>	-2.36	-2.69	-1.80	-2.13
Fc/Fc <sup>+</sup>	0.22			

<sup>a</sup>Conversion used for measurement of Fc/Fc<sup>+</sup> vs. SCE in THF <sup>12</sup>.

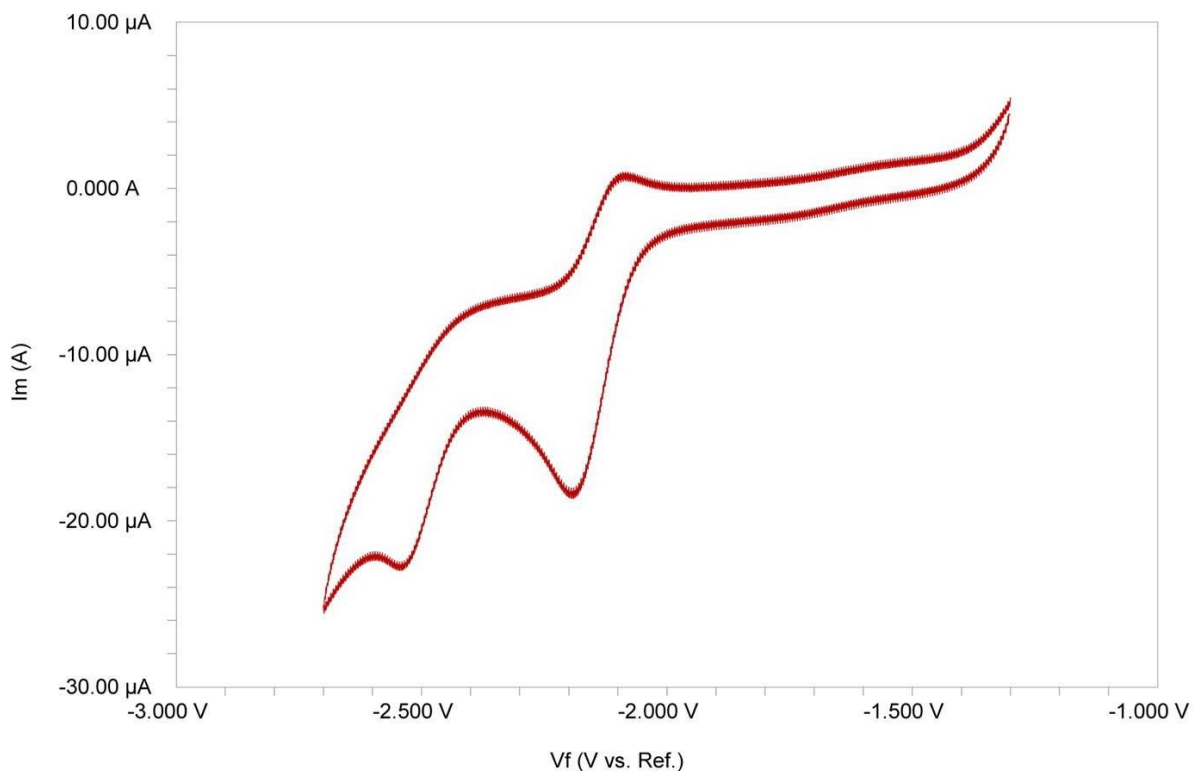


Fig. S5.33. Cyclic voltammogram of PC 7 (1 mM in THF) with 200 eq. Bu<sub>4</sub>NOH showing two reduction events.

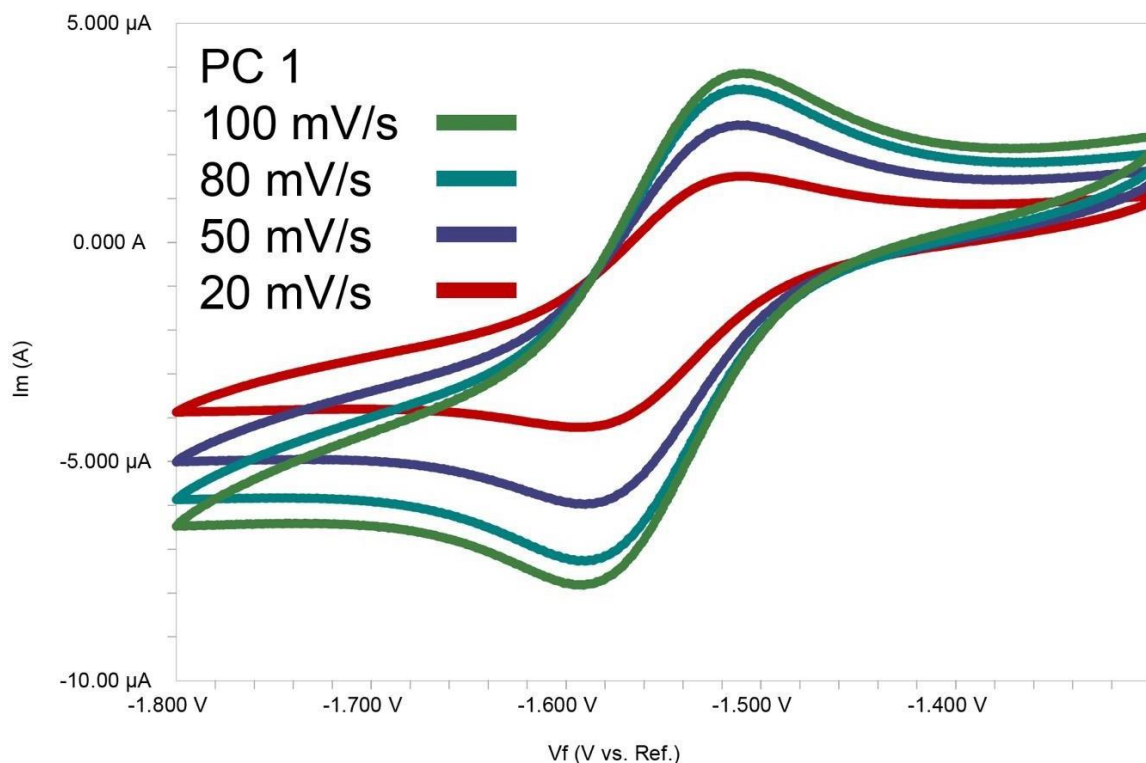


Fig. S5.34. Cyclic voltammograms of PC 1 (DMAc) with sweeps at 100 mV/s, 80 mV/s, 50 mV/s, and 20 mV/s.

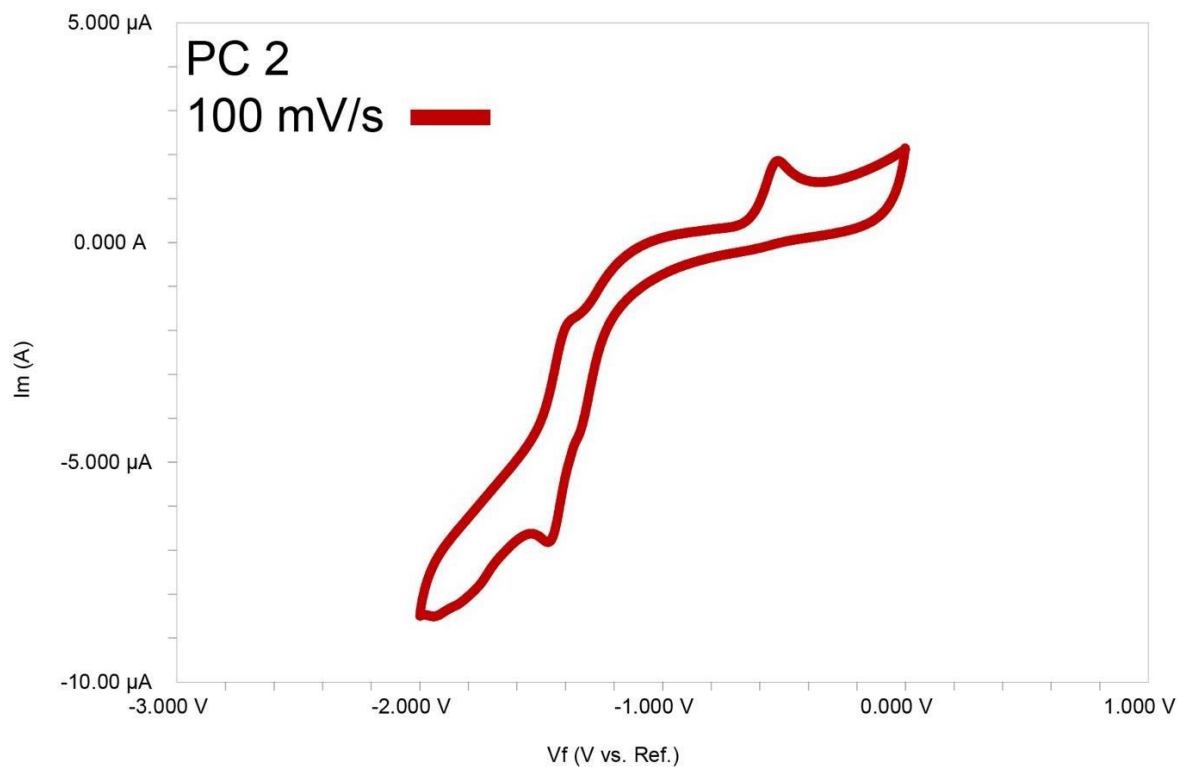


Fig. S5.35. Cyclic voltammogram of PC 2 (DMAc) with sweeps at 100 mV/s (not reversible).

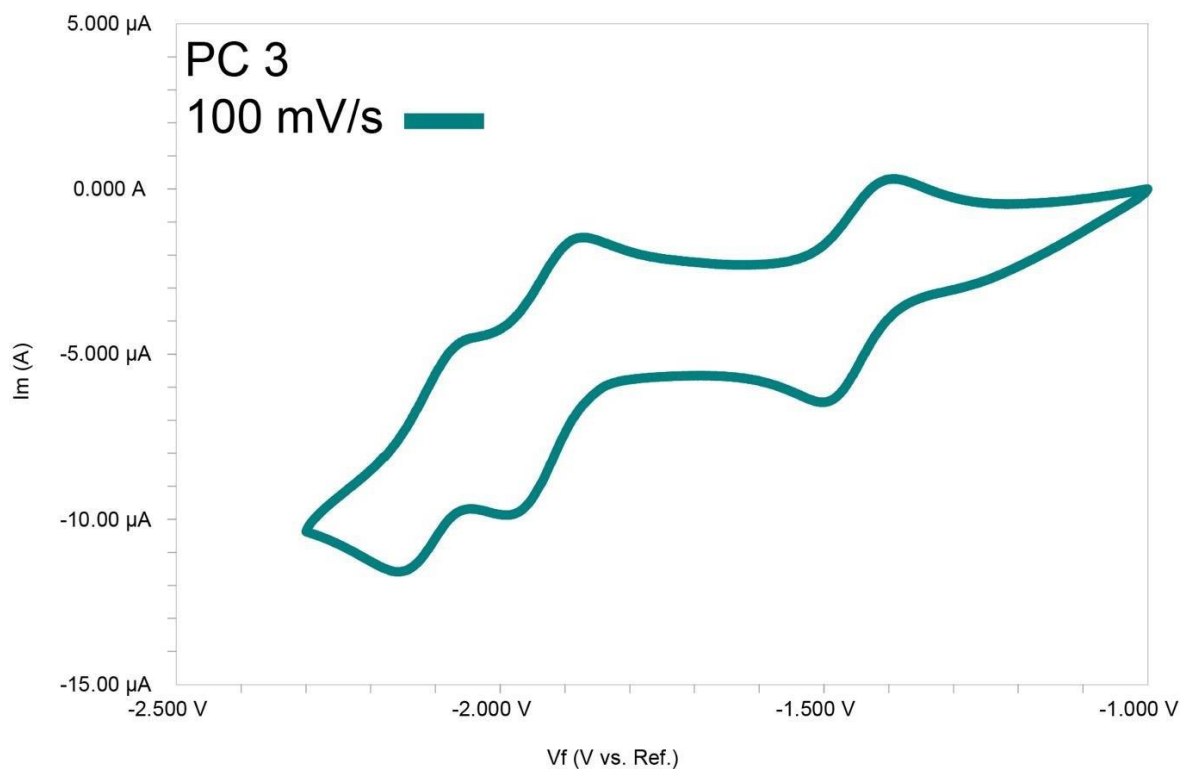


Fig. S5.36: Cyclic voltammogram of PC 3 (DMAc) with sweeps at 100 mV/s (quasi reversible).

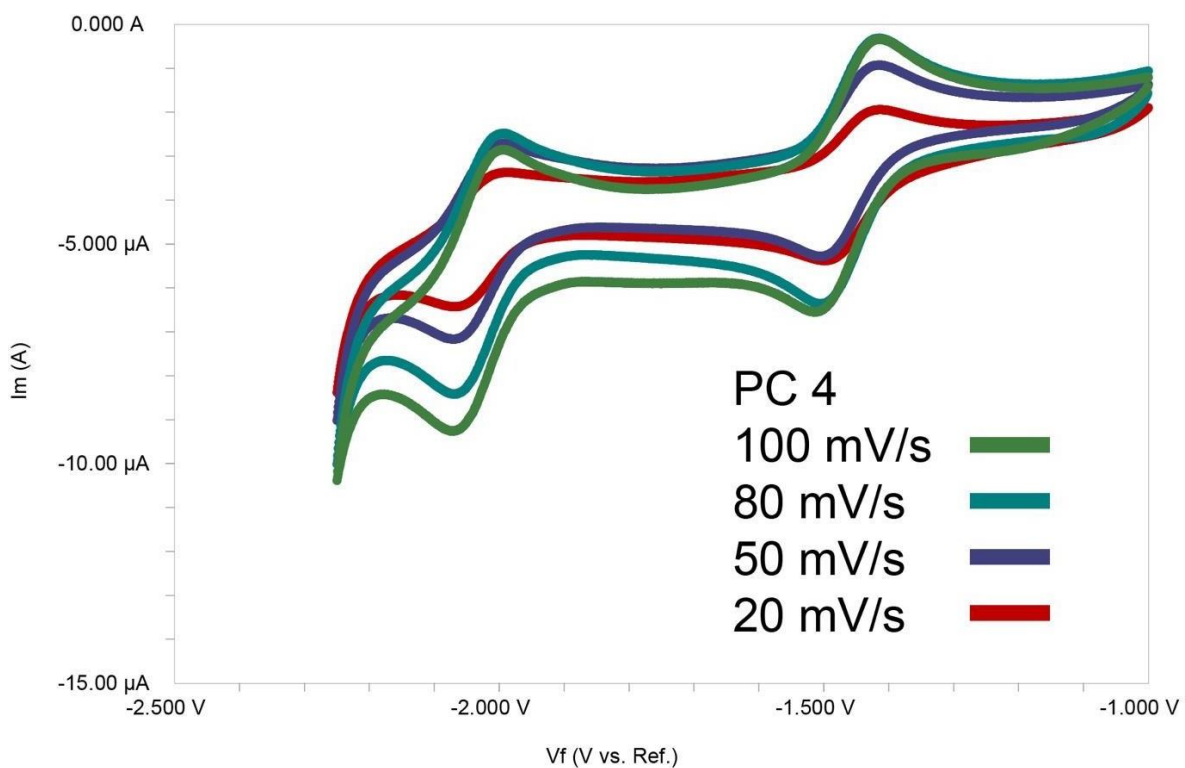


Fig. S5.37. Cyclic voltammograms of PC 4 (DMAc) with sweeps at 100 mV/s, 80 mV/s, 50 mV/s, and 20 mV/s (two quasi reversible reduction events).

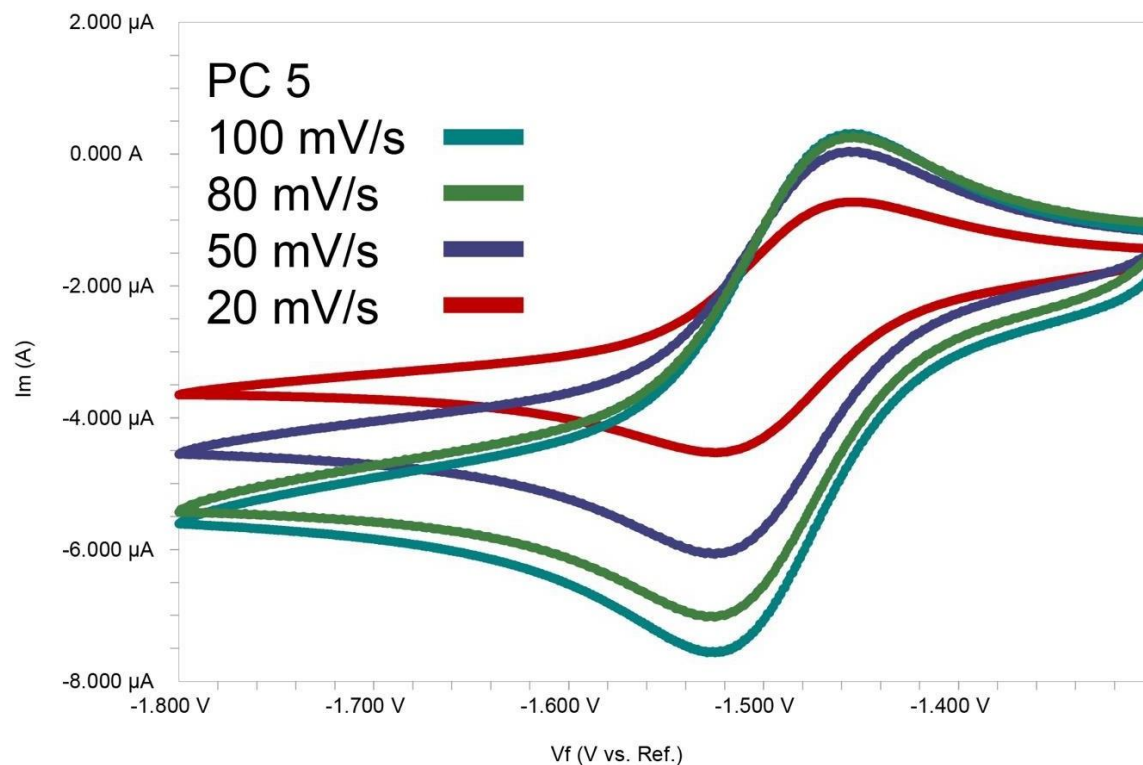


Fig. S5.38. Cyclic voltammograms of PC 5 (DMAc) with sweeps at 100 mV/s, 80 mV/s, 50 mV/s, and 20 mV/s (reversible).

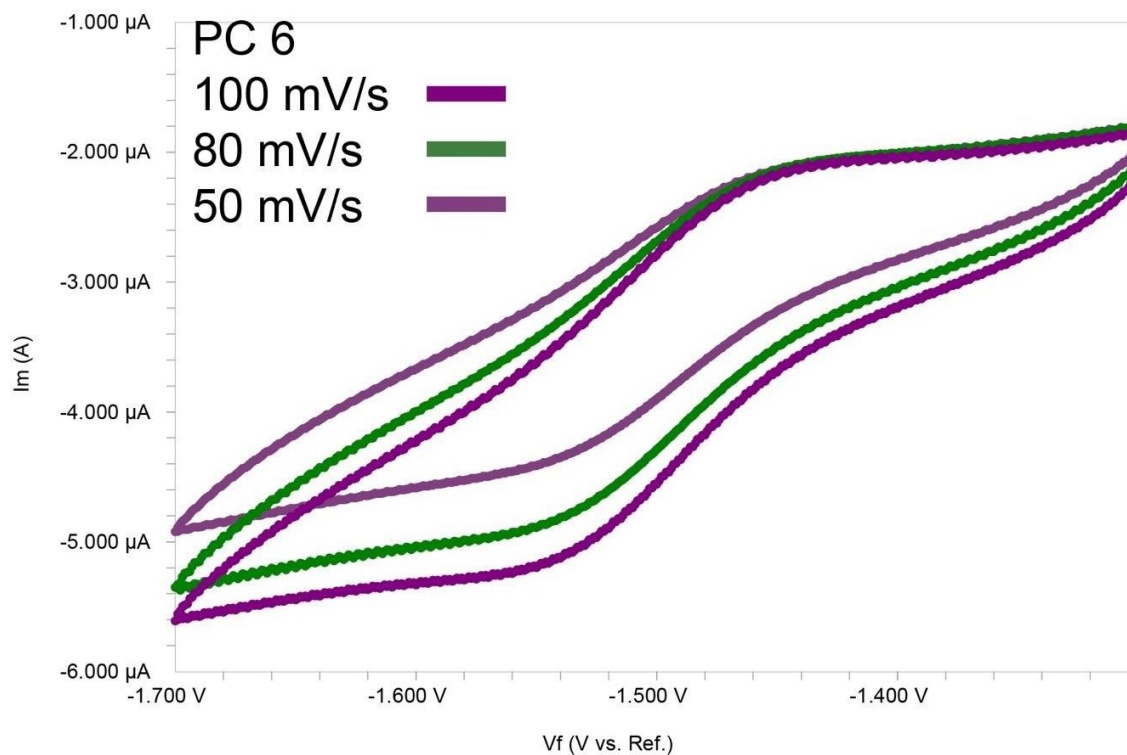


Fig. S5.39. Cyclic voltammograms of PC 6 (DMAc) with sweeps at 100 mV/s, 80 mV/s, and 50 mV/s (reversible).

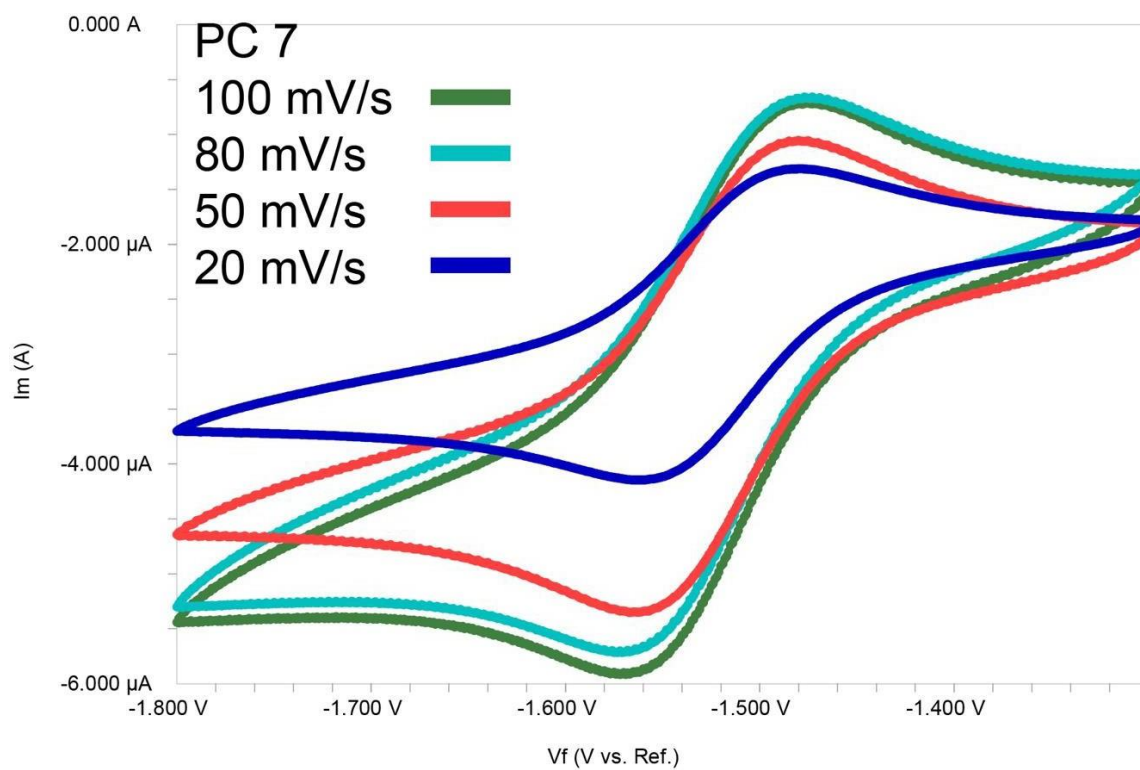


Fig. S5.40. Cyclic voltammograms of PC 7 (DMAc) with sweeps at 100 mV/s, 80 mV/s, 50 mV/s, and 20 mV/s (reversible).

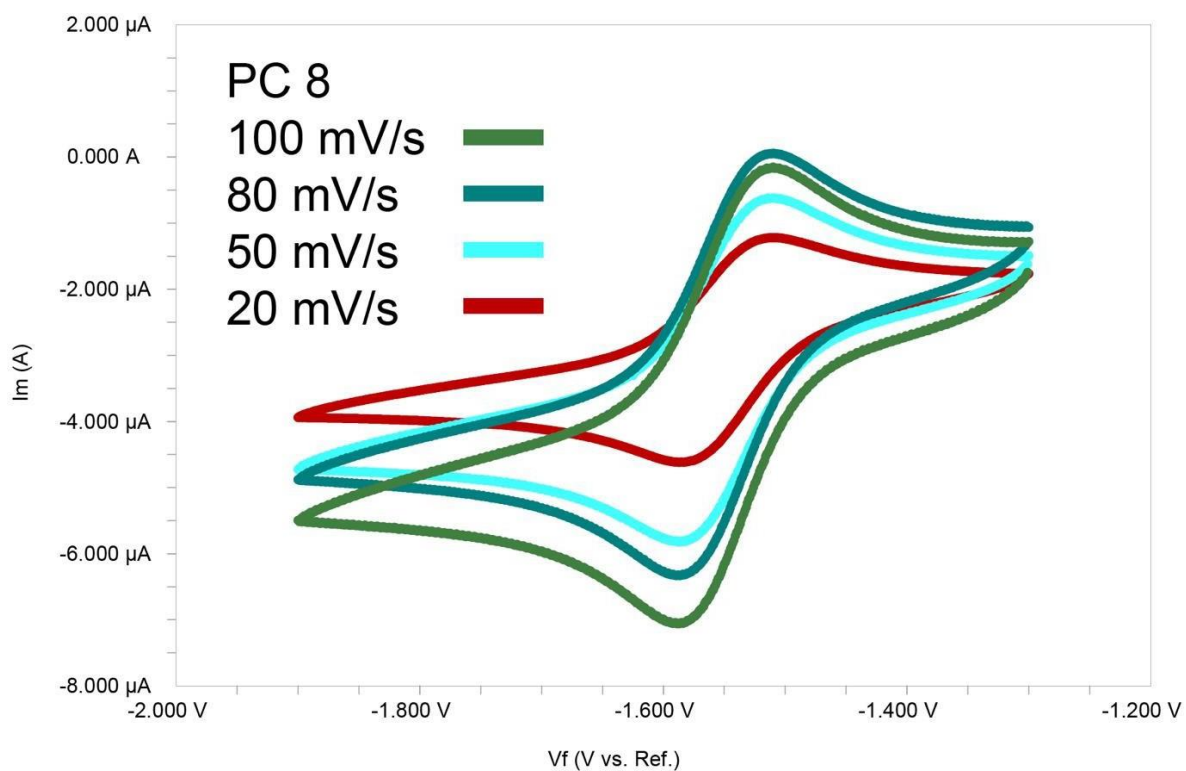


Fig. S5.41: Cyclic voltammograms of PC 8 (DMAc) with sweeps at 100 mV/s, 80 mV/s, 50 mV/s, and 20 mV/s (reversible).

## 5. Electron Paramagnetic Resonance Characterization of PC 7

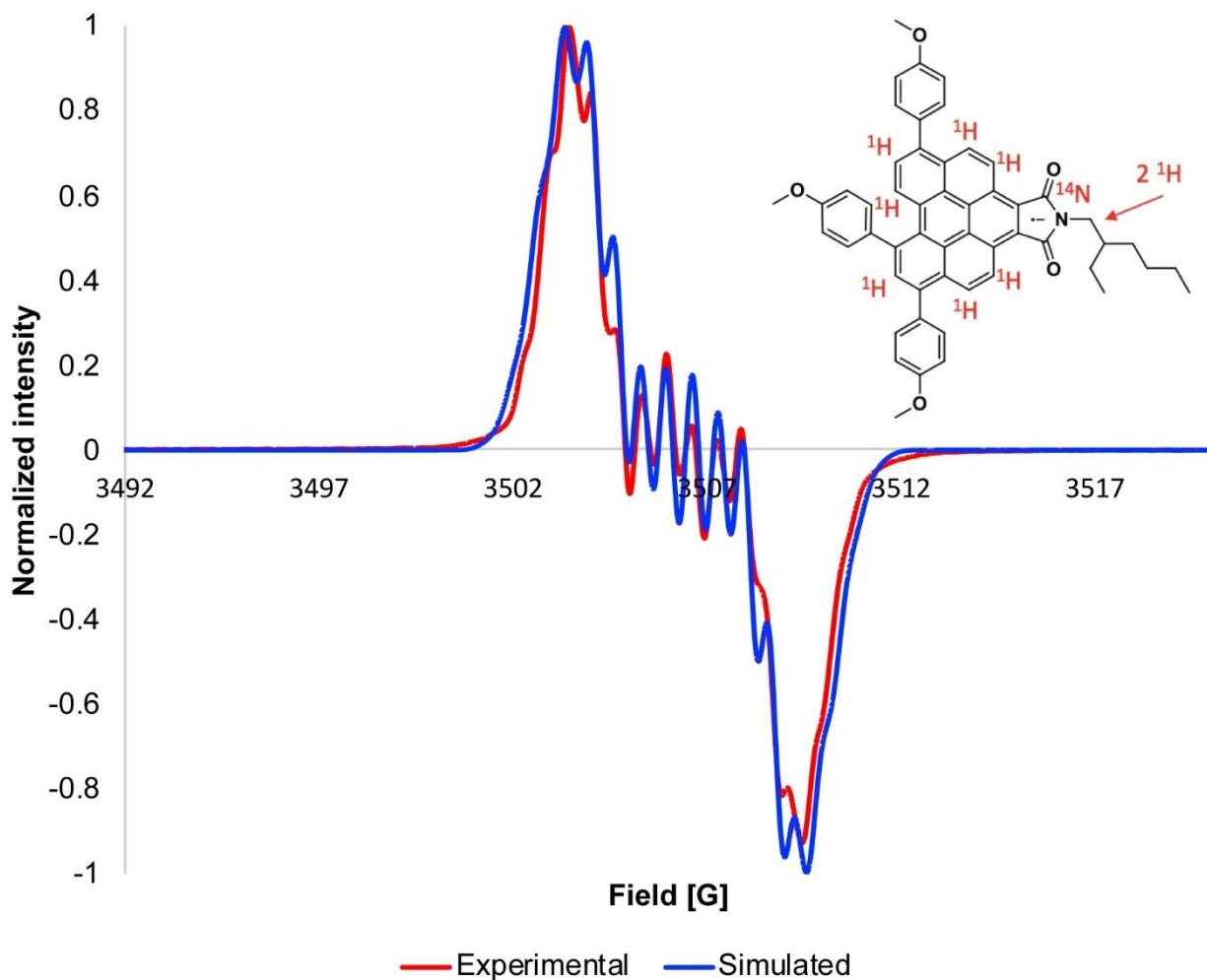


Fig. S5.42. Red: EPR spectrum of PC 7<sup>•+</sup> (5 mM THF, ambient temperature) + TBAF (100 eq.) after 30 sec. irradiation with 405 nm LED. Blue: Simulated EPR spectrum.

Table S5.7. Parameters used in the simulation of the EPR spectrum of PC 7<sup>•+</sup>

PC	$g_{iso}$	$a_{iso}$ (G)	Line Width (G)	Line Shape
7	2.00171	1.9853 (1H), 0.5397 (2H), 0.6388 (1H), 0.6450 (1H), 0.6119 (1H), 0.6108 (1H), 0.6451 (1H), 0.6444 (1H), 0.6443 (1H)	0.6663	Gaussian

## 6. NMR Spectra of Photocatalysts

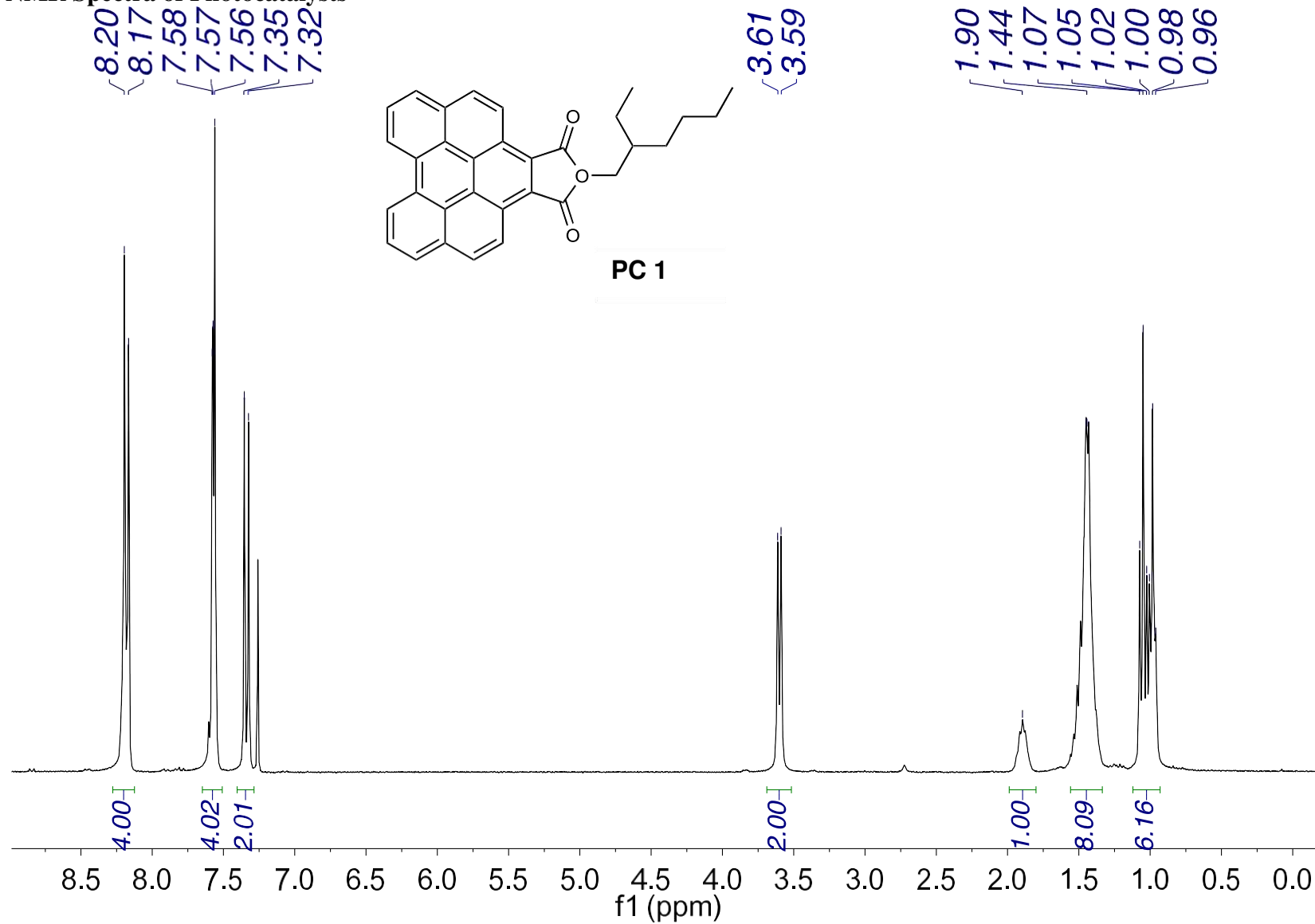


Fig. S5.43. <sup>1</sup>H NMR of compound PC 1 (CDCl<sub>3</sub>, 300 MHz).



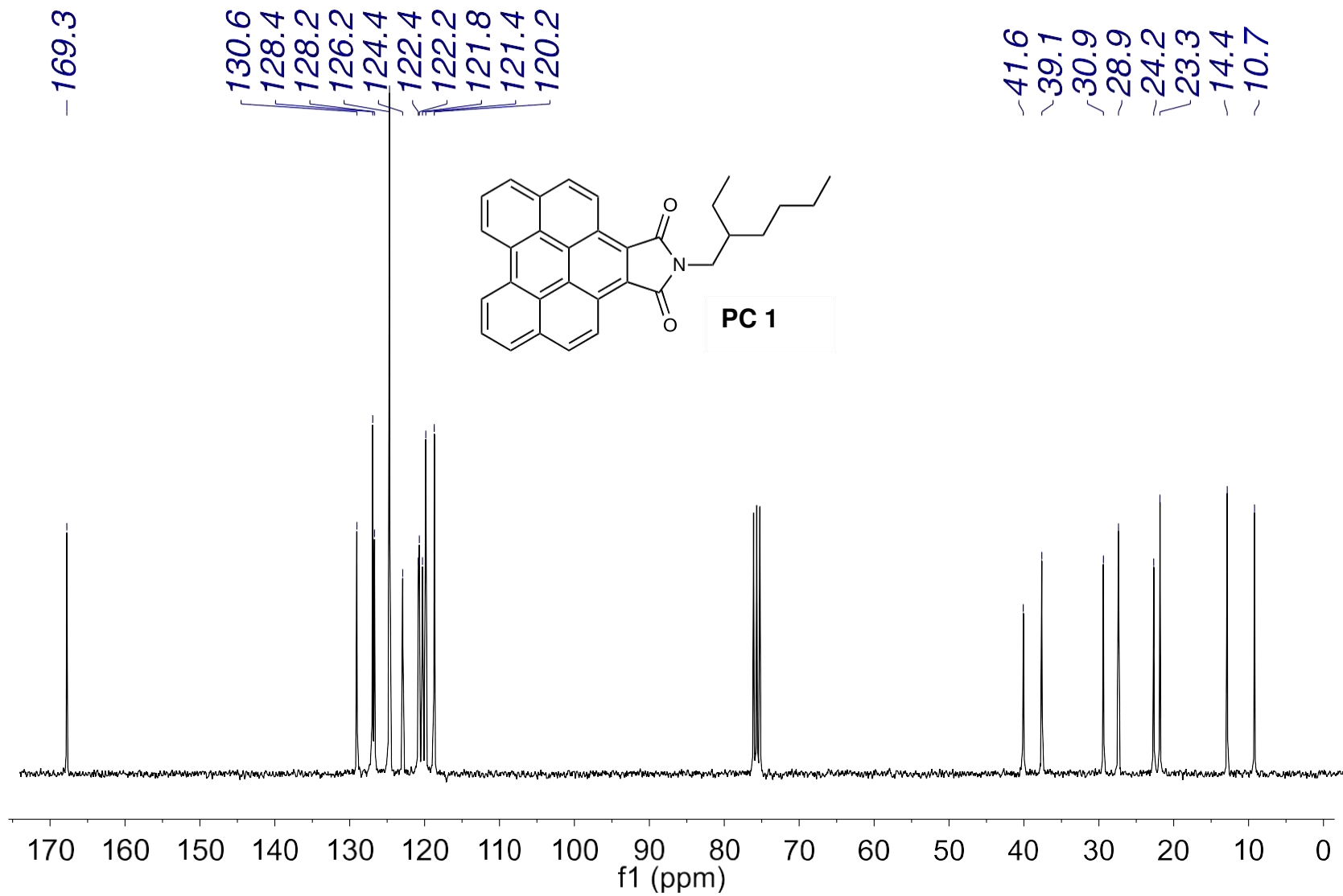


Fig. S5.44.  $^{13}\text{C}$  NMR of compound PC 1 ( $\text{CDCl}_3$ , 75 MHz).

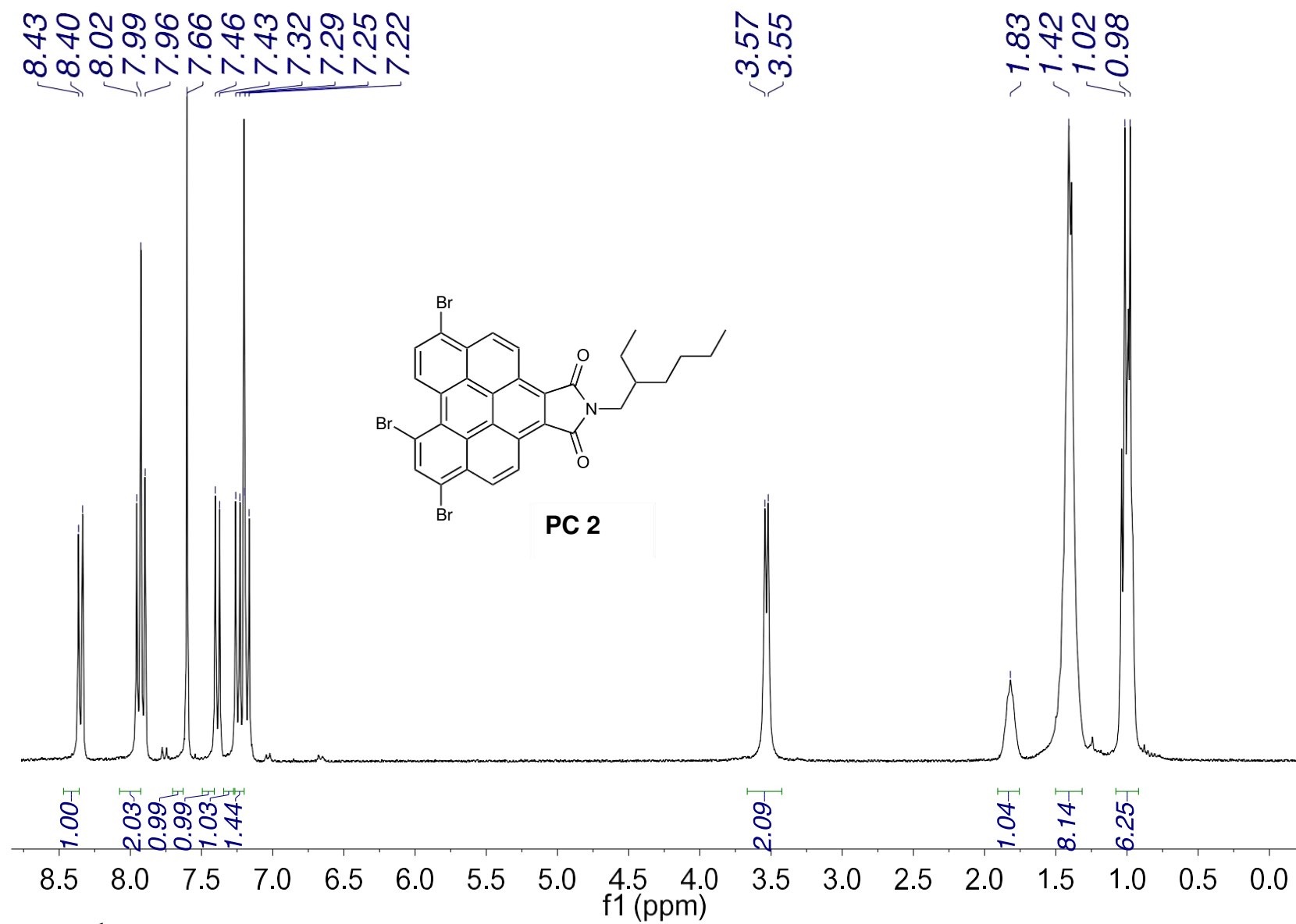


Fig. S5.45.  $^1\text{H}$  NMR of compound PC 2 ( $\text{CDCl}_3$ , 300 MHz).

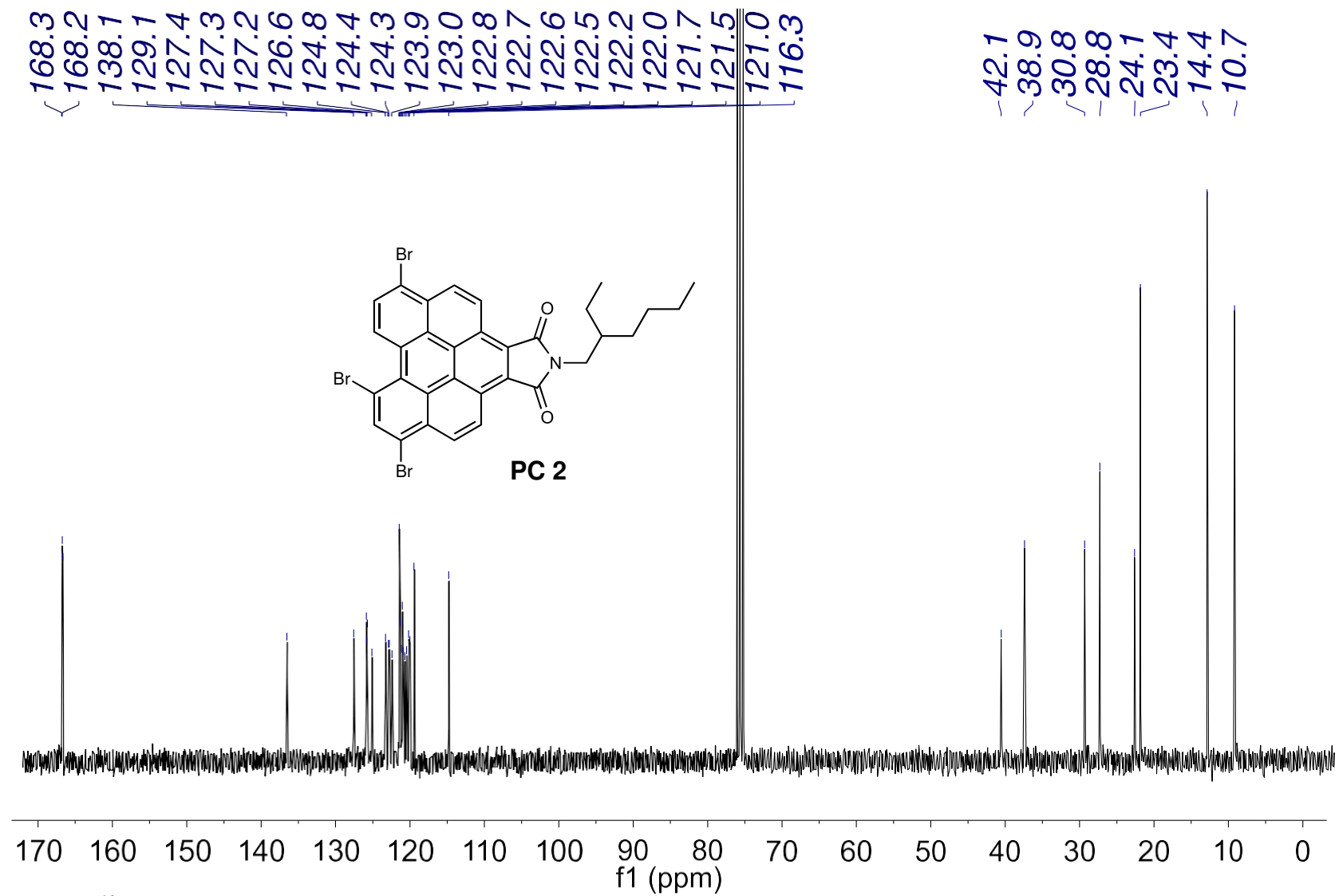


Fig. S5.46. <sup>13</sup>C NMR of compound PC 2 (CDCl<sub>3</sub>, 75 MHz).

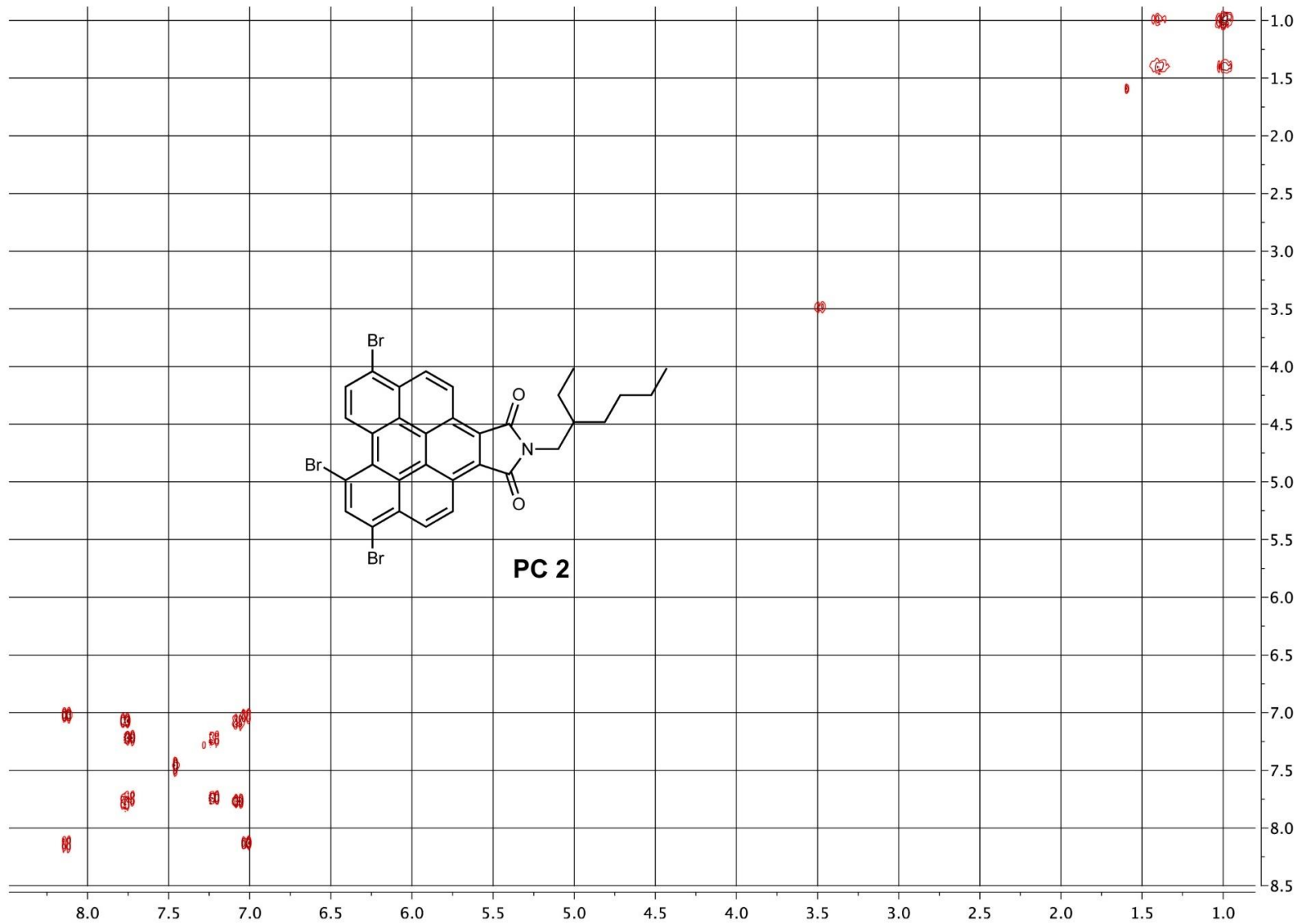


Fig. S5.47. COSY of compound PC 2 (CDCl<sub>3</sub>, 300 MHz).

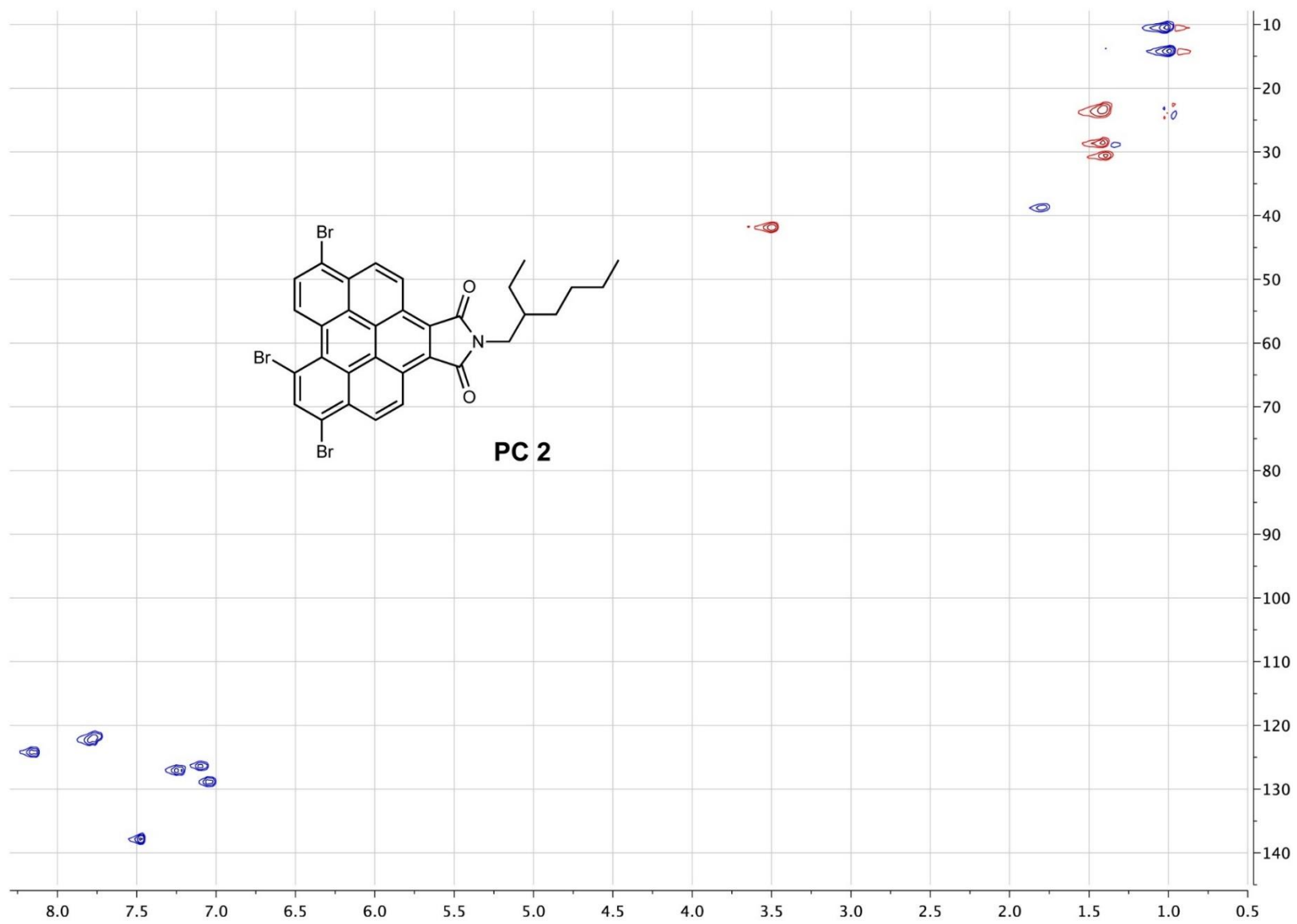


Fig. S5.48. HSQC of compound PC 2 (CDCl<sub>3</sub>, 300 MHz).

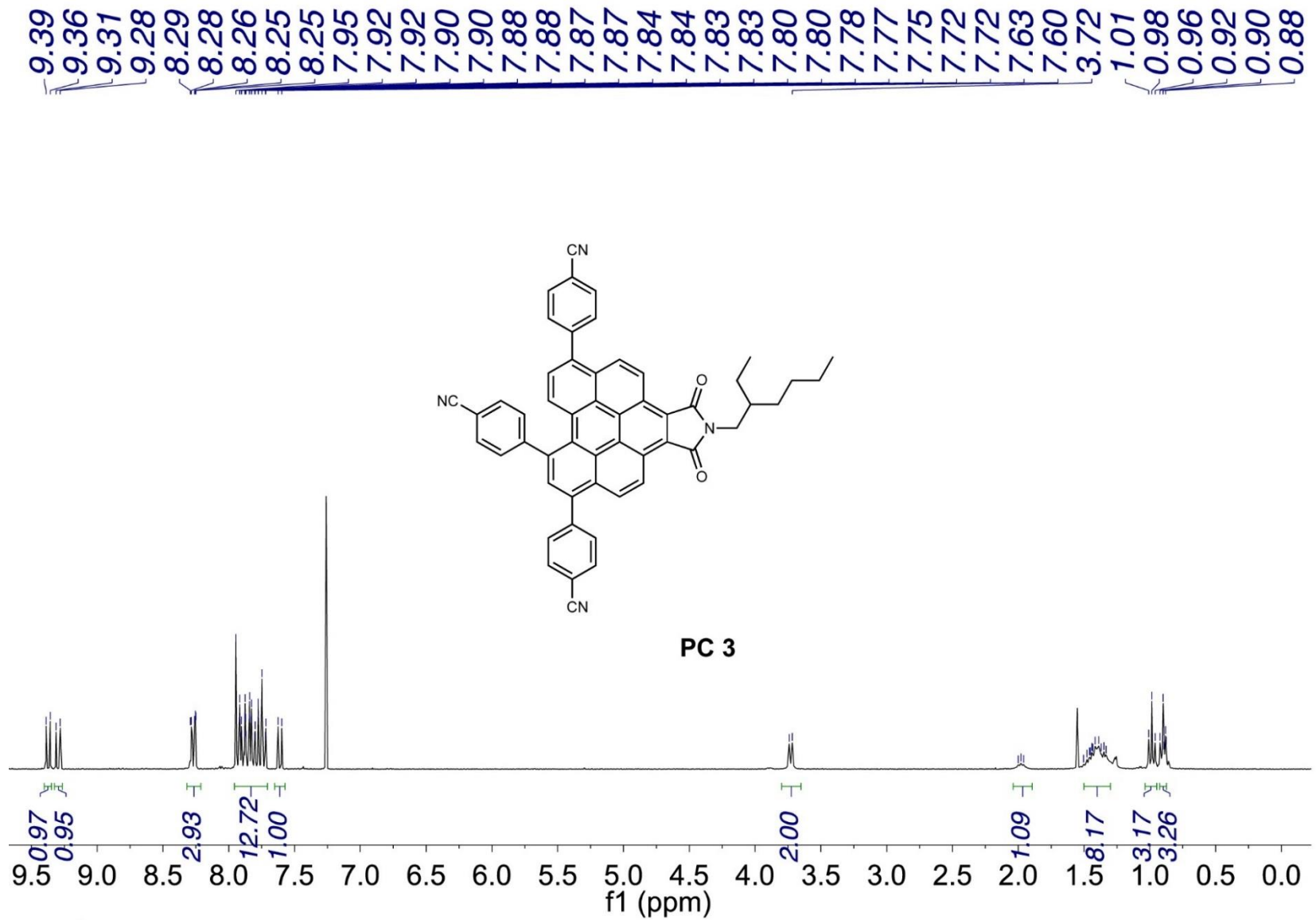


Fig. S5.49.  $^1\text{H}$  NMR of compound PC 3 ( $\text{CDCl}_3$ , 300 MHz).

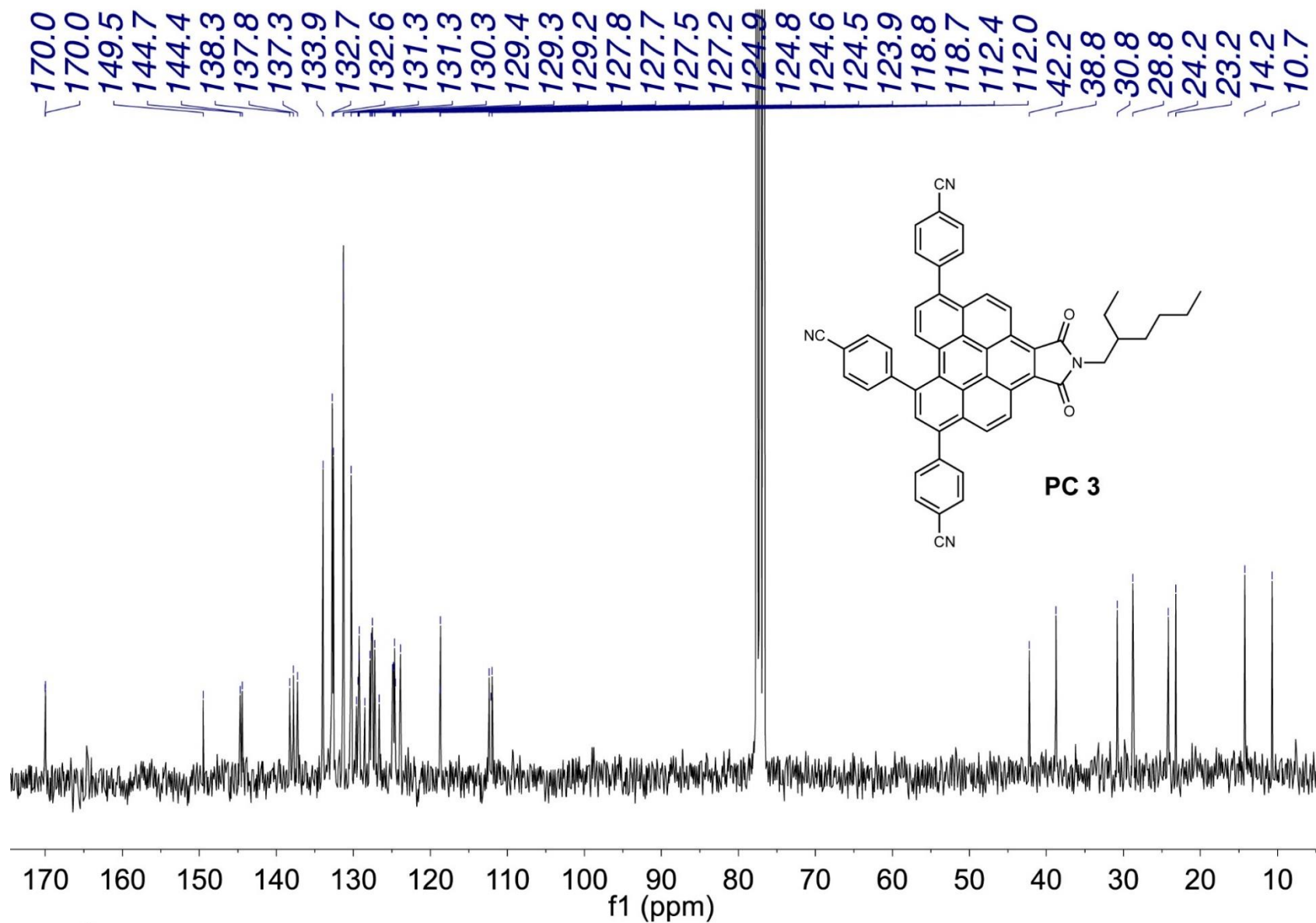


Fig. S5.50.  $^{13}\text{C}$  NMR of compound PC 3 ( $\text{CDCl}_3$ , 300 MHz).

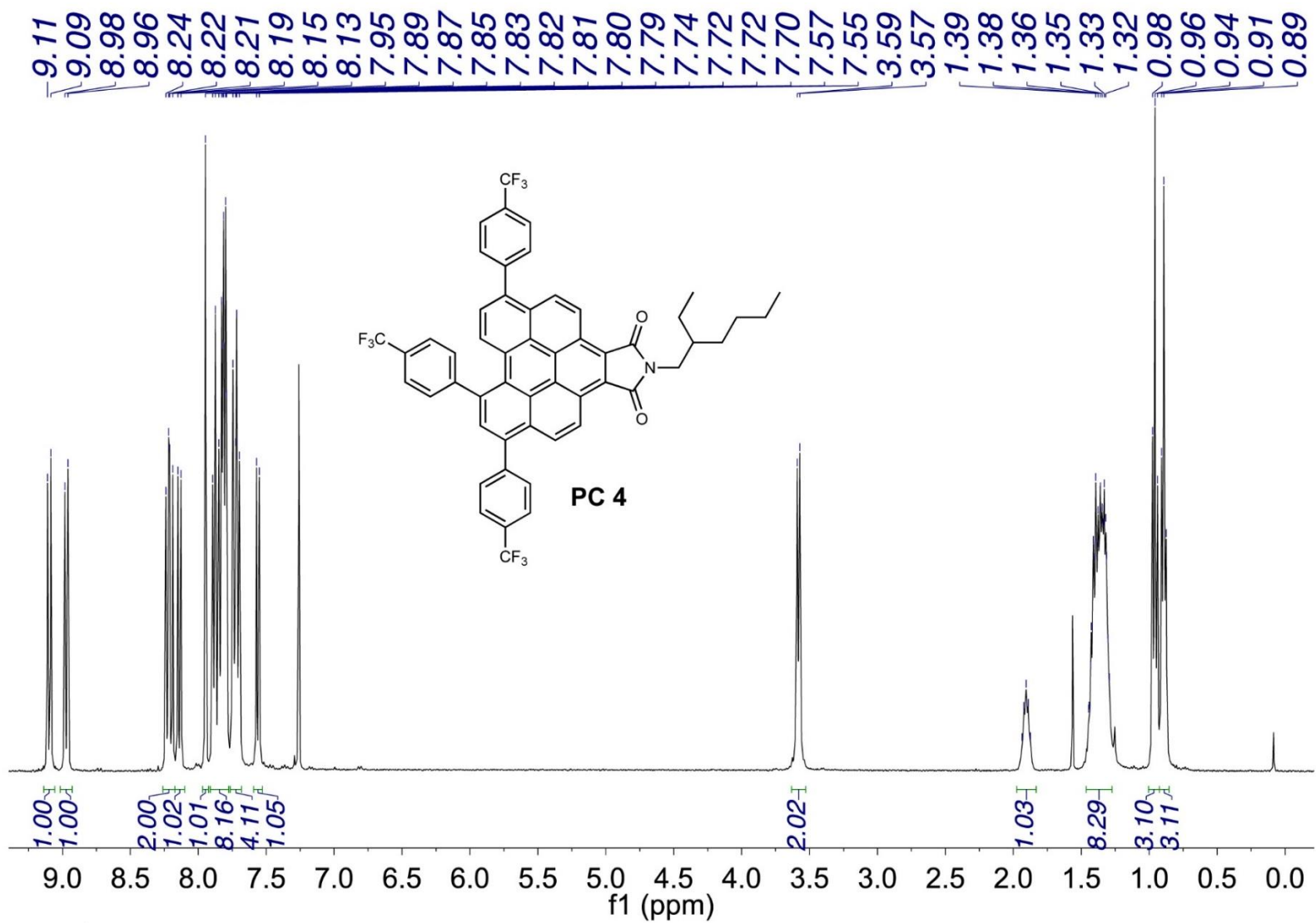


Fig. S5.51.  $^1\text{H}$  NMR of compound PC 4 ( $\text{CDCl}_3$ , 300 MHz).



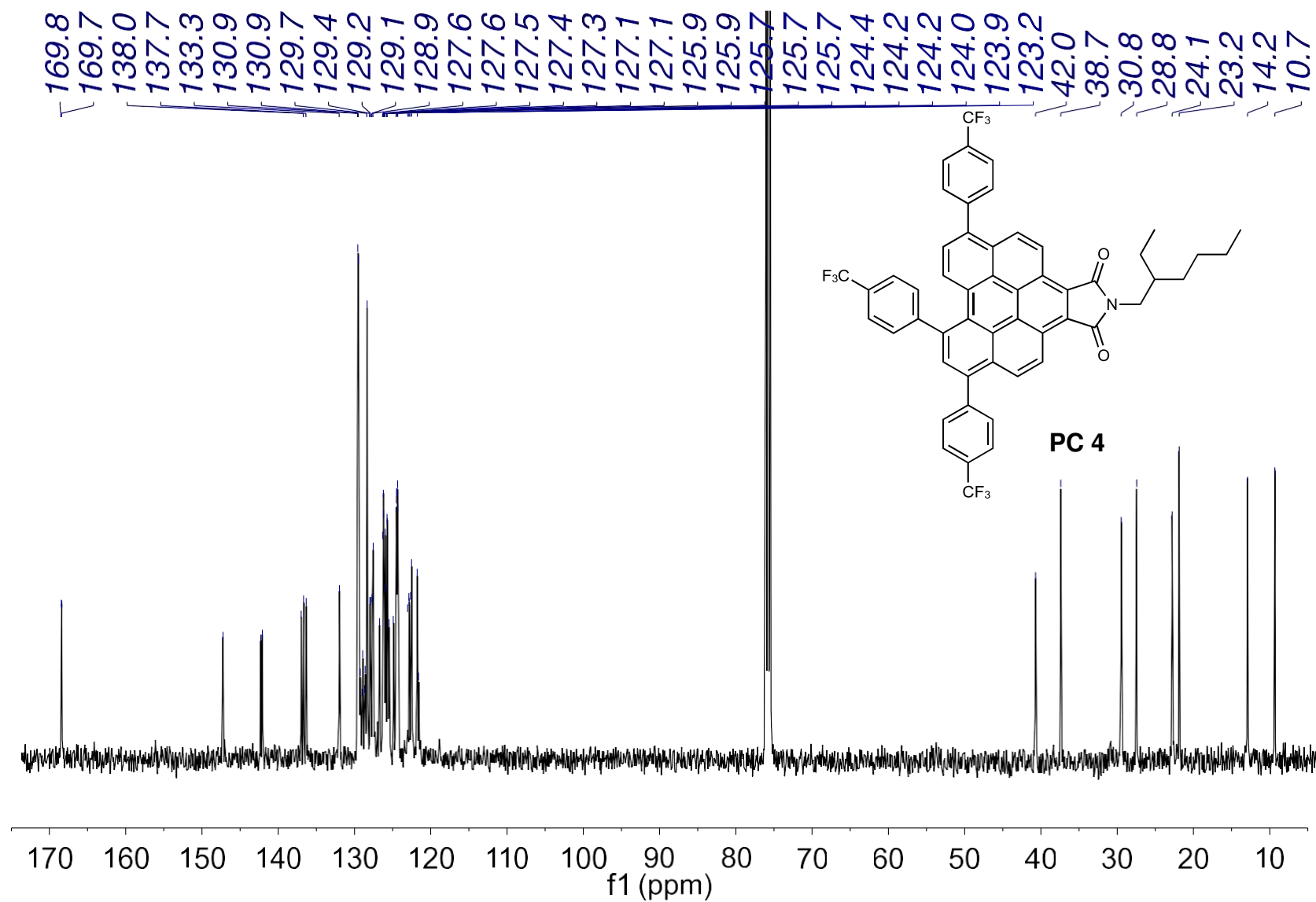


Fig. S5.52. <sup>13</sup>C NMR of compound PC 4 (CDCl<sub>3</sub>, 101 MHz).

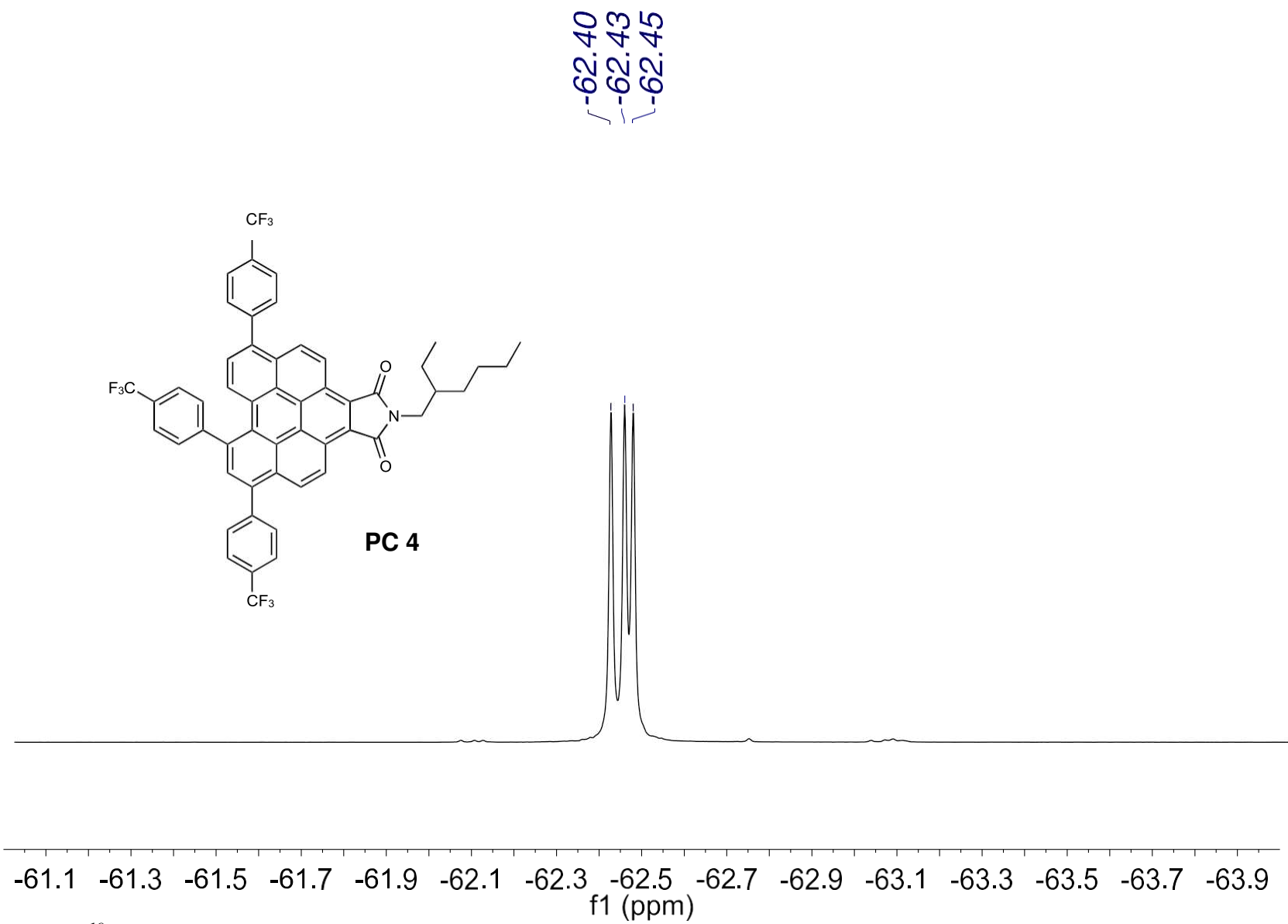


Fig. S5.53.  $^{19}\text{F}$  NMR of compound PC 4 ( $\text{CDCl}_3$ , 282 MHz).

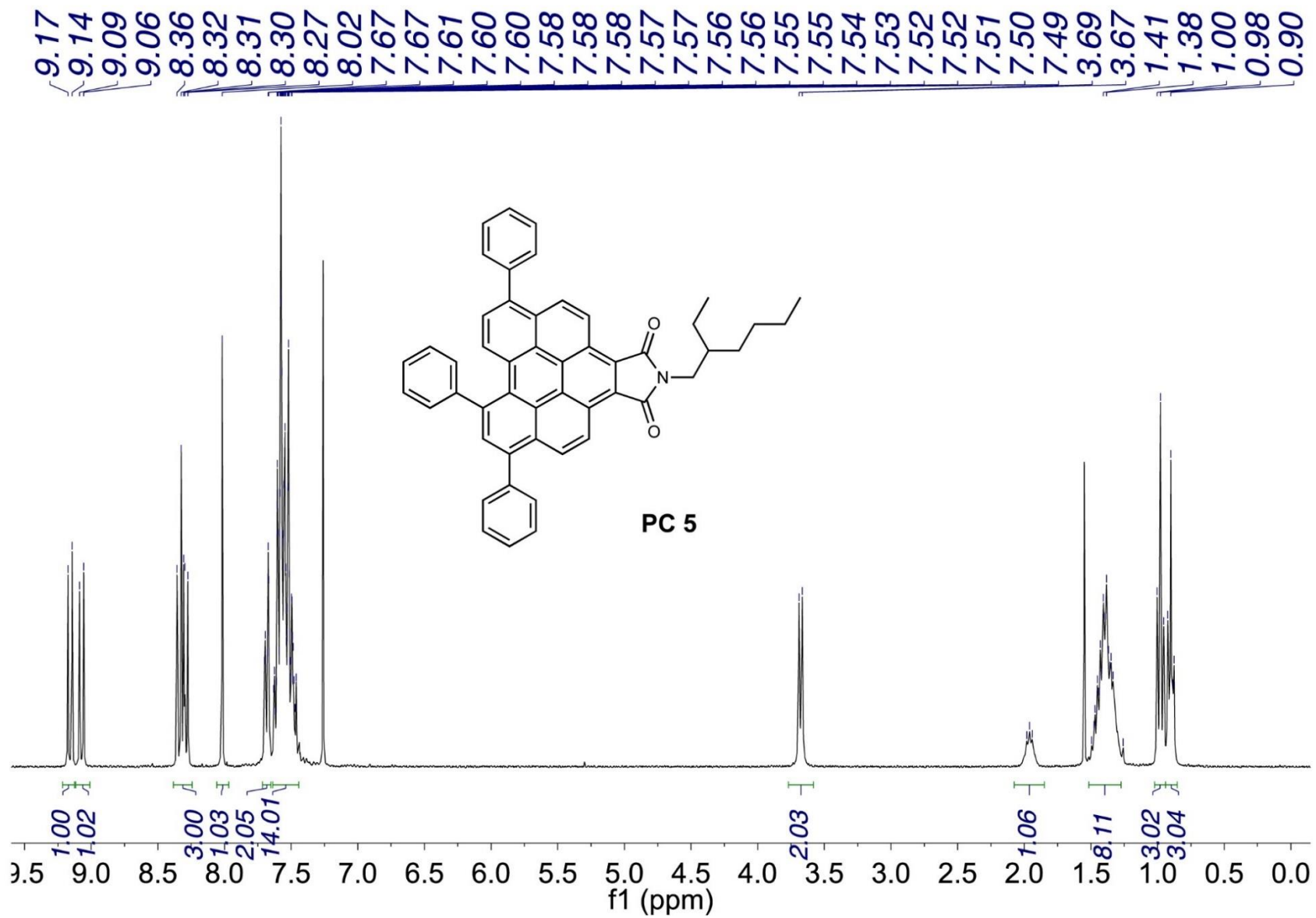


Fig. S5.54.  $^1\text{H}$  NMR of compound PC 5 ( $\text{CDCl}_3$ , 282 MHz).

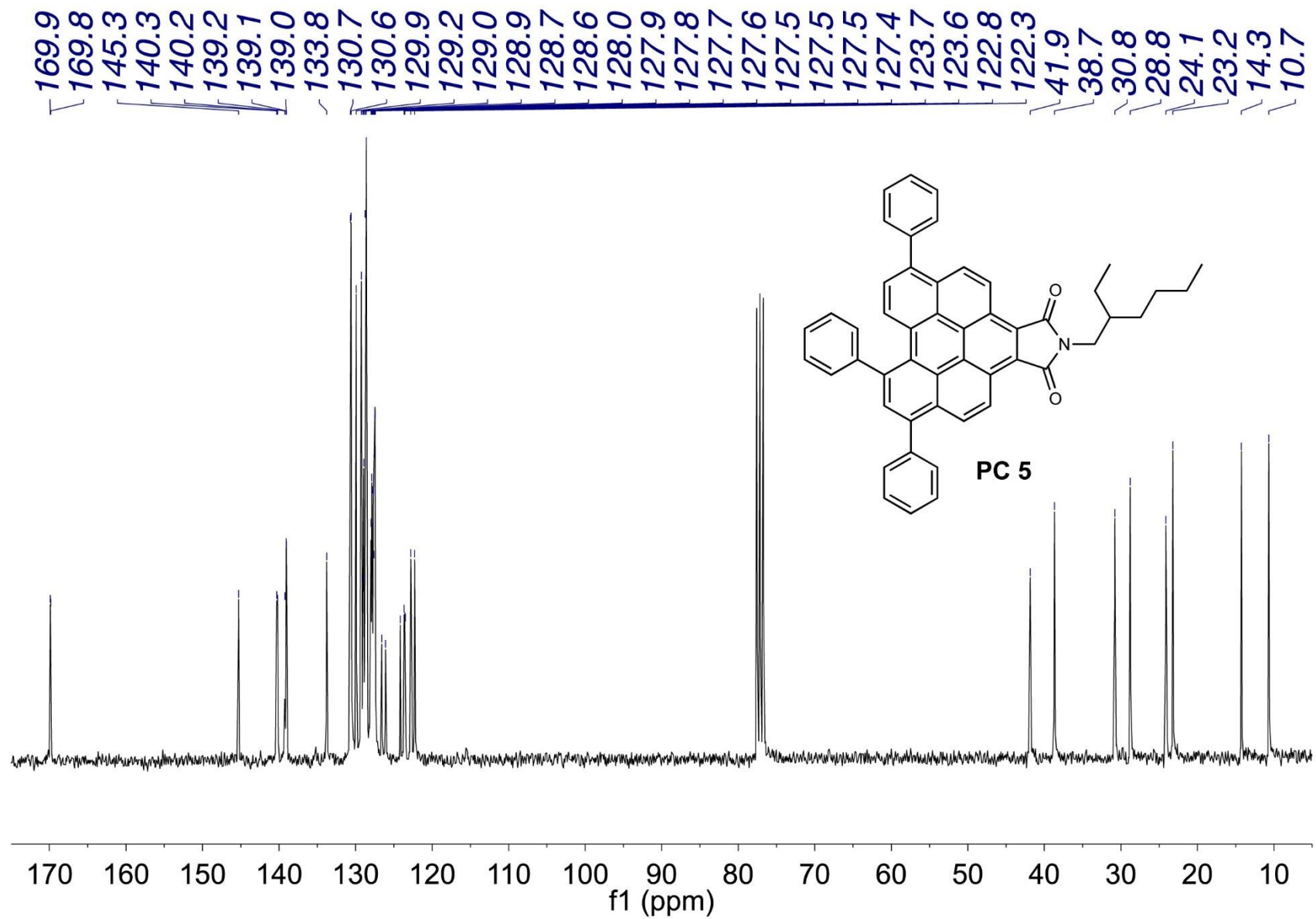


Fig. S5.55.  $^{13}\text{C}$  NMR of compound PC 5 ( $\text{CDCl}_3$ , 282 MHz).

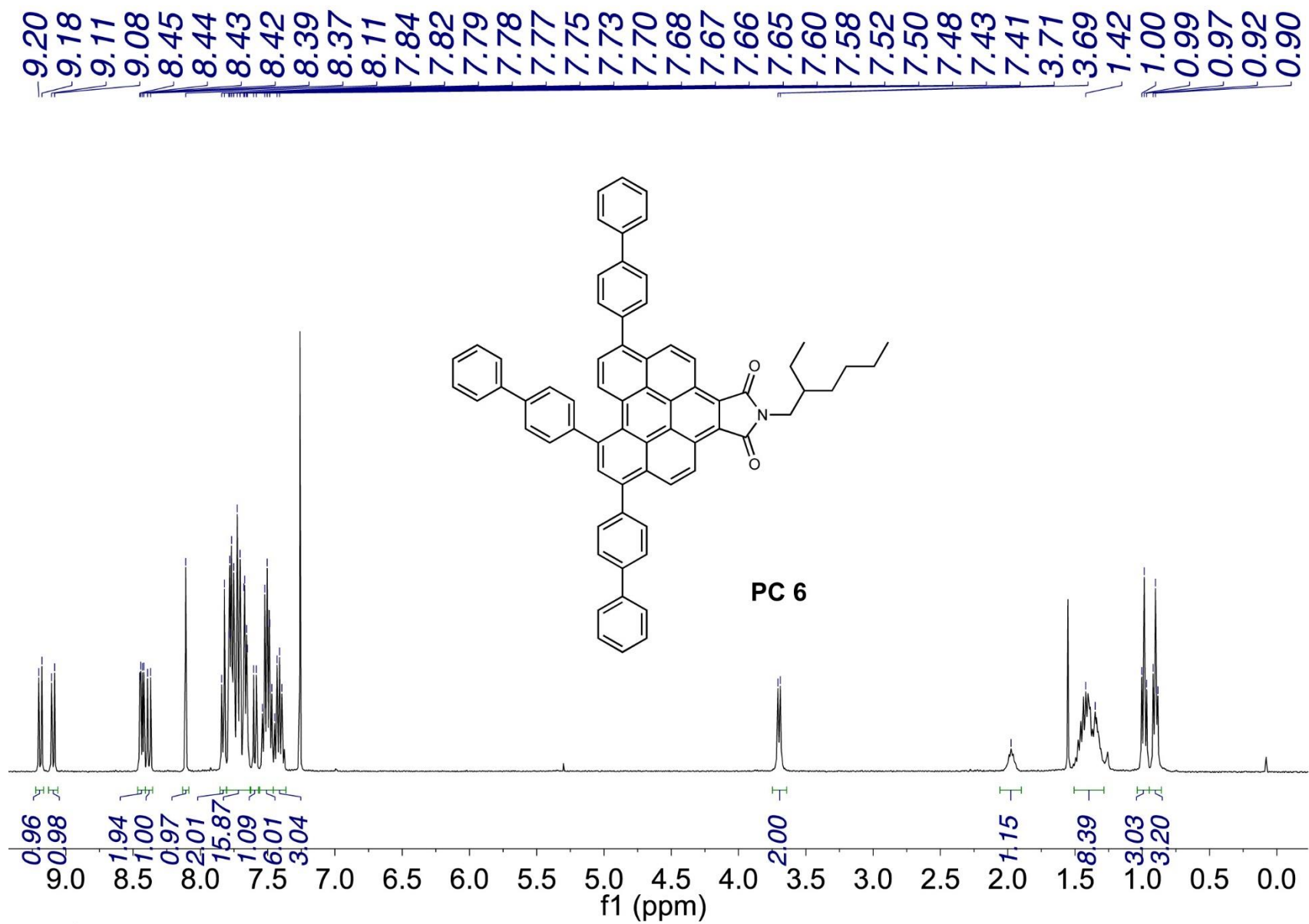


Fig. S5.56.  $^1\text{H}$  NMR of compound PC 6 ( $\text{CDCl}_3$ , 282 MHz).

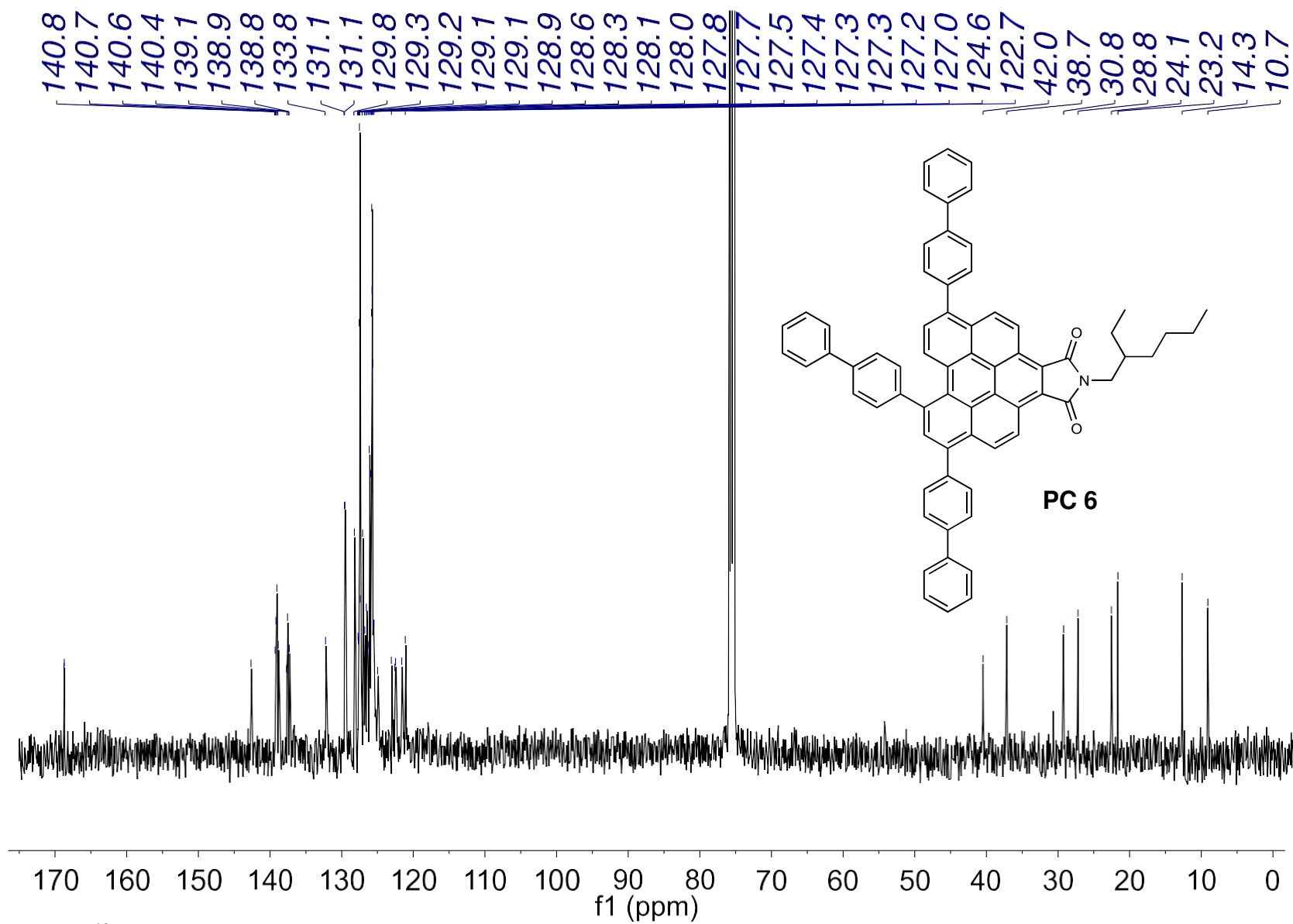


Fig. S5.57.  $^{13}\text{C}$  NMR of compound PC 6 ( $\text{CDCl}_3$ , 101 MHz).

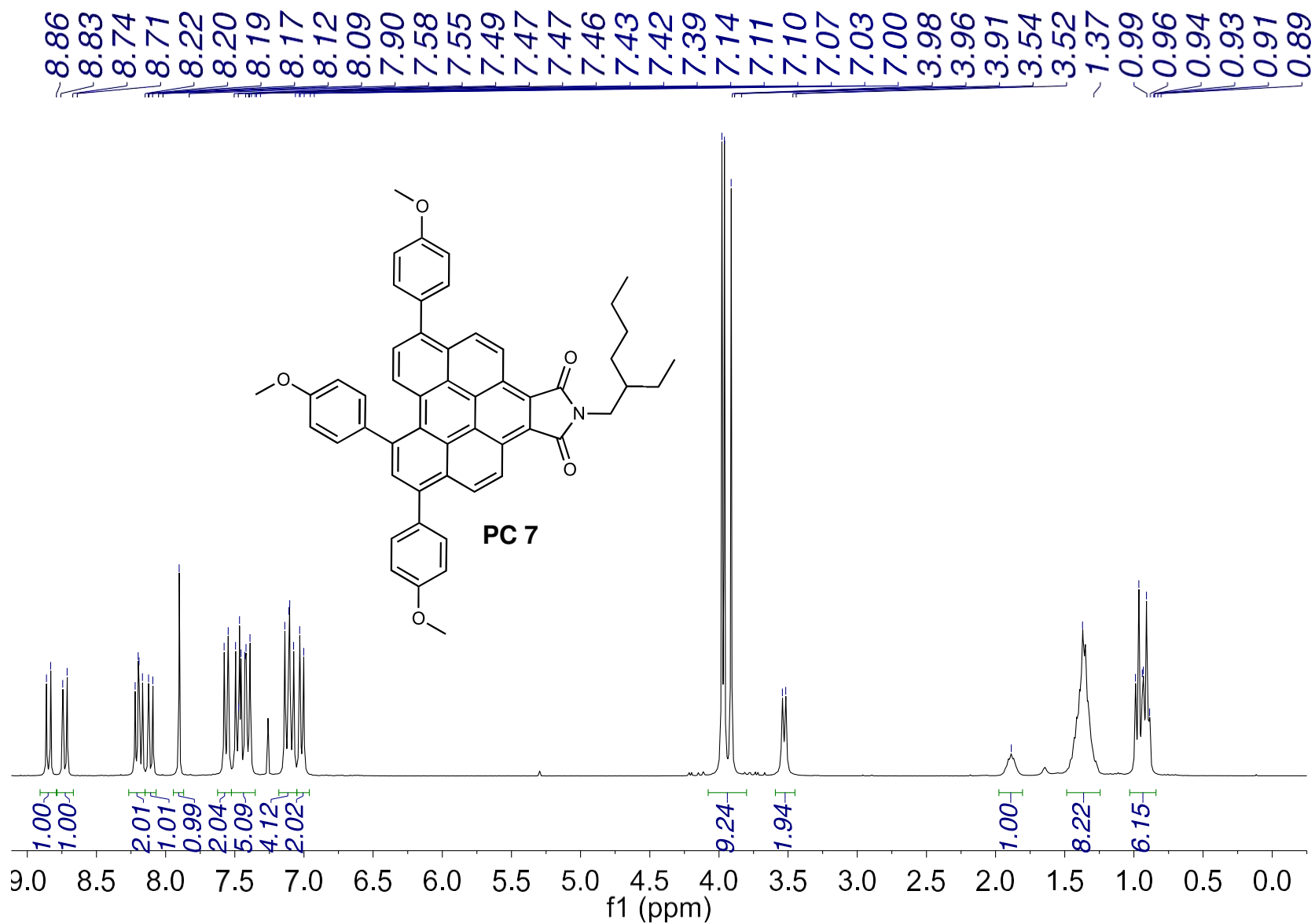


Fig. S5.58.  $^1\text{H}$  NMR of compound PC 7 ( $\text{CDCl}_3$ , 300 MHz).

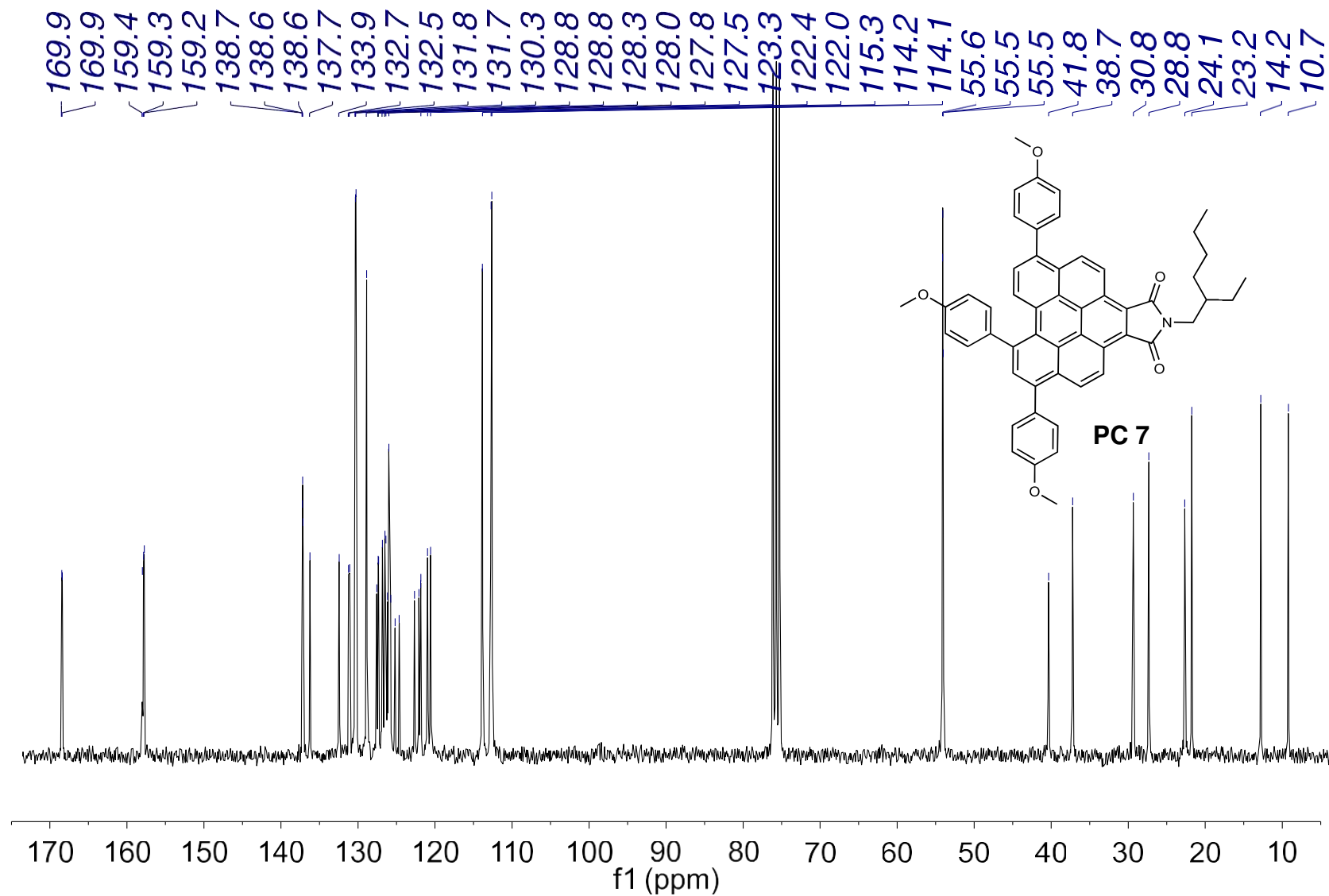


Fig. S5.59.  $^{13}\text{C}$  NMR of compound PC 7 ( $\text{CDCl}_3$ , 75 MHz).



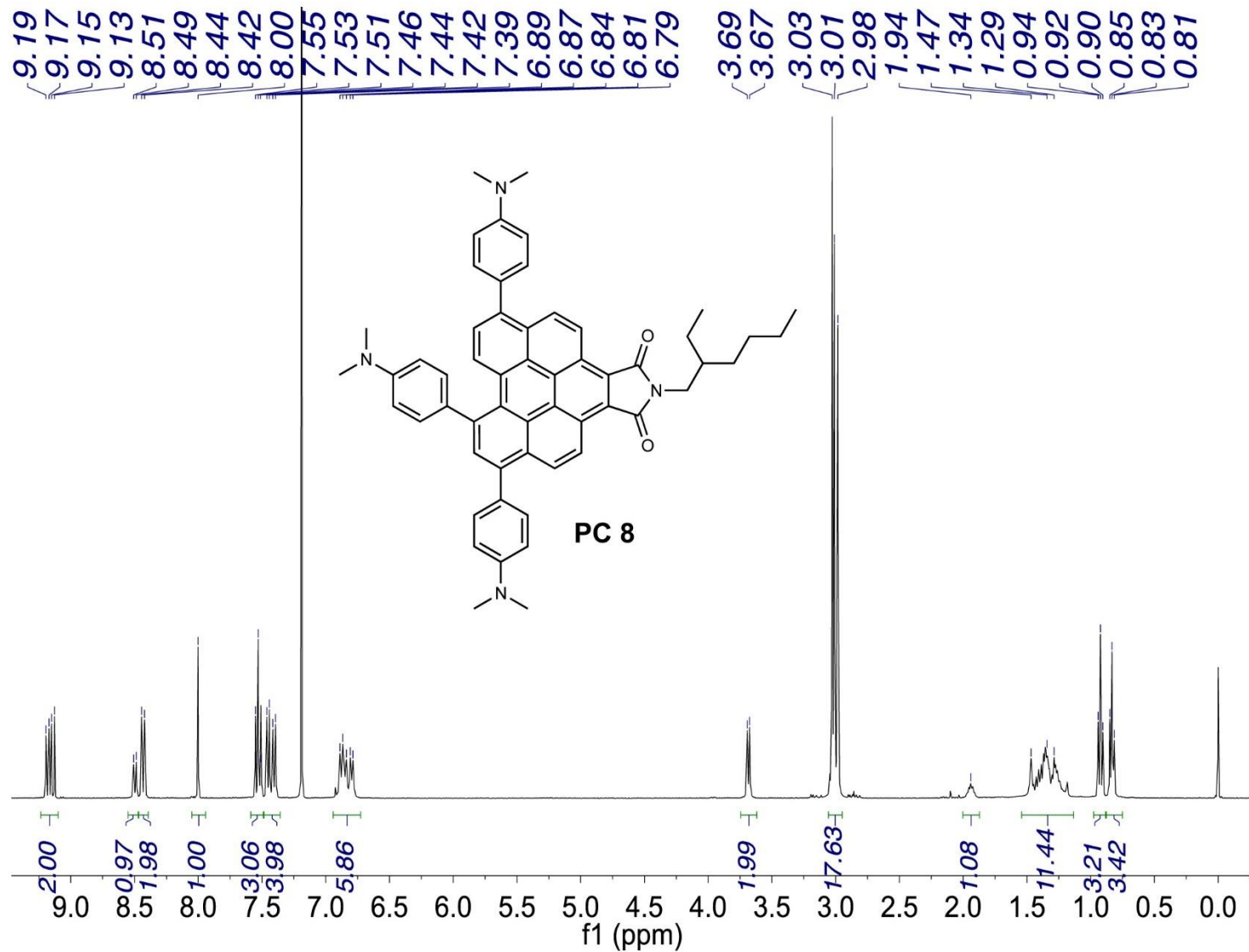


Fig. S5.60. <sup>1</sup>H NMR of compound PC 8 (CDCl<sub>3</sub>, 400 MHz).

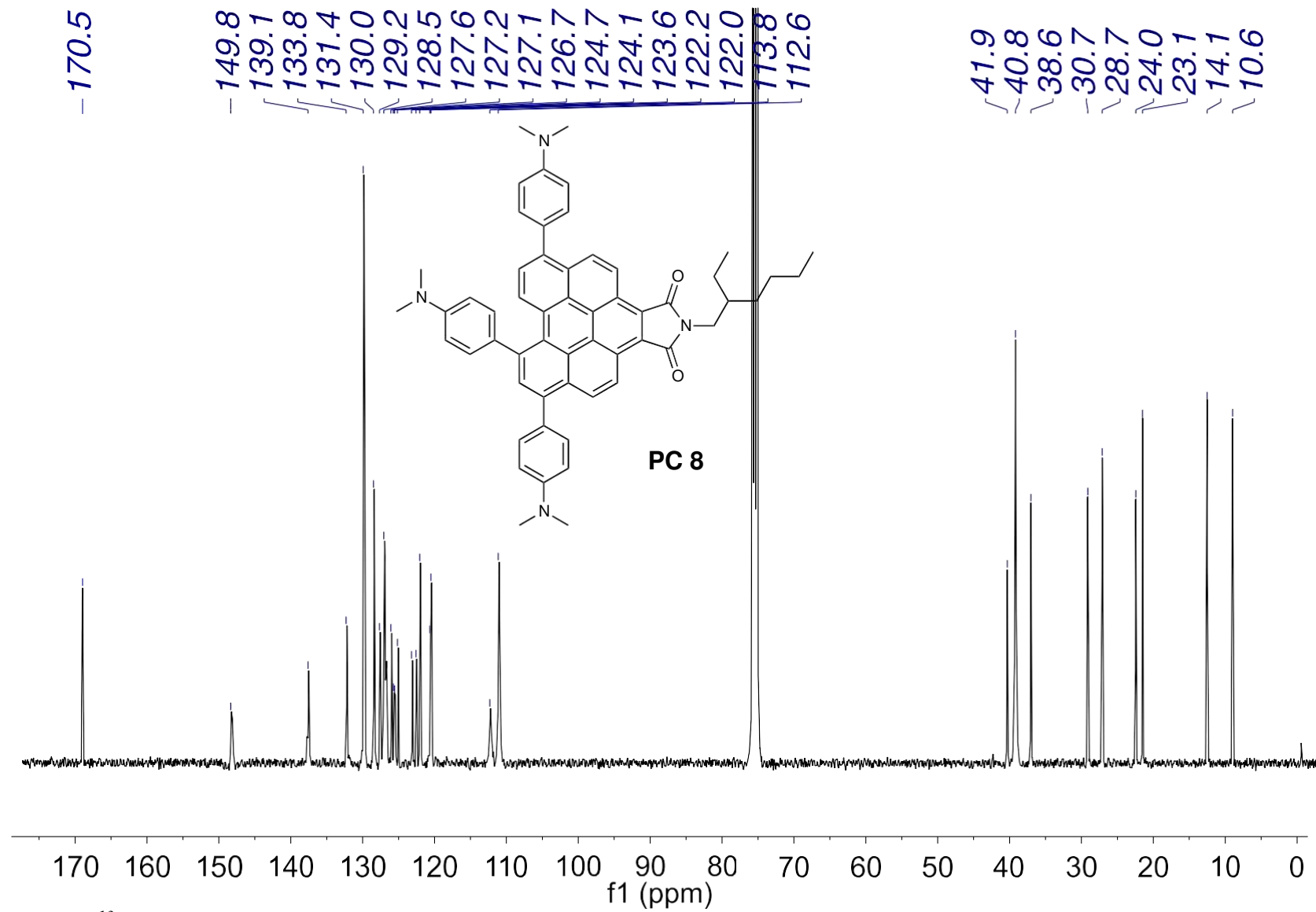


Fig. S5.61.  $^{13}\text{C}$  NMR of compound PC 8 ( $\text{CDCl}_3$ , 101 MHz).

# NMR Spectra of Substrates

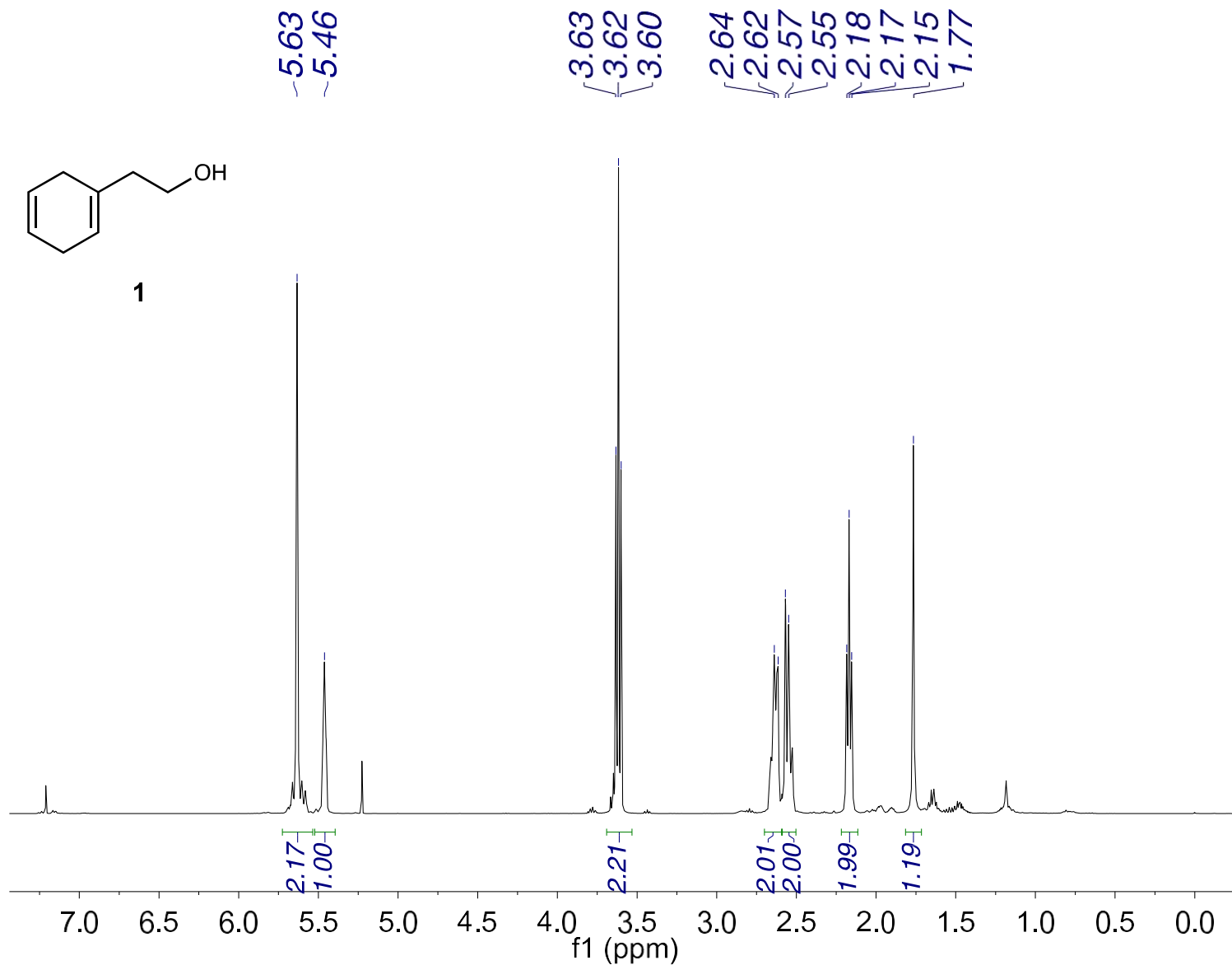


Fig. S5.62: <sup>1</sup>H NMR of 2-(cyclohexa-1,4-dien-1-yl)ethan-1-ol (1) (CDCl<sub>3</sub>, 400 MHz).

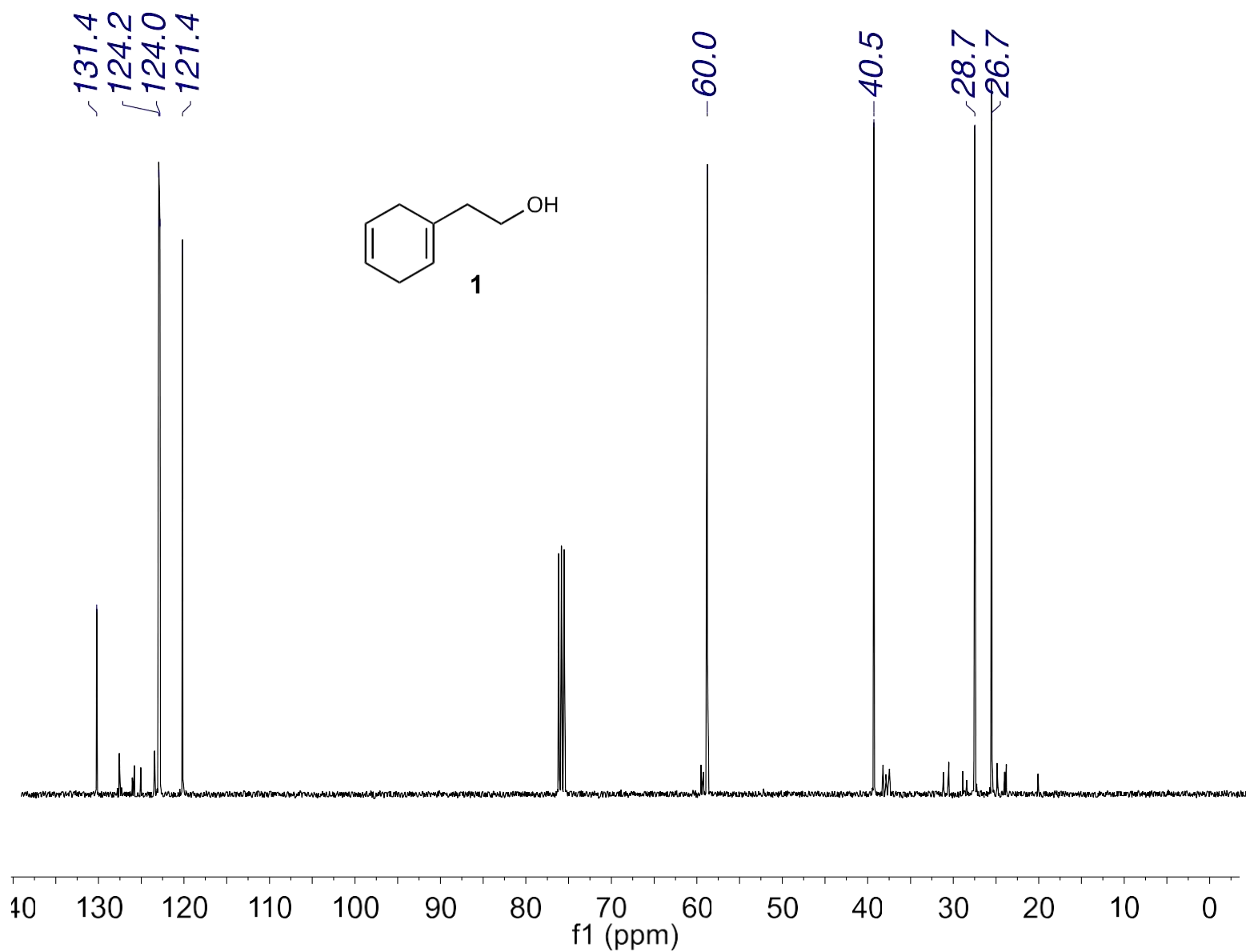


Fig. S5.63.  $^{13}\text{C}$  NMR of 2-(cyclohexa-1,4-dien-1-yl)ethan-1-ol (1) ( $\text{CDCl}_3$ , 101 MHz).

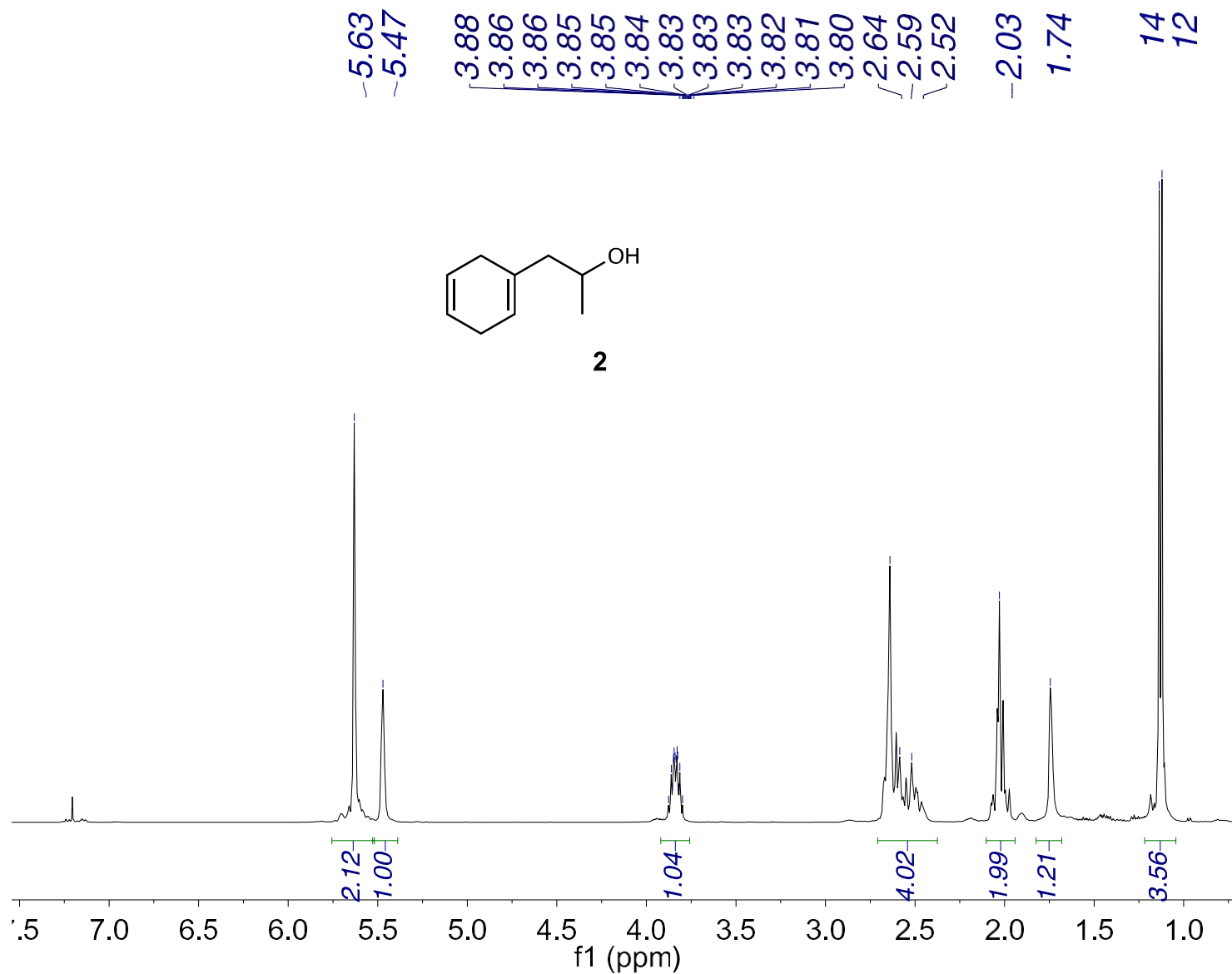


Fig. S5.64.  $^1\text{H}$  NMR of 1-(cyclohexa-1,4-dien-1-yl)propan-2-ol (2) ( $\text{CDCl}_3$ , 400 MHz).

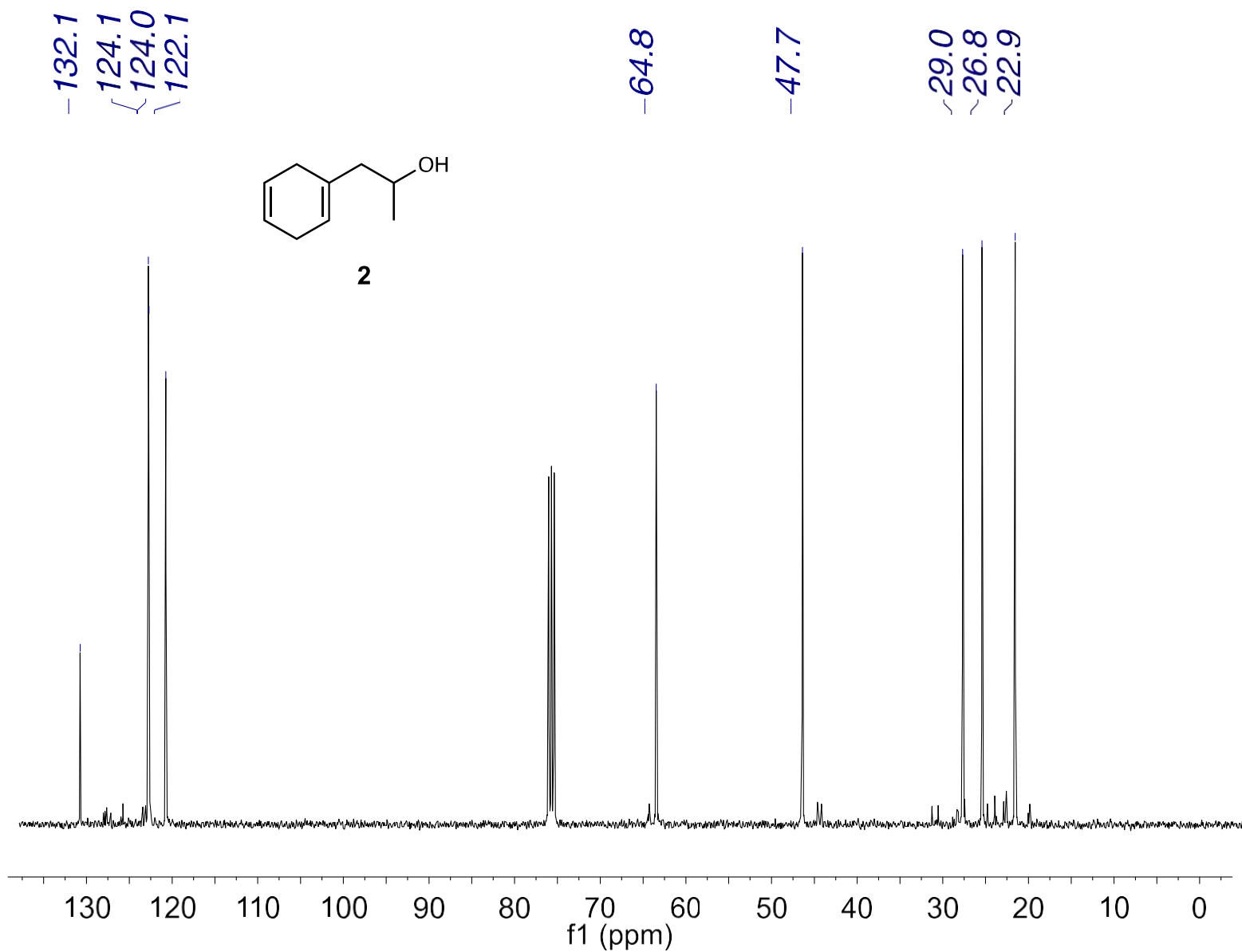


Fig. S5.65.  $^{13}\text{C}$  NMR of 1-(cyclohexa-1,4-dien-1-yl)propan-2-ol (2) ( $\text{CDCl}_3$ , 101 MHz).

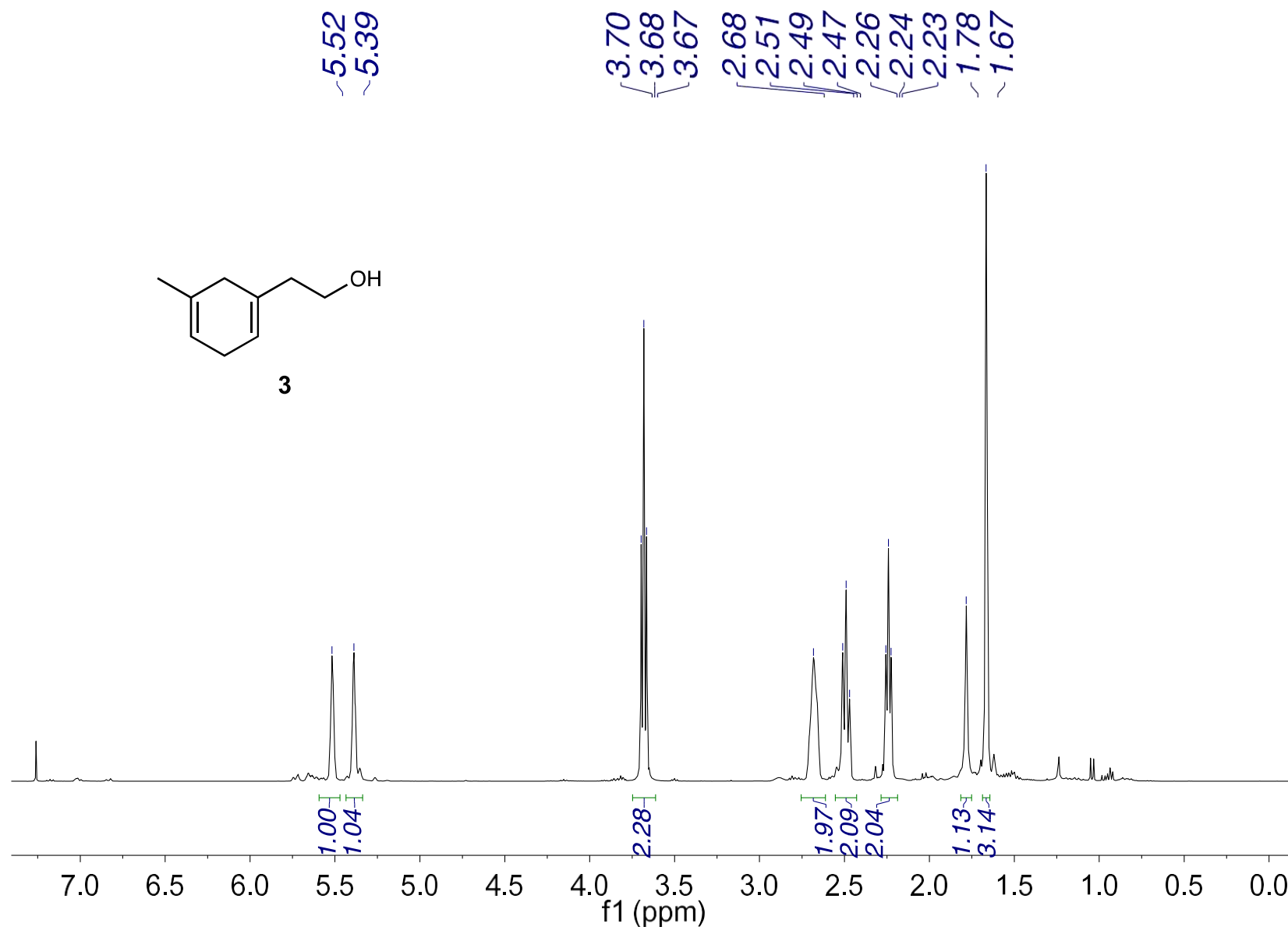


Fig. S5.66.  $^1\text{H}$  NMR of 2-(5-methylcyclohexa-1,4-dien-1-yl)ethan-1-ol (3) ( $\text{CDCl}_3$ , 400 MHz)

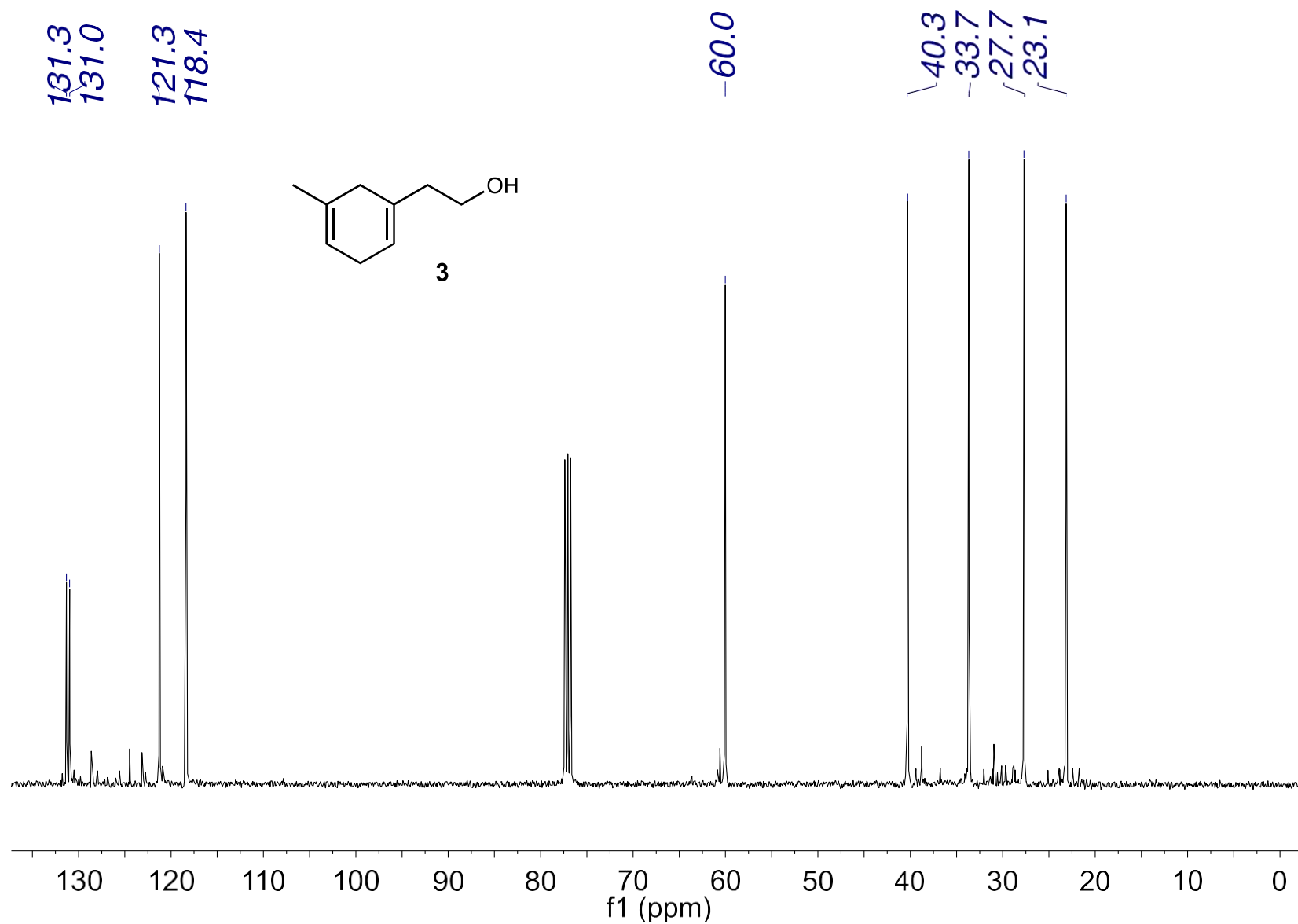


Fig. S5.67.  $^{13}\text{C}$  NMR of 2-(5-methylcyclohexa-1,4-dien-1-yl)ethan-1-ol (3) ( $\text{CDCl}_3$ , 101 MHz)



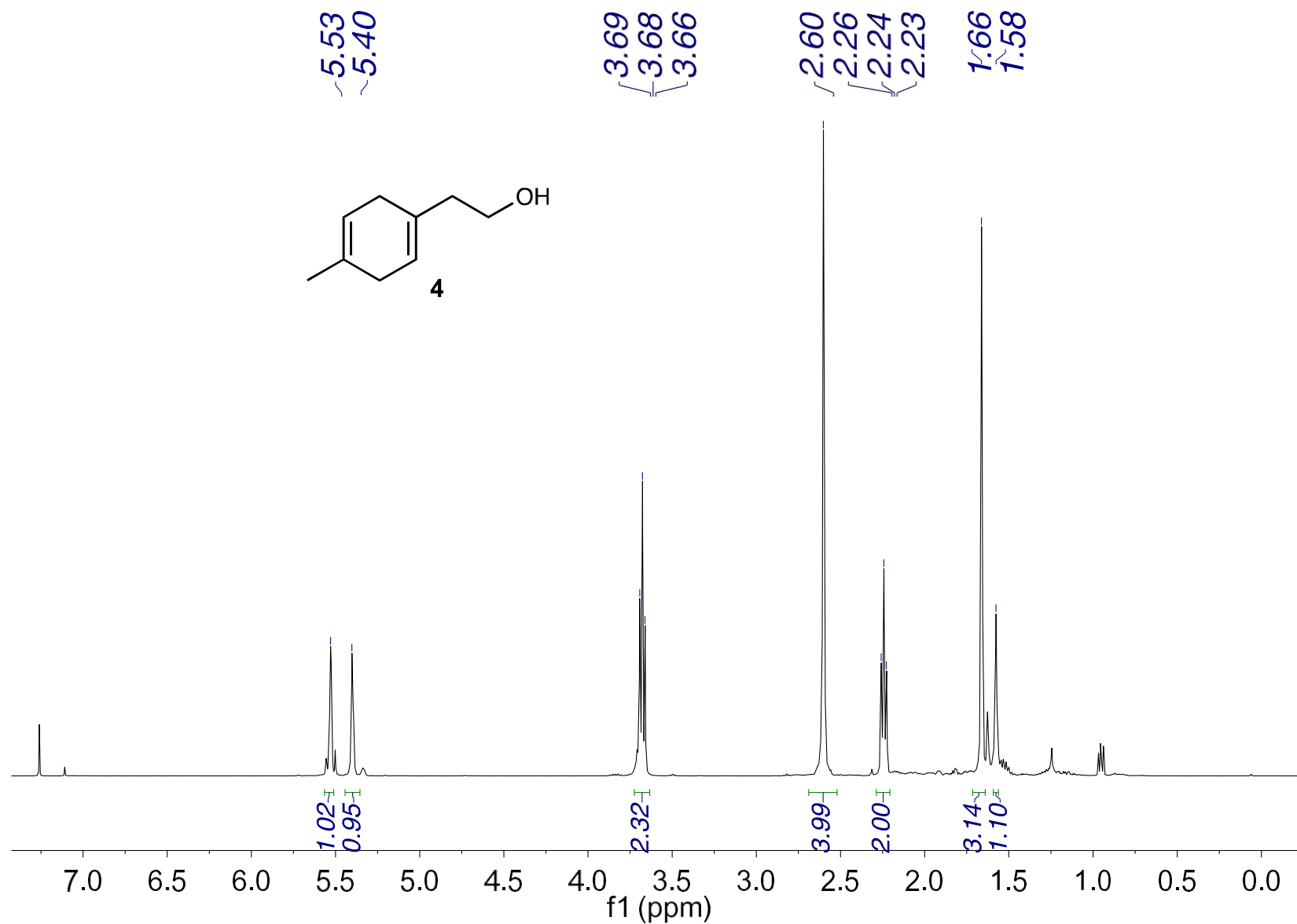
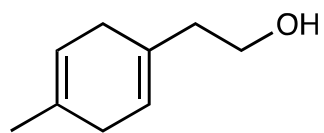


Fig. S5.68. <sup>1</sup>H NMR of 2-(4-methylcyclohexa-1,4-dien-1-yl)ethan-1-ol (4) (CDCl<sub>3</sub>, 400 MHz)



**4**

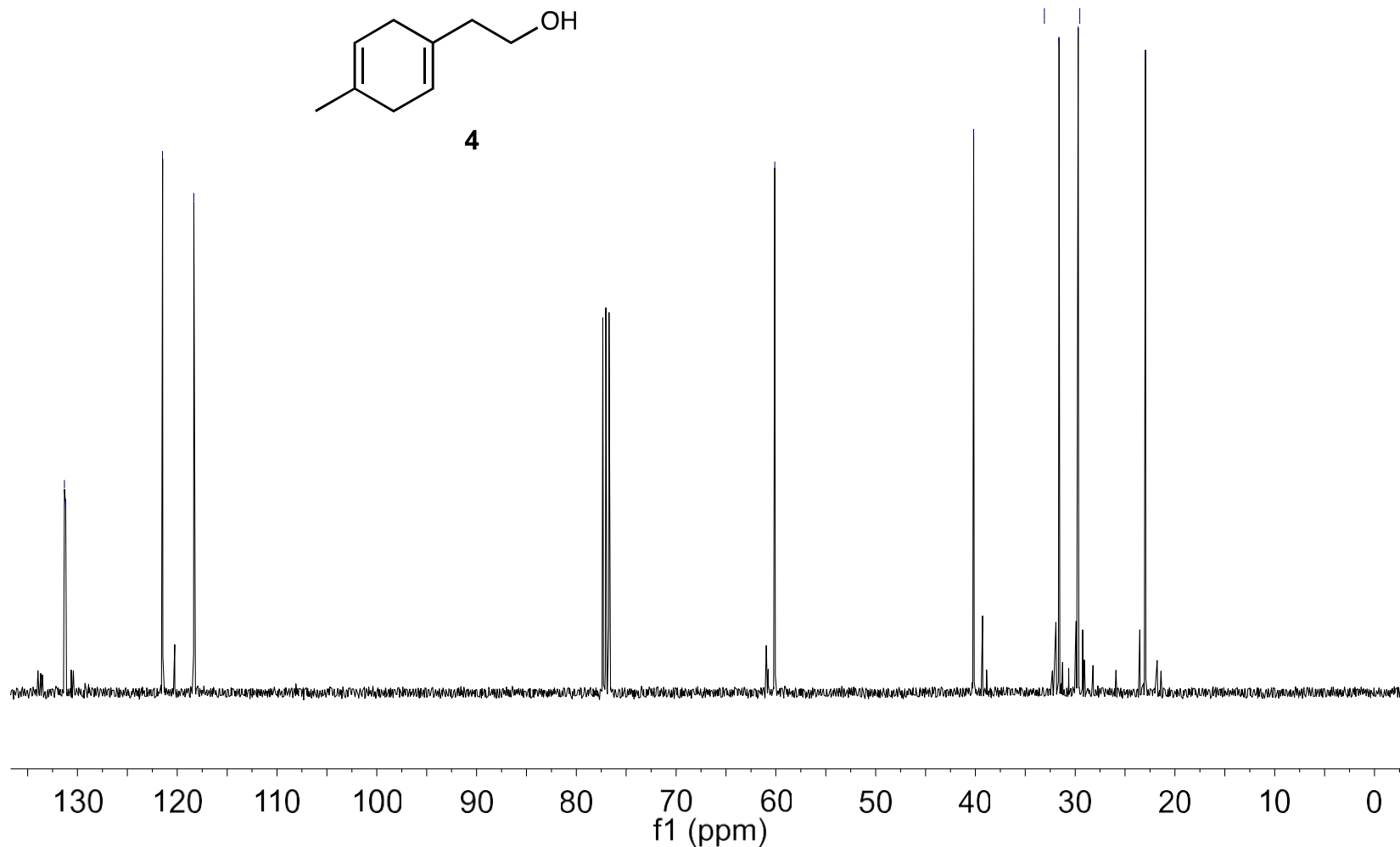


Fig. S5.69.  $^{13}\text{C}$  NMR of 2-(4-methylcyclohexa-1,4-dien-1-yl)ethan-1-ol (4) ( $\text{CDCl}_3$ , 101 MHz)

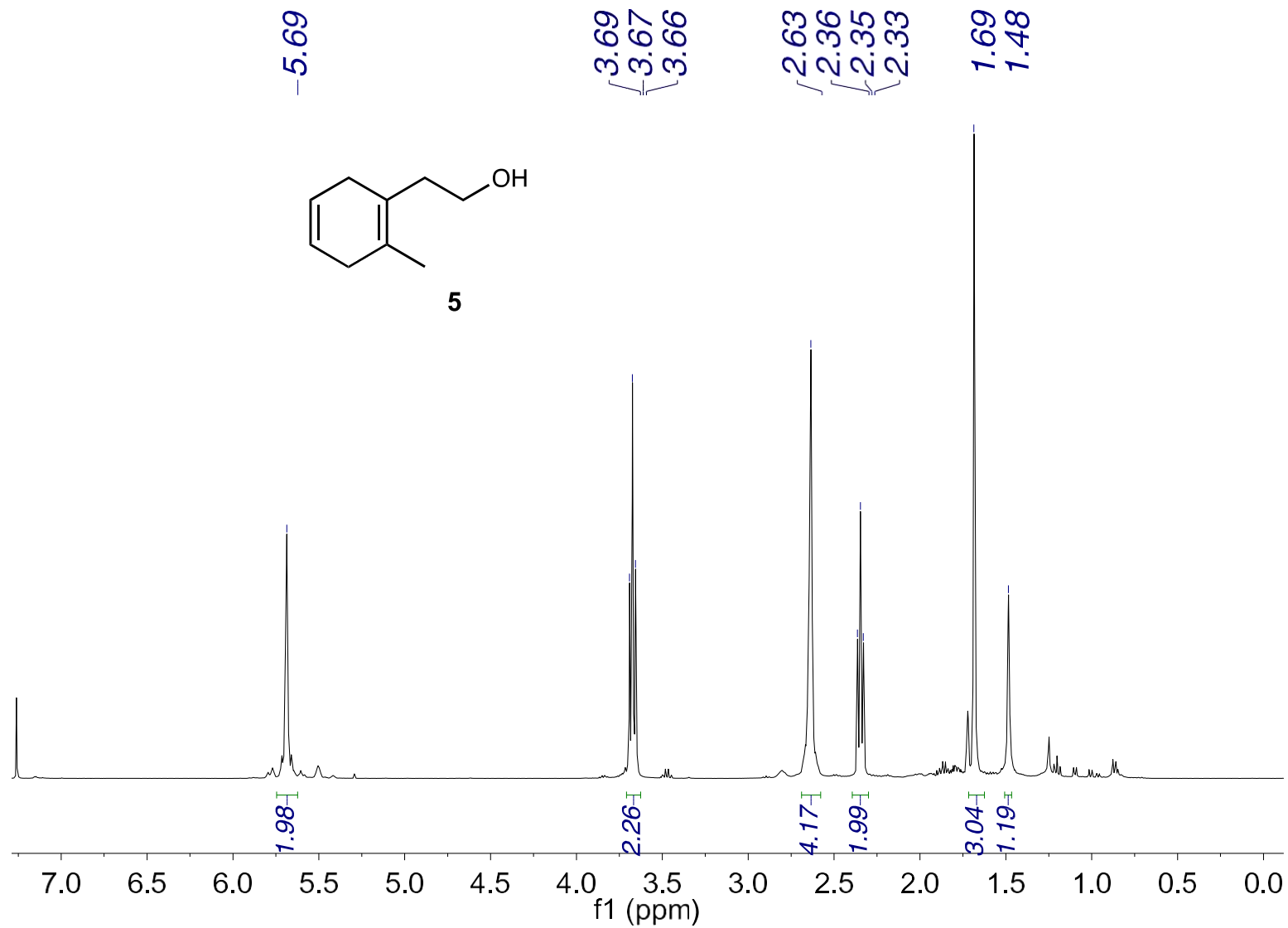


Fig. S5.70. <sup>1</sup>H NMR of 2-(2-methylcyclohexa-1,4-dien-1-yl)ethan-1-ol (5) (CDCl<sub>3</sub>, 400 MHz)

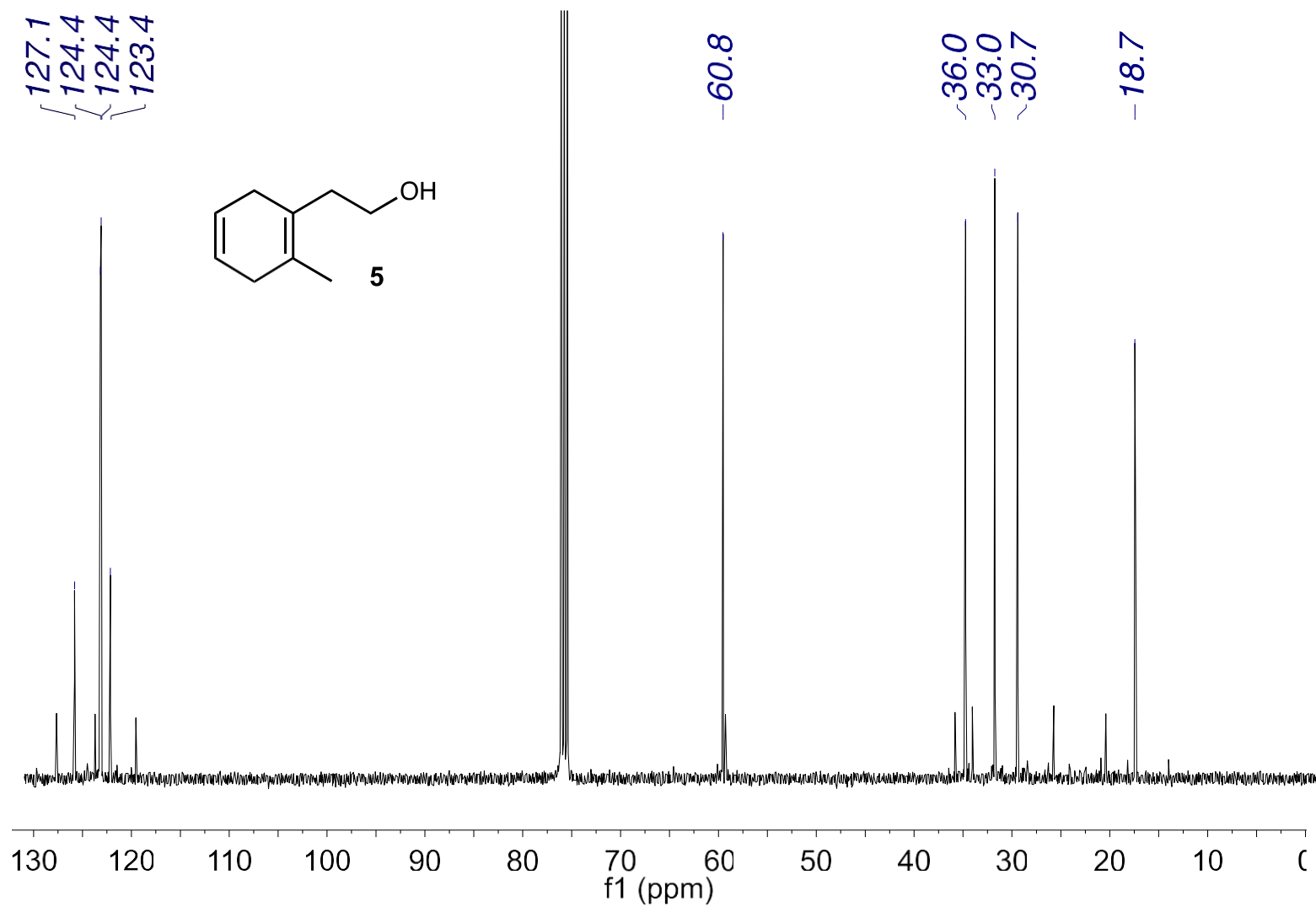


Fig. S5.71. <sup>13</sup>C NMR of 2-(2-methylcyclohexa-1,4-dien-1-yl)ethan-1-ol (5) (CDCl<sub>3</sub>, 101 MHz)

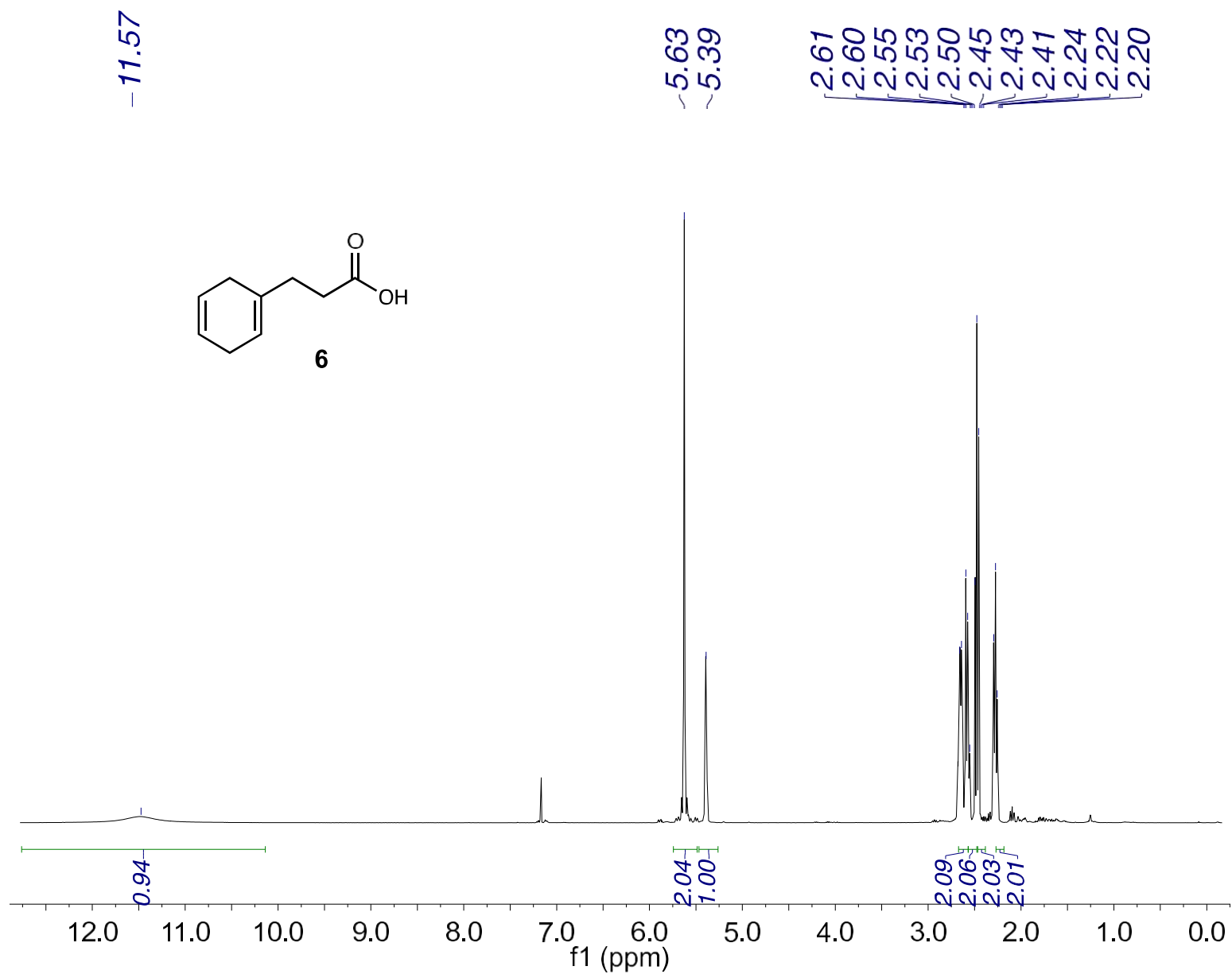


Fig. S5.72. <sup>1</sup>H NMR of 3-(cyclohexa-1,4-dien-1-yl)propanoic acid (6) (CDCl<sub>3</sub>, 400 MHz).

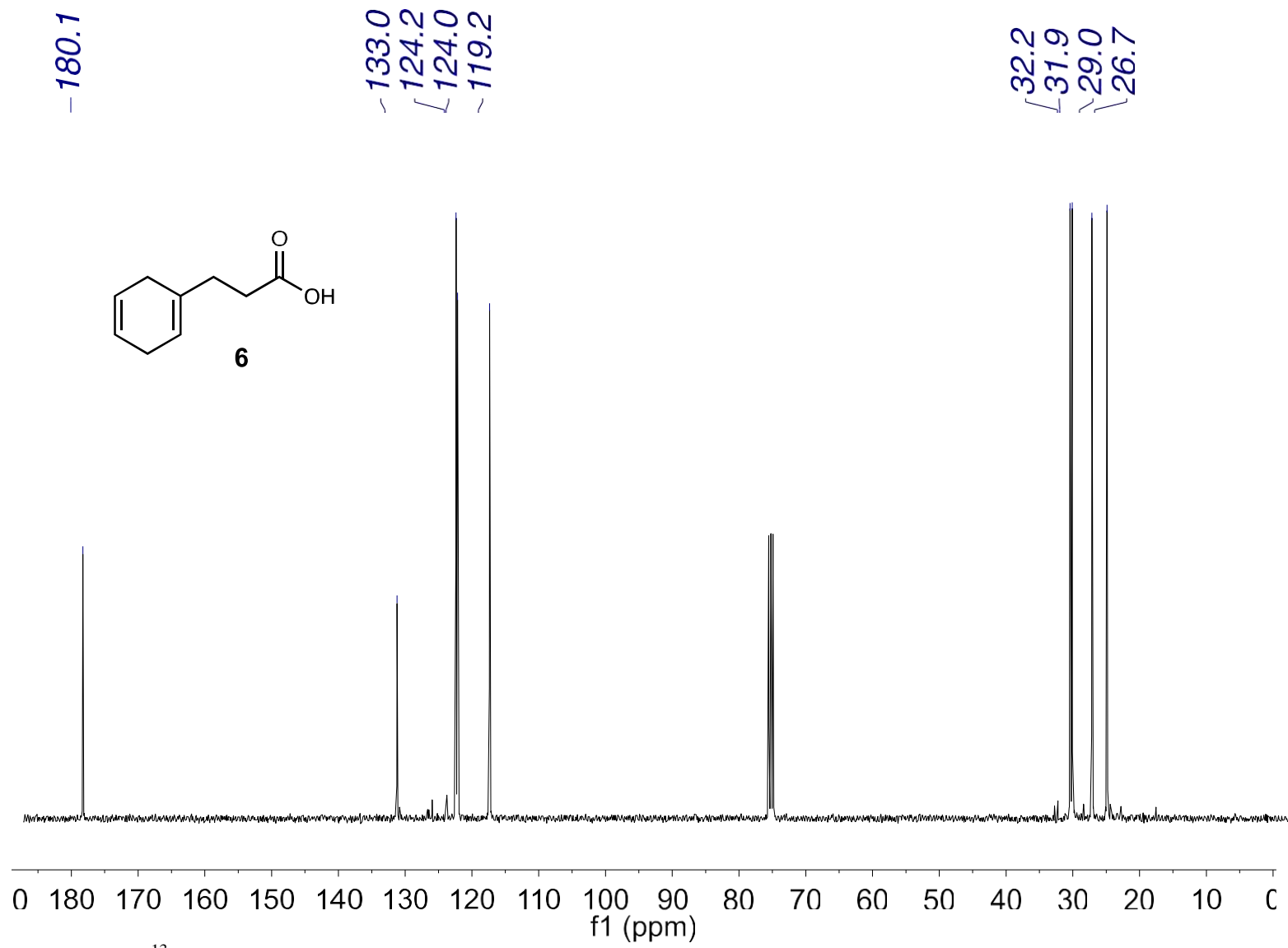


Fig. S5.73.  $^{13}\text{C}$  NMR of 3-(cyclohexa-1,4-dien-1-yl)propanoic acid (6) ( $\text{CDCl}_3$ , 101 MHz).

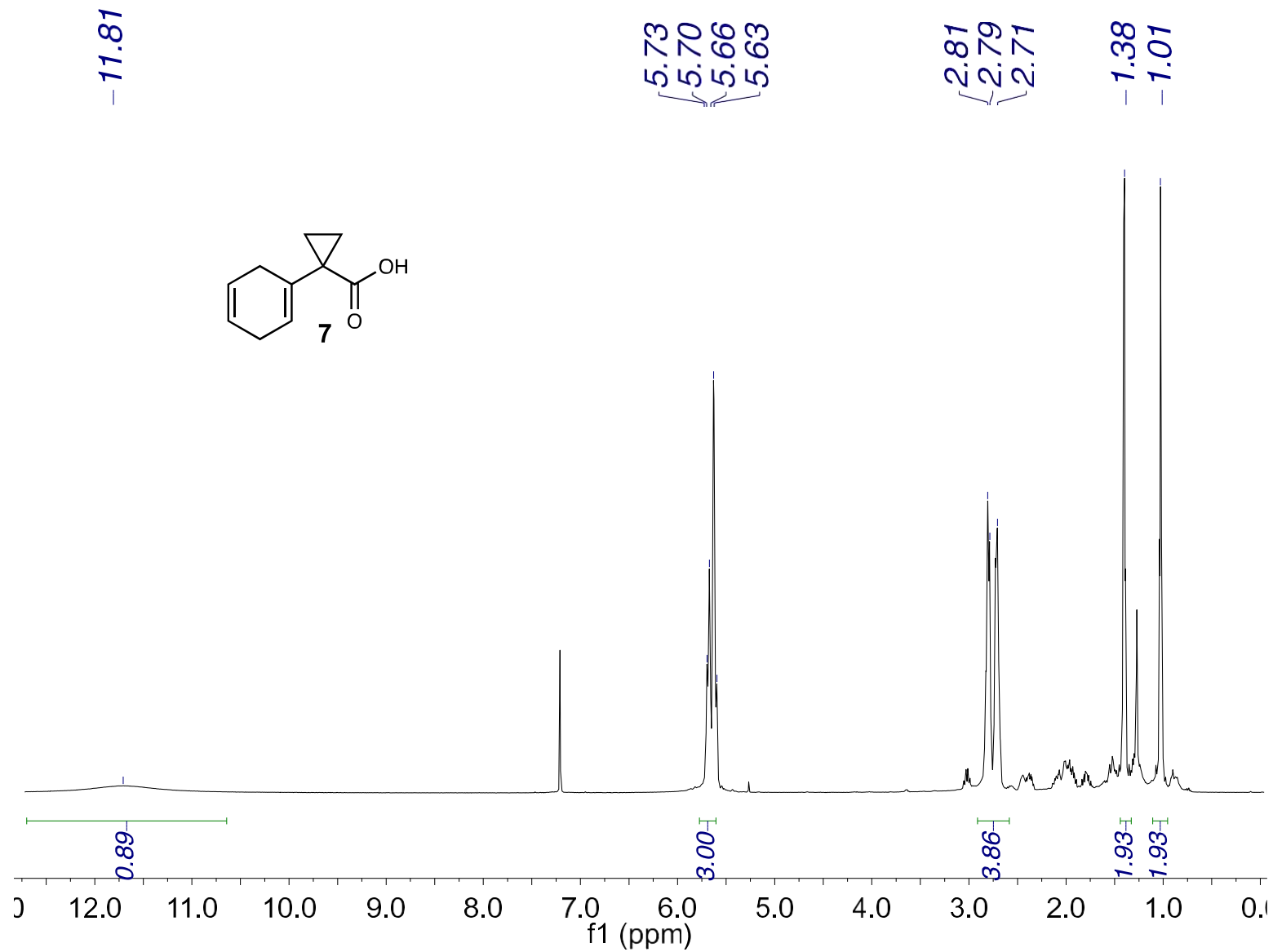


Fig. S5.74. <sup>1</sup>H NMR of 1-(cyclohexa-1,4-dien-1-yl)cyclopropane-1-carboxylic acid (7) (CDCl<sub>3</sub>, 400 MHz).

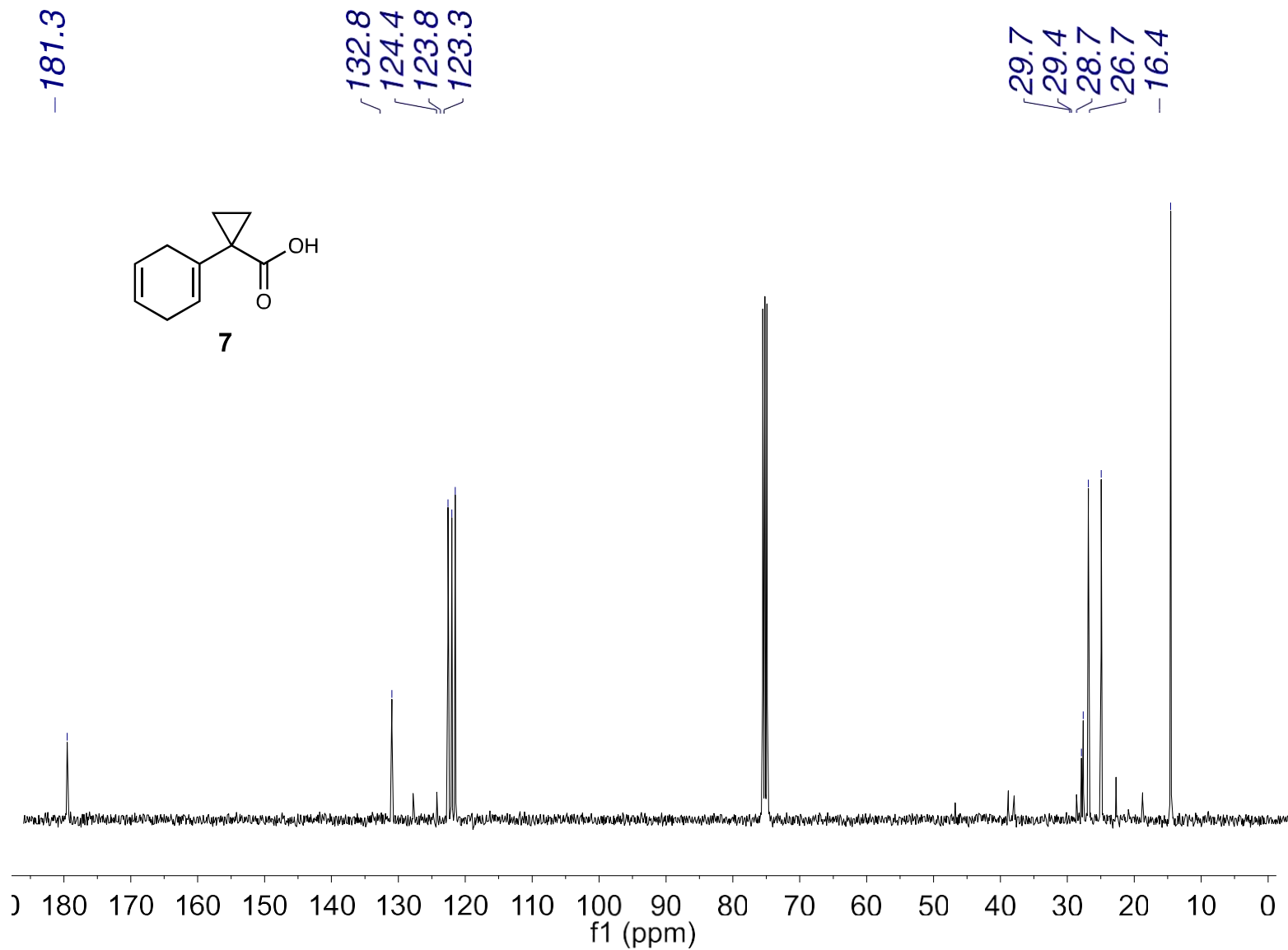


Fig. S5.75.  $^{13}\text{C}$  NMR of 1-(cyclohexa-1,4-dien-1-yl)cyclopropane-1-carboxylic acid (7) ( $\text{CDCl}_3$ , 101 MHz).



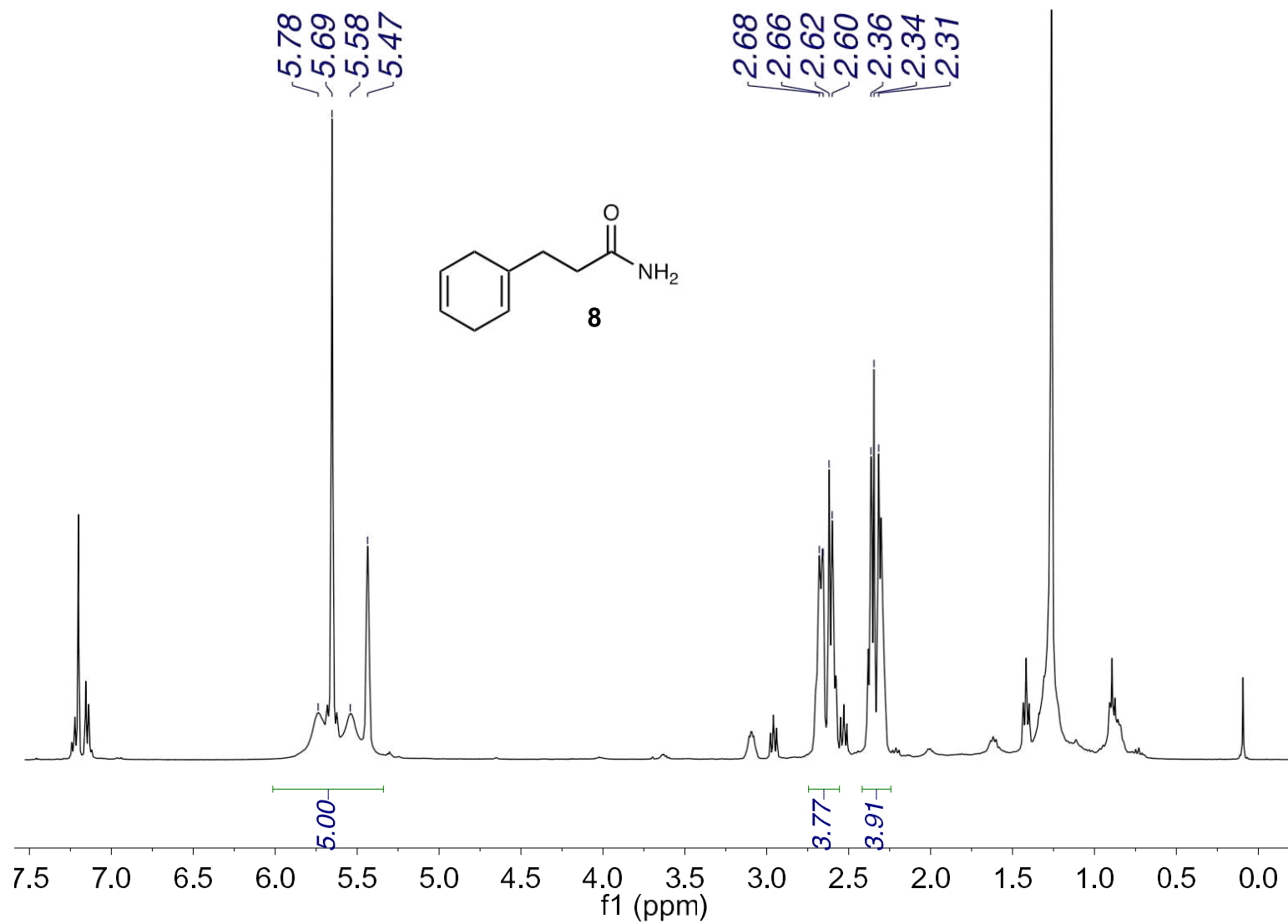


Fig. S5.76.  $^1\text{H}$  NMR of 3-(cyclohexa-1,4-dien-1-yl)propanamide (8) ( $\text{CDCl}_3$ , 400 MHz).

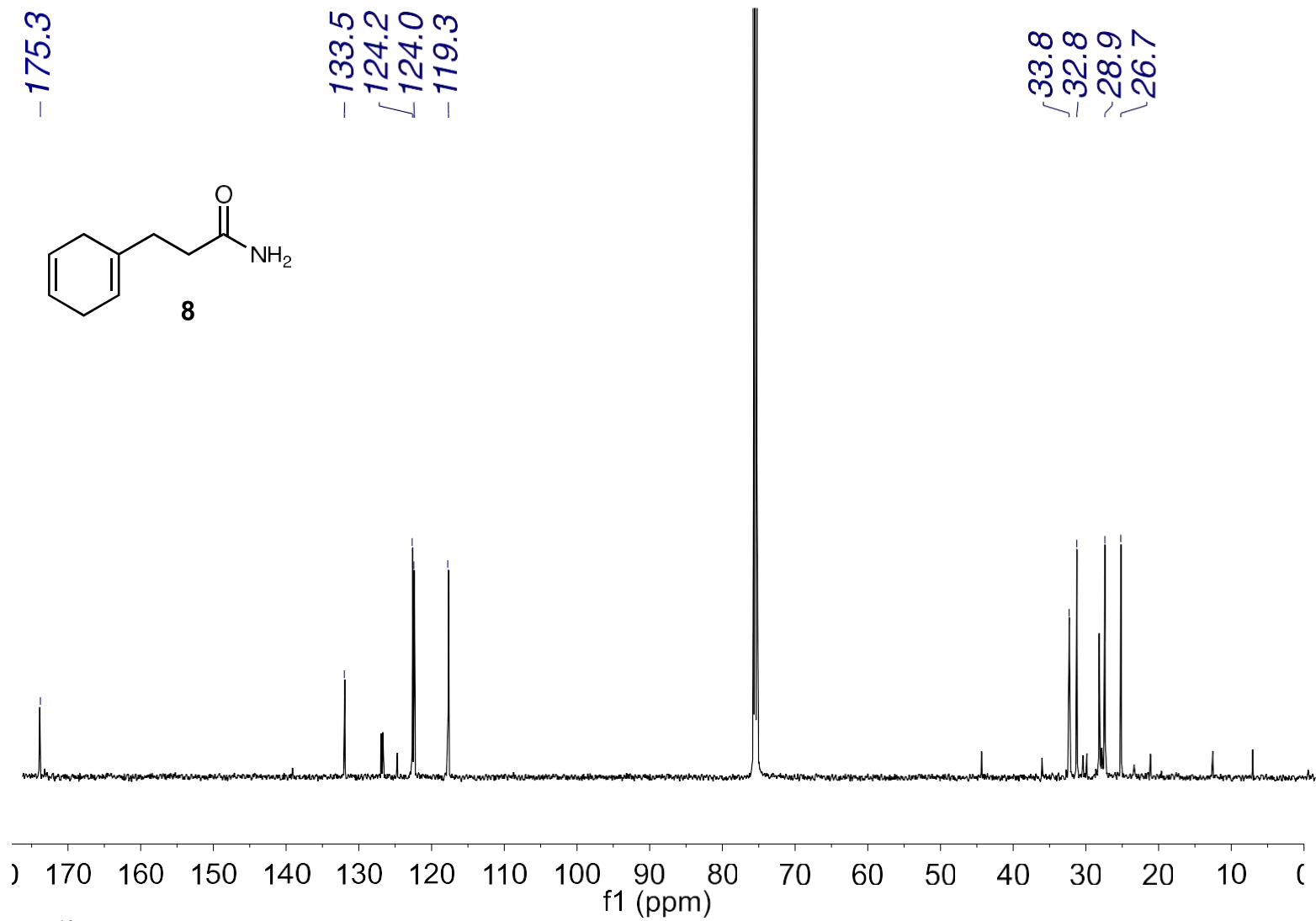


Fig. S5.77. <sup>13</sup>C NMR of 3-(cyclohexa-1,4-dien-1-yl)propanamide (8) (CDCl<sub>3</sub>, 101 MHz).

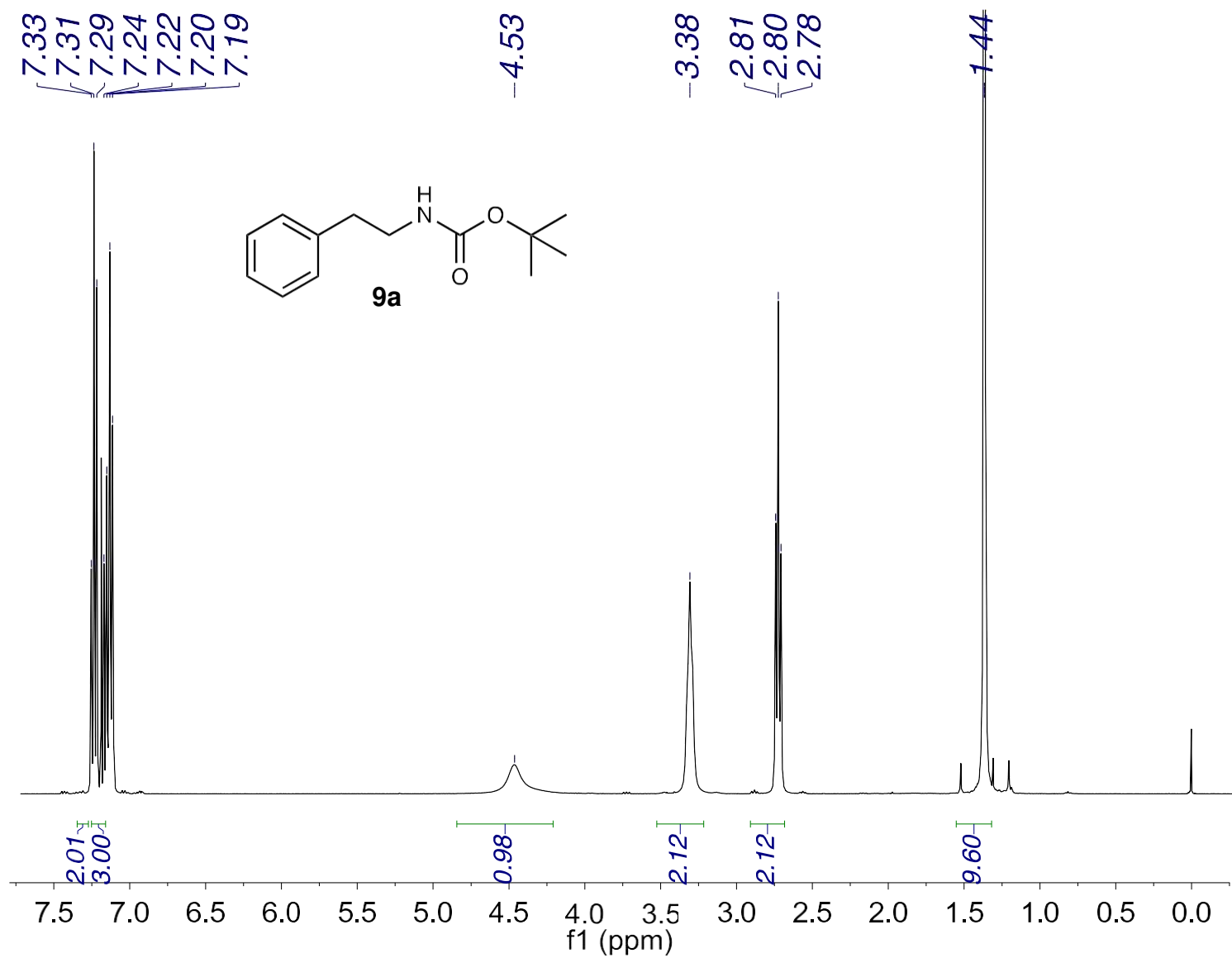


Fig. S5.78. <sup>1</sup>H NMR of *t*-butyl phenylethylcarbamate (9a) (CDCl<sub>3</sub>, 400 MHz).

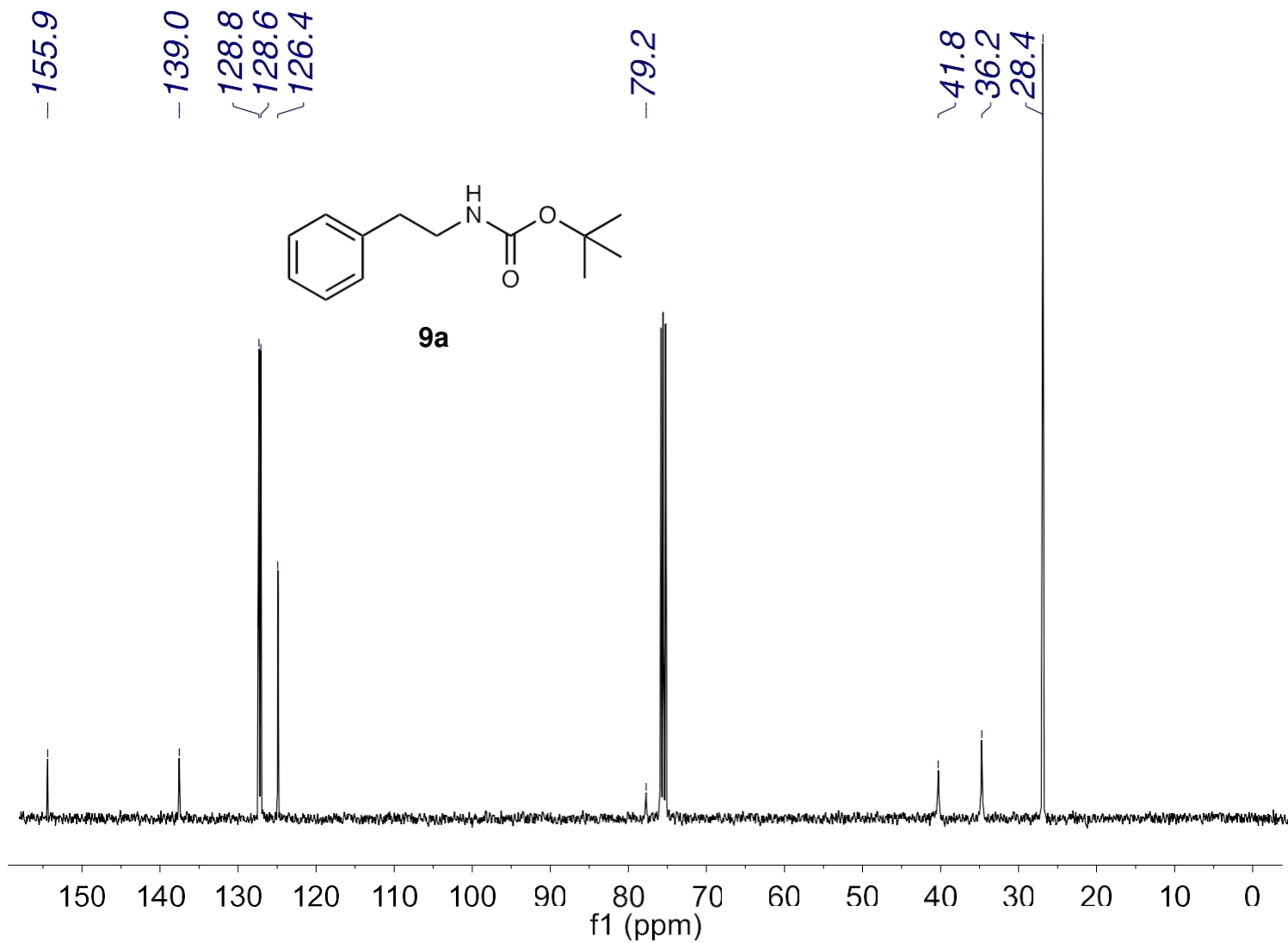


Fig. S5.79.  $^{13}\text{C}$  NMR of *t*-butyl phenylethylcarbamate (9a) ( $\text{CDCl}_3$ , 101 MHz).

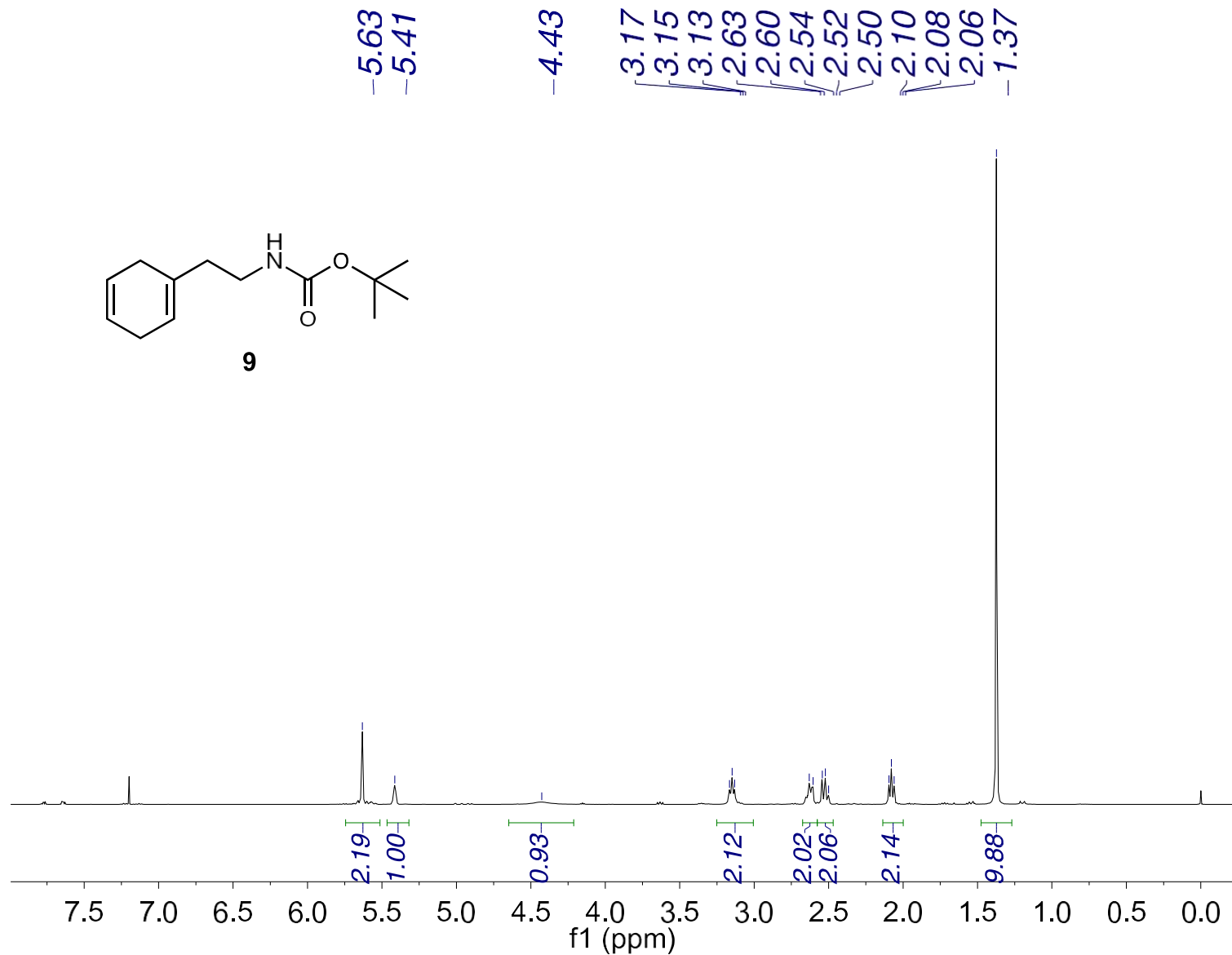


Fig. S5.80. <sup>1</sup>H NMR of tert-butyl (2-(cyclohexa-1,4-dien-1-yl)ethyl)carbamate (**9**) (CDCl<sub>3</sub>, 400 MHz)

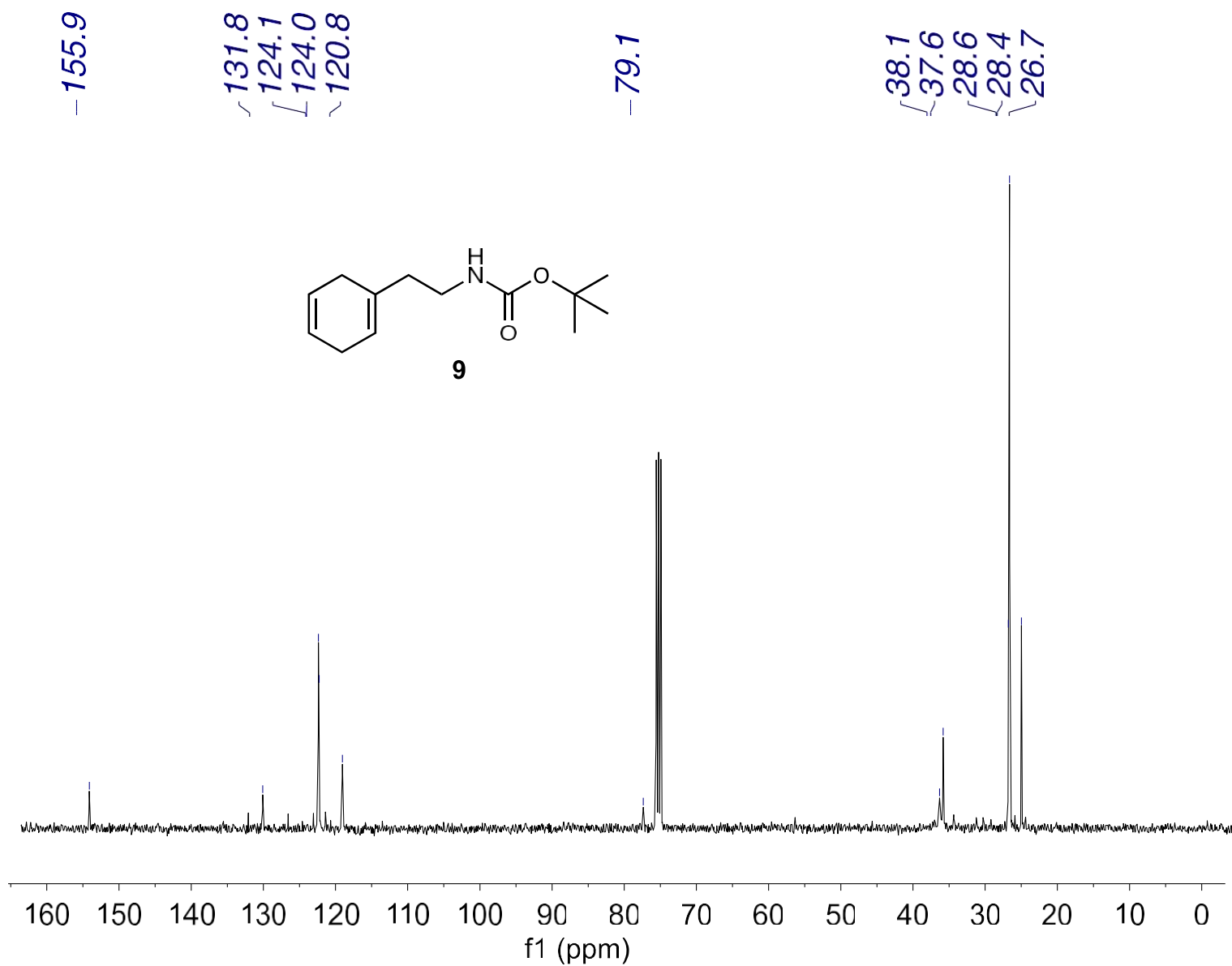


Fig. S5.81. <sup>13</sup>C NMR of tert-butyl (2-(cyclohexa-1,4-dien-1-yl)ethyl)carbamate (9) (CDCl<sub>3</sub>, 101 MHz)

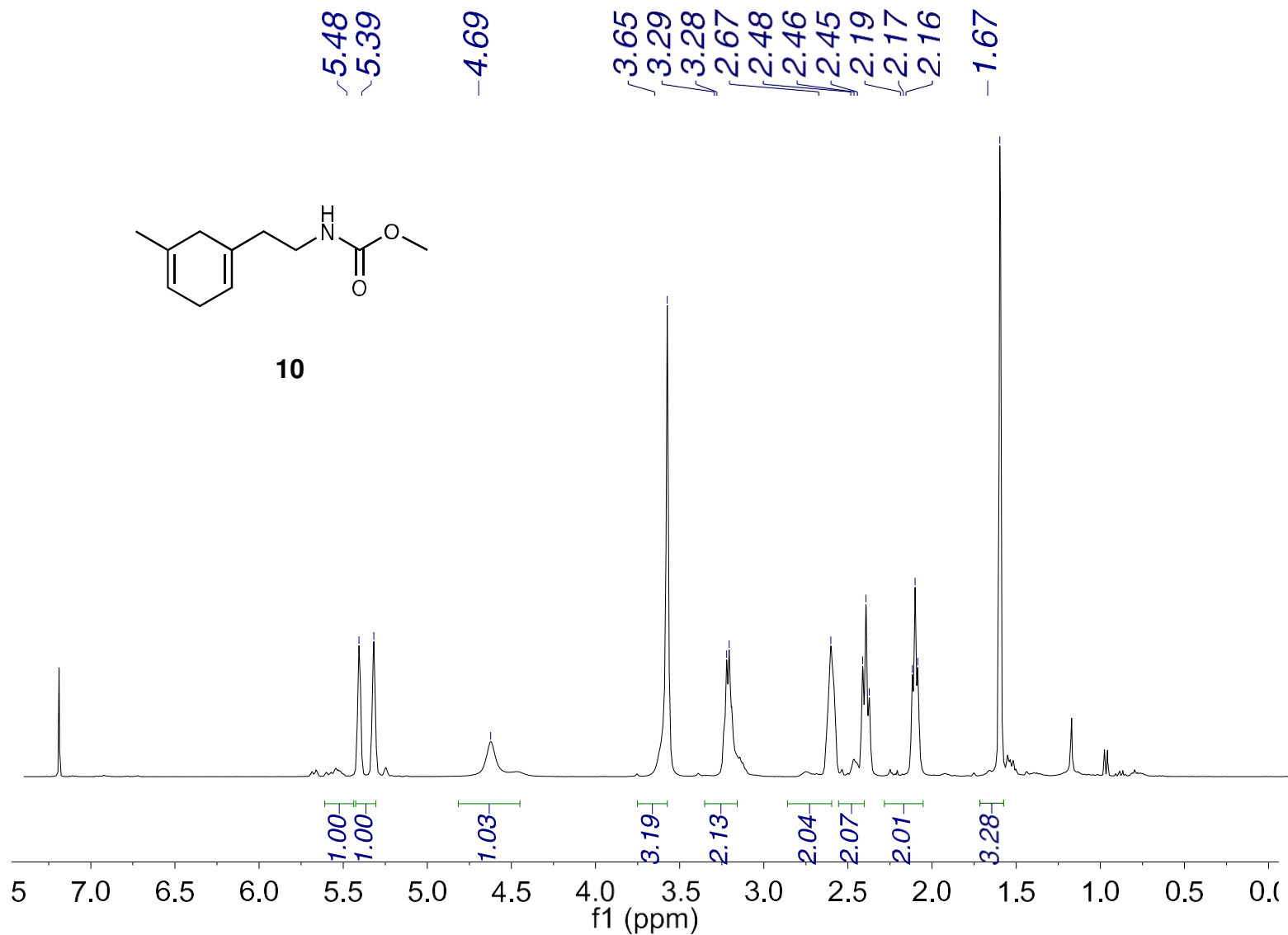


Fig. S5.82.  $^1\text{H}$  NMR of methyl (2-(5-methylcyclohexa-1,4-dien-1-yl)ethyl)carbamate (10) ( $\text{CDCl}_3$ , 400 MHz)

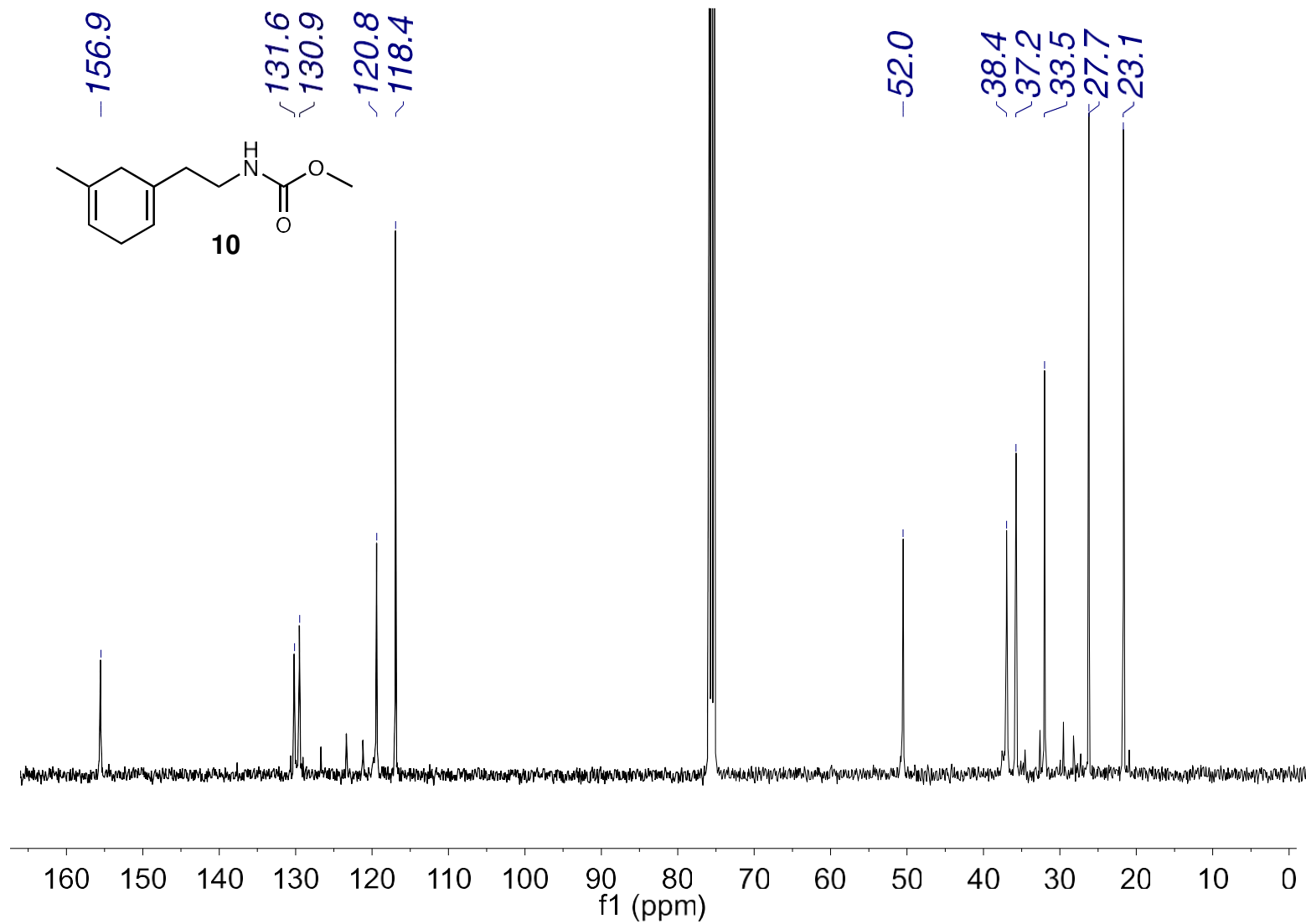


Fig. S5.83.  $^{13}\text{C}$  NMR of methyl (2-(5-methylcyclohexa-1,4-dien-1-yl)ethyl)carbamate (10) ( $\text{CDCl}_3$ , 101 MHz)



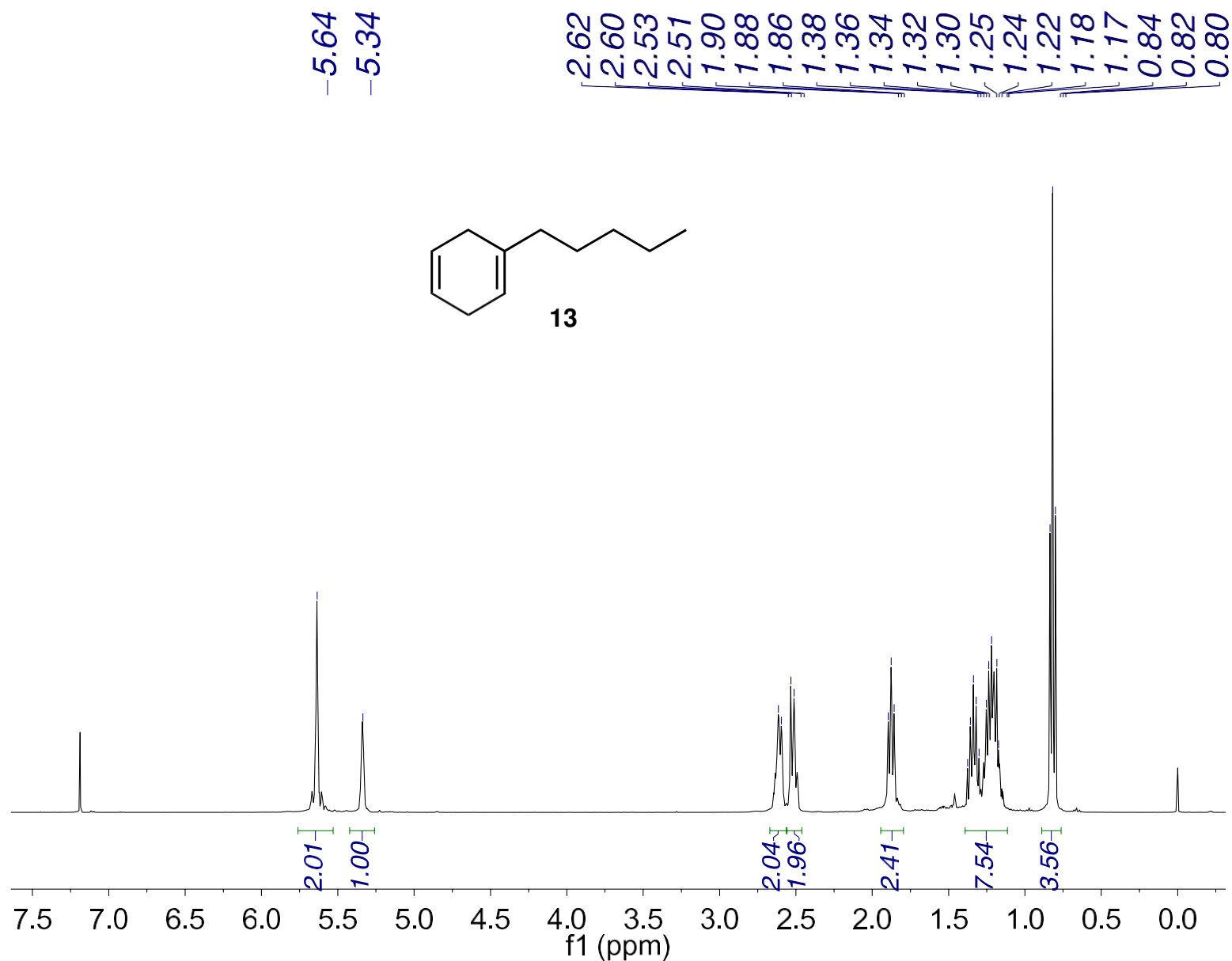


Fig. S5.84. <sup>1</sup>H NMR of 1-pentylcyclohexa-1,4-diene (13) (CDCl<sub>3</sub>, 400 MHz)

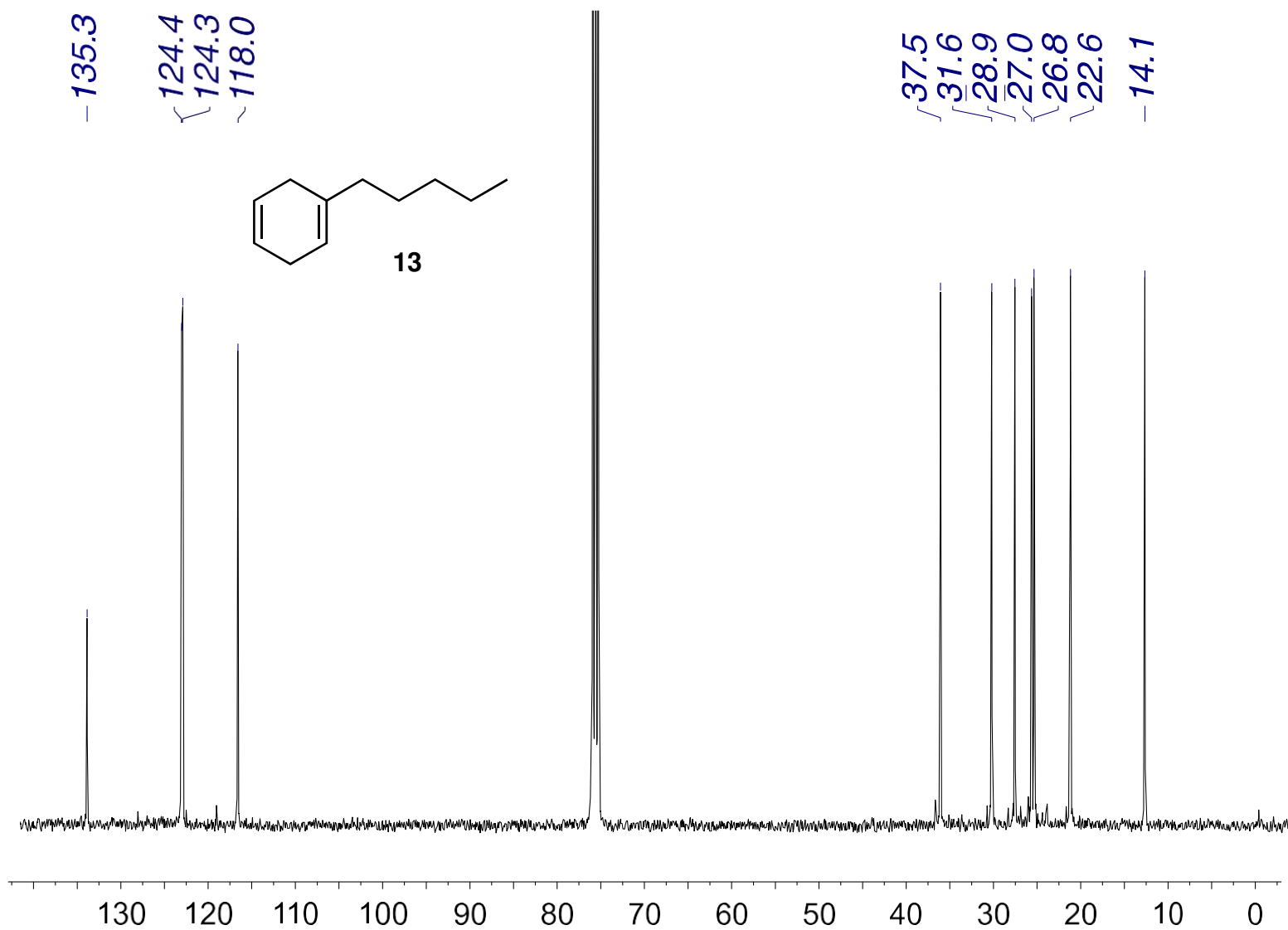


Fig. S5.85.  $^{13}\text{C}$  NMR of 1-pentylcyclohexa-1,4-diene (13) ( $\text{CDCl}_3$ , 101 MHz)

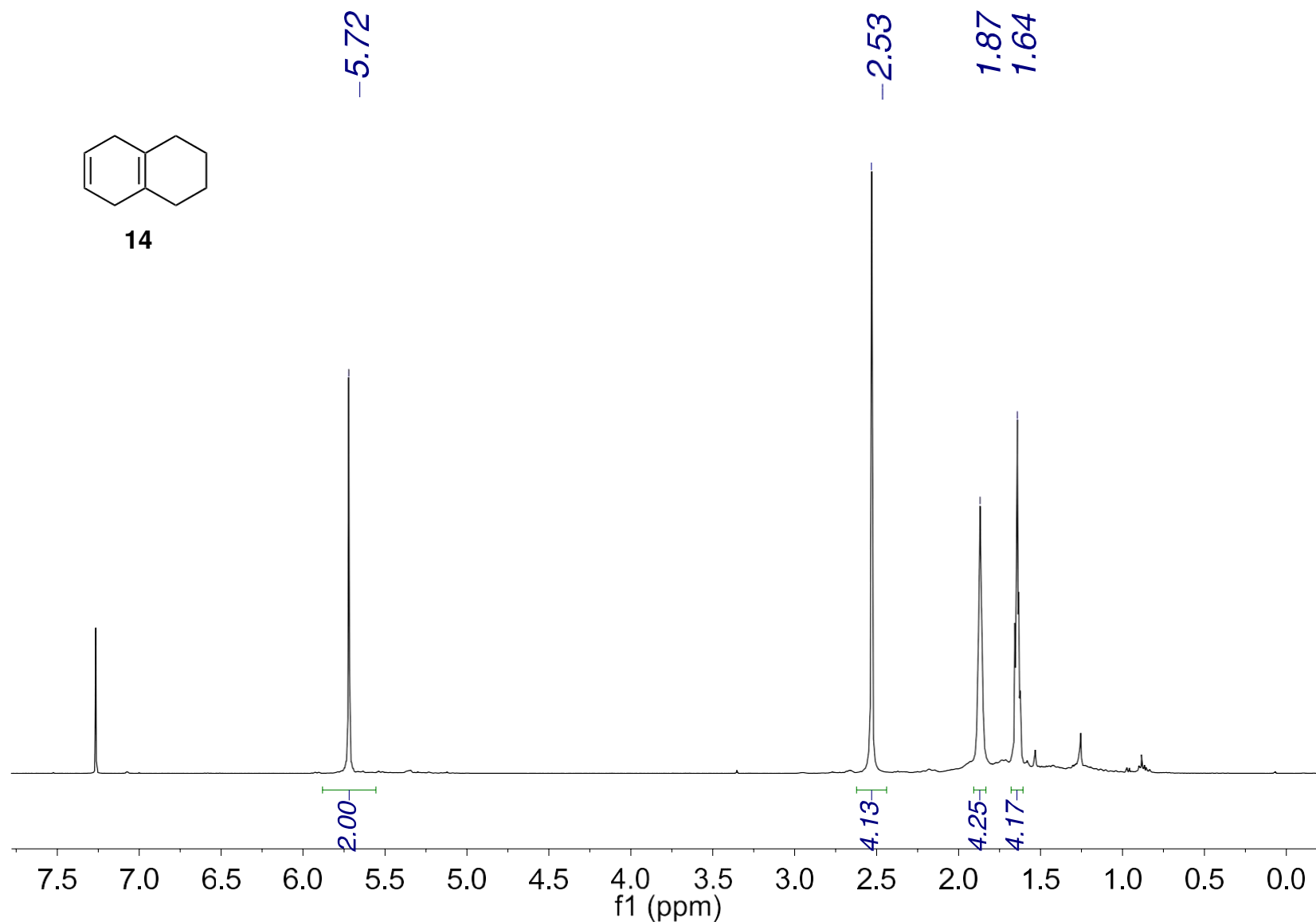


Fig. S5.86. <sup>1</sup>H NMR of 1,2,3,4,5,8-hexahydronaphthalene (14) (CDCl<sub>3</sub>, 400 MHz)

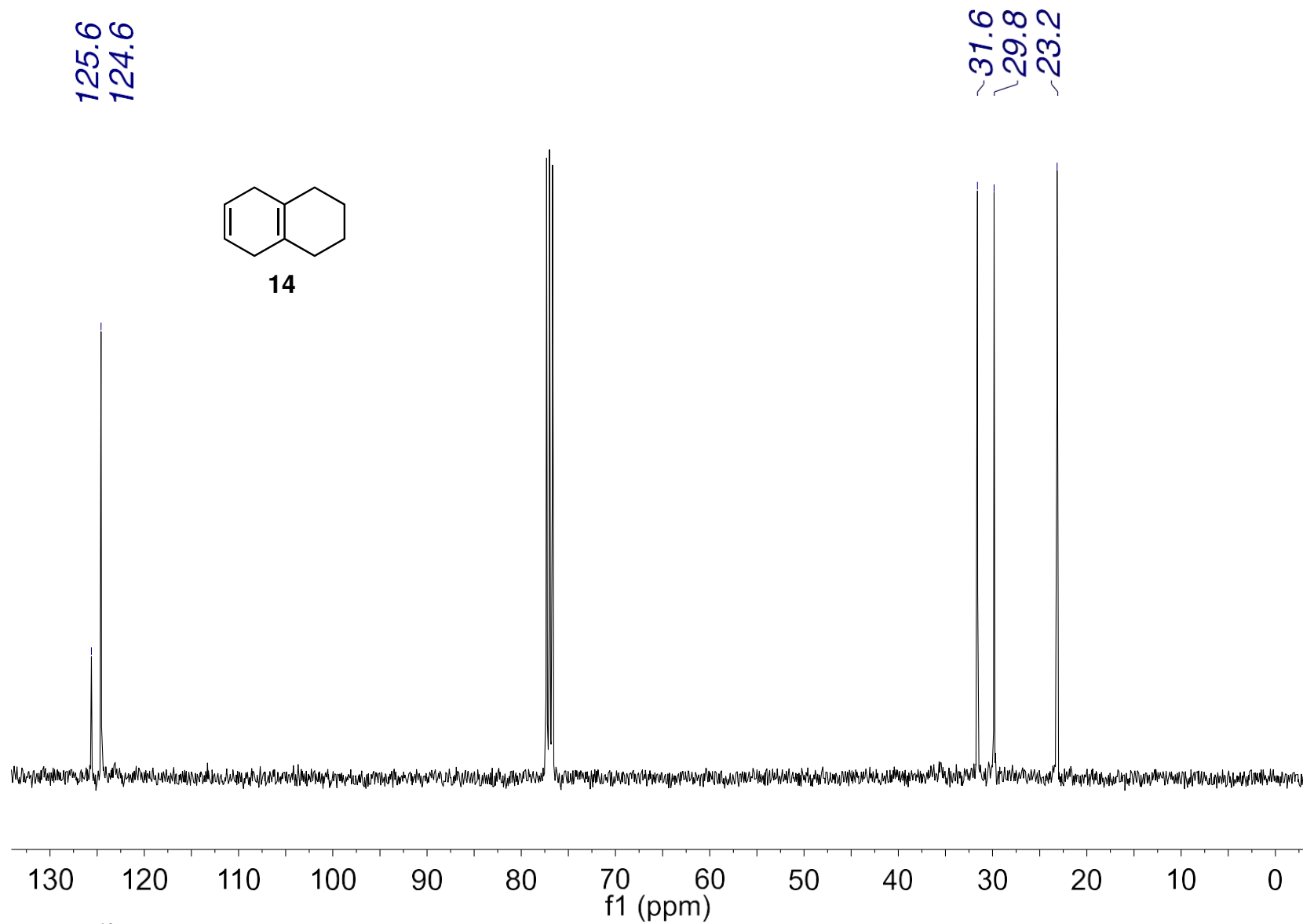


Fig. S5.87.  $^{13}\text{C}$  NMR of 1,2,3,4,5,8-hexahydronaphthalene (14) ( $\text{CDCl}_3$ , 101 MHz)

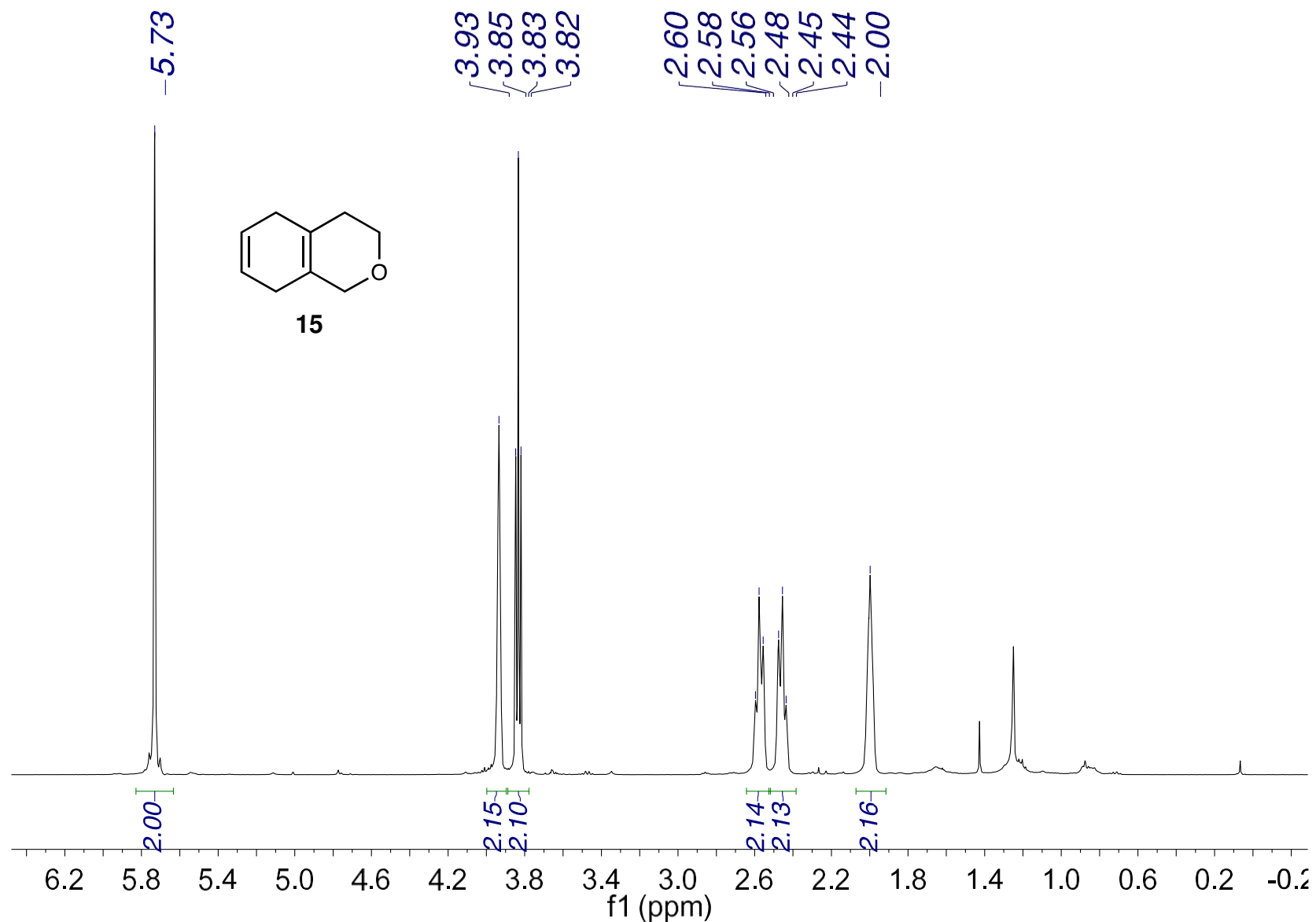


Fig. S5.88.  $^1\text{H}$  NMR of 3,4,5,8-tetrahydro-1H-isochromene (15) ( $\text{CDCl}_3$ , 400 MHz).

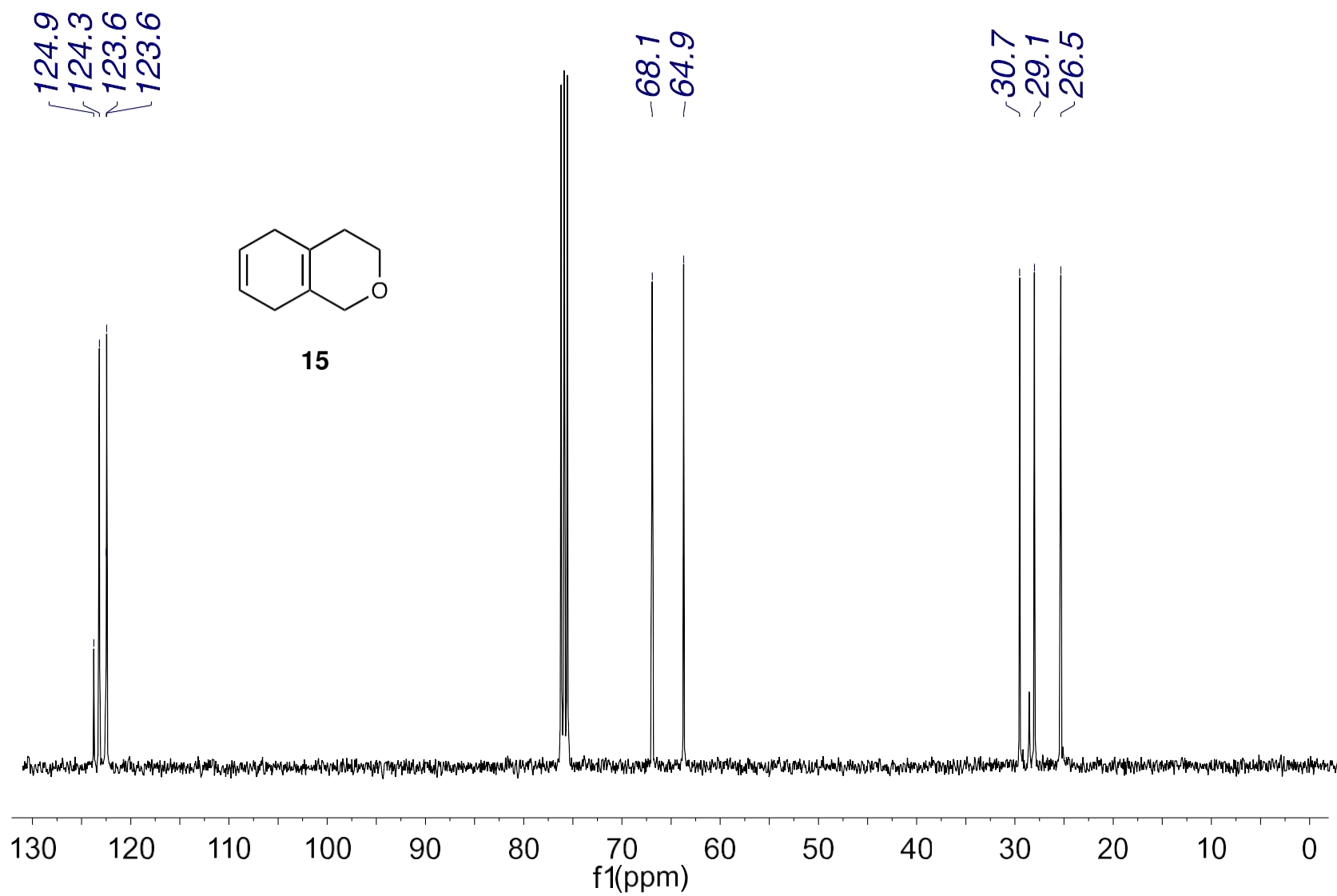


Fig. S5.89.  $^{13}\text{C}$  NMR of 3,4,5,8-tetrahydro-1H-isochromene (15) ( $\text{CDCl}_3$ , 101 MHz).

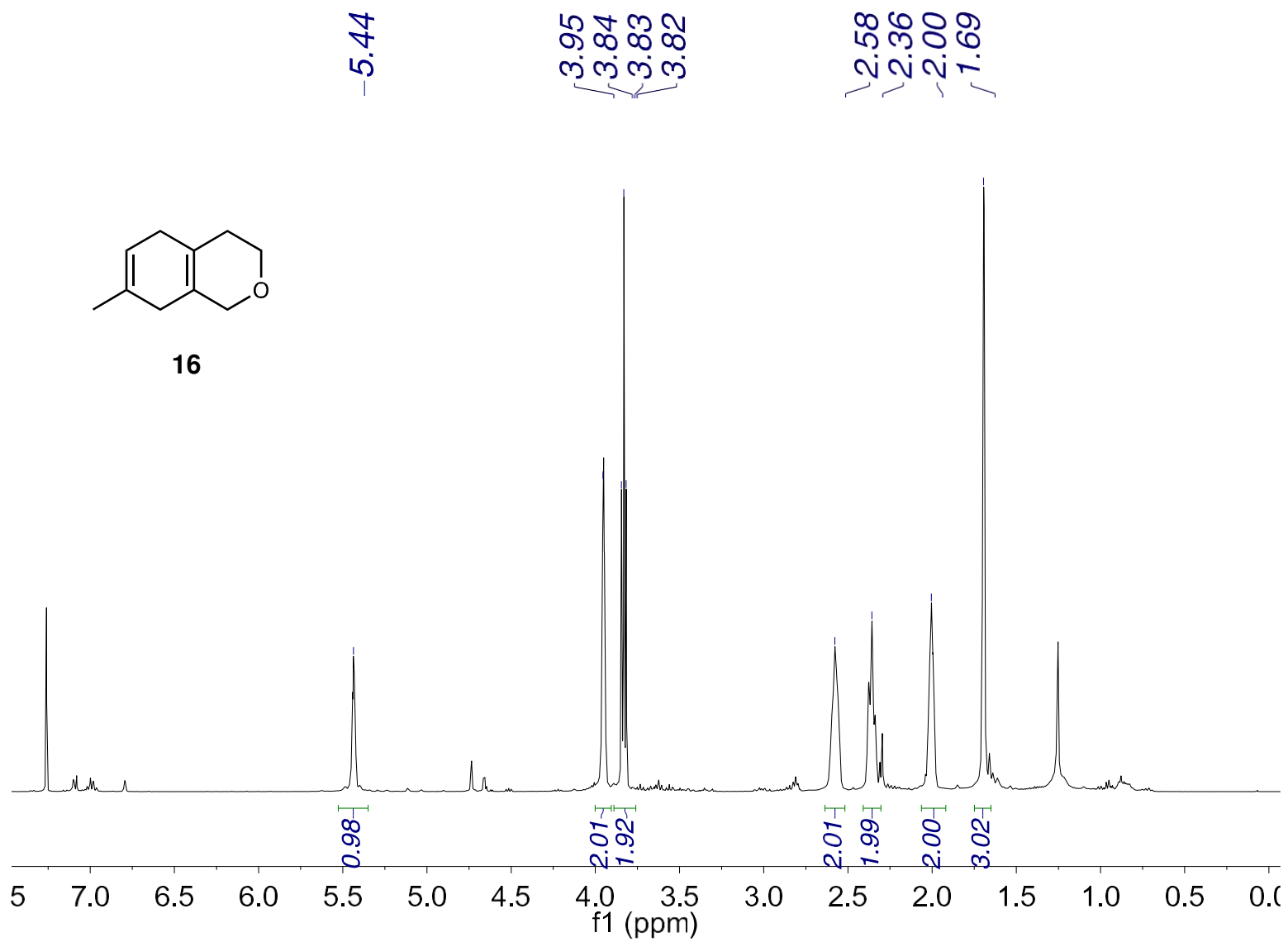


Fig. S5.90. <sup>1</sup>H NMR of 7-methyl-3,4,5,8-tetrahydro-1H-isochromene (16) (CDCl<sub>3</sub>, 400 MHz).

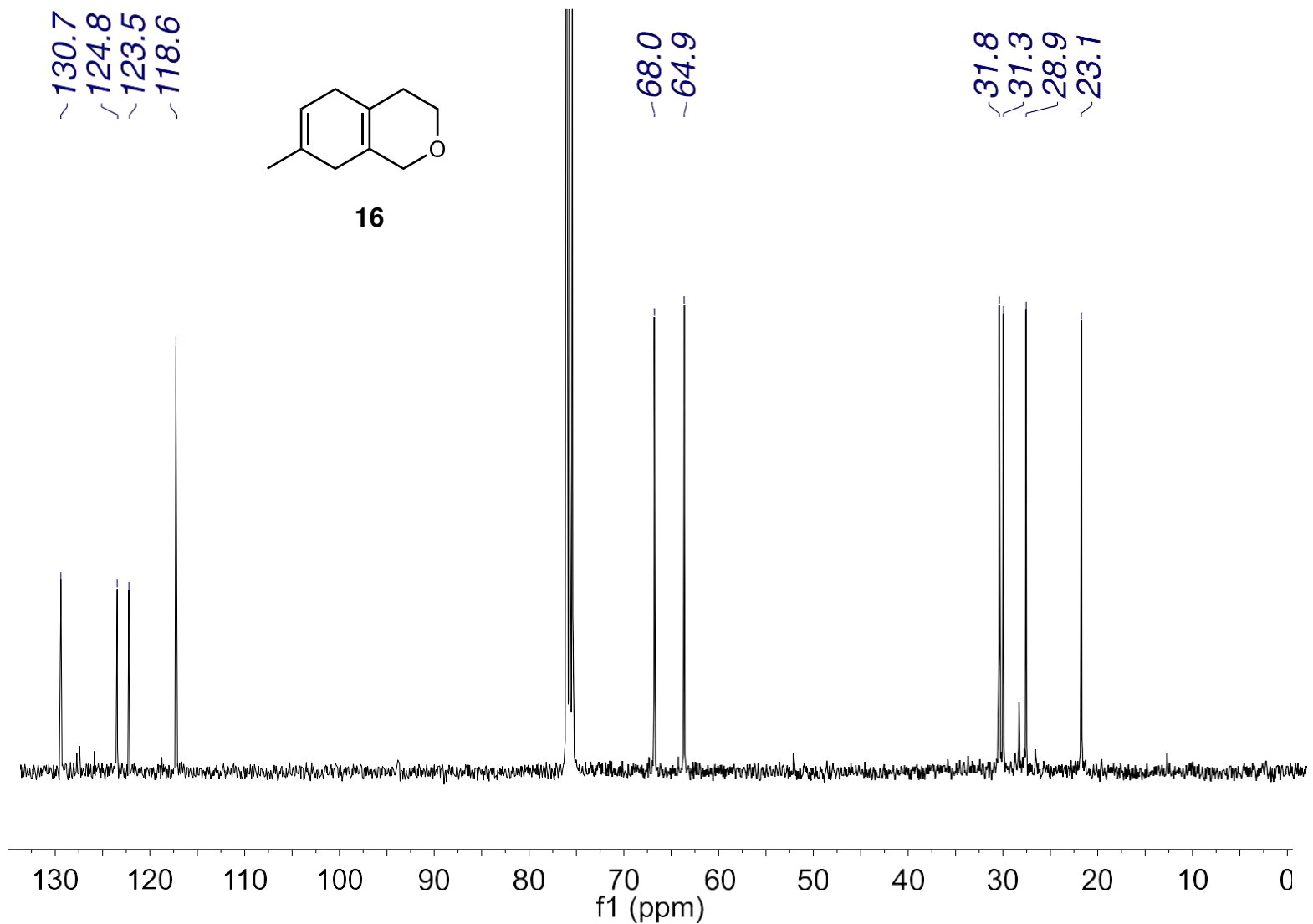


Fig. S5.91.  $^{13}\text{C}$  NMR of 7-methyl-3,4,5,8-tetrahydro-1H-isochromene (16) ( $\text{CDCl}_3$ , 101 MHz).



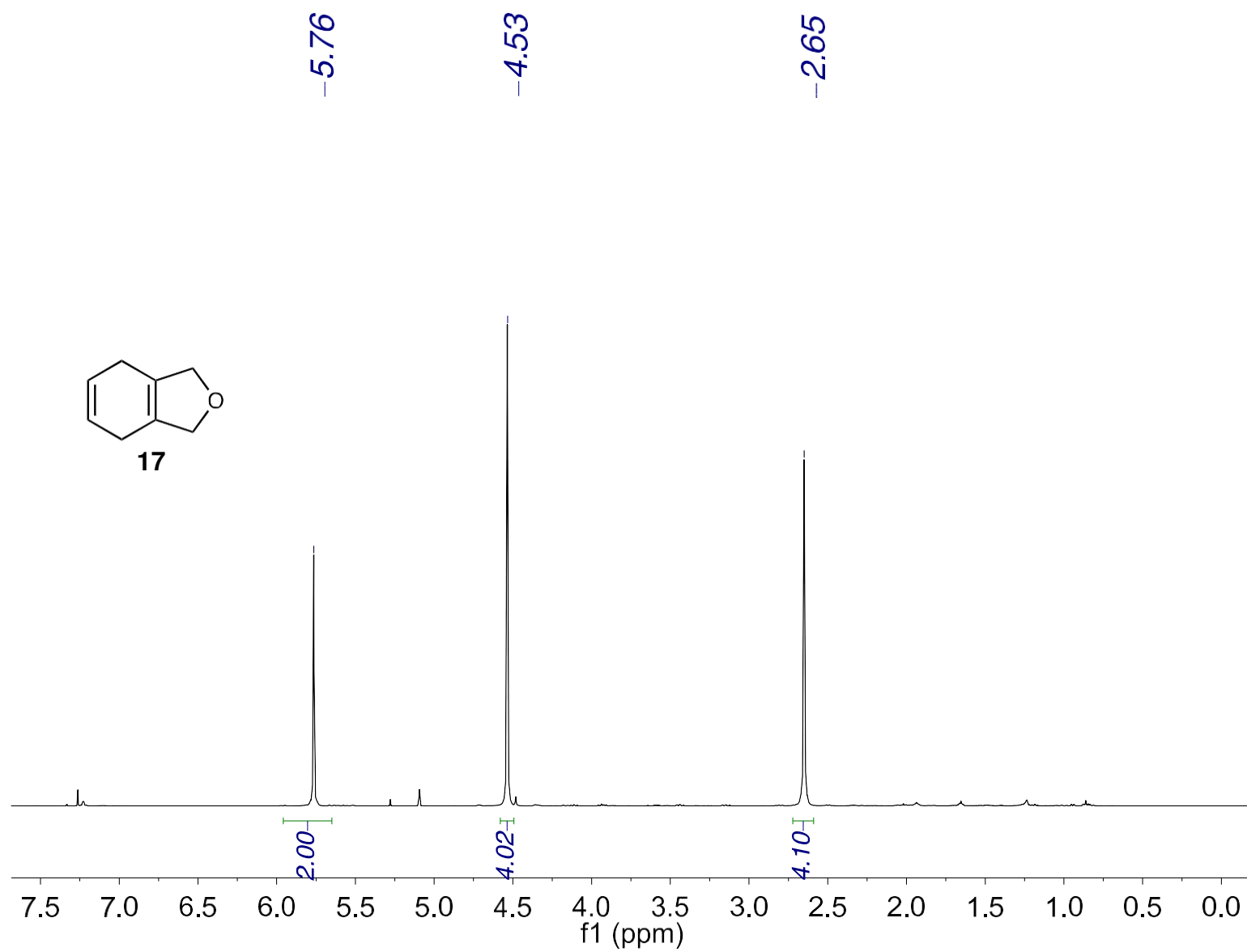


Fig. S5.92. <sup>1</sup>H NMR of 1,3,4,7-tetrahydroisobenzofuran (17) (CDCl<sub>3</sub>, 400 MHz).

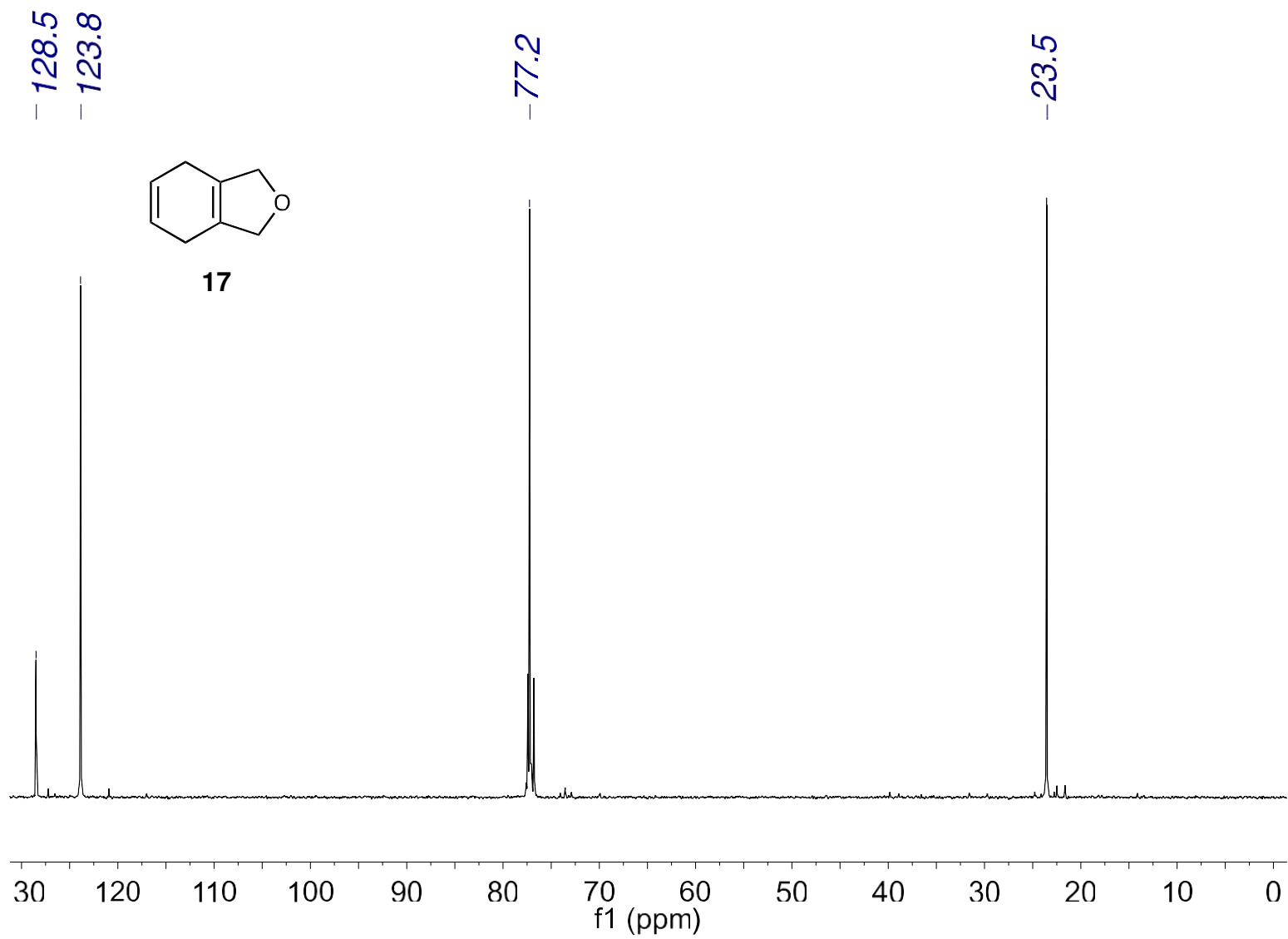


Fig. S5.93.  $^{13}\text{C}$  NMR of 1,3,4,7-tetrahydroisobenzofuran (17) ( $\text{CDCl}_3$ , 101 MHz).

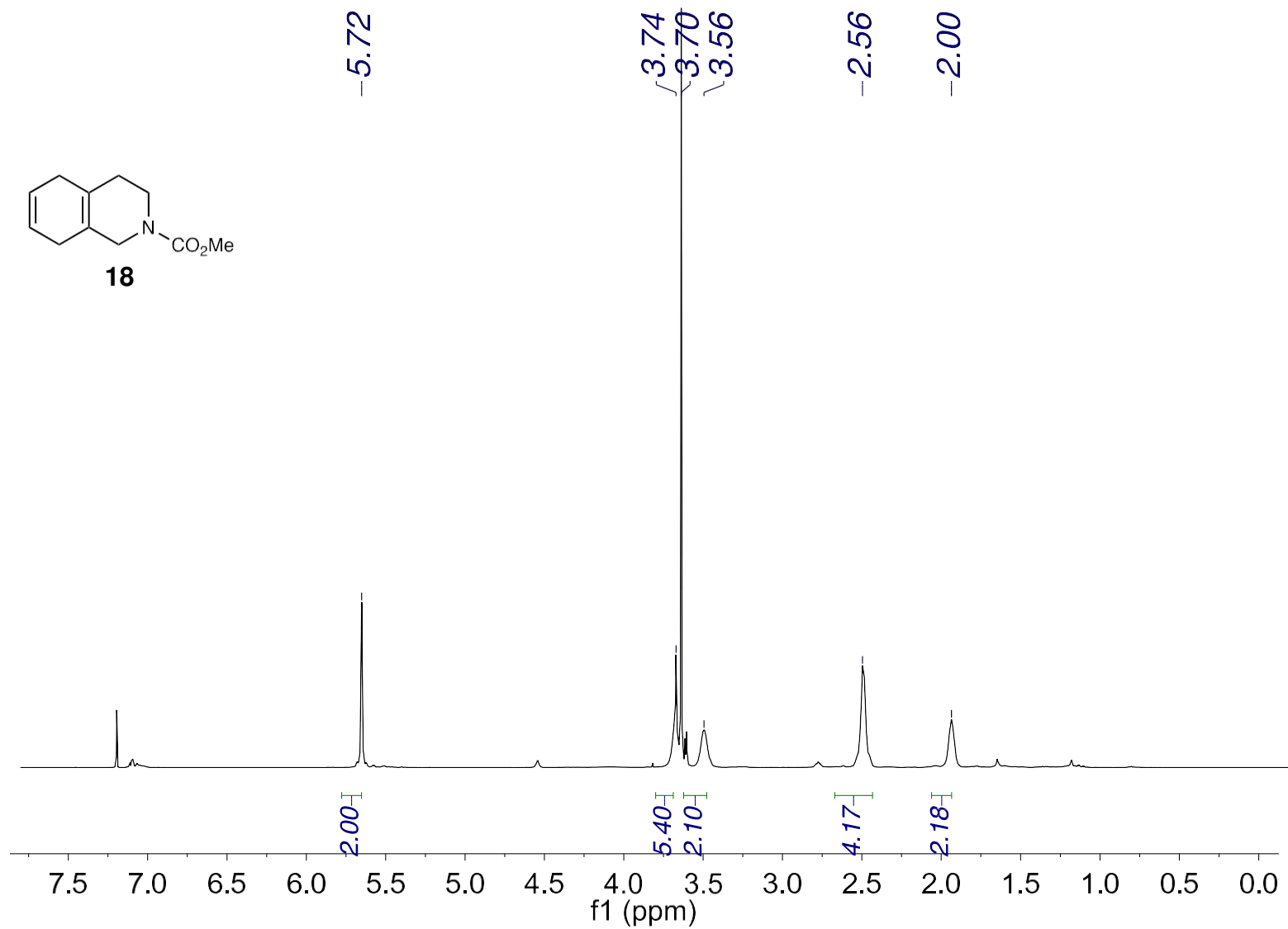


Fig. S5.94. <sup>1</sup>H NMR of methyl 3,4,5,8-tetrahydroisoquinoline-2(1H)-carboxylate (18) (CDCl<sub>3</sub>, 400 MHz).

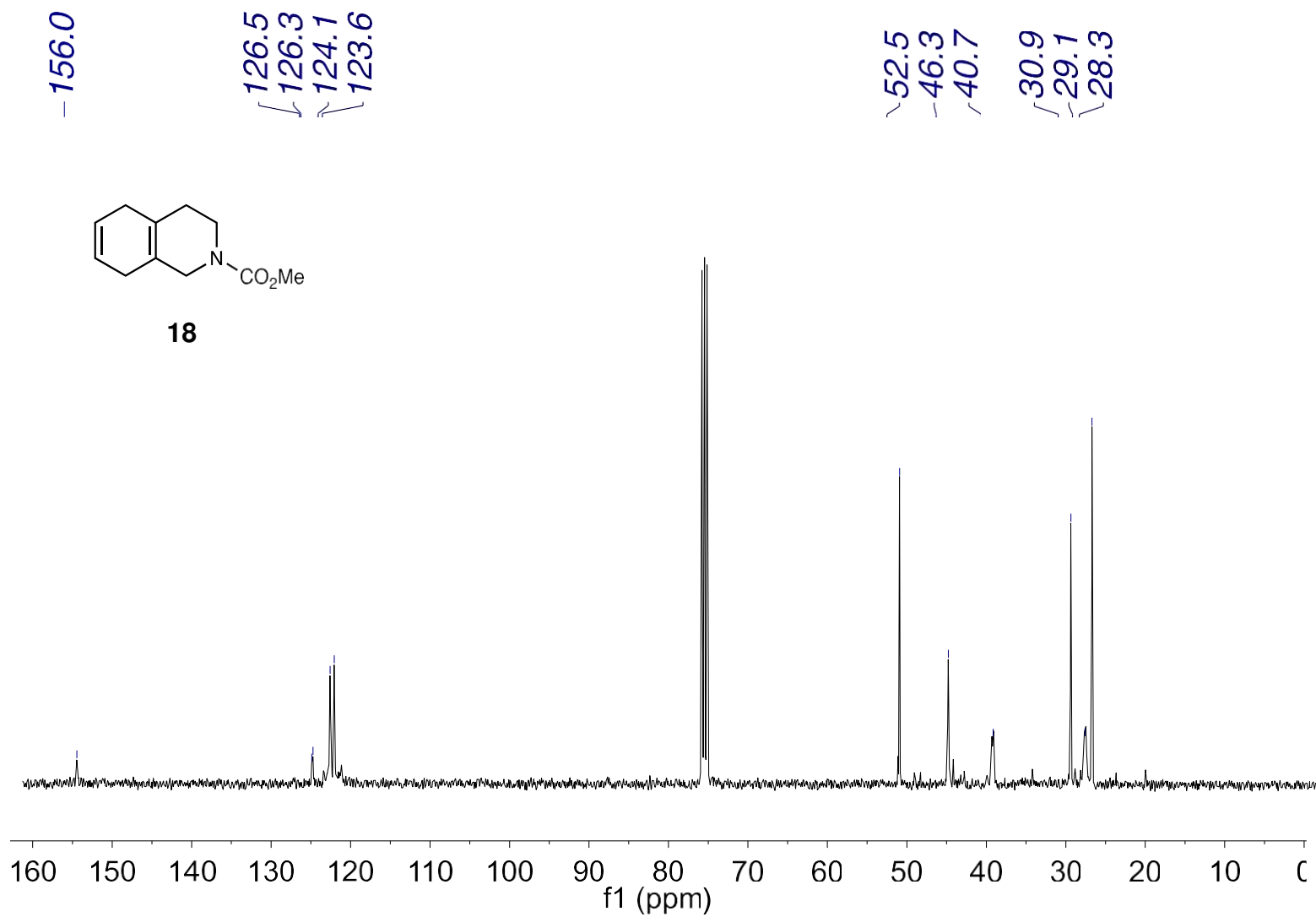


Fig. S5.95.  $^{13}\text{C}$  NMR of methyl 3,4,5,8-tetrahydroisoquinoline-2(1H)-carboxylate (18) ( $\text{CDCl}_3$ , 101 MHz).

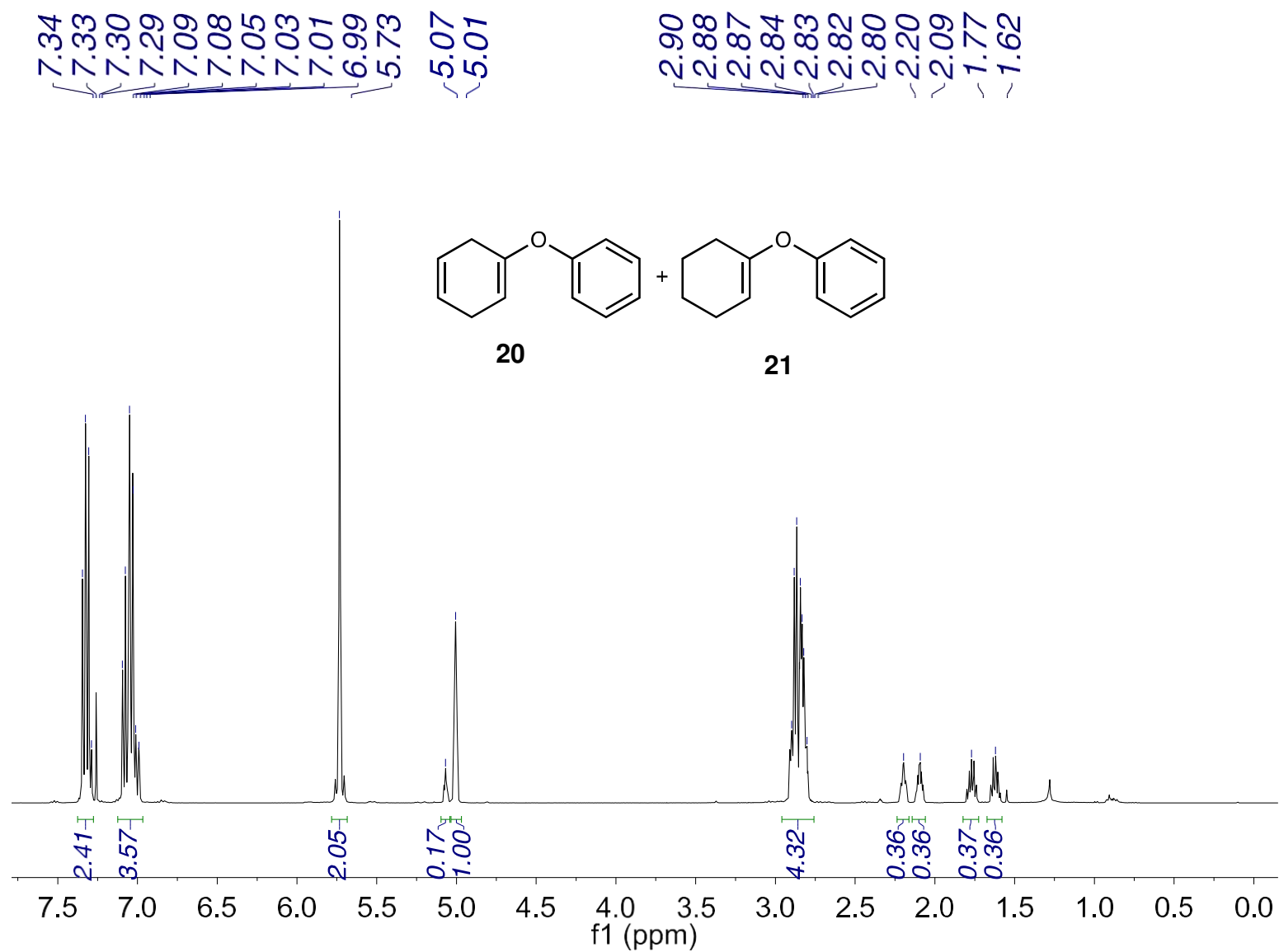


Fig. S5.96. <sup>1</sup>H NMR of (cyclohexa-1,4-dien-1-yloxy)benzene and (cyclohex-1-en-1-yloxy)benzene (20 and 21) (CDCl<sub>3</sub>, 400 MHz).

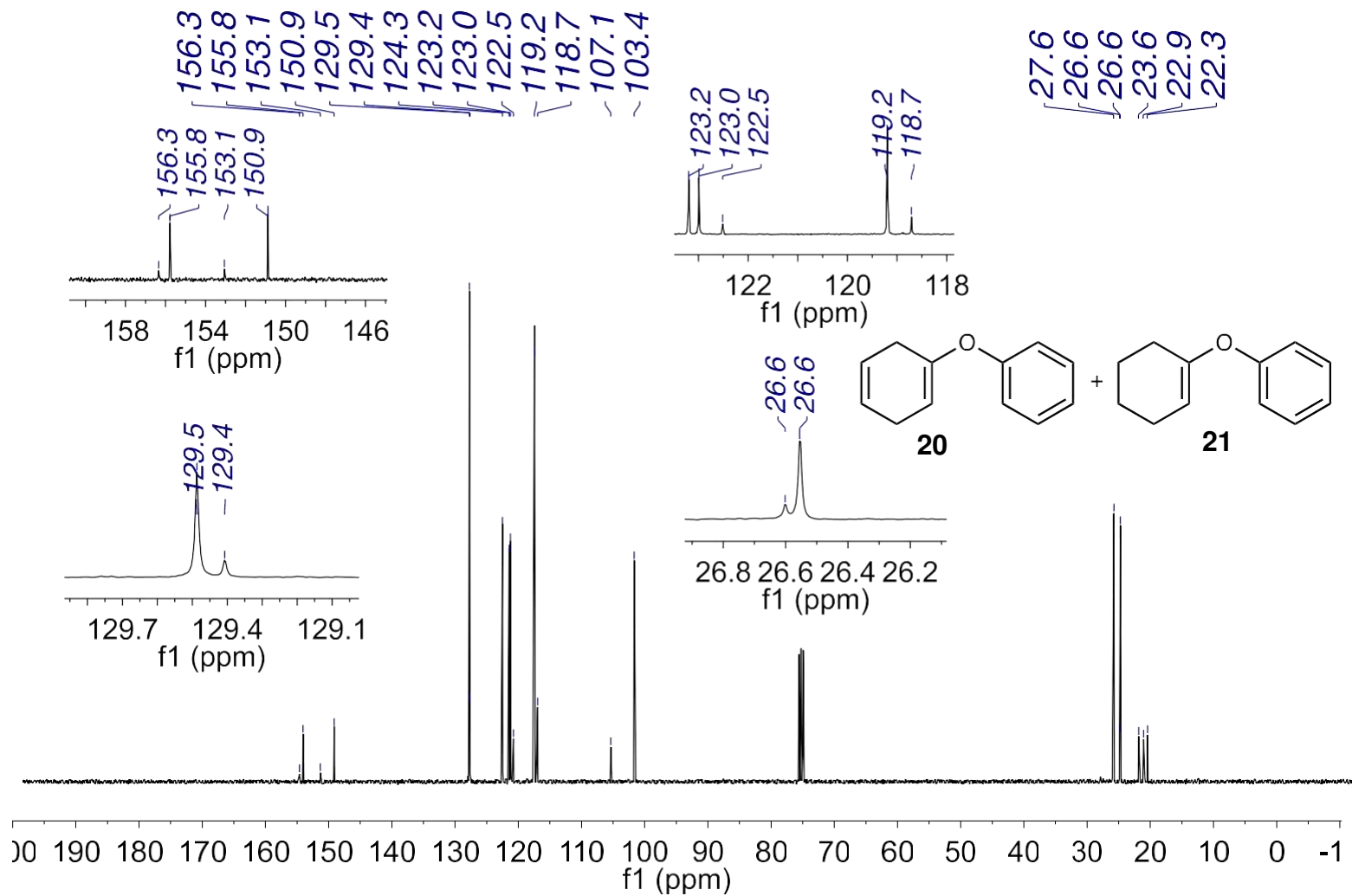


Fig. S5.97.  $^{13}\text{C}$  NMR of (cyclohexa-1,4-dien-1-yloxy)benzene and (cyclohex-1-en-1-yloxy)benzene (20 and 21) ( $\text{CDCl}_3$ , 101 MHz).

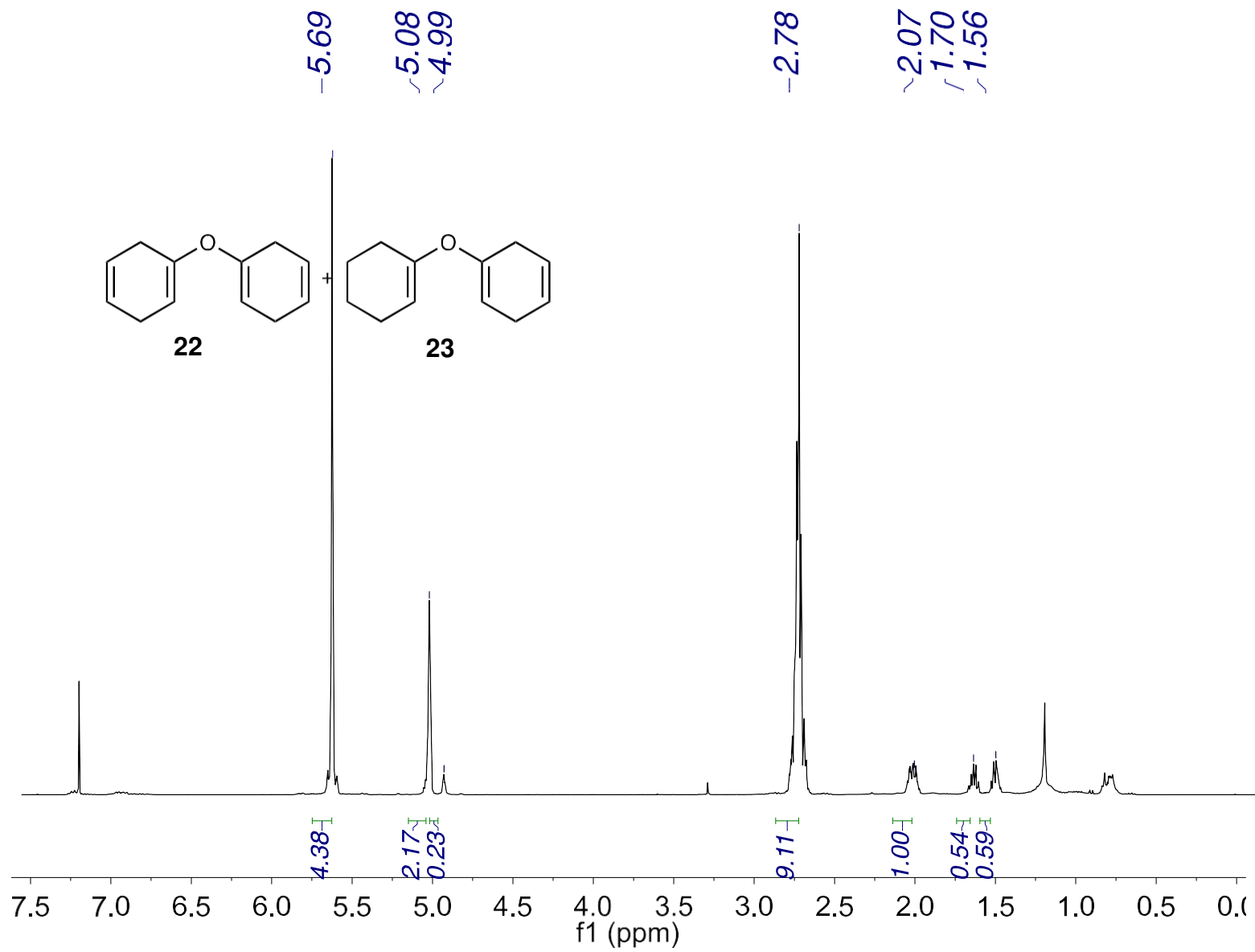


Fig. S5.98.  $^1\text{H}$  NMR of 1,1'-oxydicyclohexa-1,4-diene and 1-(cyclohex-1-en-1-yloxy)cyclohexa-1,4-diene (22 and 23) ( $\text{CDCl}_3$ , 400 MHz).

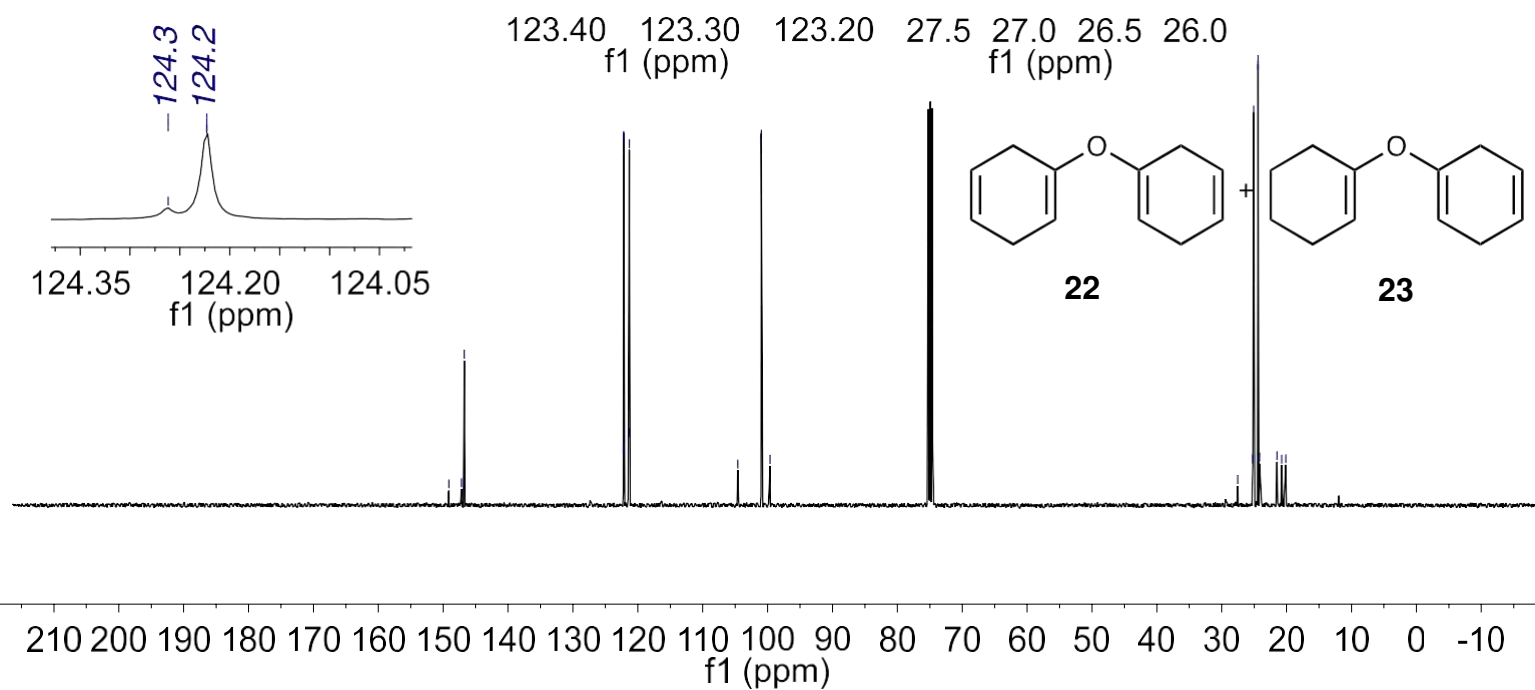
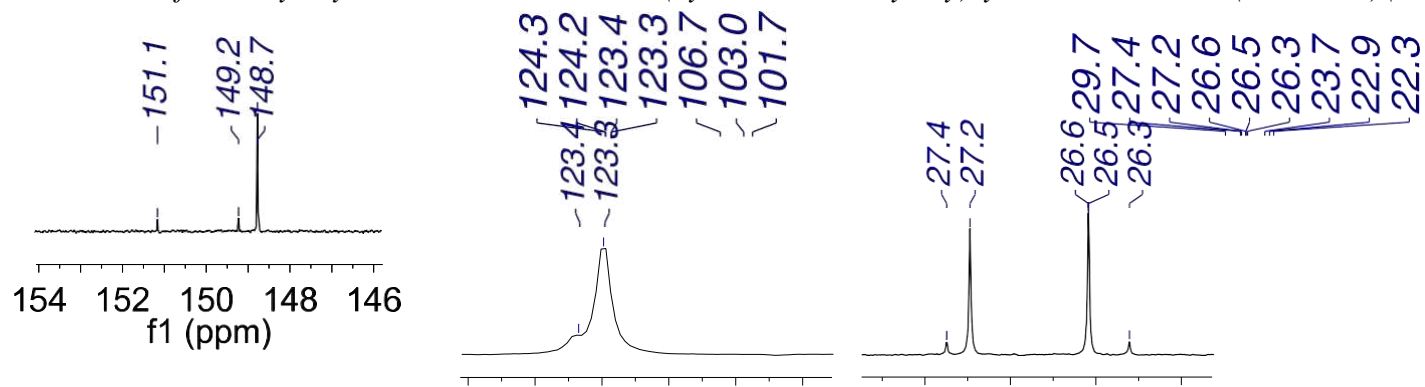


Fig. S5.99.  $^{13}\text{C}$  NMR of 1,1'-oxydicyclohexa-1,4-diene and 1-(cyclohex-1-en-1-yloxy)cyclohexa-1,4-diene (22 and 23) ( $\text{CDCl}_3$ , 101 MHz).



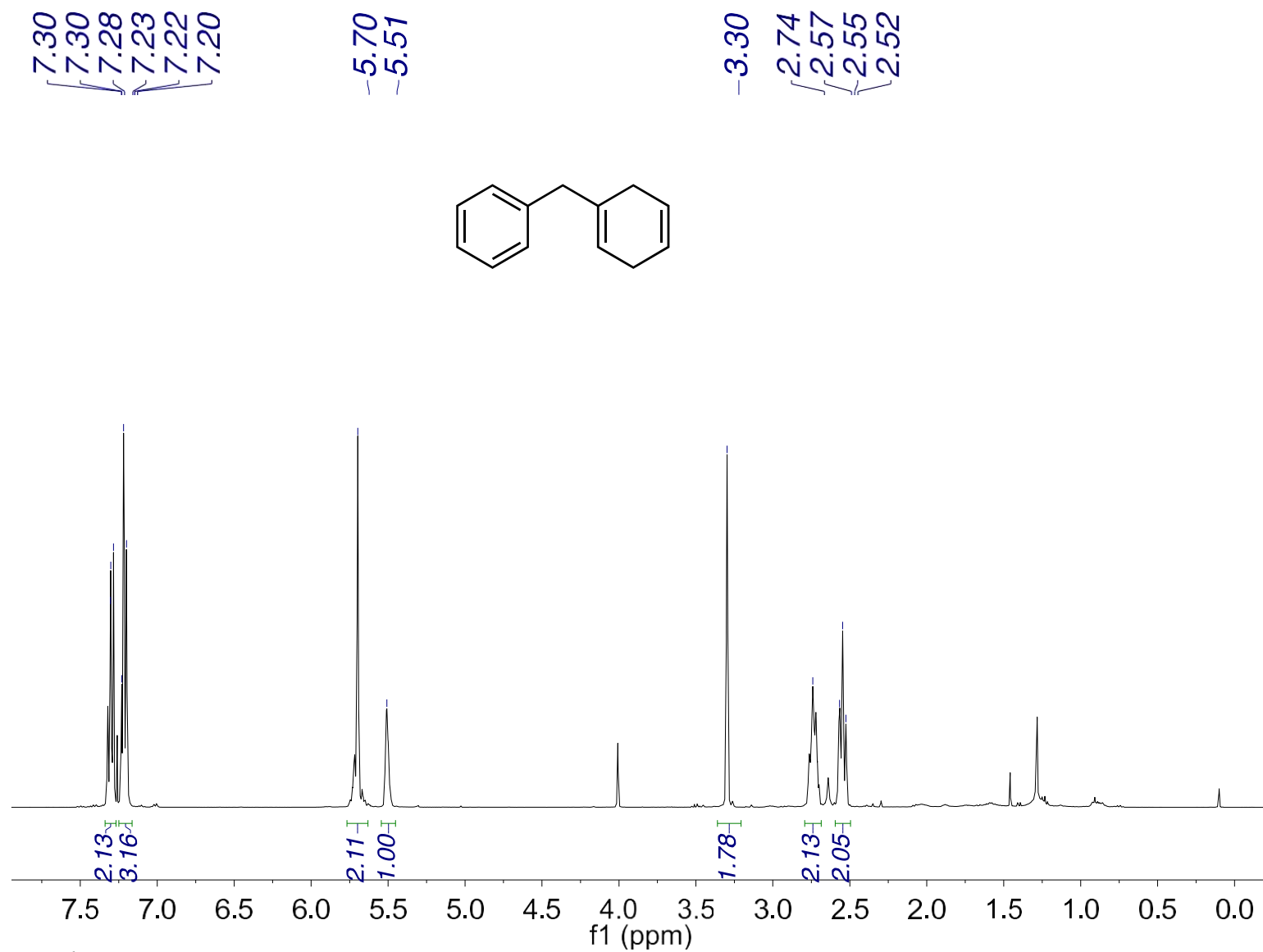


Fig. S5.100. <sup>1</sup>H NMR of (cyclohexa-1,4-dien-1-ylmethyl)benzene (25) (CDCl<sub>3</sub>, 400 MHz).

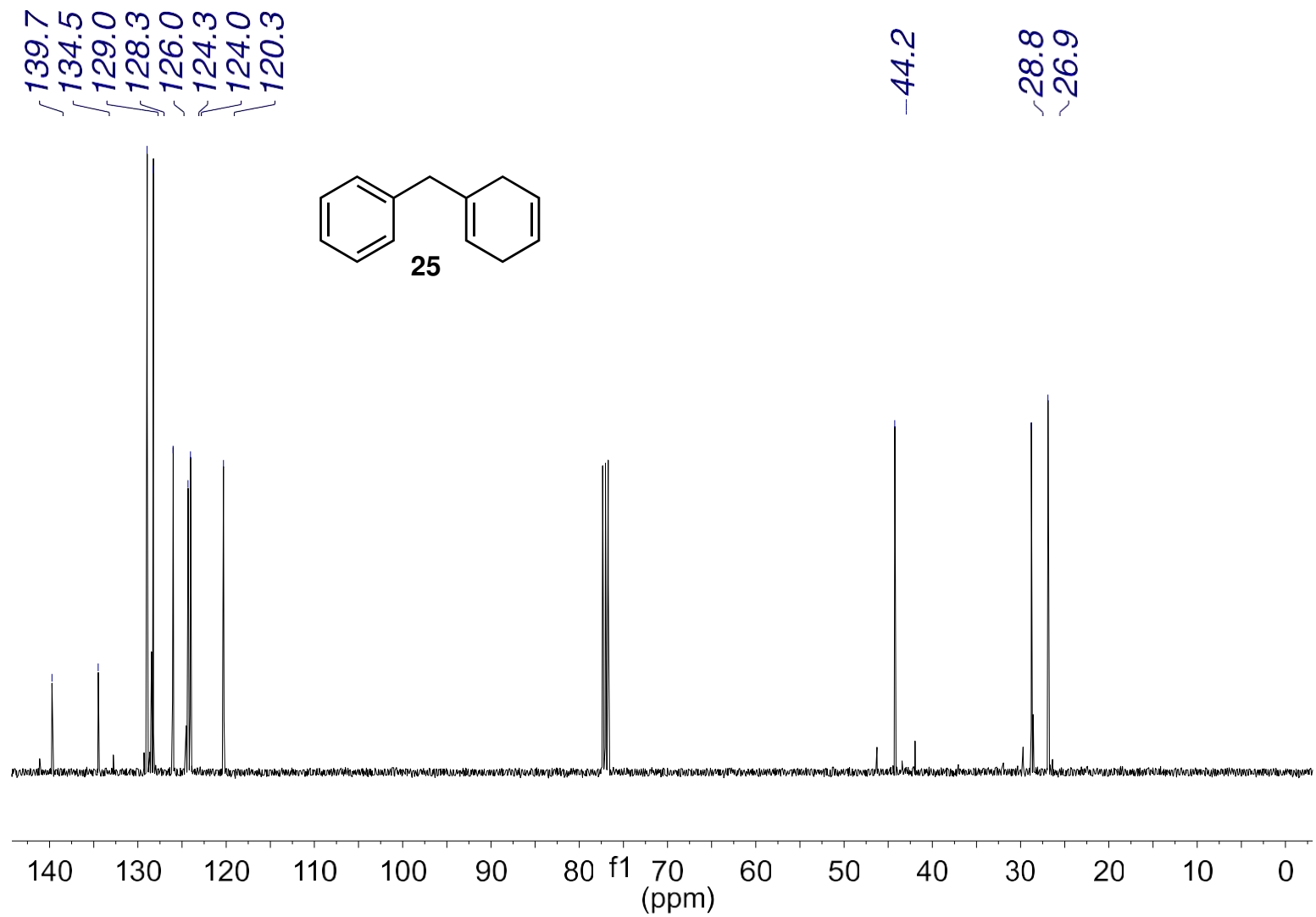


Fig. S5.101.  $^{13}\text{C}$  NMR of (cyclohexa-1,4-dien-1-ylmethyl)benzene (25) ( $\text{CDCl}_3$ , 101 MHz).

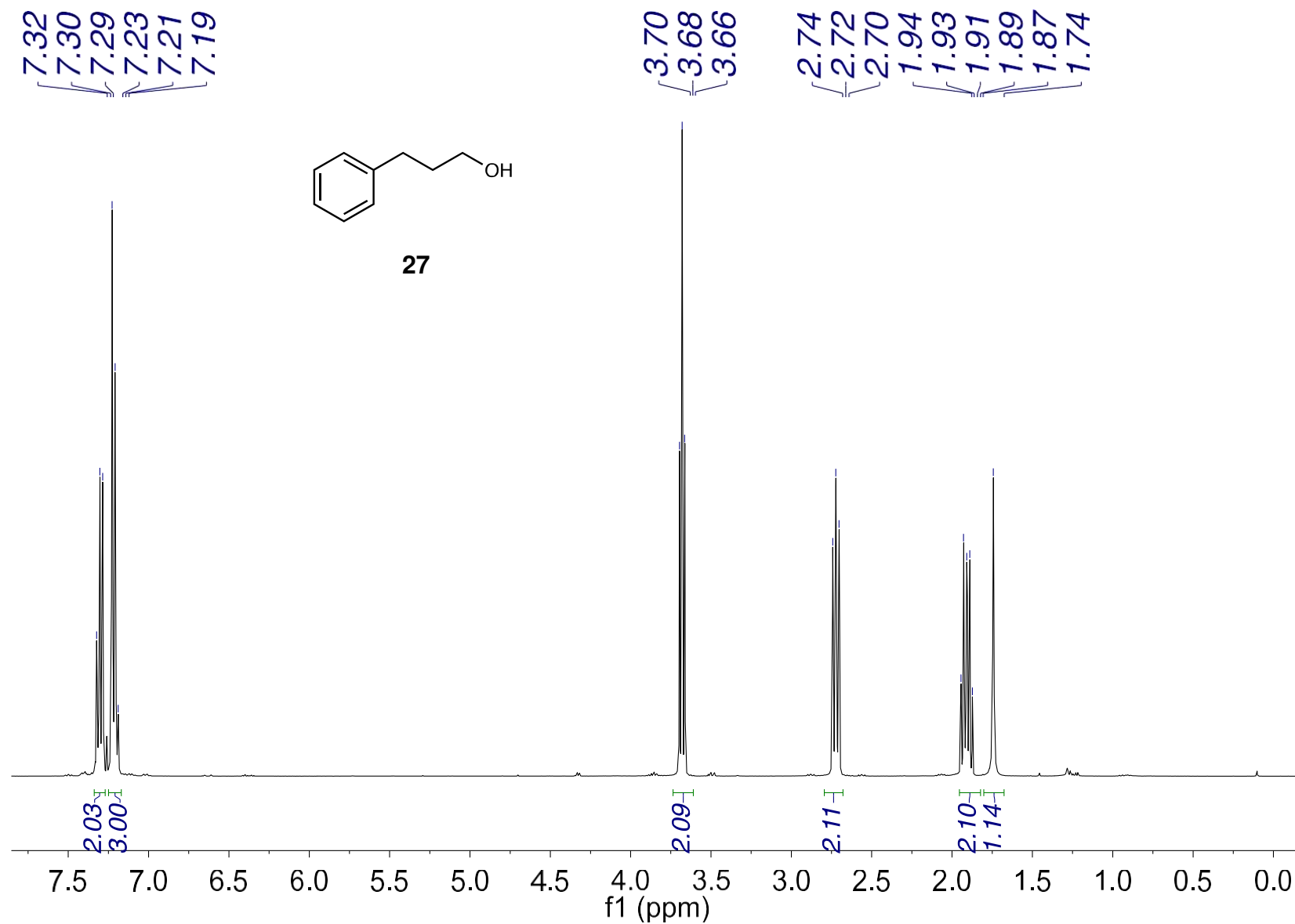


Fig. S5.102.  $^1\text{H}$  NMR of phenylpropan-3-ol (27) ( $\text{CDCl}_3$ , 400 MHz).

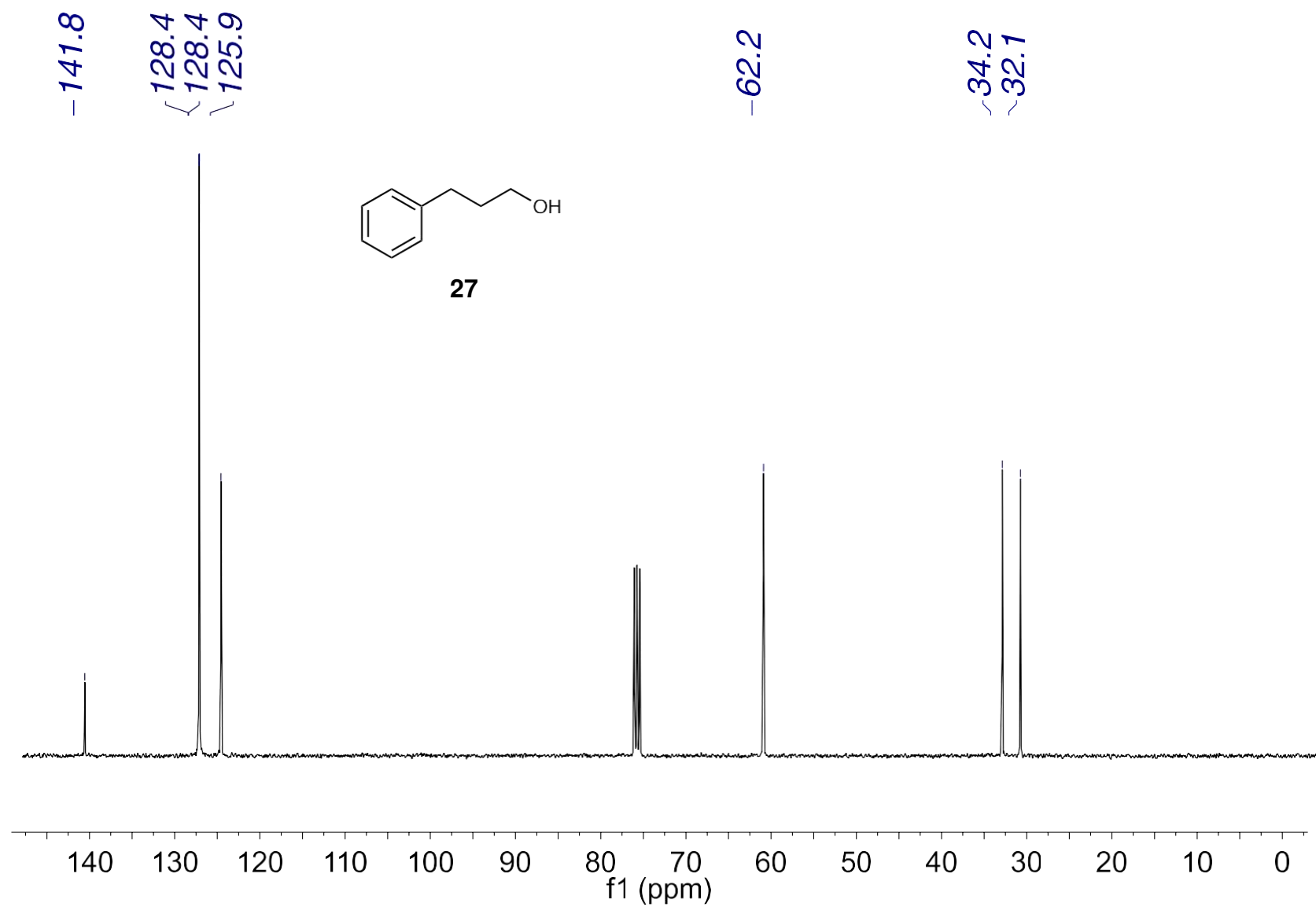


Fig. S5.103.  $^{13}\text{C}$  NMR of phenylpropane-3-ol (27) ( $\text{CDCl}_3$ , 101 MHz).

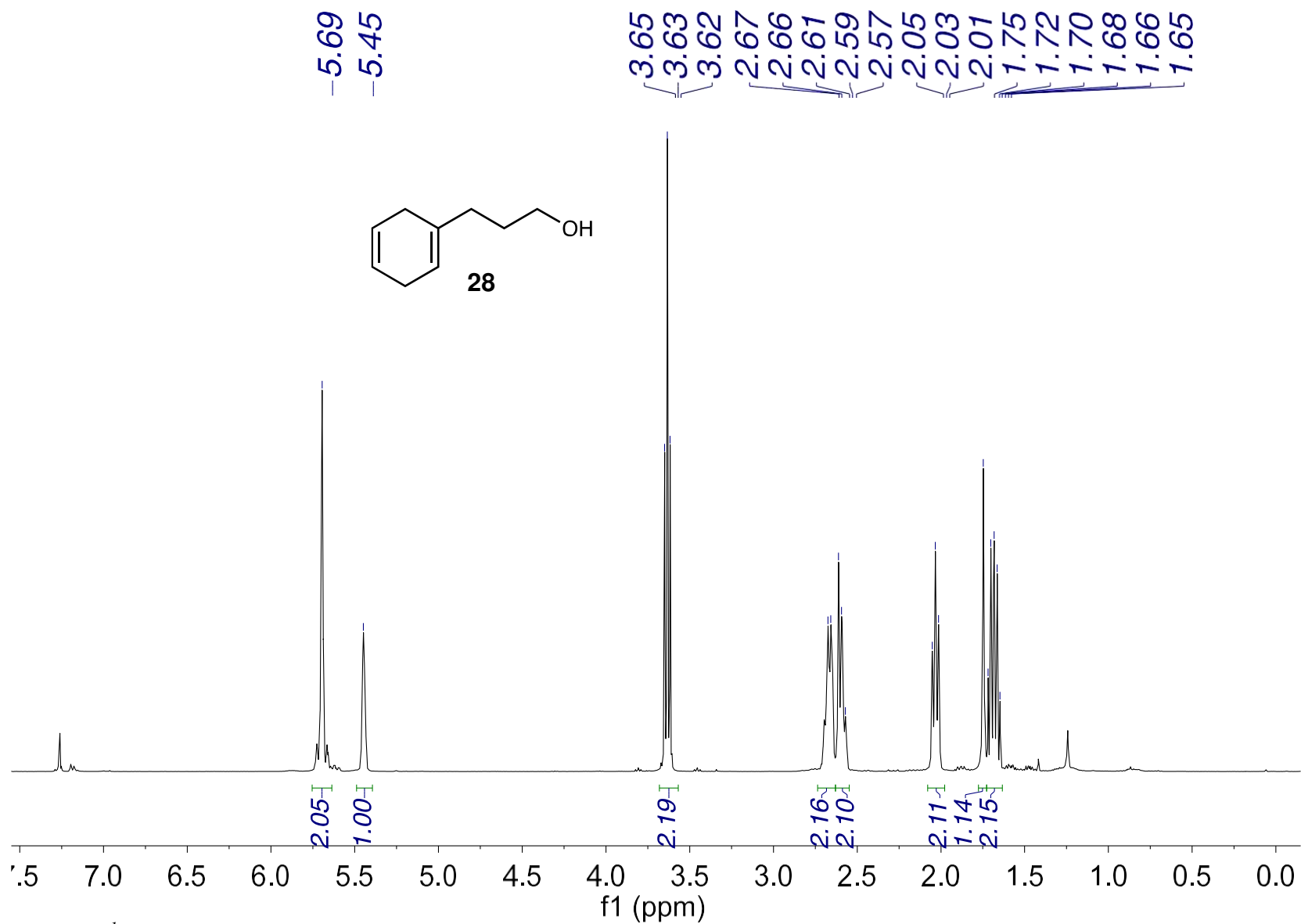


Fig. S5.104. <sup>1</sup>H NMR of 3-(cyclohexa-1,4-dien-1-yl)propan-1-ol (28) (CDCl<sub>3</sub>, 400 MHz).

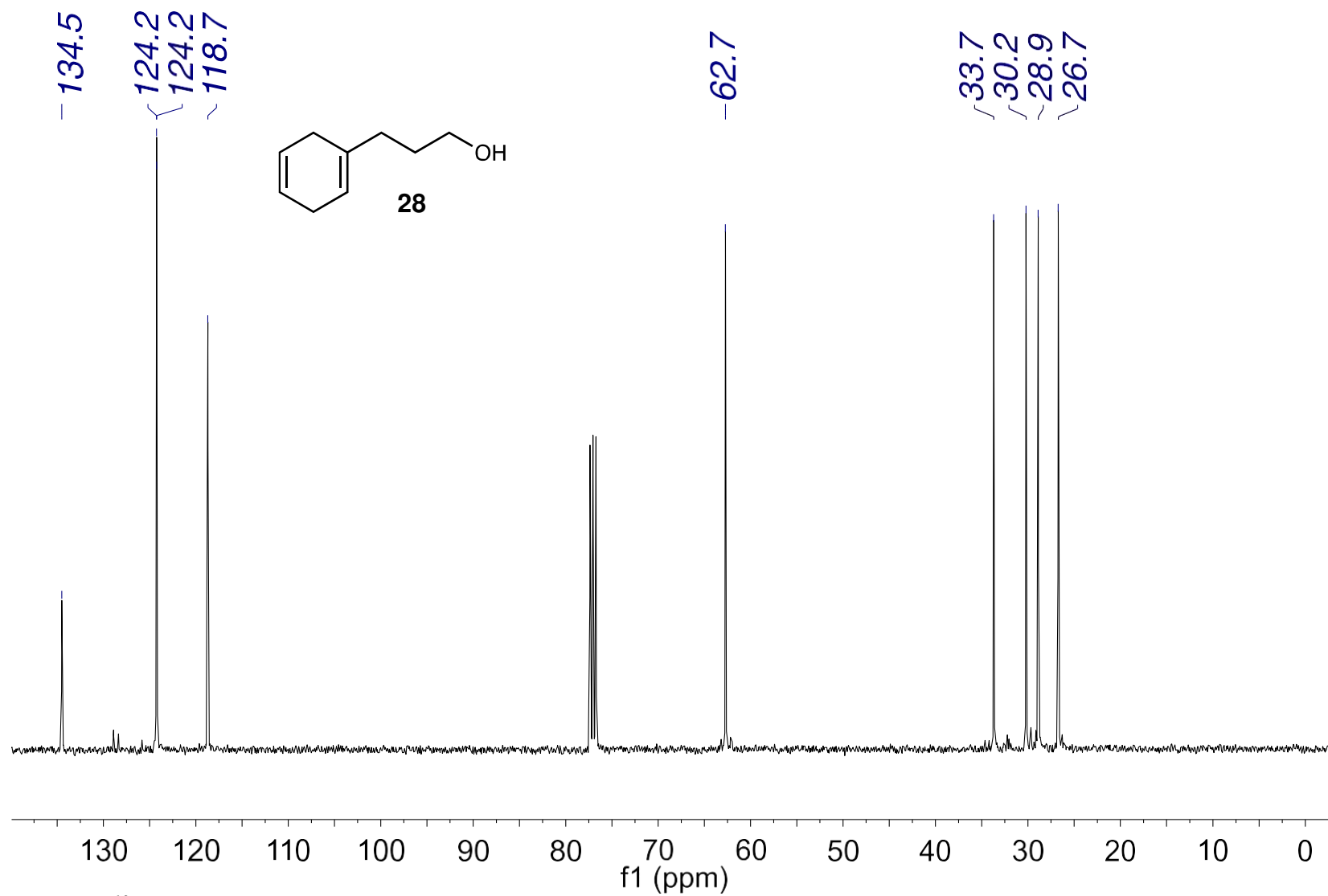


Fig. S5.105.  $^{13}\text{C}$  NMR of 3-(cyclohexa-1,4-dien-1-yl)propan-1-ol (28) ( $\text{CDCl}_3$ , 101 MHz).

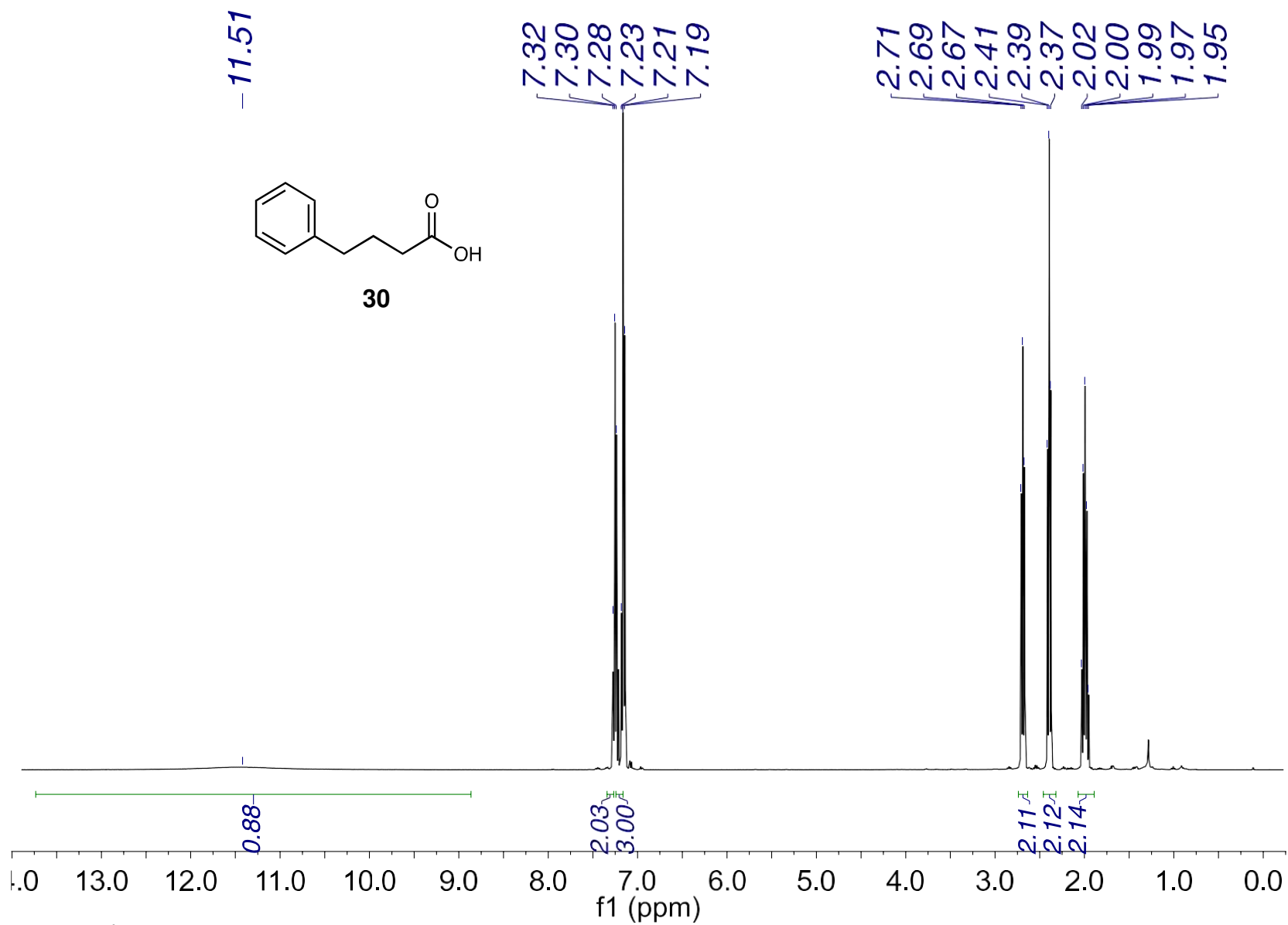


Fig. S5.106. <sup>1</sup>H NMR of 4-phenylbutanoic acid (30) (CDCl<sub>3</sub>, 400 MHz).

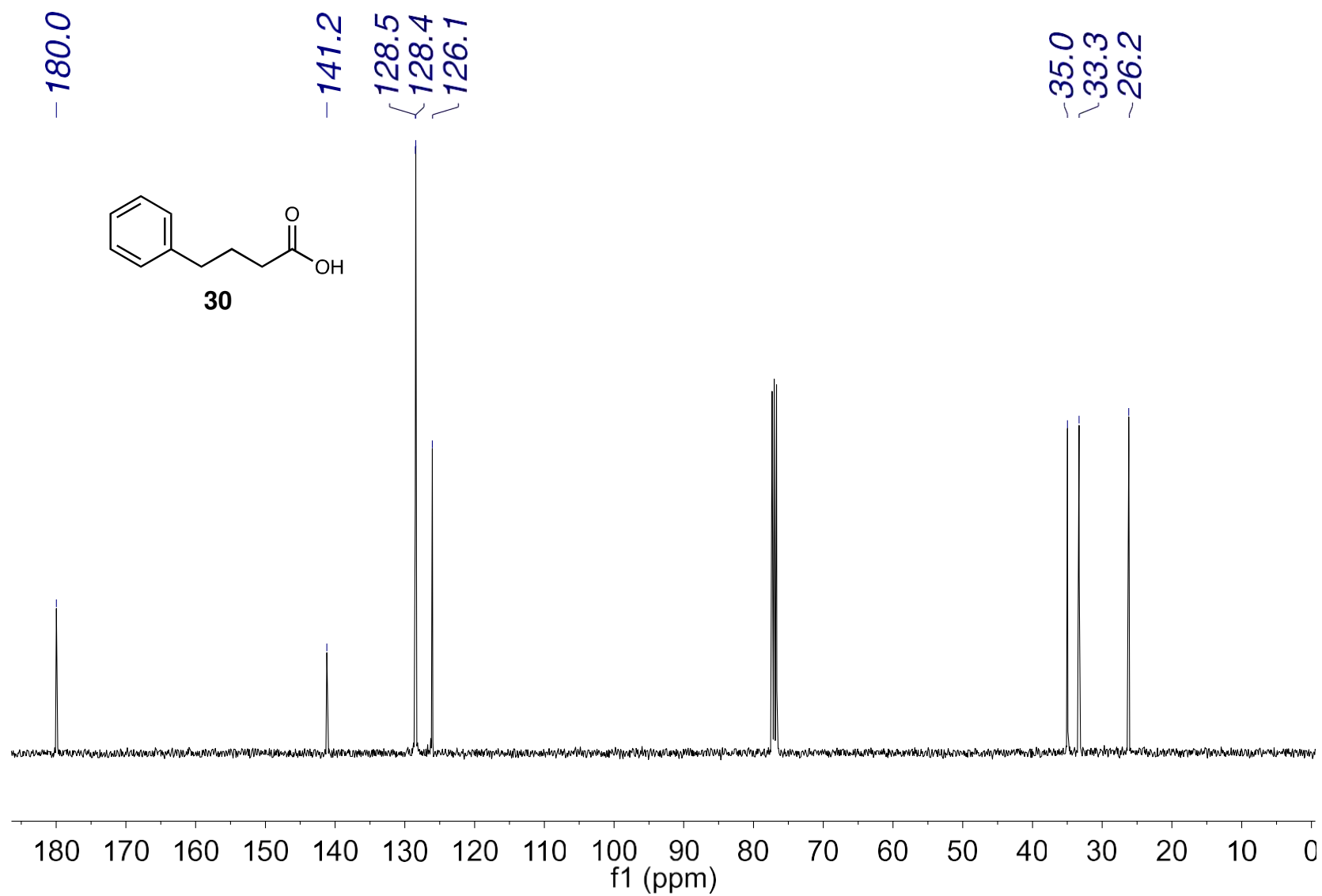


Fig. S5.107.  $^{13}\text{C}$  NMR of 4-phenylbutanoic acid (30) ( $\text{CDCl}_3$ , 101 MHz).



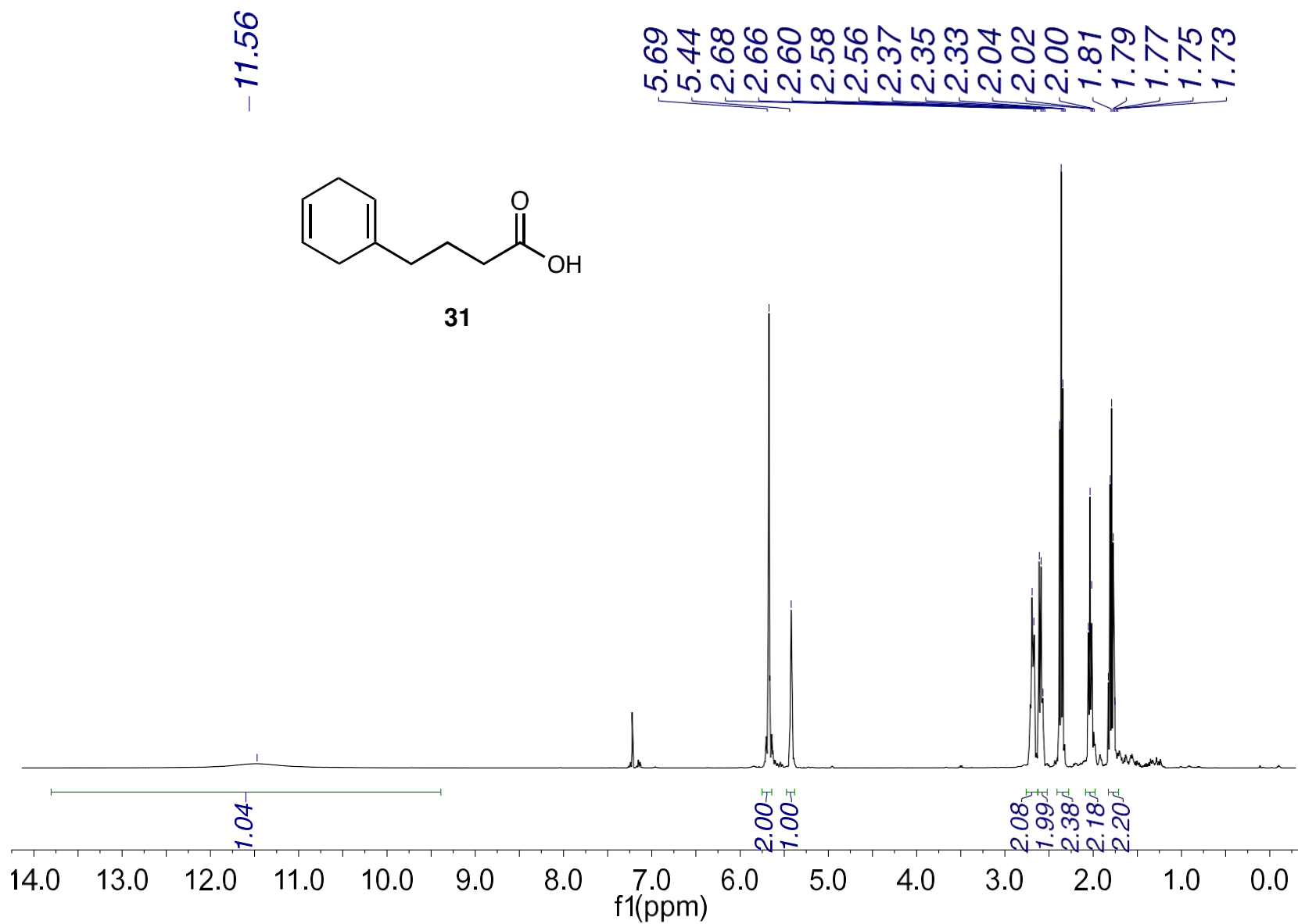


Fig. S5.108.  $^1\text{H}$  NMR of 4-(cyclohexa-1,4-dien-1-yl)butanoic acid (31) ( $\text{CDCl}_3$ , 400 MHz).

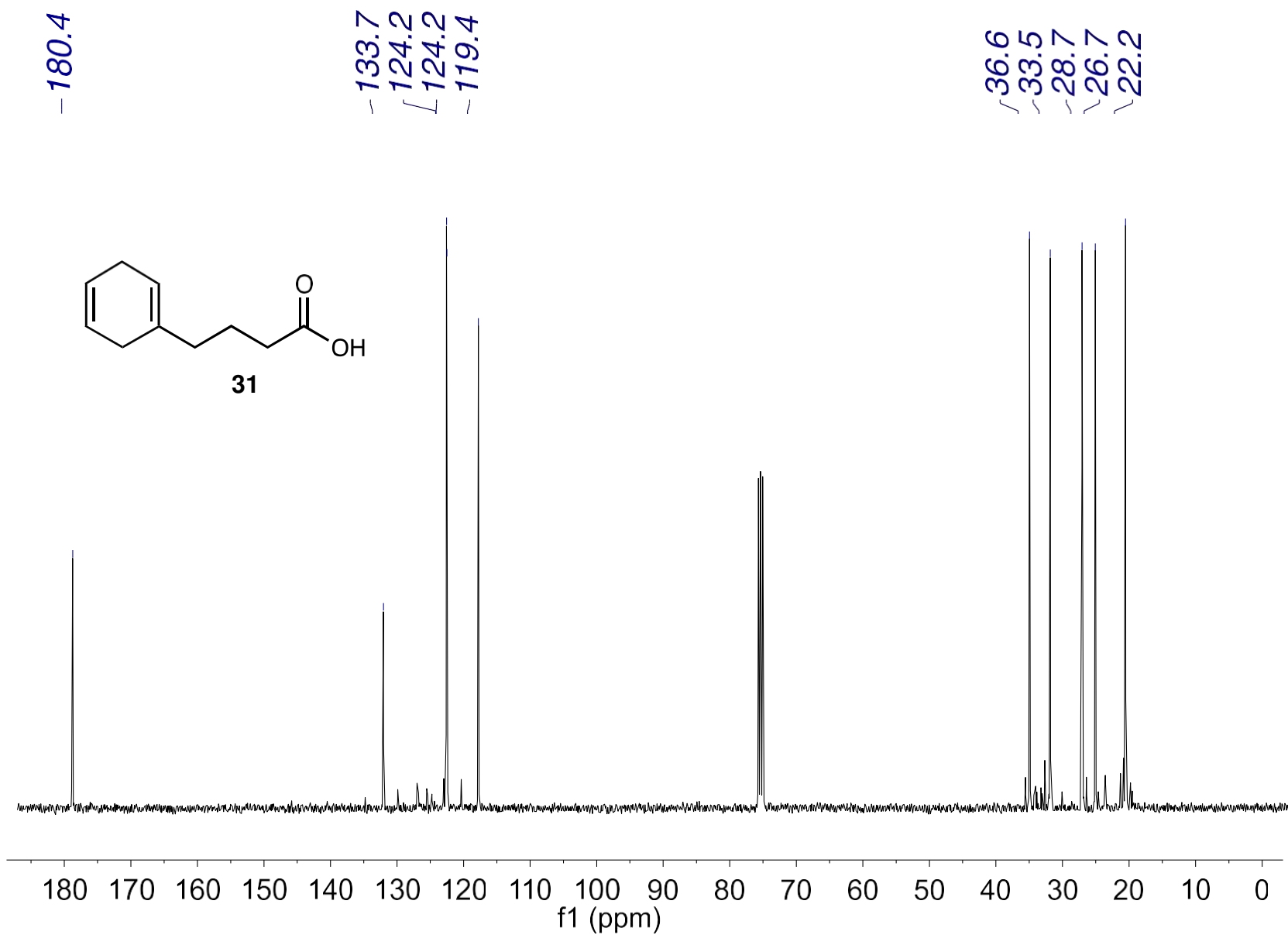


Fig. S5.109.  $^{13}\text{C}$  NMR of 4-(cyclohexa-1,4-dien-1-yl)butanoic acid (31) ( $\text{CDCl}_3$ , 101 MHz).

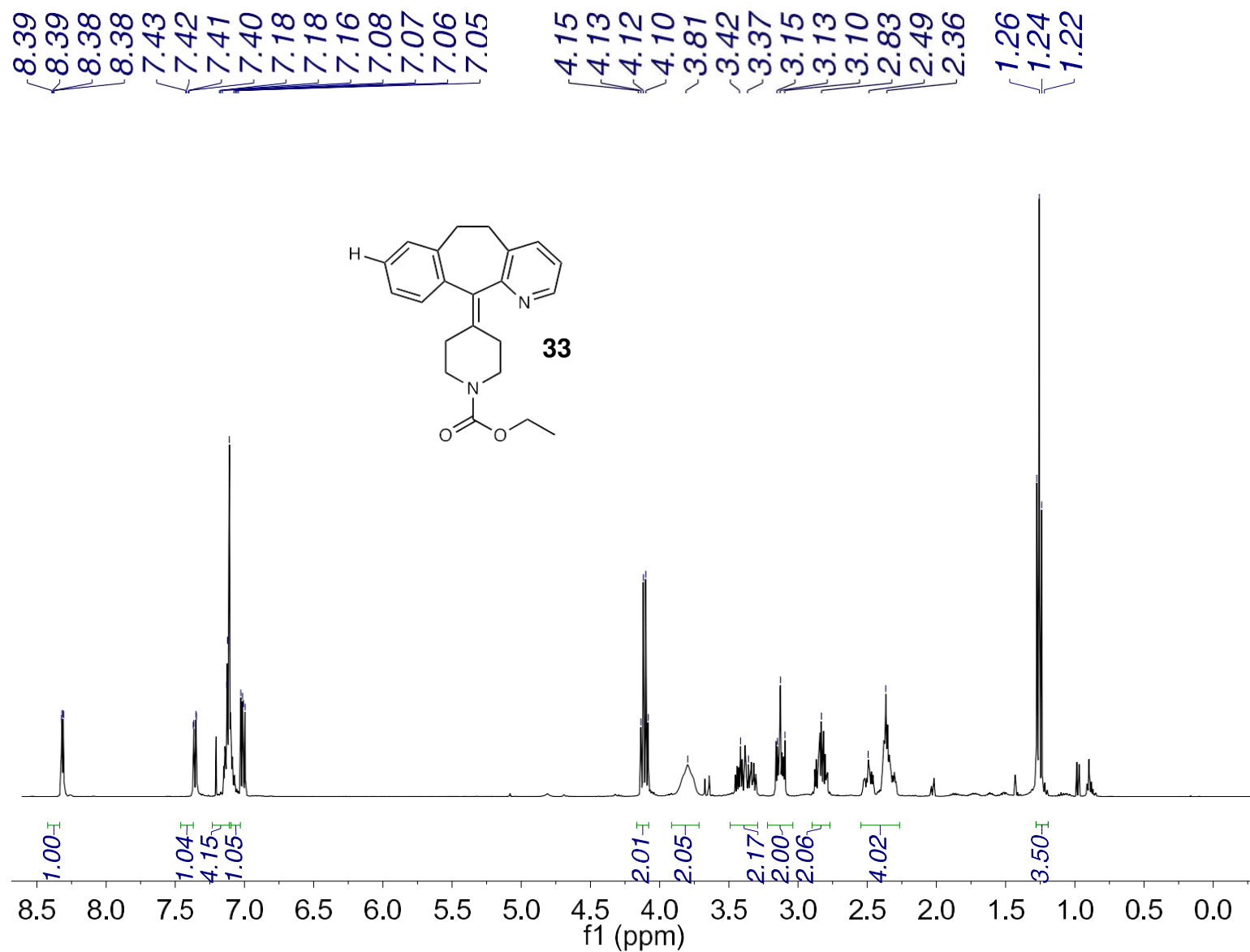


Fig. S5.110. <sup>1</sup>H NMR of ethyl 4-(5,6-dihydro-11H-benzo[5,6]cyclohepta[1,2-b]pyridin-11-ylidene)piperidine-1-carboxylate (**33**) (CDCl<sub>3</sub>, 400 MHz).

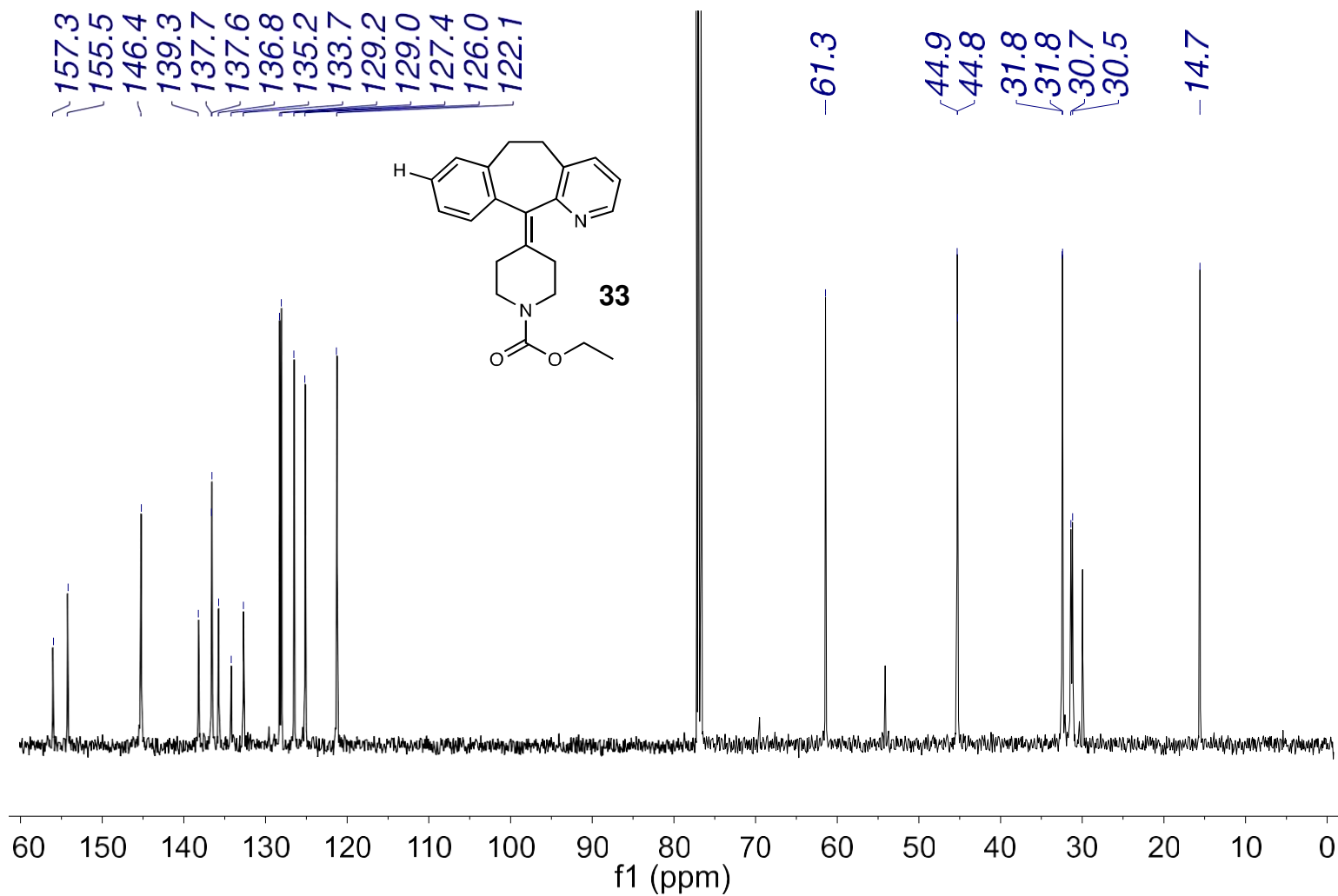


Fig. S5.111. <sup>13</sup>C NMR of ethyl 4-(5,6-dihydro-11H-benzo[5,6]cyclohepta[1,2-b]pyridin-11-ylidene)piperidine-1-carboxylate (33) (CDCl<sub>3</sub>, 101 MHz).

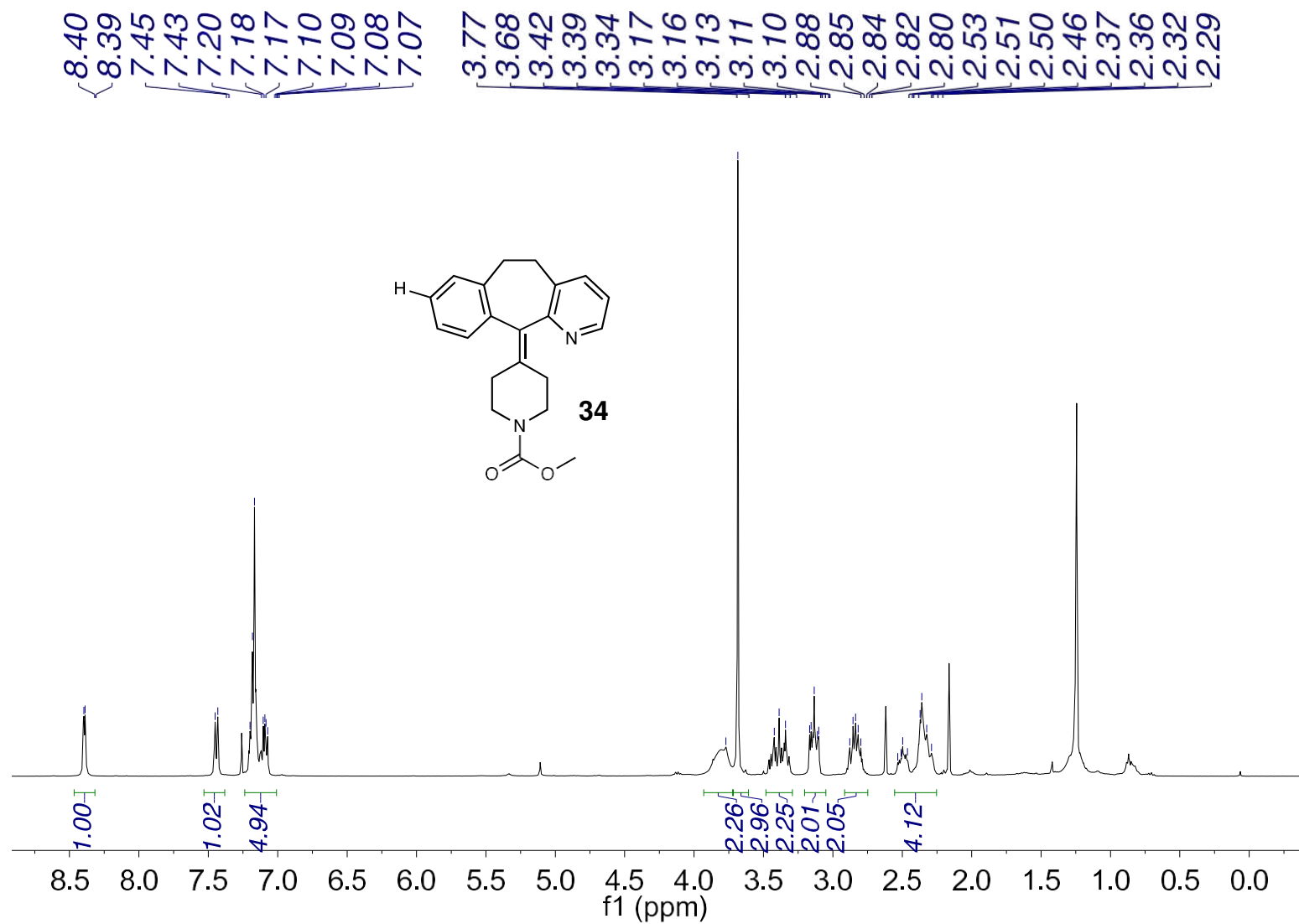


Fig. S5.112. <sup>1</sup>H NMR of methyl 4-(5,6-dihydro-11H-benzo[5,6]cyclohepta[1,2-b]pyridin-11-ylidene)piperidine-1-carboxylate (34) (CDCl<sub>3</sub> 400 MHz).

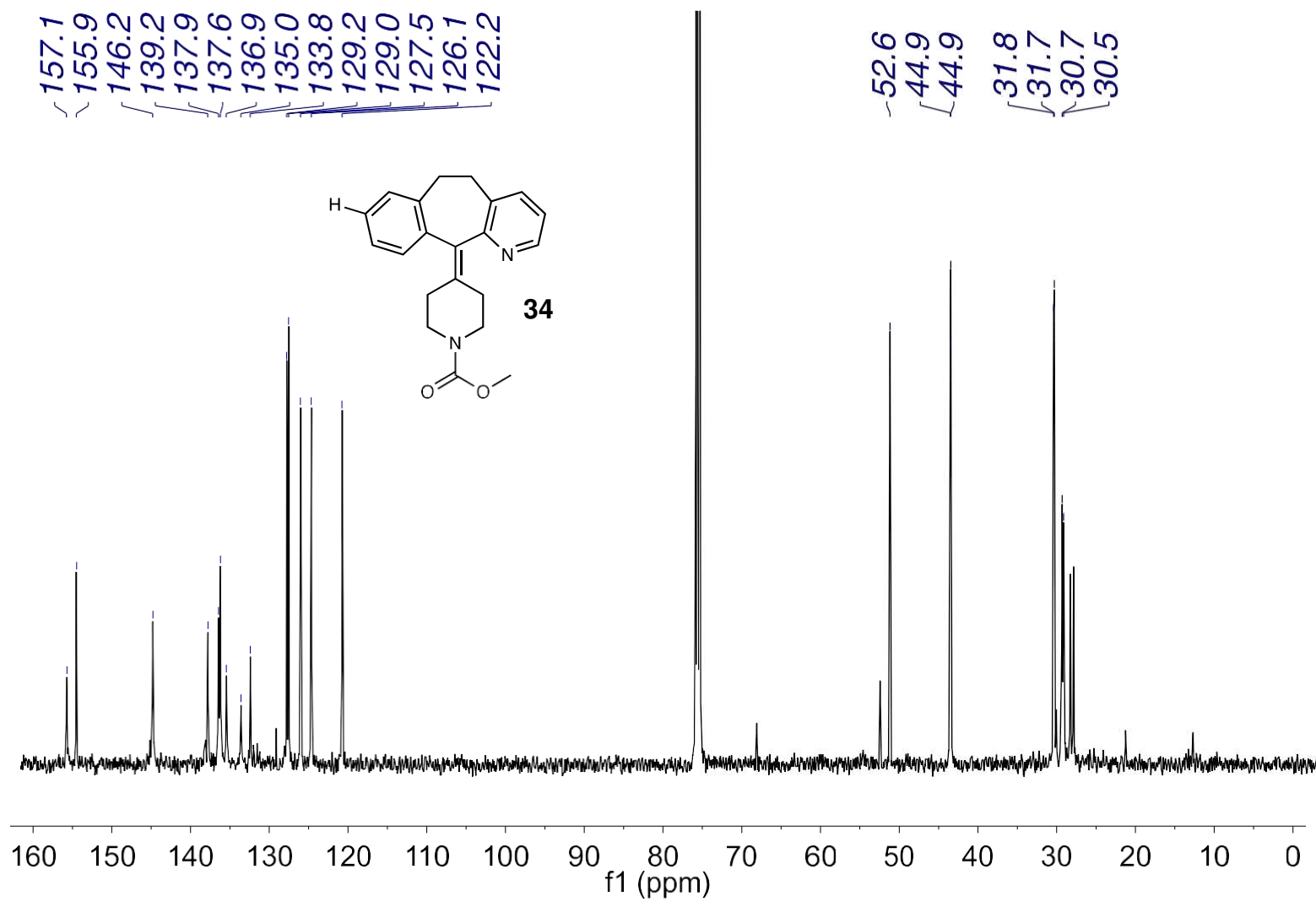


Fig. S5.113. <sup>13</sup>C NMR of methyl 4-(5,6-dihydro-11H-benzo[5,6]cyclohepta[1,2-b]pyridin-11-ylidene)piperidine-1-carboxylate (34) (CDCl<sub>3</sub> 101 MHz).

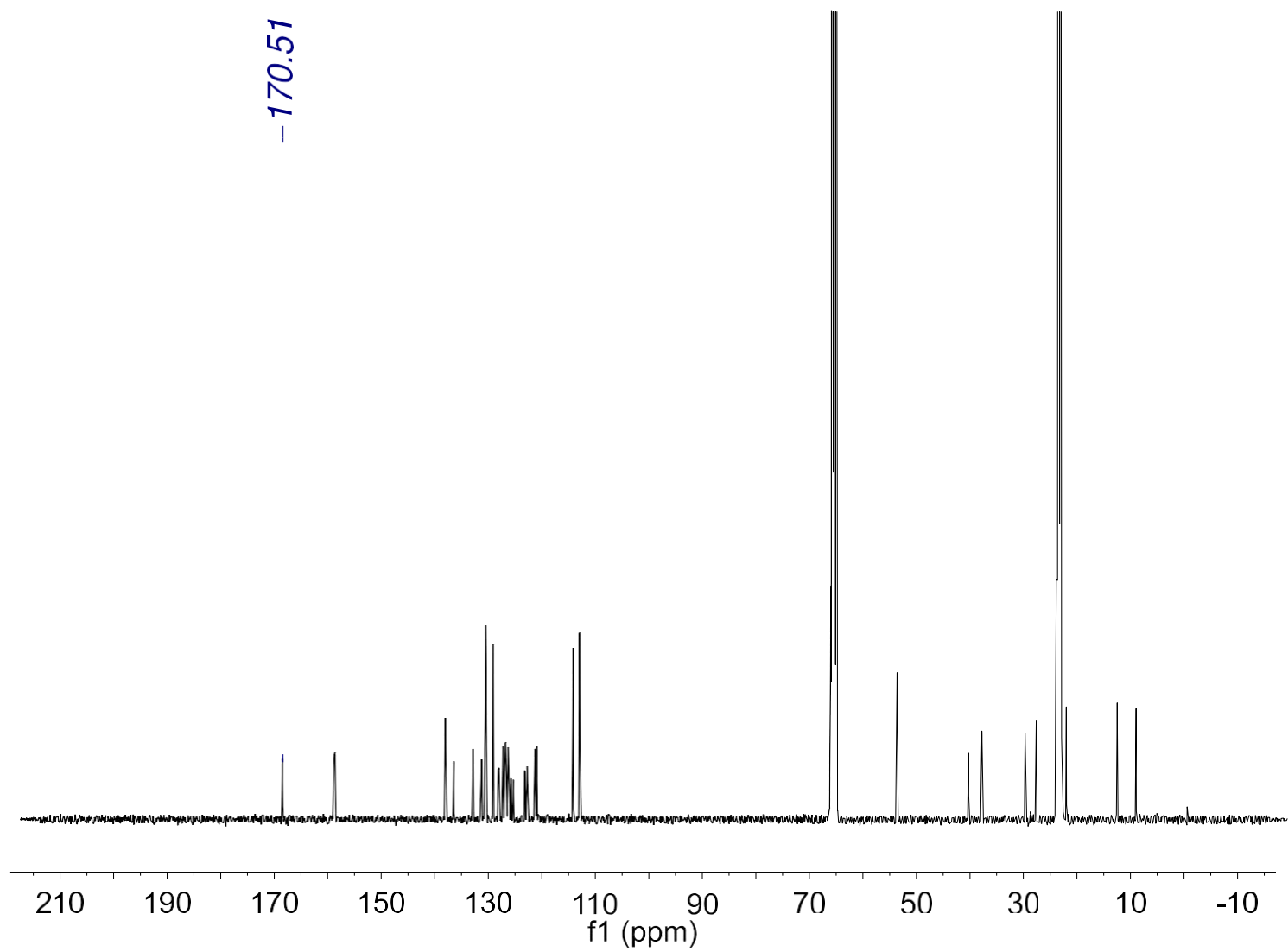


Fig. S5.114.  $^{13}\text{C}$  NMR of compound PC 7 (THF- $d_8$  101 MHz).

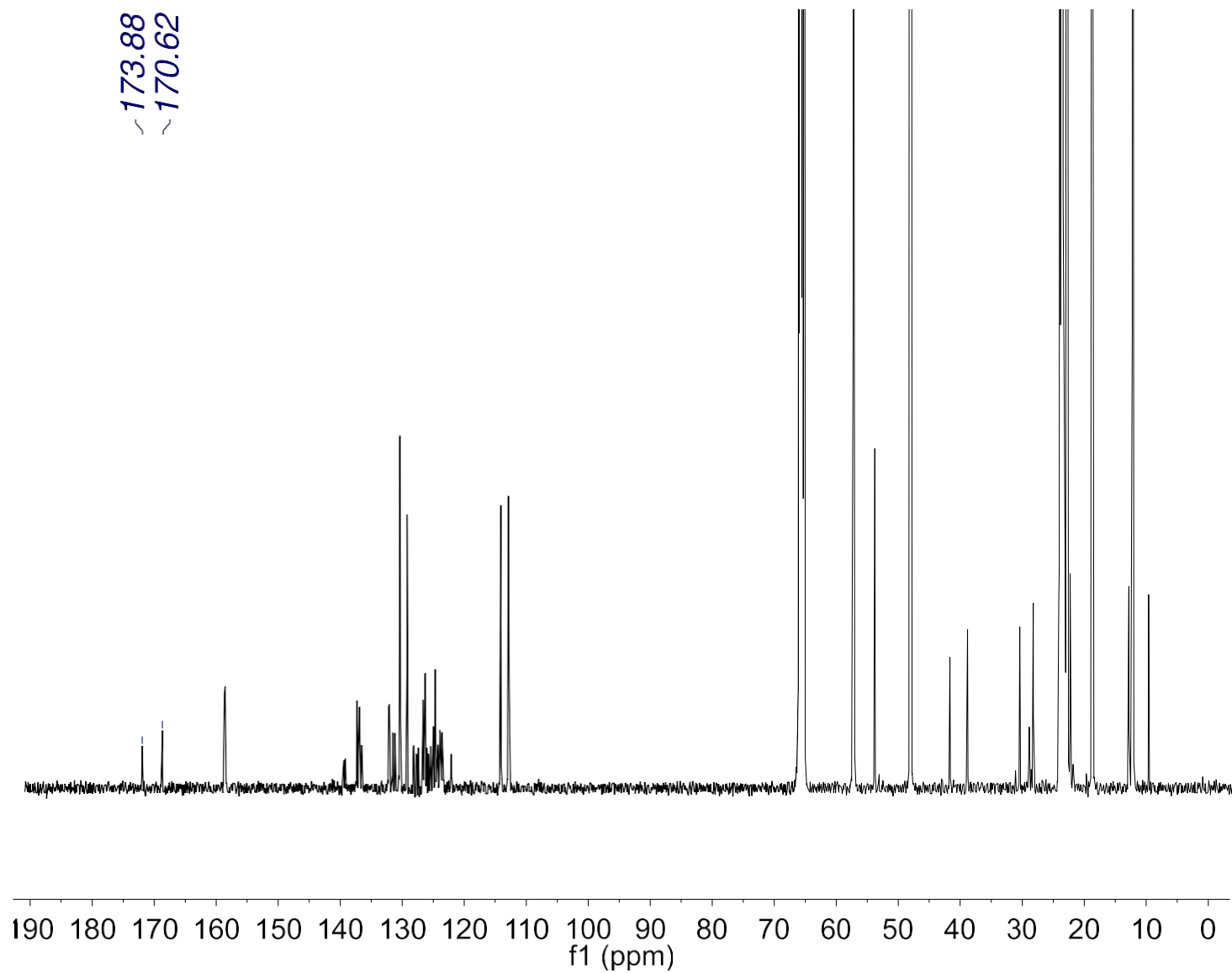


Fig. S5.115.  $^{13}\text{C}$  NMR of compound  $[\text{PC 7-OH}]^-$  complex ( $\text{THF-d}_8$  101 MHz).



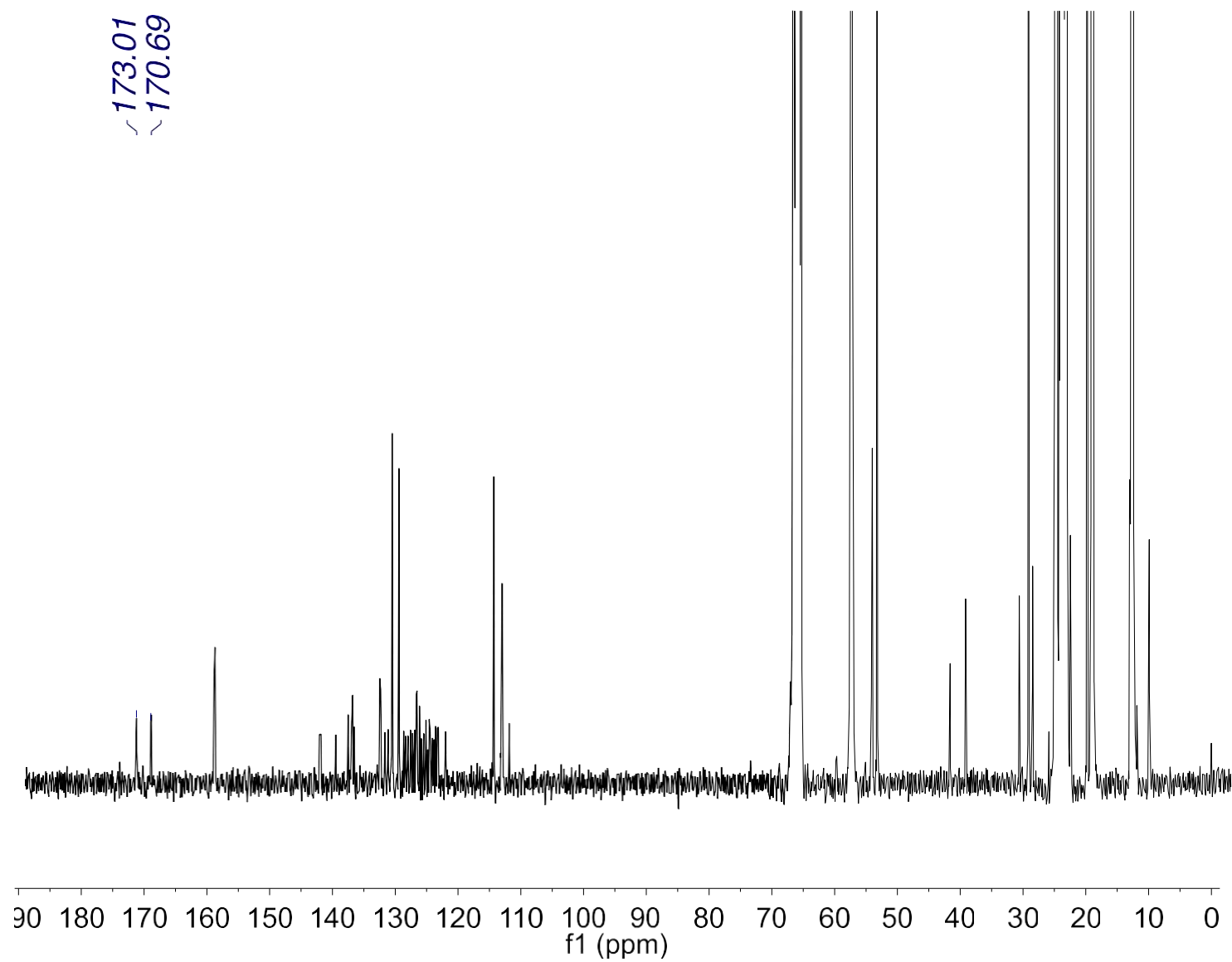


Fig. S5.116.  $^{13}\text{C}$  NMR of compound  $[\text{PC } 7\text{-F}]^-$  complex ( $\text{THF-d}_8$  101 MHz).

## 7. Computational Data and Methods

All calculations were performed using computational chemistry software package Gaussian 16 ver. C01<sup>13</sup>. We acknowledge the use of computational resource provided by XSEDE - Comet supercomputer (grant number CHE 160041).

### Thermochemistry

Geometries of all molecular structures were optimized at the unrestricted M06/6-31G(d,p)/CPCM-methanol level of theory<sup>14</sup> followed by frequency calculations to obtain zero point energy (ZPE) corrections, thermal corrections, and entropic TS terms using ideal gas approximations. The obtained Gibbs free energy,  $G^{0*}(298\text{K}, 1\text{atm})$ , by default has a standard reference state of 298.15K and 1 atm. However, a standard reference state of 298.15K and 1 mole/liter [ $G^0(298\text{K}, 1\text{M})$ ] is more relevant for reactions carried out in the liquid phase as in our reaction conditions.

To obtain the Gibbs free energy with relevant standard state reference,  $G^0(298\text{K}, 1\text{M}) = G^{0*}(298\text{K}, 1\text{atm}) + RT \ln(0.08206T)$ , where R is the gas constant and T is the temperature.  $\Delta G^0(298\text{K}, 1\text{M}) = \Delta G^{0*}(298\text{K}, 1\text{atm})$  when there is no mole change from the reactant to the product. However, for every net mole change  $\Delta G^0(298\text{K}, 1\text{M}) = \Delta G^{0*}(298\text{K}, 1\text{atm}) - 1.89$  kcal/mol.

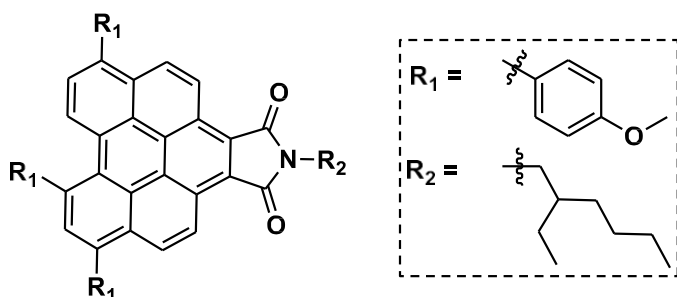
At the converged geometries, single point calculations at uM06/6-311+G(d,p)/CPCM-methanol were performed; the various corrections and entropic TS terms from uM06/6-31G(d,p) calculations were then applied to the energy obtained with uM06/6-311+G(d,p).

### Reduction Potential (E0) Calculations

Standard reduction potentials ( $E^0$ ) were calculated following previously reported procedures 15,16. A value of -100.5 kcal/mol was assumed 15 for the reduction free energy of the standard hydrogen electrode (SHE). Thus,  $E^0 = (-100.5 - \Delta G_{\text{red}})/23.06$  (V vs. SHE); for  $E^0$  ( $\text{PC}^{*+}/\text{PC}^*$ ),  $\Delta G_{\text{red}} = G(\text{PC}^*) - G(\text{PC}^{*+})$  while for  $E^0$  ( $\text{PC}/\text{PC}^{\bullet-}$ ),  $\Delta G_{\text{red}} = G(\text{PC}^{\bullet-}) - G(\text{PC})$ . The Gibbs were calculated at the unrestricted M06/6-311+G(d,p) level of theory in CPCM- $\text{H}_2\text{O}$  solvent (single point energy) using geometries optimized at unrestricted M06/6-31G(d,p) level of theory in CPCM- $\text{H}_2\text{O}$  solvent. To reference to the Saturated Calomel Electrode (SCE),  $E^0$  (vs. SHE) is converted to  $E^0$  (vs. SCE) using  $E^0$  (vs. SCE) =  $E^0$  (vs. SHE) - 0.24 V. The lowest singlet excited state  $S_1$  energy [ $E(S_1)$ ] was obtained from TD-DFT optimization detailed below.

### Excited State Calculation

Ground state geometries of BPI derivatives were first obtained from optimization calculations at CAM-B3LYP/6-31G(d,p)/CPCM-methanol<sup>17</sup>. Using these geometries, single point time dependent density functional theory (TD-DFT) calculations were then performed at the CAM-B3LYP/6-31G(d,p)/CPCM-methanol level of theory. The first 5 excited states of PC and  $[\text{PC-OH}]^-$  were reported below, which correspond to their vertical excitation energies. The orbitals involved in a given transition are reported, followed by the contribution of those orbitals to the transition.



Excited State 1: Singlet-?Sym 3.0415 eV 407.64 nm f=0.2401 <S\*\*2>=0.000

201 -> 206 0.13375

202 -> 207 0.12928

204 -> 207 -0.10547

205 -> 206 0.64896

Excited State 2: Singlet-?Sym 3.2502 eV 381.47 nm f=0.5002 <S\*\*2>=0.000

202 -> 206 -0.16345

203 -> 206 0.12498

204 -> 206 0.13101

205 -> 207 0.64514

Excited State 3: Singlet-?Sym 3.6576 eV 338.98 nm f=0.4524 <S\*\*2>=0.000

194 -> 206 0.15635

201 -> 206 0.19349

202 -> 206 0.40782

203 -> 206 -0.27895

204 -> 206 -0.31117

205 -> 207 0.25099

Excited State 4: Singlet-?Sym 4.0920 eV 302.99 nm f=0.8011 <S\*\*2>=0.000

202 -> 207 -0.25893

203 -> 207 0.27375

204 -> 206 -0.11850

204 -> 207 0.47280

205 -> 206 0.19544

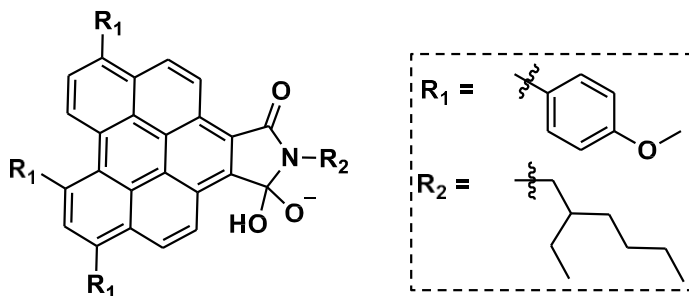
205 -> 211 -0.10597

Excited State 5: Singlet-?Sym 4.1282 eV 300.33 nm f=0.0075 <S\*\*2>=0.000

193 -> 206 0.64705

193 -> 210 0.14005

193 -> 211 -0.12618



Excited State 1: Singlet-?Sym 3.2944 eV 376.34 nm f=0.7093 <S\*\*2>=0.000

210 -> 211 0.68444

Excited State 2: Singlet-?Sym 3.5521 eV 349.05 nm f=0.0207 <S\*\*2>=0.000

203 -> 211 0.10337

207 -> 211 -0.27034

209 -> 211 0.36930

210 -> 212 0.47396

Excited State 3: Singlet-?Sym 4.0387 eV 306.99 nm f=0.0951 <S\*\*2>=0.000

207 -> 211 0.15324

207 -> 212 0.15155

209 -> 211 0.22833

209 -> 212 0.55927

209 -> 222 0.13119

210 -> 212    -0.11481  
 Excited State 4:    Singlet-?Sym 4.1495 eV 298.79 nm f=0.3895 <S\*\*2>=0.000  
 208 -> 211    -0.14261  
 209 -> 211    0.48681  
 209 -> 212    -0.25211  
 210 -> 212    -0.29958  
 210 -> 213    0.12363  
 Excited State 5:    Singlet-?Sym 4.2753 eV 290.00 nm f=0.7796 <S\*\*2>=0.000  
 204 -> 211    -0.11070  
 207 -> 211    0.27133  
 207 -> 212    0.12806  
 208 -> 211    -0.28823  
 208 -> 212    -0.17236  
 210 -> 212    0.27074  
 210 -> 213    0.33302

For [PC-OH], its relaxed S<sub>1</sub> geometry was obtained from TD-DFT optimization at the same CAM-B3LYP/6-31G(d,p)/CPCM-methanol level of theory. The first 3 excited state energies from this relaxed S<sub>1</sub> geometry are reported below. The fluorescence or E(S<sub>1</sub>) energy was predicted to be 2.44 eV (507 nm). The orbitals involved in a given transition are reported, followed by the contribution of those orbitals to the transition.

Excited State 1:    Singlet-?Sym 2.4439 eV 507.32 nm f=0.9254 <S\*\*2>=0.000  
 210 -> 211    0.69743

Total Energy, E(TD-HF/TD-DFT) = -2552.27748931

Excited State 2: Singlet-?Sym 3.2633 eV 379.93 nm f=0.0096 <S\*\*2>=0.000

203 -> 211 0.11262

205 -> 211 -0.11005

207 -> 211 -0.23037

208 -> 211 0.17873

209 -> 211 0.34007

210 -> 212 0.48065

Excited State 3: Singlet-?Sym 3.6948 eV 335.57 nm f=1.9448 <S\*\*2>=0.000

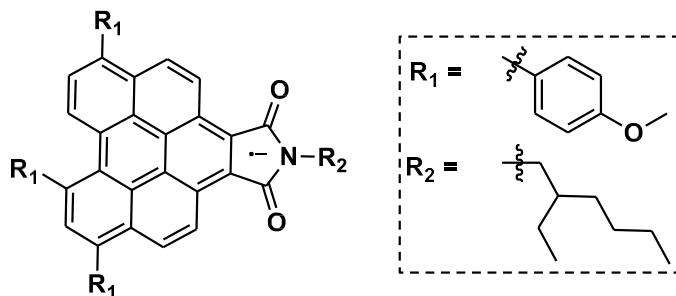
207 -> 211 -0.20680

208 -> 211 0.15427

209 -> 211 0.43047

210 -> 212 -0.45548

The first 10 excited states of PC<sup>+</sup> are shown below:



Excited State 1: 2.348-?Sym 1.1324 eV 1094.93 nm f=0.0200

<S\*\*2>=1.129

205A -> 207A -0.18412

206A -> 207A 0.91332

206A -> 209A	0.13430
206A -> 210A	-0.14507
206A -> 211A	-0.13685
205B -> 206B	-0.21080

This state for optimization and/or second-order correction.Total Energy, E(TD-HF/TD-DFT) = -  
2476.54049979

Excited State 2: 3.195-?Sym 2.0773 eV 596.84 nm f=0.0031 <S\*\*2>=2.303

205A -> 207A	0.53460
206A -> 207A	0.23762
206A -> 208A	0.11523
206A -> 210A	-0.12405
206A -> 211A	-0.13538
204B -> 207B	0.24321
205B -> 206B	0.62904
205A <- 207A	0.10531
205B <- 206B	0.11680

Excited State 3: 2.267-?Sym 2.6606 eV 466.00 nm f=0.2164 <S\*\*2>=1.035

206A -> 207A	-0.10807
206A -> 209A	0.82634
206A -> 210A	0.27203
206A -> 211A	-0.10330
206A -> 214A	0.11617
206A -> 215A	0.21721



205B -> 207B 0.13176

Excited State 4: 2.221-?Sym 2.7304 eV 454.09 nm f=0.0562 <S\*\*2>=0.983

206A -> 207A 0.18213

206A -> 208A 0.44076

206A -> 209A -0.23415

206A -> 210A 0.63740

206A -> 211A 0.18938

206A -> 214A 0.37316

206A -> 218A -0.13026

Excited State 5: 2.392-?Sym 2.7628 eV 448.76 nm f=0.0086 <S\*\*2>=1.181

205A -> 207A 0.11120

205A -> 208A -0.15040

206A -> 207A -0.18407

206A -> 208A 0.69576

206A -> 210A -0.29815

206A -> 211A -0.27939

206A -> 217A -0.20569

201B -> 206B 0.10995

204B -> 207B -0.20393

205B -> 206B -0.20617

205B -> 208B -0.11714

Excited State 6: 2.626-?Sym 2.9802 eV 416.03 nm f=0.0135 <S\*\*2>=1.474

197A -> 207A	-0.14934
202A -> 207A	-0.12869
204A -> 207A	-0.15555
205A -> 211A	-0.15197
206A -> 208A	0.15424
206A -> 209A	0.26971
206A -> 210A	-0.18099
206A -> 211A	0.61346
206A -> 213A	0.17409
206A -> 214A	0.19421
206A -> 216A	0.33103
197B -> 206B	0.15244
202B -> 206B	0.12280
205B -> 210B	-0.14641
Excited State 7:	3.296-?Sym 3.1096 eV 398.71 nm f=0.0182 <S**2>=2.465
197A -> 207A	-0.13232
203A -> 207A	-0.11163
204A -> 207A	0.43081
205A -> 210A	0.11776
205A -> 211A	-0.13452
206A -> 210A	0.12546
197B -> 206B	0.16155
202B -> 206B	0.10743

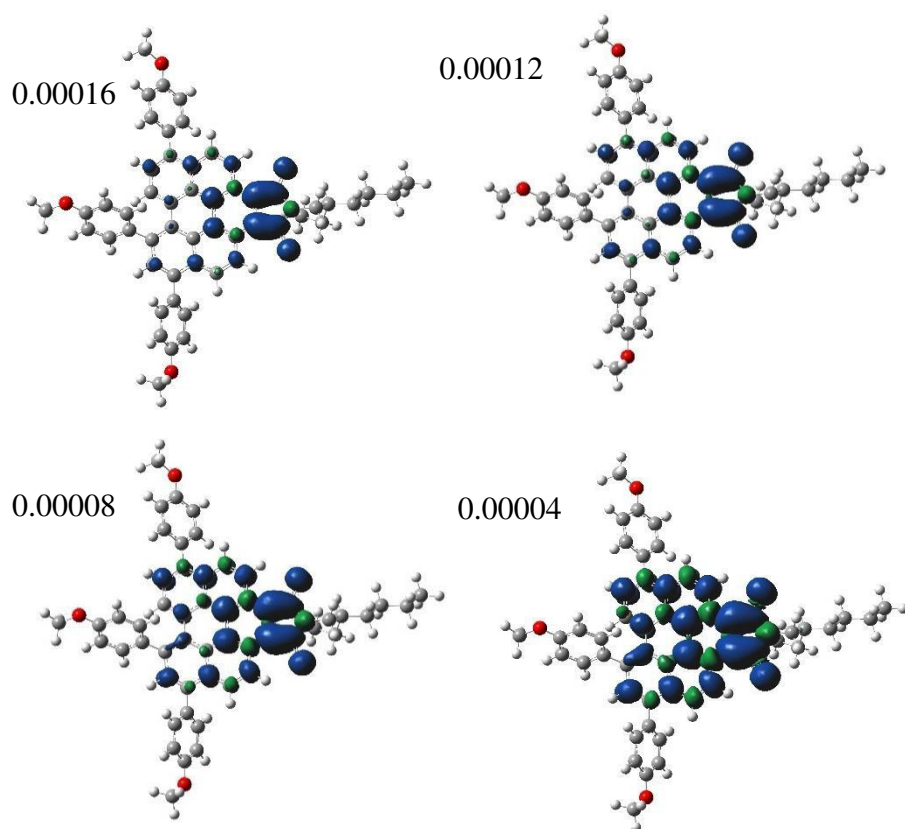
204B -> 206B	0.50287			
204B -> 208B	0.12456			
205B -> 207B	0.29246			
205B -> 209B	-0.12592			
205B -> 210B	-0.14832			
Excited State 8:	2.304-?Sym	3.2307 eV	383.77 nm	f=0.0470 <S**2>=1.077
205A -> 207A	-0.26090			
206A -> 207A	-0.13234			
206A -> 208A	0.17202			
206A -> 210A	-0.11077			
206A -> 211A	-0.18243			
191B -> 207B	0.14365			
204B -> 207B	0.79797			
205B -> 206B	-0.11298			
205B -> 207B	0.14974			
Excited State 9:	2.518-?Sym	3.2709 eV	379.06 nm	f=0.0104 <S**2>=1.335
201B -> 207B	-0.16422			
204B -> 206B	-0.57470			
204B -> 209B	-0.11391			
205B -> 207B	0.72872			
205B -> 215B	-0.10199			
Excited State 10:	3.364-?Sym	3.4050 eV	364.12 nm	f=0.0523 <S**2>=2.580
192A -> 214A	0.11458			

193A -> 213A	-0.10099
194A -> 213A	0.15046
196A -> 214A	-0.10604
201A -> 215A	0.19942
202A -> 215A	0.11643
203A -> 207A	-0.24055
203A -> 208A	0.11827
203A -> 209A	0.10122
203A -> 210A	-0.15304
203A -> 217A	0.17763
205A -> 207A	-0.15248
205A -> 209A	0.12233
205A -> 215A	-0.15074
206A -> 215A	0.12956
192B -> 211B	-0.11432
192B -> 214B	-0.10152
193B -> 212B	-0.12598
194B -> 212B	0.11516
201B -> 213B	-0.13831
201B -> 215B	-0.15364
203B -> 206B	0.23648
203B -> 208B	-0.13504
203B -> 209B	-0.17390

203B -> 217B	-0.18788
205B -> 206B	0.16829
205B -> 213B	-0.13178

### Spin Density Calculation

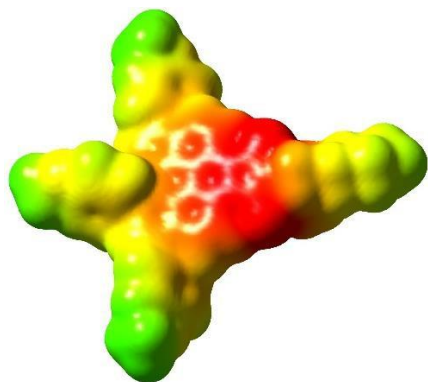
Spin density of PC<sup>-</sup> was computed at uM06/6-31G(d,p)/CPCM-methanol level of theory. In the manuscript, the spin density was visualized at density isovalue = 0.00012. Other density isovalues are shown below.



### Electrostatic Potential (ESP) Calculation

At the converged geometry of PC<sup>-</sup>, single point energy calculation with CHELPG ESP population analysis were performed at uM06/6-31G(d,p)/CPCM-methanol level of theory. Total

electron density of  $PC^{\bullet-}$  was first plotted and then were mapped with ESP derived charges to show distribution of charges on  $PC^{\bullet-}$  shown below. Range of ESP charges plotted = -0.150 to 0.150.



Proposed generation of solvated electron by  $PC^{\bullet-}$ \*

For the one electron reduction of PC to  $PC^{\bullet-}$ , the  $E^0$  was predicted to be -1.30 V vs. SCE, which is close to the experimental value of -1.24 V vs. SCE.  $PC^{\bullet-}$  can be photoexcited, where the first six excited states (ES) as predicted from TDDFT calculations, can be accessed by a 405 nm photon. These excited states have predicted  $E^0(PC/PC^{\bullet-*})$  values ranging from -2.43 to -4.28 V vs. SCE. In particular, ES(2-6) have sufficient thermodynamic force to generate a solvated electron at  $E^0_{\text{exp}} = -3.01$  V vs. SCE<sup>18</sup> with rate constant  $k_{\text{ET},1}$ . Benzene can be reduced to its anion radical ( $E^0_{\text{exp}} = -3.46$  V vs. SCE)<sup>19</sup> by a solvated electron with rate constant  $k_{\text{ET},2}$ . As a competing pathway, the solvated electron may deactivate to low-lying ES1 with rate constant  $k_{\text{ET},3}$ . ES1 can also be accessed from high-lying ES2-6 via internal conversion processes ( $k_{\text{IC}}$ ).

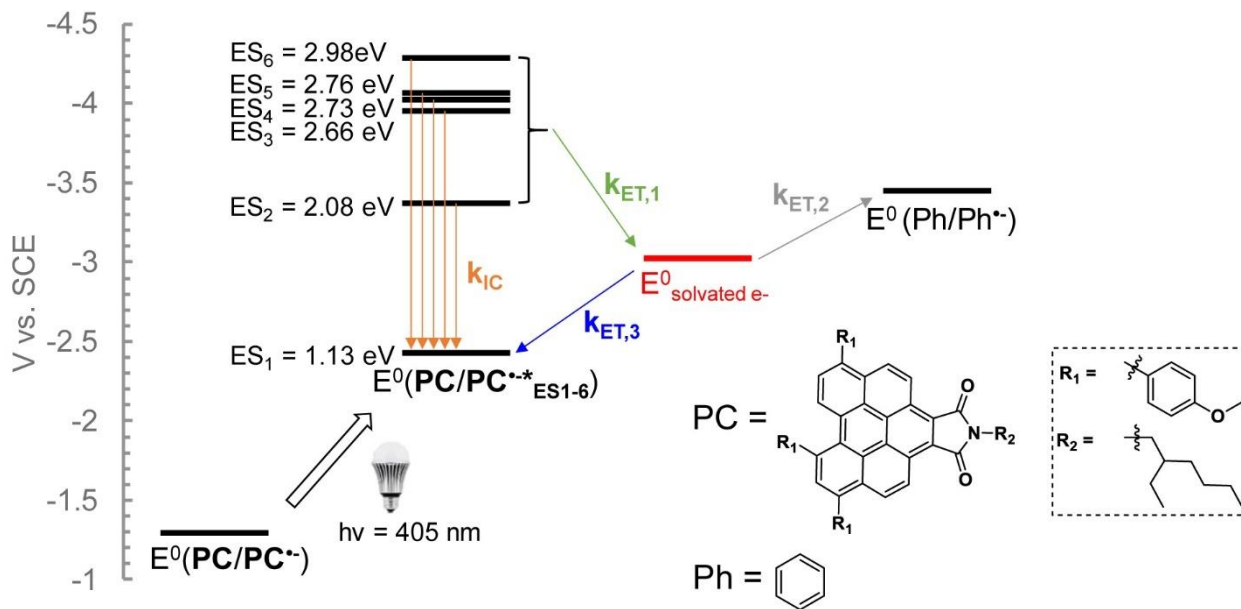


Fig. S5.117. Reduction potentials of PC<sup>\*•</sup> relative to a solvated electron and benzene.

### Nature of Photoexcitation of [PC-OH]<sup>-</sup>

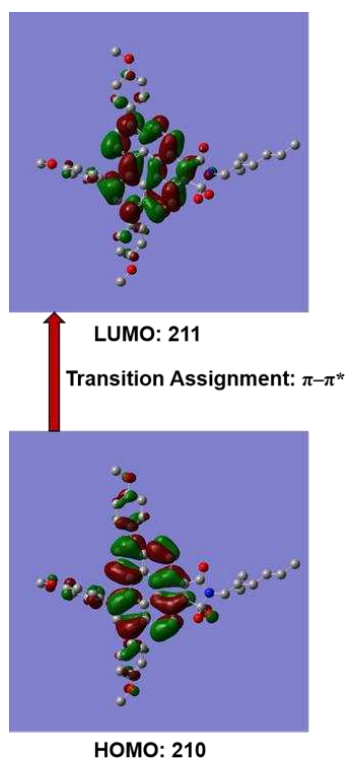
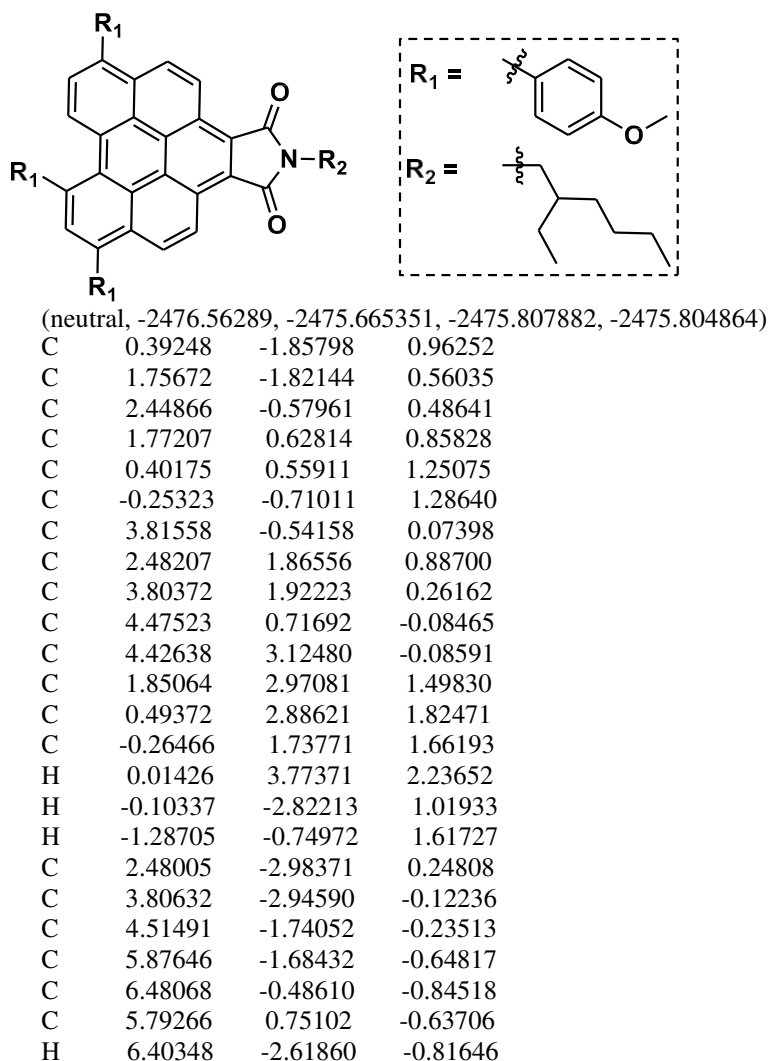


Fig. S5.118. Ground state highest occupied molecular orbital (HOMO) and lowest occupied molecular orbital (LUMO) for [PC-OH] computed at the CAM-B3LYP/6-31Gdp/CPCM-MeOH level of theory. The HOMO-LUMO transition can be assigned as  $\pi$ - $\pi^*$ .

### Coordinates of Molecular Structures

All coordinates are reported as XYZ Cartesian coordinates. Converged geometries were obtained from uM06/6-31G(d,p)/CPCM-methanol level of theory unless otherwise specified. Single point energies computed at uM06/6-311+G\*\* level of theory (reported in parentheses) are arranged in the following order:  $E_{0K}$  (not ZPE and thermally corrected), H (298.15 K, 1atm),  $G^{0*}$  (298.15 K, 1 atm), and  $G^0$  (298.15 K, 1 M). They are stated in Hartrees units.





C	5.68178	3.15433	-0.67316
H	6.11053	4.11380	-0.95556
C	6.39770	1.99270	-0.94506
C	2.03690	-4.40185	0.24965
C	4.26038	-4.33771	-0.37139
N	3.14974	-5.14902	-0.14152
O	5.35316	-4.75171	-0.70530
O	0.95007	-4.87401	0.51898
C	3.16988	-6.59381	-0.27456
H	4.07437	-6.96175	0.22583
H	2.30022	-6.96808	0.28127
C	-1.70810	1.78152	1.97767
C	-2.15943	2.35382	3.16859
C	-2.67214	1.31033	1.07239
C	-3.51491	2.45018	3.46829
H	-1.43332	2.71883	3.89289
C	-4.02301	1.40250	1.35277
H	-2.35269	0.88330	0.12347
C	-4.45556	1.97133	2.55580
H	-3.82187	2.89199	4.41118
H	-4.77066	1.04662	0.64838
C	3.12358	-7.10483	-1.71377
H	4.04703	-6.77297	-2.21981
C	3.12704	-8.63367	-1.66983
H	2.12556	-8.98088	-1.36157
H	3.81900	-8.97985	-0.88528
C	3.51915	-9.29444	-2.98192
H	2.86454	-8.94755	-3.79754
H	4.53655	-8.97282	-3.25824
C	3.46973	-10.81354	-2.91883
H	2.45160	-11.13020	-2.64608
H	4.12109	-11.16242	-2.10305
C	3.88271	-11.46621	-4.22685
H	3.84378	-12.55929	-4.17064
H	3.22592	-11.15114	-5.04757
H	4.90677	-11.18282	-4.50108
C	1.91425	-6.56266	-2.48980
H	1.06469	-6.45890	-1.79695
H	1.60117	-7.31424	-3.22782
C	2.16219	-5.25323	-3.22477
H	1.28181	-4.94641	-3.79981
H	2.41094	-4.42815	-2.54717
H	2.99762	-5.35790	-3.92845
H	7.51732	-0.45452	-1.16767
H	3.91500	4.06678	0.07240
C	2.53496	4.22109	1.90682
C	2.05484	5.47032	1.51773
C	3.64477	4.17856	2.76439
C	2.66747	6.65086	1.93440
H	1.19409	5.52782	0.85343
C	4.25865	5.33948	3.19251
H	4.02793	3.21418	3.09334
C	3.77785	6.58702	2.77501
H	2.27125	7.60386	1.59778
H	5.11575	5.31178	3.86083
C	7.72912	2.11246	-1.57736

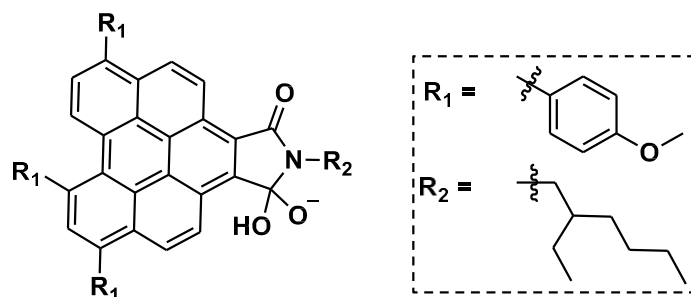
C	8.68301	2.98271	-1.04564
C	8.05735	1.42728	-2.75792
C	9.92795	3.16081	-1.64172
H	8.45345	3.52633	-0.13068
C	9.28807	1.59597	-3.36553
H	7.32330	0.76892	-3.21867
C	10.23596	2.46167	-2.80921
H	10.64396	3.83900	-1.18793
H	9.53909	1.07282	-4.28484
O	11.41154	2.55654	-3.47398
O	4.45202	7.66455	3.24238
O	-5.79579	2.01345	2.74093
C	12.39557	3.42681	-2.95206
H	12.70605	3.12472	-1.94325
H	13.25296	3.36291	-3.62363
H	12.03954	4.46491	-2.92141
C	4.00005	8.94479	2.84980
H	4.66520	9.66738	3.32489
H	4.04963	9.07274	1.76047
H	2.97093	9.12883	3.18519
C	-6.27792	2.58504	3.94057
H	-7.36642	2.52813	3.89490
H	-5.92560	2.03100	4.82046
H	-5.97634	3.63642	4.03500

(neutral [CPCM-water], -2476.563302, -2475.665779, -2475.808276, -2475.805258)

C	0.39199	-1.85775	0.96256
C	1.75621	-1.82136	0.56033
C	2.44825	-0.57955	0.48642
C	1.77177	0.62823	0.85842
C	0.40143	0.55934	1.25086
C	-0.25364	-0.70984	1.28648
C	3.81514	-0.54159	0.07387
C	2.48191	1.86556	0.88729
C	3.80347	1.92220	0.26177
C	4.47485	0.71689	-0.08473
C	4.42615	3.12479	-0.08574
C	1.85064	2.97079	1.49885
C	0.49368	2.88637	1.82510
C	-0.26489	1.73800	1.66206
H	0.01434	3.77388	2.23700
H	-0.10402	-2.82181	1.01939
H	-1.28746	-0.74941	1.61732
C	2.47945	-2.98365	0.24793
C	3.80572	-2.94591	-0.12261
C	4.51437	-1.74057	-0.23538
C	5.87590	-1.68436	-0.64855
C	6.48014	-0.48615	-0.84559
C	5.79221	0.75100	-0.63736
H	6.40294	-2.61858	-0.81694
C	5.68142	3.15433	-0.67323
H	6.11014	4.11383	-0.95557
C	6.39728	1.99267	-0.94538
C	2.03629	-4.40175	0.24944
C	4.25959	-4.33772	-0.37175
N	3.14895	-5.14898	-0.14201

O	5.35238	-4.75180	-0.70573
O	0.94944	-4.87389	0.51897
C	3.16899	-6.59382	-0.27502
H	4.07296	-6.96193	0.22619
H	2.29888	-6.96795	0.28018
C	-1.70837	1.78199	1.97758
C	-2.15985	2.35478	3.16825
C	-2.67230	1.31055	1.07230
C	-3.51536	2.45133	3.46772
H	-1.43389	2.72008	3.89254
C	-4.02321	1.40291	1.35247
H	-2.35282	0.88322	0.12354
C	-4.45593	1.97219	2.55526
H	-3.82242	2.89354	4.41039
H	-4.77072	1.04684	0.64801
C	3.12372	-7.10505	-1.71420
H	4.04756	-6.77343	-2.21968
C	3.12699	-8.63390	-1.66985
H	2.12520	-8.98090	-1.36241
H	3.81819	-8.97992	-0.88457
C	3.52024	-9.29512	-2.98137
H	2.86635	-8.94855	-3.79771
H	4.53790	-8.97363	-3.25691
C	3.47074	-10.81420	-2.91775
H	2.45235	-11.13072	-2.64580
H	4.12137	-11.16278	-2.10125
C	3.88488	-11.46736	-4.22516
H	3.84586	-12.56041	-4.16857
H	3.22882	-11.15256	-5.04657
H	4.90919	-11.18409	-4.49855
C	1.91510	-6.56309	-2.49139
H	1.06456	-6.46049	-1.79955
H	1.60350	-7.31442	-3.23028
C	2.16293	-5.25303	-3.22529
H	1.28325	-4.94700	-3.80182
H	2.40950	-4.42791	-2.54695
H	2.99971	-5.35650	-3.92755
H	7.51674	-0.45465	-1.16823
H	3.91484	4.06677	0.07276
C	2.53527	4.22077	1.90774
C	2.05538	5.47027	1.51916
C	3.64518	4.17764	2.76515
C	2.66835	6.65051	1.93614
H	1.19454	5.52829	0.85502
C	4.25940	5.33828	3.19361
H	4.02816	3.21307	3.09378
C	3.77885	6.58610	2.77659
H	2.27231	7.60371	1.59991
H	5.11657	5.31004	3.86182
C	7.72858	2.11246	-1.57792
C	8.68239	2.98307	-1.04657
C	8.05676	1.42702	-2.75835
C	9.92720	3.16127	-1.64286
H	8.45290	3.52697	-0.13176
C	9.28738	1.59583	-3.36619
H	7.32281	0.76843	-3.21891

C	10.23519	2.46186	-2.81024
H	10.64312	3.83975	-1.18937
H	9.53827	1.07245	-4.28542
O	11.41064	2.55683	-3.47517
O	4.45330	7.66329	3.24422
O	-5.79614	2.01446	2.74020
C	12.39459	3.42769	-2.95364
H	12.70530	3.12595	-1.94482
H	13.25185	3.36384	-3.62536
H	12.03816	4.46562	-2.92326
C	4.00162	8.94391	2.85197
H	4.66702	9.66615	3.32721
H	4.05117	9.07204	1.76270
H	2.97261	9.12807	3.18752
C	-6.27845	2.58667	3.93967
H	-7.36693	2.52982	3.89385
H	-5.92626	2.03292	4.81977
H	-5.97675	3.63802	4.03364

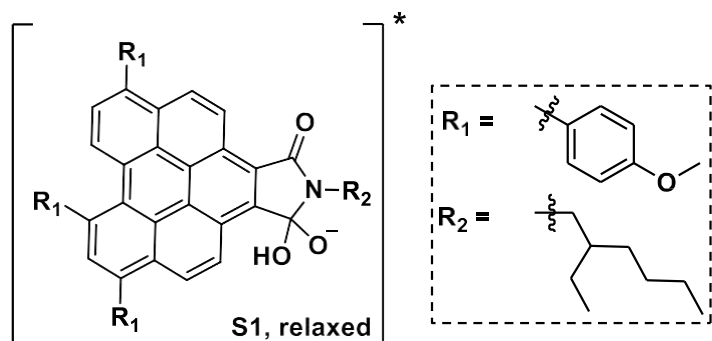


(anion, -2552.500312, -2551.587685, -2551.730744, -2551.727726)

C	0.27070	-1.77544	1.00539
C	1.63520	-1.77059	0.60023
C	2.34369	-0.54616	0.51217
C	1.69884	0.67743	0.88890
C	0.33334	0.63809	1.30381
C	-0.35222	-0.61631	1.33777
C	3.70568	-0.54447	0.07924
C	2.43783	1.89979	0.90143
C	3.75356	1.92202	0.25372
C	4.39107	0.69784	-0.09816
C	4.39844	3.10730	-0.10639
C	1.84199	3.02035	1.51682
C	0.48917	2.96536	1.87299
C	-0.29593	1.83370	1.72936
H	0.03698	3.86465	2.29078
H	-0.24068	-2.73434	1.02787
H	-1.38683	-0.63228	1.66927
C	2.31477	-2.96692	0.30651
C	3.62592	-2.96400	-0.08831
C	4.35761	-1.76401	-0.23275
C	5.71030	-1.73829	-0.67876
C	6.34635	-0.55708	-0.89236
C	5.70033	0.69917	-0.67036
H	6.20049	-2.69126	-0.85645
C	5.64945	3.10651	-0.70849
H	6.09851	4.05524	-0.99678

C	6.33207	1.92816	-0.98562
C	4.06270	-4.37105	-0.34213
N	2.98172	-5.14566	-0.13957
O	5.19333	-4.75078	-0.67410
O	0.65165	-4.62295	-0.28721
C	2.98670	-6.58056	-0.23051
H	3.75270	-7.00092	0.44184
H	2.00608	-6.91916	0.13652
C	-1.73159	1.91075	2.07786
C	-2.14301	2.48066	3.28402
C	-2.72788	1.47567	1.18970
C	-3.48922	2.61125	3.61404
H	-1.39151	2.81867	3.99557
C	-4.06982	1.60078	1.49994
H	-2.43985	1.04821	0.23095
C	-4.46146	2.16821	2.71734
H	-3.76389	3.05112	4.56788
H	-4.84165	1.27186	0.80845
C	3.21074	-7.10848	-1.64848
H	4.20513	-6.74944	-1.96224
C	3.25252	-8.63349	-1.62391
H	2.26054	-9.01410	-1.32194
H	3.95406	-8.96824	-0.84154
C	3.65420	-9.27242	-2.94366
H	2.94840	-8.97589	-3.73666
H	4.63671	-8.87934	-3.25510
C	3.71645	-10.79090	-2.87710
H	2.73519	-11.17821	-2.56261
H	4.42305	-11.08908	-2.08743
C	4.12190	-11.41973	-4.19917
H	4.16404	-12.51268	-4.13977
H	3.41185	-11.15632	-4.99343
H	5.11110	-11.06495	-4.51548
C	2.16174	-6.55396	-2.62850
H	1.54407	-5.80858	-2.10653
H	1.47691	-7.36217	-2.93069
C	2.78306	-5.91795	-3.86285
H	2.02589	-5.52948	-4.55407
H	3.43221	-5.08042	-3.57303
H	3.40635	-6.63216	-4.41752
H	7.37591	-0.55661	-1.23974
H	3.91183	4.06191	0.05592
C	2.55655	4.26152	1.90416
C	2.09751	5.51637	1.50807
C	3.67463	4.20774	2.75020
C	2.73709	6.68967	1.90592
H	1.22996	5.58371	0.85345
C	4.31672	5.36082	3.15875
H	4.04298	3.23922	3.08409
C	3.85565	6.61307	2.73395
H	2.35492	7.64676	1.56440
H	5.18118	5.32302	3.81720
C	7.66167	2.01623	-1.62887
C	8.64146	2.85995	-1.10157
C	7.96525	1.32937	-2.81507
C	9.88534	3.01311	-1.70769

H	8.43207	3.40409	-0.18205
C	9.19467	1.47238	-3.43258
H	7.21286	0.68879	-3.27121
C	10.16696	2.31344	-2.88103
H	10.62085	3.67229	-1.25682
H	9.42589	0.94741	-4.35618
O	11.33962	2.38487	-3.55633
O	4.55660	7.68311	3.18261
O	-5.79719	2.24443	2.93154
C	12.34603	3.23058	-3.03837
H	12.65812	2.91727	-2.03334
H	13.19681	3.15189	-3.71688
H	12.01316	4.27621	-2.99936
C	4.12425	8.96658	2.78078
H	4.80849	9.68227	3.23915
H	4.16245	9.08157	1.68940
H	3.10281	9.17449	3.12605
C	-6.23685	2.81453	4.14734
H	-7.32737	2.78773	4.12593
H	-5.88044	2.24144	5.01347
H	-5.90484	3.85634	4.24728
C	1.73229	-4.38192	0.36320
O	1.63006	-4.73510	1.76825
H	0.77114	-5.17810	1.77289

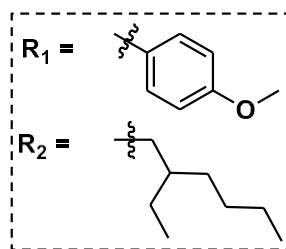
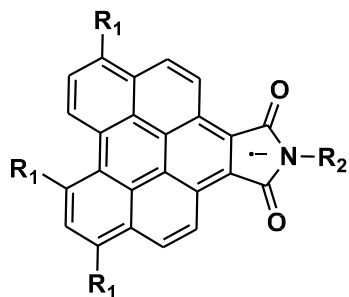


(anion; optimized S1 state, Total Energy, E(TD-HF/TD-DFT) = -2552.27748931)

C	0.34378	-1.73879	1.00231
C	1.67754	-1.73955	0.58979
C	2.38781	-0.50398	0.49236
C	1.75196	0.70860	0.88703
C	0.37215	0.68559	1.25868
C	-0.29373	-0.55257	1.31606
C	3.72740	-0.48405	0.00813
C	2.49596	1.92521	0.90559
C	3.75022	1.97208	0.23584
C	4.38700	0.76220	-0.18242
C	4.40272	3.20329	-0.09410
C	1.89326	3.07531	1.56871
C	0.52144	3.04574	1.80441
C	-0.27601	1.92681	1.60446
H	0.05416	3.93225	2.21993
H	-0.17769	-2.68740	1.03887
H	-1.32818	-0.57941	1.63403
C	2.37711	-2.94299	0.27300
C	3.66051	-2.92368	-0.15971

C	4.39011	-1.70516	-0.33279
C	5.70584	-1.65604	-0.80845
C	6.33285	-0.44729	-1.01975
C	5.68745	0.78921	-0.78101
H	6.21044	-2.59193	-1.01425
C	5.62448	3.21898	-0.71758
H	6.05519	4.17464	-0.99842
C	6.30765	2.04568	-1.07640
C	4.10474	-4.32767	-0.41546
N	3.04268	-5.11912	-0.18314
O	5.23072	-4.70073	-0.77128
O	0.70683	-4.61002	-0.27051
C	3.11220	-6.55927	-0.19753
H	3.98731	-6.88368	0.37949
H	2.22176	-6.92295	0.32428
C	-1.72902	2.02852	1.83036
C	-2.24525	2.74703	2.91504
C	-2.65776	1.46450	0.93574
C	-3.61219	2.90146	3.11573
H	-1.56347	3.18008	3.63957
C	-4.01855	1.61298	1.11923
H	-2.30045	0.92281	0.06680
C	-4.50975	2.33134	2.21410
H	-3.96154	3.45572	3.97741
H	-4.72685	1.18637	0.41739
C	3.18283	-7.17071	-1.60630
H	4.04922	-6.71038	-2.09844
C	3.45325	-8.67554	-1.47815
H	2.62019	-9.13799	-0.92933
H	4.34436	-8.82253	-0.85308
C	3.65571	-9.42580	-2.79260
H	2.74964	-9.35627	-3.40613
H	4.45491	-8.94252	-3.37046
C	4.00341	-10.89948	-2.59026
H	3.20898	-11.38002	-2.00554
H	4.91459	-10.97557	-1.98387
C	4.19855	-11.65344	-3.90215
H	4.44715	-12.70426	-3.72907
H	3.29062	-11.62214	-4.51305
H	5.00803	-11.21252	-4.49280
C	1.91712	-6.83873	-2.42124
H	1.40503	-5.99823	-1.93987
H	1.22405	-7.68958	-2.36918
C	2.18636	-6.48756	-3.88421
H	1.25568	-6.27153	-4.41841
H	2.82125	-5.59817	-3.95664
H	2.69499	-7.29445	-4.41921
H	7.35650	-0.44417	-1.37141
H	3.89135	4.13822	0.07656
C	2.66788	4.18436	2.12690
C	2.16268	5.49481	2.16273
C	3.93188	3.97021	2.72014
C	2.86224	6.53875	2.74785
H	1.21055	5.71259	1.69086
C	4.63050	4.99916	3.31975
H	4.34516	2.96883	2.74015

C	4.10691	6.29471	3.33655
H	2.43792	7.53440	2.73273
H	5.59171	4.82147	3.78962
C	7.58812	2.17422	-1.78842
C	8.53491	3.12050	-1.37357
C	7.89460	1.42801	-2.94317
C	9.73455	3.31212	-2.04790
H	8.33972	3.70906	-0.48310
C	9.07970	1.61179	-3.62735
H	7.17309	0.71583	-3.32731
C	10.01531	2.55215	-3.18304
H	10.43933	4.04549	-1.67746
H	9.30055	1.04330	-4.52420
O	11.15091	2.65390	-3.91797
O	4.87058	7.23911	3.93818
O	-5.86073	2.41705	2.31173
C	12.12626	3.60164	-3.51587
H	12.50655	3.38285	-2.51273
H	12.94086	3.52174	-4.23443
H	11.72549	4.62038	-3.53530
C	4.37760	8.56815	3.99414
H	5.13317	9.14900	4.52132
H	4.23642	8.98461	2.99156
H	3.43222	8.62062	4.54370
C	-6.40784	3.13916	3.40248
H	-7.48981	3.08695	3.28866
H	-6.12350	2.69242	4.36087
H	-6.09285	4.18767	3.38624
C	1.81823	-4.37146	0.34715
O	1.74103	-4.72807	1.75708
H	0.85642	-5.11916	1.78234



(anion radical, -2476.680773, -2475.785686, -2475.92776, -2475.924742)

C	0.39267	-1.86870	0.92608
C	1.75826	-1.84087	0.53280
C	2.43823	-0.59823	0.46036
C	1.76090	0.60542	0.82675
C	0.38843	0.54328	1.22672
C	-0.26333	-0.72159	1.25354
C	3.82466	-0.55649	0.05133
C	2.46901	1.85044	0.85271
C	3.78960	1.91083	0.21197
C	4.47257	0.70139	-0.11797
C	4.39304	3.11249	-0.15354
C	1.84690	2.95107	1.46975
C	0.48711	2.87113	1.81421



C	-0.26979	1.72662	1.65464
H	0.01351	3.76072	2.22883
H	-0.09702	-2.83804	0.97615
H	-1.29865	-0.76778	1.58129
C	2.47147	-3.02540	0.23502
C	3.84049	-2.98333	-0.12786
C	4.52479	-1.75356	-0.23993
C	5.88770	-1.68133	-0.64334
C	6.49246	-0.47994	-0.85131
C	5.79786	0.75040	-0.65934
H	6.41512	-2.61852	-0.80334
C	5.65834	3.15562	-0.73302
H	6.07537	4.11746	-1.02626
C	6.38889	2.00188	-0.97721
C	2.04003	-4.40154	0.25070
C	4.30083	-4.33261	-0.34989
N	3.17963	-5.14528	-0.11288
O	5.41183	-4.78402	-0.67326
O	0.93953	-4.91750	0.50792
C	3.20237	-6.58050	-0.24490
H	4.11351	-6.95714	0.24032
H	2.33608	-6.96238	0.31328
C	-1.71077	1.76989	1.98683
C	-2.14944	2.32944	3.18840
C	-2.68771	1.31170	1.08866
C	-3.50201	2.42979	3.50344
H	-1.41361	2.68409	3.90818
C	-4.03573	1.40620	1.38383
H	-2.37927	0.88995	0.13377
C	-4.45394	1.96495	2.59634
H	-3.79710	2.86324	4.45415
H	-4.79208	1.05946	0.68390
C	3.14336	-7.09788	-1.68318
H	4.06932	-6.77576	-2.19152
C	3.12505	-8.62577	-1.64750
H	2.12084	-8.96116	-1.33349
H	3.81721	-8.98536	-0.86848
C	3.49731	-9.28769	-2.96475
H	2.84383	-8.92361	-3.77412
H	4.51841	-8.98203	-3.24634
C	3.42223	-10.80609	-2.91206
H	2.40038	-11.10715	-2.63512
H	4.07210	-11.17183	-2.10235
C	3.81599	-11.45783	-4.22656
H	3.75818	-12.55052	-4.17766
H	3.16023	-11.12562	-5.04141
H	4.84327	-11.19060	-4.50515
C	1.93882	-6.53265	-2.45051
H	1.11021	-6.38492	-1.74097
H	1.58723	-7.28204	-3.17454
C	2.22222	-5.23808	-3.19836
H	1.34016	-4.89023	-3.74820
H	2.53099	-4.43325	-2.52120
H	3.03054	-5.38204	-3.92728
H	7.53000	-0.44921	-1.17339
H	3.86649	4.04911	-0.00920

C	2.53420	4.20232	1.87461
C	2.04591	5.45370	1.50251
C	3.65398	4.16154	2.71951
C	2.65665	6.63497	1.92262
H	1.17645	5.51286	0.84953
C	4.26833	5.32190	3.14971
H	4.04555	3.19618	3.03561
C	3.77679	6.57044	2.74912
H	2.25086	7.58868	1.59915
H	5.13362	5.29254	3.80765
C	7.72697	2.12905	-1.59676
C	8.66744	3.01462	-1.06664
C	8.07684	1.43526	-2.76618
C	9.91637	3.20223	-1.65339
H	8.42203	3.56556	-0.16012
C	9.31166	1.61123	-3.36425
H	7.35592	0.76075	-3.22418
C	10.24400	2.49427	-2.80951
H	10.61969	3.89420	-1.20024
H	9.57790	1.07978	-4.27470
O	11.42650	2.59524	-3.46491
O	4.45162	7.64915	3.21901
O	-5.79398	2.01096	2.79575
C	12.39394	3.48190	-2.94190
H	12.69739	3.19466	-1.92640
H	13.25972	3.42180	-3.60322
H	12.02600	4.51638	-2.92520
C	3.98717	8.92846	2.84179
H	4.65279	9.65257	3.31429
H	4.02247	9.06571	1.75280
H	2.96055	9.10396	3.18995
C	-6.25915	2.57235	4.00580
H	-7.34858	2.52208	3.97263
H	-5.90003	2.00801	4.87663
H	-5.95080	3.62121	4.10853

(anion radical [CPCM-water], -2476.682467, -2475.787391, -2475.929461, -2475.926442)

C	0.39283	-1.86877	0.92667
C	1.75838	-1.84093	0.53327
C	2.43831	-0.59830	0.46074
C	1.76095	0.60543	0.82719
C	0.38849	0.54328	1.22704
C	-0.26321	-0.72164	1.25402
C	3.82472	-0.55647	0.05153
C	2.46908	1.85041	0.85331
C	3.78966	1.91090	0.21255
C	4.47258	0.70156	-0.11776
C	4.39317	3.11260	-0.15276
C	1.84691	2.95095	1.47052
C	0.48705	2.87101	1.81462
C	-0.26996	1.72659	1.65479
H	0.01344	3.76061	2.22919
H	-0.09695	-2.83804	0.97692
H	-1.29854	-0.76779	1.58170
C	2.47167	-3.02552	0.23539
C	3.84061	-2.98339	-0.12768

C	4.52489	-1.75345	-0.23988
C	5.88767	-1.68107	-0.64361
C	6.49231	-0.47962	-0.85172
C	5.79770	0.75065	-0.65948
H	6.41527	-2.61812	-0.80381
C	5.65829	3.15580	-0.73260
H	6.07525	4.11775	-1.02557
C	6.38882	2.00216	-0.97734
C	2.04040	-4.40167	0.25116
C	4.30087	-4.33260	-0.34973
N	3.17987	-5.14541	-0.11252
O	5.41205	-4.78396	-0.67322
O	0.93985	-4.91768	0.50878
C	3.20252	-6.58071	-0.24495
H	4.11343	-6.95762	0.24046
H	2.33619	-6.96268	0.31308
C	-1.71102	1.76978	1.98661
C	-2.15004	2.32996	3.18781
C	-2.68765	1.31099	1.08840
C	-3.50266	2.43018	3.50250
H	-1.41455	2.68525	3.90761
C	-4.03575	1.40540	1.38323
H	-2.37907	0.88900	0.13365
C	-4.45437	1.96467	2.59541
H	-3.79806	2.86413	4.45288
H	-4.79184	1.05828	0.68319
C	3.14357	-7.09803	-1.68326
H	4.06965	-6.77623	-2.19160
C	3.12487	-8.62594	-1.64749
H	2.12050	-8.96101	-1.33368
H	3.81674	-8.98566	-0.86830
C	3.49724	-9.28806	-2.96462
H	2.84397	-8.92401	-3.77416
H	4.51847	-8.98267	-3.24605
C	3.42184	-10.80644	-2.91168
H	2.39987	-11.10723	-2.63490
H	4.07150	-11.17217	-2.10180
C	3.81569	-11.45841	-4.22602
H	3.75763	-12.55106	-4.17692
H	3.16012	-11.12622	-5.04103
H	4.84309	-11.19148	-4.50446
C	1.93935	-6.53258	-2.45088
H	1.11031	-6.38552	-1.74171
H	1.58834	-7.28164	-3.17547
C	2.22274	-5.23757	-3.19800
H	1.34089	-4.88982	-3.74825
H	2.53091	-4.43289	-2.52035
H	3.03142	-5.38102	-3.92661
H	7.52974	-0.44879	-1.17412
H	3.86680	4.04924	-0.00794
C	2.53430	4.20205	1.87562
C	2.04638	5.45356	1.50336
C	3.65394	4.16089	2.72068
C	2.65748	6.63462	1.92339
H	1.17698	5.51306	0.85033
C	4.26861	5.32109	3.15088

H	4.04515	3.19548	3.03706
C	3.77755	6.56982	2.75006
H	2.25204	7.58843	1.59982
H	5.13373	5.29146	3.80903
C	7.72677	2.12936	-1.59713
C	8.66722	3.01516	-1.06724
C	8.07649	1.43548	-2.76654
C	9.91603	3.20278	-1.65415
H	8.42197	3.56630	-0.16080
C	9.31121	1.61152	-3.36482
H	7.35558	0.76097	-3.22459
C	10.24361	2.49471	-2.81029
H	10.61932	3.89492	-1.20123
H	9.57725	1.08006	-4.27533
O	11.42584	2.59571	-3.46577
O	4.45262	7.64818	3.21983
O	-5.79427	2.01049	2.79450
C	12.39339	3.48300	-2.94331
H	12.69722	3.19604	-1.92790
H	13.25886	3.42288	-3.60497
H	12.02502	4.51727	-2.92690
C	3.98862	8.92794	2.84260
H	4.65452	9.65165	3.31523
H	4.02414	9.06511	1.75366
H	2.96210	9.10367	3.19079
C	-6.26008	2.57296	4.00411
H	-7.34945	2.52249	3.97047
H	-5.90121	2.00932	4.87543
H	-5.95187	3.62189	4.10590

## 8. X-Ray Diffraction Experiments

The single-crystal X-ray diffraction data for compound 8 is deposited at the Cambridge Crystallographic Data Center under CCDC 1912318 and is contained in the .CIF file attached to this manuscript.

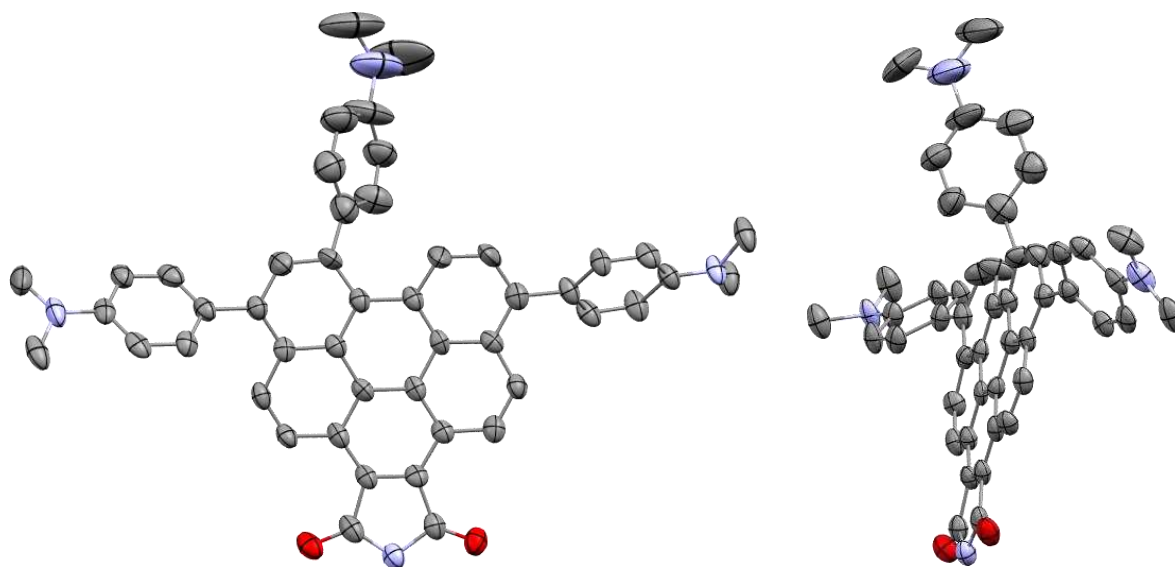


Fig. S5.119. Molecular structure of Compound 8 derived by single crystal X-ray diffraction. Two different orientations are shown: top (left) and side (right). Hydrogen atoms and alkyl tail have been omitted for clarity. ORTEP plots with anisotropic displacement parameters set at 50% probability. Atoms are represented as the following colors: carbon: gray, nitrogen: blue, oxygen: red.

### 9. References — EXPERIMENTAL 3

- (1) Lim, C.-H.; Kudisch, M.; Liu, B.; Miyake, G. M. *J. Am. Chem. Soc.* 2018, *140*, 7667.
- (2) Manning, S. J.; Bogen, W.; Kelly, L. A. *J. Org. Chem.* 2011, *76*, 6007.
- (3) Peters, B. K.; Rodriguez, K. X.; Reisberg, S. H.; Beil, S. B.; Hickey, D. P.; Kawamata, Y.; Collins, M.; Starr, J.; Chen, L.; Udyavara, S.; Klunder, K.; Gorey, T. J.; Anderson, S. L.; Neurock, M.; Minter, S. D.; Baran, P. S. *Science* 2019, *363*, 838.
- (4) Dörfler, J.; Bytyqi, B.; Hüller, S.; Mann, N. M.; Brahms, C.; Schmidtman, M.; Doye, S. *Adv. Synth. Catal.* 2015, *357*, 2265.
- (5) Kurouchi, H.; Kawamoto, K.; Sugimoto, H.; Nakamura, S.; Otani, Y.; Ohwada, T. *J. Org. Chem.* 2012, *77*, 9313.
- (6) Reisman, S. E.; Doyle, A. G.; Jacobsen, E. N. *J. Am. Chem. Soc.* 2008, *130*, 7198.
- (7) Peterson, S. L.; Stucka, S. M.; Dinsmore, C. J. *Org. Lett.* 2010, *12*, 1340.

- (8) Chen, G.; Fu, C.; Ma, S. *Tetrahedron* 2006, 62, 4444.
- (9) Cafiero, L. R.; Snowden, T. S. *Org. Lett.* 2008, 10, 3853.
- (10) supramolecular.org. <http://supramolecular.org> (accessed 2019).
- (11) Thordarson, P. *Chem. Soc. Rev.* 2011, 40, 1305.
- (12) Connelly, N. G.; Geiger, W. E. *Chem. Rev.* 1996, 96, 877.
- (13) Frisch, M. J.; Trucks, G. W.; Schlegel, H. B.; Scuseria, G. E.; Robb, M. A.; Cheeseman, J. R.; Scalmani, G.; Barone, V.; Petersson, G. A.; Nakatsuji, H.; Li, X.; Caricato, M.; Marenich, A. V.; Bloino, J.; Janesko, B. G.; Gomperts, R.; Mennucci, B.; Hratchian, H. P.; Ortiz, J. V.; Izmaylov, A. F.; Sonnenberg, J. L.; Williams; Ding, F.; Lipparini, F.; Egidi, F.; Goings, J.; Peng, B.; Petrone, A.; Henderson, T.; Ranasinghe, D.; Zakrzewski, V. G.; Gao, J.; Rega, N.; Zheng, G.; Liang, W.; Hada, M.; Ehara, M.; Toyota, K.; Fukuda, R.; Hasegawa, J.; Ishida, M.; Nakajima, T.; Honda, Y.; Kitao, O.; Nakai, H.; Vreven, T.; Throssell, K.; Montgomery Jr., J. A.; Peralta, J. E.; Ogliaro, F.; Bearpark, M. J.; Heyd, J. J.; Brothers, E. N.; Kudin, K. N.; Staroverov, V. N.; Keith, T. A.; Kobayashi, R.; Normand, J.; Raghavachari, K.; Rendell, A. P.; Burant, J. C.; Iyengar, S. S.; Tomasi, J.; Cossi, M.; Millam, J. M.; Klene, M.; Adamo, C.; Cammi, R.; Ochterski, J. W.; Martin, R. L.; Morokuma, K.; Farkas, O.; Foresman, J.B.; Fox, D. J.: Gaussian 16 Rev. C.01. Wallingford, CT, 2016.
- (14) Zhao, Y.; Truhlar, D. *Theor. Chem. Acc.* 2008, 120, 215.
- (15) He, H.; Zapol, P.; Curtiss, L. A. *J. Phys. Chem. C* 2010, 114, 21474.
- (16) Tossell, J. A. *Comput. Theor. Chem.* 2011, 977, 123.
- (17) Yanai, T.; Tew, D. P.; Handy, N. C. *Chem. Phys. Lett.* 2004, 393, 51.
- (18) Goez, M.; Kerzig, C.; Naumann, R. *Angew. Chem. Int. Ed.* 2014, 53, 9914.
- (19) Mortensen, J.; Heinze, J. *Angew. Chem. Int. Ed.* 1984, 23, 84.

## REFERENCES

- (1) Narayanam, J. M. R.; Stephenson, C. R. J. *Chem. Soc. Rev.* 2011, *40*, 102.
- (2) Prier, C. K.; Rankic, D. A.; MacMillan, D. W. C. *Chem. Rev.* 2013, *113*, 5322.
- (3) Schultz, D. M.; Yoon, T. P. *Science* 2014, *343*, 6174.
- (4) Romero, N. A.; Nicewicz, D. A. *Chem. Rev.* 2016, *116*, 10075.
- (5) Mortensen, J.; Heinze, J. *Angew. Chem., Int. Ed.* 1984, *23*, 84.
- (6) Ishikawa, H.; Noyes, W. A. *J. Am. Chem. Soc.* 1962, *84*, 1502.
- (7) Birch, A. J. *J. Chem. Soc.* 1944, 430.
- (8) Birch, A. J. *Pure Appl. Chem.* 1996, *68*, 553.
- (9) Lei, P.; Ding, Y.; Zhang, X.; Adijiang, A.; Li, H.; Ling, Y.; An, J. *Org. Lett.* 2018, *20*, 3439.
- (10) Birch, A. J. *Nature* 1946, *158*, 60.
- (11) Peters, B. K.; Rodriguez, K. X.; Reisberg, S. H.; Beil, S. B.; Hickey, D. P.; Kawamata, Y.; Collins, M.; Starr, J.; Chen, L.; Udyavara, S.; Klunder, K.; Gorey, T. J.; Anderson, S. L.; Neurock, M.; Minter, S. D.; Baran, P. S. *Science* 2019, *363*, 838.
- (12) Yasuda, M.; Pac, C.; Sakurai, H. *J. Org. Chem.* 1981, *46*, 788.
- (13) Glaser, F.; Kerzig, C.; Wenger, O. S. *Angew. Chem., Int. Ed.* 2020, *59*, 10266.
- (14) Kerzig, C.; Guo, X.; Wenger, O. S. *J. Am. Chem. Soc.* 2019, *141*, 2122.
- (15) Chatterjee, A.; König, B. *Angew. Chem., Int. Ed.* 2019, *58*, 14289.
- (16) Ghosh, I.; Ghosh, T.; Bardagi, J. I.; König, B. *Science* 2014, *346*, 725.
- (17) Zeman, C. J.; Kim, S.; Zhang, F.; Schanze, K. S. *J. Am. Chem. Soc.* 2020, *142*, 2204.
- (18) MacKenzie, I. A.; Wang, L.; Onuska, N. P. R.; Williams, O. F.; Begam, K.; Moran, A. M.; Dunitz, B. D.; Nicewicz, D. A. *Nature* 2020, *580*, 76.

- (19) Cowper, N. G. W.; Chernowsky, C. P.; Williams, O. P.; Wickens, Z. K. *J. Am. Chem. Soc.* 2020, *142*, 2093.
- (20) Kim, H.; Kim, H.; Lambert, T. H.; Lin, S. *J. Am. Chem. Soc.* 2020, *142*, 2087.
- (21) Theriot, J. C.; Lim, C.-H.; Yang, H.; Ryan, M. D.; Musgrave, C. B.; Miyake, G. M. *Science* 2016, *352*, 1082.
- (22) Pearson, R. M.; Lim, C.-H.; McCarthy, B. G.; Musgrave, C. B.; Miyake, G. M. *J. Am. Chem. Soc.* 2016, *138*, 11399.
- (23) Buss, B. L.; Lim, C.-L.; Miyake, G. M. *Angew. Chem., Int. Ed.* 2020, *59*, 3209.
- (24) Manning, S. J.; Bogen, W.; Kelly, L. A. *J. Org. Chem.* 2011, *76*, 6007.
- (25) Gerber, L. C. H.; Frischmann, P. D.; Fan, F. Y.; Doris, S. E.; Qu, X.; Scheuermann, A. M.; Persson, K.; Chiang, Y.-M.; Helms, B. A. *Nano Lett.* 2016, *16*, 549.
- (26) Gosztola, D.; Niemczyk, M. P.; Svec, W.; Lukas, A. S.; Wasielewski, M. R. *J. Phys. Chem. A* 2000, *104*, 6545.
- (27) Guha, S.; Goodson, F. S.; Corson, L. J.; Saha, S. *J. Am. Chem. Soc.* 2012, *134*, 13679.
- (28) Roth, H. G.; Romero, N. A.; Nicewicz, D. A. *Synlett* 2016, *27*, 714.
- (29) Yoshimi, Y.; Ishise, A.; Oda, H.; Moriguchi, Y.; Kanezaki, H.; Nakaya, Y.; Katsuno, K.; Itou, T.; Inagaki, S.; Morita, T.; Hatanaka, M. *Tetrahedron Lett.* 2008, *49*, 3400.
- (30) Hayyan, M.; Hashim, M. A.; AlNashef, I. M. *Chem. Rev.* 2016, *116*, 3029.
- (31) Almena, J.; Foubelo, F.; Yus, M. *Tetrahedron* 1995, *51*, 3365.
- (32) Thordarson, P. *Chem. Soc. Rev.* 2011, *40*, 1305.
- (33) Dawson, R. E.; Hennig, A.; Weimann, D. P.; Emery, D.; Ravikumar, V.; Montenegro, J.; Takeuchi, T.; Gabutti, S.; Mayor, M.; Mareda, J.; Schalley, C. A.; Matile, S. *Nat. Chem.* 2010, *2*, 533.



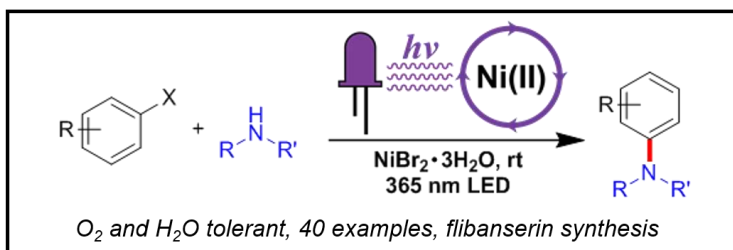
- (34) Saha, S. *Acc. Chem. Res.* 2018, *51*, 2225.
- (35) Goodson, F. S.; Panda, D. K.; Ray, S.; Mitra, A.; Guha, S.; Saha, S. *Org. Biomol. Chem.* 2013, *11*, 4797.
- (36) Buxton, G. V.; Greenstock, C. L.; Helman, W. P.; Ross, A. B. *J. Phys. Chem. Ref. Data* 1988, *17*, 513.
- (37) Asmus, K. D.; Moeckel, H.; Henglein, A. *J. Phys. Chem.* 1973, *77*, 1218.
- (38) Stoll, S.; Schweiger, A. *J. Magn. Reson.* 2006, *178*, 42.
- (39) Kenney-Wallace, G. A.; Jonah, C. D. *J. Phys. Chem.* 1982, *86*, 2572.
- (40) Jou, F. Y.; Dorfman, L. M. *J. Chem. Phys.* 1973, *58*, 4715.
- (41) Thurnauer, M. C.; Meisel, D. *Chem. Phys. Lett.* 1982, *92*, 343.
- (42) Okamura, T.; Sancar, A.; Heelis, P. F.; Hirata, Y.; Mataga, N. *J. Am. Chem. Soc.* 1989, *111*, 5967.
- (43) Demchenko, A. P.; Tomin, V. I.; Chou, P.-T. *Chem. Rev.* 2017, *117*, 13353.

## CHAPTER 6 | SUMMARY AND CONCLUSIONS

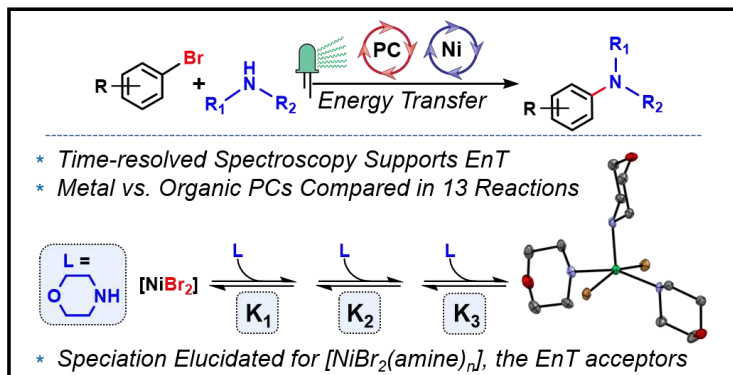
In Part 1 of this thesis, two discoveries were made in the area of light-driven Ni catalysis which have advanced the field. Firstly, a new reaction for C–N bond formation was discovered which avoided use of a precious metal Ir PC through the direct photoexcitation of Ni-amine complexes under UV light (Fig. 6.1a).<sup>1</sup> This reaction was found to exhibit a broad scope with 40 examples demonstrated, including synthesis of the medicine flibanserin and several new flibanserin derivatives. Mechanistically, DFT calculations and spectroscopic experiments were consistent with a reaction cycle involving a Ni-centered excited state that facilitates intramolecular

### Summary of Work Included in this Thesis

#### (a) Chapter 2: C–N Coupling via Photoexcitation of Ni-amine Complexes



#### (b) Chapter 3: Energy Transfer to Ni-amine Complexes in C–N Coupling



#### (c) Chapter 5: Organocatalyzed Birch Reduction Driven by Visible Light

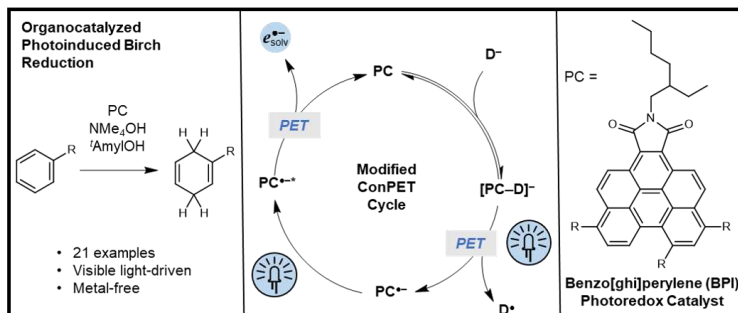


*Fig. 6.1. Summary of the 3 main thesis chapters of this work. (a) C–N coupling via the photoexcitation of Ni-amine complexes. (b) Energy transfer to Ni-amine complexes in light-driven, Ni-catalyzed C–N coupling reactions. (c) Organocatalyzed Birch reduction driven by visible light.*

electron transfer to produce an amino radical and Ni(I) complex, from which several pathways to product formation are possible. Notably, several other reaction manifolds have been published in which photoexcitation of a Ni complex leads to comparable reactivity to achieve C–C or C–O bond formation.<sup>2-4</sup>

Given this broader importance of Ni-centered excited states in cross coupling reactions, it is not surprising that several mechanistic studies have now emerged that are focused on photophysical characterization of these types of states for potentially representative Ni complexes.<sup>5-6</sup> Further, direct evidence has now been obtained for photoexcitation-induced reductive elimination from Ni(II) complexes.<sup>7</sup> Importantly, any bond forming event initiated by photoexcitation of a Ni complex can be viewed as an opportunity to effect the same chemistry through an energy transfer pathway if a suitable PC is added into the system. The work described in Chapter 3 involves the discovery of an energy transfer pathway of this type to achieve C–N coupling (Fig. 6.1b),<sup>8</sup> but the same logic could be extended to other systems to develop new energy transfer reactions.

In addition, the Ni-amine complexes that were identified and characterized in this work may form in many other systems involving Ni(II) and amines, and therefore this knowledge will be broadly useful. In addition, their discovery suggests that speciation should be studied in any reaction in which a component could bind to the Ni catalyst (especially if it is used in stoichiometric quantities). Further, the binding study was the first to elucidate stepwise equilibrium constants for a 1:3 transition metal:ligand system through the method developed in this work. This modeling method could be extended to other 1:3 systems which may have previously been too

difficult to deconvolute. Finally, the spectroscopic support and computational framework developed for a Förster type energy transfer pathway could potentially be used as a new way to predict reactivity in dual PC/Ni catalyzed systems which proceed via energy transfer.

This mechanistic study further fits into a rapidly growing sub-field of detailed mechanistic studies in light-driven Ni catalysis. In addition to this work, detailed studies have now been published on three C—O coupling systems,<sup>7, 9-10</sup> two additional C—N systems,<sup>11-12</sup> and a C—S coupling system.<sup>13</sup> Very recently, pulse radiolysis has been utilized to study oxidative addition at Ni(I) complexes with bipyridine or terpyridine type ligands.<sup>14</sup> The differences between these systems suggest that catalysis involving Ni(0) or Ni(II) precatalysts involves nuanced interplay between multiple oxidation states Ni(0/I/II/III), and further detailed studies of key mechanistic steps will no doubt provide further insights relevant to reaction optimization. Some areas for future inquiry include studying reductive elimination and transmetallation steps involving Ni(III), as well as extending oxidative addition studies at Ni(I) to aryl bromides/chlorides/pseudohalides.

In Part 2, a photoinduced, organocatalytic method for Birch reduction of aromatic substrates was developed (Fig. 6.1c).<sup>15</sup> Notably, arenes commonly considered “inert” such as benzene could be coupled under this method with 21 examples demonstrated, including late stage dechlorination of a medicinal compound. To date, many other strategies have been found to generate highly reducing excited states or solvated electrons,<sup>16-22</sup> but none of these aside from this work have reported dearomatization. Given the utility of this transformation, the development of this reaction could have a profound effect on organic chemistry if its shortcomings can be overcome. Specifically, the long reaction times (4-6 days), requirement to add PC in multiple additions (implying catalyst decomposition), and poor performance with amines or electron rich heterocycles present barriers to the practicality of this reaction. In addition, mechanistic questions

remain, focusing on the detection of solvated electrons, the fate of the  $\text{OH}\cdot$ , and the mode of decomposition of the PC. Future mechanistic work focuses on gaining experimental evidence to elucidate these areas of interest, as well as applying these insights in the development of improved Birch PCs.

## REFERENCES

- (1) Lim, C.-H.; Kudisch, M.; Liu, B.; Miyake, G. M., *J. Am. Chem. Soc.* 2018, *140*, 7667.
- (2) Ishida, N.; Masuda, Y.; Ishikawa, N.; Murakami, M. *Asian J. Org. Chem.* 2017, *6*, 669.
- (3) Yang, L.; Lu, H.-H.; Lai, C.-H.; Li, G.; Zhang, W.; Cao, R.; Liu, F.; Wang, C.; Xiao, J.; Xue, D., *Angew. Chem. Int. Ed.* 2020, *59*, 12714.
- (4) Welin, E. R.; Le, C.; Arias-Rotondo, D. M.; McCusker, J. K.; MacMillan, D. W. C. *Science* 2017, *355*, 380.
- (5) Shields, B. J.; Kudisch, B.; Scholes, G. D.; Doyle, A. G. *J. Am. Chem. Soc.* 2018, *140*, 3035.
- (6) Ting, S. I.; Garakyaraghi, S.; Taliaferro, C. M.; Shields, B. J.; Scholes, G. D.; Castellano, F. N.; Doyle, A. G., *J. Am. Chem. Soc.* 2020, *142*, 5800.
- (7) Tian, L.; Till, N. A.; Kudisch, B.; MacMillan, D. W. C.; Scholes, G. D., *J. Am. Chem. Soc.* 2020, *142*, 4555.
- (8) Kudisch, M.; Lim, C.-H.; Thordarson, P.; Miyake, G. M. *J. Am. Chem. Soc.* 2019, *141*, 19479.
- (9) Sun, R.; Qin, Y.; Ruccolo, S.; Schnedermann, C.; Costentin, C.; Nocera, D. G., *J. Am. Chem. Soc.* 2019, *141*, 89.
- (10) Malik, J. A.; Madani, A.; Pieber, B.; Seeberger, P. H., *J. Am. Chem. Soc.* 2020, *142*, 11042.
- (11) Gisbertz, S.; Reischauer, S.; Pieber, B., *Nat. Catal.* 2020, *3*, 611.
- (12) Till, N. A.; Tian, L.; Dong, Z.; Scholes, G. D.; MacMillan, D. W. C., *J. Am. Chem. Soc.* 2020, *142*, 15830.
- (13) Qin, Y.; Sun, R.; Gianoulis, N. P.; Nocera, D. G., *J. Am. Chem. Soc.* 2021, *143*, 2005.
- (14) Till, N. A.; Oh, S.; MacMillan, D. W. C.; Bird, M. J., *J. Am. Chem. Soc.* 2021. *Just Accepted*.
- (15) Cole, J. P.; Chen, D.-F.; Kudisch, M.; Pearson, R. M.; Lim, C.-H.; Miyake, G. M., *J. Am. Chem. Soc.* 2020, *142*, 13573.

- (16) MacKenzie, I. A.; Wang, L.; Onuska, N. P. R.; Williams, O. F.; Begam, K.; Moran, A. M.; Dunietz, B. D.; Nicewicz, D. A. *Nature* 2020, 580, 76.
- (17) Kerzig, C.; Guo, X.; Wenger, O. S. *J. Am. Chem. Soc.* 2019, 141, 2122.
- (18) Glaser, F.; Kerzig, C.; Wenger, O. S., *Angew. Chem. Int. Ed.* 2020, 59, 10266.
- (19) Cowper, N. G. W.; Chernowsky, C. P.; Williams, O. P.; Wickens, Z. K. *J. Am. Chem. Soc.* 2020, 142, 2093.
- (20) Kim, H.; Kim, H.; Lambert, T. H.; Lin, S. *J. Am. Chem. Soc.* 2020, 142, 2087.
- (21) Graml, A.; Neveselý, T.; Jan Kutta, R.; Cibulka, R.; König, B., *Nat. Commun.* 2020, 11, 3174.
- (22) Glaser, F.; Larsen, C. B.; Kerzig, C.; Wenger, O. S., *Photochem. Photobiol. Sci.* 2020, 19, 1035.